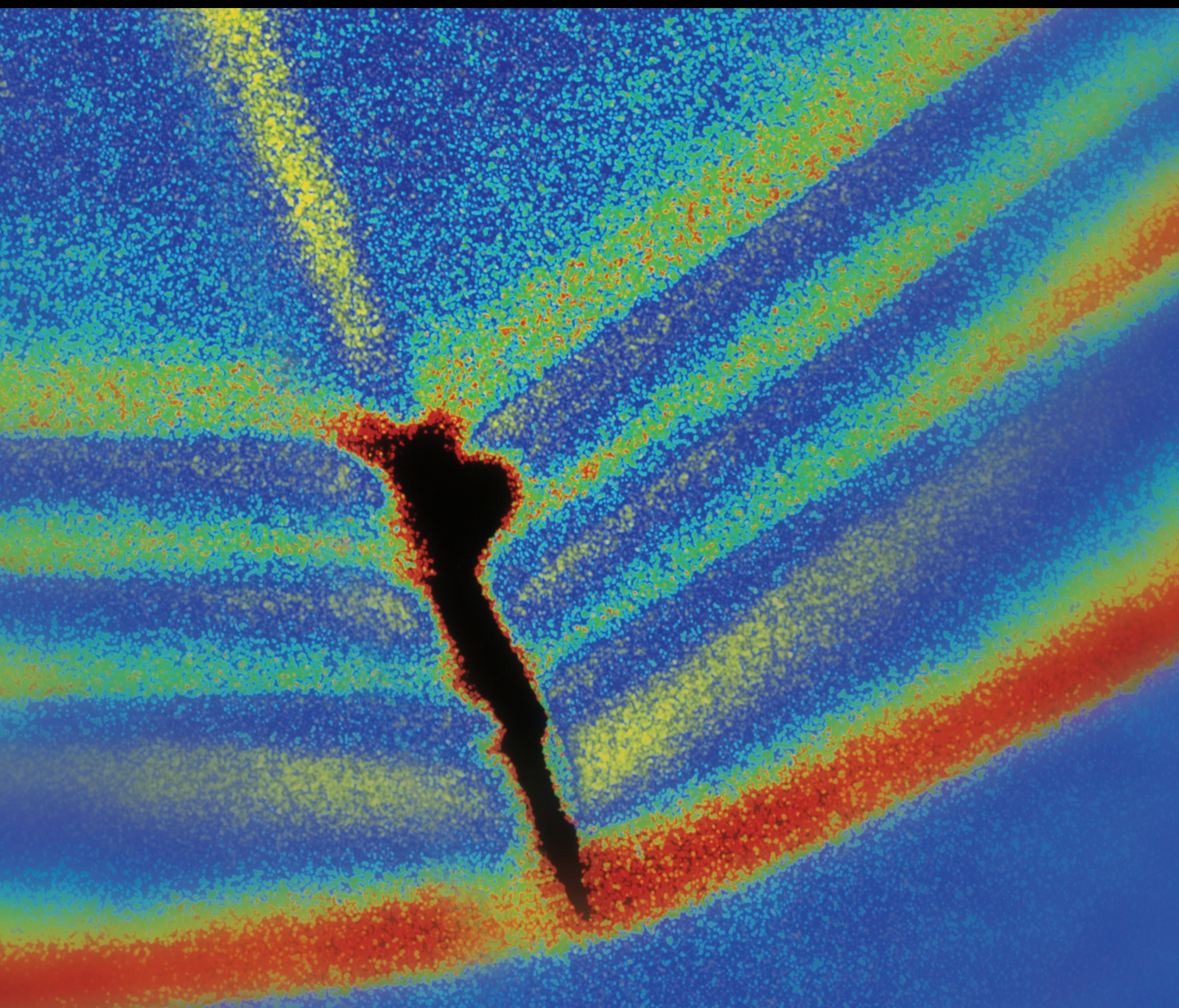


Resilient Civil Infrastructure under Dynamic Loadings

Lead Guest Editor: Xing Ma

Guest Editors: Nawawi Chouw, Mohamed ElGawady, and Songye Zhu





Resilient Civil Infrastructure under Dynamic Loadings

Shock and Vibration

Resilient Civil Infrastructure under Dynamic Loadings

Lead Guest Editor: Xing Ma

Guest Editors: Nawawi Chouw, Mohamed ElGawady,
and Songye Zhu



Copyright © 2018 Hindawi. All rights reserved.

This is a special issue published in "Shock and Vibration." All articles are open access articles distributed under the Creative Commons Attribution License, which permits unrestricted use, distribution, and reproduction in any medium, provided the original work is properly cited.

Editorial Board

- Brij N. Agrawal, USA
Felix Albu, Romania
Marco Alfano, Italy
Sumeet S. Aphale, UK
Hassan Askari, Canada
Lutz Auersch, Germany
Matteo Aureli, USA
Mahmoud Bayat, Iran
Marco Belloli, Italy
Giosuè Boscato, Italy
Francesco Braghin, Italy
Rafał Burdzik, Poland
Salvatore Caddemi, Italy
Ivo Caliò, Italy
Antonio Carcaterra, Italy
Dumitru I. Caruntu, USA
Cristina Castejón, Spain
Nicola Caterino, Italy
Gabriele Cazzulani, Italy
Noel Challamel, France
Athanasios Chasalevris, UK
Xavier Chimentin, France
Nawawi Chouw, New Zealand
Simone Cinquemani, Italy
Pedro A. Costa, Portugal
Alvaro Cunha, Portugal
Giorgio Dalpiaz, Italy
Farhang Daneshmand, Canada
Sergio De Rosa, Italy
Silvio L.T. de Souza, Brazil
Dario Di Maio, UK
Luigi Di Sarno, Italy
Longjun Dong, China
Lorenzo Dozio, Italy
Mohamed El Badaoui, France
Mohammad Elahinia, USA
Fiorenzo A. Fazzolari, UK
Matteo Filippi, Italy
Piotr Folegą, Poland
Paola Forte, Italy
Francesco Franco, Italy
Juan C. G. Prada, Spain
Pedro Galvín, Spain
Gianluca Gatti, Italy
Marco Gherlone, Italy
- Anindya Ghoshal, USA
Nere Gil-Negrete, Spain
Adam Glowacz, Poland
Itzhak Green, USA
Hassan Haddadpour, Iran
M.I. Herreros, Spain
Hamid Hosseini, Japan
Reza Jazar, Australia
Sakdirat Kaewunruen, UK
Yuri S. Karinski, Israel
Jeong-Hoi Koo, USA
Georges Kouroussis, Belgium
Mickaël Lallart, France
Luca Landi, Italy
Marco Lepidi, Italy
Zhixiong Li, China
Manuel Lopez Aenlle, Spain
Nuno M. Maia, Portugal
Stefano Manzoni, Italy
Giuseppe Carlo Marano, Italy
Stefano Marchesiello, Italy
Francesco S. Marulo, Italy
Jean-Mathieu Mencik, France
Laurent Mevel, France
Fabio Minghini, Italy
Mahdi Mohammadpour, UK
Rui Moreira, Portugal
Emiliano Mucchi, Italy
Sara Muggiasca, Italy
Tony Murmu, UK
Pedro Museros, Spain
Roberto Nascimbene, Italy
Sundararajan Natarajan, India
Toshiaki Natsuki, Japan
Miguel Neves, Portugal
Nicola Nisticò, Italy
Roberto Palma, Spain
A. Papageorgiou, Greece
Francesco Pellicano, Italy
Paolo Pennacchi, Italy
Evgeny Petrov, UK
Giuseppe Piccardo, Italy
Antonina Pirrotta, Italy
Franck Poisson, France
Luca Pugi, Italy
- Mohammad Rafiee, Canada
Carlo Rainieri, Italy
José J. Rangel-Magdaleno, Mexico
Didier Rémond, France
Francesco Ripamonti, Italy
Riccardo Rubini, Italy
Salvatore Russo, Italy
Giuseppe Ruta, Italy
Edoardo Sabbioni, Italy
Filippo Santucci de Magistris, Italy
Onome E. Scott-Emuakpor, USA
Roger Serra, France
Chengzhi Shi, USA
Vadim V. Silberschmidt, UK
Kumar V. Singh, USA
Jean-Jacques Sinou, France
Isabelle Sochet, France
Alba Sofi, Italy
Jussi Sopanen, Finland
Stefano Sorace, Italy
Andrea Spaggiari, Italy
Shuaishuai Sun, Australia
Chao Tao, China
Marco Tarabini, Italy
Gloria Terenzi, Italy
Mario Terzo, Italy
Tai Thai, Australia
Marc Thomas, Canada
Hamid Toopchi-Nezhad, Iran
Carlo Trigona, Italy
Federica Tubino, Italy
Nerio Tullini, Italy
Angelo Marcelo Tusset, Brazil
Jens Twiefel, Germany
Filippo Ubertini, Italy
Marcello Vanali, Italy
F. Viadero, Spain
M. Ahmer Wadee, UK
Jörg Wallaschek, Germany
Matthew J. Whelan, USA
Agnieszka Wylomanska, Poland
Enrico Zappino, Italy
Radoslaw Zimroz, Poland

Contents

Resilient Civil Infrastructure under Dynamic Loadings

Xing Ma , Nawawi Chouw , Mohamed ElGawady, and Songye Zhu 
Editorial (1 page), Article ID 9458023, Volume 2018 (2018)

High Performance Damage-Resistant Seismic Resistant Structural Systems for Sustainable and Resilient City: A Review

Junhua Wang  and Hua Zhao 
Review Article (32 pages), Article ID 8703697, Volume 2018 (2018)

Nonlinear Dynamic Analysis of High-Voltage Overhead Transmission Lines

Meng Zhang , Guifeng Zhao , and Jie Li 
Research Article (35 pages), Article ID 1247523, Volume 2018 (2018)

Adaptive Reconstruction of a Dynamic Force Using Multiscale Wavelet Shape Functions

Wen-Yu He , Yang Wang, and Songye Zhu 
Research Article (11 pages), Article ID 8213105, Volume 2018 (2018)

Development of Practical Finite Element Models for Collapse of Reinforced Concrete Structures and Experimental Validation

Mario Bermejo, Anastasio P. Santos, and José M. Goicolea
Research Article (9 pages), Article ID 4636381, Volume 2017 (2018)

Wind-Induced Coupling Vibration Effects of High-Voltage Transmission Tower-Line Systems

Meng Zhang, Guifeng Zhao, Lulu Wang, and Jie Li
Research Article (34 pages), Article ID 1205976, Volume 2017 (2018)

Study on Vibration Reduction Method for a Subway Station in Soft Ground

Xian-Feng Ma, Ning-Ning Feng, Guo-Bo Wang, and Xu Fang
Research Article (9 pages), Article ID 4029385, Volume 2017 (2018)

Study on Progressive Collapse Behavior of SRC Column-Steel Beam Hybrid Frame Based on Pushdown Analysis

Liusheng Chu, Gaoju Li, Danda Li, and Jun Zhao
Research Article (12 pages), Article ID 3075786, Volume 2017 (2018)

Source Parameter Estimation Method for Assessment of Structural Resiliencies

Zijun Wang and Boming Zhao
Research Article (7 pages), Article ID 5830124, Volume 2017 (2018)

Mitigation of Ground Vibration due to Collapse of a Large-Scale Cooling Tower with Novel Application of Materials as Cushions

Feng Lin and Qiheng Zhong
Research Article (14 pages), Article ID 6809246, Volume 2017 (2018)

Shake Table Study on the Effect of Mainshock-Aftershock Sequences on Structures with SFSI

Xiaoyang Qin and Nawawi Chouw
Research Article (12 pages), Article ID 9850915, Volume 2017 (2018)

Numerical Study on the Seismic Response of Structure with Consideration of the Behavior of Base Mat Uplift

Guo-Bo Wang, Xin Zhou, Xian-Feng Ma, and Jun Wu

Research Article (19 pages), Article ID 2030462, Volume 2017 (2018)

Computation of Rayleigh Damping Coefficients for the Seismic Analysis of a Hydro-Powerhouse

Zhiqiang Song and Chenhui Su

Research Article (11 pages), Article ID 2046345, Volume 2017 (2018)

Editorial

Resilient Civil Infrastructure under Dynamic Loadings

Xing Ma ¹, Nawawi Chouw ², Mohamed ElGawady,³ and Songye Zhu ⁴

¹*School of Natural and Built Environments, University of South Australia, Adelaide, SA, Australia*

²*Department of Civil and Environmental Engineering, The University of Auckland, Auckland, New Zealand*

³*Department of Civil, Architectural and Environmental Engineering, Missouri University of Science and Technology, Rolla, MO, USA*

⁴*Department of Civil and Environmental Engineering, The Hong Kong Polytechnic University, Hung Hom, Hong Kong*

Correspondence should be addressed to Xing Ma; xing.ma@unisa.edu.au

Received 13 March 2018; Accepted 13 March 2018; Published 6 June 2018

Copyright © 2018 Xing Ma et al. This is an open access article distributed under the Creative Commons Attribution License, which permits unrestricted use, distribution, and reproduction in any medium, provided the original work is properly cited.

A resilient infrastructural system is an important component of a modern city. The main principles are safety, sustainability, functionality, maintainability, and fast recoverability following natural and/or man-made hazards. This special issue addresses new research developments in resilient infrastructural systems under dynamic loadings, for example, wind, traffic, tsunamis, and earthquakes.

In total, 39 submissions have been received and 12 papers have been finally selected for publication. Two papers address the interactional response of soil and structures: “Study on Vibration Reduction Method for a Subway Station in Soft Ground” by Ma et al. and “Numerical Study on the Seismic Response of Structure with Consideration of the Behavior of Base Mat Uplift” by Wang et al. The structural collapse behaviour and its influence on ground vibration are addressed in “Development of Practical Finite Element Models for Collapse of Reinforced Concrete Structures and Experimental Validation” by Bermejo et al., “Study on Progressive Collapse Behavior of SRC Column-Steel Beam Hybrid Frame Based on Pushdown Analysis” by Chu et al., and “Mitigation of Ground Vibration due to Collapse of a Large-Scale Cooling Tower with Novel Application of Materials as Cushions” by F. Lin and Q. Zhong. Three articles focus on the seismic load estimation and seismic structural behaviour as shown in “Source Parameter Estimation Method for Assessment of Structural Resiliencies” by Z. Wang and B. Zhao, “High Performance Damage-Resistant Seismic Resistant Structural Systems for Sustainable and Resilient City” by J. Wang and H. Zhao, and “Shake Table Study on the Effect of Mainshock-Aftershock Sequences on Structures with SFSI” by X. Qin and N. Chouw. Zhang et al. present the nonlinear behaviour

of transmission tower-line systems in “Wind-Induced Coupling Vibration Effects of High-Voltage Transmission Tower-Line Systems” and “Nonlinear dynamic analysis of high-voltage overhead transmission lines.” He et al. propose a new dynamic force reconstruction method in “Adaptive Reconstruction of a Dynamic Force Using Multiscale Wavelet Shape Functions.” Z. Song and C. Su present an approach for estimating structural damping in “Computation of Rayleigh Damping Coefficients for the Seismic Analysis of a Hydro-Powerhouse.”

We hope that the papers in this special issue are useful to readers, and the publication of the special issue will stimulate further research in the area of resilient infrastructures.

Xing Ma
Nawawi Chouw
Mohamed ElGawady
Songye Zhu

Review Article

High Performance Damage-Resistant Seismic Resistant Structural Systems for Sustainable and Resilient City: A Review

Junhua Wang ^{1,2} and Hua Zhao ²

¹College of Civil Engineering, Nanjing Tech University, Nanjing, Jiangsu, China

²State Key Laboratory of Geohazard Prevention and Geoenvironment Protection, Chengdu University of Technology, Chengdu, Sichuan, China

Correspondence should be addressed to Hua Zhao; zardhua@gmail.com

Received 14 July 2017; Revised 11 December 2017; Accepted 10 January 2018; Published 30 April 2018

Academic Editor: Mohamed ElGawady

Copyright © 2018 Junhua Wang and Hua Zhao. This is an open access article distributed under the Creative Commons Attribution License, which permits unrestricted use, distribution, and reproduction in any medium, provided the original work is properly cited.

This paper presents a review of high performance damage-resistant seismic resistant structural (DRSRS) systems for the sustainable and resilient city. Firstly, the motivation and the basic principle as well as methodology of the developing DRSRS system are briefly illustrated. Then, the structural detailing and the seismic behaviors of three types of existing DRSRS systems, namely, the replaceable structural element (RSE), rocking seismic resisting structural (RSRS) system, and self-centering seismic resisting structural (SCSRS) system, are summarized in detail. The theoretical and extensive experimental study results indicated that the three existing types of DRSRS system can minimize the postdamage after loading. Types of energy dissipation devices and dampers, as well as fuse sections, can largely enhance the energy dissipation capacity of the proposed structural system. Many numerical and finite element models have been proposed to analyze the dynamic and static cyclic responses of them. The residual deformation after the dynamic response is smaller compared to that following the cyclic response. Then, the current research challenges of DRSRS system are illustrated, and the new research highlights that emerged in recent years are stated. Finally, the conclusions of this paper are summarized; furthermore, the recommendations for the future studies are pointed out at the end of the paper.

1. Introduction

The majority of the world's population, over 3.96 billion people, lives in cities [1]. As the centers of population, politics, and economics activity as well as culture, the natural hazards bring more severe destructions and disasters to cities compared to before. Therefore, the sustainable and resilient city has been paid more and more enthusiasm in recent years. A “resilient city” is demanded to quickly rehabilitate or maintain its essential functions from any shock or stress [2]. The shocks or stresses include heat waves, storms, earthquake, flood, and an accelerated rate of sea level rise.

The Wenchuan earthquake in 2008 caused 86000 deaths and approximately 138.33 billion USD economical loss [3]. The Great Kobe earthquake led 6434 deaths and caused about 170 billion USD loss in economics [4]. 15870 persons died in the Great East Japan Earthquake which caused about 100

billion loss USD in economics [5]. The 7.8 magnitude earthquake in Nepal in April 2015 occurred with close to 9,000 victims and 6 billion USD estimated losses including damage reported in India, China, and Bangladesh [6]. On 16 April 2016, a series of earthquakes hit Kumamoto, Japan, leading to 64 deaths and infrastructure damage of approximately 5.6 billion USD. On the same day, an earthquake attacked Ecuador and murdered 668 people [7]. In August 2016, Italy's Umbria region suffered from a 6.2 earthquake that caused 293 deaths and left 4000 people homeless; the damage is estimated at 3.96 billion USD [8]. Other invisible losses in culture, human emotion, and quality of life are inestimable.

The earthquake caused a mass of economical loss and destructions of infrastructures; this leads to big difficulty for the sustainable and resilient city. Thus the American and Japanese earthquake engineering researchers pointed out that the resilient city needs to be the next objective of

earthquake engineering at the seventh joint planning meeting of NEES/E-Defense Collaborative Research on Earthquake Engineering [9]. Actually, to minimize the residual deformation of engineering structure after an earthquake, engineers and researchers have developed some innovative structure systems including replaceable structural element (RSE) and rocking seismic resisting structural (RSRC) system as well as self-centering seismic resisting structural (SCSRS) system in recent decades; all the above-mentioned structural systems are called high performance damage-resistant seismic structural (DRSS) system in this paper.

The RSE is developed through actively artificially forming relative weakening structural element which will be easily failed before other protective structural elements and can be easily replaced after an earthquake; as a result, the whole structure can be quickly rehabilitated and decontaminated. So far, the most popular studied DRSS systems are RCRC system and SCSRS system that is created in accordance with the elastic gap opening mechanisms to soften the seismic response of the structure; posttension tendon or strand is used to return the whole structure to a plumb position. In order to dissipate the seismic energy, the energy dissipating devices or types of dampers are usually included in the DRSS system. In addition, using the inherent strong elastic recovery force of high strength tension longitudinal bar to pull the structure back after loading is another new way to develop the DRSS system in recent years.

The objectives of this paper are to review the current research status of high performance DRSS systems and to outline current research challenges for the aforementioned structural systems. First, the motivation and the basic principles, as well as methodology of DRSS system, are briefly reviewed. Then, the seismic behaviors of several current different types of DRSS systems including the RSE, RCRC, and SCSRS systems are overviewed in detail. Finally, some current research challenges and the recommendations for future studies for DRSS system are summarized and discussed.

2. Motivation of High Performance DRSS Systems

For the sake of protecting the lives of the occupants, structures are typically designed for “life-safety” performance according to the most modern building codes and are expected to undergo significant structural or nonstructural damage referred as residual deformation during a severe earthquake. Repairing damaged structures with large residual deformation is expensive and time-consuming, even the structures with significant severe residual deformation have to be demolished due to the high cost.

Since the 1990s, the performance-based design method has been adopted by most engineers and researchers in the world, and this designed method has been developed three generations [10–12]. It is expected that the structure designed according to the performance-based design method can have prospective seismic behaviors to withstand the possible earthquake and have the safety to protect the lives of the occupants and that the seismic damage of the structure

due to the possible earthquake can be controlled within the expectant degree. The principle of “undamaged under minor earthquake, repairable under moderate earthquake, and uncanceled under large earthquake” proposed by the Chinese seismic code and Japanese seismic code is similar to the purpose of the performance-based design method. However, due to the uncertainty of the earthquake, the structures possibly suffer from larger earthquake than the predicted level, causing the seismic damage of structure to be more serious than the predicted damage. The structures with severe seismic damage bring a big difficulty to the repairing of building and the rehabilitation of the society.

The reconstruction after the Kobe Earthquake lasted 10 years and the money for reconstruction reached up to 145 billion USD [13]. After the Great East Japan Earthquake in 2011, the first time budget fund applied from Japan government for the reconstruction is up to 35 billion USD, which could not satisfy the need of reconstruction; this also caused a heavy burden on the Japanese economy [14]. The estimated cost of rebuilding after the earthquake occurred in Christchurch, New Zealand, in 2011 is 28 billion USD, which is approximately 20% GDP of New Zealand without including economic losses associated with business downtime, and the Christchurch reconstruction is still underway until 2014 [15, 16]. Therefore, the importance of minimizing the residual deformation to make the repairing of structure easier was pointed out [17, 18].

It is understood that engineering structures with large residual deformation are harm to the sustainable and resilient city because it is necessary to consume lots of time and social wealth for reconstruction after the earthquake. Consequently, there is a consensus to develop a new generation of the seismic resisting structural system to withstand the earthquake, which has a strong resilient capacity and very small structural damage after the earthquake.

3. Basic Principles and Methodology of High Performance DRSS Systems

In order to understand how to control the damage of structure, it is necessary to understand the mechanism of damage of the conventional seismic resisting structure. The conventional approach to earthquake resistant design of buildings depends upon providing the building with strength, stiffness, and inelastic deformation capacity. Figure 1 schematically shows the seismic performances of the conventional seismic structural system.

As shown in Figure 1(a), conventional seismic structural system satisfies the demand of deformation through plastic hinges at the bottoms of the column and the ends of the beam. The conventional seismic resisting structural system undertakes two responsibilities simultaneously: (1) resisting the earthquake force through strong stiffness; (2) dissipating the earthquake energy through inelastic buckling or yielding of longitudinal bars and crushing of concrete at compression zone, as shown in Figure 1(b); this leads to the hysteretic loop of the conventional seismic resisting system is plump, shown as in Figure 1(c). However, the plump hysteretic loop indicates that severe damage and large residual drift are possible after

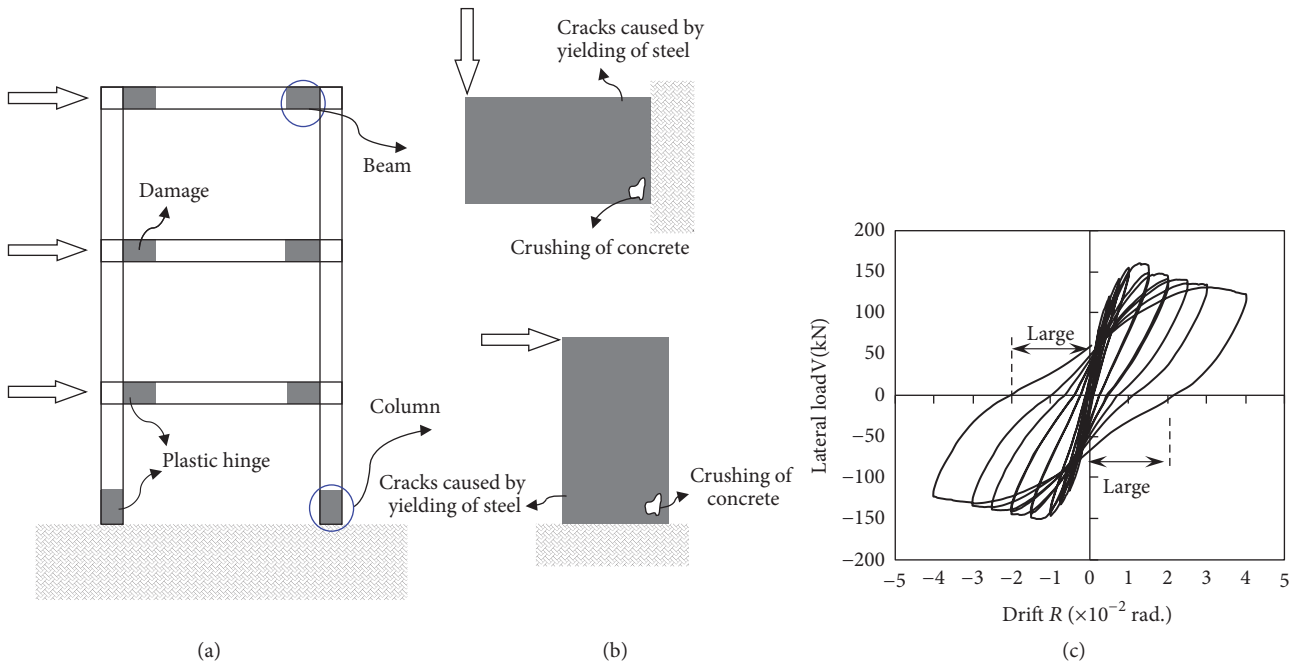


FIGURE 1: Seismic performance of conventional seismic structural system: (a) seismic resisting structural frame; (b) damage of structural element; (c) hysteretic curve of lateral force (adopted from [19], copyright 2014 JCI).

the lateral seismic force is removed, shown as in Figure 1(c). The stations above indicate that controlling the damage of a structure should emphasize the interface of two structural members and the plastic hinge zones.

To reduce the damage of conventional seismic resisting structural system, more advanced techniques are not to strengthen the structure, but to soften the earthquake-generated forces acting upon it. Among the most important advanced techniques of earthquake resistant design and construction are (1) energy dissipation devices and (2) base isolation. In particular, the base-isolated structure reduces the damage through a series of bearing pads which are placed between the building and the foundation. The foundation and the upper building are separated, and the connection between them is weakened. The bearing pads dissipate the most seismic energy, while the base-isolated structure itself escapes the deformation and damage.

The principle of weakening the connection between upper structure and the foundation is adopted into developing the rocking structural system. The upper structure-foundation intersection of the rocking structure could undertake the compressive force but could not bear the tensile force. A certain uplift (rocking) is promised at the upper structure-foundation intersection under the lateral earthquake load; however, the upper structure does not bear the bending deformation, as shown in Figure 2(a). The weight of structure returns the whole structure back to the vertical location without or with little residual deformation. The posttensioned tendons or strands are included to provide the restoring force for the rocking structure, as shown in Figure 2(b). Figure 2 implies that the damage of both two structures is eliminated by the rocking weakening behavior at the intersection;

however, the resilient forces are different. The self-centering forces of structural systems shown in Figures 2(a) and 2(b) are provided by the uncontrolled gravity of structure and the controlled recovery force of tendon or strand, respectively. In order to distinguish them, two types of structures shown in Figures 2(a) and 2(b) are called rocking seismic resisting structural (RSRS) system and self-centering seismic resisting structural (SCSRS) system in this paper, respectively.

On the other hand, the RSE is based on the mechanism that the structure fails in the relative weak location under loading. The RSE designed at the relative weakening location can be easily replaced after the earthquake; as a result, the entire structure can be quickly rehabilitated and desterilized.

In order to enhance the seismic energy dissipation capacity, types of energy dissipation devices and dampers, as well as fuse sections, are included the DRSSRS systems including the RSE and RSRS system as well as the SCSRS system.

4. Replaceable Structural Elements

As is well known, there is somehow an essential mechanism that the structure failed at the weakening structural elements under loading condition. Consequently, it is possible that the structure failed at one or some artificial weakening structural elements which are called RSE. In general, RSE is used by mechanics; application in structural engineering is limited and focuses on the steel structure and bridge structure as well as the precast structural system until now.

4.1. Bridge Engineering Structure. A new concept [20] for bridge tower designs in seismic zones using sacrificial inelastic shear link schemes was adopted by TY Lin International

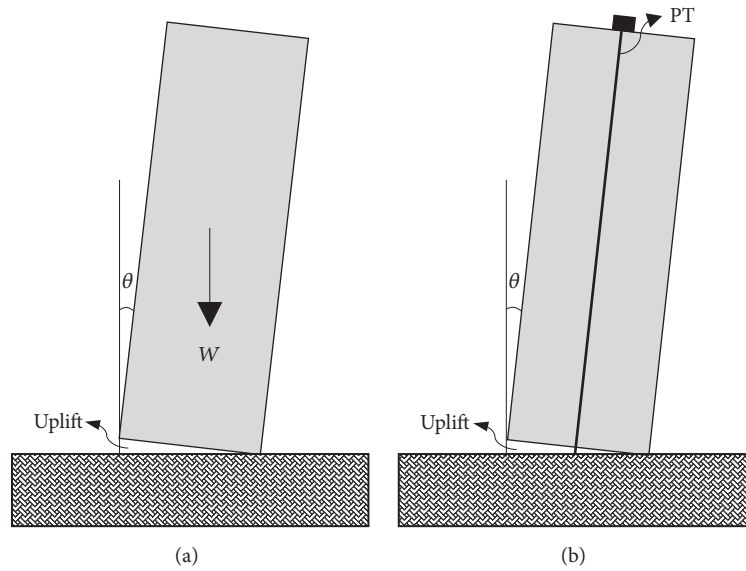


FIGURE 2: The principles of RSS system and SCS system: (a) DRSRS system; (b) SCSRS system.

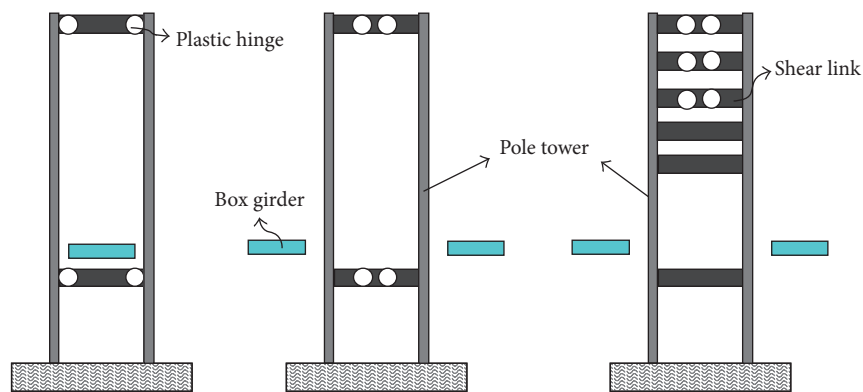


FIGURE 3: Concept of shear links of San Francisco–Oakland Bay Bridge (adopted from [20], copyright 2004 ASCE).

in 2000, shown in Figure 3. The sacrificial inelastic shear link could enable the new San Francisco–Oakland Bay Bridge (SFOBB) signature tower shafts to remain elastic during large seismic events and capable of carrying the large axial loads delivered by the suspension cables. In addition, the shear links are bolted to the tower shafts; therefore, the links are replaceable if required after large seismic events. It was shown that the inelastic tower links could be used to tune the dynamic response of bridge towers in regions of high seismicity through global seismic time history analysis [33].

4.2. Coupling Beam of Shear Wall System. The RSE design philosophy is most applied to coupling beam between wall systems. Fortney et al. firstly proposed a new type of fuse coupling beam (FCB) [21, 22], as shown in Figure 4. It is assumed that all inelastic deformations will be concentrated in the middle section (fuse section) of the beam such that the two outer steel beam parts could be protected. The fuse section is connected to the outer steel beam section via the flange splice plates at top and bottom flange and web splice plate, as well as

slip critical bolted connections. The compared experimental results showed that FCB led to early energy dissipation and lower stiffness relative to the typical steel coupling beam (SCB); nevertheless, postdamage repair/replacement difficulties and expenses are minimized [22]. Additionally, in order to enhance the stiffness and energy absorption capacity and to reduce construction difficulties of RSE, some innovated alternative schemes were performed [34, 35].

Lu et al. proposed three types of steel coupling beams for the shear wall structural system with replaceable fuse [23, 43], as shown in Figure 5. Type I fuse is a steel I-beam whose web has a diamond-shaped hole; type II fuse is two webs of the steel I-beam, filled with lead between the webs; type III is two round steel tubes, filled with lead in the tube. The experimental results indicated that the shear capacities of shear wall systems with replaceable fuses were close to that of the conventional shear wall system. Moreover, the inelastic deformation and damage of specimens were concentrated in the fuse section as expected [44, 45]. In order to reduce the damage at the bottom of the shear wall, new replaceable foot

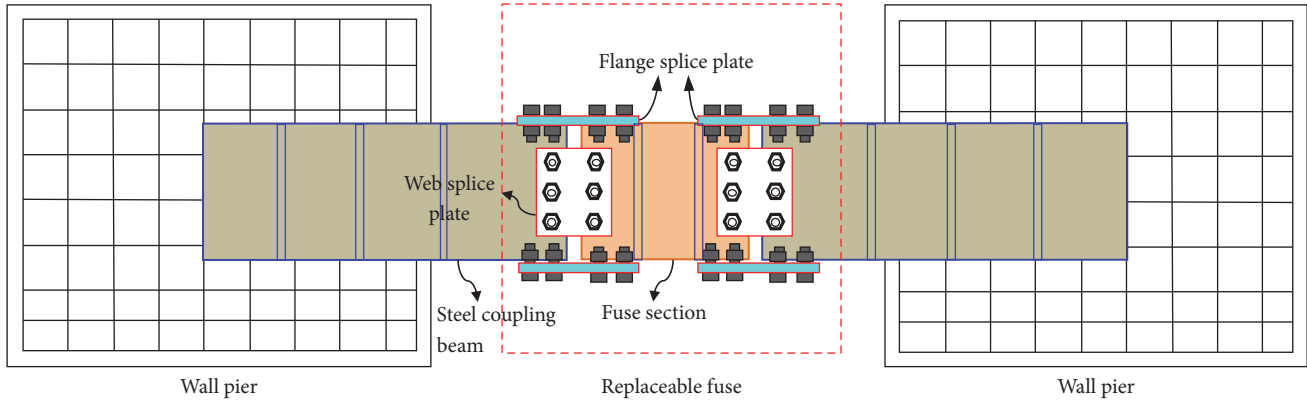


FIGURE 4: Details of replaceable fuse steel coupling beam (adopted from [21, 22], copyright 2006, 2007 ASCE).

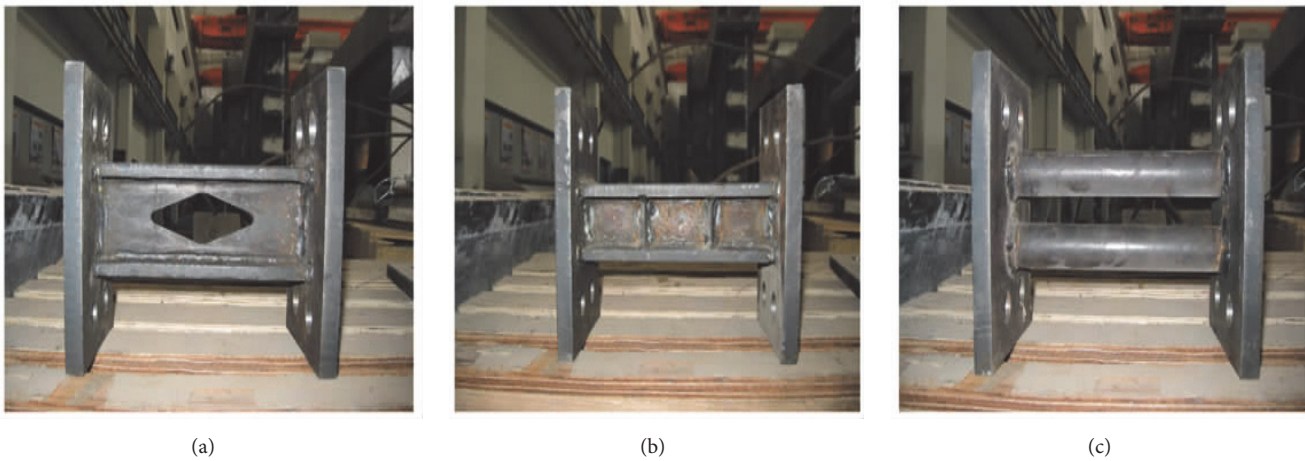


FIGURE 5: The new replaceable coupling beams proposed by Lu: (a) type I; (b) type II; (c) type III. (adopted from [23], copyright 2013 Journal of Earthquake Engineering and Engineering Vibration).

parts for the shear wall were proposed [46]; it was experimentally revealed that the proposed foot parts wall could greatly minimize the damage at the bottom of the shear wall. Similar to the replaceable coupling beam type III proposed by Deng et al., replaceable steel truss coupling beams were developed and used into the shear wall structural system [47, 48].

The replaceable steel coupling beam (RSCB) shown as in Figure 6 was proposed by Ji et al. [24]. The cyclic behavior of short shear link was experimentally studied in detail [49]. Furthermore, the scheme of proposed RSCB was further innovated and the seismic behaviors were experimentally numerically studied [24, 50]. The test results showed that the wall systems with shear link had a good shear strength and large inelastic rotation capacity; in particular, the damaged shear link was replaced within very short time [50].

The replaceable steel coupling beams (RSCB) aforementioned can be taken as shear links with weakening section relative to protected normal beam segment and shear walls; the earthquake energy is dissipated by RSCB through inelastic deformation. If the RSCB is attached to a damper, more earthquake energy can be dissipated, and the shear wall can

be preferably protected. Chuang et al. used a friction damper in the replaceable coupling beam of shear wall to enhance the earthquake energy dissipation capacity [25]. Figure 7 shows the configuration of the proposed friction damper which consists of two sets of an I-beam, a gusset plate, a steel plate for connection, and a brass plate used as the friction material, as shown in Figures 7(a) and 7(b). The earthquake energy is dissipated by the friction damper through the vertical deformation of the slot hole, shown as in Figure 7(c).

Teng et al. developed a mild metallic beam damper for coupled shear wall system [26], as shown in Figure 8; the proposed beam damper is a steel plate with low yielding strength and rectangular column holes. The experimental results showed that the global buckling in plane occurred under loading, and the damper behaved with great energy dissipation capacity [26]. The pseudodynamic test result indicated that the proposed mild metallic beam damper could reduce the seismic response of shear wall system and make the earthquake energy larger [58].

Mao et al. proposed a type of shape memory alloy damper (SMA) to dissipate the earthquake energy of coupling beam in RC frame-shear wall structural system [27]; the assembly

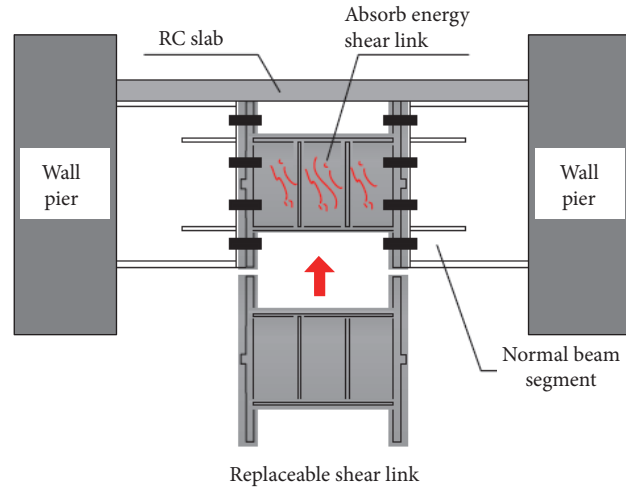


FIGURE 6: Replaceable steel coupling beam (RSCB) (adopted from [24], copyright 2016 Engineering Mechanics).

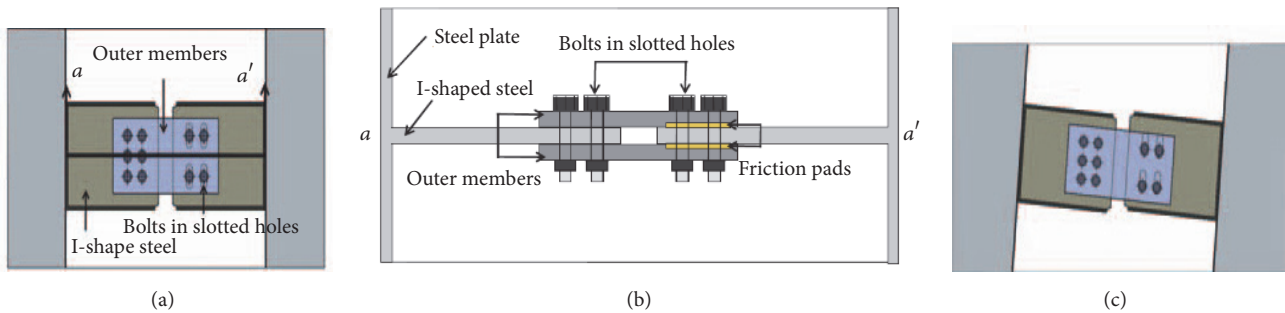


FIGURE 7: Slot bolt-type connection installed between coupled beams. (a) Elevation. (b) Sectional view. (c) Slip of slot bolt-type connection by the flexural deformation of walls (adopted from [25], copyright 2009 Structural Design Tall Spectral Building).

of SMA is schematically shown in Figure 9. The SMA damper contains four steel components (assembly parts I–IV) and two groups of SMA wires (group A and B); the earthquake energy is dissipated through tension of SMA wires located around the ears on part II and III (or part II and IV) when relative vertical displacement occurs between cantilever shear wall ends.

Kumagai et al. developed a type of RC shear wall structural system with coupling beam damper [28, 29], as shown in Figure 10. The coupling beam damper is a rectangular steel shear plate with a low yielding point, which is connected to the steel beam embedded in shear walls. Experimental result showed that the proposed coupling beam damper behaved with stable hysteretic response, and the load carrying capacity did not deteriorate up to 1/20 drift angle. So far, there were nine building structures adopting the proposed coupling beam damper [59].

A new viscoelastic coupling damper (VCD) device was developed by Lyons et al. [30] to use into the coupled wall of the high-rise building. As shown in Figure 11, the VCD consists of multiple layers of viscoelastic (VE) material, placed between layers of steel plate which are anchored at alternating ends to the coupled RC walls using a number

of different connection details. In addition, ductile “fuse” mechanism can be added in series with the VE material. The experimental result validated that the VE material exhibited stable hysteretic behavior under the loading conditions that are expected in high-rise buildings under wind and earthquake loading. The full-scale test results also demonstrated the targeted viscoelastic response during the wind and low-level earthquake loading and the targeted viscoelastic-plastic response for extreme earthquakes, where the response is a combination of the VE response and the nonlinear behavior of the structural fuses [60].

Kim et al. proposed a hybrid energy dissipative device (HEDD) applicable to RC shear wall structural system which consists of U-shaped steel plates and high damping rubbers [31, 32]; the HEDD is schematically shown in Figure 12. The high damping rubber damper placed between the casings (Casing 1 and Casing 2) is designed to accommodate shear deformation when the rotation of building occurs. Experimental investigations were conducted to validate the excellent seismic performances of RC shear walls connected by hybrid energy dissipative coupling beams.

Kurama and Shen proposed unbonded posttensioned hybrid coupled wall for shear wall structural system [36],

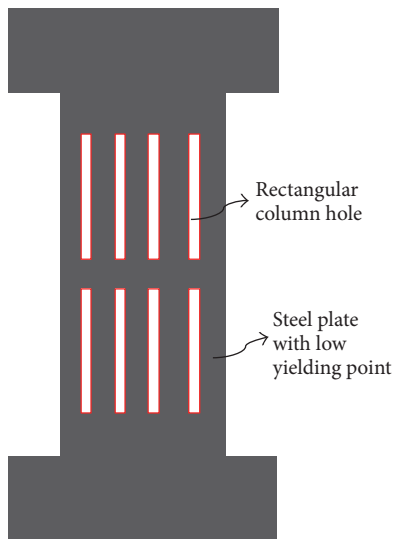


FIGURE 8: Elevation of mild metallic damper (adopted from [26], copyright 2010 Journal of Building Structures).

shown as in Figure 13; reinforced concrete walls are coupled using steel beams and unbonded posttensioning, without embedding the beams into the walls. The beam-to-wall connection regions include top and bottom angles bolted to the beam flanges and to steel plates embedded in the walls (using welded headed studs); the angles are to yield and provide energy dissipation during an earthquake and resist sliding of the beams along the beam-to-wall connections. The seismic behavior of the proposed unbonded posttensioned hybrid coupled wall was experimentally studied in detail [67, 68]. The nonlinear load-deformation behavior of proposed hybrid coupled wall system was analyzed, and a simple design method based on fiber elements to estimate the nonlinear load-deformation was proposed. The results indicated that unbonded posttensioned steel coupling beams with initial stiffness similar to embedded steel beams can be designed to provide stable levels of coupling without experiencing significant damage over large nonlinear cyclic deformations [69, 70], and the design approach was proposed for the unbonded posttensioned hybrid coupled shear wall structural system [71].

4.3. Frame Structural System. In order to prevent damage to columns or infill walls and to minimize life-safety hazards during potentially earthquakes, Aliaari et al. developed a seismic infill wall isolator subframe (SIWIS) system [37, 72, 73], shown as in Figure 14. The SIWIS system consists of two vertical and one horizontal sandwiched light-gauge steel studs with “rigid-brittle” elements in the vertical members. As a “sacrificial” component or a “structural fuse” to protect the infill wall and frame from failure, the SIWIS is designed to allow infill wall-frame interaction under wind loading and minor-to-moderate earthquakes for reduced building drift but to disengage them under damaging events. The seismic performances of SIWIS system were experimentally investigated in detail [37, 74] and analyzed using nonlinear finite

element models [75, 76]. Analysis results showed that the concept of SIWIS system works in providing initially high stiffness followed by an isolation of infill wall from interaction with the confining frame. Practical design guidelines are proposed, and the result of the study demonstrates that the proposed isolation system has merits and can potentially improve the seismic performance of masonry infill walls by protecting the infill wall and the frame from damage due to their interaction [77].

5. Rocking Seismic Resisting Structural Systems

In 1963 the first time analysis of the rocking motion of structures was performed by Housner who found that several golf-ball-on-a-tee types of elevated water tanks survived the ground shaking due to the effect of uplift despite the appearance of instability; on the other hand, much more stable-appearing reinforced concrete, elevated water tanks were severely damaged during the Chilean earthquakes of May 1960 [81].

Since the 1970s, the principle of rocking motion of structure was largely applied to research on the seismic resisting structural system. Hukelbridge and Clough studied the effects of allowing column uplift in steel building frames on seismic response under severe seismic loading; the table test results indicated that allowing column uplift was shown for this frame to significantly reduce both the seismic loading and ductility demand [82, 83]. Priestley et al. verified the mechanism of energy dissipation of rocking structural system through table test and proposed a simple design method for assessing maximum rocking displacements, using equivalent elastic characteristics and a response-spectra approach [84]. Basically, the analysis of the seismic response of rocking structural system under the earthquake lateral loading was gradually deeply studied before the 1980s [85–88].

After completing the theoretical mechanism analysis of the seismic response of rocking structural system, the experimental studies on types of engineering structural systems such as bridge engineering and building structures were started from the 1990s. The methodologies of rocking structural system were through not only softening the connection between structure and foundation but softening the connection between structural elements such as beam-column joint.

5.1. Rocking Bridge Pier Structure. Aslam et al. studied the rocking motion of a major pier in the bridge, a semirigid seismic connection was used at the base of the pier and the rocking of the pier was permitted to take place during the future major earthquakes [87, 88]. Priestley et al. proposed rocking bridge pier as a strengthened design and seismic design scheme of bridge engineering [89]. Mander and Cheng developed a new paradigm called Damage Avoidance Design (DAD), in which the bridge piers is free to rock under large lateral loads such that damage is avoided by the special detailing of the connections [90]. Mashal et al. used dissipative controlled rocking (DCR) systems with types of external and internal dissipation devices into Accelerated Bridge

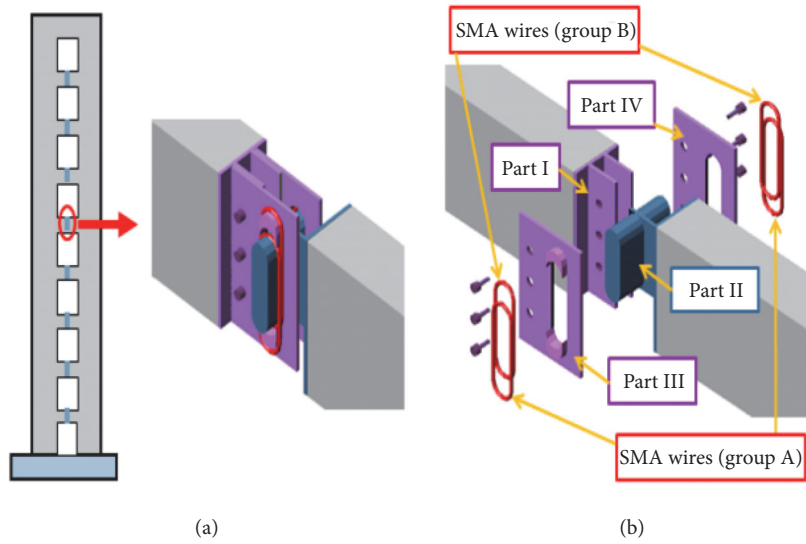


FIGURE 9: The location and assembly parts of the SMA damper in the coupling beam: (a) location of the SMA damper; (b) assembly parts of the damper (adopted from [27], copyright 2012 WCEE).

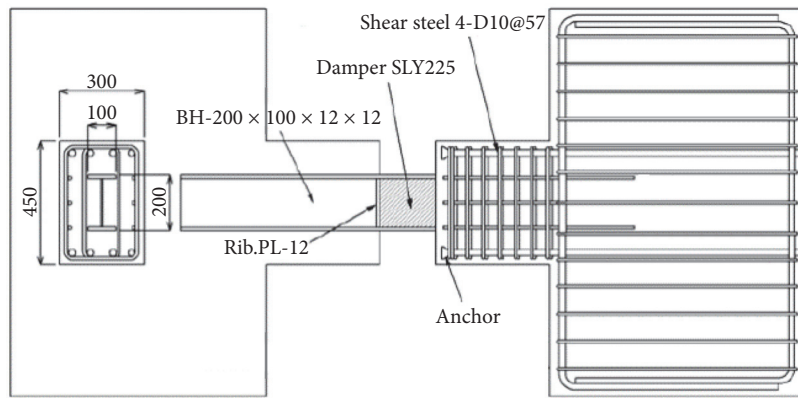


FIGURE 10: Dimensions and reinforcement of replaceable coupling beams (adopted from [28, 29], copyright 2009 AIJ and 2010 Tokyo University).

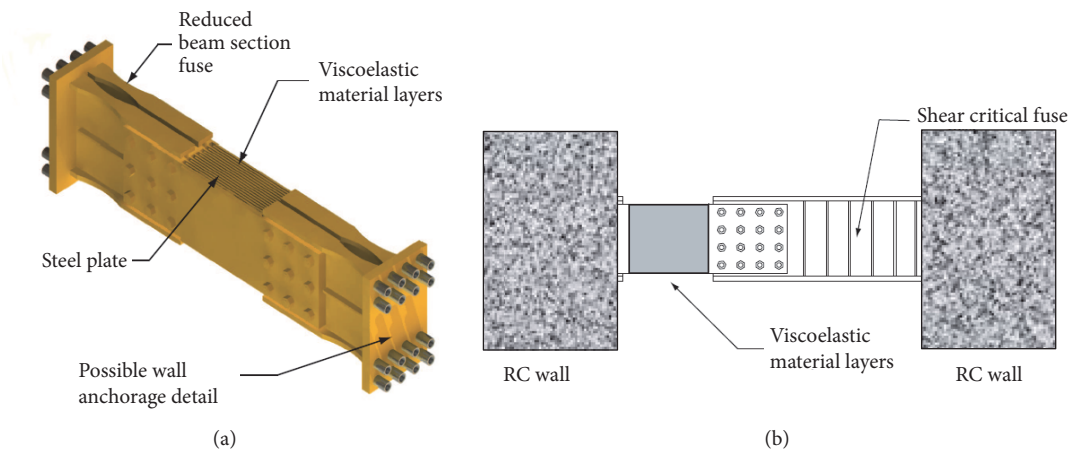


FIGURE 11: RC coupled wall high-rise building with viscoelastic coupling dampers: (a) viscoelastic coupling damper (VCD); (b) alternative design using VCD for prototype structure (adopted from [30], copyright 2012 WCEE).

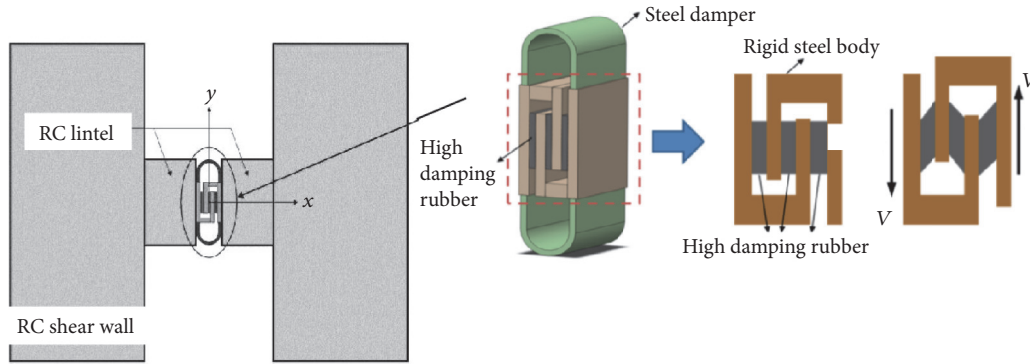


FIGURE 12: Schematic drawing of a hybrid damper embedded into a coupling beam connecting RC shear walls and the deformed shapes of a hybrid damper (adopted from [31, 32], copyright 2012, 15 WCEE).

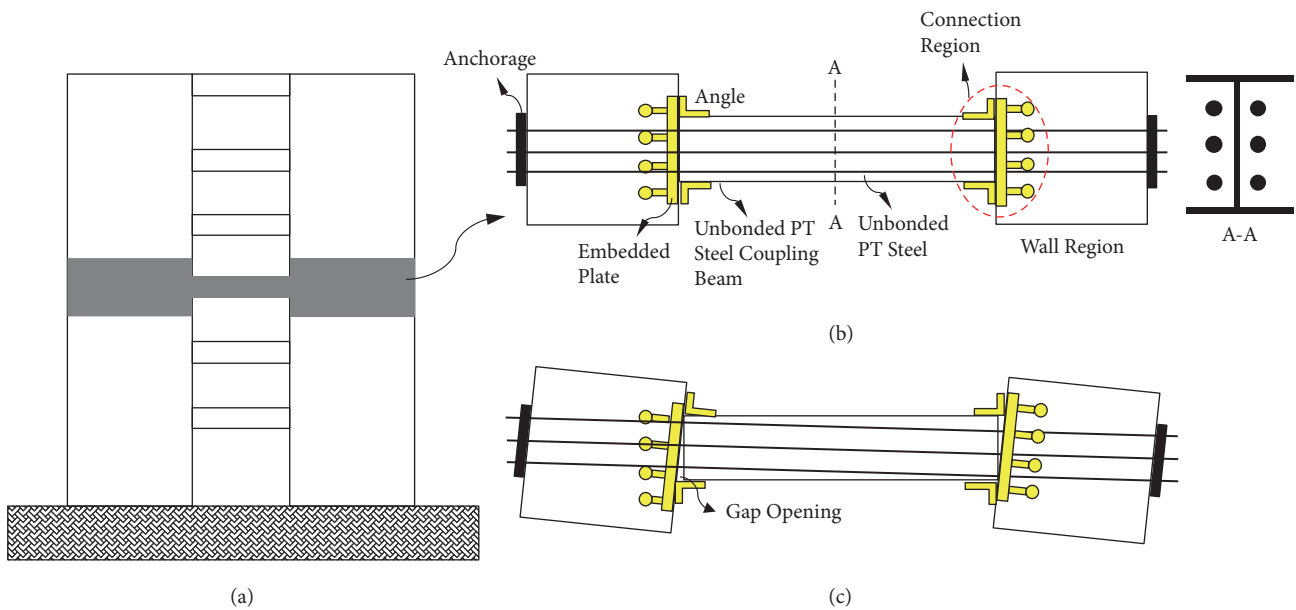


FIGURE 13: Unbonded posttensioned hybrid coupled wall subassemblage: (a) location of coupled beam; (b) elevation; (c) deformed shape (adopted from [36]).

Construction (ABC) to enhance the seismic behavior of Accelerated Bridge Construction (ABC) structures [91].

5.2. *Rocking Concrete Frame System.* Roh used the “rocking columns,” a type of double hinged gravity column or cracked base and top column which resists vertical loads with minimum or no lateral strength, to reduce the strength of the part of the lateral load resisting system (i.e., weaken the structure) for controlling the story accelerations [92]. Roh and Reinhorn firstly proposed a macroscopic analytical approach applicable for analysis of rocking column [93]. The proposed model is verified through the quasi-static cyclic of 1:3 scale rocking column and the IDARC2D computational model [94]. Subsequently, the seismic performance of a span prototype structure with the proposed rocking column and damper was analyzed; the results indicated that the proposed rocking column and damper could effectively reduce the seismic response of structure [93].

Cao et al. [95] developed a new type of connection to assemble the frame and concrete rocking walls; test results showed the rocking wall with the novel connections effectively controlled the interstory drift concentration and endowed the structure with a uniform deformation mode when subjected to different loading patterns.

5.3. *Rocking Steel Frame System.* Eatherton et al. of Stanford University experimentally investigated the seismic behaviors of controlled posttensioned rocking steel framed buildings with replaceable energy dissipation fuses [38]; the rocking steel framed building is as shown in Figure 15; the experimental results indicated that the proposed rocking steel frame exhibited excellent recovery properties, and the seismic energy dissipation and damage were concentrated in the replaceable fuse elements. Midorikawa et al. conducted the three-dimensional table test of posttensioned steel frame in 2009 [96, 97], and Ma et al. performed a table test of 2:3

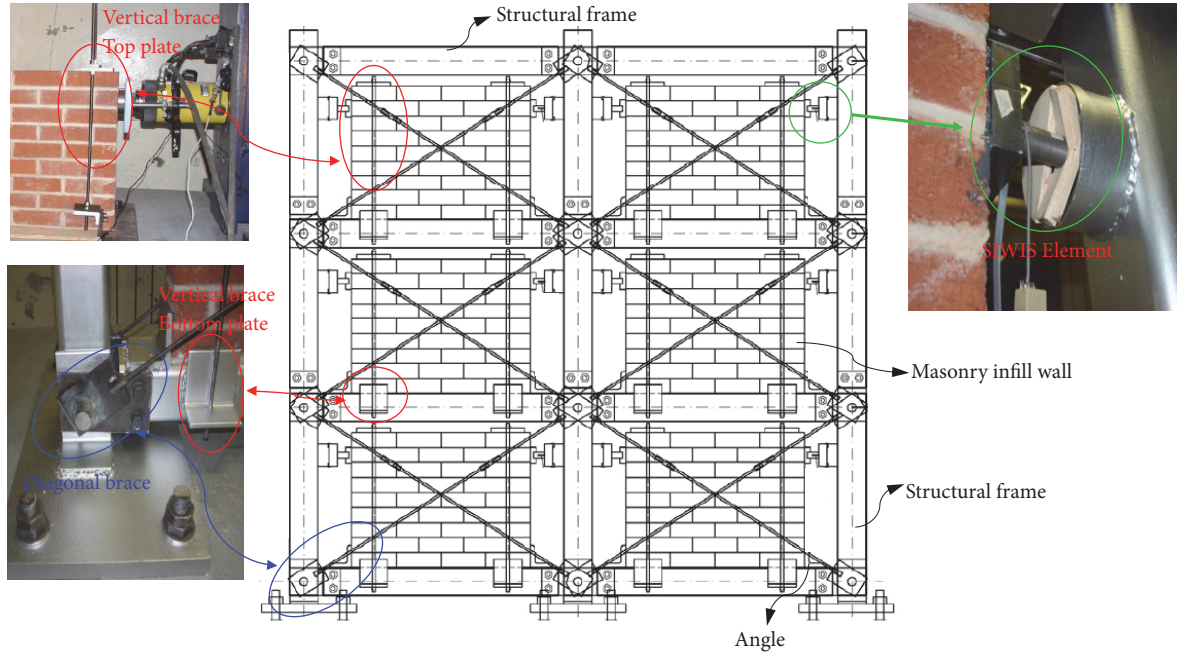


FIGURE 14: Schematic design of scaled two-bay three stories SIWIS frame (adopted from [37], copyright 2005 The Pennsylvania State University).

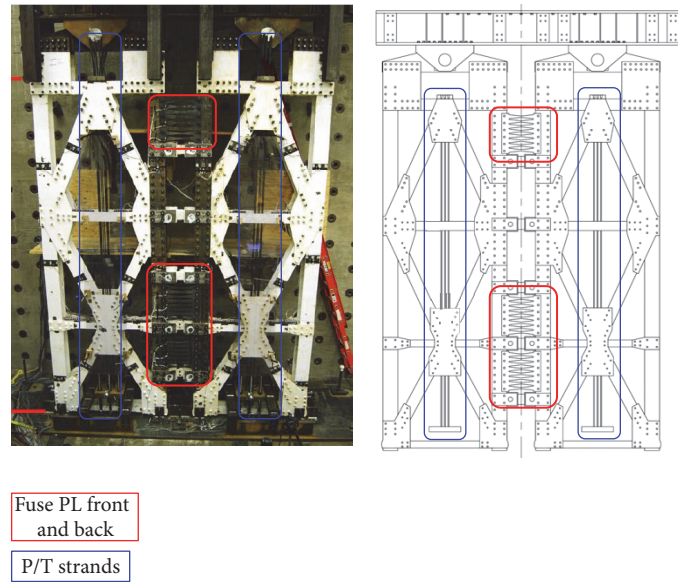


FIGURE 15: Posttensioned controlled rocking steel framed building with replaceable energy dissipation fuses (adopted from [38], copyright 2008 the 14th WCEE).

scale steel frame with controlled rocking column and earthquake energy dissipation device in E-Defense of Japan [98], Eatherton et al. also conducted similar test on this kind of steel frame [99].

5.4. *Rocking Concrete Shear Wall System.* Anderson studied the influence of the rocking of foundation on seismic response of the shear wall under seismic loading through the proposed computational model [100]. Gajan and Kutter

[101, 102] proposed that using rocking footings in place of, or in combination with, structural base isolation and energy dissipation devices improves the performance of the structure during seismic loading; results showed that a footing with large A/A_c ratio (A is actual footing area, and A_c is the area required to support the vertical and shear loads) possesses a well moment capacity that is insensitive to soil properties and suffers small permanent settlements [101]. The effects of static vertical factor of safety (F_{SV}) and the applied normalized

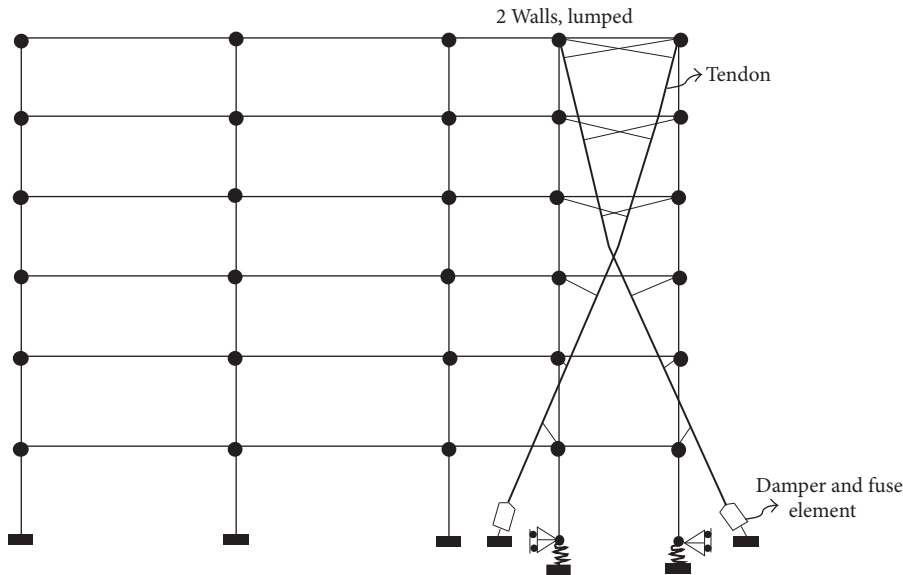


FIGURE 16: Scheme of a six-story rocking wall-frame building (adopted from [39], copyright 2004 Journal of Structural Engineering ASCE).

moment-to-shear ratio (M/HL) at the footing-soil interface on footing-soil system behavior were analyzed; the results indicated that, for a particular F_{SV} , footings with a large moment-to-shear ratio dissipate considerably more energy through rocking and suffer less permanent settlement than footings with a low moment-to-shear ratio [103].

Ajrab et al. [39] designed a six-story rocking wall-frame building with various supplemental system configurations which include prestressed tendons and energy dissipation devices using performance-based design methodology, shown as in Figure 16. Seismic performance and response evaluation, using nonlinear time history analyses, suggests that desired performance levels, minor to no damage, can be achieved with added equivalent viscous damping, and the seismic response was not sensitive to the prestress level in tendons and to wall base width. However, this rocking wall-frame building system is complicated such that it could not be extensively applied into constructions.

Lu [104] analyzed the influences of rocking wall and wall-neutral axis as well as the 3D effect on the seismic response of RC wall-frame; the result indicated that uncontrolled wall rocking could cause beam-wall connection failure, leading to accelerated deterioration of the entire system. Pushover and dynamic time history analyses showed that by incorporating wall-neutral axis migration, more satisfactory prediction of the inelastic response of the wall-frame can be made. A systematic improvement of the wall-frame inelastic behavior can be achieved by involving the 3D effect.

Hitaka and Sakino [40] developed a new type of hybrid coupled wall (HCW) system which consists of rolled steel coupling beams, reinforced concrete (RC) wall piers, and concrete-filled tube (CFT) short columns, shown as in Figure 17. In this new system (HCW), the bases of the wall piers are connected to the base beams only through CFT short columns, and the yielding occurs in the coupling beams and the short columns. The experimental results indicated that the proposed HCW could fail in the expected location such

as the coupling beam and CFT column with ductile behavior and large energy dissipation.

Wiebe and Christopoulos [105, 106] considered that structural forces of the base-rocking system can be increased significantly even when the base moment is limited because of higher mode effects. They suggested that higher mode effects may be substantially reduced by designing to allow rocking to occur at multiple locations over the height of a base-rocking system. The statistical study results showed that the bending moment envelope above the base of the wall is greatly reduced by providing multiple rocking sections, while the peak displacements do not increase in magnitude or in variability.

Mulligan et al. [107] analyzed a scaled semiactive rocking wall system using real-time, high-speed hybrid testing. The results showed that the semiactive devices are controlled to provide supplementary resistance only for the upward rocking motion of the wall, providing semiactive energy dissipation over half of each cycle and relying on radiation damping for the other half. Marriott et al. [108] proposed a displacement-based retrofit procedure based on targeting predefined performance criteria, such as joint shear and/or column curvature deformation limits; an extensive experimental program investigating the use of rocking wall systems to retrofit existing poorly detailed frame structures is promised.

Wada et al. [41] developed a retrofit system of prestressed concrete rocking walls and steel dampers to control the seismic damage mode and increase the strength and energy dissipating capacity of an 11-story steel reinforced concrete frame in Japan, shown as in Figure 18. The extensive nonlinear time analyzed results showed that the rocking system can significantly reduce both the seismic responses to different earthquake ground motions and their scattering.

5.5. Rocking Masonry Structural Wall System. Toranzo et al. used the principle of rocking wall system into confined

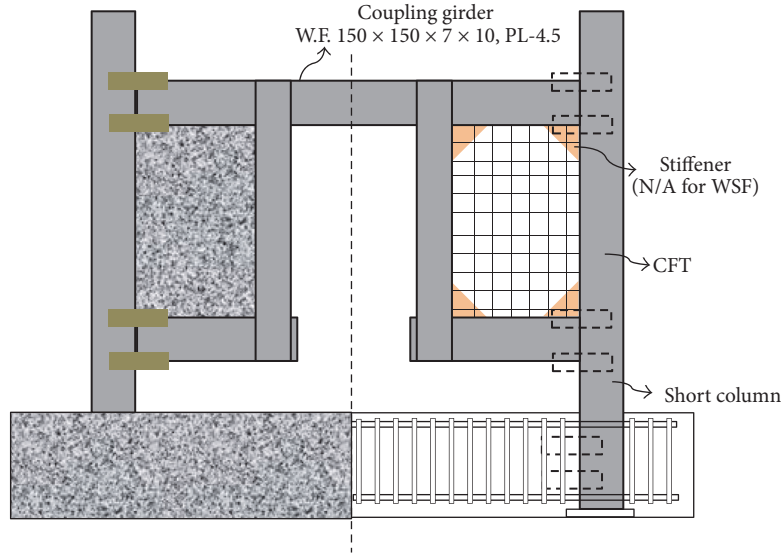


FIGURE 17: Rocking hybrid coupled wall (adopted from [40], copyright 2008 Earthquake Engineering and Structural Dynamics).

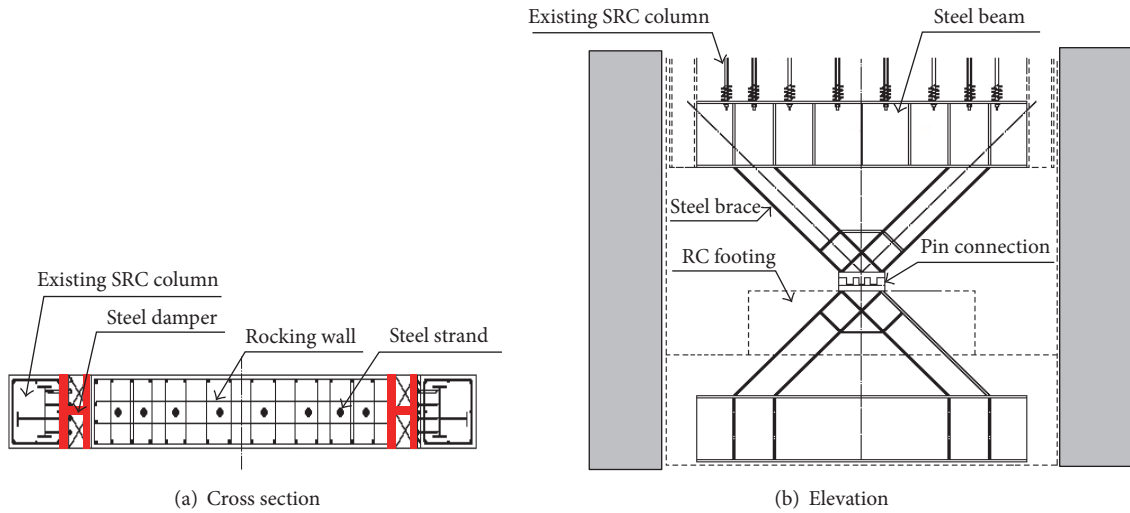


FIGURE 18: Structural retrofitting of rocking walls and steel dampers in Tokyo Institute of Technology (adopted from [41], copyright 2009 Applied Technology Council).

masonry structural system [42, 109–111], shown as in Figure 19. A shake table investigation was conducted to validate the concept of rocking walls as primary seismic systems; as the inherent damping of this system was low, a pair of supplemental steel hysteretic energy dissipating dampers were used at the base of the wall. The results indicated that with careful detailing, not only the damage was eliminated but the structure recenters itself following a large earthquake. They considered that the rocking wall concept can be extended to any rocking wall system.

5.6. *Rocking Timber Structural System.* Loo et al. [51] used a new concept in shear wall design into timber shear wall structure; the new concept involves the use of slip-friction connectors in lieu of traditional hold-down connectors [112], as shown in Figure 20. Slip-friction connectors, originally

developed for the steel framing industry, rely on the mobilization of friction across steel plates to resist loading up to a predetermined threshold. Upon this threshold being exceeded, relative sliding between the steel plates allows the shear wall to be displaced in an inelastic manner. The numerical results suggested that slip-friction connectors hold the promise of being able to effectively protect sheathing, framing, and nail connections from excessive stresses and deformations during earthquake events of design level intensity or higher. Kishiki and Wada also utilized the philosophy of rocking into timber structural system and designed controlled wood wall structural system [113].

5.7. *Rocking Core Wall System.* The numerical results performed by Nielsen et al. [114] showed that the rocking core wall structural system possesses the recentering capacity due

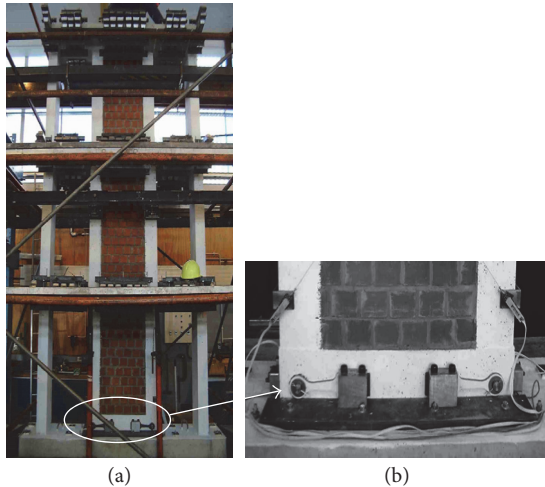


FIGURE 19: Three-story rocking confined masonry wall: (a) the elevation of the wall; (b) details of the energy dissipations (adopted from [42], copyright 2004, 13 WCEE).

to the effect of gravity, and the moment at the foundation of rocking core wall structural system is smaller by 30% than that of common core wall structural system having fixed foundation. Zhou et al. also obtained similar numerical results through compared analysis [115].

6. Self-Centering Seismic Resisting Structural Systems

On the basis of rocking structural system, the posttensioned tendons or strands are included into to externally provide a self-centering capacity to the structural system. The seismic resisting structural system with posttension is called self-centering seismic resisting structural systems (SCSRSS).

6.1. Self-Centering RC Frame System. Priestley and Tao [52] developed a new type of self-centering precast concrete frame using partial debonded prestressing tendons in which the beam can rotate; the beam-column interface is shown as in Figure 21. Cheok and Lew [116] experimentally verified the above-mentioned self-centering precast concrete frame system.

In 1996, Priestley and MacRae developed precast concrete beam-column joint subassembly with two ungrouted posttensioned tendons, shown in Figure 22, and performed experiment under cyclic reversal seismic load; the test results showed that energy absorption of the hysteretic response was larger than expected, and the residual displacements were negligible [53]. El-Sheikh et al. conducted pushover analysis and time history analysis of the developed precast concrete beam-column joint subassembly [117]. Cai et al. [118] developed a kind of new self-centering posttensioned precast concrete beam-column connection in which prestressed bar was used to provide the self-centering capacity to structures and the steel angle clamped at the beam-column joint was used to dissipate the energy. Lu et al. [119] conducted a shake table test of a self-centering reinforced concrete frame; test results indicated that the designed reinforced concrete frame has good

seismic performance and self-centering capacity subjected to earthquake ground motions; the self-centering structures can undergo large deformation with minor residual displacement after the strong earthquake excitations.

Morgen and Kurama developed a new type of friction damper for unbonded posttensioned precast concrete building moment frame structures in seismic regions, shown as in Figure 23; the proposed friction dampers were placed at beam-column joints. The compared test results showed that the dampers can provide a significant amount of supplemental energy dissipation at the beam ends, while the self-centering capability of the structure is preserved [54].

6.2. Self-Centering RC Shear Wall System. Kurama et al. [55, 120–122] utilized unbonded posttensioned tendon or PT bar across horizontal joints to develop precast concrete wall, shown as in Figure 24; the unbonded posttensioned precast walls can soften and undergo large nonlinear lateral displacements with little damage, and the nonlinear behavior is primarily due to the opening of gaps along the horizontal joints; however, the energy dissipation capacity was low. Consequently, Kurama et al. [123, 124] used supplemental viscous damping to reduce the lateral drift of unbonded posttensioned precast concrete walls under earthquakes; the nonlinear dynamic time history analyses showed that the proposed energy dissipation system was effective in reducing the maximum roof drift to prevent significant damage to the walls, and Perez et al. [125, 126] also performed similar experiments and analysis. Smith et al. [127, 128] used the posttensioned tendon or PT bar technology into the hybrid wall which was constructed by stacking rectangular precast concrete wall panels across horizontal joints at the floor levels.

Holden et al. [129, 130] innovated the unbonded posttensioned precast concrete wall proposed by Kurama by adding longitudinal mild steel reinforcement crossing the joint between the walls and the foundation to enhance energy dissipation capacity. Marriott et al. [131] conducted shake table test of the proposed wall system with variable dampers; the test results showed that the proposed wall system had a great self-centering capacity. Sritharan et al. [56, 132] designed a jointed wall system in which two or more single precast walls designed with unbonded posttensioning are connected to each other with the help of special connectors along the vertical joints, as shown in Figure 25.

Panian et al. [133, 134] believed that the shear wall system with posttensioned prestressed tendon has a better economic benefit and seismic result. Furthermore, Stevenson et al. [135] had utilized posttensioned prestress steel bar into the design of shear walls in David Brower Center to resist the potential earthquake. Rahman and Sritharan [136] proposed the calculated model of a self-centering shear wall system. Pennucci et al. [137, 138] proposed the displacement-based design method of precast shear walls with additional dampers. Aaleti and Sritharan [139] proposed a simplified method to characterize the seismic responses of unbonded posttensioned precast wall systems. Erkmen and Schultz [140] performed a series of compared tests to study the self-centering capacity of precast walls. Twigden et al. [141] investigated a single posttensioned concrete wall subjected to

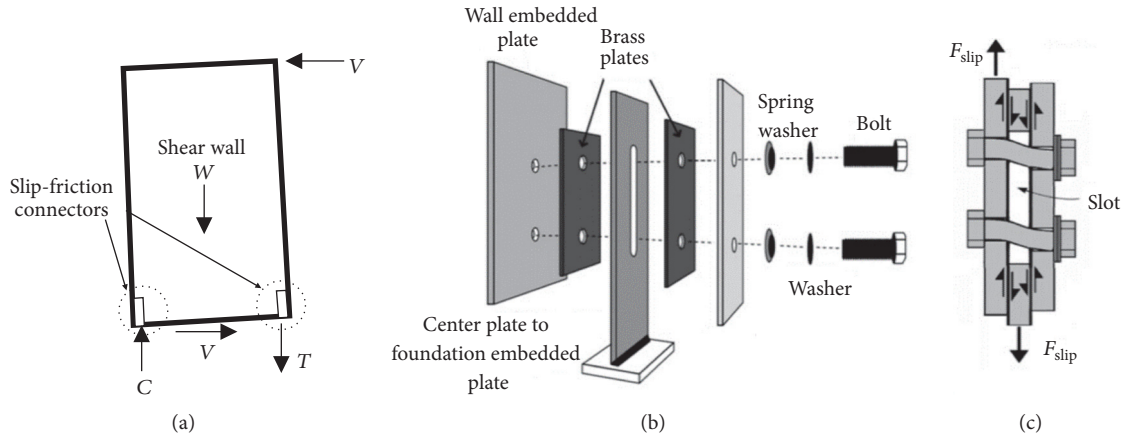


FIGURE 20: Slip-friction connectors with shear walls: (a) capping of lateral force on the shear wall; (b) connector assemblage for the precast concrete wall; (c) activated friction forces. (adopted from [51], copyright 2012 Engineering Structures).

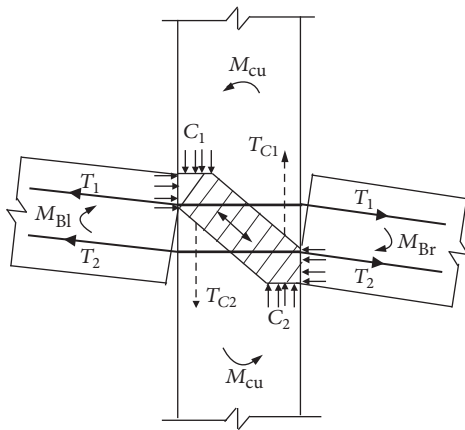


FIGURE 21: Beam-column connection with partially debonded prestressing tendons (adopted from [52], copyright 1993 PCI Journal).

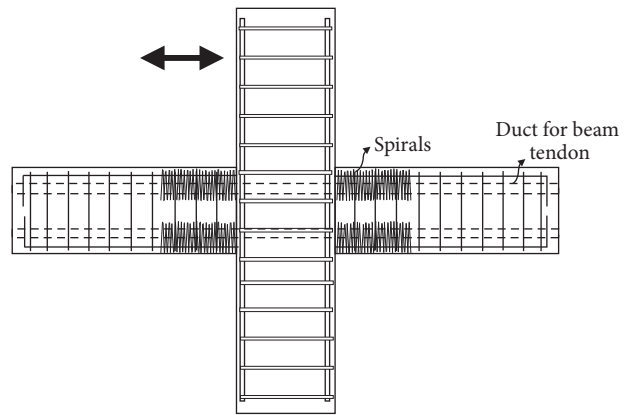


FIGURE 22: Precast concrete beam-column joint subassembly with two ungrouted posttensioned tendons (adopted from [53], copyright 1996 PCI Journal).

pseudostatic cyclic loading, high-speed cyclic loading, free vibration, and dynamic forced-vibration testing.

6.3. *Self-Centering Steel Frame System.* Ricles et al. [57] of Lehigh University designed a new kind of steel beam-column interface connection of moment resisting frames (MRFs) with self-centering capacity using posttension high strength strands, shown as in Figure 26; the top and seat angles are added to provide energy dissipation and redundancy under seismic loading. This new type of connection has the following advantages: (1) field welding is not required; (2) the connection stiffness is similar to that of a welded connection; (3) the connection is self-centering; and (4) significant damage to the MRF is confined to the angles of the connection. Time history analysis results showed that the seismic performance of a posttensioned steel MRF subject to the earthquake records exceeds the performance of an MRF with typical welded connections subject to the same earthquake records. Consequently, many other researchers innovated this new type of steel beam-column connection [66, 142, 143], Rojas et al. [144] added a posttensioned friction

damped connection (PFDC) into the above-mentioned steel beam-column connection to enhance the earthquake energy dissipation capacity.

Sause et al. [64, 145] developed self-centering moment resisting frames (SC-MRFs) and self-centering concentrically braced frame (SC-CBF) systems with the goal of providing adequate nonlinear drift capacity without significant damage or residual drift under the design basis earthquake. Both experimental results and analytical results indicated that all SC-MRFs and SC-CBF possess self-centering behavior, and no significant structural damage occurred. In order to use this new types of MRFs and SC-CBF into design and construction, the performance-based seismic design approach for PT steel frame systems was proposed; seismic performance levels, seismic input levels, structural limit states and capacities, and structural demands for PT frame systems were defined; the design objectives were outlined; design criteria were given; and a step-by-step design procedure was given [65].

Clayton [61] developed the self-centering steel plate shear wall (SC-SPSW) system, shown schematically in Figure 27,

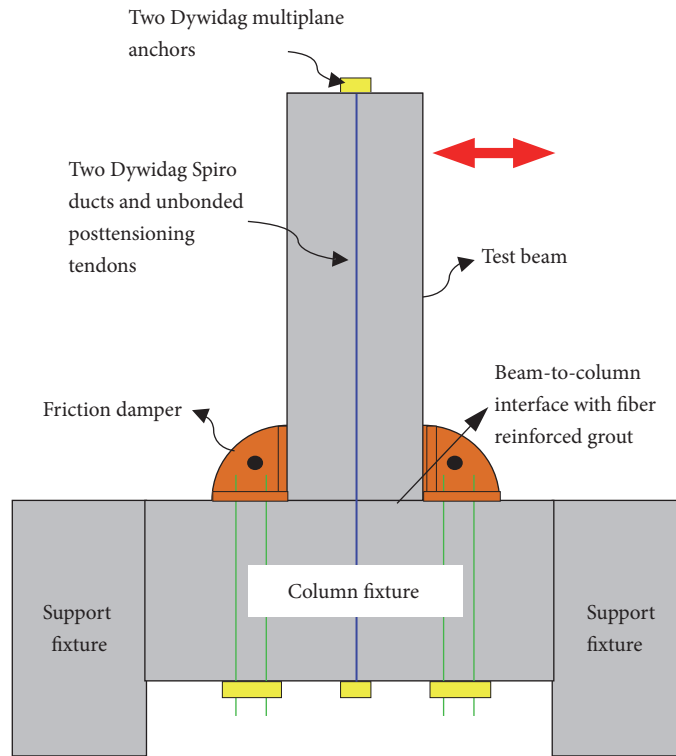


FIGURE 23: Schematic of the columns with damper (adopted from [54], copyright 2004 PCI Journal).

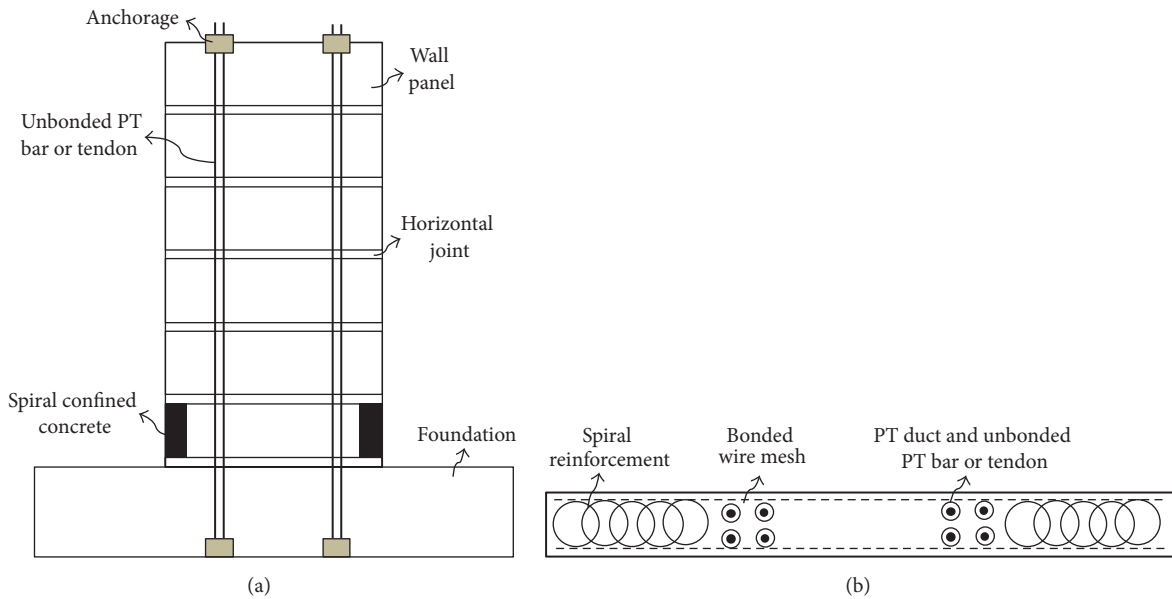


FIGURE 24: Unbonded posttensioned precast wall: (a) elevation; (b) cross section near base. (adopted from [55], copyright 1999 PCI Journal).

which consists of thin steel web plates that resist lateral loads and dissipate energy through the development of diagonal tension field action, just as in conventional SPSWs. However, the moment resisting beam-to-column connections of conventional SPSWs are replaced by posttensioned beam-to-column connections to introduce the recentering capability. Winkley [146] conducted comprehensively experimental

studied in detail, and Clayton et al. [147, 148] proposed design method applicable for the SC-SPSW based on the experiments.

6.4. Self-Centering Masonry Structural Wall System. Wight et al. studied seismic response of partially grouted post-tensioned concrete masonry (PCM) walls with unbonded

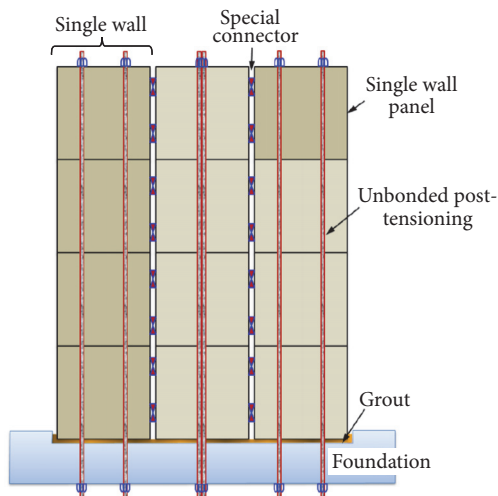


FIGURE 25: The jointed precast wall system (adopted from [56], copyright 2007 Iowa State University).

tendons by means of shake table testing. The shake table tests demonstrated the self-centering nature of posttensioned masonry walls and their ability to achieve large displacements with minimal accumulation of damage [149, 150].

Laursen and Ingham [151, 152] found that the energy dissipation capacity of the posttensioned fully grouted concrete masonry (PCM) wall is limited but can be enhanced by incorporating the internal energy dissipation mild steels with “dog-bone” shape [153, 154]. The energy dissipation device has little influence on the decrease of the ductility capacity [155].

Hassanli et al. investigated the influence of axial stress ratio on seismic behaviors of unbonded posttensioned masonry wall (PT-MW) [156–160]; both experimental and numerical results showed that low axial stress ratio causes higher increase in lateral strength and better displacement ductility, but larger residual drift to PT-MW; the axial stress ratio is limited to 0.15. The wall length is another most influential factor contributing to the rotation and the compression zone length of unbonded PT-MW. Both axial stress ratio and wall length are used to predict the flexural strength of unbonded PT-MW.

6.5. Self-Centering Timber Structural System. The NMIT Arts and Media Building is the new generation of multistory timber structures which employs an advanced damage avoidance earthquake design that is the first in the world for a timber building [62]. As shown in Figure 28, the NMIT seismic system relies on pairs of coupled LVL shear walls that incorporate high strength steel tendons posttensioned through a central duct. The walls are centrally fixed to allow them to rock during a seismic event. A series of U-shaped steel plates placed between the walls form a coupling mechanism and act as dissipators to absorb seismic energy. The design allows the primary structure to remain essentially undamaged while readily replaceable connections act as plastic fuses.

6.6. Self-Centering Bridge Pier Structural System. Cheng developed a self-centering bridge model that can eliminate residual deformations after earthquakes [63]. A bridge model consists of two precast RC bridge columns posttensioned to the concrete deck and foundations by high strength rods, as shown in Figure 29. The hybrid system is extended to bridge engineering, in which precast elements are connected via posttensioning techniques; self-centering and energy dissipating properties are adequately combined to achieve the target maximum displacement with negligible residual displacements; the reliability of hybrid system was confirmed by quasi-static cyclic and nonlinear time history analysis based on lumped plasticity numerical models [161].

Mohammed et al. utilized the concrete segment which has hollow double skin cross section and situated it within the plastic hinge zone of bridge column, to mitigate the damage after earthquake; simultaneously, they used the unbonded PT strands located within the void of the inner skin to provide the self-centering force for bridge column [162–165]. The shaking table test result showed that the residual drift of the bridge column proposed by Ayman and ElGawady was smaller than the conventional RC bridge column [166]. However, the void of the hollow cross section of the proposed bridge column infilled by concrete had better seismic performance because the twist angle was smaller when it was subjected to the bidirectional cyclic loading [167].

Guo et al. [168, 169] developed a self-centering bridge pier system connected by unbonded posttensioned tendons to minimize the residual deformation after the earthquake and mild steel to stably dissipate the earthquake energy.

Dong et al. developed a new type of brace (SC-BRB) for bridge column system; the SC-BRB consists of the traditional buckling restrained brace (BRB) having excellent energy dissipation capacity and the self-centering brace (SC brace). The numerical results demonstrated that the bridge equipped with the SC-BRB system has smaller residual displacement and a moderate energy dissipation capability compared to the ones equipped with traditional BRB and SCB systems [170].

7. Analysis and Design Seismic Behavior of DRSRS System

The high performance damage-resistant seismic resisting structural (DRSRS) system is capable of eliminating the most or full residual deformation when the lateral load is removed. In general, the DRSRS system consists of posttensioned bar (PT) and energy dissipation element (EDE) such that the dominant structural element can be protected through the gap opening mechanism, and the PT is used to eliminate the residual deformation due to the self-centering capacity of it, the EDE is used to dissipate the earthquake energy.

The PTs contain high strength strands, tendons, or bars [57, 68, 171], and the PTs should have high strength and high yield strain. The EDEs consist of hysteretic damping elements, viscous damping elements, and frictional damping elements. Hysteretic damping elements used in self-centering systems include buckling restrain braces [172–174], short yielding elements similar to the buckling restrain braces [175, 176],

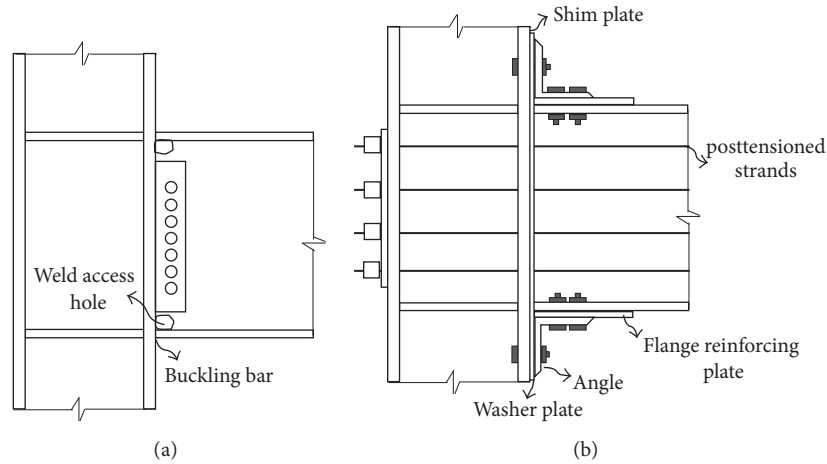
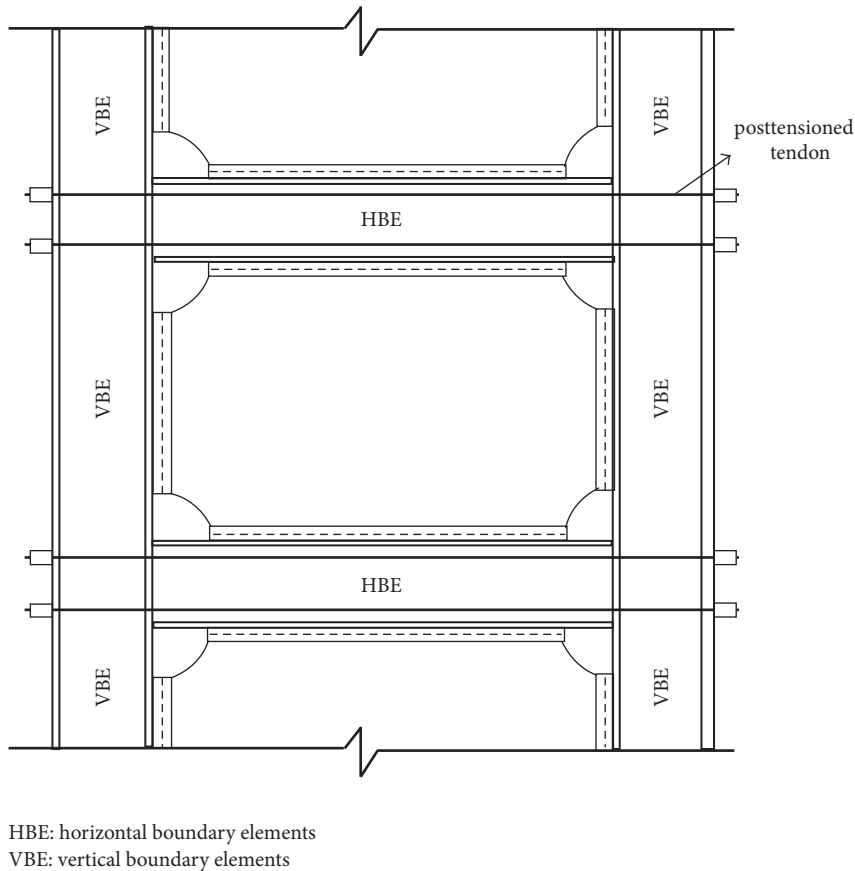


FIGURE 26: Moment connections: (a) pre-Northridge welded connection; (b) posttensioned connection (adopted from [57], copyright 2001 Journal of Structural Engineering, ASCE).



HBE: horizontal boundary elements
 VBE: vertical boundary elements

FIGURE 27: Schematic elevation of intermediate story of SC-SPSW (adopted from [61], copyright 2010 University of Washington).

unbonded mild steel reinforcement [177, 178], steel reinforcement with reduced sections [129], yielding anchor bolts [179], fuse plates [180], yielding end plates [181, 182], yielding angles [69, 183], web hourglass pins [184], and tapered steel cantilever plates [111]. The frictional damping elements used contain frictional slide plate [185], frictional plates with spring washers [186], frictional fuse angle with slotted holes

[187], and viscous fluid damper [188] embedded in the foundation or mounted beside the columns above the foundation.

The hysteretic behavior of structural systems with PT and EDE is as shown in Figure 30; the PT has strong recentering force to pull the whole structural element back, shown in Figure 30(a); however, it has little energy dissipation capacity. The EDEs have great energy dissipation capacity,

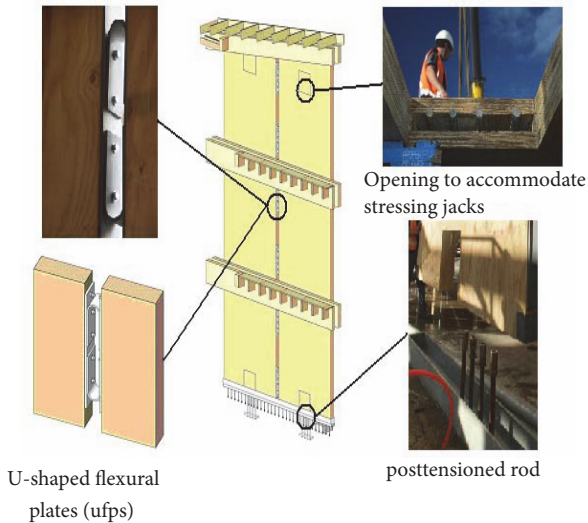


FIGURE 28: LVL coupled shear walls showing posttensioning rods and U-shape flexural plates (UFPs) energy dissipating devices (adopted from [62], copyright 2011, 9th Pacific Conference on Earthquake Engineering).

shown as in Figure 30(b); consequently, they are incorporated into the DRSRS system to enhance the energy dissipation capacity, as shown in Figure 30(c). The overall response of the DRSRS system can be decomposed into the nonlinear elastic contribution from the prestressed tendon or strand (PT) and the bilinear elastoplastic hysteretic contribution from the energy dissipation element (EDE).

7.1. Analysis of Monotonic Seismic Behavior and Design of DRSRS System. To estimate the seismic behavior of DRSRS system in numerical method, some works have been performed. Wight [189] developed a finite element model to assess the monotonic response of posttensioned masonry wall; a reasonable seismic strength and postrocking behavior could be simulated; however, the initial stiffness was overestimated and the strength degradation could not be predicted. Smith et al. [127, 128] attempted to use two different analytical models to evaluate the seismic behaviors of the test structure: a fiber-element model (DRAIN-2DX) and a finite element model (ABAQUS); in the models the fiber beam-column elements are to represent the precast wall panels and truss elements for the unbonded PT steel.

A finite element model was proposed by Ryu et al. [190] to analyze the reversed cyclic seismic response of unbonded posttensioned (PT) fully grouted clay brick walls, and a good comparison between the experimental results and the numerical results was presented. The ABAQUS software was used by Henry et al. [191] to the cyclic lateral load response of the PreWEC which consists of a precast wall with end columns. The precast wall and the end columns are connected by some O-shape connectors. The model could predict good results of the PreWEC system for both the global and local responses.

The multispring element to model the opening and closing of the gap at the critical interface section is used to

predict the seismic behavior of the hybrid pier systems [161, 192]. Li et al. [193] utilized the ABAQUS numerically to study the seismic performance of precast segmental concrete columns reinforced by the posttensioned tendon at the center of the cross section; the opening and closing between the concrete segments are simulated by using the surface to surface contact elements. This finite element method could rationally estimate the self-centering behaviors of test columns subjected to the cyclic loading.

Although the finite element method can effectively evaluate the seismic response, it involves computational difficulties that make it unsuitable for the designer. Kurama et al. [55] assumed that the responses of posttensioned concrete wall can be characterized by some limit states, graphically shown in Figure 31. As the wall displacement increases, the limit states are summarized: (1) decompression state, which identifies the initiation of a gap opening along the horizontal joint between wall and foundation; (2) softening state, which identifies the beginning of significant reduction in the lateral stiffness of the wall due to the gap opening along the horizontal joint and the nonlinear behavior of the concrete in compression; (3) yielding state, which identifies the point at which the posttensioned steel yields; (4) failure state, which identifies the axial-flexure of the wall which occurs as a result of crushing of the confined concrete. Furthermore, the design approach, design objectives shown in Figure 31, design criteria, and seismic design procedure were proposed in detail by Kurama et al. [55].

Perez et al. [126] proposed a trilinear model to predict the nonlinear lateral response of unbonded PT-CWs based on the above-mentioned limit states shown as in Figure 31. Aaleti and Sritharan [139] developed a simplified approach using a trilinear function of the neutral axis depth at a drift of 2%. Hassanli et al. [194] developed an analysis procedure to characterize the lateral force behavior of unbonded posttensioned concrete walls (PT-CWs) based on the mechanics of rocking walls and geometric compatibility conditions; the force-displacement curve of unbonded PT-CW could be predicted with a very good accuracy.

Madan et al. [195] proposed an analytical approach for predicting the nonlinear in-plane flexural behavior of longitudinally posttensioned hollow block masonry shear walls under reversed cyclic lateral loading based on a modified fiber-element model. Kalliontzis and Schultz [196] developed a simplified procedure based on the equivalent stress block analysis and the neutral axis depth (NAD) versus wall rotation relationship proposed by Thomas and Sritharan [197]; the comparison with the finite element method showed that the above-proposed analysis method could adequately capture the experimental force-displacement responses. Furthermore, the in-plane flexural strength of unbonded PT-CW for the designer can be evaluated using the equation proposed by Hassanli et al. [160].

For the self-centering posttensioned steel frame (SCPTSF) systems, the desired limit state progressions of the SCPTSF system using PT bars and PT strands are schematically shown in Figures 32(a) and 32(b). Similar to the self-centering concrete wall system, the limit states of SCPTSF system are summarized as follows [64, 65]: (1) decompression and uplift of the

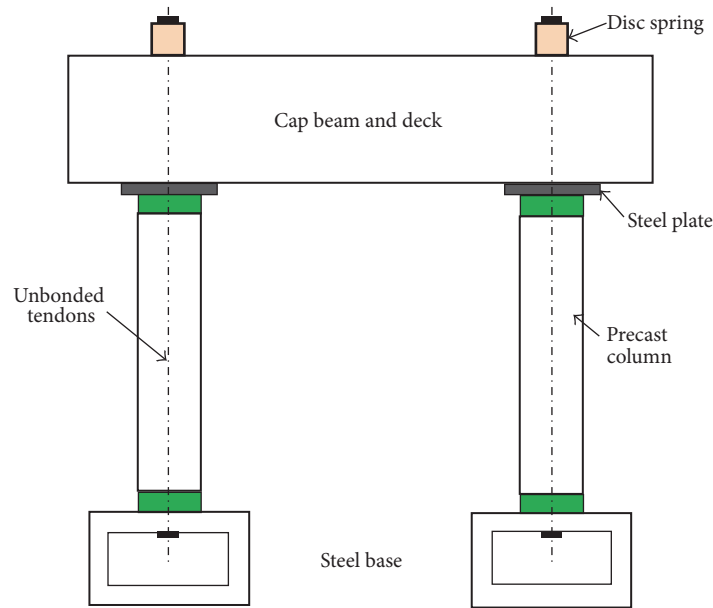


FIGURE 29: A self-centering designed bridge model (adopted from [63], copyright 2008 Engineering Structures).

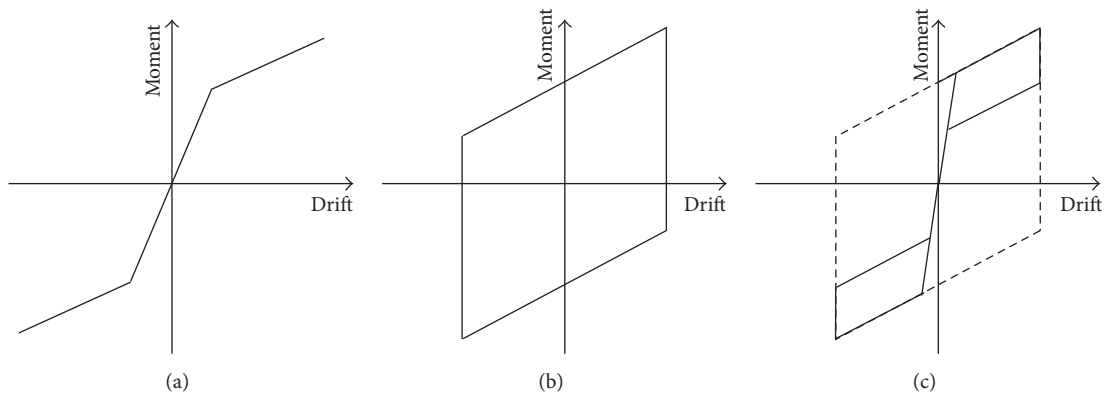


FIGURE 30: Idealized hysteretic behavior of the DRSRS SYSTEM: (a) contribution of prestressed tendon (PT); (b) contribution of energy dissipation element (EDE); (c) moment-drift relationship of DRSRS SYSTEM.

“tension” column at the base; (2) yielding of the PT steel: this limit state progression depends on the type of PT steel used and the type of self-centering system; the rocking steel braced frames with PT bars; this limit state is due to the yielding of PT bar, shown in Figure 32(a); for the moment resisting frame with PT strands, the limit state is caused by system, shown in Figure 32(b); (3) significant yielding of the beams, columns, or braces of self-centering braced frame; (4) failure of the beams, columns, or braces of the self-centering braced frame or PT strand yields. Similar research works were done by Garlock et al. for SCPTSFS [65], as shown in Figures 32(a) and 32(b).

7.2. Residual Deformation of DRSRS System. The DRSRS system is developed to eliminate the residual deformation, and its self-centering capacity is characterized by the resistances due to the restoring force from PT and the force in the energy dissipation element. Two independent response parameters α

and β were considered to control the self-centering capacity of DRSRS system, shown as in Figure 33; the coefficients α and β reflect the postyielding stiffness and the energy dissipation capacity of the DRSRS system, respectively. The influence of the variation of the parameters α and β on the hysteretic behavior and ductility of DRSRS SYSTEM was discussed in detail, the displacement ductility was reduced in all cases for increasing values of α and β [78]; the residual drift decreases with increasing the postyielding stiffness α and decreasing the coefficient β [198].

Christopoulos et al. [199, 200] estimated the residual deformations of the SDOF and MDOF systems which are representative of frame structures, the analysis results showed that the residual deformations are significantly sensitive to the hysteretic rules, the postyielding stiffness, the expected global inelastic mechanisms, and the seismic intensity.

Although the response of self-centering system can be characterized as an idealized flag-shape behavior, it is no

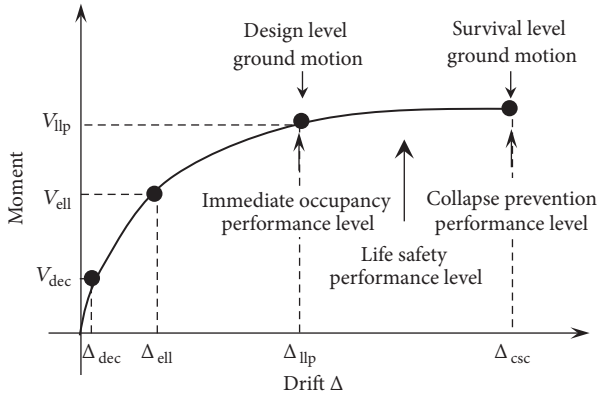


FIGURE 31: Base shear-roof drift relationship and design objectives of SCPTPSWS (adopted from [55], copyright 1999 PCI Journal).

possible to exist for the real entire structure system due to (1) the interaction with other structural and/or non-structural elements in a building [198, 201] and (2) the fact that the responses of the PT member and energy dissipating components cannot be simply added together because energy dissipating elements are only engaged after decompression followed by uplift at the tension zone [202].

The realistic hysteresis response of a self-centering structural system needs to consider the effects of dynamic self-centering capacity. Christopoulos et al. found that the residual drift at the end of dynamic response is typically less than the maximum residual drift of the cyclic hysteretic loop due to the postpeak behavior called the “shake-down” phenomenon, respectively [199, 203]. Henry et al. [202] found that the residual drift ratio, which is defined as the ratio of the residual drift at the end of the dynamic analysis to the maximum static or cyclic residual drift, has no significant correlation with the fundamental period, hysteretic energy dissipation, the ground motion parameters, and the viscous damping of structural system by investigating the dynamic self-centering behavior of the PreWEC concrete wall system. Henry et al. further established the residual drift limit for the real self-centering PreWEC concrete wall system, which is limited to 0.2% for a design level earthquake and 0.3% for a maximum considered earthquake, based on the recommendations by Rahman and Sritharan [136, 178].

For designing the expected self-centering PT concrete member, ACI design guidelines [204] limited the moment contribution from energy dissipating (ED) reinforcement so that it must be less than 50% of the probable flexural moment of the member, and the value proposed in New Zealand [205] is 46%. ITG-5 [206] indicated that the self-centering capacity may be significant loss if the ED device contributes more than 40% of the flexural capacity. Henry et al. [202] found that the PT and ED moment contributions are only critical when the structure is unloaded to zero, meaning that the above-proposed value may result in conservative and unconservative estimation of the self-centering ability of structure.

8. Current Research Challenges in High Performance DRSRS Systems

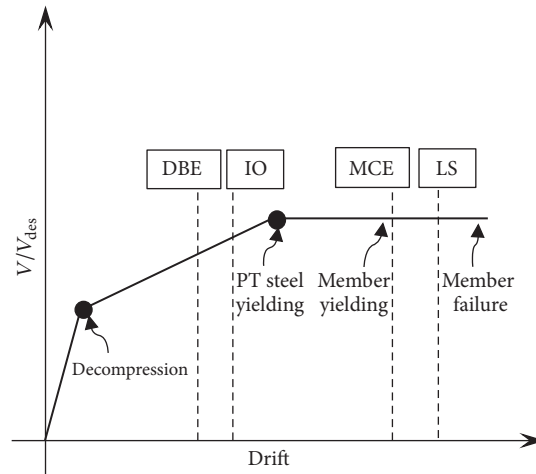
8.1. Floor Diaphragm Connections in DRSRS Systems. In conventional moment resisting frame, the seismic inertial forces are transferred from the floor diaphragm to each beam; however, this mechanism is problematic for the self-centering moment resisting frame, because gap opening at the connections causes a PT frame to “expand” after decompression, as shown in Figure 34 [65]. In the deformed position, the distance between the column centerlines is larger than in the original undeformed position due to connection gap opening, and the PT frame expansion increases with the number of bays, shown in Figure 34(b).

To resolve this problem, many approaches were studied. One detailed approach was proposed in which the floor diaphragm in the moment resisting frame per floor is attached to one beam, and the floor diaphragm and beams in all other bays are noncomposite, which permits the beam to move relatively to the floor diaphragm [65]. It is proposed that the beam-column connection can rock at the beam bottom flange while the beam top flange with the column is preserved all the time [207]. A sliding slab is used to minimize restraints on the expansion of the PT frame, in which a composite slab is rigidly connected to the beams in a single bay of the PT frame, and a sliding device is installed between the floor beams and the beams in other bays such that the slab is allowed to slide [208, 209].

Henry et al. [191, 210] proposed an isolated floor connection to minimize the damage of the floor due to the rocking wall, in which the floor is connected to the end column of the rocking wall system, and the end column is connected with the wall using some O-shape connectors.

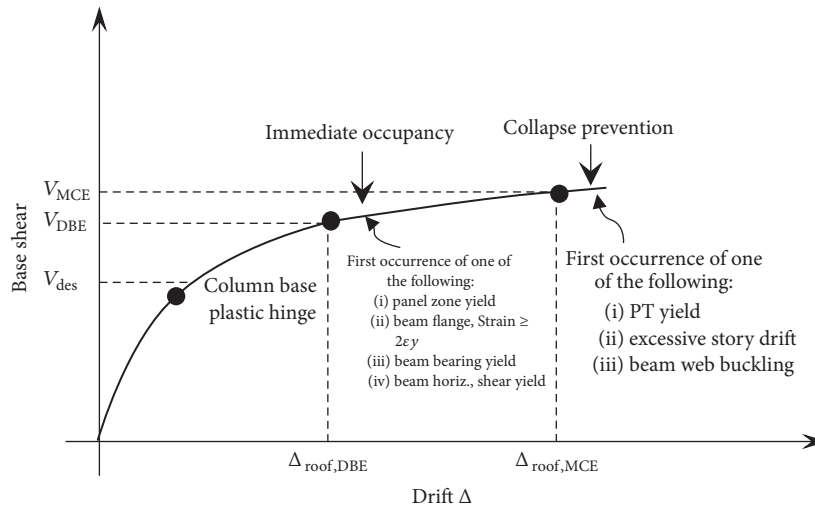
8.2. Higher Mode Effects. Some studies [211, 212] have demonstrated that the higher modes contribute significantly to the force demands of controlled rocking frame members, so rocking does not fully limit the peak seismic forces because of higher mode effects. To limit higher mode effects in controlled rocking steel frames, Wiebe et al. [105, 213–215] proposed two types of higher mode mitigation mechanisms: the first mitigation mechanism is formed by allowing the upper section of the frame to rock, so as to better control the mid-height overturning moment; the second mitigation mechanism is formed by replacing the conventional first-story brace with a self-centering energy dissipative (SCED) brace, so as to better control the base shear. Experimental and numerical results suggested that the proposed mechanisms can enable better capacity design by reducing the variability of peak seismic force demands without causing excessive displacements. Although this approach could reduce the effect, further research is needed on this topic.

8.3. Collapse Safety Assessment. The DRSRS system is developed to reduce or eliminate residual deformation under design seismic level; however, it is still possible to undergo the very rare and intense earthquakes which are not included in the predicted design seismic level, meaning that the DRSRS system may collapse. So far studies on this topic are very



DBE: designed basis earthquake
 IO: immediate occupancy
 MCE: maximum considered earthquake
 LS: life safety

(a)



(b)

FIGURE 32: Base shear-roof drift relationship and design objectives of SCPTPSWS: (a) rocking braced frame with PT bars (adopted from [64], copyright 2006, 5th International Conference on Behavior of Steel Structures in Seismic Areas); (b) moment resisting frame with PT strands (adopted from [65, 66], copyright 2007, 14WCEE, ASCE).

limited [216, 217] and the research on this topic should be ongoing.

8.4. Life Cyclic Cost Assessment. In general, the structural system of self-centering structures is different from conventional structural system, which leads to additional complexity in design, fabrication, and erection of the self-centering system. For example, the anchorage construction of prestress tendon in the foundation is difficult, which may increase construction costs; as a result, even the savings due to the damage-free performance will offset the increased initial cost over the life of the structural system. Thus, life-cycle cost analysis

must consider not only the structural repair costs but all elements of the structure. Studies on quantifying the life-cycle costs of DRSRS system are ongoing [218–221] and need to be further researched in future.

8.5. Building Code Provision for Design. The purpose of the DRSRS system differs from the conventional structure, so the design methodology and the detailing requirement of DRSRS system will be very different from the conventional structure. Despite the attempts to propose design approaches for the precast posttensioned wall system and the posttensioned steel frame system [55, 65], the entire design system which should

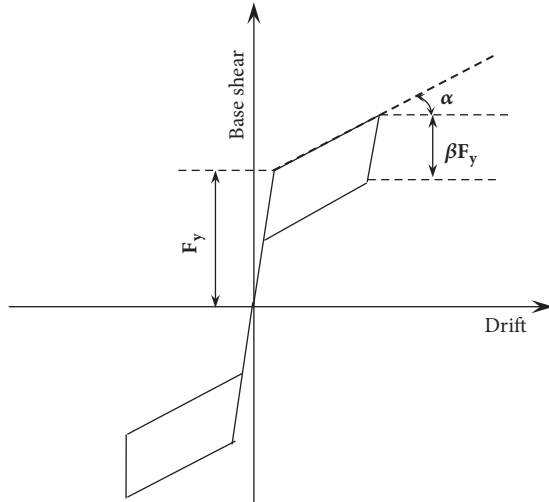


FIGURE 33: Idealized pseudo-force-drift relationship of DRSRS SYSTEM (adopted from [78], copyright 2002 John Wiley & Sons, Ltd).

be included in building code provision to guide the design of DRSRS system in the actual construction has not been established yet.

8.6. Assessment of Influence of Prestress Lost on the Structural System. So far the most popular DRSRS system mainly uses the prestress tendon or strands (PT) to provide the self-centering capacity. As is well known, the prestress methodology has inherent shortcoming “prestress loss.” Consequently, for the DRSRS system using the PT, how to evaluate the loss in the stress of the PT at large lateral deformation and the influence of the loss on seismic performances of structures is the unavoidable problem for using the PT bar, especially the prestress loss that lasts within the long serviceable period of DRSRS system.

9. Current New Research Highlights in High Performance DRSRS Systems

In order to reduce the additional constructed cost due to the difficulties in the detailing requirement such as the anchorage of PT and the designation and to avoid the shortcoming of prestress methodology used in the DRSRS system, recently, another method to develop resilient concrete structures by using the inherent elastic resilient capacity of tensile longitudinal bar was proposed, which should be paid more attention.

In order to obtain enough ductility, Pandey et al. [222–225] experimentally and numerically found that decreasing properties of bond strength of longitudinal bars could greatly improve the ductility of concrete. Tanaka et al. [226] thus used the unbonded high strength steel bar as the tensile longitudinal bar to reinforce the concrete columns; the experimental result showed that the columns exhibited strong self-centering hysteresis response performance; however, the lateral resistance capacity is smaller than that calculated by the current design codes.

To overcome the problems in the method of using PT or unbonded rebars, Sun et al. [227–229] have recently proposed using a special ultrahigh strength rebar (SBPDN 1275/1420 rebar) with low bond strength as longitudinal rebar in concrete members. The SBPDN rebar has a spiral groove on its surface and has a low bond strength of about 1/5 of deformed rebar [79]; the difference between the SBPDN bar and conventional high strength steel bar USD 685 is shown as in Figure 35. The structural detailing of column proposed by Sun et al. is shown in Figure 36; the reinforcement ployout of the proposed column is the same as that of the conventional column; however, due to the poor flexibility of SBPDN rebar, all the SBPDN bars are anchored by steel tie plates which are connected by nuts and bolts at both ends and middle contraflexure section of column. In addition, due to the ultrahigh strength of SBPDN rebar, the column section is confined by two semisteel plates which are connected by nuts and bolts to enhance the shear-resisting capacity such that the shear failure can be avoided.

In recent years, they performed extensive experimental study on the seismic behaviors of rectangular or circular columns reinforced by SBPDN bars; the results demonstrated that concrete columns using SBPDN rebar and steel plates exhibited stable cyclic behavior up to large deformation and very small residual deformation compared to the columns using conventional high strength steel rebar (USD685) [230–234].

Wang et al. proposed sustainable and resilient concrete columns with a large quantity of fly ash (LQFA) reinforced by SBPDN bars in order to use largely fly ash into concrete construction [19, 80]. The experimental results of resilient LQFA concrete columns showed that columns using SBPDN rebar having low bond strength as the longitudinal bar had excellent drift angle up to 0.04 rad~0.05 rad and small residual deformation.

To assess the seismic responses of concrete columns reinforced by SBPDN bars having low bond strength, Funato et al. [79] have proposed an integrated analytical method that could evaluate reasonably cyclic behaviors of concrete columns by considering the slippage of longitudinal bars. This method, however, involves tedious double-loop iteration procedures to find the balanced depth of neutral axis in the targeted column section and to obtain the slippage of longitudinal rebars from their anchorage zones. Consequently, Wang [235] proposed a simple analytical procedure to calculate the structural performances of concrete member reinforced by steel having different bond strength and an equation to calculate the deformation at the maximum lateral load. The comparison results indicated that the proposed analytical method and equation could reasonably assess the seismic responses of concrete column reinforced by steel with different bond strength level.

10. Conclusions

Beacuse the majority of the population in the world lives concentrically in cities, basically, it is consensus to develop high performance seismic resisting structural (DRSRS) system for the sustainable and resilient city. The high cost of repairing

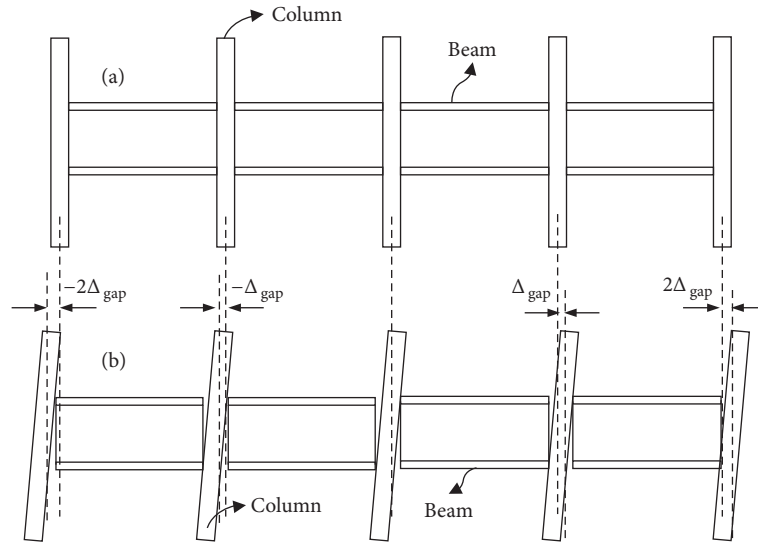


FIGURE 34: Elevation of one floor of a DRSRS SYSTEM: (a) undeformed; (b) deformed configurations (adopted from [65], copyright 2007 Journal of Structural Engineering, ASCE).

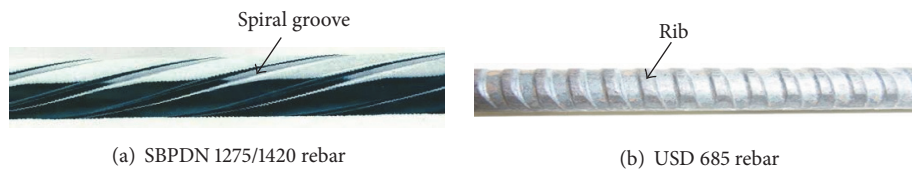


FIGURE 35: The difference between conventional steel and SBPDN steel (adopted from [79], copyright 2012 JCI).

the damaged engineering structures after earthquake compels engineers and researchers to develop the innovative structural system which can eliminate the residual deformation. Based on the principles of “replaceable” and weakening the connections between structural elements such as upper structures and foundation, beam-column intersection, three types of DRSRS systems are developed and ongoingly studied: (1) replaceable structural element (RSE); (2) rocking seismic resisting structural (RSRS) system; (3) self-centering seismic resisting structural (SCRS) system.

This paper summarized the research status and achievements of the existing DRSRS systems; the main conclusions are illustrated as follows:

- (1) The test results indicated that the shear wall system with replaceable coupling beam has smaller post-earthquake damage compared to the conventional shear wall system. The energy dissipation devices can be utilized as either an independently replaceable coupling fuse section or jointly used with replaceable coupling beam together into the shear wall system.
- (2) Rocking seismic resisting structural (RSRS) systems have been extended into bridge engineering structure, RC frame system, steel frame system, RC shear wall system, masonry wall and timber structural system, and core wall system. The extensive experimental study results showed that RSRS systems with types of

energy dissipation devices can greatly limit the damage and the residual deformation of the structural system after loading and can possess good energy dissipation capacity.

- (3) The posttensioned prestress tendon and strand are used to provide the self-centering capacity for the structural system. The dissipation devices are included to enhance energy dissipation capacity of the self-centering seismic structural (SCSS) systems. Extensive experimental programs indicated that the combination of posttensioned tendon and energy dissipation devices could minimize the damage and the residual deformation after loading and behave with good energy dissipation capacity.
- (4) Types of numerical models including the finite element method can reasonably analyze the cyclic and dynamical responses of RSRS and SCSS systems. Some equations have been proposed to design the self-centering shear wall system.
- (5) The residual deformation at the end dynamic response is smaller compared to the static cyclic loading; despite the attempts to propose design limit of residual deformation for the precast concrete shear wall system, the analyses of the residual deformation

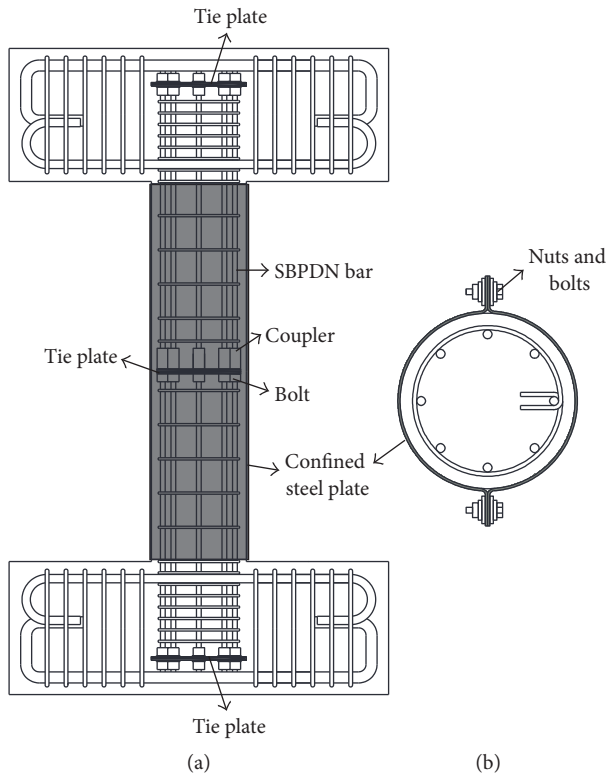


FIGURE 36: The layout of specimen with SBPDN steel bar: (a) elevation of column; (b) cross section (adopted from [80], copyright 2015 JCI).

for other resilient structural forms and for the entire structural system are limited.

- (6) Ongoing challenges for SCSRSS include (1) addressing the floor diaphragm connections to beam and column, (2) mitigating the adverse effect of higher mode effects, (3) collapse safety assessment, (4) life cyclic cost assessment, (5) building code provision for design, and (6) assessment of influence of prestress loss on seismic responses of the structural system.
- (7) The new research viewpoint using high strength steel bar with the low bond strength to develop the resilient structural system which showed stable cyclic behavior up to large deformation and good self-centering capacity should be paid more attention and enthusiasm due to its simple structural technology.

11. Recommendations for Future Studies

- (1) The principle of the replaceable structural element (RSE) should be extensively used to the other structural system, for example, the plastic hinge zones of the column and beam and the foot toes of the wall systems where concrete is crushed due to the compression in usual. Furthermore, the analysis and design approach of RSE should be further studied.
- (2) The analysis and experiments on the response of the entire structural system with self-centering member and other nonstructural elements which may

decrease the self-centering capacity should be further performed.

- (3) The dynamic analysis to determine the residual deformation of the DRSRS system or structural system using other materials such as high strength FRP rebar and SBPDN rebar should be conducted. The design equation of the residual deformation under reversed cyclic seismic loading should be proposed.
- (4) It is not advocated to use complicated and high cost engineering technology to develop DRSRS systems; on the contrary, simple and low-cost technology is encouraged when considering the future popularization specially in the poverty area or country.
- (5) The potential imperfections of DRSRS system such as higher mode effect, the connection of floor and the self-centering member, prestress loss, and degradation in the initial stiffness should be deeply studied and eliminated.
- (6) Due to the simple structural technology and detailing, using high strength steel with poor bond strength property to develop the self-centering structural system is an alternative that should be paid more attention and deeply studied.

Additional Points

Highlights. (i) The current research status and achievement of existing DRSRS systems such as replaceable structural element, rocking structural system, and self-centering structural system for sustainable and resilient city are summarized in detail. (ii) The current research highlights that emerged using high strength steel bar with poor bond strength property to develop DRSRS system are illustrated. (iii) The current research challenges of DRSRS system and the recommendations for the future studies are pointed out and discussed.

Conflicts of Interest

The authors declare that they have no conflicts of interest.

Acknowledgments

The research reported in this paper was supported by the National Natural Science Foundation of China (Project no. 51708288), the National Natural Science Foundation of China (Project no. 41772317), and the Opening Fund of State Key Laboratory of Geohazard Prevention and Geoenvironment Protection of Chengdu University of Technology (Project no. SKLGP2016K005). The authors also would like to express their gratitude and sincere appreciation to the Department of Architecture, Graduate School of Engineering, Kobe University, and College of Civil Engineering at Nanjing Tech University.

References

- [1] United Nations, “Department of Economic and Social Affairs (UNDESA), Population Division, World Population Prospects: The 2015 Revision, Key Findings and Advance Tables,” 2015, <https://esa.un.org/unpd/wpp/>.
- [2] ICLEI, “ICLEI Seoul Strategic Plan 2015-2021: Building a World of Local Actions for a Sustainable Urban Future,” 2015, http://www.iclei.org/fileadmin/user_upload/ICLEI_WS/Documents/Publications/Strategic_Plan_low-res_rev.pdf.
- [3] X. Wang, X. Ding, L. Wang, and Y. Wang, “A study on fast earthquake loss assessment and its application to 2008 Wenchuan M8 earthquake,” *Earthquake Science*, vol. 31, no. 2, pp. 205–211, 2009.
- [4] K. Norio, “The Great Hanshin Awaji Earthquake, Housing,” *Livelihood*, Kobe, K TEC, 2013.
- [5] Y. Honjo, *Summary of damages from and reconstruction measures for, Great East Japan Earthquake*, Kobe, Kobe Institute of Urban Research, 2013.
- [6] Resilient Cities Report, “Global developments in urban adaptation and resilience,” in *The 7th Global Forum on Urban Resilience and Adaptation*, Bonn, Germany, July 2016.
- [7] R. E. Swiss, *Preliminary sigma estimates for first-half 2016: natural catastrophes drive global insured losses to USD 31 billion, Preliminary sigma estimates for first half 2016 natural catastrophes drive global insured losses to USD*, 2016, <http://www.swissre.com/media/newsreleases>.
- [8] R. E. Swiss, 2016, Earthquake Italy, August 2016: First Facts For You At A Glance, <http://www.swissre.com/library/factsheet-publication/earthquake>.
- [9] *Report of the seventh joint planning meeting of NEES/E-defense collaborative research on earthquake engineering*, Berkeley, University of California, Berkeley, PEER, 2010.
- [10] FEMA 273, NEHRP guidelines and commentary for seismic rehabilitation of buildings. Wash, DC, USA, Federal Emergency Management Agency, 1997.
- [11] FEMA 356, Prestandard and commentary for the seismic rehabilitation of buildings. Wash, DC, USA, Federal Emergency Management Agency, 2000.
- [12] FEMA 445, Next-generation performance-based seismic design guidelines: program plan for new and existing buildings. Wash, DC, USA, Federal Emergency Management Agency, 2007.
- [13] T. Zhang, T. Bo, and JY. Lai, “Comparative study of earthquake recovery and reconstruction between China and Japan,” *Journal of Natural Disasters*, vol. 23, no. 4, p. 12, 2004.
- [14] R. P. Jiang, “The influence of the Great Japan Earthquake on Japanese economics,” in *Japanese Studies*, 2011.
- [15] New Zealand Treasury, Budget Policy Statement, New Zealand Government, 2013.
- [16] S. H. Potter, J. S. Becker, D. M. Johnston, and K. P. Rossiter, “An overview of the impacts of the 2010-2011 Canterbury earthquakes,” *International Journal of Disaster Risk Reduction*, vol. 14, pp. 6–14, 2015.
- [17] S. Ohtani, “Development of performance-based design methodology in Japan,” in *Proceedings of International Conference at Bled*, pp. 59–68, 1997.
- [18] K. Kawashima, “Japanese seismic design specifications of highway bridges and the performance-based design,” in *Proceedings of International Conference at Bled*, pp. 229–240, 1996.
- [19] J. H. Wang, T. Takeuchi, T. Koyama, and Y. P. Sun, “Seismic Behavior of Circular Fly Ash Concrete Columns Reinforced by Ultra High Strength Rebar and Steel Plates,” in *Proceedings of the Japan Concrete Institute*, vol. 36, pp. 115–120, 2014.
- [20] M.-C. Tang and R. Manzanarez, “San Francisco-Oakland Bay Bridge design concepts and alternatives,” in *Proceedings of the 2001 Structures Congress and Exposition, Structures 2001*, USA, May 2001.
- [21] P. J. Fortney, B. M. Shahrooz, and G. A. Rassati, “The next generation of coupling beams,” in *Proceedings of the 5th International Conference on Composite Construction in Steel and Concrete V*, pp. 619–630, zaf, July 2004.
- [22] P. J. Fortney, B. M. Shahrooz, and G. A. Rassati, “Large-scale testing of a replaceable “fuse” steel coupling beam,” *Journal of Structural Engineering*, vol. 133, no. 12, pp. 1801–1807, 2007.
- [23] X. L. Lu, Y. Chen, and H. J. Jiang, “Research progress in new replaceable coupling beams,” *Journal of Earthquake Engineering and Engineering Vibration*, vol. 33, no. 1, pp. 9–15, 2013.
- [24] X. D. Ji, D. Liu, and Y. Sun, *Seismic performance assessment of a hybrid coupled wall system with replaceable steel coupling beams versus traditional RC coupling beams*. *Earthquake Engineering & Structural Dynamics*, 2016.
- [25] H.-S. Chung, B.-W. Moon, S.-K. Lee, J.-H. Park, and K.-W. Min, “Seismic performance of friction dampers using flexure of RC shear wall system,” *The Structural Design of Tall and Special Buildings*, vol. 18, no. 7, pp. 807–822, 2009.
- [26] J. Teng, B. Ma, W. Li, H. Zhang, and D. Cao, “Pseudo-static test for coupling beam damper of coupled shear wall structure,” *Jianzhu Jiegou Xuebao/Journal of Building Structures*, vol. 31, no. 12, pp. 92–100, 2010.
- [27] C. X. Mao, Z. Y. Wang, and L. Q. Zhang, “Seismic performance of RC frame-shear wall structure with novel shape memory alloy dampers in coupling beams,” in *Proceeding of 15WCEE*, Lisbon, Portugal, 2012.
- [28] H. Kumagai, K. Shimazaki, and S. Hayashi, “Restoring force characteristics of coupling beam dampers: Coupling beam dampers with low yield point steel (Part 2),” *Journal of Structural and Construction Engineering*, vol. 74, no. 643, pp. 1677–1684, 2009.
- [29] H. Kumagai, *Studies on seismic performance of high-rise buildings with RC shear walls and coupling beam dampers. Doctoral dissertation [Doctoral, thesis]*, Tokyo University, 2010.
- [30] R. M. Lyons, C. Christopoulos, and M. S. Montgomery, “Enhancing the seismic performance of RC coupled wall high-rise buildings with viscoelastic coupling dampers,” in *Proceeding of 15WCEE*, Lisbon, Portugal, 2012.
- [31] H. J. Kim, K. S. Choi, and S. H. Oh, “Comparative study on seismic performance of conventional RC coupling beams and hybrid energy dissipative coupling beams used for RC shear walls,” in *Proceeding of 15WCEE*, Lisbon, Portugal, 2012.
- [32] S. H. Oh, K. Y. Choi, H. J. Kim, and et al., “Experimental validation on dynamic response of RC shear wall systems coupled with hybrid energy dissipative devices,” in *Proceedings of 15WCEE*, p. 1422, Lisbon, Portugal, 2012.
- [33] C. C. McDaniel and F. Seible, “Influence of inelastic tower links on cable-supported bridge response,” *Journal of Bridge Engineering*, vol. 10, no. 3, pp. 272–280, 2005.
- [34] G. A. Rassati, P. J. Fortney, and B. M. Shahrooz, “Design of innovative coupling beams for use in hybrid coupled core wall system,” in *Proceedings of the NSF CMMI Research and Innovation Conference*, Honolulu, Hawaii, USA, 2009.
- [35] G. A. Rassati, P. J. Fortney, B. M. Shahrooz, and P. W. Johnson, “Performance evaluation of innovative hybrid coupled core wall

- systems,” in *Proceedings of the 6th International Conference on Composite Construction in Steel and Concrete*, pp. 479–492, USA, July 2008.
- [36] Y. C. Kurama and Q. Shen, “Seismic design and response evaluation of unbonded post-tensioned hybrid coupled wall structures,” *Earthquake Engineering & Structural Dynamics*, vol. 37, no. 14, pp. 1677–1702, 2008.
- [37] M. Aliaari, *Development of seismic infill wall isolator subframe (SIWIS) system, Doctoral dissertation*, The Pennsylvania State University, 2005.
- [38] M. R. Eatherton, J. F. Hajjar, G. G. Deierlein, and et al., “Controlled rocking of steel-framed buildings with replaceable energy dissipating fuses,” in *The 14th World Conference on Earthquake Engineering*, Beijing, China, 2008.
- [39] J. J. Ajrab, G. Pekcan, and J. B. Mander, “Rocking wall-frame structures with supplemental tendon systems,” *Journal of Structural Engineering*, vol. 130, no. 6, pp. 895–903, 2004.
- [40] T. Hitaka and K. Sakino, “Cyclic tests on a hybrid coupled wall utilizing a rocking mechanism,” *Earthquake Engineering & Structural Dynamics*, vol. 37, no. 14, pp. 1657–1676, 2008.
- [41] A. Wada, Z. Qu, H. Ito, S. Motoyui, H. Sakata, and K. Kasai, “Seismic retrofit using rocking walls and steel dampers,” in *Proceedings of the 2009 ATC and SEI Conference on Improving the Seismic Performance of Existing Buildings and Other Structures*, pp. 1010–1021, USA, December 2009.
- [42] L. A. Toranzo, J. I. Restrepo, and A. J. Carr, “Rocking confined masonry walls with hysteretic energy dissipators and shaketable validation,” in *Proceedings of the Proceeding of 13th World Conference on Earthquake Engineering*, Vancouver, Canada, 2004.
- [43] X. L. Lu, Y. J. Mao, and Y. Chen, “Test and analysis on shear walls with replaceable devices under cyclic loading for earthquake resilient structures,” in *Proceedings of the 9th CUEE and 4th ACEE Joint Conference*, Tokyo, Japan, 2012.
- [44] X. L. Lu, Y. Y. Mao, and Y. Cheng, “Earthquake resilience of tall buildings using replaceable energy dissipation members,” in *Proceedings of the Tenth U.S. National Conference on Earthquake Engineering Frontiers of Earthquake Engineering (10NCEE)*, Anchorage, Alaska, USA, 2014.
- [45] Y. Lu, M. Panagiotou, and I. Koutromanos, “Three-dimensional beam-truss model for reinforced concrete walls and slabs - part I: modeling approach, validation, and parametric study for individual reinforced concrete walls,” *Earthquake Engineering & Structural Dynamics*, vol. 45, no. 9, pp. 1495–1513, 2016.
- [46] X. Lu, Y. Mao, Y. Chen, J. Liu, and Y. Zhou, “New structural system for earthquake resilient design,” *Journal of Earthquake and Tsunami*, vol. 7, no. 3, Article ID 1350013, 2013.
- [47] Z.-H. Deng, Q. Lin, Q. Hu, Z.-M. Pan, and D.-X. Xu, “Test for aseismic behavior of new steel truss coupling beams,” *Zhendong yu Chongji*, vol. 31, no. 1, pp. 76–81, 2012.
- [48] X. Li, Lu. HL, and YL. She, “Experimental study on seismic behavior of replaceable steel truss coupling beams with energy-dissipating devices,” *Journal of Building Structures (Supplement)*, vol. 31, no. 1, pp. 389–394, 2013.
- [49] X. Ji, Y. Wang, Q. Ma, and T. Okazaki, “Cyclic Behavior of Very Short Steel Shear Links,” *Journal of Structural Engineering*, vol. 142, no. 2, p. 04015114, 2016.
- [50] X. Ji, Y. Wang, Q. Ma, and T. Okazaki, “Cyclic Behavior of Replaceable Steel Coupling Beams,” *Journal of Structural Engineering*, vol. 143, no. 2, p. 04016169, 2017.
- [51] W. Y. Loo, P. Quenneville, and N. Chouh, “A numerical study of the seismic behaviour of timber shear walls with slip-friction connectors,” *Engineering Structures*, vol. 34, pp. 233–243, 2012.
- [52] M. J. N. Priestley and J. R. Tao, “Seismic response of precast prestressed concrete frames with partially debonded tendons,” *PCI journal*, vol. 38, no. 1, pp. 58–69, 1993.
- [53] M. J. N. Priestley and G. A. MacRae, “Seismic tests of precast beam-to-column joint subassemblages with unbonded tendons,” *PCI journal*, vol. 41, no. 1, pp. 64–80, 1996.
- [54] B. G. Morgen and Y. C. Kurama, “A friction damper for post-tensioned precast concrete moment frames,” *Precast Concrete Institute journal*, vol. 49, no. 4, pp. 112–133, 2004.
- [55] Y. Kurama, S. Pessiki, R. Sause, and L.-W. Lu, “Seismic behavior and design of unbonded post-tensioned precast concrete walls,” *PCI journal*, vol. 44, no. 3, pp. 72–89, 1999.
- [56] S. Sritharan, S. Aaleti, and D. Thomas, *Seismic analysis and design of precast concrete jointed wall systems. ISU-ERI-Ames Report ERI-07404*, Iowa State University, 2007.
- [57] J. M. Ricles, R. Sause, M. M. Garlock, and C. Zhao, “Post-tensioned seismic-resistant connections for steel frames,” *Journal of Structural Engineering*, vol. 127, no. 2, pp. 113–121, 2001.
- [58] J. Teng, B. Ma, W. Li et al., “Seismic simulation test for coupling beam damper of coupled shear wall structure,” *Jianzhu Jieqou Xuebao/Journal of Building Structures*, vol. 31, no. 12, pp. 101–107, 2010.
- [59] H. Kumagai, “Earthquake response of a high-rise building with reinforced concrete shear walls and coupling beam dampers,” *Research report of Shimizu Corporation*, 2010.
- [60] M. Montgomery and C. Christopoulos, “Experimental validation of viscoelastic coupling dampers for enhanced dynamic performance of high-rise buildings,” *Journal of Structural Engineering (United States)*, vol. 141, no. 5, Article ID 4014145, 2015.
- [61] P. M. Clayton, *Self-centering steel plate shear walls: Development of design procedure and evaluation of seismic performance*, University of Washington, Department of Civil and Environmental Engineering, Seattle, Wash, USA, 2010.
- [62] C. P. Devereux, T. J. Holden, and A. H. Buchanan, “NMIT arts media building-damage mitigation using post-tensioned timber walls,” in *Proceedings of the 9th Pacific Conference on Earthquake Engineering*, Auckland, New Zealand, 2011.
- [63] C.-T. Cheng, “Shaking table tests of a self-centering designed bridge substructure,” *Engineering Structures*, vol. 30, no. 12, pp. 3426–3433, 2008.
- [64] R. Sause, J. M. Ricles, D. Roke, and et al., “Self-centering seismic resistant steel concentrically-braced frames,” in *Proceedings of 5th International Conference on Behaviour of Steel Structures in Seismic Areas*, pp. 85–90, Yokohama, Taylor, 2006.
- [65] M. M. Garlock, R. Sause, and J. M. Ricles, “Behavior and design of posttensioned steel frame systems,” *Journal of Structural Engineering*, vol. 133, no. 3, pp. 389–399, 2007.
- [66] Y.-C. Lin, J. Ricles, R. Sause, and C.-Y. Seo, “Earthquake simulations on a self-centering steel moment resisting frame with web friction devices,” in *Proceedings of the 2009 Structures Congress - Don't Mess with Structural Engineers: Expanding Our Role*, pp. 1364–1373, USA, May 2009.
- [67] Y. Kurama, Q. Shen, and B. Weldon, “Coupling of RC walls using unbonded post-tensioning: application in hybrid construction,” in *Proceedings of the 13th World Conference on Earthquake Engineering*, Vancouver, B.C., Canada, 2004.
- [68] Y. C. Kurama, B. D. Weldon, and Q. Shen, “Experimental evaluation of posttensioned hybrid coupled wall subassemblages,”

- Journal of Structural Engineering*, vol. 132, no. 7, Article ID 002607QST, pp. 1017–1029, 2006.
- [69] Q. Shen and Y. Kurama, “Nonlinear behavior of posttensioned hybrid coupled wall subassemblages,” *Journal Structural Engineering*, vol. 128, no. 10, pp. 1290–1300, 2002.
- [70] Y. C. Kurama and Q. Shen, “Posttensioned hybrid coupled walls under lateral loads,” *Journal of Structural Engineering*, vol. 130, no. 2, pp. 297–309, 2004.
- [71] Q. Shen, Y. C. Kurama, and B. D. Weldon, “Seismic design and analytical modeling of posttensioned hybrid coupled wall subassemblages,” *Journal of Structural Engineering*, vol. 132, no. 7, Article ID 001607QST, pp. 1030–1040, 2006.
- [72] A. M. Memari and M. Aliaari, “Seismic infill wall isolator subframe (SIWIS) system for use in buildings,” *Proc., ATC-17-2 Seismic on Response Modification Technologies for Performance-Based Design*, Los Angeles, Calif, USA, 2002.
- [73] A. M. Memari, “Recent developments in seismic isolation systems for masonry infill and brick veneer walls,” in *Proceedings of the Building Integration Solutions: Proceedings of the Architectural Engineering 2003 Conference*, pp. 258–262, usa, September 2003.
- [74] M. Aliaari and A. M. Memari, “Experimental evaluation of a sacrificial seismic fuse device for masonry infill walls,” *Journal of Architectural Engineering*, vol. 13, no. 2, pp. 111–125, 2007.
- [75] A. M. Memari and M. Aliaari, “Analysis of masonry infilled steel frames with seismic isolator subframes,” *Engineering Structures*, vol. 27, no. 4, pp. 487–500, 2005.
- [76] A. M. Memari and M. Aliaari, “Pushover analysis of masonry infilled steel frames with seismic infill wall isolator subframe (SIWIS) system,” pp. 191–202.
- [77] M. Aliaari and A. M. Memari, “Development of a seismic design approach for infill walls equipped with structural fuse,” *The Open Civil Engineering Journal*, vol. 6, no. 1, pp. 249–263, 2012.
- [78] C. Christopoulos, A. Filiatrault, and B. Folz, “Seismic response of self-centring hysteretic SDOF systems,” *Earthquake Engineering & Structural Dynamics*, vol. 31, no. 5, pp. 1131–1150, 2002.
- [79] Y. Funato, Y. P. Sun, T. Takeuchi, and G. C. Cai, “Modeling and Application of Bond Characteristic of High-strength Reinforcing Bar with Spiral Grooves,” in *Proceedings of the Cai GC. Modeling and Application of Bond Characteristic of High-strength Reinforcing Bar with Spiral Grooves. Proceedings of the Japan Concrete Institute*, vol. 34, pp. 157–162.
- [80] J. H. Wang, T. Takeuchi, T. Koyama, and Y. P. Sun, “Seismic behavior of circular fly ash concrete beam-column reinforced by SBPDN rebars and steel-plate jacketing,” in *Proceedings of the Japan Concrete Institute*, vol. 37, pp. 93–198, 2015.
- [81] G. W. Housner, “The behavior of inverted pendulum structures during earthquakes,” *Bulletin of the Seismological Society of America*, vol. 53, no. 2, pp. 403–417, 1963.
- [82] A. A. Hukelbridge and R. W. Clough, “Preliminary experimental study of seismic uplift of a steel frame,” Tech. Rep., Berkley, University of California, Berkeley, Calif, USA, 1977.
- [83] A. A. Hukelbridge, “Earthquake simulation tests of a nine story steel frame with columns allowed to uplift,” Tech. Rep., Berkeley, University of California, Berkeley, Calif, USA, 1977.
- [84] M. J. N. Priestley, R. J. Evison, and A. J. Carr, “Seismic response of structures free to rock on their foundation,” *Bulletin of the New Zealand Society for Earthquake Engineering*, vol. 11, no. 3, pp. 141–150, 1978.
- [85] J. W. Meek, “Dynamic response of tipping core buildings,” *Earthquake Engineering & Structural Dynamics*, vol. 6, no. 5, pp. 437–454, 1978.
- [86] C.-S. Yim, A. K. Chopra, and J. Penzien, “Rocking response of rigid blocks to earthquakes,” *Earthquake Engineering & Structural Dynamics*, vol. 8, no. 6, pp. 565–587, 1980.
- [87] M. Aslam, W. G. Godden, and D. T. Scalise, “Earthquake rocking response of rigid bodies,” *Journal of the Structural Division*, vol. 106, no. 2, pp. 377–392, 1980.
- [88] I. N. Psycharis and P. C. Jennings, “Rocking of slender rigid bodies allowed to uplift,” *Earthquake Engineering & Structural Dynamics*, vol. 11, no. 1, pp. 57–76, 1983.
- [89] M. J. N. Priestley, F. Seible, and G. M. Calvi, *Seismic Design and Retrofit of Bridges*, John Wiley & Sons, New York, NY, USA, 1996.
- [90] J. B. Mander and C. T. Cheng, “Seismic resistance of bridge piers based on damage avoidance design,” Technical Report MCEER-97-0014, Buffalo: University at Buffalo, The State University of New York. Multidisciplinary Center for Earthquake Engineering Research, 1997.
- [91] M. Mashal, S. White, and A. Palermo, “Concepts and developments for accelerated bridge construction and dissipative controlled rocking,” in *Proceedings of the 15 WCEE*, Lisboa, Portugal, 2012.
- [92] H. Roh, *Seismic behavior of structures using rocking columns and viscous dampers*, Buffalo, University at Buffalo, The State University of New York. Department of Civil, Structural and Environmental Engineering, 2007.
- [93] H. Roh and A. M. Reinhorn, “Nonlinear static analysis of structures with rocking columns,” *Journal of Structural Engineering*, vol. 136, no. 5, pp. 532–542, 2010.
- [94] H. Roh and A. M. Reinhorn, “Modeling and seismic response of structures with concrete rocking columns and viscous dampers,” *Engineering Structures*, vol. 32, no. 8, pp. 2096–2107, 2010.
- [95] H. Y. Cao, P. Pan, S. J. Wu, L. P. Ye, and et al., “Experimental study of connections of frame-rocking wall system,” *Journal of Building Structures*, vol. 33, no. 12, pp. 38–46, 2012.
- [96] M. Midorikawa, T. Azuhata, T. Ishihara, and A. Wada, “Three dimensional shaking table tests on seismic response of reduced-scale steel rocking frames,” in *Proceedings of the 3rd International Conference on Advances in Experimental Structural Engineering*, Earthquake Engineering Research Center, San Francisco, USA, 2009.
- [97] M. Midorikawa, T. Ishihara, T. Azuhata, and et al., *Seismic Behavior of Steel Rocking Frames by Three-Dimensional Shaking Table Tests*, 7 CUEE & 5 IC, Tokyo Institute of Technology, Tokyo, Japan, 2010.
- [98] X. Ma, G. Deierlein, H. Krawinkler, M. Eatherton, and et al., “Large-scale shaking table test of steel braced frame with controlled rocking and energy dissipating fuses,” in *Proceedings of the 9th US National and 10th Canadian Conference on Earthquake Engineering*, Canadian Association for Earthquake Engineering, Ottawa, Canada, 2010.
- [99] M. R. Eatherton, J. F. Hajjar, and G. Deierlein, “Hybrid simulation testing of a controlled rocking steel braced frame system,” in *Proceedings of the 9th US National and 10th Canadian Conference on Earthquake Engineering*, Canadian Association for Earthquake Engineering, Ottawa, Canada, 2010.
- [100] D. L. Anderson, “Effect of foundation rocking on the seismic response of shear walls,” *Canadian Journal of Civil Engineering*, vol. 30, no. 2, pp. 360–365, 2003.
- [101] S. Gajan and B. L. Kutter, “Capacity, settlement, and energy dissipation of shallow footings subjected to rocking,” *Journal of Geotechnical and Geoenvironmental Engineering*, vol. 134, no. 8, pp. 1129–1141, 2008.

- [102] S. Gajan, Physical and numerical modeling of nonlinear cyclic load-deformation behavior of shallow foundations supporting rocking shear walls. Davis, Calif, USA, Dept. of Civil and Environmental Engineering, Univ. of California, 2006.
- [103] S. Gajan and B. L. Kutter, "Effects of moment-to-shear ratio on combined cyclic load-displacement behavior of shallow foundations from centrifuge experiments," *Journal of Geotechnical and Geoenvironmental Engineering*, vol. 135, no. 8, pp. 1044–1055, 2009.
- [104] Y. Lu, "Inelastic behaviour of RC wall-frame with a rocking wall and its analysis incorporating 3-D effect," *The Structural Design of Tall and Special Buildings*, vol. 14, no. 1, pp. 15–35, 2005.
- [105] L. Wiebe and C. Christopoulos, "Mitigation of higher mode effects in base-rocking systems by using multiple rocking sections," *Journal of Earthquake Engineering*, vol. 13, no. 1, pp. 83–108, 2009.
- [106] L. Wiebe, *Mitigation of higher mode effects in self-centering walls by using multiple rocking sections [Master, thesis]*, Master dissertation, Università degli Studi di Pavia, 2008.
- [107] K. J. Mulligan, J. G. Chase, J. B. Mander, and et al., "Hybrid experimental analysis of semi-active rocking wall systems," in *Proceedings of New Zealand Society of Earthquake Engineering (NZSEE)*, Napier, New Zealand, 2006.
- [108] D. Marriott, S. Pampanin, and D. Bull, "Improving the seismic performance of existing reinforced concrete buildings using advanced rocking wall solutions," in *Proceedings of New Zealand Society of Earthquake Engineering (NZSEE)*, Palmerston North, New Zealand, 2007.
- [109] L. A. Toranzo, A. Carr J, and J. I. Restrepo, "Displacement based design of rocking walls incorporating hysteretic energy dissipators," *Passive Energy Dissipation and Active Control of Vibration of Structures*, 2001.
- [110] L. A. Toranzo, *The use of rocking walls in confined masonry structures: a performance-based approach [Doctoral, thesis]*, Department of Civil Engineering, University of Canterbury, New Zealand, 2002.
- [111] L. A. Toranzo, J. I. Restrepo, J. B. Mander, and A. J. Carr, "Shake-table tests of confined-masonry rocking walls with supplementary hysteretic damping," *Journal of Earthquake Engineering*, vol. 13, no. 6, pp. 882–898, 2009.
- [112] C. Bora, M. G. Oliva, S. D. Nakaki, and R. Becker, "Development of a precast concrete shear-wall system requiring special code acceptance," *PCI journal*, vol. 52, no. 1, pp. 122–135, 2007.
- [113] S. Kishiki and A. Wada, "Shaking table test on controlled rocking frame of wooden structures," in *7CUEE & 5ICEE*, pp. 1091–1095, Tokyo Institute of Technology, Tokyo, Japan, 2010.
- [114] G. Nielsen M, I. Almufti, and S. A. Mahin, "Performance of rocking core walls in tall buildings under severe seismic motions," in *Proceedings of the 9th US National and 10th Canadian Conference on Earthquake Engineering*, Ottawa, Canada, 2010.
- [115] Y. Zhou, R. Li, and X. L. Lu, "Earthquake-resilient tall buildings using rocking walls," in *Proceeding of 15 WCEE*, Lisboa, Portugal, 2012.
- [116] G. S. Cheok and H. S. Lew, "Model Precast Concrete Beam-to-Column Connections Subject to Cyclic Loading," *PCI journal*, vol. 38, no. 4, pp. 80–92, 1993.
- [117] M. T. El-Sheikh, R. Sause, S. Pessiki, and L.-W. Lu, "Seismic behavior and design of unbonded post-tensioned precast concrete frames," *PCI journal*, vol. 44, no. 3, pp. 54–71, 1999.
- [118] X. Cai, S. Meng, and W. Sun, "Experimental study on behaviors of beam-column connections for self-centering post-tensioned precast frame," *Tumu Gongcheng Xuebao/China Civil Engineering Journal*, vol. 45, no. 12, pp. 29–37, 2012.
- [119] X. L. Lu, Y. Cui, and J. J. Liu, "Shaking table test of a self-centering reinforced concrete frame," *Journal of Building Structures*, vol. 30, no. 9, pp. 31–35, 2014.
- [120] Y. Kurama, S. Pessiki, R. Sause Lu, and et al., "Analytical modeling and lateral load behavior of unbonded post-tensioned precast concrete Walls," Tech. Rep., Department of Civil and Environmental Engineering, Lehigh University, Bethlehem, PA, USA, 1996.
- [121] Y. C. Kurama, R. Sause, S. Pessiki, and et al., "Seismic design and response evaluation of unbonded post-tensioned precast concrete walls," Tech. Rep., Department of Civil and Environmental Engineering, Lehigh University, 1997.
- [122] Y. Kurama, R. Sause, S. Pessiki, and L.-W. Lu, "Lateral load behavior and seismic design of unbonded post-tensioned precast concrete walls," *ACI Structural Journal*, vol. 96, no. 4, pp. 622–632, 1999.
- [123] Y. C. Kurama, "Seismic design of unbonded post-tensioned precast concrete walls with supplemental viscous damping," *ACI Structural Journal*, vol. 97, no. 4, pp. 648–658, 2000.
- [124] Y. C. Kurama, R. Sause, S. Pessiki, and L.-W. Lu, "Seismic response evaluation of unbonded post-tensioned precast walls," *ACI Structural Journal*, vol. 99, no. 5, pp. 641–651, 2002.
- [125] F. J. Perez, S. Pessiki, and R. Sause, "Experimental and analytical lateral load response of unbonded post tensioned precast concrete walls," in *Center for Advanced Technology for Large Structural Systems (ATLSS). No. 04-11*, Lehigh Univ, Bethlehem, PA, USA, 2004.
- [126] F. J. Perez, R. Sause, and S. Pessiki, "Analytical and experimental lateral load behavior of unbonded posttensioned precast concrete walls," *Journal of Structural Engineering*, vol. 133, no. 11, pp. 1531–1540, 2007.
- [127] B. J. Smith, Y. C. Kurama, and M. J. McGinnis, "Design and measured behavior of a hybrid precast concrete wall specimen for seismic regions," *Journal of Structural Engineering*, vol. 137, no. 10, pp. 1052–1062, 2011.
- [128] B. J. Smith, Y. C. Kurama, and M. J. McGinnis, "Behavior of precast concrete shear walls for seismic regions: comparison of hybrid and emulative specimens," *Journal of Structural Engineering*, vol. 139, no. 11, pp. 1917–1927, 2013.
- [129] T. Holden, J. Restrepo, and J. B. Mander, "Seismic performance of precast reinforced and prestressed concrete walls," *Journal of Structural Engineering*, vol. 129, no. 3, pp. 286–296, 2003.
- [130] J. I. Restrepo and A. Rahman, "Seismic performance of self-centering structural walls incorporating energy dissipators," *Journal of Structural Engineering*, vol. 133, no. 11, pp. 1560–1570, 2007.
- [131] D. Marriott, S. Pampanin, D. Bull, and A. Palermo, "Dynamic testing of precast, post-tensioned rocking wall systems with alternative dissipating solutions," *Bulletin of the New Zealand Society for Earthquake Engineering*, vol. 41, no. 2, pp. 90–103, 2008.
- [132] G. Mannasa and S. Reddy, "A study on analysis and design of precast concrete wall system," in *Proceedings of the International Journal of Advanced Technology and Innovative Research*, vol. 8, pp. 2707–2712, 2016.
- [133] L. Panian, M. Steyer, and S. Tipping, "Post-Tensioned concrete walls for seismic resistance," *Journal of the Post-tensioning Institute*, vol. 5, no. 1, p. 12, 2007.

- [134] L. Panian, M. Steyer, and S. Tipping, "Post-Tensioned shotcrete shear walls," in *Post-Tensioned shotcrete shear walls*, vol. 29, Farmington Hills, Mich, USA, 2007.
- [135] M. Stevenson, L. Panian, and M. Korolyk, "Post-tensioned concrete walls and frames for seismic resistance - a case study of the David Brower Center," in *Proceedings of the SEAOC Annual Convention*, Hawaii, USA, 2008.
- [136] M. A. Rahman and S. Sritharan, "An evaluation of force-based design vs. direct displacement-based design of jointed precast post-tensioned wall systems," *Earthquake Engineering and Engineering Vibration*, vol. 5, no. 2, pp. 285–296, 2006.
- [137] D. Pennucci, "Displacement-based design of precast walls with additional dampers," in *Italy, European School for Advanced Studies in Reduction of Seismic Risk*, ROSE School, University of Pavia, 2008.
- [138] D. Pennucci, G. M. Calvi, and T. J. Sullivan, "Displacement-based design of precast walls with additional dampers," *Journal of Earthquake Engineering*, vol. 13, no. 1, pp. 40–65, 2009.
- [139] S. Aaleti and S. Sritharan, "A simplified analysis method for characterizing unbonded post-tensioned precast wall systems," *Engineering Structures*, vol. 31, no. 12, pp. 2966–2975, 2009.
- [140] B. Erkmen and A. E. Schultz, "Self-centering behavior of unbonded, post-tensioned precast concrete shear walls," *Journal of Earthquake Engineering*, vol. 13, no. 7, pp. 1047–1064, 2009.
- [141] K. M. Twigden, R. S. Henry, and Q. T. Ma, "Dynamic testing of post-tensioned rocking walls," in *Proceedings of the Proceeding of 15th World Conference on Earthquake Engineering*, Lisbon, Portugal, 2012.
- [142] H.-J. Kim and C. Christopoulos, "Friction damped posttensioned self-centering steel moment-resisting frames," *Journal of Structural Engineering*, vol. 134, no. 11, pp. 1768–1779, 2008.
- [143] M. Wolski, J. M. Ricles, and R. Sause, "Experimental study of a self-centering beam-column connection with bottom flange friction device," *Journal of Structural Engineering*, vol. 135, no. 5, pp. 479–488, 2009.
- [144] P. Rojas, J. M. Ricles, and R. Sause, "Seismic performance of post-tensioned steel moment resisting frames with friction devices," *Journal of Structural Engineering*, vol. 131, no. 4, pp. 529–540, 2005.
- [145] R. Sause, J. M. Ricles, and Y. Lin, "Self-centering damage-free seismic-resistant steel frame systems," in *7 CUEE & 5ICEE*, pp. 39–48, Tokyo Institute of Technology, Tokyo, Japan, 2010.
- [146] T. B. Winkley, *Self-centering steel plate shear walls. Large scale experimental investigation*, University of Washington, Department of Civil and Environmental Engineering, Seattle, Wash, USA, 2011.
- [147] P. M. Clayton, T. B. Winkley, J. W. Berman, and L. N. Lowes, "Experimental investigation of self-centering steel plate shear walls," *Journal of Structural Engineering (United States)*, vol. 138, no. 7, pp. 952–960, 2012.
- [148] D. M. Dowden, R. Purba, and M. Bruneau, "Behavior of self-centering steel plate shear walls and design considerations," *Journal of Structural Engineering (United States)*, vol. 138, no. 1, pp. 11–21, 2012.
- [149] G. D. Wight, J. M. Ingham, and M. J. Kowalsky, "Shaketable testing of rectangular post-tensioned concrete masonry walls," *ACI Structural Journal*, vol. 103, no. 4, pp. 587–595, 2006.
- [150] G. D. Wight, M. J. Kowalsky, and J. M. Ingham, "Shake table testing of posttensioned concrete masonry walls with openings," *Journal of Structural Engineering*, vol. 133, no. 11, pp. 1551–1559, 2007.
- [151] P. T. Laursen and J. M. Ingham, "In-plane Response of Posttensioned Concrete Masonry," *Journal of the Structural Engineering Society of New Zealand*, vol. 12, no. 2, pp. 21–39, 1999.
- [152] P. T. Laursen and J. M. Ingham, "Structural Testing of Single-Storey Post-Tensioned Concrete Masonry Walls," *Journal of the Masonry Society*, vol. 19, no. 1, pp. 69–82, 2001.
- [153] P. T. Laursen and J. M. Ingham, "Structural Testing of Enhanced Post-Tensioned Concrete Masonry Walls," *ACI Structural Journal*, vol. 101, no. 6, pp. 852–862, 2004.
- [154] P. T. Laursen and J. M. Ingham, "Structural testing of large-scale posttensioned concrete masonry walls," *Journal of Structural Engineering*, vol. 130, no. 10, pp. 1497–1505, 2004.
- [155] P. T. Laursen, "Seismic performance of prestressed concrete masonry walls incorporating energy dissipators," in *Proceedings of the The 14th World Conference on Earthquake Engineering*, Beijing, China, 2008.
- [156] R. Hassanli, M. A. Elgawady, and J. E. Mills, "Experimental Investigation of In-Plane Cyclic Response of Unbonded Post-tensioned Masonry Walls," *Journal of Structural Engineering (United States)*, vol. 142, no. 5, Article ID 04015171, 2016.
- [157] R. Hassanli, *Behavior of unbonded post-tentioned masonry walls. Doctoral dissertation*, University of South Australia, 2015.
- [158] R. Hassanli, M. A. ElGawady, and J. E. Mills, "Strength and seismic performance factors of posttensioned masonry walls," *Journal of Structural Engineering*, vol. 141, no. 11, 2015.
- [159] J. Abouzar, R. G. Mohammad, A. B. Habib, and et al., *Seismic performance and damage incurred by monolithic concrete self-centering rocking walls under the effect of axial stress ratio. Bulletin Earthquake Engineering*, 2017.
- [160] R. Hassanli, M. A. ElGawady, and J. E. Mills, "In-plane flexural strength of unbonded post-tensioned concrete masonry walls," *Engineering Structures*, vol. 136, pp. 245–260, 2017.
- [161] A. Palermo, S. Pampanin, and G. M. Calvi, "Concept and development of hybrid solutions for seismic resistant bridge systems," *Journal of Earthquake Engineering*, vol. 9, no. 6, pp. 899–921, 2005.
- [162] EI. Mohanmed, SL. Ahmad, and MD. Haitham, "Seismic behavior of segmented frames," in *Proceedings of the 9th US National and 10th Canadian Conference on Earthquake Engineering*, Toronto, Canada, 2010.
- [163] S. L. Ahmad, *Seismic performance of self-centering frames composed of precast post-tensioned concrete encased in FRP tubes; Master dissertation [Master, thesis]*, 2009.
- [164] M. Elgawady, A. J. Booker, and H. M. Dawood, "Seismic behavior of posttensioned concrete-filled fiber tubes," *Journal of Composites for Construction*, vol. 14, no. 5, pp. 616–628, 2010.
- [165] M. D. Haitham, *Seismic behavior and design of segment precast post-tensioned concrete piers. Master dissertation [Master, thesis]*, Washington State University, 2010.
- [166] M. Ayman and M. A. ElGawady, "Damage-resistant segmental double-skin bridge column with replaceable energy dissipaters," in *The Sixth International Conference on Structural Engineering, Mechanics and Computation*, Aapril 2016, M. Ayman, M. A. ElGawady, Damage-resistant segmental double-skin bridge column with replaceable energy dissipaters, The Sixth International Conference on Structural Engineering, Mechanics and Computation, April 2016.
- [167] S. Ichikawa, H. Matsuzaki, A. Moustafa, M. A. Elgawady, and K. Kawashima, "Seismic-resistant bridge columns with ultrahigh-performance concrete segments," *Journal of Bridge Engineering*, vol. 21, no. 9, Article ID 04016049, 2016.

- [168] J. Guo, K. G. Xin, M. H. He, and L. Hu, *Experimental study and analysis on the seismic performance of a self-centering bridge pier. Engineering Mechanics (Suppl I)*, 29, 34, 2012.
- [169] M. H. He, K. G. Xin, and J. Guo, "Local stability study of new bridge piers with self-centering joints," *Engineering Mechanics*, vol. 29, no. 4, pp. 122–127, 2012.
- [170] H. Dong, X. Du, Q. Han, H. Hao, K. Bi, and X. Wang, "Performance of an innovative self-centering buckling restrained brace for mitigating seismic responses of bridge structures with double-column piers," *Engineering Structures*, vol. 148, pp. 47–62, 2017.
- [171] N. Gonner, N. B. Chancellor, R. Sause, J. M. Ricles, and D. Roke, "Experimental Setup, and Testing of Self-Centering Steel Concentrically-Braced Frame Test Structure," Tech. Rep., Lehigh University, Bethlehem, PA, USA, 2010.
- [172] D. J. Miller, L. A. Fahnestock, and M. R. Eatherton, "Development and experimental validation of a nickel-titanium shape memory alloy self-centering buckling-restrained brace," *Engineering Structures*, vol. 40, pp. 288–298, 2012.
- [173] M. Pollino and M. Bruneau, "Seismic testing of a bridge steel truss pier designed for controlled rocking," *Journal of Structural Engineering*, vol. 136, no. 12, pp. 1523–1532, 2010.
- [174] X. Ma, H. Krawinkler, and G. Deierlein, Seismic Design, Simulation and Shake Table Testing of Self-Centering Braced Frame with Controlled Rocking and Energy Dissipating Fuses, Stanford University: Stanford, CA, USA, 2011.
- [175] Z. Sun and C. C. Chang, "Structural damage assessment based on wavelet packet transform," *Journal of Structural Engineering*, vol. 128, no. 10, pp. 1354–1361, 2002.
- [176] A. Maurya and M. R. Eatherton, "Self-centering beams with resilient seismic performance," in *Proceedings of the Structures Congress 2014*, pp. 2442–2453, USA, April 2014.
- [177] A. Palermo, S. Pampanin, and D. Marriott, "Design, modeling, and experimental response of seismic resistant bridge piers with posttensioned dissipating connections," *Journal of Structural Engineering*, vol. 133, no. 11, pp. 1648–1661, 2007.
- [178] M. A. Rahman and S. Sritharan, "Performance-based seismic evaluation of two five-story precast concrete hybrid frame buildings," *Journal of Structural Engineering*, vol. 133, no. 11, pp. 1489–1500, 2007.
- [179] T. Takamatsu, H. Tamai, T. Yamanishi, and A. Matsuo, "Self-centering performance of non-slip-type exposed column base," in *Proceedings of the 5th International Conference on Behaviour of Steel Structures in Seismic Areas - Stessa 2006*, pp. 357–362, jpn, August 2006.
- [180] X. Ma, E. Borchers, A. Peña, H. Krawinkler, and G. Deierlein, *Design and Behavior of Steel Shear Plates with Openings as Energy-Dissipating Fuses*, Stanford University, Stanford, CA, USA, 2010.
- [181] M. Midorikawa, T. Azuhata, T. Ishihara, and A. Wada, "Shaking table tests on seismic response of steel braced frames with column uplift," *Earthquake Engineering & Structural Dynamics*, vol. 35, no. 14, pp. 1767–1785, 2006.
- [182] A. Wada, S. Yamada, O. Fukuta, and M. Tanigawa, "Passive Controlled Slender Structures Having Special Devices at Column Connections," in *Proceedings of the 7th International Seminar on Seismic Isolation, Passive Energy Dissipation and Active Control of Vibrations of Structures*, Assisi, Italy, 2001.
- [183] M. M. Garlock, J. M. Ricles, and R. Sause, "Experimental studies of full-scale posttensioned steel connections," *Journal of Structural Engineering*, vol. 131, no. 3, pp. 438–448, 2005.
- [184] G. Vasdravellis, T. L. Karavasilis, and B. Uy, "Large-scale experimental validation of steel posttensioned connections with web hourglass pins," *Journal of Structural Engineering (United States)*, vol. 139, no. 6, pp. 1033–1042, 2013.
- [185] M. Wolski, J. M. Ricles, and R. Sause, "Seismic resistant self-centering steel moment resisting frames with bottom flange friction devices," in *Proceedings of the 5th International Conference on the Behavior of Steel Structures in Seismic Areas (STESSA '06)*, pp. 481–487, Yokohama, Japan, August 2006.
- [186] Y.-C. Lin, R. Sause, and J. Ricles, "Seismic performance of a large-scale steel self-centering moment-resisting frame: MCE hybrid simulations and quasi-static pushover tests," *Journal of Structural Engineering (United States)*, vol. 139, no. 7, pp. 1227–1236, 2013.
- [187] C. Christopoulos, R. Tremblay, H.-J. Kim, and M. Lacerte, "Self-centering energy dissipative bracing system for the seismic resistance of structures: Development and validation," *Journal of Structural Engineering*, vol. 134, no. 1, pp. 96–107, 2008.
- [188] R. Trmblay, L. P. Poirier, N. Bouaanani, M. Leclerc, and V. Rene, "Innovative viscously damped rocking braced steel frames," in *Proceedings of the Proceeding of 14 WCEE*, Beijing, China, 2008.
- [189] G. Wight, *Seismic performance of a post-tensioned concrete masonry wall system [Ph.D. thesis]*, University of Auckland, New Zealand, 2006, Ph.D dissertation.
- [190] D. Ryu, A. C. Wijeyewickrema, M. A. Elgawady, and M. A. K. M. Madurapperuma, "Effects of tendon spacing on in-plane behavior of posttensioned masonry walls," *Journal of Structural Engineering*, vol. 140, no. 4, Article ID 4013096, 2014.
- [191] R. S. Henry, S. Sritharan, and J. M. Ingham, "Finite element analysis of the PreWEC self-centering concrete wall system," *Engineering Structures*, vol. 115, pp. 28–41, 2016.
- [192] H. A. Spieth, A. J. Carr, and A. G. Murahidy, "Modelling of post-tensioned precast reinforced concrete frame structures with rocking beam-column connections," in *Proceedings of the NZSEE Conference*, Rotorua, New Zealand, 2004.
- [193] C. Li, H. Hao, and K. Bi, "Numerical study on the seismic performance of precast segmental concrete columns under cyclic loading," *Engineering Structures*, vol. 148, pp. 373–386, 2017.
- [194] R. Hassanli, M. A. ElGawady, and J. E. Mills, "Force-displacement behavior of unbonded post-tensioned concrete walls," *Engineering Structures*, vol. 106, pp. 495–505, 2016.
- [195] A. Madan, A. M. Reinhorn, and J. B. Mander, "Fiber-element model of posttensioned hollow block masonry shear walls under reversed cyclic lateral loading," *Journal of Structural Engineering*, vol. 134, no. 7, pp. 1101–1114, 2008.
- [196] D. Kalliontzis and A. E. Schultz, "Characterizing the In-Plane Rocking Response of Masonry Walls with Unbonded Posttensioning," *Journal of Structural Engineering (United States)*, vol. 143, no. 9, Article ID 04017110, 2017.
- [197] D. J. Thomas and S. Sritharan, "An evaluation of seismic design guidelines proposed precast jointed wall systems," ISU-ERI-Ames Rep ERI-04643, Dept. of Civil, Construction, and Environmental Engineering, Iowa State Univ, 2004.
- [198] M. R. Eatherton and J. F. Hajjar, "Residual drifts of self-centering systems including effects of ambient building resistance," *Earthquake Spectra*, vol. 27, no. 3, pp. 719–744, 2011.
- [199] C. Christopoulos, S. Pampanin, and M. J. N. Priestley, "Performance-based seismic response of frame structures including residual deformations, part I: single-degree of freedom systems," *Journal of Earthquake Engineering*, vol. 7, no. 1, pp. 97–118, 2003.

- [200] S. Pampanin, C. Christopoulos, and M. J. N. Priestley, "Performance-based seismic response of frame structures including residual deformations. Part II: multi-degree of freedom systems," *Journal of Earthquake Engineering*, vol. 7, no. 1, pp. 119–147, 2003.
- [201] R. S. Henry, S. Aaleti, S. Sritharan, and J. M. Ingham, "Seismic analysis of a low-damage Precast Wall with End Columns (PreWEC) including interaction with floor diaphragms," *Journal of the Structural Engineering Society New Zealand (SESOC)*, vol. 25, no. 1, pp. 69–81, 2012.
- [202] R. S. Henry, S. Sritharan, and J. M. Ingham, "Residual drift analyses of realistic self-centering concrete wall systems," *Earthquake and Structures*, vol. 10, no. 2, pp. 409–428, 2016.
- [203] G. A. Macrae and K. Kawashima, "Post-earthquake residual displacements of bilinear oscillators," *Earthquake Engineering & Structural Dynamics*, vol. 26, no. 7, pp. 701–716, 1997.
- [204] ACI Innovation Task Group 5, Requirements for Design of a Special Unbonded Post-Tensioned Precast Shear Wall Satisfying ACI ITG-5.1 (ITG 5.2-09), American Concrete Institute, Farmington Hills, MA, USA, 2009.
- [205] NZS 3101, Concrete Structures Standard, Wellington, New Zealand, Standards New Zealand, 646, 2006.
- [206] ACI Innovation Task Group 5, Acceptance criteria for special unbonded post-tensioned precast structural walls based on validation testing (ITG 5.1-07), American Concrete Institute, Farmington Hills, MI, USA, 2007.
- [207] D. M. Dowden and M. Bruneau, "NewZ-BREAKSS: Post-tensioned rocking connection detail free of beam growth," *Engineering Journal*, vol. 48, no. 2, pp. 153–158, 2011.
- [208] C.-C. Chou and J.-H. Chen, "Seismic design and shake table tests of a steel post-tensioned self-centering moment frame with a slab accommodating frame expansion," *Earthquake Engineering & Structural Dynamics*, vol. 40, no. 11, pp. 1241–1261, 2011.
- [209] C.-C. Chou and J.-H. Chen, "Development of floor slab for steel post-tensioned self-centering moment frames," *Journal of Constructional Steel Research*, vol. 67, no. 10, pp. 1621–1635, 2011.
- [210] R. S. Henry, *Self-centering precast concrete walls for buildings in regions with low to high seismicity. PhD thesis [Ph.D. thesis]*, Civil and Environmental Engineering, Auckland, University of Auckland, 2011.
- [211] D. Roke, R. Sause, J. M. Ricles, and N. Gonner, Damage-free seismic-resistant self-centering steel concentrically-braced frames. Proc., STESSA 2009, Taylor & Francis, London, 2009.
- [212] M. Eatherton and J. Hajjar, "Large-scale cyclic and hybrid simulation testing and development of a controlled-rocking steel building system with replaceable fuses," Tech. Rep., Dept. of Civil and Env. Eng., Univ. of Illinois at Urbana-Champaign, 2010.
- [213] L. Wiebe, *Design of controlled rocking steel frames to limit higher mode effects. Doctoral dissertation*, University of Toronto, 2013.
- [214] L. Wiebe, C. Christopoulos, R. Tremblay, and M. Leclerc, "Mechanisms to limit higher mode effects in a controlled rocking steel frame. 1: Concept, modelling, and low-amplitude shake table testing," *Earthquake Engineering & Structural Dynamics*, vol. 42, no. 7, pp. 1053–1068, 2013.
- [215] L. Wiebe, C. Christopoulos, R. Tremblay, and M. Leclerc, "Mechanisms to limit higher mode effects in a controlled rocking steel frame. 2: Large-amplitude shake table testing," *Earthquake Engineering & Structural Dynamics*, vol. 42, no. 7, pp. 1069–1086, 2013.
- [216] E. Tahmasebi, N. B. Chancellor, R. Sause, J. M. Ricles, A. L. Joó, and G. Akbas, "Collapse Performance of Steel Self-Centering Braced Frame Systems," in *In Proceedings of the 7th International Conference on Behavior of Steel Structures in Seismic Areas*, pp. 9–11, Santiago, Chile, 2012.
- [217] E. Tahmasebi, R. Sause, J. M. Ricles, N. B. Chancellor, and T. Akbas, "Probabilistic collapse performance assessment of self-centering concentrically braced frames," in *Proceedings of the 10th U.S. National Conference on Earthquake Engineering: Frontiers of Earthquake Engineering, NCEE 2014*, usa, July 2014.
- [218] G. MacRae, "Low Damage construction Some Systems Issues," in *Proceedings of the In Proceedings of the 10th International Conference on Urban Earthquake Engineering*, Tokyo, Japan, 2013.
- [219] D. A. Roke, A. Chandra, Q. Huang, and K. Sett, "Methodology for Life Cycle Cost Assessment of Self-Centering Concentrically Braced Frame Systems," in *Proceedings of the In Proceedings of the 10th International Conference on Urban Earthquake Engineering*, Tokyo, Japan, 2013.
- [220] G. Deodatis, B. Ellingwood, and D. Frangopol, *Safety, Reliability, Risk and Life-Cycle Performance of Structures and Infrastructures*, CRC Press, 2014.
- [221] M. Dyanati, Q. Huang, and D. A. Roke, "Structural and nonstructural performance evaluation of self-centering, concentrically braced frames under seismic loading," in *Proceedings of the Structures Congress 2014*, pp. 2393–2404, USA, April 2014.
- [222] G. R. Pandey and H. Mutsuyoshi, "Seismic damage mitigation of reinforced concrete bridge piers by unbonding longitudinal reinforcements," in *Proceedings of the Proceeding of 13WCEE, No.154*, Vancouver, Canada, 2004.
- [223] G. R. Pandey, H. Mutsuyoshi, T. Maki, and H. Uchibori, "Numerical study on seismic behavior of RC bridge piers with bond controlled reinforcement," in *Proceedings of the Uchibori H. Numerical study on seismic behavior of RC bridge piers with bond controlled reinforcement. Proceeding of JCI*, vol. 26, pp. 1207–1212, 2004.
- [224] G. R. Pandey and H. Mutsuyoshi, "Seismic performance of reinforced concrete piers with bond-controlled reinforcements," *ACI Structural Journal*, vol. 102, no. 2, pp. 295–304, 2005.
- [225] G. R. Pandey, H. Mutsuyoshi, and T. Maki, "Seismic performance of bond controlled RC columns," *Engineering Structures*, vol. 30, no. 9, pp. 2538–2547, 2008.
- [226] M. Tanaka, F. Esaki, and M. Ono, "Hysteresis response of R/C column with high strength unbonded longitudinal reinforcing bars," in *Proceedings of the Japan Concrete Institute*, vol. 26, pp. 181–186, 2004.
- [227] Y. P. Sun, G. C. Cai, and T. Takeshi, "Seismic behavior and performance-based design of resilient concrete columns," *Applied Mechanics and Materials*, vol. 438–439, pp. 1453–1460, 2013.
- [228] S. M. Nakai, Y. P. Sun, and T. Takeuchi, "Effects axial load level and longitudinal steel ratio on seismic performance of RC Columns reinforced by ultra-high strength rebar," in *Proceedings of the Japan Concrete Institute*, pp. 33–157, 2011, [in Japanese].
- [229] M. Tani, YP. Sun, and T. Fujinaga, "Experimental Study of Concrete Columns with High Resilience," in *Proceedings of the Japan Concrete Institute*, pp. 31–565, 2009, [in Japanese].
- [230] S. Y. Kittaka, M. Tani, and Y. P. Sun, "Study on the bending-shear properties of RC Columns reinforced with ultra-high-strength rebar," in *Proceedings of the Japan Concrete Institute*, vol. 32, pp. 79–84, 2010.

- [231] Y. P. Sun and T. Takeuchi, “Fundamental Study of Earthquake-resilient Concrete Columns,” in *Proceedings of the Japan Concrete Institute*, vol. 35, pp. 1501–1506, 2013, [in Japanese].
- [232] G. C. Cai and Y. Sun, “Experimental Study of Seismic Performance of Circular Concrete Columns with High Yield Strength and Low Bond Strength rebars,” in *Proceedings of the Japan Concrete Institute*, vol. 35, pp. 145–150, 2013.
- [233] G. C. Cai, *Seismic Performance and Evaluation of Resilient Circular Concrete Columns. Doctoral dissertation [Doctoral, thesis]*, Kobe University, 2014.
- [234] S. Grigor, Y. Tanaka, T. Takeuchi, and Y. P. Sun, “Seismic Behavior and Assessment of Circular Concrete Columns Reinforced by Ultra-High Strength Rebars,” in *Proceedings of the Japan Concrete Institute*, vol. 38, pp. 193–198, 2016.
- [235] J. H. Wang, *Seismic behavior and evaluation of concrete members made of a large quantity of fly ash. Doctoral dissertation [Doctoral, thesis]*, Kobe University, 2016.

Research Article

Nonlinear Dynamic Analysis of High-Voltage Overhead Transmission Lines

Meng Zhang ¹, Guifeng Zhao ¹, and Jie Li ^{2,3}

¹School of Civil Engineering, Zhengzhou University, Zhengzhou 450001, China

²College of Civil Engineering, Tongji University, Shanghai 200092, China

³State Key Laboratory for Disaster Reduction in Civil Engineering, Tongji University, Shanghai 200092, China

Correspondence should be addressed to Guifeng Zhao; gfzhao@zzu.edu.cn

Received 24 July 2017; Revised 15 February 2018; Accepted 8 March 2018; Published 19 April 2018

Academic Editor: Songye Zhu

Copyright © 2018 Meng Zhang et al. This is an open access article distributed under the Creative Commons Attribution License, which permits unrestricted use, distribution, and reproduction in any medium, provided the original work is properly cited.

According to a generalized Hamilton's principle, three-dimensional (3D) nonlinear vibration equations for overhead transmission lines that consider geometric nonlinearity are established. Based on the characteristics of an actual transmission line, the 3D equations are simplified to two-dimensional equations, and the nonlinear vibration behavior of transmission lines is investigated by combining theoretical analysis with numerical simulation. The results show that transmission lines have inherently nonlinear vibration characteristics. When in free vibration, a transmission line can undergo nonlinear internal resonance, even when its initial out-of-plane energy is relatively low; as its initial out-of-plane energy increases, the coupling of in-plane and out-of-plane vibration becomes stronger. When forced to vibrate by an external excitation, due to the combined action of internal and primary resonance, the vibration energy of a transmission line transfers from the out-of-plane direction to the in-plane direction that is not directly under the excitation, resulting in an increase in the dynamic tension and the displacement amplitude of the transmission line. Increasing damping can consume the vibration energy of a transmission line but cannot prevent the occurrence of internal resonance.

1. Introduction

High-voltage overhead transmission lines (HVOTLs) are important carriers within power systems, and their safety directly affects the normal operation of the whole power system. Currently, aluminum conductor steel-reinforced (ACSR) cables are the most widely used transmission lines in engineering applications. ACSR cables, characterized by their light weight, small damping, and long spans, can only bear axial tension. Generally, the vibration of a transmission line in the plane where the transmission line is located under the action of gravity is referred to as in-plane vibration, and the vibration in the plane vertical to the aforementioned plane is referred to as out-of-plane vibration. A transmission line is often considered as a single-cable structure in calculation. According to the suspended cable theory [1], the in-plane stiffness of a transmission line is a result of its internal force, and the out-of-plane stiffness of a transmission line is relatively low. Therefore, the vibration of a transmission

line exhibits conspicuous “large displacement, small-strain” geometrically nonlinear characteristics. In particular, when induced by wind and rain or strong wind, transmission lines are more prone to relatively strong nonlinear vibration. In severe cases, such vibration can cause damage to transmission lines. Therefore, an in-depth investigation of the nonlinear vibration of HVOTLs is of great significance.

Research on cables has progressed from statics to dynamics and from the linear theory to the nonlinear theory [1–14]. In the static theory, cables are viewed as two-force bars with an aim to simplify calculation. As a result, the results of calculation based on the static theory differ relatively significantly from the actual situation [1, 2]. In comparison, the natural frequencies of the out-of-plane and in-plane vibration of a suspended cable obtained based on the linear dynamic theory of cables are relatively accurate. Moreover, it can also be derived from the linear dynamic theory of cables that out-of-plane and in-plane modes of vibration are completely independent of one another [3]. However, cables are flexible

structures; consequently, their motion exhibits significantly nonlinear motion characteristics and very complex forms that are a result of the combined action of external and internal resonance. In addition, the geometric and physical parameters of cables also have an impact on their dynamic response [4–14]. Evidently, even the linear dynamic theory cannot accurately describe the forms of motion of cables. It is irrefutable that the wind-induced vibration response of long-span, lightweight, and small-damping transmission lines has inherently nonlinear characteristics [15–24]. However, the current design specification still requires the use of the linear static theory of suspended cables to design transmission lines, which clearly cannot meet the engineering demand. The abovementioned linear design theory is easily mastered and applied in engineering, but its shortcomings are also obvious. For example, it assumes that the relationship between the static load and the response of the whole line is a linear function in calculations, which obviously does not conform to the nonlinear mechanical properties of a transmission line. Furthermore, there is a significant difference between the in-plane and out-of-plane vibration of a transmission line, and the former has obvious nonlinearity stiffness that will induce additional tension of the transmission line. Therefore, it is not enough to calculate the response of a transmission line only by its first-order out-of-plane vibration. In fact, as a highly flexible line system, it is inevitable to consider the multiorder vibrations of a transmission line, and the dynamic tension generated by the vibration of the transmission line under the action of the pulsating wind is the main load that acts on the transmission tower.

Based on the aforementioned analysis, according to a generalized *Hamilton's* principle, three-dimensional (3D) nonlinear differential equations of motion for horizontally suspended transmission lines that consider the initial deflection are established in this work. Based on the characteristics of an actual transmission line, the 3D equations are simplified to two-dimensional (2D) equations. On this basis, the method of multiple scales is employed to theoretically study the nonlinear internal resonance behavior of transmission lines. Moreover, a higher-order *Runge-Kutta* method is also used to perform a numerical analysis of the nonlinear vibration characteristics of transmission lines to reveal the characteristics of the coupled action of the out-of-plane and in-plane vibration of transmission lines when in nonlinear vibration, with the aim of providing a basis for the reasonable design of HVOTLs.

2. 3D Nonlinear Equations of Motion for Elastic Transmission Lines

2.1. Establishing 3D Equations of Motion. Figure 1 shows an elastic transmission line with its two ends hinge-supported at the same height. The initial static equilibrium geometric configuration S_0 of the transmission line in the plane Oxy is used as the reference location and is represented by function $x(y)$. d_c , L_c , and $T_c(y, t)$ represent the sag and span of the dynamic tension in the transmission line, respectively. S_D represents the 3D dynamic configuration of the transmission

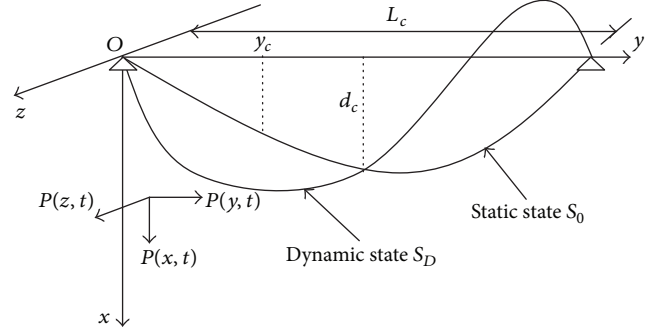


FIGURE 1: Spatial configuration of a transmission line.

line under an external excitation $P(t)$. $P(x, t)$, $P(y, t)$, and $P(z, t)$ represent the components of the external excitation $P(t)$ in the x -, y -, and z -axes, respectively. E_c and A_c represent the elastic modulus and the cross-sectional area of the transmission line, respectively. γ_c represents the dead weight of the transmission line per unit length ($\gamma_c = m_c g$, where g represents the acceleration of gravity). $u_c(y, t)$, $v_c(y, t)$, and $w_c(y, t)$ represent the displacements of the transmission line along the longitudinal in-plane vibration (y -axis direction), the transverse in-plane vibration (x -axis direction), and the transverse out-of-plane vibration (z -axis direction), respectively.

To simplify analysis, the following assumptions [12, 25] are made: (a) the flexural, torsional, and shear stiffness of the transmission line is sufficiently low and thus negligible; (b) the transmission line only bears tension in the axial direction, and its axial strain, when vibrating, is sufficiently small and thus negligible; (c) only geometric nonlinearity is considered, whereas material nonlinearity is not considered.

When the tension in the transmission line is in the initial static equilibrium state, the length ds_0 of the differential element at any arbitrary location y_c along the y -axis direction is

$$ds_0 = \sqrt{1 + \left(\frac{\partial x}{\partial y}\right)^2} dy. \quad (1)$$

According to the definition of Lagrangian strain, initially, the length ds of the differential element of the transmission line under the action of gravity is

$$ds = \frac{\sqrt{1 + (\partial x / \partial y)^2}}{1 + \epsilon_{c0}} dy, \quad (2)$$

where ϵ_{c0} represents the initial static strain of the transmission line, which is calculated using the following equation:

$$\epsilon_{c0} = \frac{T_c(y, 0)}{E_c A_c}, \quad (3)$$

where $T_c(y, 0)$ represents the initial tension in the transmission line.

The length of the differential element of the transmission line after it has undergone dynamic deformation under an external excitation $P(t)$ is

$$ds_D = \sqrt{\left(1 + \frac{\partial u_c}{\partial y}\right)^2 + \left(\frac{\partial x}{\partial y} + \frac{\partial v_c}{\partial y}\right)^2 + \left(\frac{\partial w_c}{\partial y}\right)^2} dy. \quad (4)$$

The total dynamic strain [12] of the transmission line in a motion state under the external excitation is

$$\varepsilon_c = \frac{ds_D - ds}{ds} = \frac{1 + \varepsilon_{c0}}{\sqrt{1 + (\partial x/\partial y)^2}} \cdot \sqrt{\left(1 + \frac{\partial u_c}{\partial y}\right)^2 + \left(\frac{\partial x}{\partial y} + \frac{\partial v_c}{\partial y}\right)^2 + \left(\frac{\partial w_c}{\partial y}\right)^2} - 1. \quad (5)$$

The transient total tension $T_c(y, t)$ in the differential element of the transmission line in a motion state is

$$T_c(y, t) = T_c(y, 0) + E_c A_c \varepsilon_c = T_c(y, 0) + \left(\frac{1}{\sqrt{1 + (\partial x/\partial y)^2}} \cdot \sqrt{\left(1 + \frac{\partial u_c}{\partial y}\right)^2 + \left(\frac{\partial x}{\partial y} + \frac{\partial v_c}{\partial y}\right)^2 + \left(\frac{\partial w_c}{\partial y}\right)^2} - 1 \right) \cdot E_c A_c. \quad (6)$$

According to a generalized *Hamilton's* principle,

$$\delta \int_{t_1}^{t_2} (K^v - U) dt + \int_{t_1}^{t_2} \delta W dt = 0, \quad (7)$$

where K^v , U , δW represent the kinetic energy and the strain energy of the transmission line and the virtual work done by nonconservative forces (including the virtual work δW_c done by the damping force and the virtual work δW_p done by the external excitation), respectively.

The kinetic energy of the transmission line is

$$K^v = \frac{1}{2} \int_0^{L_c} \frac{\gamma_c \sqrt{1 + (\partial x/\partial y)^2}}{g(1 + \varepsilon_{c0})} (\dot{u}_c^2 + \dot{v}_c^2 + \dot{w}_c^2) dy, \quad (8)$$

where $\gamma_c \sqrt{1 + (\partial x/\partial y)^2}/g(1 + \varepsilon_{c0})$ represents the mass of the transmission line in the static equilibrium state per unit length and \dot{u}_c , \dot{v}_c , and \dot{w}_c represent the vibration velocities of the transmission line in the y -, x -, and z -axis directions, respectively.

According to the aforementioned assumptions, the strain energy of the transmission line can only be generated by an axial tension. According to the principle of virtual work, the strain energy is

$$U = \int_0^{L_c} T_c(y, 0) \varepsilon_c ds + \frac{1}{2} \int_0^{L_c} E_c A_c \varepsilon_c^2 ds. \quad (9)$$

The virtual work done by the damping force is

$$\delta W_c = - \int_0^{L_c} c_c (\dot{u}_c \delta u_c + \dot{v}_c \delta v_c + \dot{w}_c \delta w_c) dy, \quad (10)$$

where c_c represents the structural damping of the transmission line.

The virtual work done by the external excitation $P(t)$ is

$$\delta W_p = \int_0^{L_c} (P(y, t) \delta u_c + P(x, t) \delta v_c + P(z, t) \delta w_c) dy. \quad (11)$$

By substituting (8)–(11) into (7) and considering the boundary conditions, the following is satisfied at the locations $y_c = 0$ and $y_c = L_c$:

$$\delta u_c = \delta v_c = \delta w_c = 0. \quad (12)$$

Thus, the *Euler* equations for the transmission line along the virtual displacement δu_c , δv_c , and δw_c directions are obtained:

$$\begin{aligned} & \frac{\partial}{\partial y} \left(\frac{E_c A_c (1 + \partial u_c/\partial y)}{\sqrt{1 + (\partial x/\partial y)^2}} \right) \\ & + \frac{(T_c(y, 0) - E_c A_c) (1 + \partial u_c/\partial y)}{\sqrt{(1 + \partial u_c/\partial y)^2 + (\partial x/\partial y + \partial v_c/\partial y)^2 + (\partial w_c/\partial y)^2}} \\ & = \frac{\gamma_c \sqrt{1 + (\partial x/\partial y)^2}}{g(1 + \varepsilon_{c0})} \ddot{u}_c + c_c \dot{u}_c - P(y, t), \\ & \frac{\partial}{\partial y} \left(\frac{E_c A_c (\partial x/\partial y + \partial v_c/\partial y)}{\sqrt{1 + (\partial x/\partial y)^2}} \right) \\ & + \frac{(T_c(y, 0) - E_c A_c) (\partial x/\partial y + \partial v_c/\partial y)}{\sqrt{(1 + \partial u_c/\partial y)^2 + (\partial x/\partial y + \partial v_c/\partial y)^2 + (\partial w_c/\partial y)^2}} \\ & = \frac{\gamma_c \sqrt{1 + (\partial x/\partial y)^2}}{g(1 + \varepsilon_{c0})} \ddot{v}_c + c_c \dot{v}_c - P(x, t), \\ & \frac{\partial}{\partial y} \left(\frac{E_c A_c (\partial w_c/\partial y)}{\sqrt{1 + (\partial x/\partial y)^2}} \right) \\ & + \frac{(T_c(y, 0) - E_c A_c) (\partial w_c/\partial y)}{\sqrt{(1 + \partial u_c/\partial y)^2 + (\partial x/\partial y + \partial v_c/\partial y)^2 + (\partial w_c/\partial y)^2}} \\ & = \frac{\gamma_c \sqrt{1 + (\partial x/\partial y)^2}}{g(1 + \varepsilon_{c0})} \ddot{w}_c + c_c \dot{w}_c - P(z, t). \end{aligned} \quad (13)$$

Because the sag-to-span ratio d_c/L_c of a transmission line is generally very small, $\partial u_c/\partial y \ll 1$, $\partial v_c/\partial y \ll 1$, $\partial w_c/\partial y \ll 1$,

and $\partial x/\partial y \ll 1$ under small-strain conditions. Thus, these small quantities can each be expanded in a Taylor series, and their higher-order terms are negligible. In other words, in the abovementioned equations,

$$\begin{aligned} & \frac{1}{\sqrt{(1 + \partial u_c/\partial y)^2 + (\partial x/\partial y + \partial v_c/\partial y)^2 + (\partial w_c/\partial y)^2}} \\ & \approx 1 - \left\{ \frac{\partial u_c}{\partial y} - \left(\frac{\partial u_c}{\partial y} \right)^2 + \frac{\partial x}{\partial y} \cdot \frac{\partial v_c}{\partial y} + \frac{1}{2} \left(\frac{\partial x}{\partial y} \right)^2 \right. \\ & \left. + \frac{1}{2} \left(\frac{\partial v_c}{\partial y} \right)^2 + \frac{1}{2} \left(\frac{\partial w_c}{\partial y} \right)^2 \right\}. \end{aligned} \quad (14)$$

Let

$$\begin{aligned} \eta = & \frac{\partial u_c}{\partial y} - \left(\frac{\partial u_c}{\partial y} \right)^2 + \frac{\partial x}{\partial y} \cdot \frac{\partial v_c}{\partial y} + \frac{1}{2} \left(\frac{\partial x}{\partial y} \right)^2 \\ & + \frac{1}{2} \left(\frac{\partial v_c}{\partial y} \right)^2 + \frac{1}{2} \left(\frac{\partial w_c}{\partial y} \right)^2. \end{aligned} \quad (15)$$

By substituting (15) into (13), nonlinear equations of motion for the elastic transmission line that is horizontally hinge-supported at the two ends are obtained:

$$\begin{aligned} \frac{\partial}{\partial y} \left\{ \left[\frac{E_c A_c}{\sqrt{1 + (\partial x/\partial y)^2}} + (T_c(y, 0) - E_c A_c)(1 - \eta) \right] \right. \\ \left. \cdot \left(1 + \frac{\partial u_c}{\partial y} \right) \right\} = & \frac{\gamma_c \sqrt{1 + (\partial x/\partial y)^2}}{g(1 + \epsilon_{c0})} \ddot{u}_c + c_c \dot{u}_c \\ & - P(y, t), \end{aligned} \quad (16)$$

$$\begin{aligned} \frac{\partial}{\partial y} \left\{ \left[\frac{E_c A_c}{\sqrt{1 + (\partial x/\partial y)^2}} + (T_c(y, 0) - E_c A_c)(1 - \eta) \right] \right. \\ \left. \cdot \left(\frac{\partial x}{\partial y} + \frac{\partial v_c}{\partial y} \right) \right\} = & \frac{\gamma_c \sqrt{1 + (\partial x/\partial y)^2}}{g(1 + \epsilon_{c0})} \ddot{v}_c + c_c \dot{v}_c \\ & - P(x, t), \end{aligned} \quad (17)$$

$$\begin{aligned} \frac{\partial}{\partial y} \left\{ \left[\frac{E_c A_c}{\sqrt{1 + (\partial x/\partial y)^2}} \right. \right. \\ \left. \left. + (T_c(y, 0) - E_c A_c)(1 - \eta) \right] \frac{\partial w_c}{\partial y} \right\} \\ = & \frac{\gamma_c \sqrt{1 + (\partial x/\partial y)^2}}{g(1 + \epsilon_{c0})} \ddot{w}_c + c_c \dot{w}_c - P(z, t). \end{aligned} \quad (18)$$

In (16)–(18), \ddot{u}_c , \ddot{v}_c , \ddot{w}_c represent the accelerations of vibration of the transmission line along the y -, x -, and z -axes, respectively.

The above set of partial differential equations contains all the main vibration characteristics of the initial elastic transmission line continuum system, that is, the quadratic and cubic coupling terms associated with the initial deflection, the axial tension, and the spatial motion, which can be used to analyze the nonlinear dynamic behavior of the transmission line.

2.2. Equations of Coupled In-Plane and Out-of-Plane Motion for a Hinge-Supported Transmission Line. Considering that the axial stiffness $E_c A_c$ of a transmission line is generally relatively high and its axial elongation due to vibration is far smaller than its transverse vibration amplitude, the axial inertia force of a transmission line when in vibration is negligible. Under normal circumstances, the axial damping of a transmission line is relatively small; thus, the axial damping force of a transmission line when in motion is negligible. In addition, in Figure 1, since there is no external excitation along the axial direction of the transmission line (y -axis direction), $P(y, t) = 0$. Thus, (16) can be rewritten as

$$\begin{aligned} \frac{\partial}{\partial y} \left\{ \left[\frac{E_c A_c}{\sqrt{1 + (\partial x/\partial y)^2}} + (T_c(y, 0) - E_c A_c)(1 - \eta) \right] \right. \\ \left. \cdot \left(1 + \frac{\partial u_c}{\partial y} \right) \right\} = 0. \end{aligned} \quad (19)$$

The following approximation relation is then used:

$$\frac{1}{\sqrt{1 + (\partial x/\partial y)^2}} \approx 1 - \frac{1}{2} \left(\frac{\partial x}{\partial y} \right)^2. \quad (20)$$

By substituting (20) into (19), integrating the two sides of (19) over the span $[0, L_c]$ of the transmission line once, and ignoring the terms unrelated to time t , we have

$$\begin{aligned} T_c(y, 0) \left[1 - \frac{1}{2} \left(\frac{\partial x}{\partial y} \right)^2 \right] \cdot \frac{\partial u_c}{\partial y} - (T_c(y, 0) - E_c A_c) \eta \\ - (T_c(y, 0) - E_c A_c) \eta \cdot \frac{\partial u_c}{\partial y} = \hbar(t), \end{aligned} \quad (21)$$

where $\hbar(t)$ is an arbitrary function. By dividing the two sides of (21) by $E_c A_c$ and considering that the initial tension $T_c(y, 0)$ in a transmission line is generally far smaller than its axial stiffness $E_c A_c$ and that the axial deformation of a transmission line is a higher-order small quantity compared to its vertical in-plane deformation and out-of-plane deformation, we have

$$\frac{\partial u_c}{\partial y} + \frac{\partial x}{\partial y} \cdot \frac{\partial v_c}{\partial y} + \frac{1}{2} \left(\frac{\partial w_c}{\partial y} \right)^2 + \frac{1}{2} \left(\frac{\partial v_c}{\partial y} \right)^2 \approx \frac{\hbar(t)}{E_c A_c}. \quad (22)$$

To determine $\dot{h}(t)$, the two sides of (22) are integrated over the interval $[0, L_c]$ and the transmission line boundary conditions represented by (23) are used. After simplification, we have (24).

$$\begin{aligned} u_c(0, t) &= 0, \\ u_c(L_c, t) &= 0, \end{aligned} \quad (23)$$

$$\begin{aligned} \frac{\dot{h}(t)}{E_c A_c} \cdot L_c &= \int_0^{L_c} \left[\frac{\partial u_c}{\partial y} + \frac{\partial x}{\partial y} \cdot \frac{\partial v_c}{\partial y} + \frac{1}{2} \left(\frac{\partial w_c}{\partial y} \right)^2 \right. \\ &\quad \left. + \frac{1}{2} \left(\frac{\partial v_c}{\partial y} \right)^2 \right] dy. \end{aligned} \quad (24)$$

Let us set

$$\begin{aligned} \lambda(t) &= \frac{\dot{h}(t)}{E_c A_c} = \frac{1}{L_c} \int_0^{L_c} \left[\frac{\partial u_c}{\partial y} + \frac{\partial x}{\partial y} \cdot \frac{\partial v_c}{\partial y} \right. \\ &\quad \left. + \frac{1}{2} \left(\frac{\partial w_c}{\partial y} \right)^2 + \frac{1}{2} \left(\frac{\partial v_c}{\partial y} \right)^2 \right] dy. \end{aligned} \quad (25)$$

By substituting (22) and (25) into (17) and (18), respectively, we have

$$\begin{aligned} &\frac{\partial}{\partial y} \left(T_c(y, 0) \cdot \left[1 - \frac{1}{2} \left(\frac{\partial x}{\partial y} \right)^2 \right] \cdot \frac{\partial v_c}{\partial y} \right. \\ &\quad \left. - (T_c(y, 0) - E_c A_c) \cdot \lambda(t) \cdot \frac{\partial x}{\partial y} \right) \\ &\quad - \frac{\partial}{\partial y} \left((T_c(y, 0) - E_c A_c) \cdot \lambda(t) \cdot \frac{\partial v_c}{\partial y} \right) \\ &= \frac{\gamma_c \sqrt{1 + (\partial x / \partial y)^2}}{g(1 + \varepsilon_{c0})} \ddot{v}_c + c_c \dot{v}_c - P(x, t), \\ &\frac{\partial}{\partial y} \left(T_c(y, 0) \cdot \left[1 - \frac{1}{2} \left(\frac{\partial x}{\partial y} \right)^2 \right] \cdot \frac{\partial w_c}{\partial y} \right. \\ &\quad \left. - (T_c(y, 0) - E_c A_c) \cdot \lambda(t) \cdot \frac{\partial w_c}{\partial y} \right) \\ &= \frac{\gamma_c \sqrt{1 + (\partial x / \partial y)^2}}{g(1 + \varepsilon_{c0})} \ddot{w}_c + c_c \dot{w}_c - P(z, t). \end{aligned} \quad (26)$$

For ease of analysis, by use of *Galerkin's* modal truncation method, the in-plane and out-of-plane response of the transmission line is represented by

$$\begin{aligned} v_c(y, t) &= \sum_{i=1}^N \varphi_i(y) \cdot q_i(t), \\ w_c(y, t) &= \sum_{i=1}^N \varphi_i(y) \cdot q_i(t). \end{aligned} \quad (28)$$

In (28), $\varphi_i(y) = \sin(i\pi y/L_c)$ is the i th-order vibration mode function (the two ends of the conductor line are

considered to be hinge-connected), N represents the retained mode order, and $q_i(t)$ represents the generalized coordinates. By substituting it into (26) and (27), (28) can be transformed to ordinary differential equations of motion, which are subsequently solved. Equation (28) is subjected to first-order model truncation using *Galerkin's* modal truncation method; that is, set

$$\begin{aligned} v_c(y, t) &= \varphi_v(y) \cdot q_v(t) = \sin\left(\frac{\pi y}{L_c}\right) \cdot q_v(t), \\ w_c(y, t) &= \varphi_w(y) \cdot q_w(t) = \sin\left(\frac{\pi y}{L_c}\right) \cdot q_w(t). \end{aligned} \quad (29)$$

By substituting (29) into (26) and (27), subsequently multiplying the two sides of (26) by $\varphi_v(y)$, integrating the resulting equation over the interval $[0, L_c]$, multiplying the two sides of (27) by $\varphi_w(y)$, and integrating the resultant equation over the interval $[0, L_c]$, discrete equations of coupled in-plane and out-of-plane motion for the transmission line are obtained:

$$\begin{aligned} &a_1 \ddot{q}_v(t) + a_2 q_v(t) + a_3 \dot{q}_v^2(t) + a_4 \dot{q}_w^2(t) + a_5 q_v^3(t) \\ &\quad + a_6 q_w^2(t) q_v(t) + a_7 \dot{q}_v(t) = P_v, \\ &b_1 \ddot{q}_w(t) + b_2 q_w(t) + b_3 q_v(t) q_w(t) + b_4 \dot{q}_v^2(t) q_w(t) \\ &\quad + b_5 \dot{q}_w^3(t) + b_6 \dot{q}_w(t) = P_w. \end{aligned} \quad (30)$$

The factors in (30) are calculated as follows:

$$\begin{aligned} a_1 &= \int_0^{L_c} \frac{\gamma_c \sqrt{1 + (\partial x / \partial y)^2}}{g(1 + \varepsilon_{c0})} \varphi_v^2(y) dy, \\ a_2 &= - \int_0^{L_c} \frac{\partial}{\partial y} \left[T_c(y, 0) \cdot \left(1 - \frac{1}{2} \left(\frac{\partial x}{\partial y} \right)^2 \right) \cdot \varphi_v'(y) \right. \\ &\quad \left. - \left(\frac{T_c(y, 0) - E_c A_c}{L_c} \right) \cdot \frac{\partial x}{\partial y} \cdot \int_0^{L_c} \frac{\partial x}{\partial y} \cdot \varphi_v'(y) dy \right] \\ &\quad \cdot \varphi_v(y) dy, \\ a_3 &= \int_0^{L_c} \frac{\partial}{\partial y} \left[\left(\frac{T_c(y, 0) - E_c A_c}{2L_c} \right) \cdot \frac{\partial x}{\partial y} \right. \\ &\quad \cdot \int_0^{L_c} \varphi_v'^2(y) dy + \left(\frac{T_c(y, 0) - E_c A_c}{L_c} \right) \\ &\quad \cdot \varphi_v'(y) \int_0^{L_c} \frac{\partial x}{\partial y} \cdot \varphi_v'(y) dy \left. \right] \varphi_v(y) dy, \\ a_4 &= \int_0^{L_c} \frac{\partial}{\partial y} \left[\left(\frac{T_c(y, 0) - E_c A_c}{2L_c} \right) \cdot \frac{\partial x}{\partial y} \right. \\ &\quad \cdot \int_0^{L_c} \varphi_w'^2(y) dy \left. \right] \varphi_w(y) dy, \end{aligned}$$

$$\begin{aligned}
a_5 &= \int_0^{L_c} \frac{\partial}{\partial y} \left[\left(\frac{T_c(y,0) - E_c A_c}{2L_c} \right) \cdot \varphi'_v(y) \right. \\
&\quad \left. \cdot \int_0^{L_c} \varphi_v'^2(y) dy \right] \varphi_v(y) dy, \\
a_6 &= \int_0^{L_c} \frac{\partial}{\partial y} \left[\left(\frac{T_c(y,0) - E_c A_c}{2L_c} \right) \cdot \varphi'_w(y) \right. \\
&\quad \left. \cdot \int_0^{L_c} \varphi_w'^2(y) dy \right] \varphi_w(y) dy, \\
a_7 &= \int_0^{L_c} c_c \varphi_v^2(y) dy, \\
P_v &= \int_0^{L_c} P(x,t) \varphi_v(y) dy, \\
b_1 &= \int_0^{L_c} \frac{\gamma_c \sqrt{1 + (\partial x / \partial y)^2}}{g(1 + \varepsilon_{c0})} \varphi_w^2(y) dy, \\
b_2 &= - \int_0^{L_c} \frac{\partial}{\partial y} \left[T_c(y,0) \cdot \left(1 - \frac{1}{2} \left(\frac{\partial x}{\partial y} \right)^2 \right) \cdot \varphi'_w(y) \right] \\
&\quad \cdot \varphi_w(y) dy, \\
b_3 &= \int_0^{L_c} \frac{\partial}{\partial y} \left[\left(\frac{T_c(y,0) - E_c A_c}{L_c} \right) \cdot \varphi'_w(y) \right. \\
&\quad \left. \cdot \int_0^{L_c} \frac{\partial x}{\partial y} \cdot \varphi'_v(y) dy \right] \varphi_w(y) dy, \\
b_4 &= \int_0^{L_c} \frac{\partial}{\partial y} \left[\left(\frac{T_c(y,0) - E_c A_c}{2L_c} \right) \cdot \varphi'_w(y) \right. \\
&\quad \left. \cdot \int_0^{L_c} \varphi_v'^2(y) dy \right] \varphi_w(y) dy, \\
b_5 &= \int_0^{L_c} \frac{\partial}{\partial y} \left[\left(\frac{T_c(y,0) - E_c A_c}{2L_c} \right) \cdot \varphi'_w(y) \right. \\
&\quad \left. \cdot \int_0^{L_c} \varphi_w'^2(y) dy \right] \varphi_w(y) dy, \\
b_6 &= \int_0^{L_c} c_c \varphi_w^2(y) dy, \\
P_w &= \int_0^{L_c} P(z,t) \varphi_w(y) dy.
\end{aligned} \tag{31}$$

As demonstrated in (30), the in-plane and out-of-plane motion of the transmission line exhibits cubic nonlinearity, whereas the coupled in-plane and out-of-plane motion exhibits linearity, quadratic nonlinearity, and cubic nonlinearity; that is, the nonlinear coupling is very strong.

3. Theoretical Analysis of the Characteristics of the Nonlinear Coupled In-Plane and Out-of-Plane Internal Resonance of Transmission Lines

To further study the nonlinear coupled in-plane and out-of-plane dynamic characteristics of an overhead transmission line, we conducted the following analysis with the help of the multiple-scale (MS) method [26–29], which is an effective method for the analysis of nonlinear dynamics.

Assume that the external excitation is a harmonic excitation: that is,

$$\begin{aligned}
P(x,t) &= A_v \cos(\Omega_x t), \\
P(z,t) &= A_w \cos(\Omega_z t),
\end{aligned} \tag{32}$$

where A_v and A_w represent the amplitudes of the in-plane excitation and the out-of-plane excitation, respectively, on the transmission line, and Ω_x and Ω_z represent the circular frequencies of the in-plane excitation and the out-of-plane excitation, respectively.

Here, the in-plane excitation on the transmission line is not considered, that is, the generalized in-plane excitation load P_v is assumed to be zero. Now, the generalized out-of-plane excitation load on the transmission line is set to $P_w = P_0 \cos \Omega_z t$. In addition, the parameters ε , α_1 , α_2 , μ_1 , μ_2 , κ_1 , κ_2 , β_1 , β_2 , γ_1 , and f_2 are introduced to transform (30) to dimensionless equations:

$$\begin{aligned}
\ddot{q}_v(t) + \omega_1^2 q_v(t) + \varepsilon \alpha_1 q_v^2(t) + \varepsilon \kappa_1 q_w^2(t) + \varepsilon \beta_1 q_v^3(t) \\
+ \varepsilon \gamma_1 q_w^2(t) q_v(t) + 2\varepsilon \mu_1 \dot{q}_v(t) &= 0, \\
\ddot{q}_w(t) + \omega_2^2 q_w(t) + \varepsilon \alpha_2 q_v(t) q_w(t) + \varepsilon \kappa_2 q_v^2(t) q_w(t) \\
+ \varepsilon \beta_2 q_w^3(t) + 2\varepsilon \mu_2 \dot{q}_w(t) &= 2\varepsilon f_2 \cos(\Omega_z t),
\end{aligned} \tag{33}$$

where ω_1 and ω_2 represent the circular frequencies of the in-plane and out-of-plane vibrations of the transmission line, respectively. The abovementioned parameters have the following conversion relationships:

$$\begin{aligned}
\omega_1^2 &= \frac{a_2}{a_1}, \\
2\varepsilon \mu_1 &= \frac{a_7}{a_1}, \\
\varepsilon \alpha_1 &= \frac{a_3}{a_1}, \\
\varepsilon \kappa_1 &= \frac{a_4}{a_1}, \\
\varepsilon \beta_1 &= \frac{a_5}{a_1}, \\
\varepsilon \gamma_1 &= \frac{a_6}{a_1}, \\
\omega_2^2 &= \frac{b_2}{b_1},
\end{aligned}$$

$$\begin{aligned}
2\varepsilon\mu_2 &= \frac{b_6}{b_1}, \\
\varepsilon\alpha_2 &= \frac{b_3}{b_1}, \\
\varepsilon\kappa_2 &= \frac{b_4}{b_1}, \\
\varepsilon\beta_2 &= \frac{b_5}{b_1}, \\
2\varepsilon f_2 &= \frac{P_0}{b_1}.
\end{aligned} \tag{34}$$

The abovementioned set of nonlinear equations can be solved using the MS method, the basic idea of which is to regard the expansion of the response as a function with multiple independent variables (or multiple scales) [26].

The following independent variables are introduced:

$$T_n = \varepsilon^n t \quad (n = 0, 1, \dots), \tag{35}$$

that is,

$$\begin{aligned}
T_0 &= t, \\
T_1 &= \varepsilon t, \dots
\end{aligned} \tag{36}$$

Thus, the derivative with respect to t is transformed to the expansion of a partial derivative with respect to T_n , that is,

$$\begin{aligned}
\frac{d}{dt} &= \frac{dT_0}{dt} \frac{\partial}{\partial T_0} + \frac{dT_1}{dt} \frac{\partial}{\partial T_1} + \dots \\
&= D_0 + \varepsilon D_1 + \varepsilon^2 D_2 + \dots, \\
\frac{d^2}{dt^2} &= \frac{dT_0}{dt} \frac{\partial^2}{\partial T_0^2} + 2\varepsilon \frac{\partial^2}{\partial T_0 \partial T_1} + \dots \\
&= D_0^2 + 2\varepsilon D_0 D_1 + \varepsilon^2 (D_1^2 + 2D_1 D_2) + \dots.
\end{aligned} \tag{37}$$

Hence, the solutions to (33) can be expressed as follows:

$$\begin{aligned}
q_v(t, \varepsilon) &= q_{v0}(T_0, T_1, T_2, \dots) + \varepsilon q_{v1}(T_0, T_1, T_2, \dots) \\
&\quad + \varepsilon^2 q_{v2}(T_0, T_1, T_2, \dots) + \dots, \\
q_w(t, \varepsilon) &= q_{w0}(T_0, T_1, T_2, \dots) + \varepsilon q_{w1}(T_0, T_1, T_2, \dots) \\
&\quad + \varepsilon^2 q_{w2}(T_0, T_1, T_2, \dots) + \dots,
\end{aligned} \tag{38}$$

By substituting (37) and (38) into (33), we have

$$\begin{aligned}
&(D_1^2 q_{v2} + 2\mu_1 D_1 q_{v2} + 2\mu_1 D_2 q_{v1} + 2D_0 D_1 q_{v3} \\
&\quad + 2\mu_1 D_0 q_{v3} + \beta_1 q_{v1}^3 + 2\alpha_1 q_{v1} q_{v2} + 6\beta_1 q_{v0} q_{v1} q_{v2}
\end{aligned}$$

$$\begin{aligned}
&\quad + 2\alpha_1 q_{v0} q_{v3} + 3\beta_1 q_{v0}^2 q_{v3} + \gamma_1 q_{w0}^2 q_{v3} \\
&\quad + 2\gamma_1 q_{v2} q_{w0} q_{w1} + \gamma_1 q_{w1}^2 q_{v1} + 2\gamma_1 q_{v1} q_{w0} q_{w2} \\
&\quad + 2\kappa_1 q_{w1} q_{w2} + 2\gamma_1 q_{v0} q_{w1} q_{w2} + 2\kappa_1 q_{w0} q_{w3} \\
&\quad + 2\gamma_1 q_{v0} q_{w0} q_{w3}) \varepsilon^4 + (D_0^2 q_{v3} + \omega_1^2 q_{v3} + 2\mu_1 D_2 q_{v0} \\
&\quad + D_1^2 q_{v1} + 2\mu_1 D_1 q_{v1} + 2D_0 D_1 q_{v2} + 2\mu_1 D_0 q_{v2} \\
&\quad + \alpha_1 q_{v1}^2 + 3\beta_1 q_{v0} q_{v1}^2 + 2\alpha_1 q_{v0} q_{v2} + 3\beta_1 q_{v0}^2 q_{v2} \\
&\quad + \gamma_1 q_{v2} q_{w0}^2 + 2\gamma_1 q_{v1} q_{w0} q_{w1} + \kappa_1 q_{w1}^2 + \gamma_1 q_{v0} q_{w1}^2 \\
&\quad + 2\kappa_1 q_{w0} q_{w2} + 2\gamma_1 q_{v0} q_{w0} q_{w2}) \varepsilon^3 + (D_0^2 q_{v2} + \omega_1^2 q_{v2} \\
&\quad + D_1^2 q_{v0} + 2\mu_1 D_0 q_{v0} + 2D_0 D_1 q_{v1} + 2\mu_1 D_0 q_{v1} \\
&\quad + 3\beta_1 q_{v0}^2 q_{v1} + 2\kappa_1 q_{w0} q_{w1} + \gamma_1 q_{w0}^2 q_{v1} \\
&\quad + 2\gamma_1 q_{w0} q_{w1} q_{v0} + 2\alpha_1 q_{v0} q_{v1}) \varepsilon^2 + (D_0^2 q_{v1} + \omega_1^2 q_{v1} \\
&\quad + 2D_0 D_1 q_{v0} + 2\mu_1 D_0 q_{v0} + \alpha_1 q_{v0}^2 + \kappa_1 q_{w0}^2 + \beta_1 q_{v0}^3 \\
&\quad + \gamma_1 q_{w0}^2 q_{v0}) \varepsilon + D_0^2 q_{v0} + \omega_1^2 q_{v0} = 0,
\end{aligned}$$

$$\begin{aligned}
&(D_1^2 q_{w2} + 2\mu_2 D_1 q_{w2} + 2\mu_2 D_0 q_{w3} + 2D_0 D_1 q_{w3} \\
&\quad + 2\mu_2 D_2 q_{w1} + \beta_2 q_{w1}^3 + \alpha_2 q_{v3} q_{w0} + 2\kappa_2 q_{v0} q_{v3} q_{w0} \\
&\quad + 2\kappa_2 q_{v1} q_{v2} q_{w0} + \kappa_2 q_{v1}^2 q_{w1} + \alpha_2 q_{v2} q_{w1} \\
&\quad + 2\kappa_2 q_{v0} q_{v2} q_{w1} + \alpha_2 q_{v1} q_{w2} + 2\kappa_2 q_{v0} q_{v1} q_{w2} \\
&\quad + 6\beta_2 q_{w0} q_{w1} q_{w2} + \alpha_2 q_{v0} q_{w3} + \kappa_2 q_{v0}^2 q_{w3} \\
&\quad + 3\beta_2 q_{w0}^2 q_{w3}) \varepsilon^4 + (D_0^2 q_{w3} + \omega_2^2 q_{w3} + 2\mu_2 D_2 q_{w0} \\
&\quad + D_1^2 q_{w1} + 2\mu_2 D_1 q_{w1} + 2D_0 D_1 q_{w2} + 2\mu_2 D_0 q_{w2} \\
&\quad + \alpha_2 q_{v2} q_{w0} + \kappa_2 q_{v1}^2 q_{w0} + 3\beta_2 q_{w0} q_{w1}^2 + \alpha_2 q_{v1} q_{w1} \\
&\quad + 3\beta_2 q_{w0}^2 q_{w2} + 2\kappa_2 q_{v0} q_{v2} q_{w0} + 2\kappa_2 q_{v0} q_{v1} q_{w1} \\
&\quad + \kappa_2 q_{v0}^2 q_{w0} + \alpha_2 q_{v0} q_{w2}) \varepsilon^3 + (D_0^2 q_{w2} + \omega_2^2 q_{w2} \\
&\quad + D_1^2 q_{w0} + 2\mu_2 D_1 q_{w0} + 2D_0 D_1 q_{w2} + 2\mu_2 D_0 q_{w2} \\
&\quad + D_1^2 q_{w1} + 2\mu_2 D_1 q_{w1} + 3\beta_2 q_{w0}^2 q_{w2} + 3\beta_2 q_{w0} q_{w1}^2 \\
&\quad + 2\kappa_2 q_{v0} q_{v1} q_{w1} + 2\kappa_2 q_{v0} q_{v2} q_{w0} + \alpha_2 q_{v2} q_{w0} \\
&\quad + \alpha_2 q_{v1} q_{w1} + \alpha_2 q_{v0} q_{w2} + \kappa_2 q_{v0}^2 q_{w2}) \varepsilon^2 + (D_0^2 q_{w1} \\
&\quad + \omega_2^2 q_{w1} + 2D_0 D_1 q_{w0} + 2\mu_2 D_0 q_{w0} + \alpha_2 q_{v0} q_{w0} \\
&\quad + \kappa_2 q_{v0}^2 q_{w0} + \beta_2 q_{w0}^3) \varepsilon + D_0^2 q_{w0} + \omega_2^2 q_{w0} = 2\varepsilon f_2 \\
&\quad \cdot \cos(\Omega_z t).
\end{aligned} \tag{39}$$

By setting the sum of the coefficients of the same power of ε to zero, we have

$$\begin{aligned} \varepsilon^0: \\ D_0^2 q_{v0} + \omega_1^2 q_{v0} &= 0, \\ D_0^2 q_{w0} + \omega_2^2 q_{w0} &= 0, \end{aligned} \quad (40)$$

ε^1 :

$$\begin{aligned} D_0^2 q_{v1} + 2D_0 D_1 q_{v0} + 2\mu_1 D_0 q_{v0} + \omega_1^2 q_{v1} + \beta_1 q_{v0}^3 \\ + a_1 q_{v0}^2 + \gamma_1 q_{w0}^2 q_{v0} + \kappa_1 q_{w0}^2 = 0, \\ D_0^2 q_{w1} + 2D_0 D_1 q_{w0} + \beta_2 q_{w0}^3 + \omega_2^2 q_{w1} + a_2 q_{v0} q_{w0} \\ + 2\mu_2 D_0 q_{w0} + \kappa_2 q_{v0}^2 q_{w0} = 2f_2 \cos(\Omega_z t), \end{aligned} \quad (41)$$

ε^2 :

$$\begin{aligned} D_0^2 q_{v2} + \omega_1^2 q_{v2} + D_1^2 q_{v0} + 2\mu_1 D_0 q_{v0} + 2D_0 D_1 q_{v1} \\ + 2\mu_1 D_0 q_{v1} + 3\beta_1 q_{v0}^2 q_{v1} + 2\kappa_1 q_{w0} q_{w1} + \gamma_1 q_{w0}^2 q_{v1} \\ + 2\gamma_1 q_{w0} q_{w1} q_{v0} + 2\alpha_1 q_{v0} q_{v1} = 0, \\ D_0^2 q_{w2} + \omega_2^2 q_{w2} + D_1^2 q_{w0} + 2\mu_2 D_1 q_{w0} + 2D_0 D_1 q_{w2} \\ + 2\mu_2 D_0 q_{w2} + D_1^2 q_{w1} + 2\mu_2 D_1 q_{w1} + 3\beta_2 q_{w0}^2 q_{w2} \\ + 3\beta_2 q_{w0} q_{w1}^2 + 2\kappa_2 q_{v0} q_{v1} q_{w1} + 2\kappa_2 q_{v0} q_{v2} q_{w0} \\ + \alpha_2 q_{v2} q_{w0} + \alpha_2 q_{v1} q_{w1} + \alpha_2 q_{v0} q_{w2} \\ + \kappa_2 q_{v0}^2 q_{w2} = 0, \end{aligned} \quad (42)$$

ε^3 :

$$\begin{aligned} D_0^2 q_{v3} + \omega_1^2 q_{v3} + 2\mu_1 D_2 q_{v0} + D_1^2 q_{v1} + 2\mu_1 D_1 q_{v1} \\ + 2D_0 D_1 q_{v2} + 2\mu_1 D_0 q_{v2} + \alpha_1 q_{v1}^2 + 3\beta_1 q_{v0} q_{v1}^2 \\ + 2\alpha_1 q_{v0} q_{v2} + 3\beta_1 q_{v0}^2 q_{v2} + \gamma_1 q_{v2} q_{w0}^2 \\ + 2\gamma_1 q_{v1} q_{w0} q_{w1} + \kappa_1 q_{w1}^2 + \gamma_1 q_{v0} q_{w1}^2 + 2\kappa_1 q_{w0} q_{w2} \\ + 2\gamma_1 q_{v0} q_{w0} q_{w2} = 0, \\ D_0^2 q_{w3} + \omega_2^2 q_{w3} + 2\mu_2 D_2 q_{w0} + D_1^2 q_{w1} + 2\mu_2 D_1 q_{w1} \\ + 2D_0 D_1 q_{w2} + 2\mu_2 D_0 q_{w2} + \alpha_2 q_{v2} q_{w0} + \kappa_2 q_{v1}^2 q_{w0} \\ + 3\beta_2 q_{w0} q_{w1}^2 + \alpha_2 q_{v1} q_{w1} + 3\beta_2 q_{w0}^2 q_{w2} \\ + 2\kappa_2 q_{v0} q_{v2} q_{w0} + 2\kappa_2 q_{v0} q_{v1} q_{w1} + \kappa_2 q_{v0}^2 q_{w0} \\ + \alpha_2 q_{v0} q_{w2} = 0. \end{aligned} \quad (43)$$

By solving the set of equations in (40), we have

$$\begin{aligned} q_{v0} &= A_v(T_1, T_2) \exp(i\omega_1 T_0) \\ &+ \bar{A}_v(T_1, T_2) \exp(-i\omega_1 T_0), \end{aligned}$$

$$\begin{aligned} q_{w0} &= A_w(T_1, T_2) \exp(i\omega_2 T_0) \\ &+ \bar{A}_w(T_1, T_2) \exp(-i\omega_2 T_0), \end{aligned} \quad (44)$$

where A_v and A_w are unknown complex functions and \bar{A}_v and \bar{A}_w are the conjugates of A_v and A_w , respectively. For ease of description, conjugate terms are denoted by *cc*. The governing equations for A_v and A_w can be solved by requiring q_{v0} , q_{v1} , q_{w0} , and q_{w1} to be functions with a period of T_0 .

By substituting (44) into (41), we have

$$\begin{aligned} D_0^2 q_{v1} + \omega_1^2 q_{v1} &= -2i\omega_1 D_1 A_v e^{i2\omega_1 T_0} \\ &- 2i\omega_1 \mu_1 A_v e^{i2\omega_1 T_0} \\ &- \gamma_1 A_w^2 A_v e^{i(2\omega_2 + \omega_1) T_0} \\ &- \gamma_1 \bar{A}_w^2 A_v e^{i(\omega_1 - 2\omega_2) T_0} \\ &- 3\beta_1 A_v^2 \bar{A}_v e^{i\omega_1 T_0} \\ &- 2\gamma_1 A_w \bar{A}_w A_v e^{i\omega_1 T_0} \\ &- \beta_1 A_v^3 e^{i3\omega_1 T_0} - \alpha_1 A_v^2 e^{i2\omega_1 T_0} \\ &- 2\alpha_1 A_v \bar{A}_v - 2\kappa_1 A_w \bar{A}_w \\ &- \kappa_1 A_w^2 e^{i2\omega_2 T_0} + cc, \\ D_0^2 q_{w1} + \omega_2^2 q_{w1} &= -2i\omega_2 D_1 A_w e^{i2\omega_2 T_0} \\ &- 2i\omega_2 \mu_2 A_w e^{i2\omega_2 T_0} \\ &- 3\beta_2 A_w^2 \bar{A}_w e^{i\omega_2 T_0} \\ &- 2\kappa_2 A_v \bar{A}_v A_w e^{i\omega_2 T_0} \\ &- \beta_2 A_w^3 e^{i3\omega_2 T_0} \\ &- \alpha_2 A_v A_w e^{i(\omega_1 + \omega_2) T_0} \\ &- \alpha_2 A_v \bar{A}_w e^{i(\omega_1 - \omega_2) T_0} \\ &- \kappa_2 A_v^2 A_w e^{i(2\omega_1 + \omega_2) T_0} \\ &- \kappa_2 \bar{A}_v A_w e^{i(\omega_2 - 2\omega_1) T_0} + f_2 e^{i\Omega_z T_0} \\ &+ cc. \end{aligned} \quad (45)$$

From (45), we can easily find that the terms that contain $e^{i2\omega_1 T_0}$ and $e^{i2\omega_2 T_0}$ can lead to secular terms in the solutions of the above equation. In addition, from (30), we know that the coupling of the in-plane and out-of-plane motion of the transmission line exhibits linearity, quadratic nonlinearity, and cubic nonlinearity. Thus, if parameters exist that allow the natural frequencies of the in-plane and out-of-plane vibration of the transmission line to satisfy any of the relations $\omega_1 \approx \omega_2$, $\omega_1 \approx 2\omega_2$, and $\omega_2 \approx 2\omega_1$, the solutions to the

abovementioned partial differential equations that describe the motion of the transmission line will contain an additional term that links q_{v1} and q_{w1} , which is exactly the secular term caused by internal resonance. Therefore, when solving (45), we should consider the cases of $\omega_1 \approx \omega_2$, $\omega_1 \approx 2\omega_2$, and $\omega_2 \approx 2\omega_1$. In view of the complexity of the problem-solving and the purpose of this study, we merely take the case of $\omega_1 \approx \omega_2$ as an example to illustrate the analysis process.

Assume that the natural frequencies of the in-plane and out-of-plane vibrations of the transmission line meet the following relationship:

$$\omega_2 - \omega_1 = \varepsilon\sigma, \quad \sigma = O(1). \quad (46)$$

Thus,

$$\begin{aligned} (\omega_2 + \omega_1)T_0 &= 2\omega_1 T_0 + \varepsilon\sigma T_0 = 2\omega_1 T_0 + \sigma T_1 \\ &= 2\omega_2 T_0 + \sigma T_1, \\ 2\omega_2 T_0 &= 2(\omega_1 + \varepsilon\sigma)T_0 = 2\omega_2 T_0 + 2\sigma T_1. \end{aligned} \quad (47)$$

By substituting (47) into (45), we can obtain the requirements to eliminate the secular terms as follows:

$$\begin{aligned} 2i\omega_1 (D_1 A_v + \mu_1 A_v) + \alpha_1 A_v^2 + \kappa_1 A_w^2 e^{i2\sigma T_1} &= 0, \\ 2i\omega_2 (D_1 A_w + \mu_2 A_w) + \alpha_2 A_v A_w e^{i\sigma T_1} &= 0. \end{aligned} \quad (48)$$

The following formulas are introduced:

$$A_r = \frac{a_r}{2} e^{j\theta_r}, \quad r = v, w. \quad (49)$$

By substituting (49) into (48) and separating the real part from the imaginary part, we have

$$\begin{aligned} D_1 a_v + \mu_1 a_v + \frac{\alpha_1 a_v^2}{2\omega_1} \sin \theta_v \\ + \frac{\kappa_1 a_w^2}{4\omega_1} \sin 2(\theta_w + \sigma T_1) \sec \theta_v &= 0, \\ a_v D_1 \theta_v \\ - \frac{\csc \theta_v}{4\omega_1} [\alpha_1 a_v^2 \cos 2\theta_v + \kappa_1 a_w^2 \cos 2(\theta_w + \sigma T_1)] \\ &= 0, \end{aligned} \quad (50)$$

$$\begin{aligned} D_1 a_w + \mu_2 a_w + \frac{\alpha_2 a_v a_w}{4\omega_2 \cos \theta_w} \sin(\theta_v + \theta_w + \sigma T_1) &= 0, \\ a_w D_1 \theta_w + \frac{\alpha_2 a_v a_w}{4\omega_2 \cos \theta_w} \cos(\theta_v + \theta_w + \sigma T_1) &= 0. \end{aligned}$$

Let us introduce the new phase angle as follows:

$$\begin{aligned} \varphi_1 &= 2(\theta_w + \sigma T_1), \\ \varphi_2 &= \theta_v + \theta_w + \sigma T_1. \end{aligned} \quad (51)$$

By substituting (51) into (50), we have

$$\begin{aligned} D_1 a_v + \mu_1 a_v + \frac{\alpha_1 a_v^2}{2\omega_1} \sin \theta_v + \frac{\kappa_1 a_w^2}{4\omega_1} \sin \varphi_1 \sec \theta_v &= 0, \\ a_v D_1 \theta_v - \frac{\csc \theta_v}{4\omega_1} [\alpha_1 a_v^2 \cos 2\theta_v + \kappa_1 a_w^2 \cos \varphi_1] &= 0, \\ D_1 a_w + \mu_2 a_w + \frac{\alpha_2 a_v a_w}{4\omega_2 \cos \theta_w} \sin \varphi_2 &= 0, \\ a_w D_1 \theta_w + \frac{\alpha_2 a_v a_w}{4\omega_2 \cos \theta_w} \cos \varphi_2 &= 0. \end{aligned} \quad (52)$$

When solving (52), we must discuss whether the damping of the system is considered. In addition, even if we can obtain the one-order approximate steady-state solution of the equation, we must investigate its asymptotic stability to determine whether it actually exists. Hence, we can see that the above issue is so complicated that it should be specifically studied. Due to the limitation of the abovementioned approximation method, it is difficult to obtain the theoretical solutions to the equations of coupled in-plane and out-of-plane motion for transmission lines. Therefore, in the subsequent section, we intend to perform the quantitative analysis of (30) by using numerical methods.

Because the main purpose of this article is to reveal the inherently nonlinear vibration characteristics of transmission lines, the above MS analysis is merely used to determine the requirements for eliminating secular terms in the solutions of the partial differential equations of transmission lines. Because the second-order approximation solutions can provide enough information for most practical problems, it is usually necessary to give only the second-order approximation solutions of a nonlinear system by using the MS method [27–29]. For this reason, we consider only the power of ε up to 2 in this paper. From the requirements for eliminating secular terms, it is clear that internal resonance is considered to exist in the transmission line if parameters exist that allow the natural frequencies of the in-plane and out-of-plane vibration of the transmission line to satisfy any of the following relations: $\omega_1 \approx \omega_2$, $\omega_1 \approx 2\omega_2$, and $\omega_2 \approx 2\omega_1$.

4. Numerical Analysis of the Characteristics of the Nonlinear Coupled In-Plane and Out-of-Plane Internal Resonance of Transmission Lines

In numerical analysis, the *Runge-Kutta* method is widely used to obtain the approximate solutions of differential equations. This method is so accurate that most computer packages designed to find numerical solutions for differential equations will use it by default—the fourth-order *Runge-Kutta method*. Therefore, we employ a higher-order *Runge-Kutta* method to obtain the numerical solutions to these equations, with the aim of revealing the nonlinear vibration characteristics of transmission lines.



FIGURE 2: A high-voltage transmission line.

The following state variables are introduced:

$$\begin{aligned} Y_1 &= q_v, \\ Y_2 &= \dot{q}_v, \\ Y_3 &= q_w, \\ Y_4 &= \dot{q}_w. \end{aligned} \quad (53)$$

Thus, (30) can be transformed to state functions:

$$\begin{aligned} \dot{Y}_1 &= Y_2, \\ \dot{Y}_2 &= \frac{(P_v - a_2 Y_1 - a_3 Y_1^2 - a_4 Y_3^2 - a_5 Y_1^3 - a_6 Y_3^2 Y_1 - a_7 Y_2)}{a_1}, \\ \dot{Y}_3 &= Y_4, \\ \dot{Y}_4 &= \frac{(P_w - b_2 Y_3 - b_3 Y_1 Y_3 - b_4 Y_1^2 Y_3 - b_5 Y_3^3 - b_6 Y_4)}{b_1}. \end{aligned} \quad (54)$$

4.1. Calculation of the Parameters. A relatively large single-span transmission line in a high-voltage transmission line system in East China (Figure 2) is selected as an example for analysis [30]. The conductors of this span of the transmission line are composed of LGJ-630/45 ASCR cables. Table 1 lists the design parameters of the selected transmission line. The maximum design wind speed at a height of 10 m above the ground for safe operation of the selected transmission line is 25.3 m/s. In the actual transmission line, the conductors of each phase are quad-bundled conductors. To simplify calculation, in the finite element (FE) modeling process, the quad-bundled conductors of each phase are equivalently simplified to one conductor based on the following principles: the bundled conductors have the same windward area, the same total operational tension, and the same linear density. Table 2 lists the parameters of the transmission line after simplification.

The sag-to-span ratio d_c/L_c of the selected transmission line is calculated based on the parameters listed in Table 1 to be approximately 1/29, which is far smaller than 1/8. Thus, (30) can be used to analyze the nonlinear vibration characteristics of this transmission line.

4.2. Modal Analysis of the Transmission Line. Based on the actual characteristics of the selected transmission line in combination with the design parameters listed in Tables 1 and 2, LINK10 elements in ANSYS are used to construct an FE model for the selected transmission line. First, a modal analysis is performed to determine the natural frequency of vibration of each order of the transmission line model; this provides a basis for the subsequent numerical simulation. To validate the FE model constructed for a single transmission line, in this section, the FE simulation results with respect to the natural vibration frequencies of the transmission line are also compared with the theoretical solutions.

A transmission line is a typical type of suspended cable structure, and the analytical solutions for the natural frequencies of its vibration can be obtained based on the single-cable theory. A transmission line resists external loading primarily by self-stretching and consequently will undergo relatively large displacement under loading. Therefore, the geometric nonlinearity of a transmission line must be taken into consideration in the calculation. When constructing an FE model of a transmission line, one crucial point is to determine the initial configuration of the cable. Specifically, on the one hand, this means to determine the spatial location of the transmission line by determining the equilibrium and deformation compatibility equations for the transmission line based on the existing suspended cable theory; on the other hand, this means to transition the transmission line from its initial stress-free state to an initial loaded state based on a certain configuration-seeking approach.

The catenary and parabolic methods are the main methods used to determine the equilibrium equation for a suspended cable. The former is an accurate method, whereas the latter is an approximate method. However, when the sag-to-span ratio d_c/L_c of a cable is less than 1/8, the parabolic method can also yield a relatively accurate solution for the initial configuration of the transmission line. Here, assuming that the vertical load on a transmission line is evenly distributed along the span, as shown in Figure 3, the equation for the spatial configuration of the transmission line is

$$x(y) = \frac{q_c}{2T_{c0}} y(L_c - y) + \frac{\Delta_c}{L_c} y, \quad (55)$$

where q_c represents the vertical load on the transmission line, which in this case is the dead weight of the transmission line; T_{c0} represents the initial horizontal tension in the transmission line ($T_{c0} = (q_c L_c^2)/(8d_c)$); L_c represents the horizontal span of the transmission line; Δ_c represents the difference in height between the two ends of the transmission line; and d_c represents the mid-span sag of the transmission line.

Considering that a transmission line generally has a small sag, the first-order natural frequency corresponding to the out-of-plane vibration of the transmission line is the smallest frequency of all the frequencies of its vibration. According to the linear vibration theory of suspended cables, for a horizontal suspended cable with two ends hinged at the same height and whose mass is evenly distributed, the natural

TABLE 1: Original design parameters of the selected transmission line.

Items	Diameter d (mm)	Cross-sectional area A_c (mm ²)	Linear density m_c (kg/m)	Elastic modulus E_c (MPa)	Average operational tension (N)	Tension at design wind speed (N)	Breaking force (N)	Span L_c (m)	Sag d_c (m)
Conductors	33.6	666.55	2.06	63,000	35,316	43,688	141,265	480	16.6

TABLE 2: Design parameters of the selected transmission line after simplification.

Items	Diameter d (mm)	Density ρ_c (kg/m ³)	Linear density m_c (kg/m)	Linear load q_c (N/m)	Initial strain ε_{c0}
Conductors	134.4	3,090.5	8.24	80.752	0.00084

frequencies of vibration and the corresponding modes under the action of gravity alone are as follows:

(a) The out-of-plane swing and the in-plane vibration of the suspended cable are not coupled. Thus, the natural circular frequencies of the out-of-plane swing and the corresponding modes can be expressed as follows:

$$\omega_w = \frac{n\pi}{L_c} \sqrt{\frac{T_{c0}}{m_c}}, \quad n = 1, 2, 3, \dots, \quad (56)$$

$$\Phi_w = A_n \sin \frac{n\pi y}{L_c}, \quad n = 1, 2, 3, \dots,$$

where ω_w represents the natural circular frequency of the out-of-plane vibration of the suspended cable, n represents the modal number, m_c represents the mass of the suspended cable per unit length, Φ_w represents the out-of-plane mode of vibration of the suspended cable, and A_n represents the modal amplitude (each of the other symbols has the same meaning as previously described).

(b) The in-plane antisymmetric vibration of the suspended cable will not generate an increment in its horizontal dynamic tension. The natural circular frequencies of its vibration and the corresponding modes can be expressed as follows:

$$\omega_v = \frac{2n\pi}{L_c} \sqrt{\frac{T_{c0}}{m_c}}, \quad n = 1, 2, 3, \dots, \quad (57)$$

$$\Phi_v = B_n \sin \frac{2n\pi y}{L_c}, \quad n = 1, 2, 3, \dots,$$

where ω_v represents the natural circular frequency of the in-plane antisymmetric vibration of the suspended cable, n represents the modal number, Φ_v represents the mode of the in-plane antisymmetric vibration of the suspended cable, and B_n represents the modal amplitude (each of the other symbols has the same meaning as previously described).

(c) The in-plane symmetric vibration of the suspended cable will generate an additional increment in its dynamic tension. The natural circular frequencies of its vibration and the corresponding modes can be determined by solving the following transcendental equations:

$$\tan \frac{\bar{\omega}}{2} = \frac{\bar{\omega}}{2} - \frac{4}{\lambda^2} \left(\frac{\bar{\omega}}{2} \right)^3,$$

$$\bar{\omega} = \frac{\omega_{\text{vant}} L_c}{\sqrt{T_{c0}/m_c}},$$

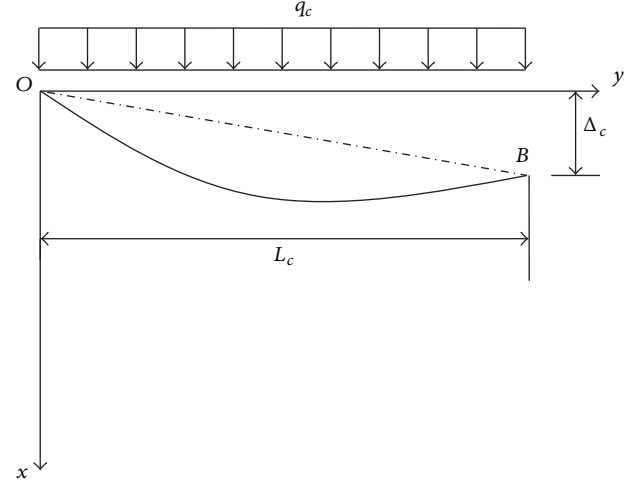


FIGURE 3: A schematic diagram of the calculation for a single cable when the load is evenly distributed along the span.

$$\lambda^2 = \frac{(m_c g L_c / T_{c0})^2 L_c}{T_{c0} L_c / (E_c A_c)},$$

$$\Phi_{\text{vant}} = \frac{\bar{h}}{T_{c0} \bar{\omega}^2} \left(1 - \tan \frac{\bar{\omega}}{2} \sin \frac{\bar{\omega} y}{L_c} - \cos \frac{\bar{\omega} y}{L_c} \right), \quad (58)$$

where ω_{vant} represents the natural circular frequency of the in-plane symmetric vibration of the suspended cable, Φ_{vant} represents the in-plane symmetric mode of vibration of the suspended cable, E_c represents the elastic modulus of the suspended cable, A_c represents the cross-sectional area of the suspended cable, and \bar{h} represents the additional tension in the suspended cable (each of the other symbols has the same meaning as previously described).

By substituting the parameters listed in Tables 1 and 2 into (55)–(58), the theoretical solutions for the natural vibration frequencies of the first eight orders of the transmission line in the three directions can be obtained (they are shown in Table 3). Table 4 summarizes the linear natural vibration frequencies of the transmission line obtained from FE simulation.

A comparison of Tables 3 and 4 shows that the natural vibration frequencies of the transmission line model obtained from FE simulation are in relatively good agreement with the theoretical values, with the largest difference being approximately 1%. This indicates that the transmission line model constructed in this work is relatively reliable. Moreover, Tables 3 and 4 also demonstrate that the following relationships between the natural frequencies of the in-plane and out-of-plane modes of vibration of the transmission line

TABLE 3: Theoretical linear natural vibration frequencies of the transmission line model.

	Calculation equation	First order	Second order	Third order	Fourth order	Fifth order	Sixth order	Seventh order	Eighth order
Out-of-plane vibration frequency f_w (Hz)	$f_w = \frac{\omega_w}{(2\pi)}$	0.136	0.273	0.409	0.546	0.682	0.818	0.955	1.091
In-plane symmetric vibration frequency f_v (Hz)	$f_v = \frac{\omega_v}{(2\pi)}$	0.344	0.46	–	–	–	–	–	–
In-plane antisymmetric vibration frequency f_{vant} (Hz)	$f_{\text{vant}} = \frac{\omega_{\text{vant}}}{(2\pi)}$	0.273	0.546	0.818	1.091	1.364	1.637	1.91	2.182

TABLE 4: Natural vibration frequencies of the transmission line model obtained from FE simulation.

	Calculation equation	First order	Second order	Third order	Fourth order	Fifth order	Sixth order	Seventh order	Eighth order
Out-of-plane vibration frequency f_w (Hz)	$f_w = \frac{\omega_w}{(2\pi)}$	0.136	0.272	0.408	0.544	0.68	0.816	0.952	1.088
In-plane symmetric vibration frequency f_v (Hz)	$f_v = \frac{\omega_v}{(2\pi)}$	0.346	0.46	0.686	0.954	1.225	1.497	1.769	2.042
In-plane antisymmetric vibration frequency f_{vant} (Hz)	$f_{\text{vant}} = \frac{\omega_{\text{vant}}}{(2\pi)}$	0.27	0.544	0.816	1.088	1.36	1.633	1.91	2.18

always exist: $\omega_v \approx \omega_w$, $\omega_v \approx 2\omega_w$, and $\omega_v \approx 3\omega_w$. In other words, within the scope of the linear theory, the natural vibration frequencies of the transmission line are always multiples of one another.

Figure 4 shows the modes of vibration of the first nine orders obtained from FE simulation. As demonstrated in Figure 4, of all the modes of vibration of the transmission line, the first-order out-of-plane vibration is the most easily excitable. The higher-order frequencies of in-plane vibration are approximately integer multiples of the fundamental frequency, and this relationship also exists between the frequencies of in-plane antisymmetric vibration and the fundamental frequency. In addition to the relationship to the fundamental frequency, the higher-order frequencies of the out-of-plane vibration are also approximately equal to those of the in-plane vibration, and the in-plane and out-of-plane modes of vibration corresponding to the same frequency are also similar to one another.

4.3. Numerical Analysis of the Nonlinear Internal Resonance of the Transmission Line When in Free Vibration. When only the free vibration of the transmission line under the action of the initial displacement is considered, in (54), $P_v = 0$ and $P_w = 0$.

The structural damping of a transmission line is often relatively small, and it can generally be set to 0.0005. In addition, the effects of the structural damping of a transmission line on its vibration, particularly under strong wind conditions, are relatively insignificant, whereas aerodynamic damping relatively significantly affects the vibration of a transmission line. By comprehensively considering the aforementioned factors, in this study, when analyzing the free vibration of the transmission line, the damping c_c of its in-plane and out-of-plane vibration is set to 0.001. In the following sections, the effects of the initial potential energy of the transmission line on its internal resonance are analyzed in two scenarios.

4.3.1. When the Initial Potential Energy of the Transmission Line Is Relatively Low (i.e., When the Initial Mid-Span Displacement of the Transmission Line Is Relatively Small). Let us set the initial out-of-plane mid-span displacement and the initial velocity of out-of-plane motion of the transmission line to 1 m and 0.00005 m/s, respectively, and both its initial in-plane mid-span displacement and the initial velocity of its in-plane motion to 0; that is, the initial conditions described in (53) are set as follows: $q_v = 0$, $\dot{q}_v = 0$, $q_w = 1$, $\dot{q}_w = 0.00005$. The displacements of the transmission line obtained from numerical simulation are then divided by the horizontal span L_c to obtain dimensionless displacements. The dimensionless velocities of in-plane and out-of-plane can also be obtained from the numerical simulation results of the in-plane and out-of-plane velocities multiplied by the first-order out-of-plane vibration period T_0 and then divided by the horizontal span L_c . The results are presented in Figures 5–7.

As demonstrated in Figure 5, when the initial energy of the transmission line is relatively low, its in-plane vibration displacement is relatively small, with the maximum amplitude being approximately 1/10 that of its out-of-plane vibration displacement; in addition, the “beat vibration” phenomenon is inconspicuous in the response time history. As demonstrated in the Fourier spectra of the displacement response of the transmission line (Figure 6), the first-order mode of vibration is the primary out-of-plane mode of vibration. The out-of-plane vibration of the transmission line gives rise to the first-order in-plane antisymmetric mode of vibration and the first-order symmetric mode of vibration. In addition, the first-order in-plane symmetric vibration energy is also greater than the first-order in-plane antisymmetric vibration energy, and the in-plane vibration energy amplitude is smaller than the out-of-plane vibration energy amplitude by one order of magnitude. This indicates that the transmission line is inherently capable of generating nonlinear internal resonance and can undergo internal resonance even

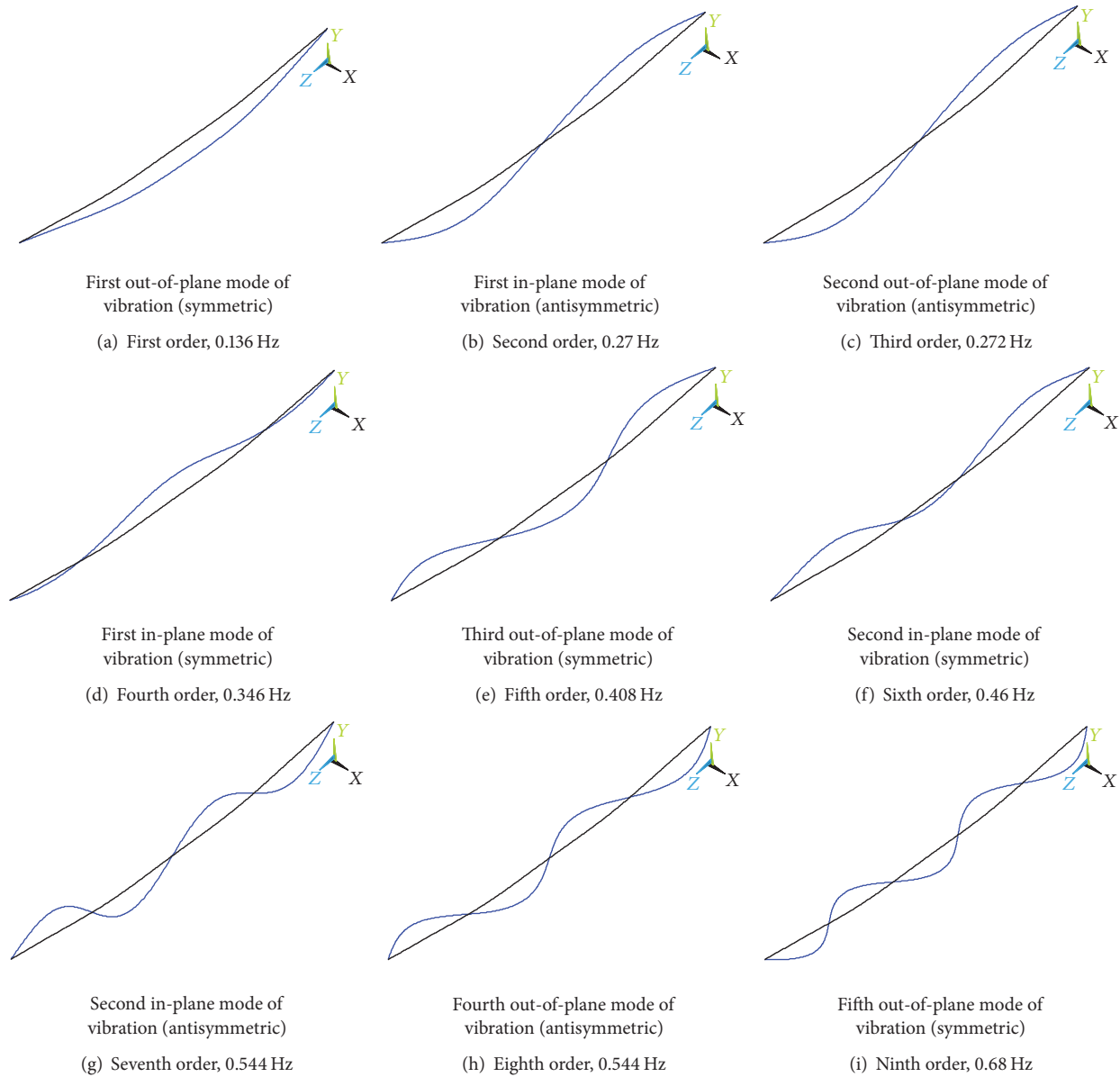


FIGURE 4: Modes of vibration of the transmission line of the first nine orders obtained from FE simulation.

when its initial energy is relatively low, but energy transfer and mode coupling are quite weak under this condition. As demonstrated in Figure 7, the out-of-plane and in-plane modes of vibration of the transmission line both exhibit periodic motion characteristics.

4.3.2. When the Initial Potential Energy of the Transmission Line Is Relatively High (i.e., When the Initial Mid-Span Displacement of the Transmission Line Is Relatively Large). Let us set the initial out-of-plane mid-span displacement of the transmission line to a relatively large value (10 m), the initial velocity of its out-of-plane mid-span motion to 0.00005 m/s, and both its initial in-plane mid-span displacement and the initial velocity of its in-plane motion to 0; that is, the initial conditions described in (53) are set as follows: $q_v = 0$, $\dot{q}_v = 0$,

$q_w = 10$, $\dot{q}_w = 0.00005$. Figures 8–10 show the numerical simulation results.

As demonstrated in Figure 8, when the initial out-of-plane displacement of the transmission line is relatively large, as a result of the internal resonance the system energy constantly transfers between the modes that are in the $\omega_v \approx \omega_w$, $\omega_v \approx 2\omega_w$, and $\omega_v \approx 3\omega_w$ relationships; in addition, the system energy also transfers between degrees of freedom that are similarly related to multiples of the frequency. On the one hand, the out-of-plane vibration energy transfers to the in-plane direction, resulting in vibration with a relatively large amplitude. Figure 8 also demonstrates that the order of magnitude of the in-plane vibration displacement amplitude is commensurate with the out-of-plane vibration displacement amplitude; a phenomenon similar to “beat vibration” is also observed in the displacement response time history; that is,

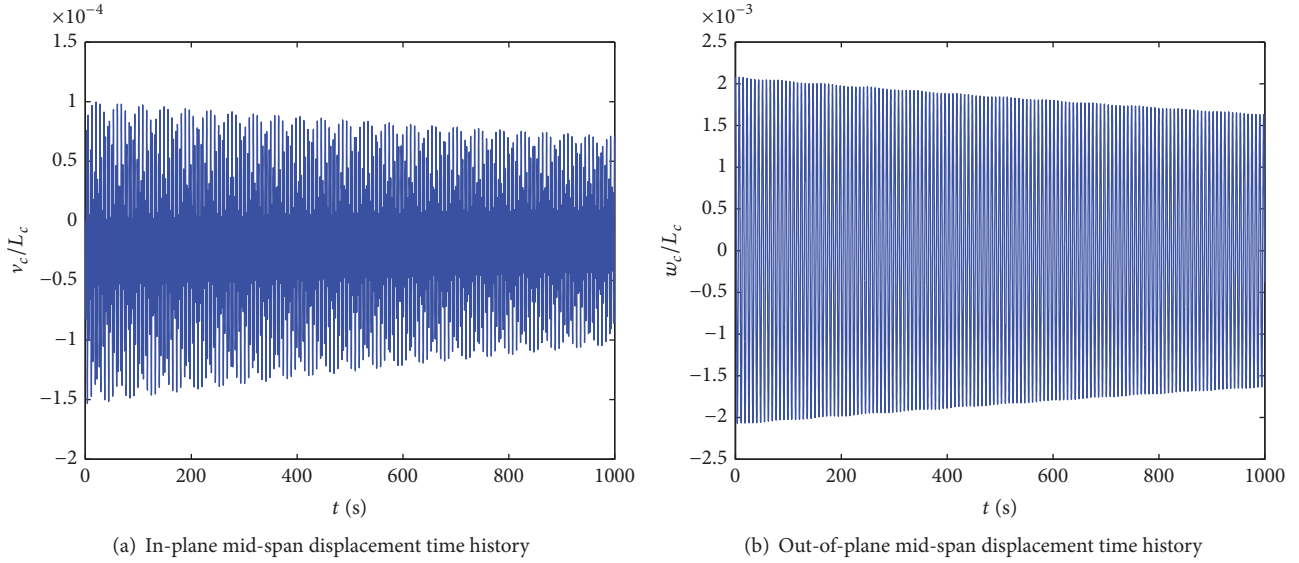


FIGURE 5: In-plane and out-of-plane mid-span displacement time histories of the transmission line when its initial potential energy is relatively low.

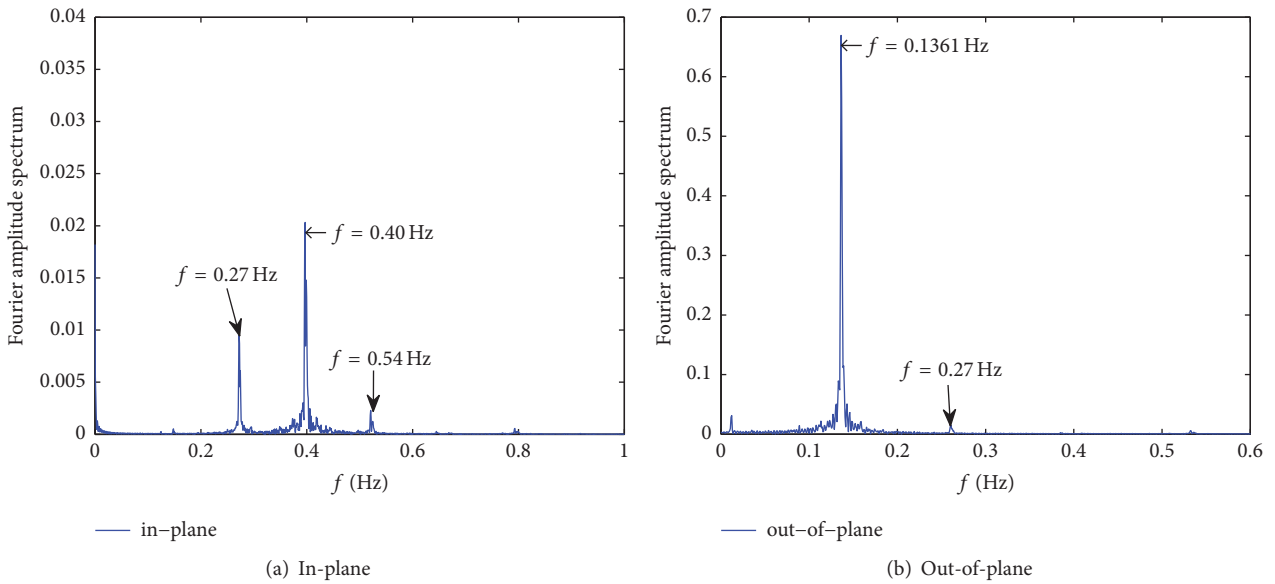
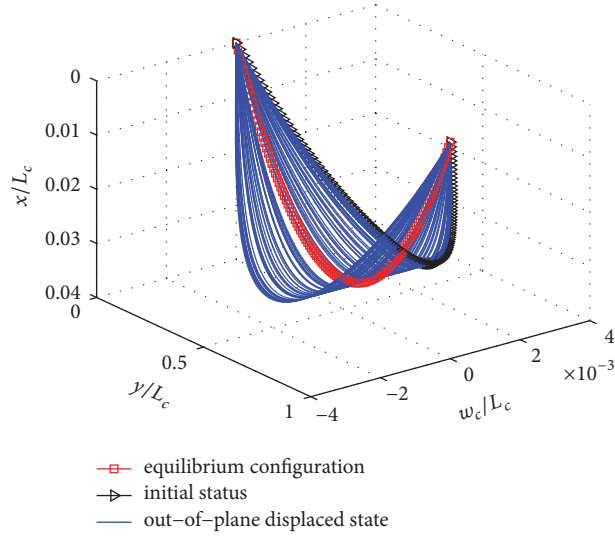


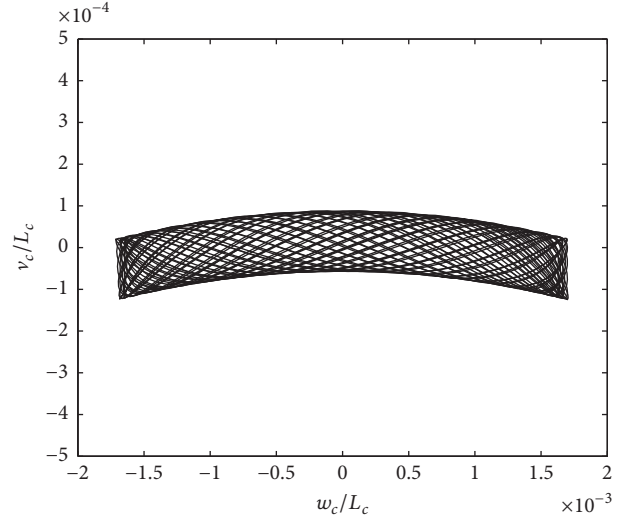
FIGURE 6: Fourier spectra of the in-plane and out-of-plane mid-span displacements of the transmission line when its initial potential energy is relatively low.

as the out-of-plane vibration response gradually decreases, the in-plane vibration response at the corresponding time gradually increases and vice versa. Furthermore, from Figures 5 and 8, we can also see that both of the maximum in-plane and out-of-plane vibration amplitudes decrease with time. This is principally because the damping dissipates the free vibration energy. On the other hand, when Galerkin's method is employed in numerical simulation to perform first-order modal truncation on the vibration response of the transmission line to simplify the analytical process, the

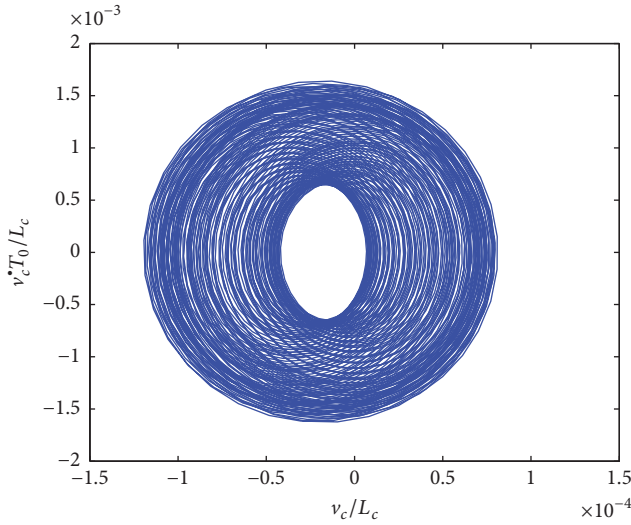
simulation results show that the second-order out-of-plane mode of vibration of the transmission line, as well as its first-order symmetric mode of vibration and its first- to fourth-order antisymmetric modes of vibration, are still excited. As a result of the internal resonance, the first-order out-of-plane mode of vibration, which has relatively high energy, gives rise to the second-order out-of-plane mode of vibration, whose frequency is twice its own frequency. Because the natural frequencies of the second-order out-of-plane mode of vibration and the first-order in-plane antisymmetric mode



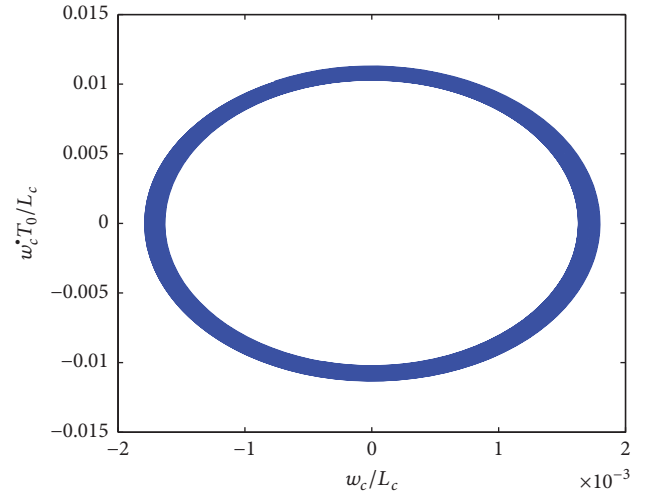
(a) Configuration of out-of-plane motion at various times



(b) In-plane and out-of-plane displacement responses in the phase space



(c) In-plane mid-span phase trajectory



(d) Out-of-plane mid-span phase trajectory

FIGURE 7: Configuration of the out-of-plane motion and the phase-space response of the transmission line when its initial potential energy is relatively low.

of vibration are closely spaced, the out-of-plane vibration energy gradually transfers to the in-plane direction. In addition, because the natural frequency of the in-plane vibration of each order is two or three times the in-plane fundamental frequency, the energy also transfers between different in-plane modes of vibration. The Fourier spectra of the displacement response shown in Figure 9 clearly demonstrate that the in-plane vibration also contains the first-order out-of-plane mode of vibration. Similarly, as demonstrated in Figure 10, the in-plane motion of the transmission line is strongly coupled to its out-of-plane motion.

The aforementioned analysis shows that the out-of-plane vibration energy of the transmission line can give rise not only to in-plane antisymmetric vibration but also to first-order in-plane symmetric vibration, whose energy is the highest

of all the in-plane modes of vibration. According to the suspended cable theory, in-plane symmetric vibration is the primary factor that causes changes in the dynamic tension in a suspended cable. To further illustrate the effects of internal resonance on the dynamic tension in the transmission line, the dynamic tension in the transmission line is calculated under the aforementioned two initial potential energy conditions (see Figure 11 for the results). In Figure 11, the tension is a dimensionless value obtained by dividing the dynamic tension T_c obtained from simulation by the initial tension T_{c0} . As demonstrated in Figure 11, when the transmission line vibrates with relatively low initial potential energy, the dynamic tension in the line is always positive, indicating that the transmission line is under tension. Meanwhile, when the line is in vibration, the dynamic tension in the transmission

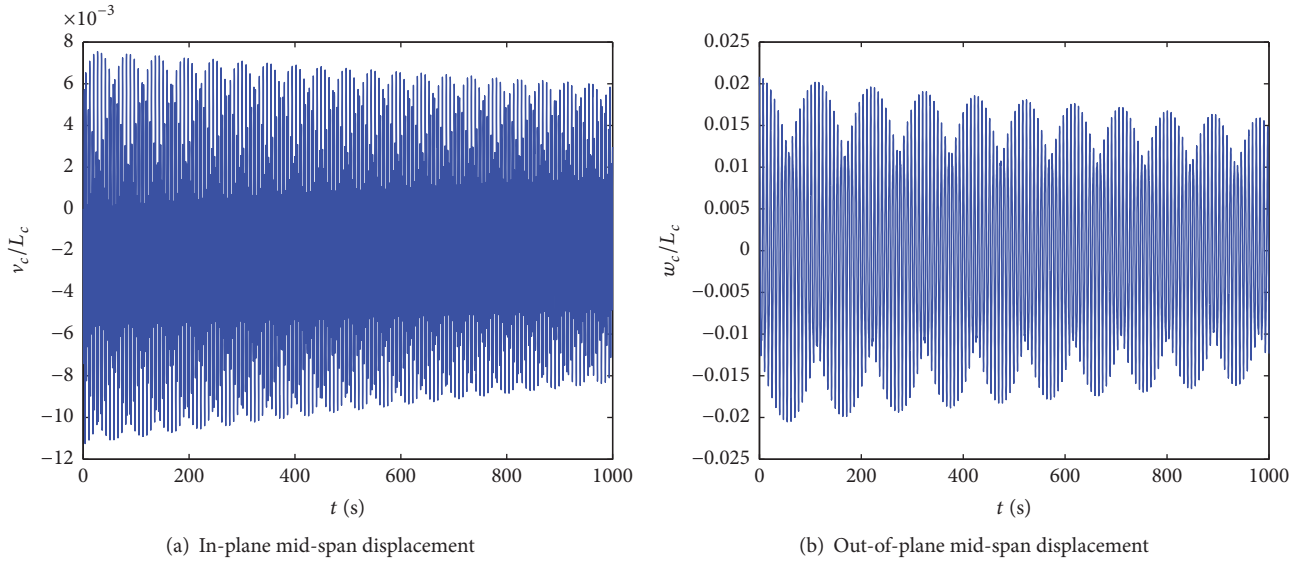


FIGURE 8: In-plane and out-of-plane mid-span displacement time histories of the transmission line when its initial potential energy is relatively high.

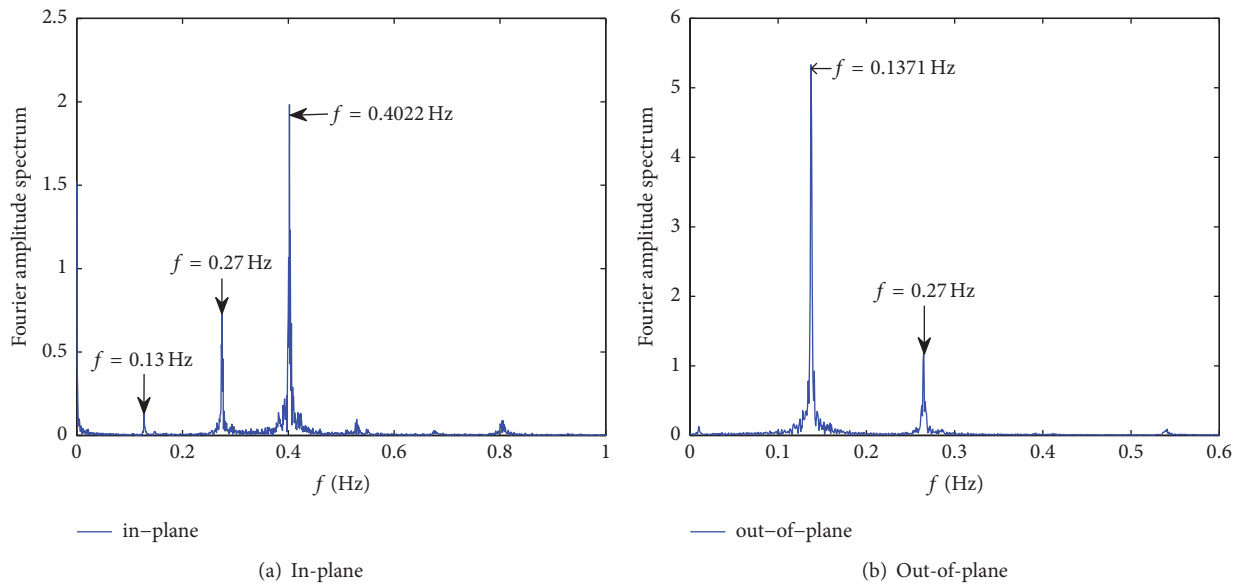


FIGURE 9: Fourier spectra of the in-plane and out-of-plane mid-span displacements of the transmission line when its initial potential energy is relatively high.

line is approximately the same as the initial tension. This suggests that when the transmission line vibrates freely with relatively low initial potential energy, the effects of internal resonance on the tension in the transmission line are negligible. The spectral distribution of the dynamic tension shown in Figure 11(c) also demonstrates that when the initial potential energy of the transmission line is relatively low, the tension in the transmission line is almost unaffected by its vibration. When the initial potential energy of the transmission line is relatively high, the dynamic tension in the transmission line may reach twice the initial tension. The spectral distribution of the dynamic tension shown in

Figure 11(d) also demonstrates that the increase in the tension in the line is related to its in-plane vibration. This indicates that when the transmission line is in motion with a large amplitude, its in-plane vibration is coupled to its out-of-plane vibration; that is, when the initial out-of-plane energy of the transmission line is relatively high, significant internal resonance occurs in the transmission line when it starts vibrating, resulting in the transfer of out-of-plane vibration energy to the in-plane direction. This in turn not only gives rise to in-plane antisymmetric vibration but also causes in-plane symmetric vibration, ultimately leading to a significant increase in the tension in the transmission line.

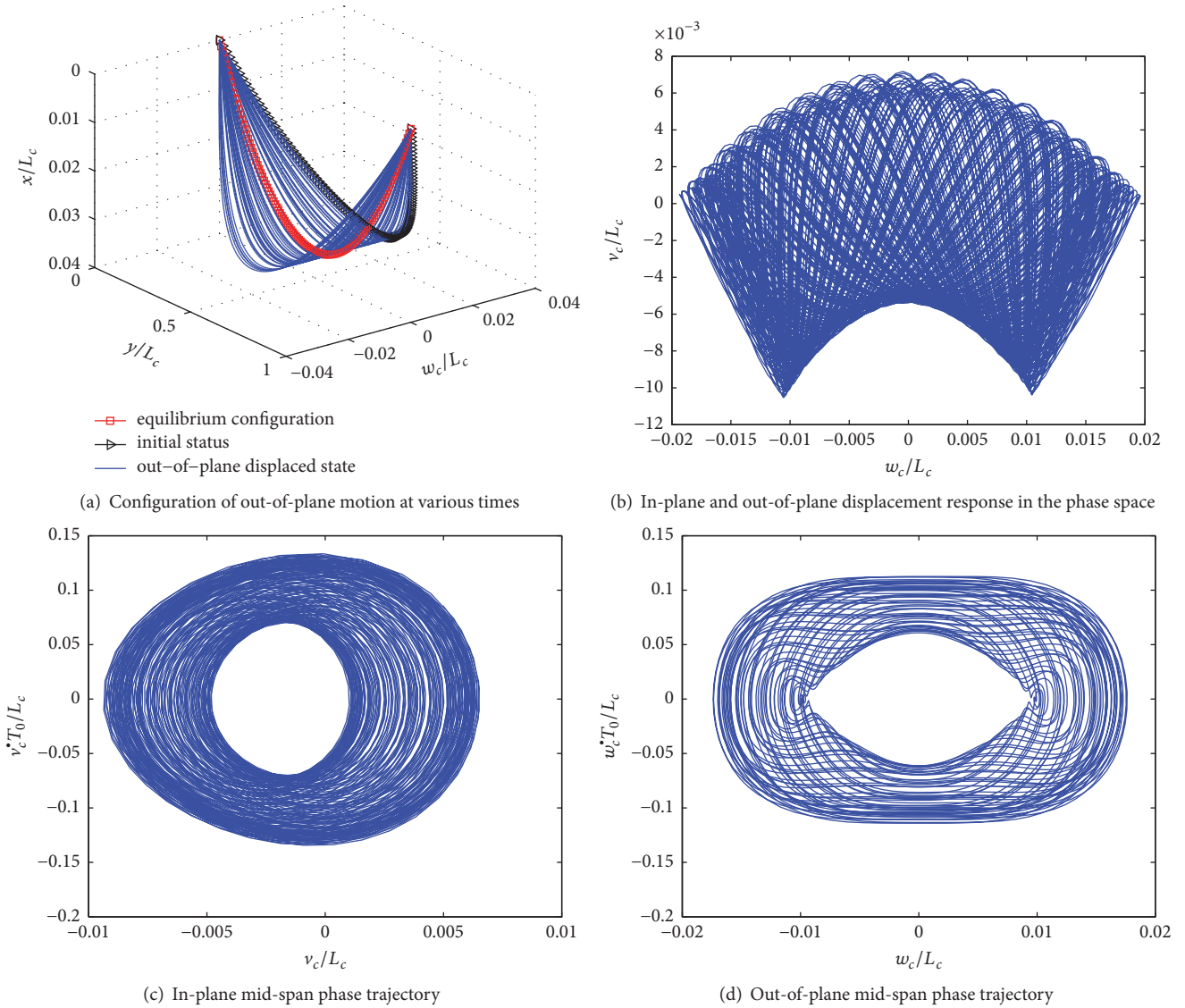


FIGURE 10: Configuration of the out-of-plane motion and the phase-space response of the transmission line when its initial potential energy is relatively high.

4.3.3. Effects of Damping on the Nonlinear Internal Resonance of the Transmission Line. It was noted in the previous sections that the structural damping of a transmission line is very small. To effectively reduce the vibration responses of transmission lines, control devices (e.g., dampers, spiral dampers, damping spacers, and damper lines) are often installed on transmission lines in engineering practice; these control devices can generate relatively large damping. Thus, in this section, the effects of damping on the internal resonance of the transmission line are analyzed.

Here, the same initial potential energy conditions as those used in Section 4.3.2 are used, but the initial damping is varied. Figures 12 and 13 show the free vibration response of the transmission line obtained in the simulation under various damping conditions. A comparison of Figures 12 and 13 with Figures 8–10 shows that, under the same conditions, increasing the damping of the transmission line results

in a significant decrease in the displacement of and the tension in the transmission line as well as a decrease in the duration of vibration of the transmission line. This indicates that increasing the damping of the transmission line can effectively consume its vibration energy, control its vibration response amplitude, and prevent an increase in its dynamic tension but cannot hamper the occurrence of its nonlinear internal resonance.

4.4. Numerical Analysis of the Nonlinear Internal Resonance of the Transmission Line When in Forced Vibration. Based on the aforementioned analysis, we know that the natural frequencies of the lower-order modes of vibration of the overhead transmission line are relatively low. However, in an actual environment, excitation energy (primarily wind load energy) is mainly distributed in the 0–1 Hz band, particularly in the 0–0.2 Hz band. Therefore, under an external excitation

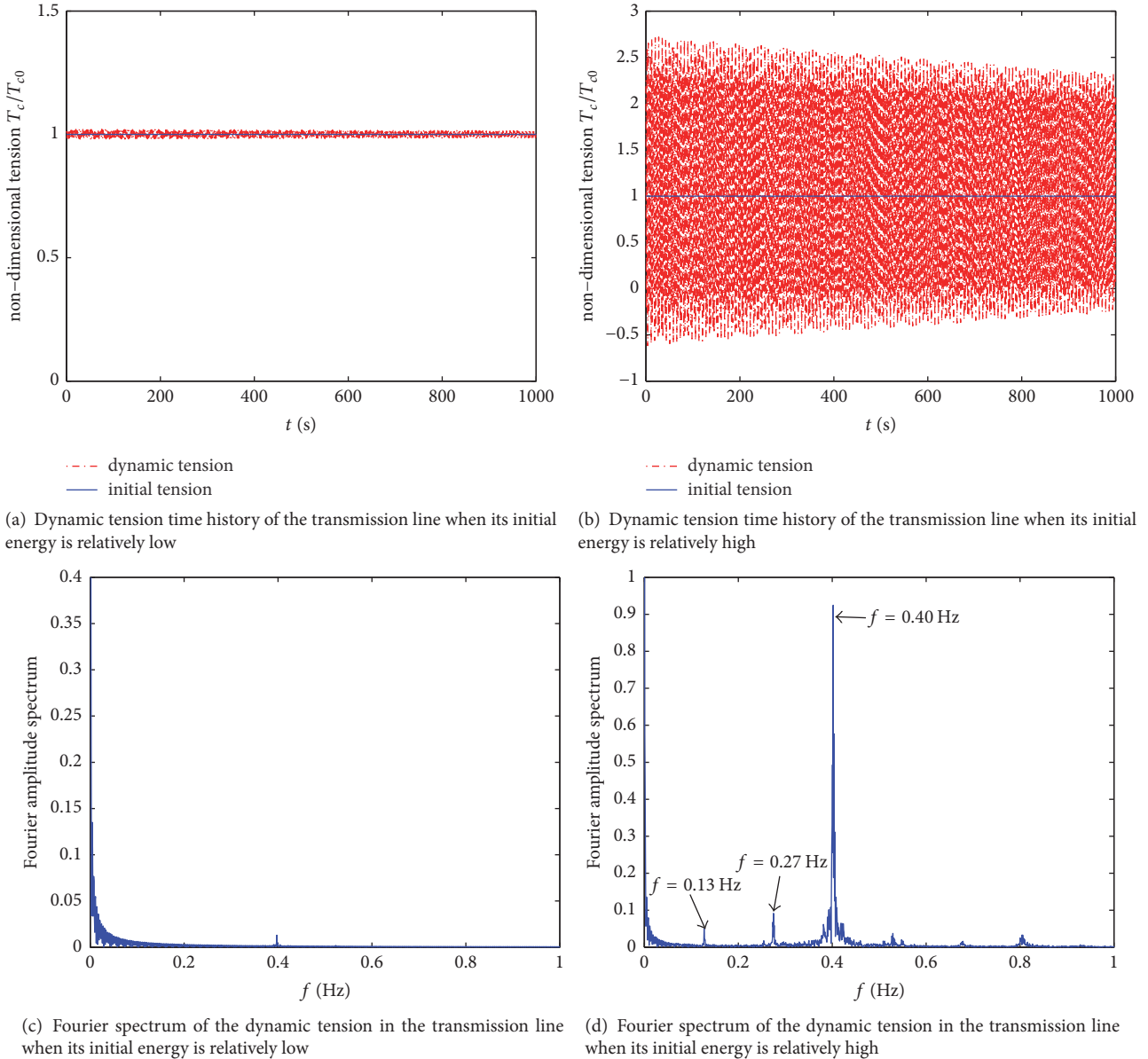


FIGURE 11: Dynamic tension in the transmission line and its Fourier spectra under two initial energy conditions.

(e.g., a wind load), there is a relatively high probability that the transmission line will resonate with it. To further study the effects of the internal resonance of the transmission line on its wind-induced vibration, in this section the effects of the internal resonance of the transmission line under a harmonic excitation on the primary resonance are first analyzed; based on the results, the forced vibration characteristics of the transmission line under a wind load are investigated.

4.4.1. Analysis of the Internal Resonance of the Transmission Line under a Harmonic Excitation. Here, it is assumed that the transmission line is only subjected to an out-of-plane harmonic excitation $P_w = P_0 \cos \Omega_z t$. The relationship between the circular frequency Ω_z of the excitation and the natural circular frequency ω_w of the out-of-plane vibration

of the transmission line is characterized by introducing a detuning parameter σ_1 , a nonnegative real number k , and a small parameter ε :

$$\Omega_z = k\omega_w + \varepsilon\sigma_1. \quad (59)$$

To study the primary resonance response of the system, k , ε , and σ_1 are set to 1, 0.001, and 10, respectively. By substituting these values into (51), the frequency f_z of the out-of-plane excitation is determined: $f_z = \Omega_z/(2\pi) = 0.146$ Hz. The natural frequency f_w of the first-order out-of-plane vibration of the transmission line that is directly induced by the excitation is as follows: $f_w = \omega_w/(2\pi) = 0.136$ Hz. f_z approximately equals f_w . Thus, it can be considered that $\Omega_z \approx \omega_w$.

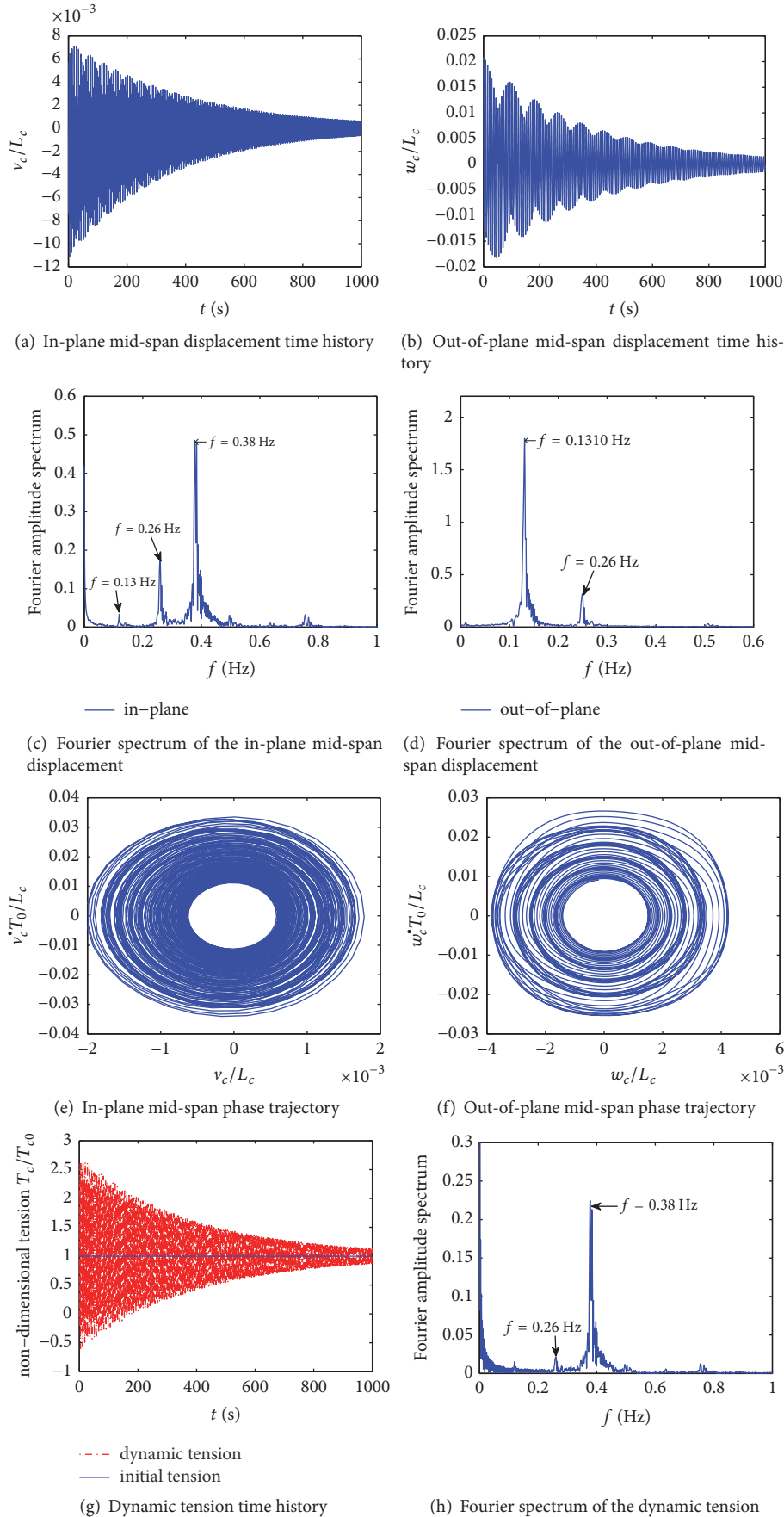


FIGURE 12: Free vibration response of the transmission line when its damping c_c is set to 0.01.

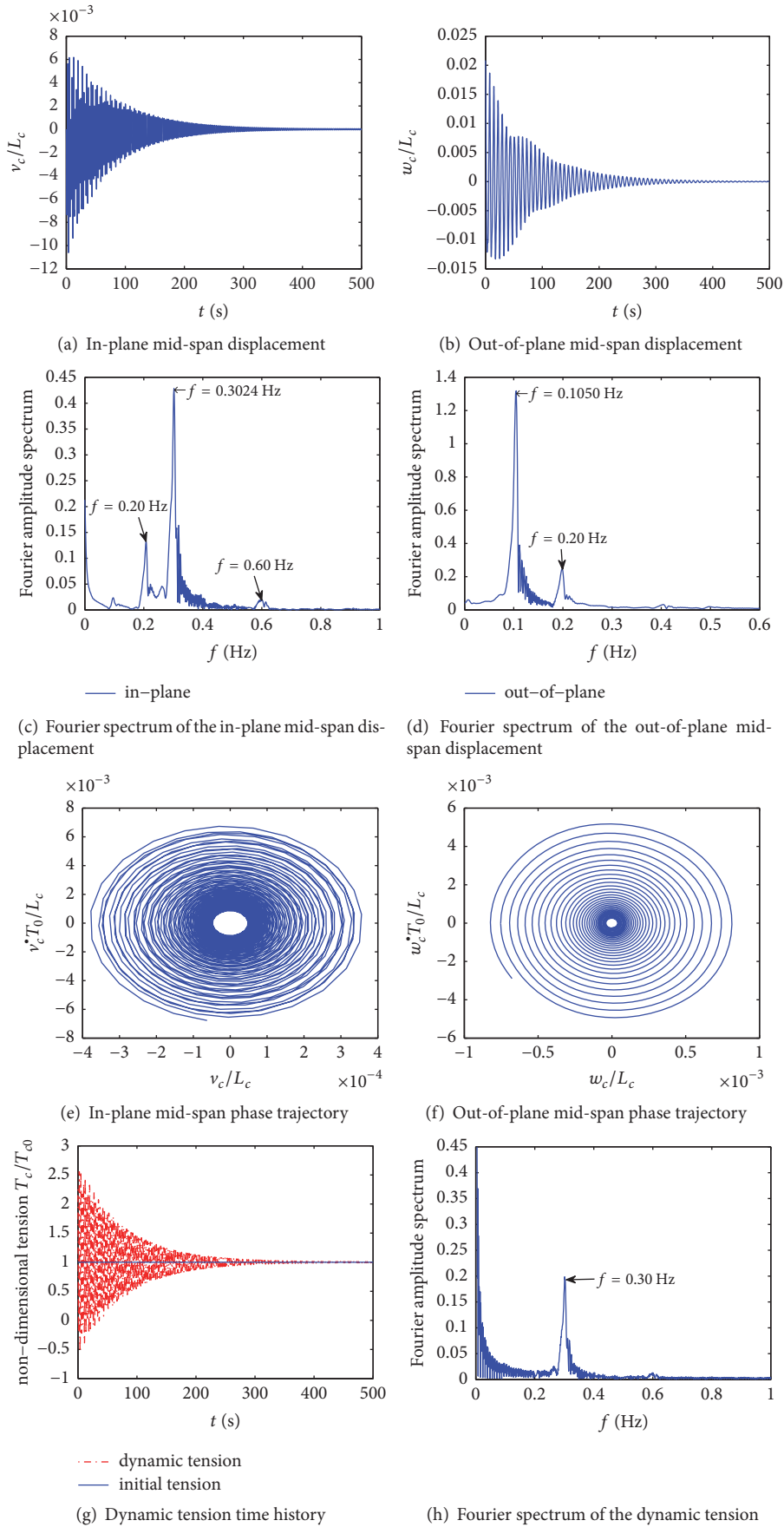


FIGURE 13: Free vibration response of the transmission line when its damping c_c is set to 0.05.

Let us set the amplitude P_0 of the generalized excitation load to 3305 N and the initial conditions for simulation to $q_v = 0$, $\dot{q}_v = 0$, $q_w = 0.1$, $\dot{q}_w = 0.00005$. By substituting these values into (54), the nonlinear forced vibration response of the transmission line under various damping conditions is determined. Figures 14–17 show the numerical simulation results obtained when the damping c_c is set to 0.001, 0.01, 0.05, and 0.1, respectively.

As demonstrated in Figure 14, the out-of-plane vibration of the transmission line directly induced by the excitation has a very large amplitude, suggesting that the transmission line is forced to resonate when $\Omega_z \approx \omega_w$. Due to the internal resonance, the vibration energy of the transmission line transfers from the out-of-plane direction to the in-plane direction, which is not directly under excitation. In addition, the in-plane vibration of the transmission line also exhibits resonance characteristics. In other words, due to the internal resonance, the forced resonance of the transmission line can involve several modes of resonance. When only considering the small structural damping, the resonance amplitude of the transmission line will jump; that is, within a certain period of time, the response occurs at a relatively small amplitude, and vibration with a relatively large amplitude occurs at a certain time and can continue steadily for an extended period of time. This differs from the resonance of a linear system. Due to the nonlinear coupling and internal resonance, the forced resonance modulates the vibration frequency of the system, and the frequencies of the out-of-plane and in-plane vibration of the transmission line are no longer linear natural frequencies and are also not the same as the excitation frequency but instead are manifested as a relatively wide distribution of vibration energy (Figures 14(c) and 14(d)). As demonstrated in the phase diagrams of the in-plane and out-of-plane response (Figures 14(e) and 14(f)), the in-plane and out-of-plane response is aperiodic with an amplitude that jumps. Considering that the external excitation has a very large amplitude due to the nonlinear internal resonance, the forced resonance excites the transmission line to resonate internally, resulting in a sharp increase in the dynamic tension in the transmission line. In addition, because of the in-plane vibration amplitude jumps, a corresponding jumping phenomenon is also observed in the dynamic tension time history curve (Figure 14(g)). As shown in the Fourier spectrum of the dynamic tension (Figure 14(h)), the dynamic tension in the transmission line is mainly significantly affected by the in-plane vibration. Because its amplitude is far greater than the design-breaking load, the dynamic tension may cause the transmission to break.

Figure 15 shows the simulation results obtained by increasing the damping c_c to 0.01, while retaining the other conditions. As demonstrated in Figure 15, amplitude jumps are eliminated due to the damping effects, but internal resonance still exists. The in-plane vibration of the transmission line not directly induced by the excitation has a large amplitude, which are of the same order of magnitude of the out-of-plane vibration. In addition, the frequency modulation by the forced resonance becomes more complicated compared to the situation in which the damping is small (Figures 15(c) and 15(d)). As demonstrated in the phase trajectory of the

steady-state response (Figures 15(e) and 15(f)), there are still jumps in the in-plane vibration amplitude of the transmission line and the corresponding dynamic tension amplitude, and the maximum value of these jumps can be as high as 3 times the initial tension. This indicates that it is still possible for the transmission line to be broken under these conditions.

Figures 16 and 17 show the simulation results that are obtained when the damping c_c is further increased to 0.05 and 0.1, respectively, while retaining the other conditions. As demonstrated in Figures 16 and 17, due to the large damping effects, the vibration amplitude of the transmission line reaches a stable state within a short period of time; however, the large damping is unable to prevent the occurrence of internal resonance, and the in-plane vibration still has a very large amplitude, the numerical value of which is commensurate with that of the out-of-plane vibration. The dynamic tension in the transmission line when it is in steady-state vibration can still reach approximately three times the initial tension. This suggests that even under relatively large damping effects, the forced resonance of the transmission line cannot be maintained as the steady-state mode of motion directly induced by the excitation but is instead manifested as the nonlinear vibration of coupled modes. Due to the frequency-modulating effect of the forced resonance, the natural frequencies of the modes of vibration of the transmission line directly induced by the excitation more accurately approach the excitation frequency, and, correspondingly, the modulated frequencies inherit the relationships between the original linear natural frequencies: they are either closely spaced with or multiples of one another. In addition, the vibration still contains higher-order modes of vibration.

As demonstrated in the phase trajectories of the response (Figures 16(e), 16(f), 17(e), and 17(f)), when its damping is relatively high, the resonance response of the transmission line reaches saturation. In other words, because the nonlinear vibration equations for the transmission line exhibit quadratic nonlinearity and the linear natural vibration frequencies of the transmission line satisfy the $\omega_w \approx \omega_v$ and $\omega_v \approx 2\omega_w$ conditions, when the frequency Ω_z of the external excitation is approximately equal to ω_w and the excitation amplitude meets a certain condition, the response energy of the mode of vibration directly induced by the excitation reaches saturation, and all the input excitation energy enters another mode. Thus, while its damping can be increased by installing energy dissipating equipment in engineering practice, the motion of a transmission line exhibits coupled in-plane and out-of-plane vibration characteristics due to the nonlinear internal resonance; in addition, a transmission line can still continue to vibrate with a relatively large amplitude under an external excitation with a relatively large amplitude, and the vibration energy continuously transfers between relevant modes without being attenuated. Due to the presence of this response saturation phenomenon, the dynamic tension in a transmission line when in vibration can still possibly reach a higher level even when its damping is set to a relatively large value, which is disadvantageous to practical engineering.

To compare the vibration response of the transmission line when not in resonance with the vibration response of

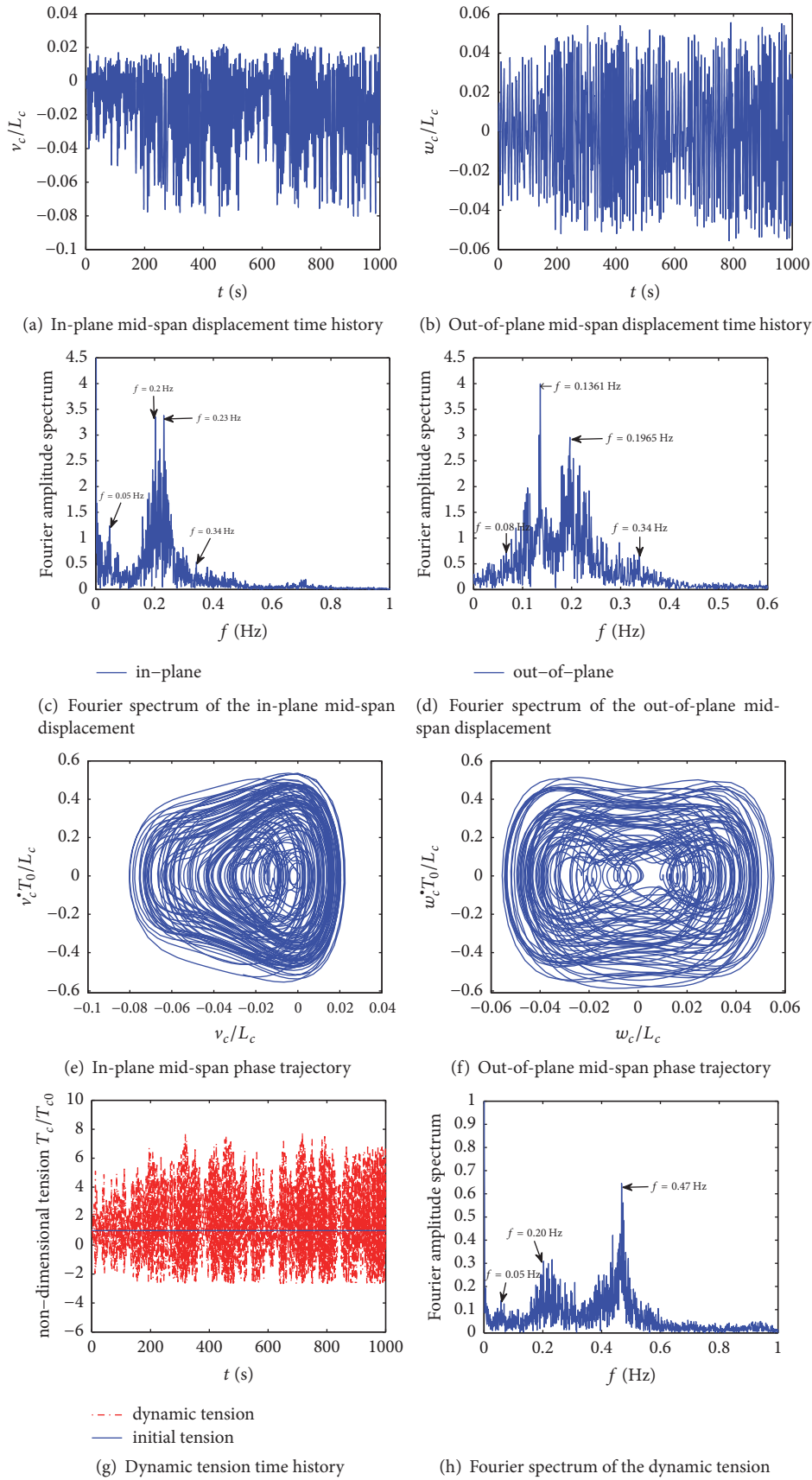


FIGURE 14: Primary resonance response of the transmission line when its damping c_c is set to 0.001.

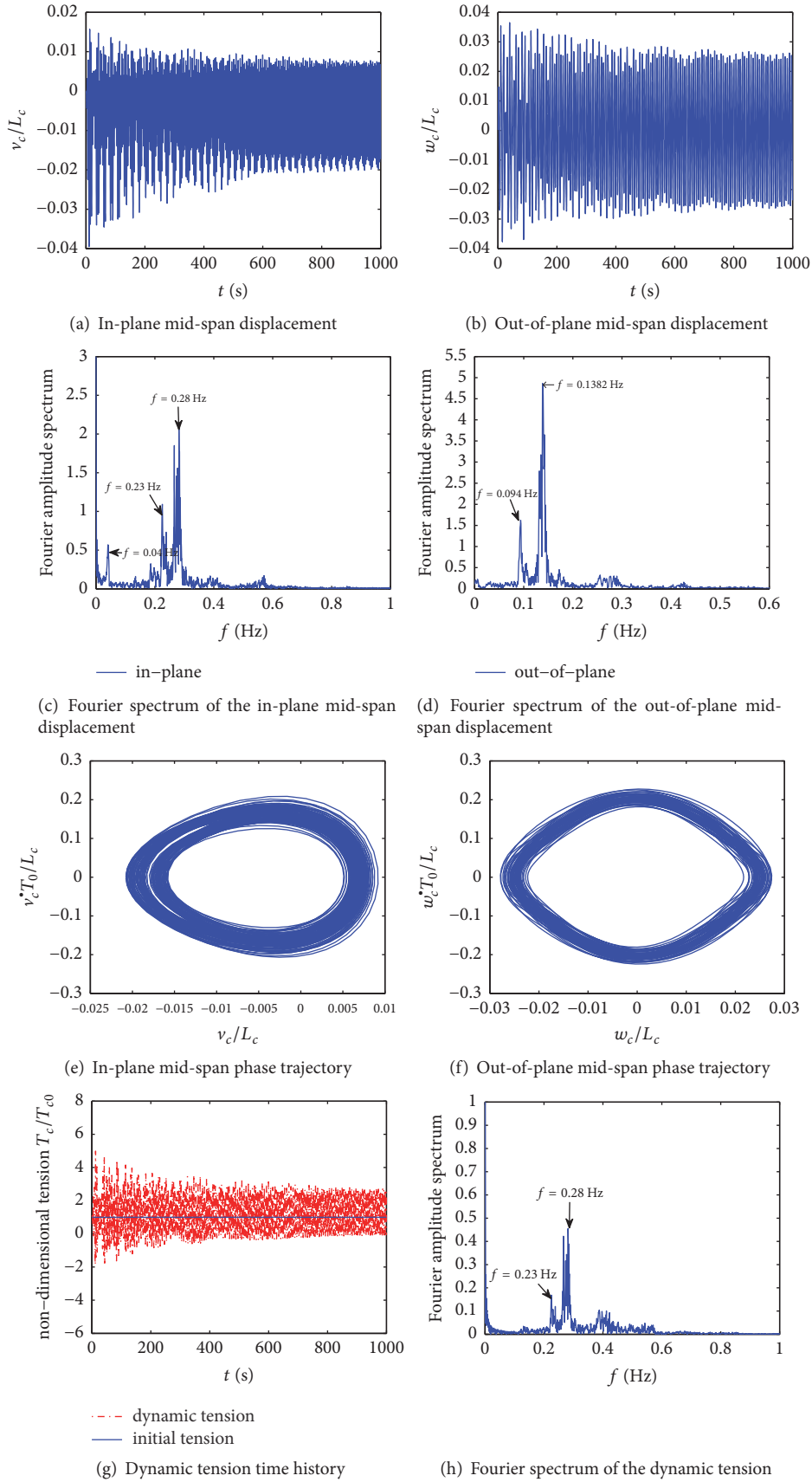


FIGURE 15: Primary resonance response of the transmission line when its damping c_c is set to 0.01.

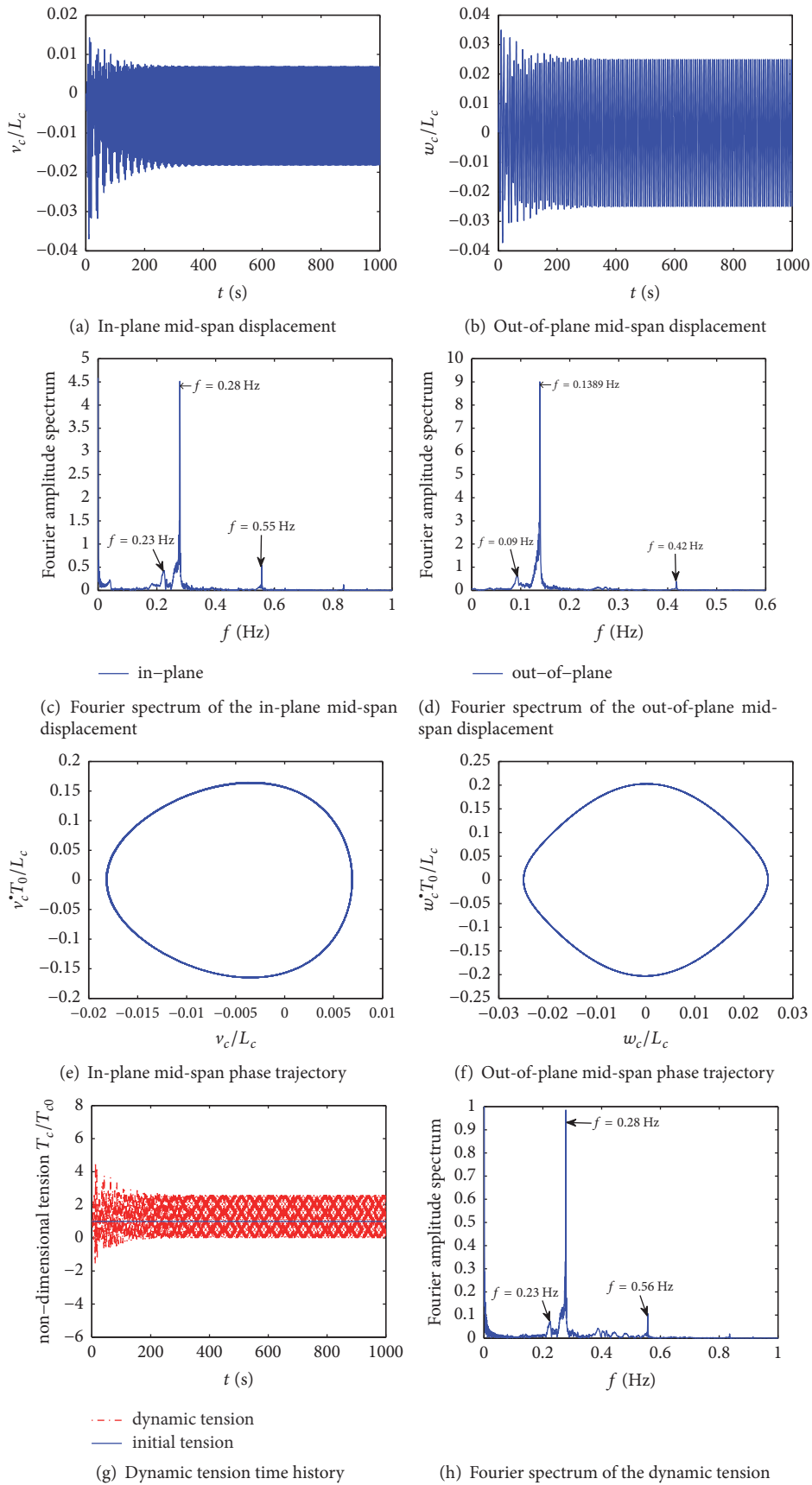


FIGURE 16: Primary resonance response of the transmission line when its damping c_c is set to 0.05.

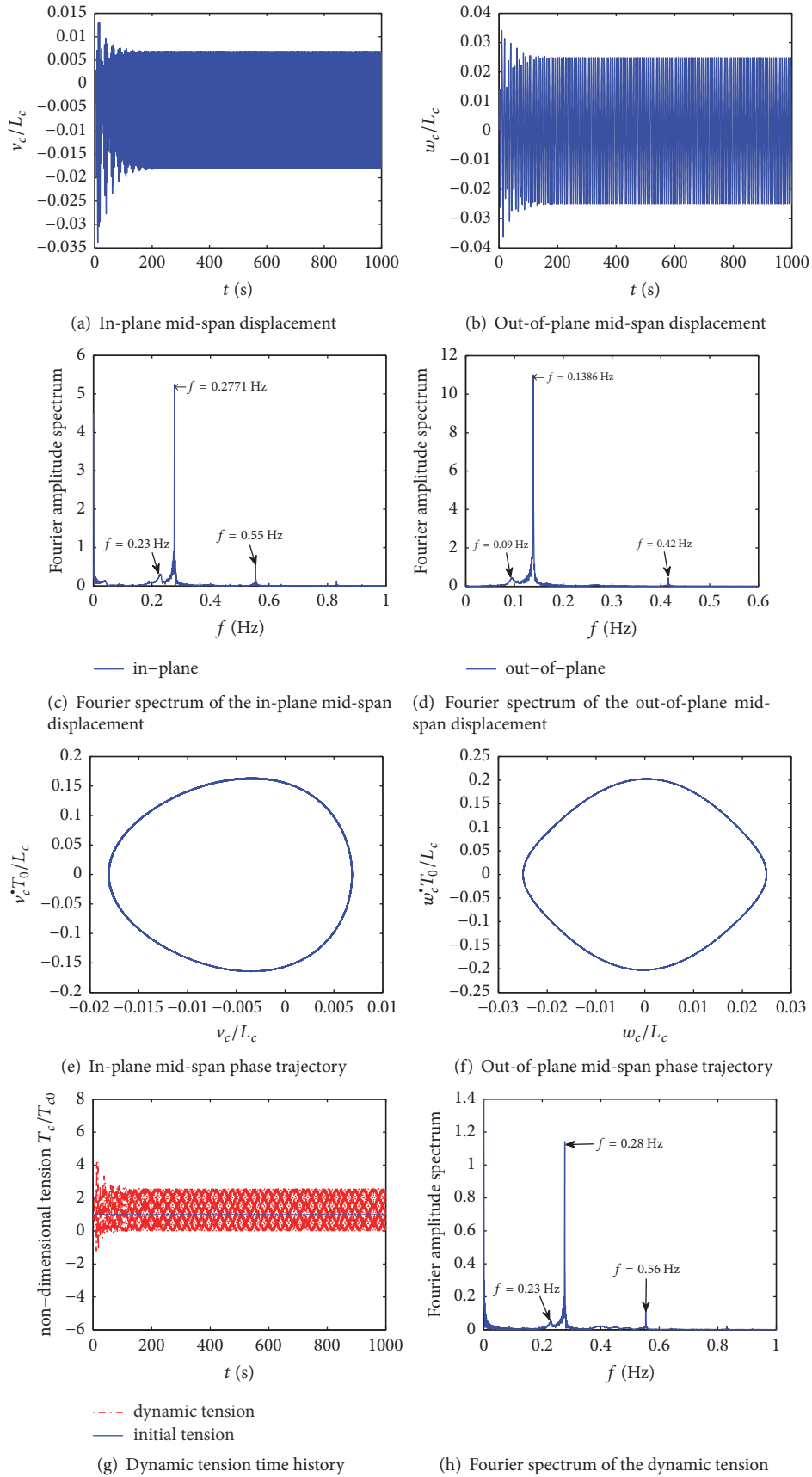


FIGURE 17: Primary resonance response of the transmission line when its damping c_c is set to 0.1.

the transmission line when in resonance, the following set of parameters is selected: frequency f_z of the external excitation: 0.68 Hz; damping c_c : 0.001; all the other parameters are the same as those used to simulate the transmission line when in resonance. Figure 18 shows the simulation results. A comparison of Figures 14 and 18 shows that when the external excitation amplitude and the damping of the transmission line remain unchanged, the vibration amplitude of the transmission line is far smaller when not in resonance than when in resonance. While an internal resonance phenomenon can still be observed numerically when the transmission line is not in resonance, the internal resonance-induced in-plane vibration amplitude is very small and is negligible. When the transmission line is not in resonance, the vibration of the system is primarily composed of the out-of-plane forced vibration induced by the out-of-plane excitation (Figure 18(d)); in addition, the dynamic tension in the transmission line changes to a relatively small extent (Figure 18(g)). It can be seen that internal resonance has a great influence on the main resonance of transmission line, so the design of transmission line needs to consider its influence reasonably.

4.4.2. Analysis of the Internal Resonance of the Transmission Line When in Wind-Induced Vibration. Under actual operating conditions, overhead transmission lines will inevitably undergo wind-induced vibration. Therefore, in this section, the nonlinear vibration characteristics of the transmission line under a wind load are studied. Considering that the vertical in-plane wind load on a transmission line is generally very small, to simplify the analytical process, it is assumed that the wind load acts in the out-of-plane direction of the transmission line. The quasi-steady hypothesis is used in calculation: when calculating the wind load on the transmission line, only the effects of the vibration of the transmission line on the wind speed are considered, whereas the aerodynamic coupling effects are not considered: that is, the load terms $P(x, t)$ and $P(z, t)$ in (26) and (27) can be expressed as follows:

$$\begin{aligned} P(x, t) &= 0.5\rho_a D_c C_D (v_{a-x} - \dot{v}_c)^2, \\ P(z, t) &= 0.5\rho_a D_c C_D (v_{a-z} - \dot{w}_c)^2, \end{aligned} \quad (60)$$

where ρ_a represents the air density; D_c represents the windward width of the transmission line; C_D represents the shape factor of the transmission line; v_{a-x} and v_{a-z} represent the wind speeds along the x - and z -axis directions, respectively; \dot{v}_c , \dot{w}_c represent the in-plane and out-of-plane vibration velocities of the transmission line, respectively.

By substituting (60) into (26) and (27) and finding the first-order modal solutions for the in-plane and out-of-plane vibration using *Galerkin's* modal truncation method, the continuous partial differential equations can be transformed to discrete ordinary partial equations, as shown in (30), in which the factors a_7 , b_6 , P_v , and P_w are calculated using the following equations (all the other factors are calculated using the same equations as introduced in Section 2.2):

$$\begin{aligned} a_7 &= \int_0^{L_c} (c_c + \rho_a D_c C_D v_{a-x}) \varphi_v^2(y) dy, \\ b_6 &= \int_0^{L_c} (c_c + \rho_a D_c C_D v_{a-z}) \varphi_w^2(y) dy, \\ P_v &= \int_0^{L_c} 0.5\rho_a D_c C_D (v_{a-x})^2 \varphi_v(y) dy, \\ P_w &= \int_0^{L_c} 0.5\rho_a D_c C_D (v_{a-z})^2 \varphi_w(y) dy. \end{aligned} \quad (61)$$

Wind speeds used in this section are selected from the database of wind speeds recorded by the field wind measurement platform installed on the transmission line (Figure 3). Three wind speed time histories with different average winds are selected, which are three wind speed records with an average value U_0 of 5.2, 9.56, and 20.1 m/s, respectively. These three wind speeds are equivalent to the Beaufort Scales 3, 5, and 8, respectively. The in-plane vertical wind load on the transmission line is converted from the vertical fluctuating wind speed recorded by the wind speed measurement device and its value is generally small and negligible. Figure 19 shows the frequency spectra corresponding to the aforementioned three wind speed time histories. As demonstrated in Figure 19, the wind speed energy is mainly distributed in the 0-1 Hz band.

Equation (30) is solved using a higher-order *Runge-Kutta* method. The damping c_c of the transmission line is set to 0.01, and the initial conditions for calculation are set as follows:

$$\begin{aligned} q_v &= 0, \\ \dot{q}_v &= 0, \\ q_w &= 0.5, \\ \dot{q}_w &= 0.00005. \end{aligned} \quad (62)$$

Based on Tables 3 and 4, we know that the natural frequencies of the first-order in-plane and out-of-plane vibration of the transmission satisfy the following condition: $\omega_v \approx 3\omega_w$. Figures 20–22 show the numerical simulation results with respect to the vibration response of the transmission line under a wind load.

As demonstrated in Figure 20, when $U_0 = 5.2$ m/s, the out-of-plane mid-span vibration amplitude of the transmission line can exceed 1 m, and its in-plane mid-span vibration amplitude is far greater than its cross-sectional diameter; in addition, the in-plane vibration is associated with a noticeable jumping phenomenon (Figure 20(a)). This indicates that the transmission line also undergoes internal resonance when in wind-induced vibration and that the vibration energy transfers between the out-of-plane and the in-plane modes of vibration. The overall vibration of the transmission line is manifested as coupled in-plane and out-of-plane vibration (Figure 20(b)). In-plane vibration amplitude jumps can also be found by observing the phase trajectories of the transmission line (Figures 20(c) and 20(d)). The out-of-plane vibration is a complex aperiodic motion. Due to the excitation from the wind load and the frequency-modulating effect of

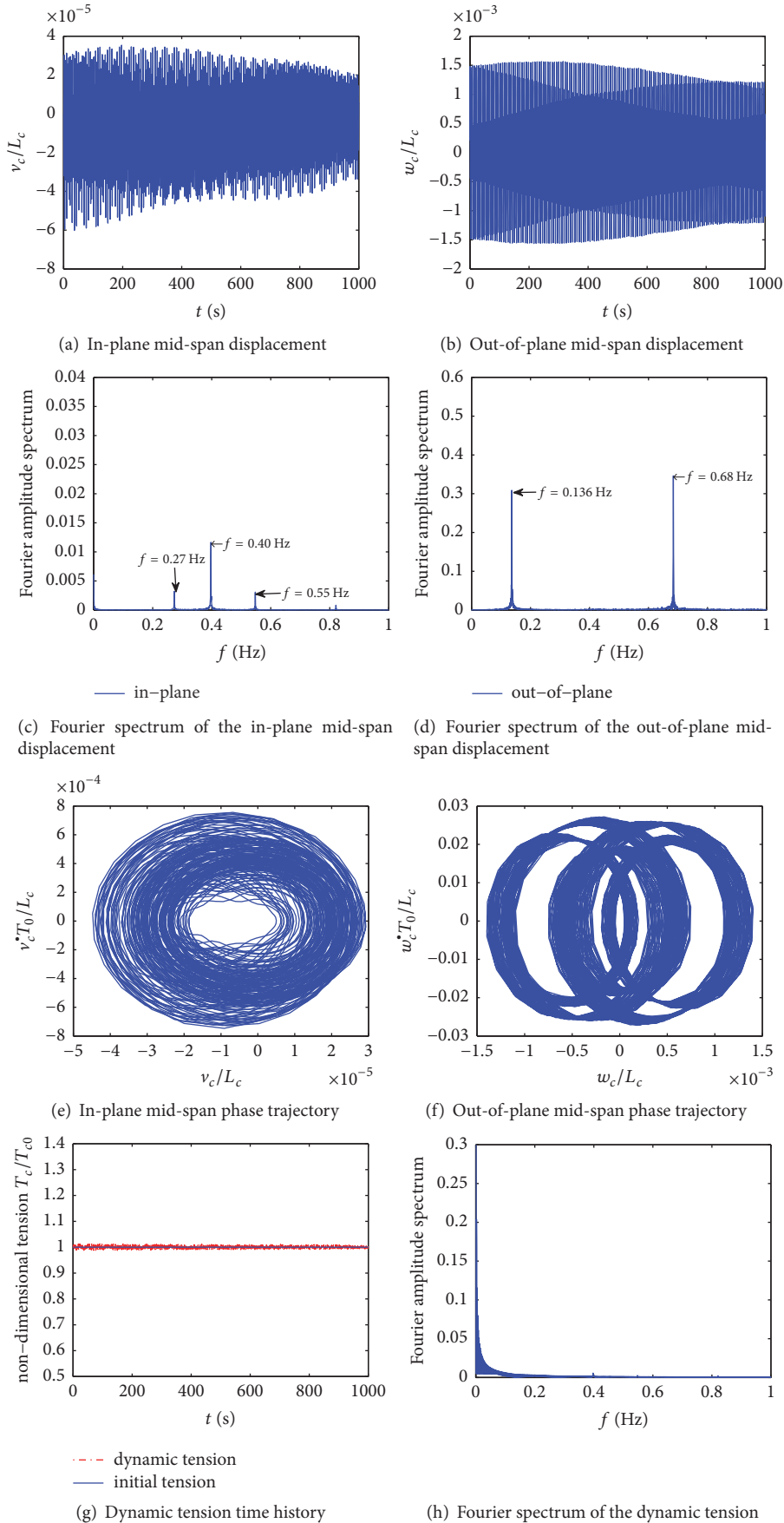


FIGURE 18: Nonresonance response of the transmission line when its damping c_c is set to 0.001.

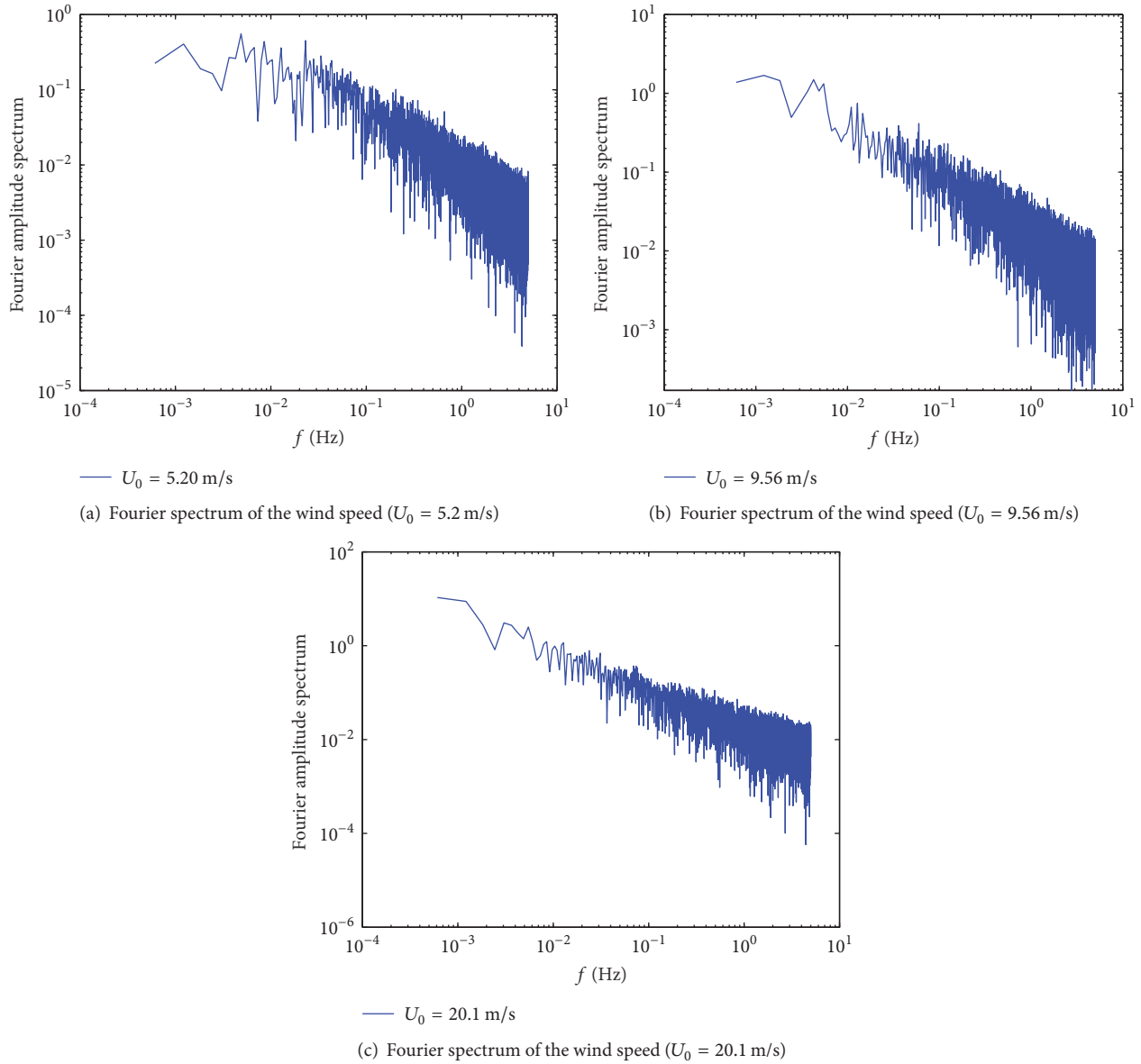


FIGURE 19: Fourier spectra of the wind speed.

the internal resonance, the natural characteristics of the in-plane and out-of-plane vibration undergo relatively significant changes, and its energy is distributed in a relatively wide frequency band (Figures 20(e) and 20(f)). In addition, due to the in-plane vibration, there are significant jumps in the dynamic tension amplitude of the transmission line (Figures 20(g) and 20(h)).

Figure 21 shows the simulation results obtained when the average wind speed U_0 is increased to 9.56 m/s. As demonstrated in Figure 21, the transmission line vibrates with a large amplitude; in addition, the out-of-plane mid-span vibration amplitude of the transmission line can reach half of its maximum sag, and its in-plane mid-span vibration amplitude can also reach half of its maximum out-of-plane vibration amplitude (Figure 21(a)); moreover, there are also jumps in the

in-plane and out-of-plane vibration amplitudes of the transmission line. However, due to the inherent randomness of a wind load, the internal resonance of the transmission line when in wind-induced vibration is not as conspicuous as the internal resonance that occurs when the line is in free vibration or under a harmonic excitation. However, as demonstrated by the response frequency spectra, changes in the natural vibration characteristics of the system are more significant than those that occur in a linear system. Higher-order in-plane and out-of-plane modes of vibration of the transmission line can be excited by a wind load with a relatively high wind speed (Figures 21(e) and 21(f)); under this condition, the phase trajectory of the response has an oval shape, and there are jumps in the displacement amplitude (the outer and inner trajectories represent lower-order and higher-order modes of

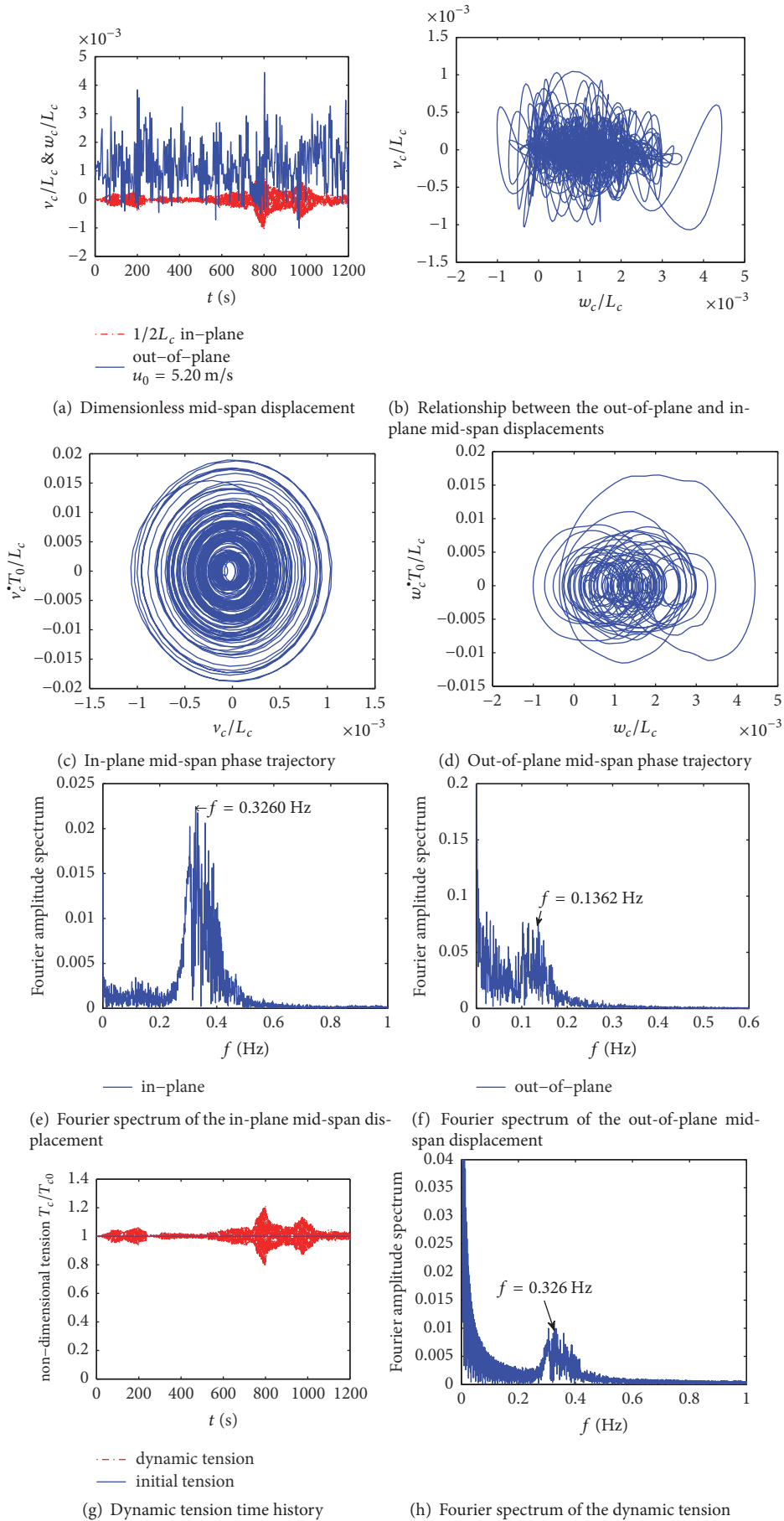


FIGURE 20: Wind-induced vibration response of the transmission line when $U_0 = 5.2$ m/s.

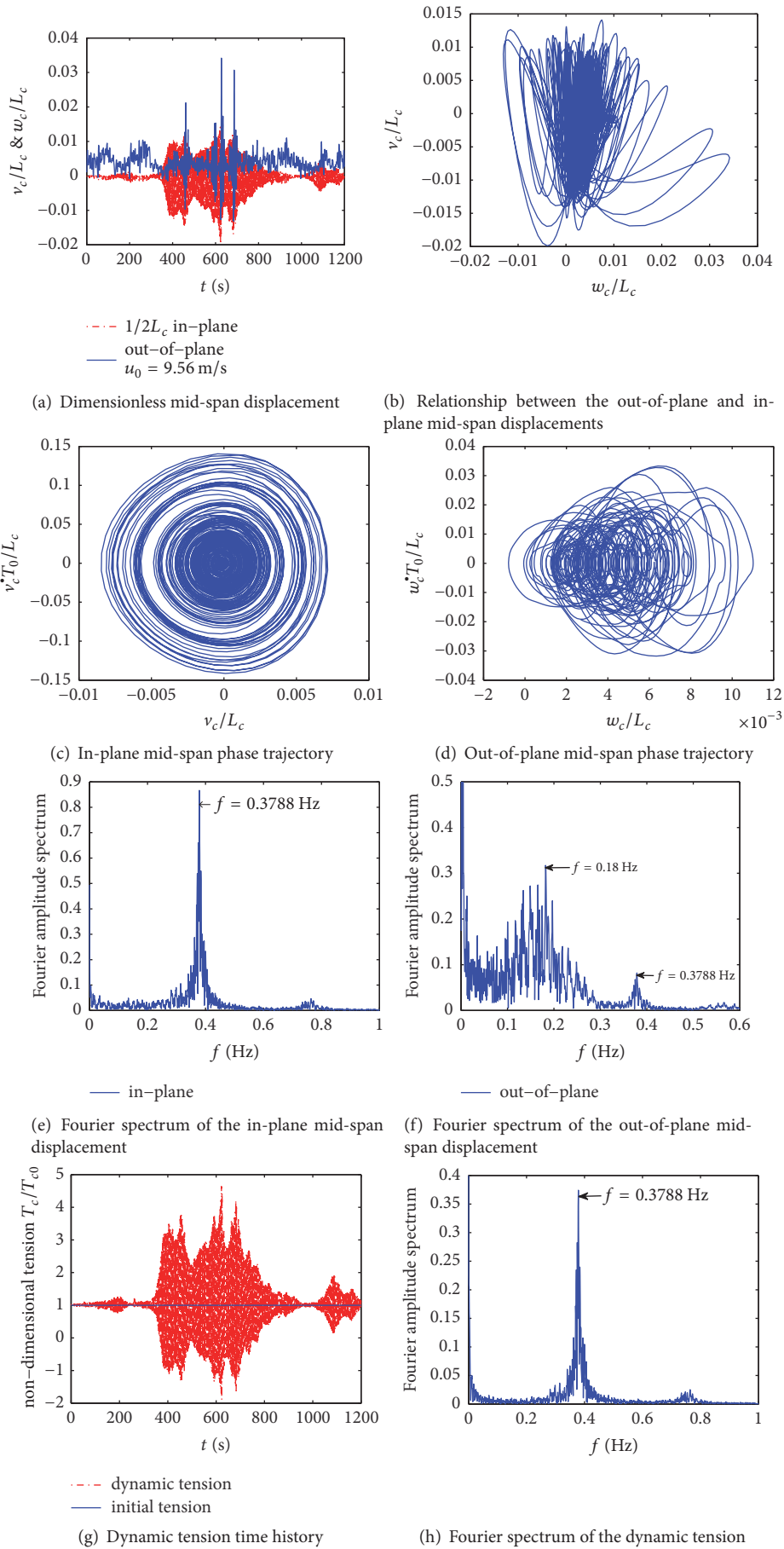


FIGURE 21: Wind-induced vibration response of the transmission line when $U_0 = 9.56$ m/s.

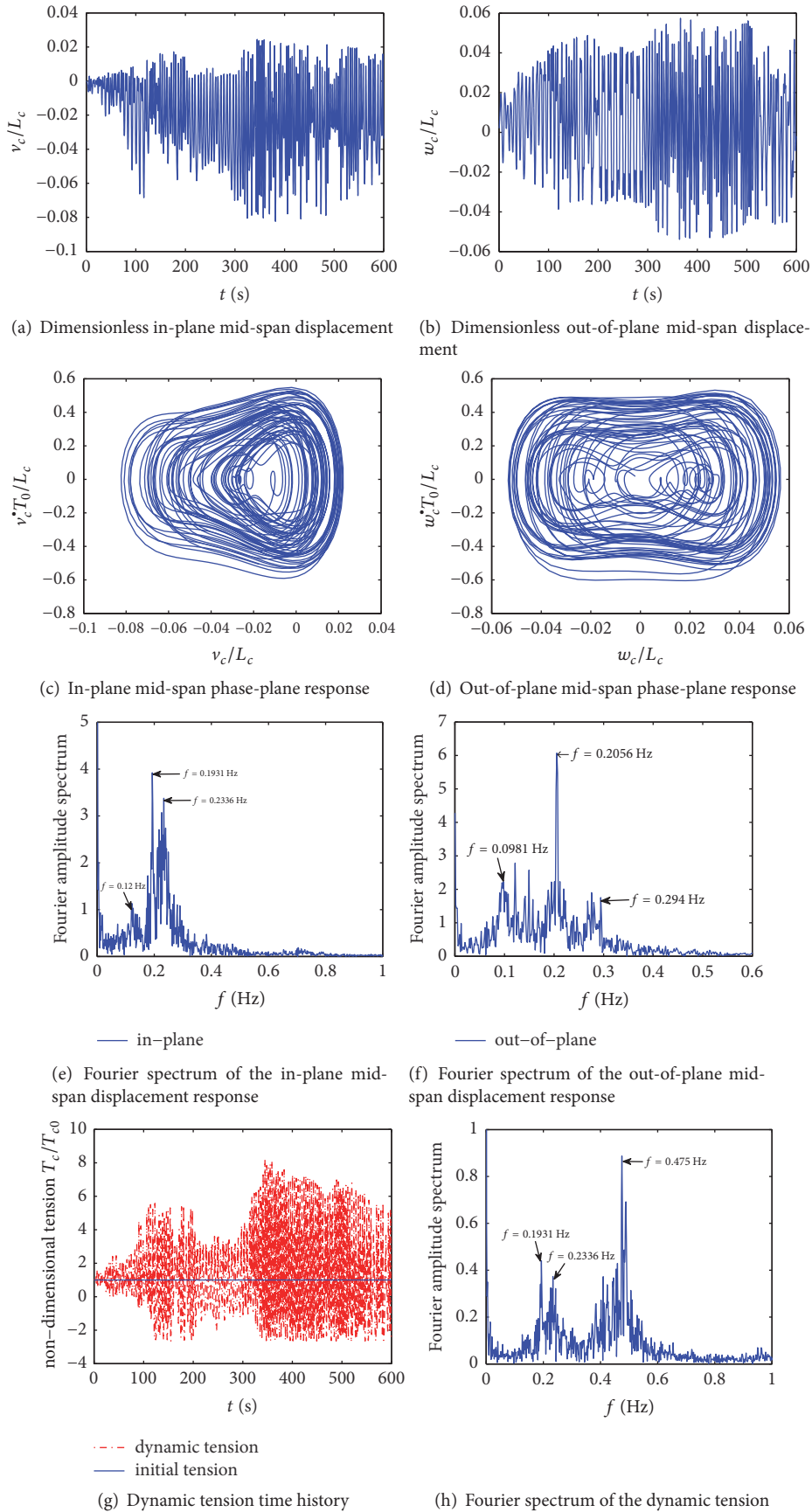


FIGURE 22: Wind-induced vibration response of the transmission line when $U_0 = 20.1$ m/s.

vibration, resp.) (Figures 21(c) and 21(d)). A comparison of Figures 20 and 21 shows that as the wind speed increases, the dynamic tension in the transmission line increases. Because the dynamic tension is mainly affected by the in-plane vibration, the jumps in the dynamic tension amplitude are quite noticeable. If the external wind excitation lasts for a sufficiently long period of time, the dynamic tension in the transmission line can even surpass its breaking load limit at some moments during the vibration process (Figures 21(g) and 21(h)), resulting in damage to the transmission line. This should warrant attention in practical engineering.

Figure 22 shows the simulation results obtained when the average wind speed U_0 is increased to 20.1 m/s. As demonstrated in Figure 22, the vibration amplitude of the transmission line further increases under a strong wind; in addition, the in-plane vibration amplitude of the transmission line is even greater than its out-of-plane vibration amplitude, and the out-of-plane and in-plane vibration amplitudes of the transmission line are of the same order of magnitude as its maximum arc sag (Figures 22(a) and 22(b)) and can even surpass its maximum arc sag, which will result in damage to the transmission line under practical conditions. As demonstrated in the in-plane and out-of-plane displacement response time histories and phase-plane response (Figures 22(c) and 22(d)), the wind-induced vibration of the transmission line exhibits significant nonlinear vibration characteristics; in addition, the out-of-plane vibration is also coupled to the in-plane vibration, and the vibration energy of the structure transfers from the out-of-plane modes that are under the wind load to the in-plane modes.

A comparison of Figures 22(e) and 22(f) shows that the energy-containing range of the out-of-plane mid-span displacement response of the transmission line is 0.09–0.294 Hz and the energy-containing range of its in-plane mid-span displacement response is 0.12–0.25 Hz, whereas the main energy-containing range of the wind load is 0.01–1 Hz. Thus, under a strong wind, the wind-induced vibration of the transmission line modulates not only the line's vibration amplitude but also its vibration frequency and can cause the transmission line to undergo high-frequency vibration; in addition, the dynamic tension in the transmission line increases significantly and can even reach or surpass its breaking load in a short time, which is very disadvantageous to the transmission line under practical conditions. A comparison of Figures 14 and 22 shows that the motion of the transmission line under a strong wind is similar to that of a primary resonance under harmonic excitation; that is, the amplitude of vibration is very large, and the in-plane vibration is strongly coupled to its out-of-plane vibration.

5. Conclusions

In this study, 3D nonlinear vibration equations for transmission lines that consider geometric nonlinearity are established. Based on the boundary conditions and the assumptions used for modeling, the 3D equations are simplified to 2D equations. *Galerkin's* modal truncation method is employed to simplify the continuous partial differential equations to discrete partial differential equations that are analyzed using

the method of multiple scales and solved by a higher-order *Runge-Kutta* method. On this basis, the nonlinear dynamic characteristics of transmission lines when in free and forced vibration, respectively, are analyzed. The main conclusions drawn from this study are summarized as follows:

(1) A transmission line has inherent nonlinear vibration characteristics. When in vibration, the in-plane motion of a transmission line is coupled to its out-of-plane motion, and linear, quadratic nonlinear, and cubic nonlinear modes of internal resonance can easily occur.

(2) When a transmission line vibrates freely, nonlinear internal resonance can occur even when the initial out-of-plane energy of the transmission line is relatively low; however, under this condition, energy transfer and mode coupling phenomena are not noticeable. As its initial out-of-plane energy increases, the internal resonance of a transmission line becomes prominent and the coupling of its in-plane and out-of-plane vibration becomes stronger, resulting in a transfer of out-of-plane vibration energy to the in-plane direction and an increase in the in-plane vibration amplitude and the dynamic tension in the transmission line. Due to the transmission line's mode coupling and nonlinear internal resonance, the out-of-plane and in-plane vibration frequencies of the line differ relatively significantly from the natural vibration frequencies of a linear system.

(3) Under a harmonic excitation, a transmission line undergoes forced resonance. Under the combined action of internal and primary resonance, the in-plane vibration of the transmission line is coupled to its out-of-plane vibration and the vibration energy transfers from the out-of-plane direction to the in-plane direction that is not directly under the excitation, resulting in a significant increase in the dynamic tension and the displacement amplitude of the transmission line. In addition, as the external excitation amplitude increases, the forced resonance effects become more significant, and the forced resonance has a modulating effect on the vibration frequency of the transmission line. As a result of the forced resonance, the in-plane and out-of-plane vibration energy of the transmission line is distributed over a relatively wide range.

(4) When a transmission line is in wind-induced vibration, as the wind speed increases, the nonlinear internal resonance of the transmission line increases; the frequency-modulating effect of its nonlinear internal resonance also increases, which may cause the transmission line to undergo high-frequency vibration. Because the in-plane vibration amplitude of a transmission line and its dynamic tension increase significantly as the wind speed increases, a noticeable amplitude jumping phenomenon occurs; consequently, when in vibration for a long period of time, the dynamic tension amplitude of the transmission line may exceed the breaking load limit, resulting in the breaking of the transmission line.

(5) Regardless of whether a transmission line is in free or forced vibration, increasing its damping can effectively consume its vibration energy, thereby allowing the vibration amplitude of the transmission line to reach a stable state within a short period of time. However, increasing the damping cannot prevent the occurrence of nonlinear internal resonance in a transmission line. When a transmission line

is in forced vibration and the external excitation has a relatively large amplitude, even if the damping of the transmission line is increased to a relatively large value, the transmission line can still maintain its nonlinear vibration of coupled modes with a large amplitude due to the nonlinear internal resonance; in addition, the vibration energy also constantly transfers between the coupled modes and does not decrease significantly. When a transmission line is in vibration for an extended period of time, this response saturation phenomenon can still cause the dynamic tension in the transmission line to surpass the design-breaking load, thereby causing damage to the transmission line.

Conflicts of Interest

The authors declare that there are no conflicts of interest regarding the publication of this paper.

Acknowledgments

This research has been funded by the National Natural Science Foundation of China (Grants nos. 51578512 and 51108425), Outstanding Young Talent Research Fund of Zhengzhou University (Grant no. 1521322004), and Foundation for University Young Key Teacher by Henan Province (Grant no. 2015GGJS-151).

References

- [1] H. M. Irvine, *Cable Structure*, MIT Press, 1981.
- [2] H. M. Irvine and J. H. Griffin, "On the dynamic response of a suspended cable," *Earthquake Engineering & Structural Dynamics*, vol. 4, no. 4, pp. 389–402, 1976.
- [3] H. Yamaguchi and M. Ito, "Linear theory of free vibrations of an inclined cable in three dimensions," *Proceedings of the Japan Society of Civil Engineers*, vol. 1979, no. 286, pp. 29–36, 1979.
- [4] H. Yamaguchi, T. Miyata, and M. Ito, "Time response analysis of a cable under harmonic excitation," *Proceedings of the Japan Society of Civil Engineers*, vol. 1981, no. 308, pp. 424–427, 1981.
- [5] N. C. Perkins and C. D. Mote Jr., "Three-dimensional vibration of travelling elastic cables," *Journal of Sound and Vibration*, vol. 114, no. 2, pp. 325–340, 1987.
- [6] G. Visweswara Rao and R. N. Iyengar, "Internal resonance and non-linear response of a cable under periodic excitation," *Journal of Sound and Vibration*, vol. 149, no. 1, pp. 25–41, 1991.
- [7] F. Benedettini, G. Rega, and R. Alaggio, "Non-linear oscillations of a four-degree-of-freedom model of a suspended cable under multiple internal resonance conditions," *Journal of Sound and Vibration*, vol. 182, no. 5, pp. 775–798, 1995.
- [8] M. Aufaure, "Three-node cable element ensuring the continuity of the horizontal tension; A clamp-cable element," *Computers & Structures*, vol. 74, no. 2, pp. 243–251, 2000.
- [9] W. K. Chang and R. A. Ibrahim, "Multiple Internal Resonance in Suspended Cables under Random In-Plane Loading," *Nonlinear Dynamics*, vol. 12, no. 3, pp. 275–303, 1997.
- [10] A. S. K. Kwan, "A new approach to geometric nonlinearity of cable structures," *Computers & Structures*, vol. 67, no. 4, pp. 243–252, 1998.
- [11] H. N. Arafat and A. H. Nayfeh, "Non-linear responses of suspended cables to primary resonance excitations," *Journal of Sound and Vibration*, vol. 266, no. 2, pp. 325–354, 2003.
- [12] N. Srinil, G. Rega, and S. Chucheepsakul, "Three-dimensional non-linear coupling and dynamic tension in the large-amplitude free vibrations of arbitrarily sagged cables," *Sound and Vibration*, vol. 269, no. 3–5, 852 pages, 2004.
- [13] N. Srinil, G. Rega, and S. Chucheepsakul, "Two-to-one resonant multi-modal dynamics of horizontal/inclined cables. I. Theoretical formulation and model validation," *Nonlinear Dynamics*, vol. 48, no. 3, pp. 231–252, 2007.
- [14] X. Xiao, J. Yang, J. Druetz, and Y. Xu, "Nonlinear oscillations of a suspended cable," *Zhendong Ceshi Yu Zhenduan/Journal of Vibration, Measurement and Diagnosis*, vol. 23, no. 2, p. 110, 2003.
- [15] D. Dempsey, "Winds wreak havoc on lines," *Transmission Distribution World*, vol. 48, no. 6, pp. 32–40, 1996.
- [16] K. Wang and G. Tang, "Response analysis of nonlinear vibration of overhead power line under suspension chain state," *Vibration and Shock*, vol. 22, no. 2, 72 pages, 2003.
- [17] N. Barbieri, O. H. de Souza Júnior, and R. Barbieri, "Dynamical analysis of transmission line cables. Part 1—Linear theory," *Mechanical Systems and Signal Processing*, vol. 18, no. 3, pp. 659–669, 2004.
- [18] R. Barbieri, N. Barbieri, and O. H. de Souza Júnior, "Dynamical analysis of transmission line cables. Part 3—Nonlinear theory," *Mechanical Systems and Signal Processing*, vol. 22, no. 4, pp. 992–1007, 2008.
- [19] A. Berlioz and C.-H. Lamarque, "A non-linear model for the dynamics of an inclined cable," *Journal of Sound and Vibration*, vol. 279, no. 3-5, pp. 619–639, 2005.
- [20] S. W. Rienstra, "Nonlinear free vibrations of coupled spans of overhead transmission lines," *Journal of Engineering Mathematics*, vol. 53, no. 3-4, pp. 337–348, 2005.
- [21] K. Tucker and A. Haldar, "Numerical model validation and sensitivity study of a transmission-line insulator failure using full-scale test data," *IEEE Transactions on Power Delivery*, vol. 22, no. 4, pp. 2439–2444, 2007.
- [22] G. F. Zhao, Q. Xie, and J. Li, "Wind-induced nonlinear interactions in the out-of-plane and in-plane dynamics of transmission line conductors," in *Proceedings of the in Proceedings of Second International Conference on Modelling and Simulation*, pp. 80–85, UK, 2009.
- [23] L. Wang and B. Fang, "Simulations on transient characteristics of 500 kV capacitor voltage transformer," *Gaodiyuan Jishu/High Voltage Engineering*, vol. 38, no. 9, pp. 2389–2396, 2012.
- [24] X. Xie, X. Hu, J. Peng, and Z. Wang, "Refined modeling and free vibration of two-span suspended transmission lines," *Acta Mechanica*, vol. 228, no. 2, pp. 673–681, 2017.
- [25] A. H. Nayfeh and D. T. Mook, *Nonlinear Oscillations*, John Wiley & Sons, New York, NY, USA, 1979.
- [26] B. Wen, Y. Li, P. Xu, and Q. Han, *Engineering Nonlinear Vibration*, Science Press, Beijing, China, 2007.
- [27] G. Veronis, "A note on the method of multiple scales," *Quarterly of Applied Mathematics*, vol. 38, no. 3, pp. 363–368, 1980/81.
- [28] H. Wang and H. Hu, "Remarks on the perturbation methods in solving the second-order delay differential equations," *Nonlinear Dynamics*, vol. 33, no. 4, pp. 379–398, 2003.

- [29] Hu. Huailei WangHaiyan, "A note on the method of multiple scales," *Journal of Dynamics and Control*, vol. 2, no. 3, pp. 10–13, 2004.
- [30] M. Zhang, G. Zhao, L. Wang, and J. Li, "Wind-induced coupling vibration effects of high-voltage transmission tower-line systems," *Shock and Vibration*, vol. 2017, 34 pages, 2017.

Research Article

Adaptive Reconstruction of a Dynamic Force Using Multiscale Wavelet Shape Functions

Wen-Yu He ¹, Yang Wang,¹ and Songye Zhu ²

¹Department of Civil Engineering, Hefei University of Technology, Hefei, Anhui, China

²Department of Civil and Environmental Engineering, The Hong Kong Polytechnic University, Hung Hom, Kowloon, Hong Kong

Correspondence should be addressed to Songye Zhu; songye.zhu@polyu.edu.hk

Received 25 July 2017; Revised 13 December 2017; Accepted 31 December 2017; Published 31 January 2018

Academic Editor: Jussi Sopanen

Copyright © 2018 Wen-Yu He et al. This is an open access article distributed under the Creative Commons Attribution License, which permits unrestricted use, distribution, and reproduction in any medium, provided the original work is properly cited.

The shape function-based method is one of the very promising time-domain methods for dynamic force reconstruction, because it can significantly reduce the number of unknowns and shorten the reconstruction time. However, it is challenging to determine the optimum time unit length that can balance the tradeoff between reconstruction accuracy and efficiency in advance. To address this challenge, this paper develops an adaptive dynamic force reconstruction method based on multiscale wavelet shape functions and time-domain deconvolution. A concentrated dynamic force is discretized into units in time domain and the local force in each unit is approximated by wavelet scale functions at an initial scale. Subsequently, the whole response matrix is formulated by assembling the responses induced by the wavelet shape function forces of all time units which are calculated by the structural finite element model (FEM). Then, the wavelet shape function-based force-response equation is established for force reconstruction. Finally, the scale of the force-response equation is lifted by refining the wavelet shape function with high-scale wavelets and dynamic responses with more point data to improve the reconstruction accuracy gradually. Numerical examples of different structural types are analyzed to verify the feasibility and effectiveness of the proposed method.

1. Introduction

Forward and inverse dynamic analyses are two typical types of structural dynamic problems, containing three basic components, namely, excitations, structures, and responses. The forward analysis refers to structural response calculation with the knowledge of excitation and structure parameters. The inverse analysis can be classified into two types: structural parameters identification using the known excitation and response and force reconstruction using the known structure parameters and response. Dynamic force reconstruction methods based on structural dynamic response have attracted great interest in the field of structural health monitoring (SHM), as it is often difficult or impractical to measure a dynamic force directly. Dynamic force reconstruction methods can generally be categorized into two groups: frequency-domain [1–4] and time-domain [5–8] methods. The frequency- and time-domain methods estimate dynamic forces by establishing the relationship between dynamic

forces and structural responses based on frequency response functions [9, 10] and impulse response functions [11, 12], respectively. Compared to the frequency-domain methods, the time-domain methods have received increasing attention in the past years because of their distinct physical meaning and relatively higher accuracy [13].

Most time-domain methods are based on discretization in the time domain. The sampling time interval size is one main factor that affects the reconstruction accuracy and efficiency. In general, a smaller size of sampling time interval can achieve higher reconstruction accuracy. However, a very small size would result in too many undetermined coefficients, which not only increases the computation cost but also tends to make the inverse problem ill-conditioned [13]. Therefore, it is challenging to set an optimal sampling time interval to balance the tradeoff between reconstruction accuracy and efficiency. Approaches based on various basis functions were proposed to address this challenge, in which unknown dynamic forces were approximated by

basis functions, such as Gaussian basis functions [14], B-spline functions [15, 16], triangle functions [17], exponential function [18], and Daubechies wavelet [19], and subsequently they were reconstructed by identifying the coefficients in these basis functions. These approaches could significantly reduce the number of unknowns (considerably less than that of data points) and shorten the identification time.

The majority of the above-mentioned basis function-based methods are whole-domain methods, which are similar to the Rize method in structural analysis. Whole-domain methods are not efficient when actual dynamic forces are complex. Therefore, Liu et al. [20] introduced the concept of “shape function” from finite element methods (FEM) into the field of force identification. A dynamic force was discretized into time units in the time domain and the local force in each time unit was approximated by shape functions. Numerical examples indicated that the shape function-based method could provide better results than traditional methods. The reconstruction accuracy of shape function-based methods depends on the approximation ability of shape functions, which is mainly determined by the length of the discrete time unit. The shape function-based methods transform the task of determining the optimal sampling time interval in traditional time-domain force identification methods into determining the optimal time unit length. In theory, shortening the time unit length can enhance the identification accuracy at the cost of an increased computation amount. However, determining the optimum time unit length in advance that can achieve the tradeoff between reconstruction accuracy and efficiency is not easy.

This paper aims to develop an adaptive method for dynamic force reconstruction based on multiscale wavelet shape functions and time-domain deconvolution. The time history of a concentrated dynamic force is discretized into time units, and wavelet scale functions at an initial scale are employed to approximate the local force within each unit. Then, the responses induced by the forces expressed using wavelet shape functions are computed by structural FEM, and the whole response matrix is formulated by assembling the responses induced by the forces expressed using different wavelet shape functions in all time units. This process is similar to assembling stiffness matrices in FEM. Subsequently, the wavelet shape function-based force-response equation is established for force reconstruction. The scale of the force-response equation is lifted by refining the wavelet shape functions with high-scale wavelets and dynamic response with more point data when necessary; consequently, the reconstruction accuracy is improved gradually. Finally, numerical examples of a simply supported beam and a two-story frame are analyzed to verify the feasibility and effectiveness of the proposed method. With this adaptive method, the challenging task in determining the time unit length can be overcome.

2. Multiscale Wavelet Shape Functions

2.1. Multiresolution Wavelet Analysis. Known as a “numerical microscope,” wavelet was firstly applied in the field of signal and image processing, and later its use was extended to

numerical computation in engineering [21]. Multiresolution analysis is one of the most important characteristics of wavelets [22]. A multiresolution analysis R of L^2 is a sequence of closed subspaces $R = \{V_j \subset L^2 \mid j \in Z\}$, such that [22]

- (1) $V_j \subset V_{j+1}$;
- (2) $\bigcup_{j \in J} V_j$ is dense in L^2 ;
- (3) for each $j \in J$, V_j has a Riesz basis given by scaling functions $\{\varphi_{j,k} \mid k \in K(j)\}$, where j is the level of resolution, J is an integer index set associated with resolution levels, $K(j)$ is some index set associated with the scaling functions of level j , and V_j denotes the approximation spaces of level j . For each V_j , a complement of V_j exists in V_{j+1} , namely, W_j . Let spaces W_j be spanned by wavelets $\psi_{j,m}(x)$ for every $m \in M(j)$, $M(j) = K(j+1) \setminus K(j)$, where $M(j)$ is the difference set of $K(j+1)$ and $K(j)$. Furthermore, let $l \in K(j+1)$ be the index at level $j+1$.

Multiresolution analysis enables wavelets to represent a finite energy function in a dynamic multiscale manner with different precision levels. For example, function $f(x)$ can be approximated in V_0 (low-scale space) as

$$f(x) \approx f^0(x) = \sum_k \bar{c}_{0,k} \phi_{0,k}, \quad (1)$$

where $\phi_{0,k}$ is the scaling function at Scale 0 and $\bar{c}_{0,k}$ represents the corresponding wavelet coefficients.

$$\bar{c}_{0,k} = \langle f(x), \phi_{0,k}(x) \rangle. \quad (2)$$

Approximation accuracy can be improved by adding high-scale wavelet terms in wavelet space W_0 , which is spanned by the wavelet functions $\psi_{0,l}$. Therefore, the approximation in space V_1 (high-scale space) is

$$f(x) \approx f^1(x) = \sum_k \bar{c}_{0,k} \phi_{0,k} + \sum_l c_{0,l} \psi_{0,l}, \quad (3)$$

where $\psi_{0,l}$ is the wavelet function at Scale 0 and $c_{0,l}$ is the corresponding wavelet coefficients in space W_0 .

$$c_{0,l} = \langle f(x), \psi_{0,l}(x) \rangle. \quad (4)$$

By further increasing the approximation order, the wavelet representation of the function approaches the exact function when $j \rightarrow \infty$.

$$f(x) \approx f^j(x) = \sum_k \bar{c}_{0,k} \phi_{0,k} + \sum_{j,l} c_{j,l} \psi_{j,l}, \quad (5)$$

$$f(x) = f^{j \rightarrow \infty}(x).$$

2.2. The Refinement of Lagrange Wavelet Function. Various wavelets, including spline wavelet [23], Daubechies wavelet [24], Hermite wavelet [25], Lagrange wavelet [26], and trigonometric wavelet [27], have been employed in numeral computation. In this study, the second-generation Lagrange

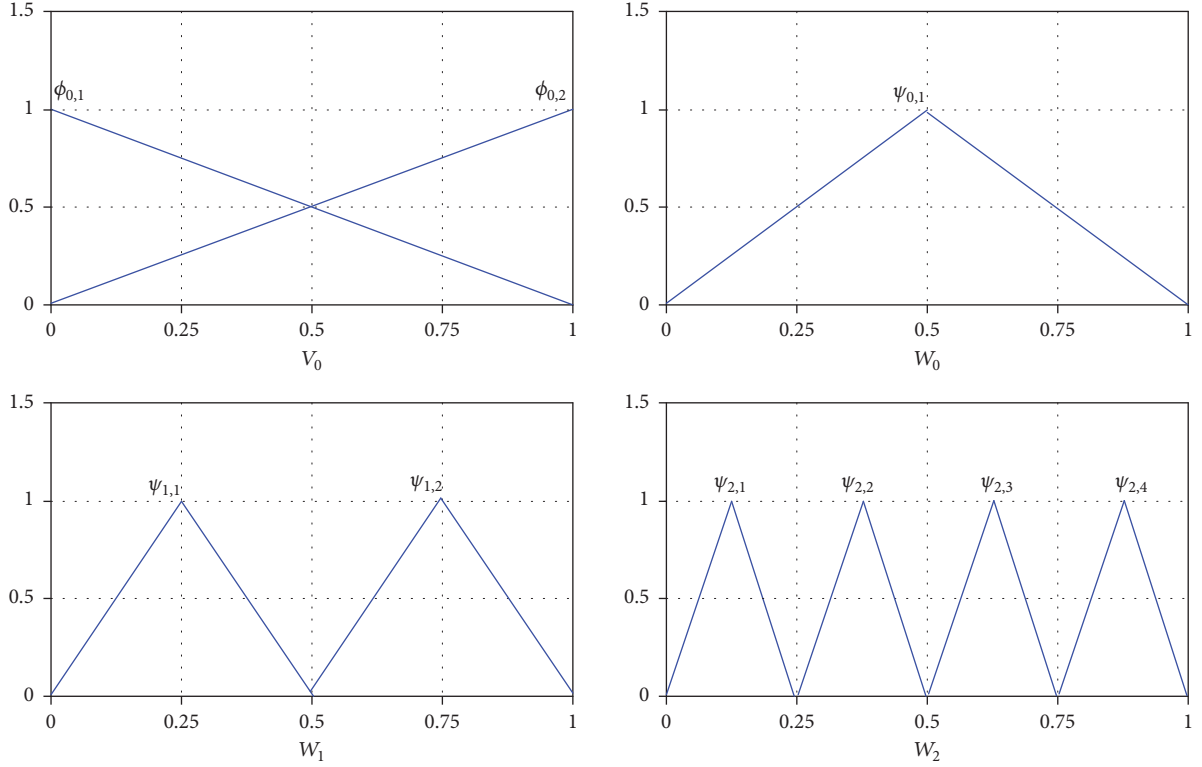


FIGURE 1: Lagrange wavelet shape functions.

wavelet [26] with convenient computational characteristics is adopted to fulfill the adaptive dynamic force reconstruction.

When defined within the interval $[0, 1]$, the scaling functions (Scale 0) of Lagrange wavelets are

$$\phi_{0,1} = \begin{cases} 1-x & x \in [0, 1] \\ 0 & \text{otherwise} \end{cases} \quad (6a)$$

$$\phi_{0,2} = \begin{cases} x & x \in [0, 1] \\ 0 & \text{otherwise} \end{cases} \quad (6b)$$

The corresponding wavelet function $\psi_{j,l}(x)$ at scale j is

$$\psi_{j,l}(x) = \begin{cases} 2^{j+1}x - 2l + 2 & x \in \left[\frac{l-1}{2^j}, \frac{l-0.5}{2^j} \right] \\ -2^{j+1}x + 2l & x \in \left[\frac{l-0.5}{2^j}, \frac{l}{2^j} \right] \\ 0 & \text{otherwise} \end{cases} \quad (7)$$

The scale functions (V_0) and wavelet functions (W_0 , W_1 , and W_2) are shown in Figure 1.

3. Adaptive Dynamic Force Reconstruction Method

Wavelet functions or scale functions are employed as elemental shape functions in the wavelet FEM to analyze structures in an adaptive manner according to actual needs.

When the wavelet FEM is employed to analyze structure problems, initial solutions with relatively low accuracy are obtained in low-scale models, and more accurate results can be acquired by lifting the model scale [21]. With this adaptive analysis, a tradeoff between the computation accuracy and computation efficiency can be achieved. In this section, this adaptive strategy will be further extended for dynamic force reconstruction to overcome the challenge in determining time unit length.

3.1. Time-Domain Deconvolution Method. Time-domain deconvolution is one of the most widely used methods for structural dynamic force reconstruction [28]. By assuming zero initial conditions, the structural response $y(t)$ can be expressed as a convolution integral of an external dynamic force $f(t)$ and the corresponding impulse response function $h(t-\tau)$ [20]:

$$y(t) = \int_0^t h(t-\tau) f(\tau) d\tau. \quad (8)$$

In a real dynamic test, structural dynamic responses are usually discrete. Suppose there are r sampling points in total. Equation (8) can be transformed into a discrete type:

$$\begin{bmatrix} y(t_1) \\ y(t_2) \\ \vdots \\ y(t_r) \end{bmatrix} = \begin{bmatrix} h(t_1) & 0 & \dots & 0 \\ h(t_2) & h(t_1) & \dots & 0 \\ \vdots & \vdots & \ddots & \vdots \\ h(t_r) & h(t_{r-1}) & \dots & h(t_1) \end{bmatrix} \begin{bmatrix} f(t_1) \\ f(t_2) \\ \vdots \\ f(t_r) \end{bmatrix} \Delta t, \quad (9)$$

where Δt is the discrete time interval. With this equation, the time history of the dynamic force $f(t)$ can be reconstructed by the measured structural response $y(t)$ and the impulse response function $h(t - \tau)$ generally obtained from the structural FEM.

The size of the sampling time interval Δt affects both the reconstruction accuracy and the efficiency. In general, a small size of sampling time interval is required to achieve high reconstruction accuracy. However, a very small size would result in too many undetermined coefficients, which not only increase the computation cost but also tend to make the inverse problem more ill-conditioned. In view of this, Liu et al. [20] introduced the concept of ‘‘shape function’’: the time history of a dynamic force was discretized into local time units and the corresponding local force was approximated by shape functions. Then, the whole response matrix was formulated by assembling the responses induced by the loads

corresponding to different shape functions in all time units. Thus, the dynamic force identification model is established through the force-response equation.

Suppose a dynamic force in the whole time domain is discretized into p time units, and each unit contains q data points, and the total sampling points are $r = p(q - 1) + 1$. Then, (9) can be further changed for shape function-based force reconstruction as follows:

$$\mathbf{Y} = \mathbf{K}\mathbf{D}, \quad (10)$$

where $\mathbf{Y} = [y(t_1) \ y(t_2) \ \cdots \ y(t_r)]^T$ and $\mathbf{D} = [d_1 \ d_2 \ \cdots \ d_r]^T$ are the response vector at r sampling points and the shape function coefficients, respectively. \mathbf{K} is the assembly of K_m , where the assembling process is similar to the method of stiffness matrices assembling in FEM [20].

$$\mathbf{K} = \sum_{m=1}^r K_m$$

$$K_m = \begin{bmatrix} 0 & \cdots & 0 & H^{N_m}(t_1) & 0 & \cdots & 0 \\ 0 & \cdots & 0 & H^{N_m}(t_2) & H^{N_m}(t_1) & \cdots & 0 \\ \vdots & & \vdots & \vdots & \vdots & \ddots & \vdots \\ 0 & \cdots & 0 & H^{N_m}(t_{r-m+1}) & H^{N_m}(t_{r-m}) & \cdots & H^{N_m}(t_1) \\ \vdots & & \vdots & \vdots & \vdots & \ddots & \vdots \\ 0 & \cdots & 0 & H^{N_m}(t_{r-1}) & H^{N_m}(t_{r-2}) & \cdots & H^{N_m}(t_{i-1}) \\ 0 & \cdots & 0 & H^{N_m}(t_r) & H^{N_m}(t_{r-1}) & \cdots & H^{N_m}(t_i) \end{bmatrix} \quad m = 1, 2, \dots, r, \quad (11)$$

$\underbrace{\hspace{10em}}_{m-1 \text{ columns}} \quad \left. \vphantom{\begin{bmatrix} 0 & \cdots & 0 & H^{N_m}(t_1) & 0 & \cdots & 0 \\ 0 & \cdots & 0 & H^{N_m}(t_2) & H^{N_m}(t_1) & \cdots & 0 \\ \vdots & & \vdots & \vdots & \vdots & \ddots & \vdots \\ 0 & \cdots & 0 & H^{N_m}(t_{r-m+1}) & H^{N_m}(t_{r-m}) & \cdots & H^{N_m}(t_1) \\ \vdots & & \vdots & \vdots & \vdots & \ddots & \vdots \\ 0 & \cdots & 0 & H^{N_m}(t_{r-1}) & H^{N_m}(t_{r-2}) & \cdots & H^{N_m}(t_{i-1}) \\ 0 & \cdots & 0 & H^{N_m}(t_r) & H^{N_m}(t_{r-1}) & \cdots & H^{N_m}(t_i) \end{bmatrix}} \right\} m \text{ rows}$

where H^{N_m} is the dynamic response induced by the m^{th} shape function N_m .

The coefficient matrix in (10) is generally ill-posed and little perturbation may cause tremendous variation in solutions. To obtain a stable and meaningful solution, it is often transformed into a Tikhonov regularization optimization problem [29]:

$$\min (\|\mathbf{Y} - \mathbf{K}\mathbf{D}\|_2^2 + \lambda \|\mathbf{D}\|_2^2), \quad (12)$$

where λ is the regularization factor. The regularization factor weighs the norm of residual and the norm of solution. It is determined by the L -curve method in this paper [30]. Generally, the relationship of the solution norm versus the residual norm is plotted for different λ , which looks like an ‘‘ L ’’ shape in the log-log scale, and the optimal regularization parameter is selected at the corner of the ‘‘ L ’’ shape [30].

The dynamic force can be estimated by the following equation:

$$\mathbf{F} = \mathbf{D}\mathbf{N}, \quad (13)$$

where \mathbf{F} and $\mathbf{N} = [N_1 \ N_2 \ \cdots \ N_r]^T$ are the dynamic force to be identified and the shape functions, respectively.

3.2. Wavelet Shape Function-Based Method. The shape function-based dynamic force reconstruction methods can considerably reduce the coefficient matrix size and enhance the computation efficiency. The accuracy of the shape function-based reconstruction method depends on the approximation ability of the shape functions, which is mainly determined by the discrete time unit length. However, it is not easy to determine the optimum time unit length that can balance the tradeoff between reconstruction accuracy and efficiency in advance. This section aims to develop an adaptive method for the reconstruction of dynamic forces based on multiresolution Lagrange wavelet shape functions and time-domain deconvolution.

Using the scaling and wavelet functions of Lagrange wavelets $\Phi_j = [\Phi_0^T, \Psi_0^T, \Psi_1^T, \dots, \Psi_{j-1}^T]$ at Scale j (described in Section 2.2) as shape functions (N), the unknown dynamic force at each unit can be approximated as

$$y = \sum_k \bar{c}_{0,k} \phi_{0,k} + \sum_{m=0}^{j-1} \sum_l c_{m,l} \Psi_{m,l} \quad (14)$$

$$= \Phi_0 \bar{\mathbf{c}} + \Psi_0 \mathbf{c}_0 + \Psi_1 \mathbf{c}_1 + \cdots + \Psi_{j-1} \mathbf{c}_{j-1} = \Phi_j \mathbf{q}_j,$$

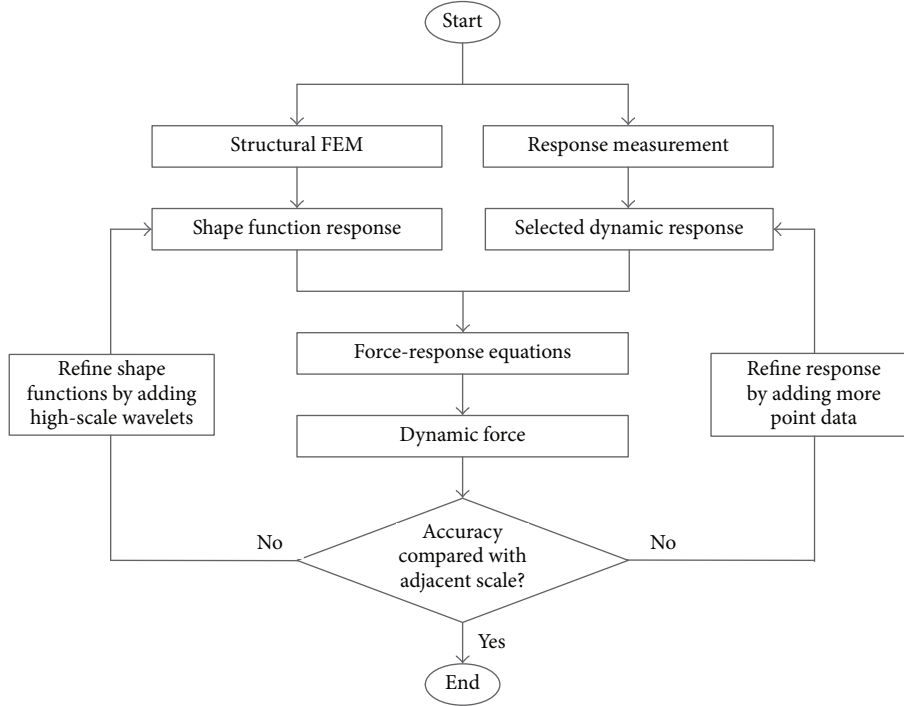


FIGURE 2: Diagram of the adaptive force reconstruction scheme.

where Φ_0 represents the scaling functions at Scale 0, Ψ_j represents the wavelet functions at Scale j , and $\mathbf{q}_j = [\bar{\mathbf{c}} \ \mathbf{c}_0 \ \mathbf{c}_1 \ \cdots \ \mathbf{c}_{j-1}]^T$ is the undetermined vector of wavelet coefficients.

Substitute (14) into (10) and (12), and then the wavelet coefficients can be obtained and the force can be reconstructed according to (13). The corresponding solution is denoted as Scale j solution. Obviously, higher scale solutions would be more accurate than lower scale ones.

Based on the multiresolution Lagrange wavelet shape functions and time-domain deconvolution, an adaptive method is developed for dynamic force reconstruction. Figure 2 presents the flowchart of this adaptive force reconstruction scheme. The detailed procedure is described as follows.

Step 1. Install a sensor on the concerned structure and measure its dynamic response (e.g., displacement, velocity, acceleration, or strain), and discretize the full dynamic response time history into p time units with an equal length.

Step 2. Use the structural FEM to calculate the response corresponding to wavelet shape functions at Scale 0.

Step 3. Establish the Scale 0 force-response equation, and obtain the corresponding solution.

Step 4. Refine the wavelet shape functions by adding high-scale wavelets, and refine dynamic responses by adding more data points. Establish the Scale 1 force-response equation and obtain the corresponding solution. Consequently, the reconstruction accuracy can be enhanced.

Step 5. Check the convergence of the solutions, and stop if the difference is smaller than a prescribed threshold. Otherwise, repeat Step 4.

During the scale lifting process for the force-response equation, the submatrices/vectors of the current scale can be retained, and only a few rows and columns need to be added. The new results can be quickly obtained via iteration, with the initial values equal to the results at the previous scale. With this adaptive strategy, the force reconstruction accuracy can be enhanced by lifting the scale of the force-response equation gradually when necessary, and thus determining the time unit length in advance, which is often a challenging task, is not required.

4. Numerical Study

Numerical examples of a simply supported beam and a double-story frame are analyzed to verify the feasibility and effectiveness of the proposed adaptive dynamic force reconstruction method. The dynamic responses and wavelet shape function responses are calculated by structural FEM in which Rayleigh damping is considered. The Newmark- β method is employed for the dynamic analysis with a time increment of 0.001 s.

To simulate a practical measurement condition environment, 5% noise is introduced by adding zero-mean Gaussian noise to the accurate displacement responses [31]:

$$\mathbf{u} = \mathbf{u}_{\text{cal}} + 5\% \times \mathbf{T}_{\text{noise}} \times \sigma(\mathbf{u}_{\text{cal}}), \quad (15)$$

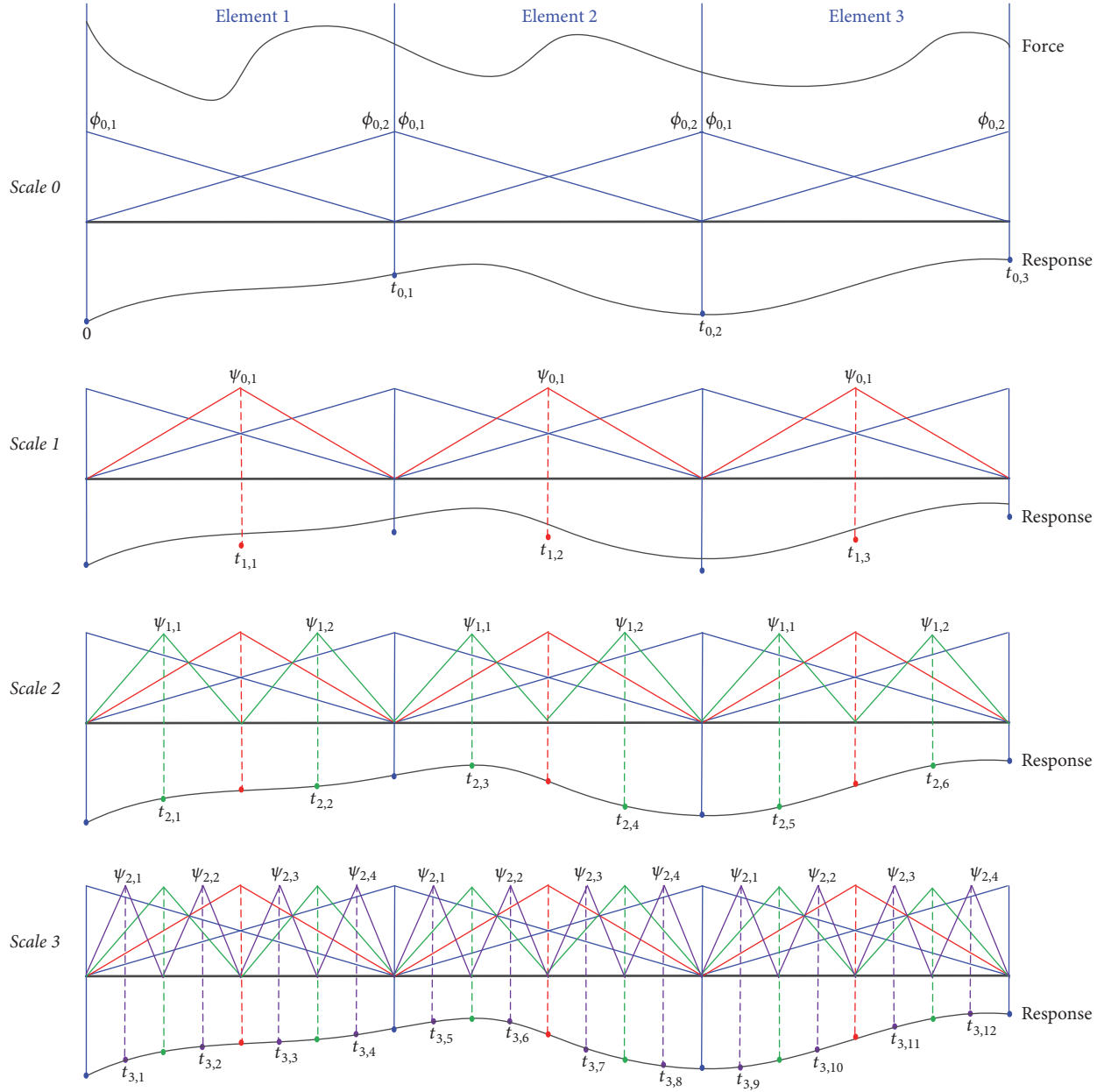


FIGURE 3: Example of the adaptive force reconstruction process.

where \mathbf{u} and \mathbf{u}_{cal} are the displacement responses with and without noise, respectively. $\mathbf{T}_{\text{noise}}$ is a vector of independent random variables following a standard normal distribution, and $\sigma(\mathbf{u}_{\text{cal}})$ is the standard deviation of the response.

A simple example is employed to illustrate the adaptive force reconstruction procedure (Figure 3). The full dynamic response time history is divided into 3 time units with equal length. In Scale 0, the responses (0 , $t_{0,1}$, $t_{0,2}$, and $t_{0,3}$) and Scale 0 Lagrange wavelet scaling functions ($\phi_{0,1}$ and $\phi_{0,2}$) are adopted to establish the force-response equation (denoted as Scale 0 force-response equation) as (10). The size of the coefficient matrix is 4×4 . Then, the Scale 0 force-response equation is changed into a Tikhonov regularization

optimization problem as (13). By solving this regularization optimization problem, the Scale 0 solutions can be obtained. Subsequently, the Scale 0 equation is lifted into Scale 1 force-response equation by adding Scale 0 Lagrange wavelet functions ($\psi_{0,1}$) and responses at time $t_{1,i}$ ($i = 1, 2, 3$). The size of the coefficient matrix in Scale 1 force-response equation is extended to 7×7 accordingly. Further, the responses at time $t_{2,i}$ ($i = 1, 2, \dots, 6$) and the Scale 1 Lagrange wavelet functions ($\psi_{1,1}$ and $\psi_{1,2}$) and the response at time $t_{3,i}$ ($i = 1, 2, \dots, 12$) and the Scale 2 Lagrange wavelet functions ($\psi_{2,1}$, $\psi_{2,2}$, $\psi_{2,3}$, and $\psi_{2,4}$) are added to formulate the Scale 2 and Scale 3 force-response equations gradually. The sizes of the coefficient matrix in Scale 2 and Scale 3 force-response equation are

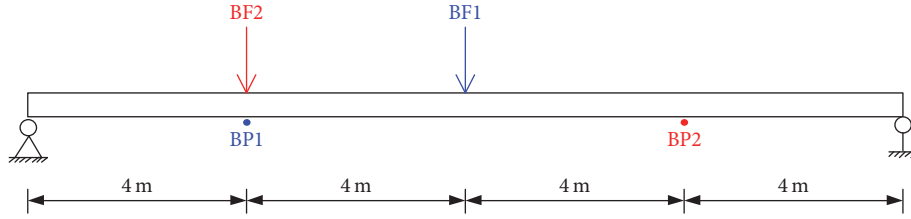


FIGURE 4: The simulated simply supported beam.

TABLE 1: Scenarios considered in the numerical simulations.

Structure type	Scenarios	Force		Measurement location
		Time history (N)	Location	
Simply supported beam	Case B1	$\sin(\pi t) + \cos(2\pi t) + \sin(4\pi t)$	BF1	BP1
	Case B2	$\sin(\pi t) + \cos(2\pi t) + \cos(3\pi t) + \cos(4\pi t)$	BF2	BP2
Double-story frame	Case F1	$\sin(\pi t) + \sin(2\pi t) + \cos(2\pi t) + \sin(4\pi t)$	FF1	FP1
	Case F2	$\cos(\pi t) + \sin(2\pi t) + \cos(2\pi t) + \sin(4\pi t)$	FF2	FP2

TABLE 2: Reconstruction parameters in numerical simulations.

Item	Scale 0	Scale 0	Scale 0	Scale 3
Time unit number	50	50	50	50
Coefficient matrix size	51×51	101×101	201×201	401×401

13×13 and 25×25 , respectively. The size of the coefficient matrix and the reconstruction accuracy would be enhanced with the scale number.

Figure 4 shows a simply supported beam with a length of $L = 16$ m, Young's modulus of 3.3×10^{11} N/m², density of 2.5×10^3 Kg/m³, and cross-sectional area of $A = 1 \times 4$ m². The scenarios, dynamic force time histories, applied locations, and measurement locations are listed in Table 1. The whole beam is divided into 16 beam elements equally, and the FEM is established accordingly.

For Case B1, the beam is excited by applying the following dynamic force at the middle span (BF1) (Figure 4):

$$BF1(t) = \sin(\pi t) + \cos(2\pi t) + \sin(4\pi t) \text{ KN} \quad (16)$$

$$(0 \leq t \leq 10).$$

The displacement response at Point BP1 in the y -direction is used to reconstruct the dynamic force. The total response time history is discrete in 50 time units with equal length. Following the procedures presented above, the dynamic force is reconstructed adaptively. The reconstruction parameters are listed in Table 2. The solutions and relative errors with respect to the maximal real force obtained at different scales are plotted in Figures 5 and 6, respectively. It can be seen that the reconstruction accuracy increases with the scale. For example, the maximal relative errors in Scale 0 to Scale 3 are about 30%, 10%, 2.5%, and 0.5% (except several starting points), respectively.

Considering the fact that the Scale 3 solution has sufficient precision, only three scales are calculated in the following cases. If higher precision is required, a higher scale

force-response equation could be formulated through the lifting process.

For Case B2, the dynamic force (BF2) with the following expression is applied at the section which is 4 m from the left end (Figure 4):

$$BF2(t) = \sin(\pi t) + \cos(2\pi t) + \cos(3\pi t) + \cos(4\pi t) \text{ KN} \quad (17)$$

$$(0 \leq t \leq 10).$$

The displacement response at Point BP2 is employed to perform the proposed adaptive dynamic force reconstruction method. The reconstruction parameters are listed in Table 2, and the solutions and relative errors of different scales are shown in Figures 7 and 8, respectively. Similar conclusions can be drawn in Case B2 as well.

Furthermore, a single-bay two-story frame is simulated, as shown in Figure 9. Young's modulus and the density of the material are 3.3×10^{11} N/m² and 2.5×10^3 Kg/m³, respectively. The cross sections are $A = 1 \times 1$ m² for all the beams and columns. Each beam and column is divided into 4 beam elements equally in developing the FEM. The scenarios, force time histories, applied locations, and measurement locations are listed in Table 1, and the reconstruction parameters are listed in Table 2. The solutions of different scales in Case F1 and Case F2 are shown in Figures 10 and 12, respectively. The corresponding relative errors are compared in Figures 11 and 13, respectively.

The simulation results of the simply supported beam and the two-story frame indicate that the reconstruction accuracy could be enhanced by lifting the scale of the wavelet shape function-based force-response equation gradually. This

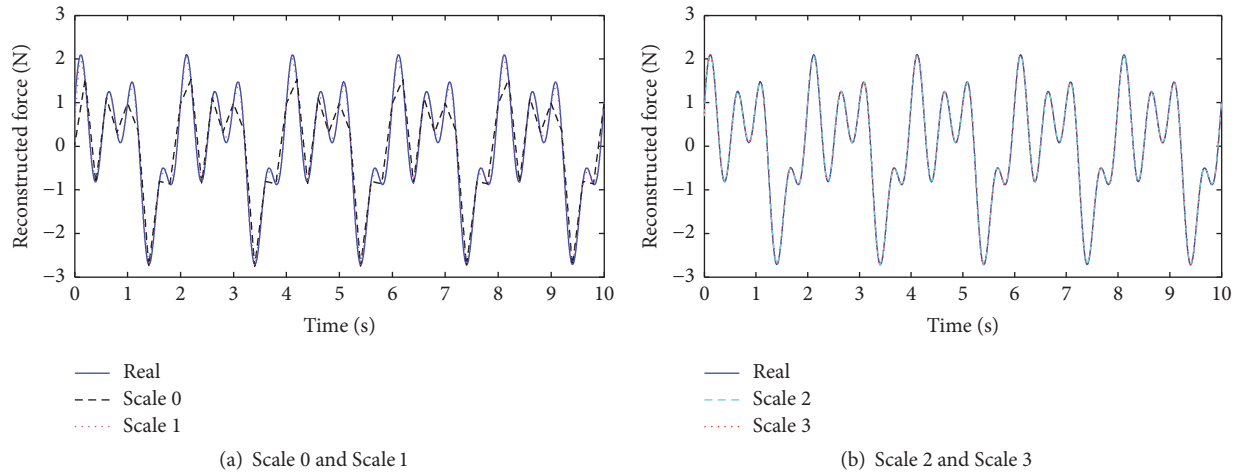


FIGURE 5: The reconstructed dynamic force in Case B1.

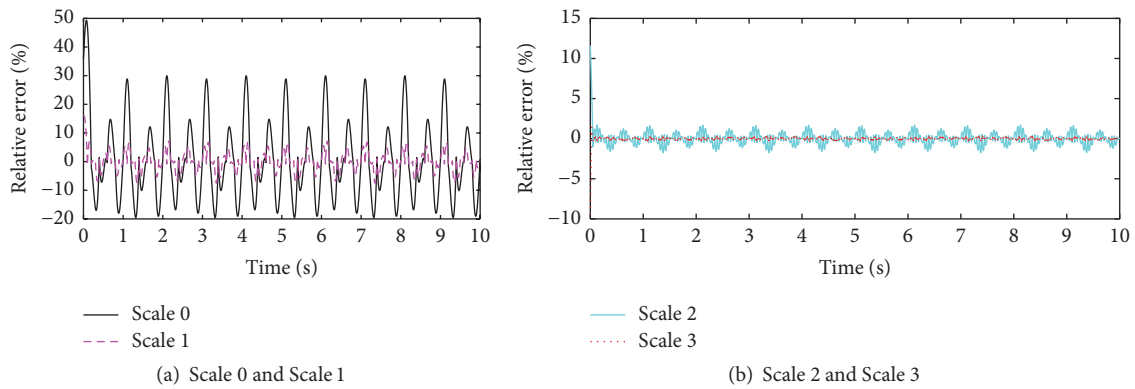


FIGURE 6: The reconstructed error in Case B1.

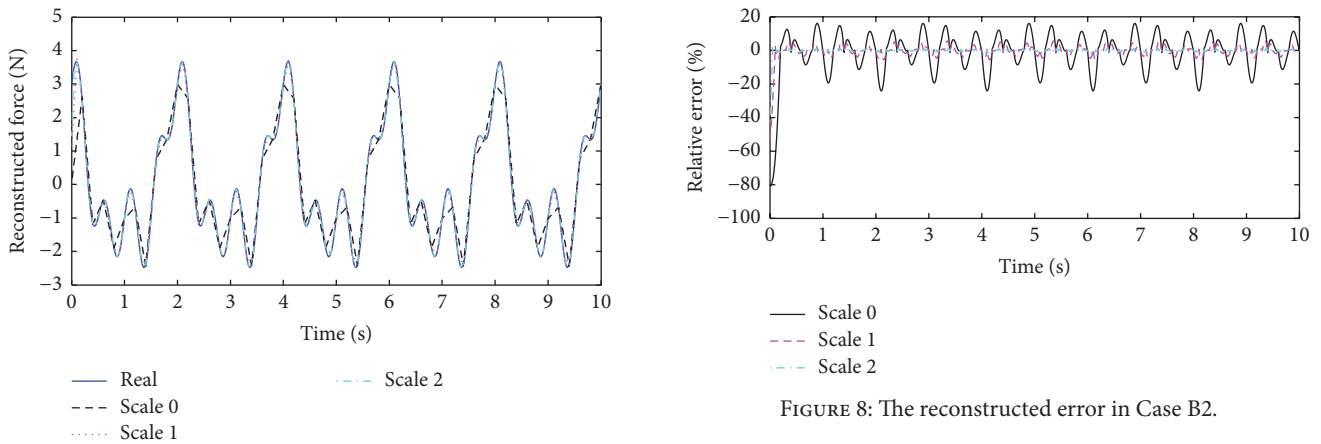


FIGURE 7: The reconstructed dynamic force in Case B2.

adaptive strategy can avoid determining the time unit length in advance, which is often a challenge in practice. The reconstruction scale that affects both the accuracy and the efficiency can be determined adaptively according to the actual needs.

5. Conclusion

As usually dynamic forces can hardly be measured, reconstructing them via structural dynamic response is essential in the field of SHM. Shape function-based methods with the ability to reduce the number of unknowns and shorten the reconstruction time significantly have attracted great interest. However, determining the optimum time unit length limits

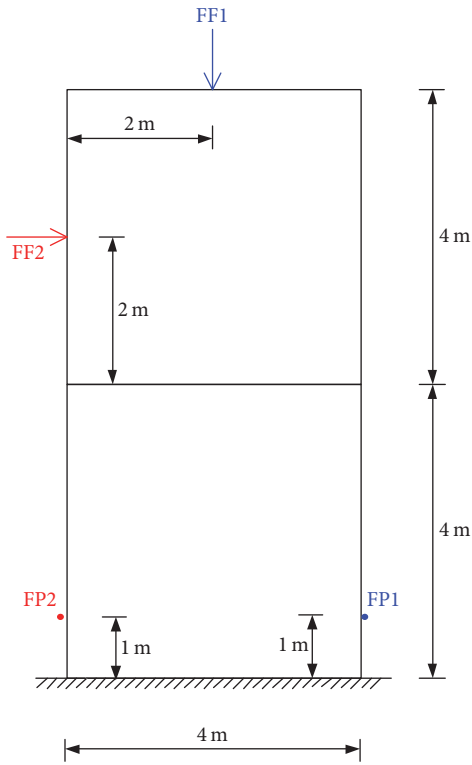


FIGURE 9: The simulated double-story frame.

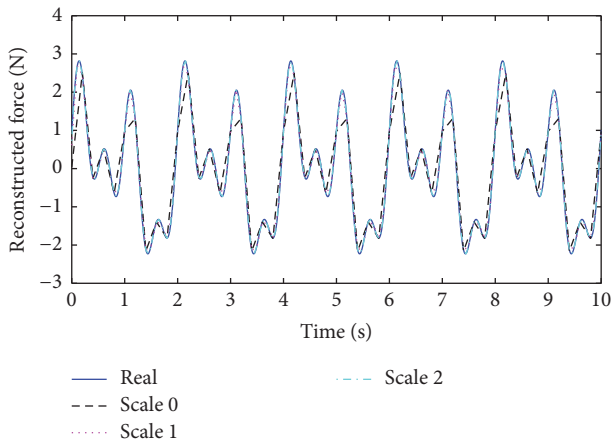


FIGURE 10: The reconstructed dynamic force in Case F1.

often presents a challenging task. In view of this, this paper developed an adaptive method for dynamic force reconstruction based on multiscale wavelet shape functions and time-domain deconvolution. The proposed method consists of four stages: (1) discretize the dynamic force into several time units in time domain, and approximate the local force in each unit by using wavelet scale functions at Scale 0; (2) formulate the whole response matrix by assembling the responses induced by the wavelet shape function-based forces in all time units; (3) establish the wavelet shape functions based force-response equation and obtain the Scale 0 solution; (4)

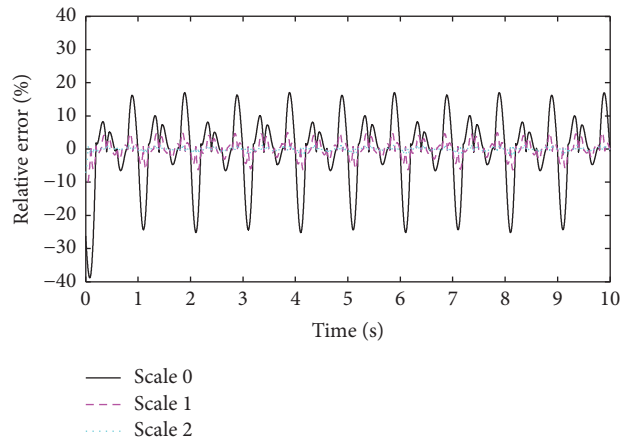


FIGURE 11: The reconstructed error in Case F1.

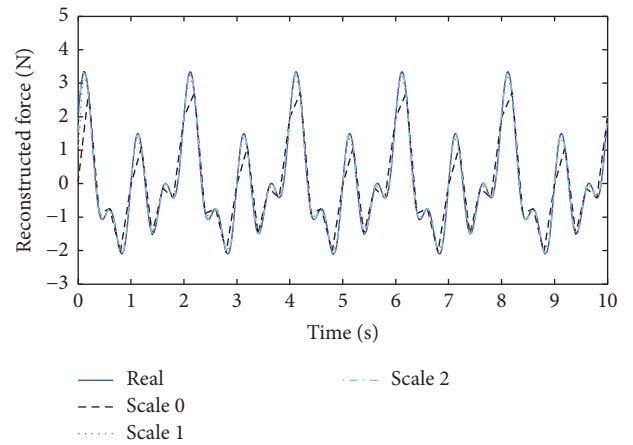


FIGURE 12: The reconstructed dynamic force in Case F2.

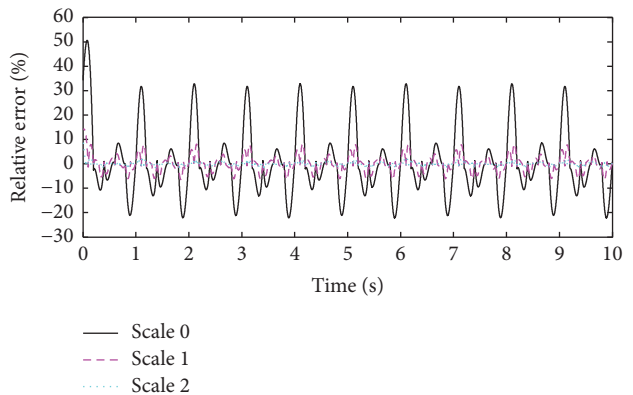


FIGURE 13: The reconstructed error in Case F2.

lift the scale of the wavelet shape functions based force-response equation and improve the reconstruction accuracy. A simply supported beam and a two-story frame subjected to different dynamic forces are simulated to verify the feasibility and effectiveness of the proposed method. The results indicate that the proposed method can significantly reduce the number of unknowns and shorten the reconstruction

time, and the reconstruction accuracy can be enhanced by lifting the scale of the wavelet shape function-based force-response equation gradually. This adaptive strategy avoids the challenging task of determining the time unit length in advance. The experimental validation of the proposed method needs to be systematically investigated in the future.

Disclosure

Findings and opinions expressed here are those of the authors alone, not necessarily the views of the sponsors.

Conflicts of Interest

The authors declare that there are no conflicts of interest regarding the publication of this paper.

Acknowledgments

The first two authors are grateful for the financial support from the National Key Research and Development Program of China (no. 2016YFC0701400), the National Natural Science Foundation of China (nos. 51508145 and 51778550), and the Fundamental Research Funds for the Central Universities (no. PA2017GDQT0022). The third author is grateful for the financial support from the Innovation and Technology Commission of the HKSAR Government to the Hong Kong Branch of National Rail Transit Electrification and Automation Engineering Technology Research Center (Project no. 1-BBY5).

References

- [1] W. S. Choi and G. J. Park, "Transformation of dynamic loads into equivalent static loads based on modal analysis," *International Journal for Numerical Methods in Engineering*, vol. 46, no. 1, pp. 29–43, 1999.
- [2] E. Turco, "A strategy to identify exciting forces acting on structures," *International Journal for Numerical Methods in Engineering*, vol. 64, no. 11, pp. 1483–1508, 2005.
- [3] Y. Liu and W. S. J. r. Shepard, "Dynamic force identification based on enhanced least squares and total least-squares schemes in the frequency domain," *Journal of Sound and Vibration*, vol. 282, no. 1-2, pp. 37–60, 2005.
- [4] E. Parloo, P. Verboven, P. Guillaume, and M. Van Overmeire, "Force identification by means of in-operation modal models," *Journal of Sound and Vibration*, vol. 262, no. 1, pp. 161–173, 2003.
- [5] H. Ronasi, H. Johansson, and F. Larsson, "A numerical framework for load identification and regularization with application to rolling disc problem," *Computers & Structures*, vol. 89, no. 1-2, pp. 38–47, 2011.
- [6] X. Sun, J. Liu, X. Han, C. Jiang, and R. Chen, "A new improved regularization method for dynamic load identification," *Inverse Problems in Science and Engineering*, vol. 22, no. 7, pp. 1062–1076, 2014.
- [7] J. Liu, X. Sun, X. Han, C. Jiang, and D. Yu, "Dynamic load identification for stochastic structures based on Gegenbauer polynomial approximation and regularization method," *Mechanical Systems and Signal Processing*, vol. 56, pp. 35–54, 2015.
- [8] D. Feng and M. Q. Feng, "Identification of structural stiffness and excitation forces in time domain using noncontact vision-based displacement measurement," *Journal of Sound and Vibration*, vol. 406, pp. 15–28, 2017.
- [9] A. N. Thite and D. J. Thompson, "The quantification of structure-borne transmission paths by inverse methods. part 1: improved singular value rejection methods," *Journal of Sound and Vibration*, vol. 264, no. 2, pp. 411–431, 2003.
- [10] H. G. Choi, A. N. Thite, and D. J. Thompson, "Comparison of methods for parameter selection in Tikhonov regularization with application to inverse force determination," *Journal of Sound and Vibration*, vol. 304, no. 3–5, pp. 894–917, 2007.
- [11] Z. R. Lu and S. S. Law, "Identification of system parameters and input force from output only," *Mechanical Systems and Signal Processing*, vol. 21, no. 5, pp. 2099–2111, 2007.
- [12] L. Wang, X. Han, and Y. Xie, "A new conjugate gradient method for solving multi-source dynamic load identification problem," *International Journal of Mechanics and Materials in Design*, vol. 9, no. 3, pp. 191–197, 2013.
- [13] J. Liu, X. Meng, C. Jiang, X. Han, and D. Zhang, "Time-domain Galerkin method for dynamic load identification," *International Journal for Numerical Methods in Engineering*, vol. 105, no. 8, pp. 620–640, 2016.
- [14] J. F. Doyle, "A wavelet deconvolution method for impact force identification," *Experimental Mechanics*, vol. 37, no. 4, pp. 403–408, 1997.
- [15] F. E. Gunawan, H. Homma, and Y. Kanto, "Two-step B-splines regularization method for solving an ill-posed problem of impact-force reconstruction," *Journal of Sound and Vibration*, vol. 297, no. 1-2, pp. 200–214, 2006.
- [16] B. Qiao, X. Zhang, X. Luo, and X. Chen, "A force identification method using cubic B-spline scaling functions," *Journal of Sound and Vibration*, vol. 337, pp. 28–44, 2015.
- [17] Y. Liu and W. S. J. r. Shepard, "An improved method for the reconstruction of a distributed force acting on a vibrating structure," *Journal of Sound and Vibration*, vol. 291, no. 1-2, pp. 369–387, 2006.
- [18] G. Yan and L. Zhou, "Impact load identification of composite structure using genetic algorithms," *Journal of Sound and Vibration*, vol. 319, no. 3–5, pp. 869–884, 2009.
- [19] Z. Li, Z. Feng, and F. Chu, "A load identification method based on wavelet multi-resolution analysis," *Journal of Sound and Vibration*, vol. 333, no. 2, pp. 381–391, 2014.
- [20] J. Liu, X. Sun, X. Han, C. Jiang, and D. Yu, "A novel computational inverse technique for load identification using the shape function method of moving least square fitting," *Computers & Structures*, vol. 144, pp. 127–137, 2014.
- [21] B. Li and X. Chen, "Wavelet-based numerical analysis: a review and classification," *Finite Elements in Analysis and Design*, vol. 81, pp. 14–31, 2014.
- [22] W. Sweldens, "The lifting scheme: a construction of second generation wavelets," *SIAM Journal on Mathematical Analysis*, vol. 29, no. 2, pp. 511–546, 1998.
- [23] W.-H. Chen and C.-W. Wu, "A spline wavelets element method for frame structures vibration," *Computational Mechanics*, vol. 16, no. 1, pp. 11–21, 1995.
- [24] L. A. Diaz, M. T. Martin, and V. Vampa, "Daubechies wavelet beam and plate finite elements," *Finite Elements in Analysis and Design*, vol. 45, no. 3, pp. 200–209, 2009.
- [25] J. Xiang and M. Liang, "Multiple damage detection method for beams based on multi-scale elements using hermite cubic

- spline-wavelet,” *CMES: Computer Modeling in Engineering & Sciences*, vol. 73, no. 3, pp. 267–298, 2011.
- [26] Y. Wang, X. Chen, Y. He, and Z. He, “The construction of finite element multiwavelets for adaptive structural analysis,” *International Journal for Numerical Methods in Biomedical Engineering*, vol. 27, no. 4, pp. 562–584, 2011.
- [27] W.-Y. He and W.-X. Ren, “Finite element analysis of beam structures based on trigonometric wavelet,” *Finite Elements in Analysis and Design*, vol. 51, pp. 59–66, 2012.
- [28] X. Q. Zhu and S. S. Law, “Structural health monitoring based on vehicle-bridge interaction: accomplishments and challenges,” *Advances in Structural Engineering*, vol. 18, no. 12, pp. 1999–2015, 2015.
- [29] C. D. Zhang and Y. L. Xu, “Comparative studies on damage identification with Tikhonov regularization and sparse regularization,” *Structural Control and Health Monitoring*, vol. 23, no. 3, pp. 560–579, 2016.
- [30] P. C. Hansen, “Analysis of discrete ill-posed problems by means of the L -curve,” *SIAM Review*, vol. 34, no. 4, pp. 561–580, 1992.
- [31] W.-Y. He and S. Zhu, “Moving load-induced response of damaged beam and its application in damage localization,” *Journal of Vibration and Control*, vol. 22, no. 16, pp. 3601–3617, 2016.

Research Article

Development of Practical Finite Element Models for Collapse of Reinforced Concrete Structures and Experimental Validation

Mario Bermejo,¹ Anastasio P. Santos,¹ and José M. Goicolea²

¹Department of Geological and Mining Engineering, Technical University of Madrid, Madrid, Spain

²Department of Mechanics and Structures, Technical University of Madrid, Madrid, Spain

Correspondence should be addressed to Mario Bermejo; mario.bermejo@upm.es

Received 25 July 2017; Revised 13 October 2017; Accepted 21 November 2017; Published 14 December 2017

Academic Editor: Nawawi Chouw

Copyright © 2017 Mario Bermejo et al. This is an open access article distributed under the Creative Commons Attribution License, which permits unrestricted use, distribution, and reproduction in any medium, provided the original work is properly cited.

This paper describes two practical methodologies for modeling the collapse of reinforced concrete structures. They are validated with a real scale test of a two-floor structure which loses a bearing column. The objective is to achieve accurate simulations of collapse phenomena with moderate computational cost. Explicit finite element models are used with Lagrangian meshes, modeling concrete, and steel in a segregated manner. The first model uses 3D continuum finite elements for concrete and beams for steel bars, connected for displacement compatibility using a penalty method. The second model uses structural finite elements, shells for concrete, and beams for steel, connected in common nodes with an eccentricity formulation. Both are capable of simulating correctly the global behavior of the structural collapse. The continuum finite element model is more accurate for interpreting local failure but has an excessive computational cost for a complete building. The structural finite element model proposed has a moderate computational cost, yields sufficiently accurate results, and as a result is the recommended methodology.

1. Introduction

In recent years a number of civil buildings have collapsed after losing one or several bearing elements, due to explosive or impact loads, from accidental events or terrorist attacks. These buildings are often made of reinforced concrete and the redistribution of loads when an element is removed had not been taken into account in their design.

The terrorist attack in Oklahoma City USA [1] on the Alfred P. Murrah Federal Building on April 19, 1995, is a well-known example of these loads. The attack claimed 168 lives and injured more than 680 people. 2300 kilograms of ANFO explosive were used resulting in enormous damage in the building and the collapse of a large part of it. Another example is the attack on the Argentine Israelite Mutual Association building in Buenos Aires on July 18, 1994 [2]. In this attack 85 people were killed and hundreds were injured. 275 kilograms of ANFO were used in this attack. The blast totally destroyed the exposed load-bearing walls and led to progressive failure of the floor slabs and collapse of the building. In Spain, the parking of the Madrid-Barajas Airport was attacked on

December 30, 2006, when a van bomb exploded, killing two and injuring 52 people; 500 to 800 kilograms of an unknown kind of explosive were used, resulting in the demolition of the five-floor structure [3]. An explosion from an accidental event occurred on February, 2012, in Astrakhan, Russia, in the fourth floor of a building, whose ten floors collapsed causing ten deaths and twelve injuries. In all these cases the damage in the structure was not only by the direct effect of the explosions but also by the subsequent collapse due to the loss of bearing elements. The damage in the structure can be catastrophic, so it is convenient to develop a practical methodology that can evaluate this phenomenon.

Several studies have been carried out on the progressive collapse of civil structures in recent years [4–6]. Some of them analyze reduced parts of the structure with detailed finite element models [7], while others propose an analytic approach [8, 9]. The most common technique used for large buildings is finite element models with a homogeneous material for reinforced concrete [10–12].

In this paper we develop, apply, and discuss two different types of finite element models for studying the collapse

of reinforced concrete structures subject to blast loads. LS-DYNA code [13] is employed for dynamic computer simulation, with Lagrangian Finite Elements, explicit time integration, and considering concrete and steel in a segregated manner. The focus of this work is on the structural collapse phenomenon; a more detailed explanation of the consideration of blast loading effects may be found in [14].

The first model uses 3D continuum finite elements for concrete and beams for steel bars, connected for displacement compatibility using a penalty method. This model is very detailed but has a high computational cost. The second model uses structural finite elements, that is, shells for concrete and beams for steel, connected in common nodes with an eccentricity formulation to take account of the position of the reinforcement. This model is less detailed than the previous one; however it reproduces the main structural features of the collapse with much lower computational cost. Both models are compared with a real scale test in order to validate the employed techniques.

2. Test Description

A six-column and two-floor structure of reinforced concrete was constructed for this test. The objective was to analyze the behavior of the structure when the bottom half of one of the central columns in the lower floor was removed. The removal was performed by blast charges located inside the column, in perforations previously disposed in the construction phase. When the charge was exploded the structure lost static equilibrium in a matter of milliseconds, entering into dynamic motion. Figure 1 shows the structure before the blast. The characteristics are as follows:

- (a) Columns:
 - (i) Dimensions: 35 cm \times 35 cm \times 300 cm.
 - (ii) Longitudinal reinforcement: 9 ribbed bars of ϕ 12 mm diameter.
 - (iii) Shear reinforcement: ϕ 6 mm diameter bars every 15 cm.
 - (iv) Concrete cover: 3.5 cm.
- (b) Slabs:
 - (i) Solid concrete, 22 cm thickness.
 - (ii) Dimensions of floor slabs: 1100 cm \times 1435 cm \times 22 cm.
 - (iii) Longitudinal reinforcement, top and bottom layers: according to Table 1 and Figure 2.
 - (iv) Punching shear reinforcement: ϕ 8 mm diameter bars every 15 cm in a zone of 90 cm \times 90 cm centered in the columns.
 - (v) Concrete cover: 3.5 cm.

The foundation of the structure was made with a reinforced concrete slab of 40 cm thickness. The materials employed in the construction were 25 MPa concrete and 500 MPa ribbed steel bars. The structure was loaded with



FIGURE 1: Photograph of the studied structure.

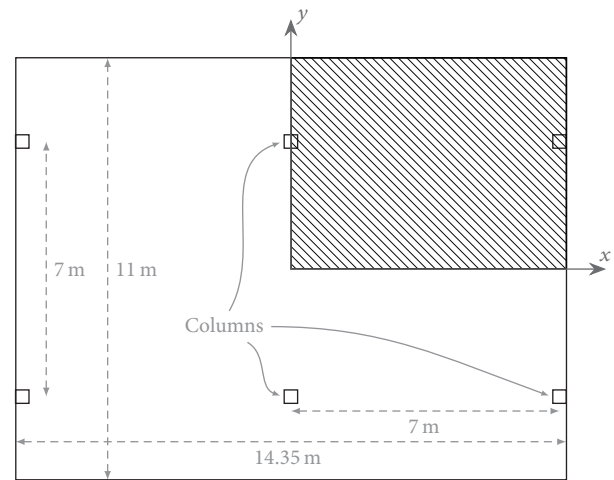


FIGURE 2: Plan view of test structure, which is symmetric with respect to x and y axes. The reinforcement of the shadowed quarter is defined in Table 1.

sandbags in the overhangs, in an 200 cm \times 1435 cm area for each. The weight of sandbags was 7 kN/m².

The process of collapse was recorded with a high-speed camera in the front of the removed column. A reel guide was 230 cm at the left of central column axis. In this guide two points were marked (1 and 2), with the 50 cm separation. The times when two points (A and B) of the first slab reach points 1 and 2 (Figure 3) were annotated and having measured the displacement an average velocity was obtained. The measured displacements and velocities are shown in the results Section 5.

3. Continuum Finite Element Model

In this model the geometry of the studied structure is reproduced accurately. The concrete is represented using continuum elements and the steel with beam type elements in a segregated manner. The two meshes are overlapped and the rebar to concrete connection is modeled via the Constrained Lagrange in Solid [15] feature in LS-DYNA, based on penalty constraints.

Eight node continuum elements with one Gauss point and hourglass control are used for concrete in the FE model.

TABLE 1: Distribution of reinforcement in a quarter of a slab (Figure 2) of the test structure.

Direction (see Figure 2)	Lines and separation	Length of reinforcement lines
Top layer reinforcement		
x direction	2 lines @ 14 cm	$\phi 10: x = 0 \text{ m to } x = 2.55 \text{ m}; \phi 8: x = 4.50 \text{ m to } x = 7.15 \text{ m}$
	5 lines @ 14 cm	$\phi 12: x = 0 \text{ m to } x = 2.55 \text{ m}; \phi 8: x = 4.50 \text{ m to } x = 7.15 \text{ m}$
	2 lines @ 14 cm	$\phi 16: x = 0 \text{ m to } x = 2.55 \text{ m}; \phi 10: x = 4.50 \text{ m to } x = 7.15 \text{ m}$
	2 lines @ 14 cm	$\phi 10: x = 0 \text{ m to } x = 2.55 \text{ m}; \phi 16: x = 4.50 \text{ m to } x = 7.15 \text{ m}$
	6 lines @ 14 cm	$\phi 16: x = 0 \text{ m to } x = 2.55 \text{ m}; \phi 16: x = 4.50 \text{ m to } x = 7.15 \text{ m}$
	2 lines @ 14 cm	$\phi 12: x = 0 \text{ m to } x = 2.55 \text{ m}; \phi 16: x = 4.50 \text{ m to } x = 7.15 \text{ m}$
	5 lines @ 14 cm	$\phi 12: x = 0 \text{ m to } x = 2.55 \text{ m}; \phi 8: x = 4.50 \text{ m to } x = 7.15 \text{ m}$
	5 lines @ 14 cm	$\phi 10: x = 0 \text{ m to } x = 2.55 \text{ m}; \phi 8: x = 4.50 \text{ m to } x = 7.15 \text{ m}$
	10 lines @ 14 cm	$\phi 8: x = 0 \text{ m to } x = 2.55 \text{ m}; \phi 8: x = 4.50 \text{ m to } x = 7.15 \text{ m}$
y direction	1 line @ 14.5 cm	$\phi 16: y = 1.00 \text{ m to } y = 5.47 \text{ m}$
	6 lines @ 14.5 cm	$\phi 12: y = 1.00 \text{ m to } y = 5.47 \text{ m}$
	7 lines @ 14.5 cm	$\phi 10: y = 1.00 \text{ m to } y = 5.47 \text{ m}$
	23 lines @ 14.5 cm	$\phi 8: y = 1.00 \text{ m to } y = 5.47 \text{ m}$
	5 lines @ 14.5 cm	$\phi 10: y = 1.00 \text{ m to } y = 5.47 \text{ m}$
	6 lines @ 14.5 cm	$\phi 12: y = 1.00 \text{ m to } y = 5.47 \text{ m}$
Bottom layer reinforcement		
x direction	10 lines @ 15 cm	$\phi 10: x = 0.55 \text{ m to } x = 7.15 \text{ m}$
	7 lines @ 12 cm	$\phi 10: x = 0 \text{ m to } x = 7.15 \text{ m}$
	20 lines @ 15 cm	$\phi 10: x = 0.55 \text{ m to } x = 7.15 \text{ m}$
y direction	44 lines @ 15 cm	$\phi 10: y = 0 \text{ m to } y = 3.10 \text{ m}; \phi 10: y = 4.00 \text{ m to } y = 5.47 \text{ m}$
	3 lines @ 15 cm	$\phi 10: y = 0 \text{ m to } y = 5.47 \text{ m}$

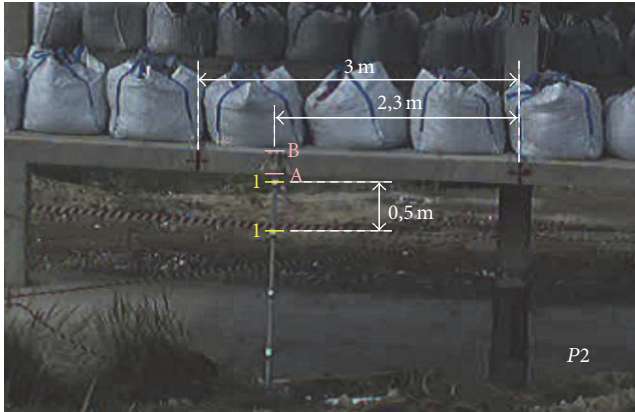


FIGURE 3: Picture of the points of measure in the slab. P2 is the half of the column before it was removed.

An hourglass formulation with Flanagan-Belytschko stiffness form of artificial viscosity [16] is used to avoid zero energy modes of deformation in the underintegrated elements.

The mesh size is composed by $5 \text{ cm} \times 5 \text{ cm} \times 5.5 \text{ cm}$ elements for the slabs and $5 \text{ cm} \times 5 \text{ cm} \times 5 \text{ cm}$ elements for the columns. Every single bar of the steel reinforcement is reproduced with Hughes-Liu beam type elements using 2×2 Gauss points in the cross section and located in the exact position within the concrete mesh.

The concrete behavior is represented using the Continuous Surface Cap Model (CSCM) [17] material model

TABLE 2: Parameters for CSCM material model for concrete.

Parameter	Value
Mass density	2300 kg/m^3
Unconfined compression strength	25 MPa
Maximum aggregate size	19 mm
Erode parameter	1.05

implemented in LS-DYNA. This material model is isotropic and has different response in tension and compression, three plasticity surfaces (TXE tensile, TOR shear, and TXC compression), softening in compression, damage in tension, and erosion formulation for elimination of material. Figure 4 shows the material response for unconfined uniaxial tension and compression. The damage formulation models both strain softening and modulus reduction ($\sigma_{ij}^d = (1 - d)\sigma_{ij}^{vp}$) where d is a scalar damage parameter that transforms the stress tensor without damage (σ_{vp}) into the stress tensor with damage (σ^d). Damage initiates and accumulates when strain-based energy terms exceed the damage threshold for brittle damage ($\tau_b = \sqrt{E\varepsilon_{\max}^2}$) and ductile damage ($\tau_d = \sqrt{0.5 \cdot \sigma_{ij}\varepsilon_{ij}}$). Elements are eroded when damage exceeds $d = 0.99$ and the maximum principal strain exceeds an erosion parameter value. The CSCM material model [17] is defined by the basic parameters shown in Table 2.

The steel behavior is represented using the Piecewise Linear Plasticity material model (Figure 5), which is an

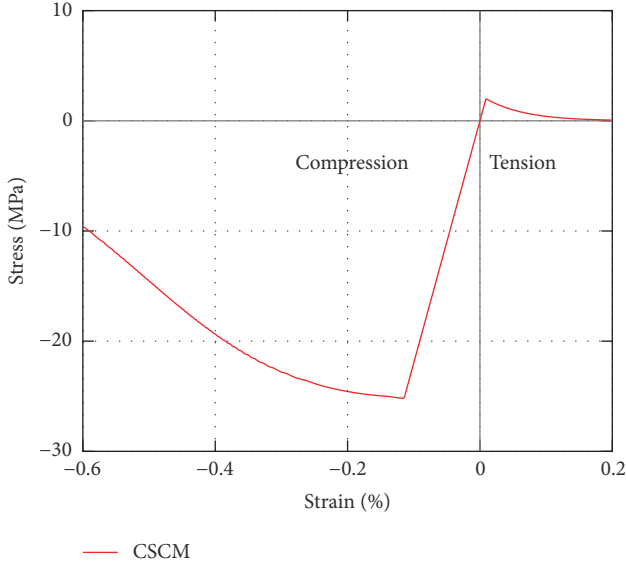


FIGURE 4: Stress-strain diagram for 25 MPa CSCM material model. Unconfined uniaxial tension and compression.

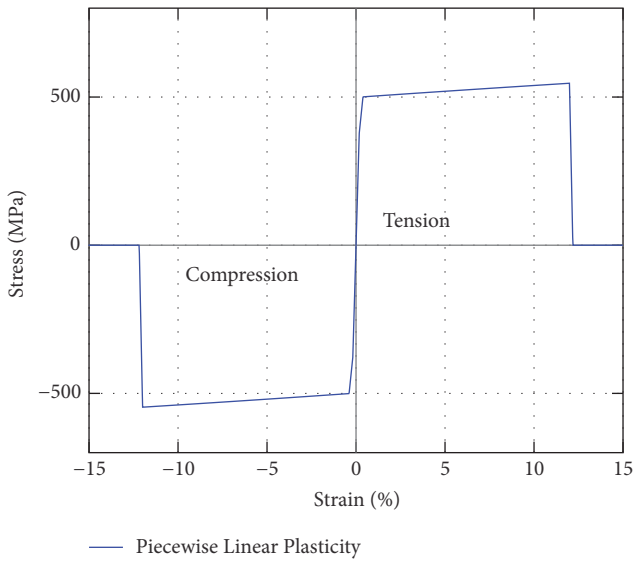


FIGURE 5: Stress-strain diagram for 500 MPa yield stress Piecewise Linear Plasticity material model.

elastoplastic material model with hardening, equal response in tension and compression, and failure when effective plastic strain reaches the ultimate strain. The material parameters are shown in Table 3.

Although distinct meshes are employed for concrete and steel, using continuum and beam type elements, respectively, their degrees of freedom are coupled with kinematic constraints which achieve full deformation compatibility. This is performed using the option *Constrained Lagrange in Solid* within LS-DYNA.

The bases of the columns are fixed and the ground is modeled as a fixed rigid slab. A penalty formulation is used for the contact between different parts of the structure, which considers the collisions between columns, slabs, and the

TABLE 3: Parameters for Piecewise Linear Plasticity material model for steel rebars.

Parameter	Value
Mass density	7850 kg/m ³
Young's modulus	210 GPa
Poisson's ratio	0.3
Yield stress	500 MPa
Tangent modulus	420 MPa
Effective plastic strain to failure	0.11

ground. The loads applied on the structure are the gravity loads caused by the sandbags and the self-weight. The load of the sandbags in the overhangs is modeled as a vertical distributed weight of 7 kN/m² (200 × 1435 cm each). The self-weight of the structure is modeled through prescribed gravity loading applied on the lumped nodal masses.

The initial state of equilibrium under the permanent loads is achieved through a dynamic relaxation step [18]. Next, the half column is eliminated, triggering the collapse process.

The LS-DYNA commands and nondefault used, respectively, for contact constraints, load of the sandbags, self-weight, and dynamic relaxation are Contact Automatic General (*sstyp: 2, mstyp: 2*); Load Segment Set (*sidr: 2, 7000 Pa*); Load Body Z (*sidr: 2, 9.8 m/s²*); Dynamic Relaxation (*nrcyck: 250, drfctr: 0.9, drterm: 0.49, idrflg: -1*)

The results obtained with this model are discussed in Section 5.

4. Structural Finite Element Model

In this model shell elements are used to represent the concrete and the steel is modeled with beam type elements in a segregated manner. The connection between the rebars and the shells is performed in the nodes with an offset formulation that takes into account the eccentricity of the reinforcement [19].

The concrete for the slabs and the columns is modeled with shell elements using two Gauss points through the thickness. The steel rebars are modeled with Hughes-Liu beam type elements using 2 × 2 Gauss points in the cross section. The individual rebars included in the model represent realistically the actual quantity of reinforcement in the structure.

For the columns 17.5 cm × 15 cm shells are used forming a section with cross form, with the same mass and inertia as the real column section (Figure 6). This modeling scheme for the columns provides a correct representation of the stiffness and strength under bending and compression, including nonlinear response and collapse, and includes simultaneously an active surface on which the blast loads will act in the case of an explosion event.

The nine bars of the longitudinal reinforcement are modeled independently, located overlapped within the longitudinal column axis, and connected to the nodes of the column concrete shell elements with the appropriate geometrical offset.

The shear reinforcement is modeled also independently with 6 mm diameter bars, their nodes being connected with

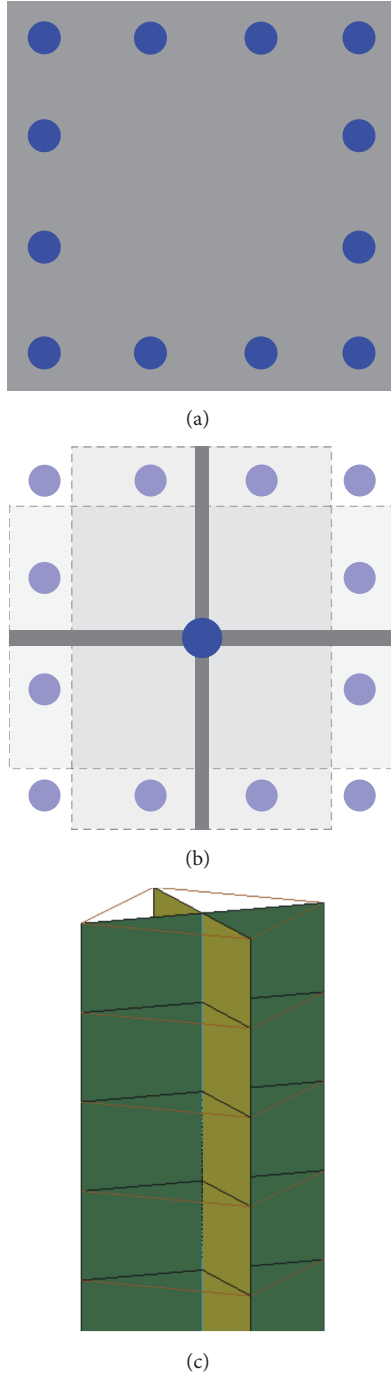


FIGURE 6: Column for structural finite element model: (a) real geometry of column section, (b) sketch of crossed shells, each with its corresponding virtual thickness, and with nine longitudinal bars overlapped at the column axis and their virtual position with geometrical offset, and (c) detail of model mesh.

the concrete shells at the nodes farther away from the column axis. Figure 6 shows the real section and the equivalent section formed by cross shells and offset reinforcement.

The slabs are modeled with flat shell elements of $20\text{ cm} \times 20\text{ cm}$ size. The distribution of reinforcement in the slabs distinguishes between support zone, central zone, top and

TABLE 4: Parameters for EC2 material model and Mat Add Erosion formulation for concrete.

Parameters for EC2 material model	Value
Mass density	2300 kg/m^3
Unconfined compression strength	25 MPa
Tensile stress to cause cracking	2.5 MPa
Tension stiffening	1.2 GPa
Parameters for Mat Add Erosion	Value
Minimum principal strain at failure	-0.032
Maximum principal strain at failure	0.025

bottom layers, and the two perpendicular directions (x , y) in the slab, following the coordinates in Figure 2:

(i) Top layer, equivalent bars:

- (a) x direction, with 20 cm of separation: 14 lines of $\phi 15.7$, $x = 0\text{ m}$ to $x = 2.60\text{ m}$ and $x = 4.60\text{ m}$ to $x = 7.20\text{ m}$; 13 lines of $\phi 10.9$, $x = 0\text{ m}$ to $x = 2.60\text{ m}$ and $x = 4.60\text{ m}$ to $x = 7.20\text{ m}$.
- (b) y direction, with 20 cm of separation: 10 lines of $\phi 13.4$, $y = 1.10\text{ m}$ to $y = 5.50\text{ m}$; 17 lines of $\phi 9.4$, $y = 1.10\text{ m}$ to $y = 5.50\text{ m}$; 8 lines of $\phi 13.4$, $y = 1.10\text{ m}$ to $y = 5.50\text{ m}$.

(ii) Bottom layer, equivalent bars:

- (a) there is no distinction between central and support zones.
- (b) x direction, with 20 cm of separation: 27 lines of $\phi 11.5$, $x = 0\text{ m}$ to $x = 7.20\text{ m}$.
- (c) y direction, with 20 cm of separation: 35 lines of $\phi 11.6$, $y = 0\text{ m}$ to $y = 5.50\text{ m}$.

Additionally, the shells of the slabs near the columns, in an $80\text{ cm} \times 80\text{ cm}$ area (4×4 shells), are modeled with 4% of transverse reinforcement to take account of punching shear reinforcement.

The concrete is modeled using the Eurocode 2 (EC2) [20] material model implemented in LS-DYNA. This material model is isotropic, with different response in tension and compression, softening in compression, damage in tension, hardening, and failure.

The steel reinforcement can be included homogenized with the concrete. This option is only used for the shear reinforcement of the slabs. This material model does not include by itself erosion, but this capability may be added with Mat Add Erosion formulation. Figure 7 shows the material response for unconfined uniaxial displacement. The parameters used for erosion were previously calibrated [14, 21] for the mesh size used in order to obtain equivalent erosion in both finite element models.

The material parameters used are shown in Table 4.

The boundary conditions, contact constraints, and loads are identical to the continuum model: columns fixed in their base, the ground as rigid slab, contact between different parts of the structure, and gravity loads for the sandbags and self-weight.

The response of the model is discussed in the next section.

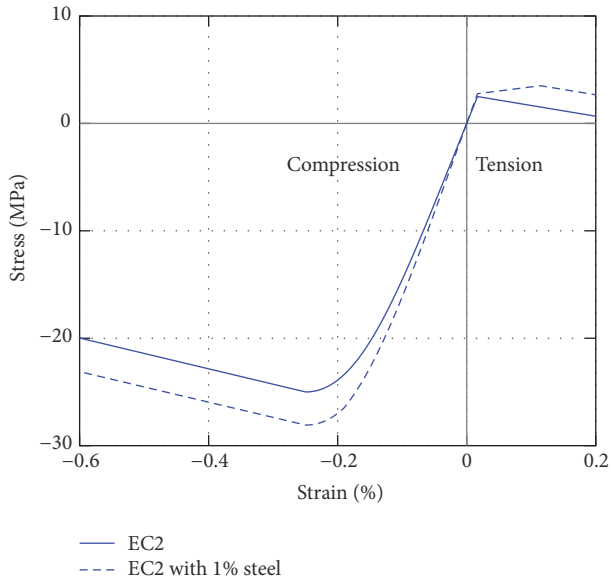


FIGURE 7: Stress-strain diagram for 25 MPa EC2 material model. Unconfined uniaxial tension and compression. Material model without homogeneous steel reinforcement and with 1% of steel reinforcement.

5. Results and Discussion

5.1. Test Results. Discrete measurements were performed for material points A and B (Figure 3), as follows:

- (i) Point A: position 1 at 0.16 s, position 2 at 0.54 s.
- (ii) Point B: position 1 at 0.33 s, position 2 at 0.71 s.

Measuring the position of these two points an average velocity of 1.3 m/s for both is obtained. Unfortunately the accelerometers that were located on the structure failed, so the displacement is the only reliable measure. The cloud of dust caused by the blast prevented reliable measures beyond one second from the collapse initiation.

5.2. Comparison between Test and Models. Figures 8 and 9 show the comparison between the measured displacements and velocities and the calculated ones for both the continuum and structural finite element models. The difference between points A and B in the calculated models is negligible and only one curve for both points A and B is drawn. Consequently, the four displacements measured in the test can be represented in one figure.

Figure 8 shows a good correlation between the four measured displacements and the displacement histories of the finite element models.

In Figure 9 the velocity histories of the continuum finite element model and the structural finite element model are compared with the measured average velocity, resulting in a good agreement between average values.

Figures 10, 11, and 12 show the evolution of the structural collapse, comparing the pictures obtained from the slow motion video with the meshes of the models at corresponding times.

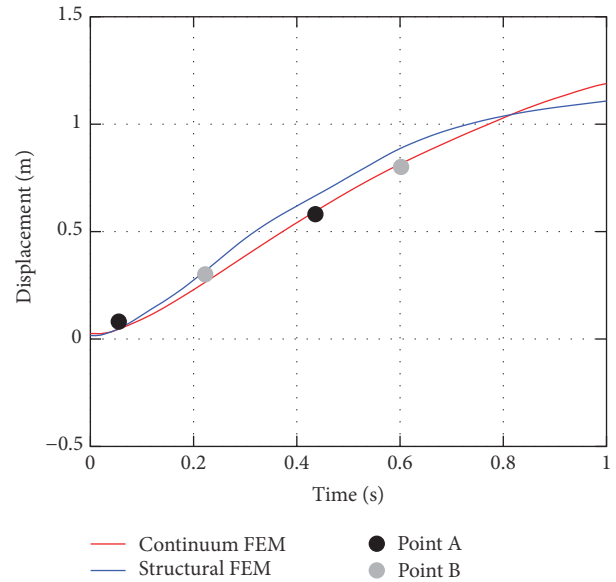


FIGURE 8: Comparison of displacements between finite element models and test.

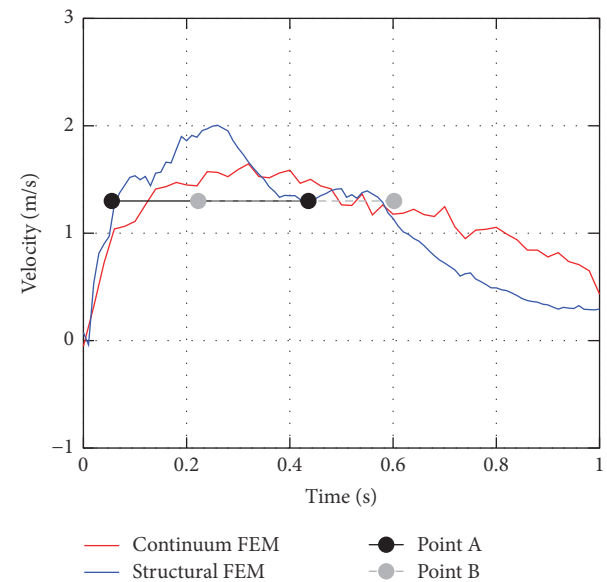


FIGURE 9: Comparison of velocities between finite element models and test.

In the first figure, at time 0.6 s, the slabs of the two floors show a large displacement because of the loss of support of the removed column. Despite these large displacements only cracking in the concrete is obtained and the reinforcement is still capable of maintaining the integrity of the slabs. The columns also maintain their structural integrity. In the second figure, at time 1.1 s, the displacements have increased in the zone of the removed column; the unions between the slabs and the columns acquire large rotations and begin to fail. However, the velocity is still low due to the contribution of the rest of the structure, and the columns keep their integrity. In the third figure, at time 2.6 s, the central column located in

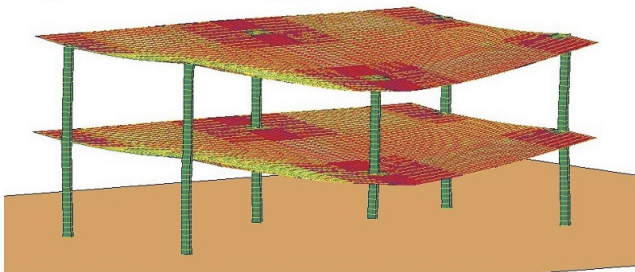
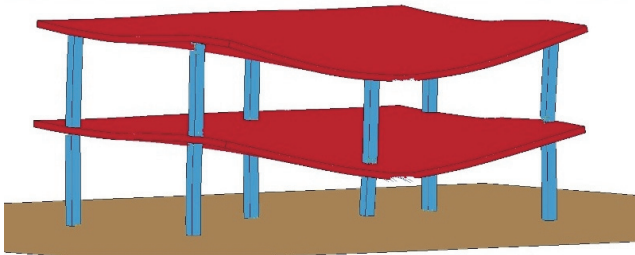


FIGURE 10: Comparison between test, continuum model, and structural model at 0.6 s after column removal.

the back and in the bottom fails due to the additional load it must support, and the complete structure collapses. Several unions between slabs and columns fail completely and the slabs fall independently of the columns. The type of collapse is the failure of concrete and reinforcement of the slabs in the center of the structure. As may be observed in the figures, the global behavior of the structure is adequately represented.

5.3. Discussion. The models used for the reinforced concrete structure have proven their capacity to reproduce the complete process of the progressive collapse. The continuum finite element model is the most accurate model, with more precision in the displacement and velocity and better prediction of concrete failure, especially in the zone where the columns support the slabs. The structural finite element model is slightly less accurate than the continuum finite element model in terms of displacement and velocity. The local failures are not represented in detail, but it has enough precision to reproduce accurately the global collapse phenomenon. The great advantage of structural finite element model is a much smaller computational cost. Table 5 shows the comparison between both models in terms of number of elements, calculation time, and memory. The structural finite element model is much more efficient.

Bearing in mind a realistic model for a complete building would be of much greater size and computational cost, for

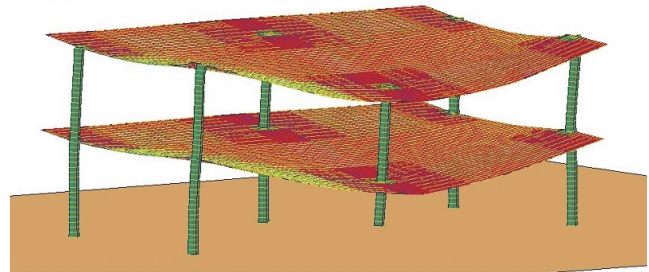
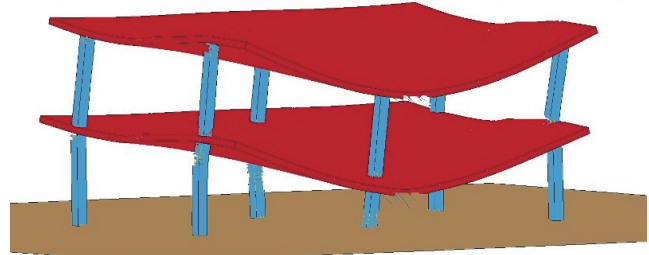


FIGURE 11: Comparison between test, continuum model, and structural model at 1.1 s after column removal.

the continuum finite element model the computer resources required render it difficult to afford. On the contrary, the structural finite element model can be used with moderate computational cost.

The same conclusion may be reached for analysis of blast loads on concrete buildings [14] and its subsequent collapse.

6. Conclusions

This paper discusses the modeling of reinforced concrete structures collapse with explicit finite element models. Two different methodologies are proposed. The finite element code LS-DYNA is used in the analysis.

The first type of model uses continuum elements for concrete and beam elements for reinforcement in a segregated way. The connection between rebars and concrete is modeled using a penalty formulation (Constrained Lagrange in Solid). CSCM and Piecewise Linear Plasticity material models are used for concrete and steel, respectively. Damage formulation and erosion parameters are shown in Section 3. Contact constraints, load of the sandbags, self-weight, and dynamic relaxation formulations are modeled with Contact Automatic General, Load Segment Set, Load Body Z, and dynamic relaxation commands of LS-DYNA.

The second type of model uses shell elements for concrete and beam elements for reinforcement in a segregated way. The

TABLE 5: Computational cost comparison between continuum FE model and structural FE model for four parallel processors Intel(R) Core(TM) i7-2600 CPU @ 3.40 GHz.

	Number of elements
Continuum FE model	540,000 continuum elements and 67,000 beams
Structural FE model	8,600 shells and 14,600 beams
	Calculation time
Continuum FE model	98 h and 23 min
Structural FE model	29 min and 24 s
	Memory (in LS-DYNA words)
Continuum FE model	192,000,000
Structural FE model	7,500,000

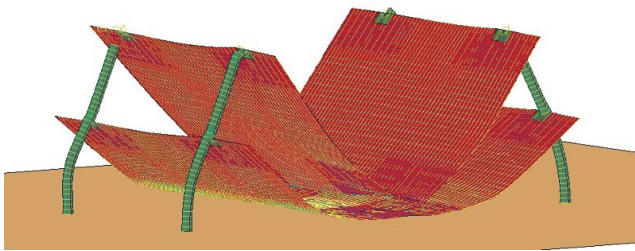
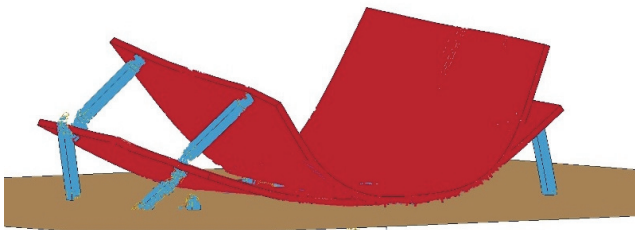


FIGURE 12: Comparison between test, continuum model, and structural model at 2.6 s after column removal.

connection between rebars and concrete is modeled using common nodes of the meshes. EC2 and Piecewise Linear Plasticity material models are used for concrete and steel, respectively. Contact constraints, load of the sandbags, self-weight, and dynamic relaxation formulations are identical to the continuum model.

The modeling techniques have been validated through the comparison with a real scale test of a two-floor structure. The numerical values for model parameters are shown in Sections 3 and 4.

Based on the results presented in this paper, the following conclusions are drawn:

- (i) The methodologies used in the two proposed finite element models have enough precision to reproduce the global collapse phenomenon in an accurate way.
- (ii) The continuum finite element model has a high precision in displacements and velocities, and in the prediction of local failures of the concrete. The structural finite element model has enough precision with lower computational cost than the continuum element model and can be used with advantage for simulation of a large frame-type building.
- (iii) For modeling the collapse of full buildings, structural finite element models with concrete shells including segregated steel beam elements coupled using common nodes are recommended.

Conflicts of Interest

The authors declare that there are no conflicts of interest regarding the publication of this paper.

Acknowledgments

This study was carried out with the support of SEGTRANS project (*Investigación, Desarrollo y Demostración de Innovadores Sistemas de Mejora de la Seguridad Integral en Terminales de Transporte*), financed by Centre for the Development of Industrial Technology of Spain (CDTI), and the experiment was realized in the Technological Institute *La Marañosa* belonging to Department of Defense of Spain.

References

- [1] P. F. Mlakar Sr., W. G. Corley, M. A. Sozen, and C. H. Thornton, "The Oklahoma City bombing: analysis of blast damage to the Murrah Building," *Journal of Performance of Constructed Facilities*, vol. 12, no. 3, pp. 113–119, 1998.
- [2] B. M. Luccioni, D. Ambrosini, and R. Danesi, "Colapso estructural bajo cargas explosivas," *Mecánica Computacional*, vol. XXII, pp. 957–970, 2003.
- [3] H. Corres and E. Romero, "Reconstrucción módulo D aparcamiento Madrid Barajas T-4," in *Resúmenes del IV Congreso de*

Asociación científico-técnica del hormigón estructural (ACHE), 2008.

- [4] J. E. Crawford, "Retrofit methods to mitigate progressive collapse," in *The Multihazard Mitigation Council of the National Institute of Building Sciences, Report on the July 2002 National Workshop and Recommendations for Future Effort*, 2002.
- [5] U. Starossek, "Typology of progressive collapse," *Engineering Structures*, vol. 29, no. 9, pp. 2302–2307, 2007.
- [6] R. Ahmadi, O. Rashidian, R. Abbasnia, F. Mohajeri Nav, and N. Usefi, "Experimental and numerical evaluation of progressive collapse behavior in scaled rc beam-column subassemblage," *Shock and Vibration*, vol. 2016, Article ID 3748435, 17 pages, 2016.
- [7] T. Krauthammer, R. L. Hall, S. C. Woodson, J. T. Baylot, J. R. Hayes, and Y. Sohn, "Development of progressive collapse analysis procedure and condition assessment for structures," Defense Technical Information Center, 2002.
- [8] G. Kaewkulchai and E. B. Williamson, "Beam element formulation and solution procedure for dynamic progressive collapse analysis," *Computers & Structures*, vol. 82, no. 7-8, pp. 639–651, 2004.
- [9] Y. Shi, Z.-X. Li, and H. Hao, "A new method for progressive collapse analysis of RC frames under blast loading," *Engineering Structures*, vol. 32, no. 6, pp. 1691–1703, 2010.
- [10] B. M. Luccioni, R. D. Ambrosini, and R. F. Danesi, "Analysis of building collapse under blast loads," *Engineering Structures*, vol. 26, no. 1, pp. 63–71, 2004.
- [11] F. Fu, "Progressive collapse analysis of high-rise building with 3-D finite element modeling method," *Journal of Constructional Steel Research*, vol. 65, no. 6, pp. 1269–1278, 2009.
- [12] L. Kwasniewski, "Nonlinear dynamic simulations of progressive collapse for a multistory building," *Engineering Structures*, vol. 32, no. 5, pp. 1223–1235, 2010.
- [13] J. O. Hallquist, *LS-Dyna*, Theory manual, 2006.
- [14] M. Bermejo, P. Anastasio, and J. M. Goicolea, "A methodology to calibrate structural finite element models for reinforced concrete structures subject to blast loads," in *Proceedings of the 9th International Conference on Structural Dynamics*, 2014.
- [15] A. Abu-Odeh, "Modeling and simulation of bogie impacts on concrete bridge rails using ls-dyna," in *Proceedings of the 10th international LS-DYNA Users Conference, Livermore Software Technology Corporations*, pp. 8–10, 2008.
- [16] D. Kosloff and G. A. Frazier, "Treatment of hourglass patterns in low order finite element codes," *Numerical and Analytical Methods in Geomechanics*, vol. 2, no. 1, pp. 57–72, 1978.
- [17] Y. D. Murray, A. Abu-Odeh, and R. Bligh, *Evaluation of LS-DYNA Concrete Material Model*, vol. 159, 2007.
- [18] A. S. Day, "An introduction to dynamic relaxation (dynamic relaxation method for structural analysis, using computer to calculate internal forces following development from initially unloaded state)," *The Engineer*, vol. 219, pp. 218–221, 1965.
- [19] M. Bermejo, J. M. Goicolea, F. Gabaldón, and A. Santos, "Impact and explosive loads on concrete buildings using shell and beam type elements," in *Proceedings of the 3rd International Conference on Computational Methods in Structural Dynamics and Earthquake Engineering (COMPDYN '11)*, May 2011.
- [20] J. O. Hallquist et al., *LS-DYNA Keyword User's Manual*, Livermore Software Technology Corporation, 2013.
- [21] M. Bermejo, A. P. Santos, J. M. Goicolea, and A. Pérez, "Evaluación de acciones explosivas sobre estructuras de hormigón armado mediante elementos finitos," *Informes de la Construcción*, vol. 67, no. 539, p. e095, 2015.

Research Article

Wind-Induced Coupling Vibration Effects of High-Voltage Transmission Tower-Line Systems

Meng Zhang,¹ Guifeng Zhao,¹ Lulu Wang,¹ and Jie Li^{2,3}

¹School of Civil Engineering, Zhengzhou University, Zhengzhou 450001, China

²College of Civil Engineering, Tongji University, Shanghai 200092, China

³State Key Laboratory for Disaster Reduction in Civil Engineering, Tongji University, Shanghai 200092, China

Correspondence should be addressed to Guifeng Zhao; gfzhao@zzu.edu.cn

Received 27 July 2017; Accepted 24 October 2017; Published 10 December 2017

Academic Editor: Xing Ma

Copyright © 2017 Meng Zhang et al. This is an open access article distributed under the Creative Commons Attribution License, which permits unrestricted use, distribution, and reproduction in any medium, provided the original work is properly cited.

A three-dimensional finite element model of a 500 kV high-voltage transmission tower-line coupling system is built using ANSYS software and verified with field-measured data. The dynamic responses of the tower-line system under different wind speeds and directions are analyzed and compared with the design code. The results indicate that wind speed plays an important role in the tower-line coupling effect. Under the low wind speed, the coupling effect is less obvious and can be neglected. With increased wind speed, the coupling effect on the responses of the tower gradually becomes prominent, possibly resulting in the risk of premature failure of the tower-line system. The designs based on the quasi-static method stipulated in the current design code are unsafe because of the ignorance of the adverse impacts of coupling vibration on the transmission towers. In practical engineering, when the quasi-static method is still used in design, the results for the design wind speed should be multiplied by the corresponding tower-line coupling effect amplifying coefficient δ .

1. Introduction

High-voltage transmission tower-line systems are important lifeline engineering infrastructures, which are vital to the harmony and sustainable development of society. A high-voltage transmission tower-line system is composed of the transmission towers and transmission lines with a large difference in stiffness between them. Because of their characteristics, including their geometric nonlinearity and closely spaced modes of vibration, the dynamic behavior of transmission lines has significant effects on the wind-induced vibration response of transmission towers. Damage to high-voltage overhead transmission lines caused by environmental impacts, especially by wind-induced vibration, has been an important issue for engineers and researchers in the power industry throughout the world [1–8]. Since the introduction of the first high-voltage transmission lines, this issue has been studied continually, but reasonable solutions have not yet been obtained. Transmission line damage caused by strong winds (the average wind speed at a height of 10 m is greater than 10.8 m/s, corresponding to a Beaufort number greater

than 6) still frequently happens. In Argentina, Australia, Brazil, Canada, Japan, South Africa, and the United States, more than 80% of the transmission lines damage in these countries is caused by extreme winds [9]. For example, in September 1961, Hurricane Carla caused over \$1.5 million in damage to utility companies in Houston, USA [10]. In September 1989, Hurricane Hugo seriously damaged the power lines from Guadeloupe Island to Virginia, USA. The most severely affected area was the Montserrat region, where all high-voltage and low-voltage transmission lines were destroyed by the hurricane [11]. On October 1, 2002, typhoon number 21 landed in Japan and caused severe accidents, leading to the collapse of the 10 high-voltage transmission towers in Ibaraki prefecture [2]. In 2005, Hurricane Katrina landed in the United States and caused outages to 2.9 million customers. Hurricane Wilma also caused 6 million customers to lose power supply [2]. On November 10, 2009, a severe thunderstorm hit the transmission lines in southern Brazil, which resulted in the collapse of three transmission lines connecting the Itaipu hydropower station to Sao Paulo, causing power outages across large areas; more than 60 million people

were affected in 12 states in Brazil [12]. China's situation is not better. From 1988 to 2009, more than 105,500 kV high-voltage transmission lines collapsed [2, 3]. Therefore, wind-induced failure of high-voltage transmission line structures has been a common issue around the world. The problems uncovered by the above-mentioned accidents are profound warnings to the power sector and national security agencies throughout the world.

Researchers in China and other countries have performed experimental research and theoretical analysis regarding the wind-induced dynamic response of high-voltage transmission tower-line coupling systems. Using aeroelastic wind tunnel models, the experimental studies have focused on the wind-induced response characteristics of tower-line coupling systems [13–19], aerodynamic damping of wires [20], dynamic tension of ice-covered wires [21], and wind-induced responses in ice-covered line structures [22–26]. Researchers have also conducted field dynamic measurement studies of transmission line structure [27–32], but due to field test conditions, the existing field tests have mostly focused on the dynamic characteristics of transmission tower structure [27–30]. The existing field measurement studies regarding wind-induced responses of tower-line coupling systems are still insufficient. At present, finite element analysis is the most frequently used method for theoretical analysis of wind-induced vibration responses of transmission tower-line coupling systems because, compared with wind tunnel tests and field measurement technology, finite element analysis not only considers the coupling vibration effect between transmission towers and cables but also better characterizes the geometric nonlinear vibration in transmission lines. Moreover, finite element analysis can be used to conveniently analyze the wind-induced vibration responses of transmission tower-line systems under different wind speeds. For these reasons, finite element analysis has been widely used in the study of wind-induced vibration of transmission line structures [33–37]. However, because the test data and the measured field wind-induced response data are limited, the applicability of finite element analysis models for tower-line systems has not been validated. Therefore, building reliable finite element analysis models for high-voltage transmission tower-line coupling systems is a common goal.

Due to the increase in power demand worldwide, the voltage levels of transmission lines continue to increase. Transmission tower-line systems have gradually been developed to use larger spans and higher overhead hanging structures, and thus the wind-induced vibration effect of the transmission lines has become even more prominent. In contrast, because of the frequent occurrence of extreme winds associated with global climate change, the probabilities of large-scale power outages caused by transmission line trips and tower collapses under strong winds are further increasing. Therefore, it is especially important to conduct detailed dynamic analysis and design of transmission lines to ensure that transmission towers can operate safely within their design service periods.

At present, the design of transmission tower-line structures as stipulated in the current codes of most countries requires that transmission towers and transmission lines to be designed separately. The adverse impacts of coupling

vibration on the transmission towers in tower-line systems under the design wind loadings are not considered. Under the action of fluctuating wind loads, the dynamic tension of the transmission lines will change continuously, which may cause the forces of the transmission tower members to be in a complex stress state and may cause the members to yield before their designed bearing capacity is reached, due to dynamic characteristics and failure mode of the tower changed. Furthermore, the dynamic characteristics and failure modes [38] of the tower are changed. Therefore, the study of the coupled vibration behavior of high-voltage transmission tower-line systems under wind load is of great theoretical significance. At the same time, it can provide guidance for the design of transmission line structures.

In recent years, researchers have realized that the effects of coupling between the towers and lines in transmission tower-line systems on the dynamic response of the transmission towers cannot be neglected. It has been suggested that the disadvantage effect of the coupling between the towers and lines should be considered when designing transmission line structures. However, studies of the specific characteristics and influence of the coupling vibration responses of tower-line systems under wind load remain limited.

To address the topics discussed above, in this study, using a 500 kV high-voltage transmission tower-line system in East China as an engineering example, a finite element analysis model matching the practical tower-line system is developed. Based on the wind speed and pressure conversion theory, the wind speeds recorded on the transmission lines are converted into wind loads. A finite element analysis of the wind-induced vibration response of the tower-line system is conducted. The results are compared with the measured data to verify the accuracy of the finite element model of the transmission tower-line system. On this basis, using the modified Davenport spectrum to simulate the wind speed time history, the dynamic responses of the transmission towers in the tower-line system under different wind speeds are analyzed. The results are compared with those provided by the static calculation method stipulated in China's "Technical Codes for Designing 110 kV–750 kV Overhead Transmission Lines" (GB50545-2010) [39]. Based on the results of this analysis, the ratio of the tower members' stress in the tower-line system to the quasi-static stress of the members of a single tower is defined as the tower-line coupling effect amplifying coefficient, δ . The variation in this coefficient under different wind speeds and directions is discussed. A quantitative design methodology is proposed. The purpose of this study is to provide technical support for the wind resistance design of high-voltage transmission tower-line systems.

2. Finite Element Model of High-Voltage Transmission Tower-Line Systems

2.1. Engineering Background and Calculation Parameters. The 500 kV high-voltage transmission line in this study is located in Jiangsu Province, China. Along the transmission line, a tower-line system consisting of 3 transmission towers (towers numbers 159, 160, and 161) and 2-span transmission lines were selected for this study, as shown in Figure 1. Transmission

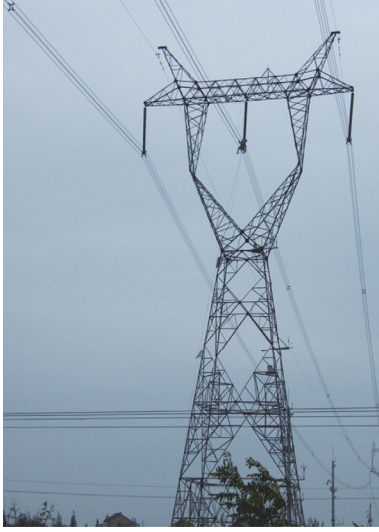


FIGURE 1: A high-voltage transmission tower-line system (tower number 160).

tower number 160 has a height of 47.1 m with cross arm 42 m above ground. The spacing between the middles of number 159 and number 160, crossing a flat field, is 280 m, and the spacing between the middles of number 160 and number 161, crossing a river with complex terrain, is 380 m. The transmission lines are in two layers. The upper layer is the lightning wires, and the lower is the electric conductors. Between number 159 and number 160, the maximum sags of the lightning wires and electric conductors are 4.3 m and 5.6 m, respectively, whereas between number 160 and number 161, the maximum sags of the lightning wires and electric conductors are 7.92 m and 10.32 m, respectively.

The transmission towers are angle steel towers. Their main members, model, and locations are shown in Table 1. The main members are Q345 steel, whereas the oblique members are Q235. The design parameters of the transmission lines are shown in Table 2. One end of the porcelain insulators is hinged at the end of the conductors. The other end is hinged in the cross arm of the tower. Three umbrella-shaped hanging insulator strings are used. Each string is composed of 27 pieces, with each piece weighing 12.0 kg. The total length of string is 4 m, the diameter is 330 mm, and the total weight is 370.29 kg.

The average wind speed at a height of 10 m is 25.3 m/s. This is used as the design wind resistance condition for these transmission lines.

2.2. The Establishment of the Finite Element Analysis Model.

To accurately calculate the wind-induced vibration response of the transmission tower-line system, a precise and reasonable finite element model of the multi-tower-line coupled system is required. Zhang [40] numerically studied the finite element modeling of transmission tower-line systems using the ANSYS software package and compared the wind-induced vibration responses of a four-tower three-wire system with those of a three-tower two-wire system. The results indicate

TABLE 1: Parameters of the main members of the transmission towers.

Number	Members specification	Applications in the tower
(1)	L180 × 16	Junction connecting insulator and crossbar, ground bracket
(2)	L100 × 10	Low crank arm in tower head
(3)	L100 × 8	Tower and tower legs (bottom)
(4)	L90 × 8	Tower head
(5)	L90 × 7	Tower oblique members, upper crank arm in tower
(6)	L80 × 7	Cross arm
(7)	L80 × 6	Tower head, crossbars; tower oblique members
(8)	L70 × 5	Oblique members, connector between tower head and crossbars
(9)	L63 × 5	Tower head, tower oblique members
(10)	L56 × 5	Tower oblique members, tower head bracing
(11)	L50 × 5	Tower bracing
(12)	L45 × 5	Tower legs (bottom), tower bracing

that the three-tower two-line model can meet the accuracy requirements for calculation with the lower computational cost. Therefore, in this study, the ANSYS software package is still used to establish the spatial finite element analysis model for the three-tower two-line system based on the actual characteristics of the transmission lines.

In the model, the angle steel member in the transmission tower is simulated using the BEAM24 element. This element is a three-dimensional thin-walled plastic beam element. All cross-sections of the beam have tensile, bending, and torsion bearing capabilities, and the model can simulate the beam element with any openings. The element has plastic, creep, and expansion bearing capacities in the axial and customized cross-section opening directions. The material of the element is simulated based on a double linear model, as the elastic and plastic properties are accommodated simultaneously. The detailed materials parameters are as follows: before the yield, the elastic modulus is 2.06×10^5 MPa, the Poisson ratio is 0.3, and the design yield strength is 310 MPa (Q345 steel) or 215 MPa (Q235 steel). After the yield, the tangent modulus is 4120 MPa.

The transmission line is a typical type of suspended cable structure. Any given conductor (ground wire) with arbitrary deflection can be discretized into a series of interconnected cable elements. After the discretization, the span-to-sag ratio of each cable element is less than that of the original cable. Therefore, the small deflection cable theory can be used to analyze each cable element. There are generally two methods currently in use to simulate the cable element. In one approach, the cable element is regarded as a straight bar with only a tensile force, and all the loads act on the nodes. This method is comparatively simple and will work accurately only when the cable pretension is far greater than the tension caused by cable deadweight (i.e., the span-to-sag ratio of the

TABLE 2: Design parameters of the transmission lines.

Item	Diameter d (mm)	Cross sectional area A_c (mm ²)	Line density m_c (kg/m)	Elastic modulus E_c (MPa)	Average operating tension (N)	Tension under design wind speed (N)	Rupture force (N)	Span L_c (m)	Sag d_c (m)
Electric conductor	33.6	666.55	2.06	63000	35316	43688	141265	280 (380)	5.6 (10.32)
Lightning wire	16	152.81	0.639	91100	14275	21929	79306	280 (380)	4.3 (7.92)

TABLE 3: Parameters of the transmission lines after equivalent processing.

Items	Diameter d (mm)	Density ρ_c (kg/m ³)	Line density m_c (kg/m)	Linear load q_c (N/m)	Initial strain ϵ_{c0}
Electric conductor	134.4	3090.5	8.24	80.752	0.00084
Lightning wire	16	4182	0.639	6.262	0.0010254

cable element is sufficiently small, often less than 1/12). The other method is to consider each cable element as a parabolic cable element, assuming that the vertical load (including the deadweight) is evenly distributed along the cable span. Similarly, this method also requires a small rise-to-span ratio of the cable element, usually less than 1/8. Considering that the maximum span sag ratio (d_c/L_c) of the transmission line in this study is approximately 1/37, much less than 1/12, we chose the first method to model the transmission line using the LINK10 element. Each element covers 1 m of length. This element can simulate rod members under axially applied tension or compressive loadings, and it can also be used to simulate relaxed suspension or chain structures. This element also has stress stiffening and geometric nonlinear analysis capabilities and can therefore meet the requirements of model building for transmission lines. The cable span between the middles of number 159 and number 160 is discretized into 280 LINK10 elements, and the cable span between the middles of number 160 and number 161 is discretized into 380 LINK10 elements. Compared with the other studies (see Gani and Légeron [34] and Fei et al. [41]), the mesh is comparatively intensive.

In practical transmission lines, each phase wire is composed of four-split wires; to simplify the calculations, in the finite element analysis model, each four-split phase wire is simplified as one piece of wire, assuming each split wire has the same windward cross-section, and thus, the operating tension of this piece of wire should be equivalent to the total operating tension, and its density should be equivalent to the averaged density of each split. The parameters of this simplified transmission line are presented in Table 3.

When establishing the finite element model of the transmission line, it is very important to determine its initial configuration. On the one hand, the balance equation and the deformation coordination equation of the transmission line should be determined based on the catenary theory, to determine the spatial location of the transmission line. On the other hand, it is necessary to transfer the transmission line from the initial stress-free state to the initial load state

in accordance with certain shape-determining methods. The main methods for determining the cable balance equation are the catenary theory method and the parabolic theory method. The former is an exact method, whereas the latter is an approximate method, but when the span-to-sag ratio of the cable is less than 1/8, the parabolic theory method also provides a relatively accurate solution. Because the maximum span sag ratio (d_c/L_c) of the transmission line in this study is approximately 1/37, much less than 1/8, the parabolic method can be used to determine the initial shape of the transmission line. Assuming that the vertical load on the transmission line is evenly distributed along the span, as shown in Figure 2, the spatial shape equation of the transmission line is

$$y(z) = \frac{q_c}{2T_{c0}} z(L_c - z) + \frac{\Delta_c}{L_c} z. \quad (1)$$

In (1), q_c is the vertical load applied on the transmission line, with only the transmission line's own weight being considered in this study; T_{c0} is the initial horizontal tension of the transmission line, $T_{c0} = (q_c L_c^2)/(8d_c)$; L_c is the horizontal span of the transmission line (half the distance between the two adjacent towers); Δ_c is the height difference between the two ends of the transmission line; and d_c is the sag in the middle of the transmission line. Using the parameters listed in Tables 2 and 3, the spatial shape equation can be determined. The initial strain that always exists in the transmission line results in the existence of the initial stress and the initial tension within the system. Therefore, the shape-determining analysis is conducted on the wire element when the finite element model is built. The purpose is to establish the initial stress state to ensure that the subsequent analysis results are correct.

The insulator is simulated with the rigid element MPC184, with rigid rod properties to simulate the spatial rigid body motion of the insulator. This choice is made because the porcelain insulator has higher stiffness than the transmission lines. The MPC184 element can be used to model a rigid constraint between two deformable bodies or as a rigid component used to transmit forces and moments in engineering

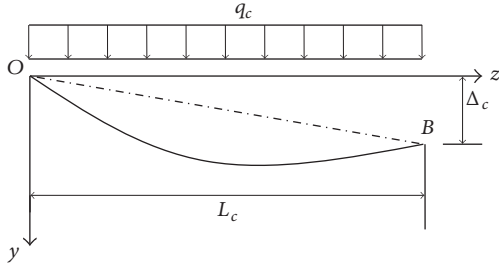


FIGURE 2: Diagram of evenly distributed vertical loadings along the span of the transmission line.

applications. This element is well suited for linear, large-rotation, and/or high-strain nonlinear applications.

To simplify the analysis, the model of the three transmission towers is built based on the parameters of tower number 160. The three-dimensional finite element models of the single tower and the tower-line coupling system are shown in Figure 3. In the model, the four nodes at the bottom of each transmission tower are rigidly constrained, and the displacement constraints in the Z coordinate direction are imposed on the connecting junctures between the transmission lines and the transmission tower. The single tower model has 1971 elements and 839 nodes in total, whereas the tower-line system model has 9210 elements and 5972 nodes in total, with 25936 degrees of freedom.

3. Analysis of the Free Vibration of the Transmission Tower-Line System

In the transmission tower-line coupling system, the tower and the line work together. The basic dynamic characteristics of the tower-line system can be obtained based on modal analysis. The dynamic characteristics include the vibration mode and frequency. Through modal analysis, the vibration response of the system when subjected to external excitation can be predicted.

The free vibrations of the transmission tower and the tower-line system discussed above are analyzed individually using the finite element model. The initial 300 orders of the natural frequency of the tower-line coupling system and the corresponding vibration modes are analyzed. The first 5 orders in the results are the rigid body motion of the insulator in the system, whose natural frequency is close to zero. Then, orders 6 to 15 are the vibration of the transmission lines, whose natural frequency is between 0.232 and 0.323 Hz. The 16th, 17th, 19th, 40th, 112th, 119th, 120th, 128th, and 161st orders represent the overall vibration model of the tower-line coupling system. The results of the rest of the higher-order vibration modes are not listed. Among the vibration models, the 16th-order mode mainly represents the vibration of the lightning wires and of the transmission towers along the z -direction (Figure 4(a)), with a corresponding frequency of 0.38 Hz. The 17th-order vibration mode is the torsion vibration of the lightning wires and of the transmission towers (Figure 4(b)), with a corresponding frequency of 0.39 Hz. The 19th-order vibration mode is the vibration of the

transmission lines and the torsion vibration of the transmission towers (Figure 4(c)), with a corresponding frequency of 0.467 Hz. The 40th-order vibration mode also represents the torsion vibrations of the tower-line transmission lines and the transmission towers (Figure 4(d)), with a corresponding frequency of 0.724 Hz. The 112th-vibration mode is the vibration of the transmission lines and of the transmission towers along x -direction (Figure 4(e)), with a corresponding frequency of 2.228 Hz. The 119th-order vibration mode also represents the vibration of the power transmission lines and of the transmission towers along the x -direction (Figure 4(f)), with a corresponding frequency of 2.295 Hz. The 120th-order vibration mode is the vibration of the transmission lines and the transmission towers along the z -axis (Figure 4(g)), with a corresponding frequency of 2.318 Hz. The 128th-order vibration mode is the vibration of the transmission lines and transmission towers along the x -direction (Figure 4(h)), with a corresponding frequency of 2.384 Hz. The 161st-order vibration mode is the vibration of the transmission lines and the torsion vibration of the transmission towers (Figure 4(i)), with a corresponding frequency of 3.138 Hz.

The results for the natural frequencies and characteristics of the vibration modes of the tower-line system are listed in Table 4. When the tower-line coupling system is vibrating as a whole, the dynamic characteristics of the transmission tower are pronouncedly different from that of an individual single transmission tower. The natural frequency of the transmission tower in the tower-line coupling system is much lower than that of the individual single tower in the corresponding vibration direction. In the tower-line system, the vibration of the transmission tower in the z - and torsion directions is more prone to occur at low frequencies, whereas the vibration in the x -direction still occurs at high frequencies. In the tower-line system, the overall vibration of the tower and the line is characterized by low-frequency, dense-mode vibration, which is different from the vibration characteristics of a single tower, demonstrating that, in the design of transmission tower-line structures, the tower-line coupling effect on the dynamic characteristics of transmission tower should be considered.

4. Comparison of Field Measurements and Finite Element Simulation of the Wind-Induced Vibration Response of the Transmission Tower-Line System

4.1. Introduction to the Field Measurements. The anemometers are placed at vertical heights of 10, 20, 28, and 43 m on tower number 160 to record the wind speed on the different parts of the transmission tower. Three wind towers were installed between transmission towers number 159 and number 160. Two ultrasonic anemometers are installed on each wind tower at heights of 10 m and 20 m. The 1st wind tower is 40 m from transmission tower number 160, the 2nd wind tower is 80 m from the 1st wind tower, and the 3rd wind tower is 120 m from the 2nd wind tower and 40 m from transmission tower number 159. The layout diagram of all wind instruments is shown in Figure 5. The acceleration sensors

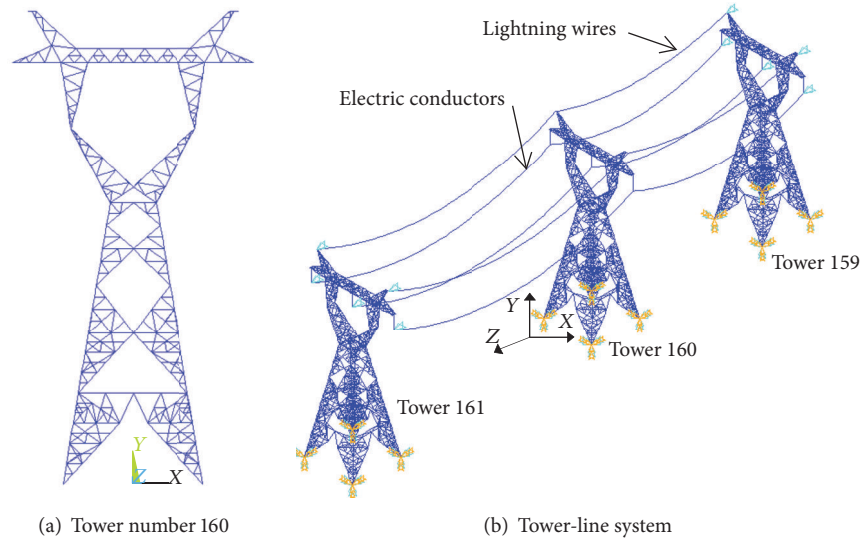


FIGURE 3: Finite element analysis model of the high-voltage transmission tower-line system.

TABLE 4: Comparison of the natural frequencies of the transmission tower-line system and a single transmission tower.

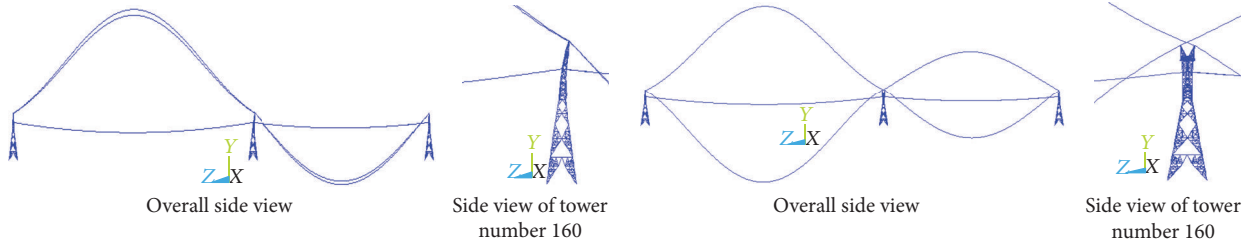
Model	Natural frequency of the transmission tower in tower-line system (Hz)	Characteristics of the vibration of the transmission tower in tower-line system	Natural frequency of a single tower (Hz)	Characteristics of the vibration of a single tower
(1)	0.38	Bending vibration in the z -direction	1.7497	Bending vibration in the z -direction
(2)	0.39	Torsion vibration	2.1481	Bending vibration in the x -direction
(3)	0.467	Torsion vibration	2.8720	Torsion vibration
(4)	0.724	Torsion vibration	4.1825	Local vibration in the tower
(5)	2.228	Vibration in the x -direction	5.0337	Coupling vibration in the z -direction and the tower's local vibration

are mounted vertically at different heights on tower number 160, noted as locations A, B, C, and D in Figure 5(a). When conducting the field measurements, the sampling frequency of the anemometers is 10 Hz, and the sampling frequency of the acceleration sensors is 100 Hz. A total of 165 seconds of acceleration response were recorded for each sample.

In September 2007, when Typhoon Wipha hit East China, the measuring equipment discussed above successfully recorded the wind speed in these locations and the acceleration response of transmission tower number 160 under the effects of the typhoon. Typhoon Wipha's strength attenuated quickly after landfall. Therefore, the average field wind speeds at heights of 10, 20, and 28 m were 6.03, 7.43, and 8.13 m/s, respectively. Figure 6 shows a dataset of wind speed time history recorded by the anemometers at 10 and 20 m on transmission tower number 160. Figure 7 shows the fluctuating wind speed power spectrum density (PSD) recorded by anemometers at 20 m on the transmission tower and on the wind tower.

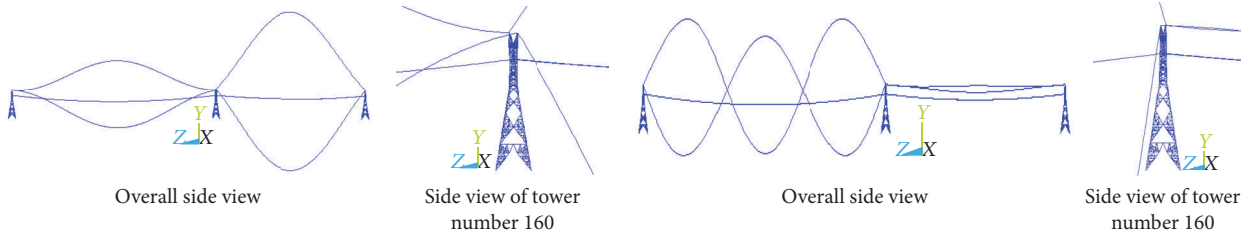
4.2. Calculation of the Wind Load on Various Locations of the Measured Transmission Lines. To provide the basis for the finite element simulation of the wind-induced vibration response of the measured transmission lines, the wind speed recorded in the field must be converted into the wind loads on the lines. When calculating the wind loads on the measured transmission lines for transmission tower number 160, considering the influence of the change of wind speed along the height of the transmission tower, as shown in Figure 8, the tower can be divided into eight sections vertically. The wind speed recorded by the anemometer at a height of 43 m is selected as the wind speed for sections 1 to 3, that at a height of 28 m is used for sections 4 and 5, that at a height of 20 m is used for section 6, and that at 10 m is employed for sections 7 and 8.

The wind loadings on the transmission lines should be calculated separately in accordance with the actual layout of the anemometers and wind towers. Because the three wind towers are installed between transmission towers number



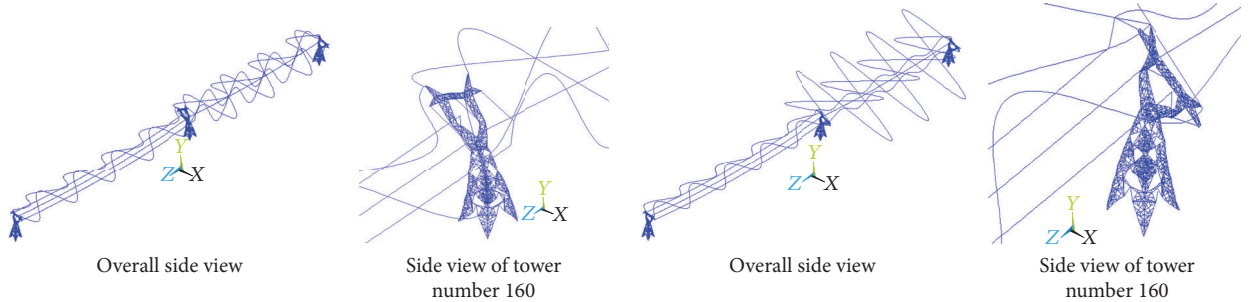
(a) The 1st-order vibration mode in the tower-line system in the z -direction (the 16th-order, $f = 0.38$ Hz)

(b) The 1st-order vibration mode in the tower-line system in the torsion direction (the 17th-order, $f = 0.39$ Hz)



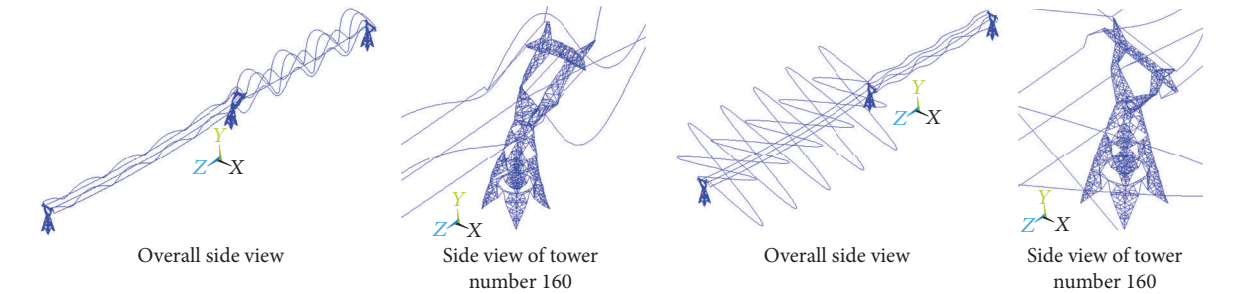
(c) The 2nd-order vibration mode in the tower-line system in the torsion direction (the 19th-order, $f = 0.467$ Hz)

(d) The 3rd-order vibration mode in the tower-line system in the torsion direction (the 40th-order, $f = 0.724$ Hz)



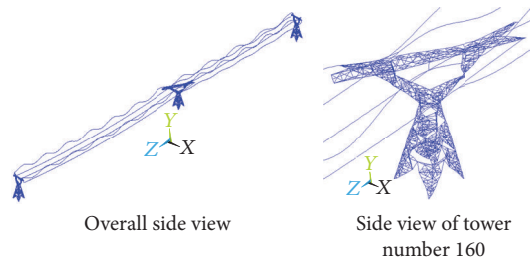
(e) The 1st-order vibration mode in the tower-line system in the x -direction (the 112th-order, $f = 2.228$ Hz)

(f) The 2nd-order vibration mode in the tower-line system in the x -direction (the 119th-order, $f = 2.295$ Hz)



(g) The 2nd-order vibration mode in the tower-line system in the z -direction (the 120th-order, $f = 2.318$ Hz)

(h) The 3rd-order vibration mode in the tower-line system in the x -direction (the 128th-order, $f = 2.384$ Hz)

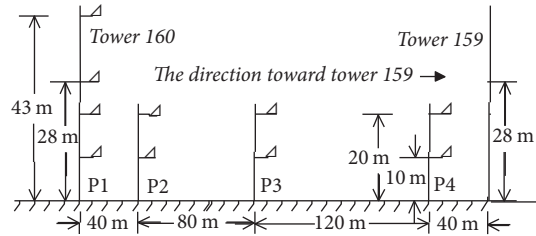


(i) The 4th-order vibration mode in the tower-line system in the torsion direction (the 161st-order, $f = 3.138$ Hz)

FIGURE 4: Vibration modes of the transmission tower-line system.



(a) The placement locations of the anemometers and acceleration sensors on tower number 160 (b) The placement of the wind tower and anemometers (c) The anemometers on transmission tower number 160



(d) Diagram of the anemometer installation locations (note: the symbol “ \angle ” represents a three-dimensional ultrasonic anemometer)

FIGURE 5: Arrangements of wind instruments and acceleration sensors in the field.

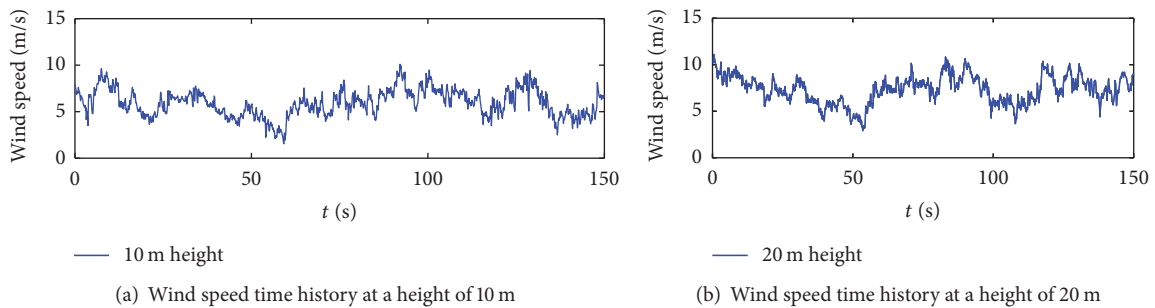


FIGURE 6: Wind speed data recorded by the anemometers on tower number 160.

160 and number 159, as shown in Figure 5, this span of the transmission lines can be divided into four sections from tower number 160 to tower number 159, and the wind loading can then be calculated section by section. Among them, the wind speed recorded by the anemometers at a height of 43 m on tower number 160 is used as the wind speed for the 1st section and that at a height of 20 m on the 1st wind tower

is used for the 2nd section; the speed at a height of 20 m on the 2nd wind tower is employed for the 3rd section and that at a height of 20 m on the 3rd wind tower is used for the 4th section. For the transmission lines between transmission towers number 160 and number 161, no wind-measuring devices are installed because of the watercourse between them and the complex terrain conditions. When calculating

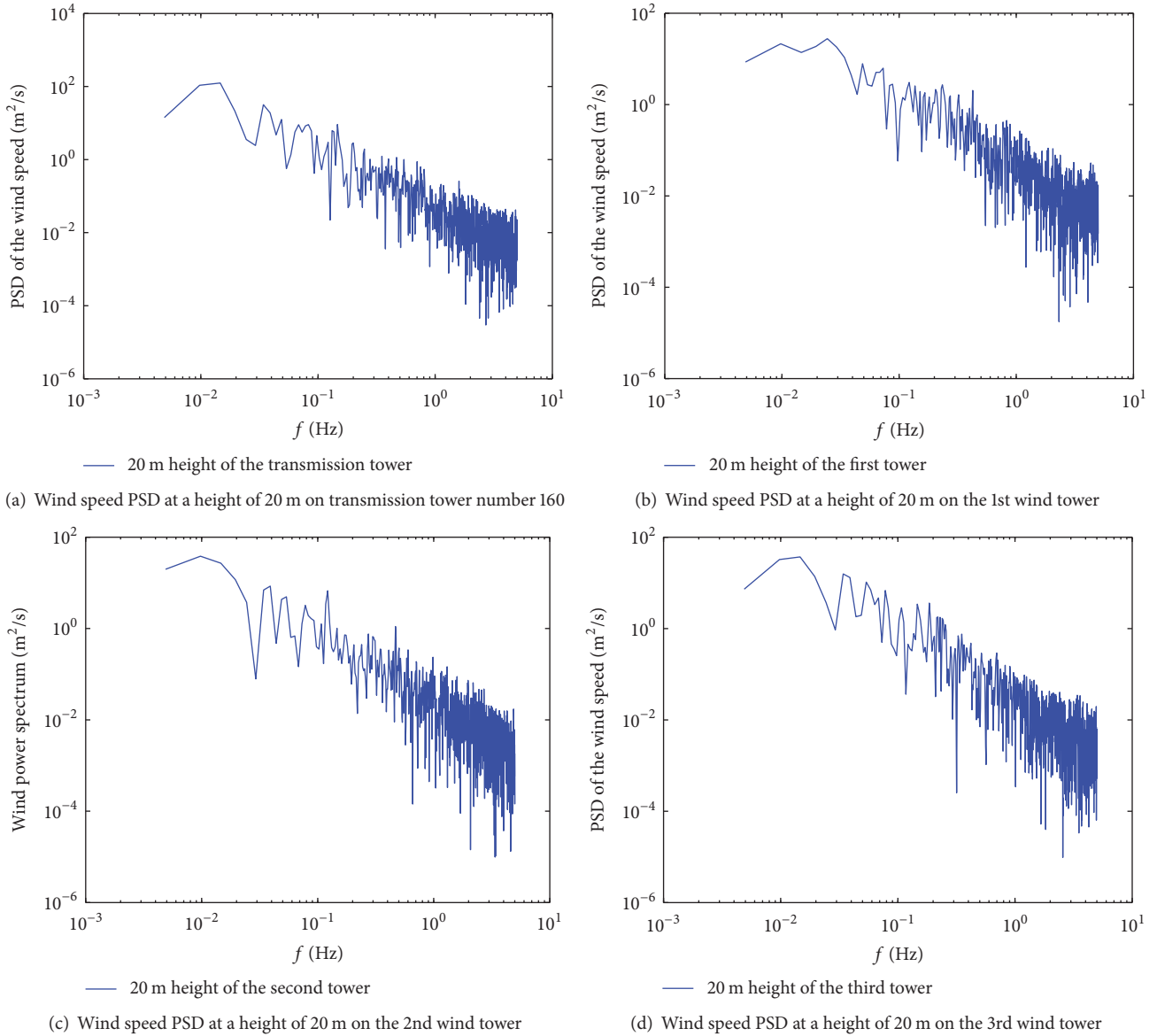


FIGURE 7: The fluctuating wind speed PSD recorded by the anemometers at each field measuring location of the transmission lines.

the wind loadings on the transmission lines in this section, the wind speed recorded by the anemometers at a height of 43 m on transmission tower number 160 is used.

The wind load applied on the insulators can be calculated based on the wind speed recorded at the corresponding height on the transmission towers.

In the matrix of field wind-measuring devices, every anemometer can record the wind speed in the main direction, the wind speed perpendicular to the main direction, and the vertical wind speed at its location. Under normal circumstances, the wind speed in the main direction is much greater than the speeds in the perpendicular and vertical directions. Considering that the transmission tower has a large stiffness, the focus should be on the impact of the horizontal wind speed, whereas the impact of vertical wind load can be neglected. For the relatively flexible transmission

lines, the effects of both the horizontal and vertical wind loads should be considered. Because the angle between the actual measured direction of the dominant wind and that of the transmission lines is approximately 106° , the main dominant wind speed and the wind speed perpendicular to the dominant wind direction can be decomposed into the wind speed perpendicular to the line direction and the wind speed parallel to the line direction.

After obtaining the wind speed vector, the wind loading on a unit length of a slender structure can be calculated based on the method proposed by Dyrbye and Hansen [42]. The wind load $F(t)$ on the tower-line structure can be expressed as follows:

$$F(t) = \frac{1}{2} \rho (U(z) + u(z, t) - \dot{x}(z, t))^2 B(z) C(z). \quad (2)$$

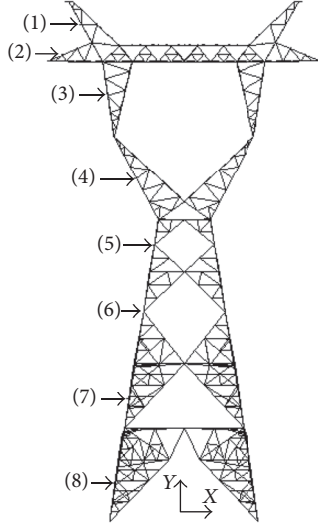


FIGURE 8: Vertical division of sections on transmission tower number 160.

In (2), ρ is the air density; $U(z)$ and $u(z, t)$ are the average wind speed and the fluctuating wind speed at height z , respectively; $\dot{x}(z, t)$ is the vibration velocity at height z ; $B(z)$ is the height of the structure perpendicular to the wind direction; and $C(z)$ is the wind load shape coefficient of the structure at height z .

Equation (2) shows that the wind load on the structure depends on the aerodynamic coupling between the wind and the motion of the structure. To simplify the analysis, this study does not consider this coupling effect in the calculations. Therefore, the wind loading is calculated based on a quasi-steady hypothesis. Equation (2) can be simplified as follows:

$$F(t) = \frac{1}{2} \rho (U(z) + u(z, t))^2 B(z) C(z). \quad (3)$$

In the detailed calculations, the wind loadings applied on the transmission towers and each section of the transmission lines can be calculated based on (3). When calculating the wind loads on the transmission towers, the towers' windward width can be calculated using its windward areas, A_s . The windward areas corresponding to each segment of transmission tower number 160 in Figure 8 are listed in Table 5.

4.3. Finite Element Simulation of the Wind-Induced Vibration Response of the Field-Measured Transmission Tower-Line System. The analysis of the wind-induced dynamic response of the transmission tower-line system can be summarized as the solutions to dynamic equations.

4.3.1. Principles of Calculation. Based on the finite element analysis method and the boundary conditions, the dynamic response of the actual transmission tower-line system can be expressed as the initial solutions of the discrete dynamic equations

$$[\mathbf{M}] \{\ddot{u}(t)\} + [\mathbf{C}] \{\dot{u}(t)\} + [\mathbf{K}] \{u(t)\} = \{\mathbf{F}(t)\}, \quad (4)$$

where $[\mathbf{M}]$, $[\mathbf{C}]$, and $[\mathbf{K}]$ are the structure's mass matrix, damping matrix, and stiffness matrix, respectively; $\{u(t)\}$, $\{\dot{u}(t)\}$ and $\{\ddot{u}(t)\}$ are the structure's displacement vectors, velocity vectors, and acceleration vectors, respectively; and $\{\mathbf{F}(t)\}$ is the wind's nodal load force vector.

The solution can be discretized in the time domain. The equation of motion can be divided into the equations of different discrete moments, and through stepwise integration, the responses of the structure in a series of discrete moments can be obtained. This method not only considers the non-linear factors of the structure but also addresses the response of the different structural modes. Therefore, the calculation is highly accurate.

When calculating the damping of the transmission tower-line system, the Rayleigh damping matrix based on the orthogonal damping assumption is used. It is expressed as

$$[\mathbf{C}] = \alpha [\mathbf{M}] + \beta [\mathbf{K}], \quad (5)$$

where α and β are the system's mass and stiffness coefficients, respectively. The equations are as follows:

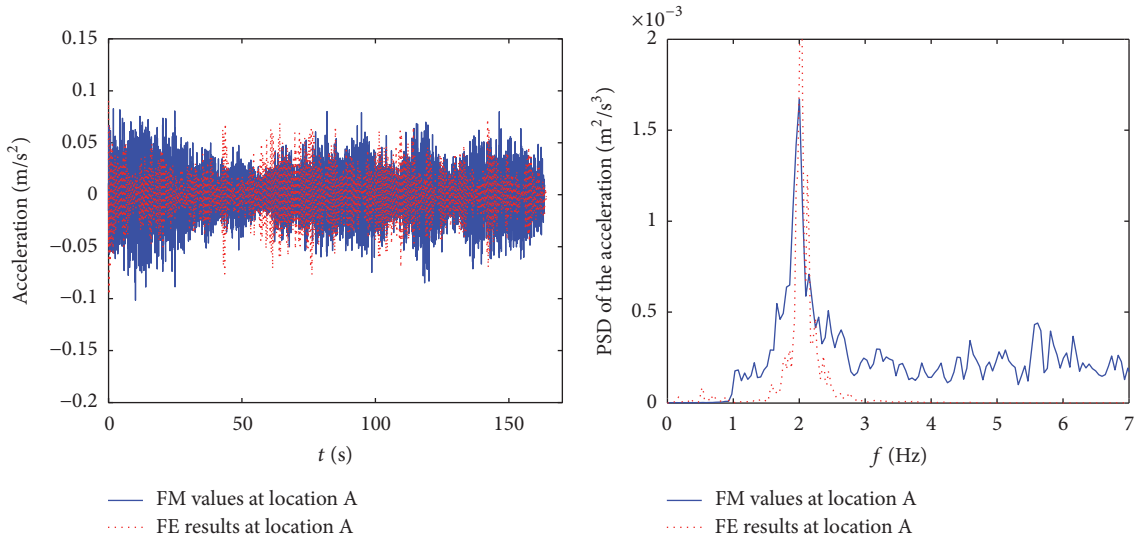
$$\alpha = \frac{2\omega_i\omega_j(\xi_j\omega_i - \xi_i\omega_j)}{\omega_i^2 - \omega_j^2}; \quad (6)$$

$$\beta = \frac{2(\xi_i\omega_i - \xi_j\omega_j)}{\omega_i^2 - \omega_j^2}.$$

In (6), ω_i and ω_j are system's i th-order and j th-order circular frequencies, and ξ_i and ξ_j are system's i th-order and j th-order damping ratios. As long as any two modes are determined, the coefficients α and β can be calculated.

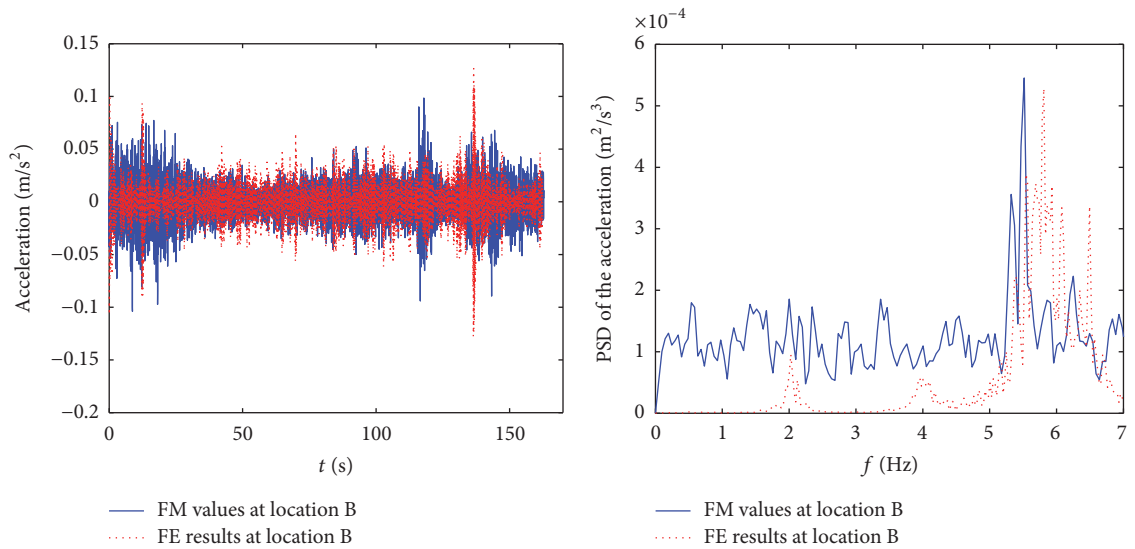
Because the sampling frequency of the measuring anemometers in the field is 10 Hz and the corresponding wind speed recorded is 165 s, 1650 load steps are designed in the finite element analysis. The wind loads calculated for each section of the measured transmission lines are used as input for the finite element model. The wind-induced dynamic response of the tower-line coupling system is calculated using the implicit *Newmark- β* stepwise integration method. The geometrical nonlinearity of the transmission lines is considered in the calculation. To accurately obtain the high-order vibration response of the structure, 0.0025 s is selected as the integral time step, and 66000 loading substeps must be calculated.

4.3.2. Comparison of Finite Element (FE) Results and Field Measurement (FM) Values. Figure 9 shows a comparison of the finite element calculation results with the field measurement results at the locations A, B, C, and D on transmission tower number 160. The left side is a comparison of the acceleration time history, and the right side is a comparison of the acceleration PSD. By and large, the finite element calculation results are clearly in good agreement with the measured results. The calculated acceleration time history and the PSD at location A are in good agreement with the measured results. At locations B, C, and D, the acceleration time history results of the finite element analysis are in good agreement with the measured results. However, the acceleration PSD



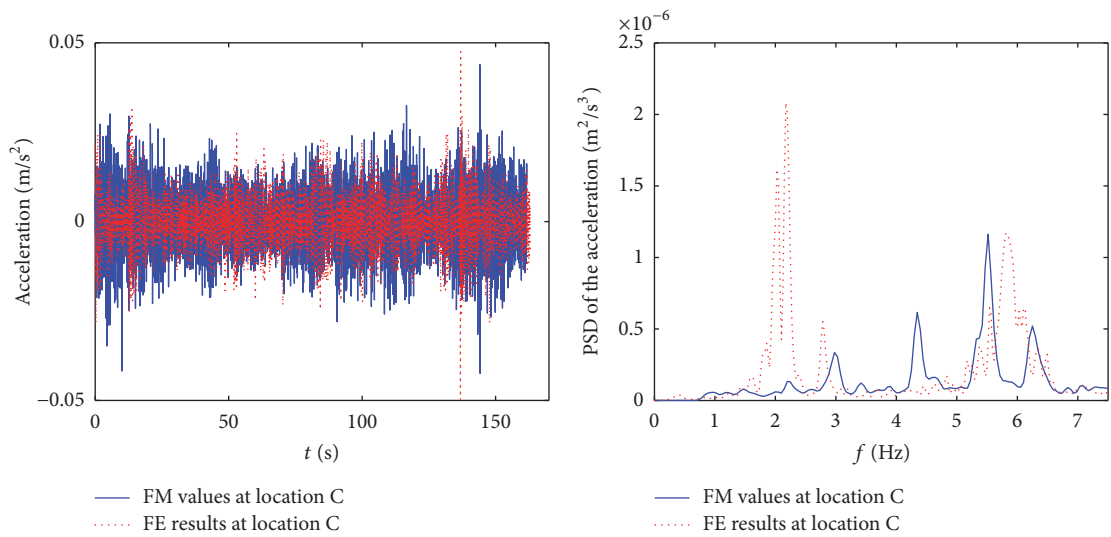
(a) Comparison of the acceleration time history at location A

(b) Comparison of the acceleration PSD at location A



(c) Comparison of the acceleration time history at location B

(d) Comparison of the acceleration PSD at location B



(e) Comparison of the acceleration time history at location C

(f) Comparison of the acceleration PSD at location C

FIGURE 9: Continued.

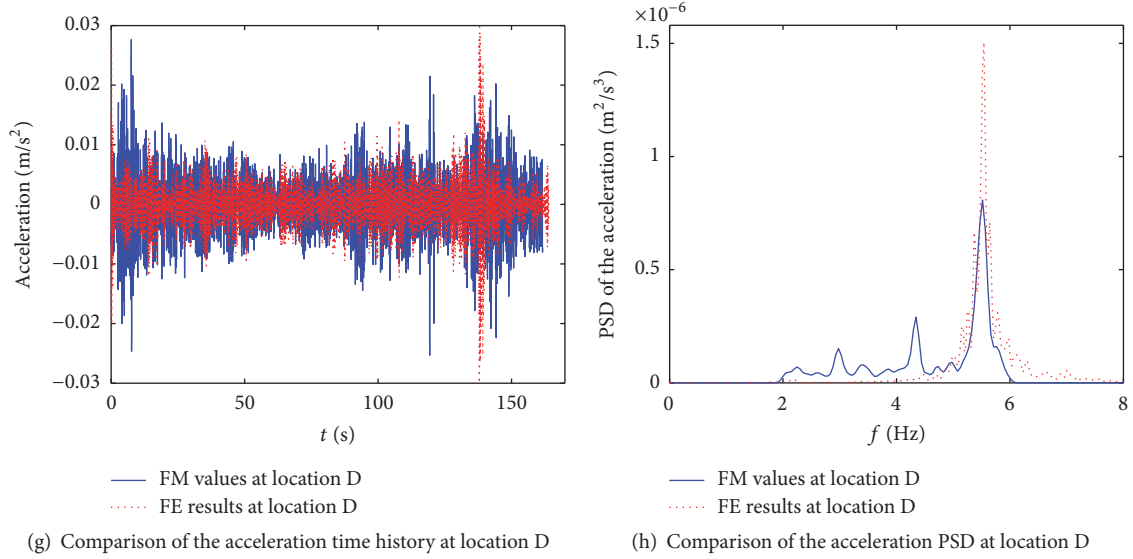


FIGURE 9: Comparison of the results of the finite element analysis calculation and the field measurements at the different measurement locations.

TABLE 5: Windward area of number 160 transmission tower.

Segment numbering	Actual area (mm ²)		Projected area (mm ²)	
	Perpendicular to the transmission line direction	Parallel to the transmission line direction	Perpendicular to the transmission line direction	Parallel to the transmission line direction
(1)	865392	1528774	752023.1	1328632
(2)	1011444	5622524	410159.4	5606444
(3)	1615828	3236466	1597591	3227210
(4)	3293370	4854699	2913509	4847745
(5)	2373116	2373116	2340374	2340374
(6)	5107037	5107037	5036575	5036575
(7)	7623368	7623368	7518187	7518187
(8)	2675226	2675226	2638316	2638316

exhibits relatively large errors, which could occur because of errors in the loads input or because the responses at these locations are affected by multiple-vibration-mode in the structure and by the influence of the measurement noise.

To vividly compare the results of the finite element analysis calculation and the measured vibration characteristics in the field, the *Hilbert-Huang Transform* (HHT) method is used in this study to identify the measured dynamic response and the dynamic response calculated by the finite element analysis method. The frequency and damping results obtained are listed in Table 6. The vibration frequency in the table is the main frequency of the structural vibration caused by the wind load at these measurement locations. Because the vibration at locations B and C is the cumulative vibration of multiple vibration modes, only the results of the high-order vibration models at these two locations are given in Table 6. Table 7 presents a comparison of the maximum acceleration and the root-mean-square responses at each measurement location.

Table 6 reveals that the vibration frequencies given by the finite element calculation method in this study are in agreement with the field measurement values, but the identified damping ratios from the two methods are quite different from each other. This difference is mainly because the *Rayleigh* damping formula is used in the finite element analysis, whereas when the actual transmission tower-line system sustains wind-induced vibration, it is affected not only by the structure damping but also by the impact of pneumatic damping, thereby resulting in larger damping ratio differences between the finite element analysis and the field measurements. However, Table 7 presents that the maximum deviation of the acceleration response at these locations does not exceed 11%, and the maximum deviation of root-mean-square response does not exceed 20%, which are acceptable deviations in engineering practice. Therefore, the finite element model for the tower-line transmission system established in this study is reliable and can be used to simulate more engineering cases.

TABLE 6: Comparison of vibration characteristics from the finite element analysis and field measurements.

Measurement location	Vibration frequency (Hz)			Damping ratio (%)		
	Finite element calculation (a)	Field measurement (b)	Deviation ((a) – (b))/(b))	Finite element calculation (a)	Field measurement (b)	Deviation ((a) – (b))/(b))
A	1.98	1.97	0.51%	1.18	1.54	–23.4%
B	5.93	5.62	5.52%	2.61	6.28	–58.4%
C	6.47	6.22	4.02%	1.30	3.00	–56.7%
D	5.41	5.41	0.00%	1.95	2.90	–32.8%

TABLE 7: Comparison of the maximum acceleration and root-mean-square responses obtained from the finite element calculation and field measurements.

Measurement location	Maximum acceleration (m/s^2)			Root mean square root (m/s^2)		
	Finite element calculation (a)	Field measurement (b)	Deviation ((a) – (b))/(b))	Finite element calculation (a)	Field measurement (b)	Deviation ((a) – (b))/(b))
A	0.1091	0.1125	–3.02%	0.0250	0.0228	9.65%
B	0.1346	0.1212	11.06%	0.0197	0.0228	–13.60%
C	0.0475	0.0438	8.45%	0.007	0.008	–12.50%
D	0.0298	0.0276	7.97%	0.0038	0.0047	–19.15%

5. Comparison of the Dynamic Response of Transmission Towers in the Tower-Line System with That of a Corresponding Single Tower

Transmission tower-line systems are complex coupling systems. The coupling effect between the towers and the lines under strong wind has a great influence on the force applied on the transmission towers. However, the existing design codes for overhead transmission lines separate the design of the transmission towers and lines. The wind loads sustained by the transmission lines are applied as static loads on the hanging points of the transmission towers, whereas the wind load adjustment factor is used to approximate the effect of wind-induced vibration on the transmission lines and towers. This linear design theory is easily implemented, but it underestimates the negative effect of the tower-line coupling vibration on the transmission towers, cannot truly reflect the loading conditions of the tower-line system under strong wind loads, and may result in designs that are unsafe. To quantitatively analyze the effect of the tower-line coupled vibration on the transmission tower, this section further calculates the dynamic response of the transmission tower in the transmission tower-line system under different wind speed conditions. The results are compared with those calculated based on the quasi-static design method stipulated in the current design codes for the corresponding single tower.

5.1. Simulation of the Wind Fields in the Transmission Tower-Line System. Because the wind speed data recorded by the wind towers in the field measurements are limited, the wind speed data equivalent to the design wind speed are not recorded. Therefore, to determine the dynamic response of the transmission tower-line system under the design wind

speed, to compare it with the response obtained based on the quasi-static method stipulated in the current design codes, and to understand the characteristics of wind-induced vibration in the tower-line system under different wind speeds, the wind fields of the tower-line system must be simulated.

Based on the description of the basic characteristics of winds by Simiu and Scanlan [43], we know that the wind speed at a certain height can be expressed as the sum of the average wind speed and the fluctuating wind speed. The average wind is a stable wind that does not change for a certain period of time. Its cyclic period is longer than the fundamental natural vibration period of most structures, and its loading effect on a structure can be treated as a static load. The fluctuating wind is characterized by being highly random, with a cyclic period similar to the fundamental natural vibration period of a common structure and a dynamic loading effect on the structure. The fluctuating wind is essentially that of three-dimensional turbulent winds, including the wind parallel to the blowing direction, the wind transverse to the blowing direction, and the perpendicular turbulence. However, in general, the values of the transverse wind and the turbulence are relatively small, and they can generally be ignored in high-rise structures. Therefore, in this study, the simulation of the wind fields focuses on the simulation of the wind speed time history of the fluctuating wind parallel to the blowing direction.

In accordance with China's "Load Code for the Design of Building Structures" GB50009-2012 [44], the terrain roughness of the measured transmission tower-line system is category B. The index of terrain roughness, z_0 , is 0.24. According to the long-term survey data collected by the wind tower array in the field, the turbulence intensity at a height of 10 m is 10%. In this study, the modified *Davenport* spectrum is used to simulate the wind speed time history of

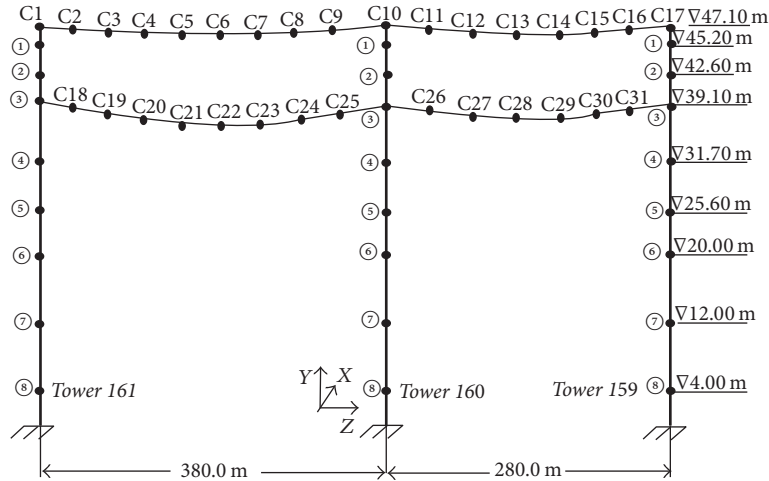


FIGURE 10: The representative nodal positions of the transmission tower-line system in the wind fields.

the transmission tower-line system. When simulating wind speed, the sampling frequency, f , is 10 Hz, and the simulated average wind speeds at a height of 10 m are 14, 16, 17, 18, 19, 20, 21, 22, 23, 24, and 25.3 m/s. These selected speeds include the design wind speed and, for engineering purposes, also strong wind speeds that have high probability of occurring. Therefore, these speeds can be used to analyze the characteristics of the wind-induced vibration of the tower-line system under different wind speeds. Because of the large geometric scale of the actual measured transmission lines, to simplify the workload of the calculation model, this study only simulates the wind speed for selected representative nodes of the tower-line system. The position and distribution of the representative nodes are shown in Figure 10. The direction of the fluctuating wind speed in the simulation is taken as the x -direction, that is, vertical to the transmission lines.

Wind speed is simulated at 8 nodal positions along the vertical direction of each transmission tower. Because of the large horizontal distance between the transmission towers, the correlation between the wind speeds at the adjacent transmission towers is weak, and thus only the vertical correlation is considered when simulating the wind speed time history of the transmission towers.

For the transmission lines, because the horizontal distances on either side of the tower-line system are not equal, to simulate the wind speed, the transmission lines between transmission towers number 160 and number 159 are divided into 7 sections, and the lines between transmission towers number 161 and number 160 are divided into 9 sections. The height difference between the two ends of the transmission lines is usually small, and both sides of the transmission lines satisfy the small sag assumption. Therefore, the difference in wind speeds caused by the height difference in the transmission lines can be ignored, and only the horizontal correlation of the wind speeds is considered. Additionally, the wind is regarded to be at the same speed between the two representative nodes of the transmission lines, as shown in Figure 10.

To verify the accuracy of the simulation results of the wind velocity field, the wind speeds at heights of 10 and 20 m on transmission tower number 160 are also simulated and compared with the field measurements, as shown in Figure 11. The simulated average field wind speeds at heights of 10 and 20 m are 6.03 and 7.15 m/s, respectively. It can be observed that the simulated results are generally in good agreement with the measurement results.

Based on the conditions discussed above, when the design wind speed, $U_{10} = 25.3$ m/s (i.e., the average wind speed at 10 m in height is 25.3 m/s), is set as the target wind speed, the wind speed time history at certain representative nodes in the tower-line system is shown in Figures 12 and 13. Figure 14 shows the wind speed power spectrum density at some representative nodes simulated in this study, when the design wind speed is set as the target. The energy dissipation region of the wind fields in this transmission line section is in the 0–0.2 Hz frequency band.

5.2. Wind-Induced Vibration Response of the Transmission Tower in the Tower-Line System under Two Different Wind Speeds. After the calculations of the wind speed time history, it can be converted into the wind loads on the tower-line system based on the method discussed in Section 4.2. The direction that the wind loads are applied is assumed to be perpendicular to the transmission lines (the x -direction); that is, the wind angle is 90 degrees. In such circumstances, the windward members of the transmission tower mainly sustain tensile stress, whereas the leeward side members mainly sustain compressive stress.

By using the implicit *Newmark- β* stepwise integration method, a transient dynamic time history analysis can be performed. Because the design wind load is so large that it might result in inelastic response of the angle members, the material nonlinearity of the angle members and the geometric nonlinearity of the transmission lines are accounted for simultaneously in the analysis. To more accurately determine the high-order response of the structure, the integration time

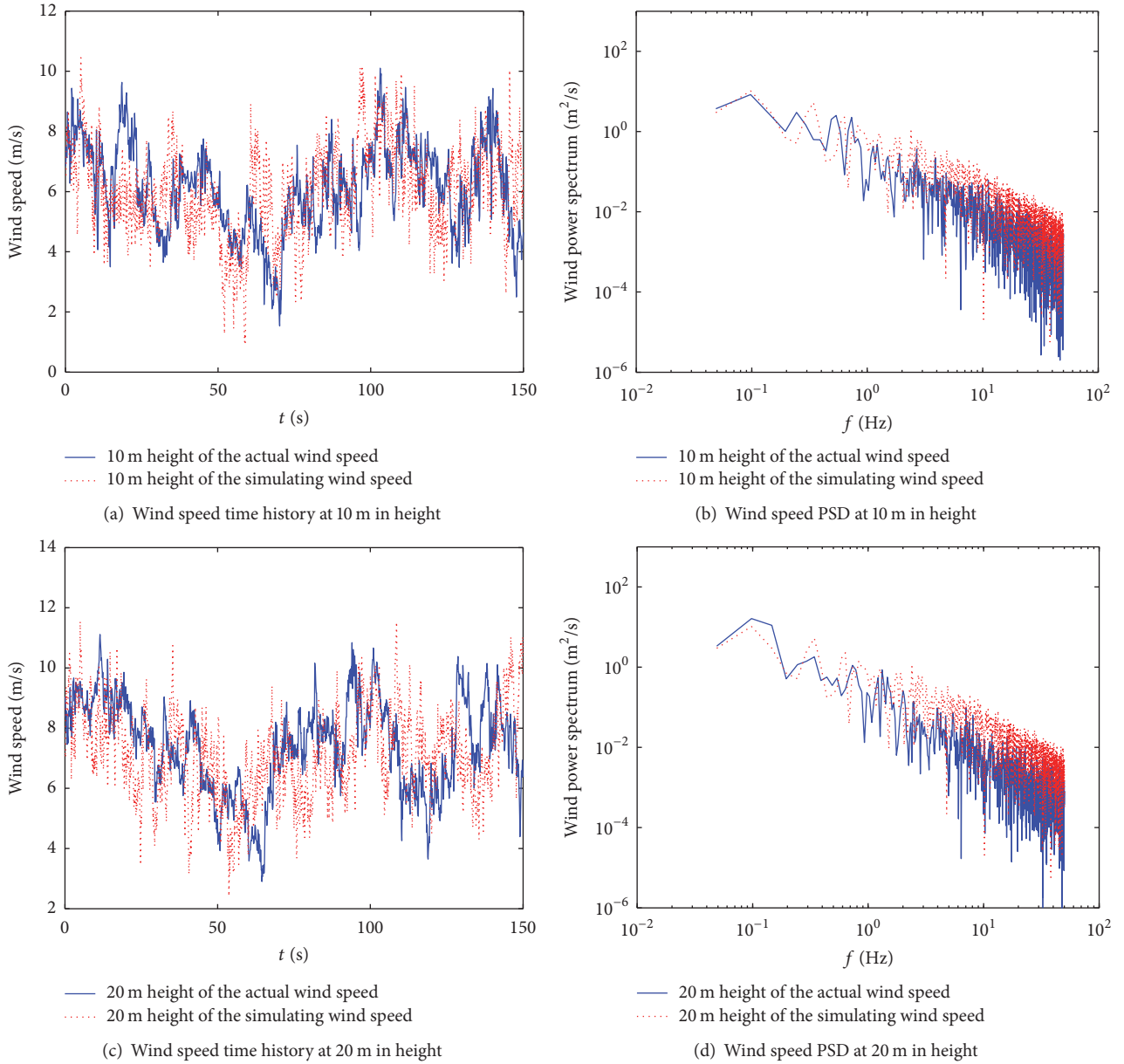


FIGURE 11: Comparison of the simulated results and the field measurements of wind velocity at heights of 10 and 20 m on transmission tower number 160.

step is set to 0.0025 s. For the input load with a sampling frequency of 10 Hz and a collection period of 150 s, a total of 60,000 load substeps are calculated.

To better understand the calculation results of the wind-induced vibration response of the tower in the tower-line system and to compare them with the calculation results of the corresponding single tower under different wind speeds, in this section, the measuring positions on transmission tower number 160 in the tower-line system are described. As shown in Figure 15, the letter “N” indicates the node, “E” represents the element, the number after the letter is the sequence number of the node or element, and the letters in brackets correspond to the placement locations of the acceleration sensors on tower number 160 (see Figure 5).

5.2.1. Responses of the Transmission Tower under the Low Wind Speed ($U_{10} = 6.03 \text{ m/s}$). The presented work is mainly focused on the displacement and acceleration responses on the top of the tower and on the maximum stress of the tower members.

(1) The Displacement and Acceleration Responses of the Nodes at the Top of the Tower. The node displacement and acceleration time history responses and the corresponding PSD at the top of transmission tower number 160 under a wind speed of $U_{10} = 6.03 \text{ m/s}$ at two different nodes on the top of the tower are shown in Figures 16 and 17.

It can be observed from the figures shown above that the displacement at the top of the tower in the tower-line system is much greater than that for the corresponding single tower.

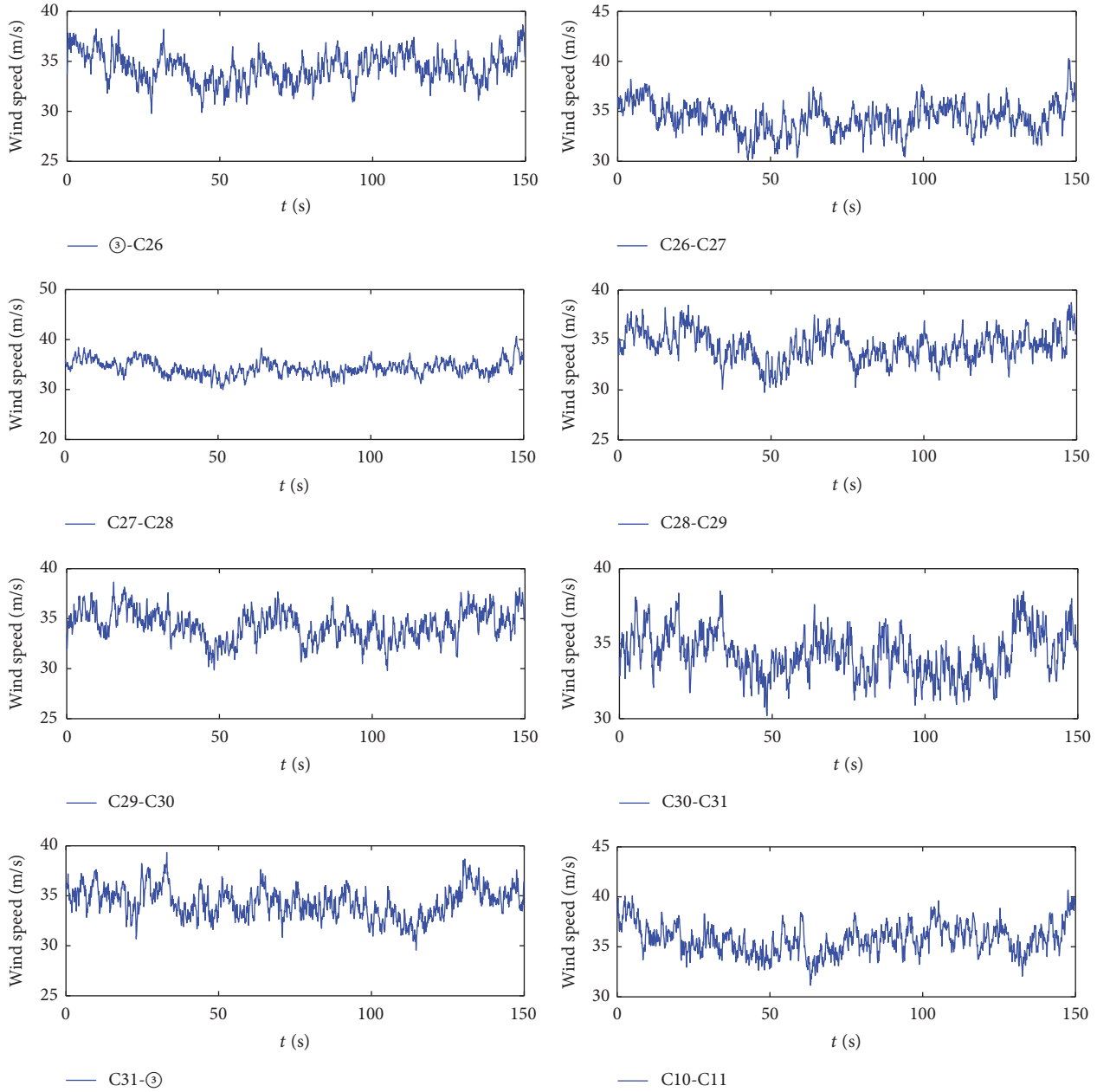


FIGURE 12: The simulated wind speed time history of the transmission lines between transmission towers number 159 and number 160.

The x -direction acceleration time history curves indicate that there is no obvious difference between the tower in the tower-line system and the corresponding single tower under the low wind speed ($U_{10} = 6.03$ m/s), whereas the z -direction results differ greatly between the two. From the frequency spectrum diagrams, we can also see that the tower vibration energy in the x -direction is mainly distributed in the frequency band of 1.8–2.2 Hz, which is very close to the fundamental natural frequency of the corresponding single tower in the x -direction. However, in the z -direction, there is a large difference, indicating that the vibration of the transmission tower is more complicated in the tower-line system than in the single tower.

(2) *Stress Responses of the Tower Members.* The stress time history and the PSD at several different elements of the tower in the tower-line system wind speed of $U_{10} = 6.03$ m/s are shown in Figures 18 and 19, respectively.

Figure 18 shows that, under the low wind speed ($U_{10} = 6.03$ m/s), the maximum stress of multiple members of the tower in the tower-line system is much less than the material design yield strength. Figure 19 shows that the maximum tensile stress (or compressive stress) of the main members of the tower in the tower-line system is caused by multimode vibration. The vibration energy is mainly distributed in the frequency band of 0–0.5 Hz, which is far from the fundamental natural frequency of the corresponding single tower.

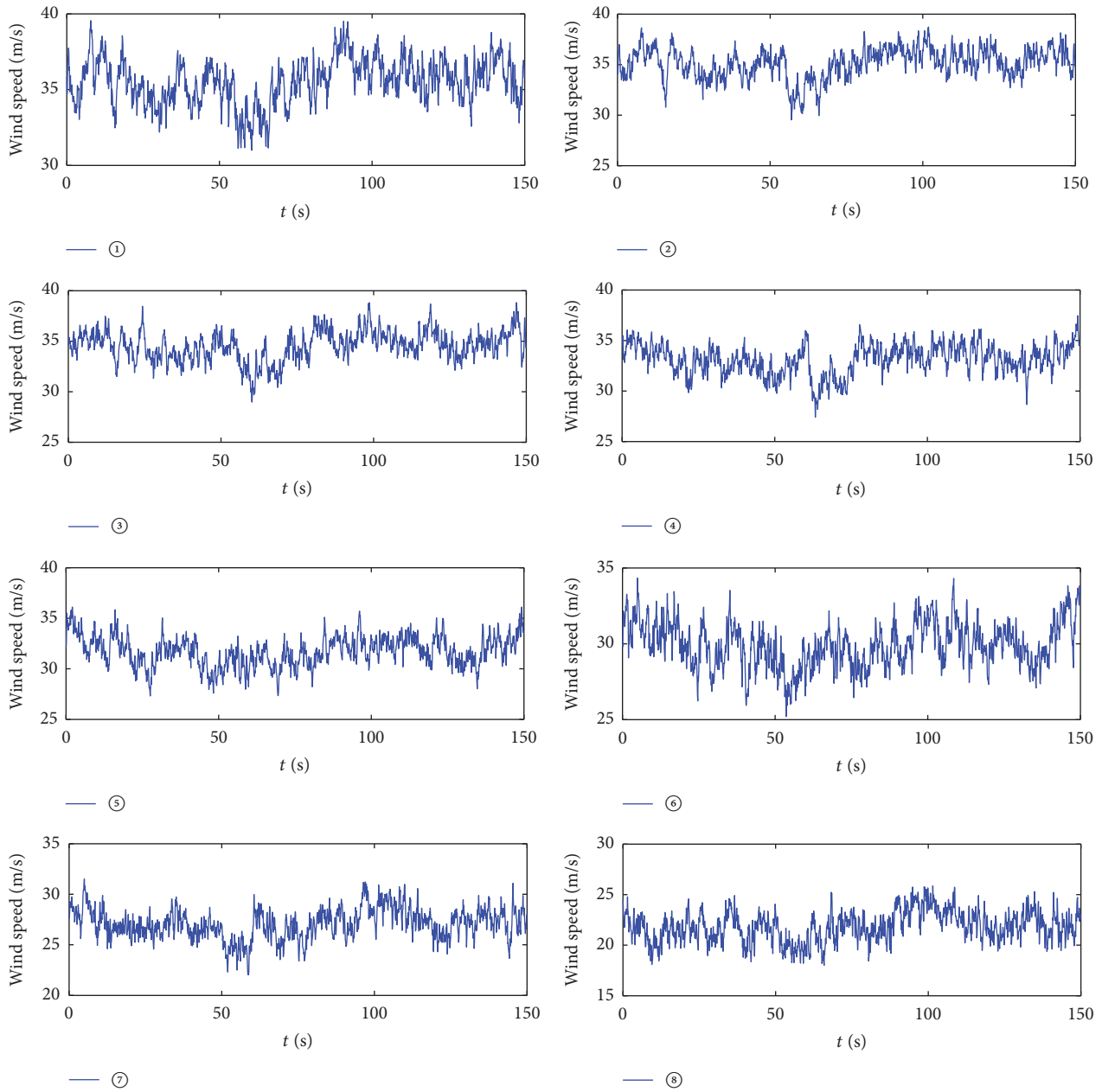


FIGURE 13: The simulated wind speed time history at the representative nodes on transmission tower number 160.

The frequency of the peak value of each high-order vibration model has an approximately multiplying relationship with the frequency of the peak value of its 1st model. Even the frequencies of the peaks of some high models also have an approximately multiplying relation.

5.2.2. Responses of the Transmission Tower under the Design Wind Speed, $U_{10} = 25.3 \text{ m/s}$

(1) *The Displacement and Acceleration Responses of the Nodes at the Top of the Tower.* The node displacement and acceleration time history responses and the corresponding PSD at the top of transmission tower number 160 under the design

speed wind ($U_{10} = 25.3 \text{ m/s}$) at two different nodes at the top of the tower are shown in Figures 20 and 21.

To demonstrate the influence of wind-induced vibration on the transmission tower in the tower-line system, the dynamic steady-state response of the corresponding single tower under the design wind speed ($U_{10} = 25.3 \text{ m/s}$) is also calculated. Comparisons of the displacement and acceleration responses at the corresponding nodes are presented in Tables 8 and 9, respectively.

Table 8 reveals that, under the design wind speed ($U_{10} = 25.3 \text{ m/s}$), the displacement at the top of the tower in the tower-line system is much greater than that for the corresponding single tower. The maximum displacement in the x -direction for the tower-line system is approximately 5.2

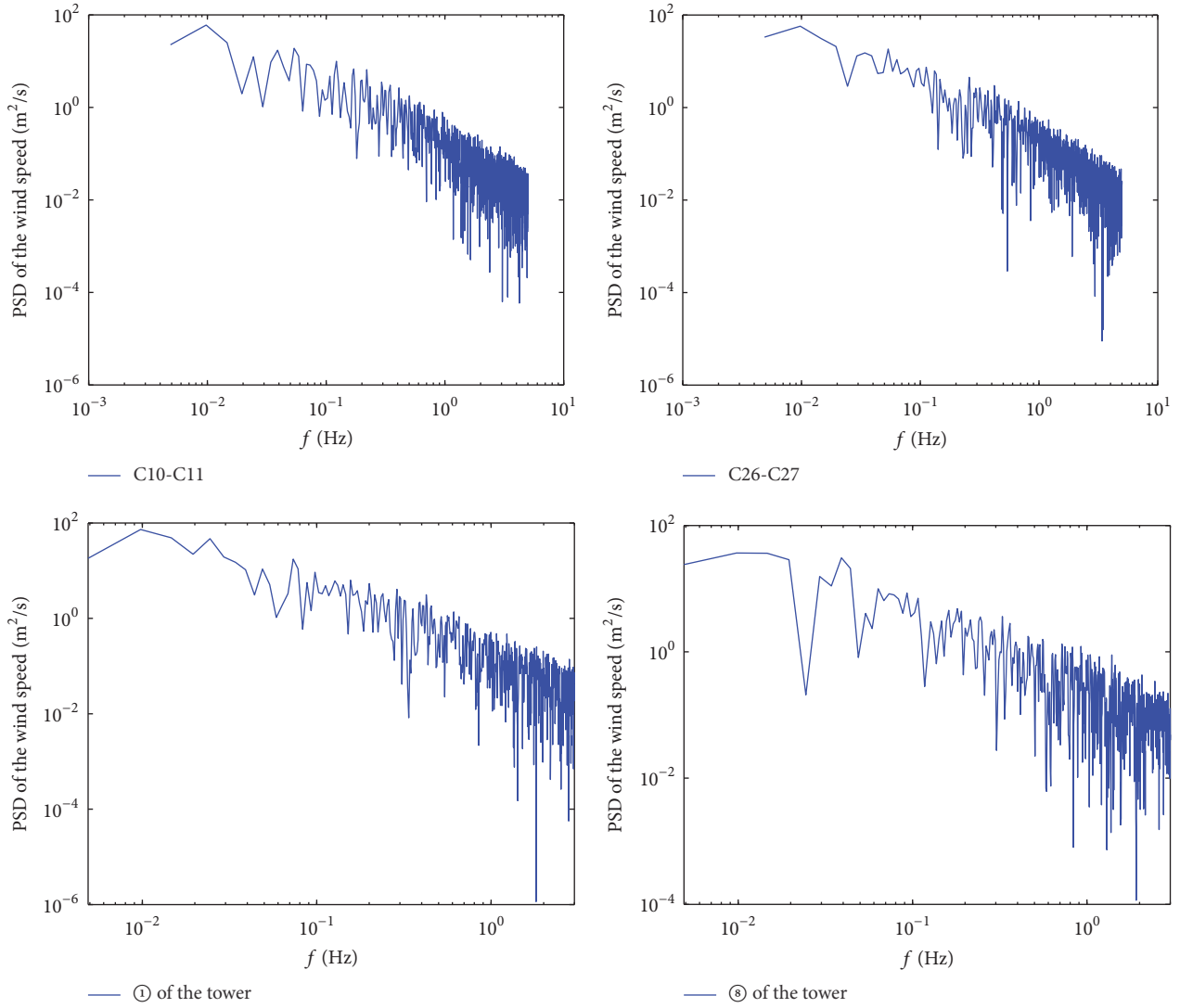


FIGURE 14: The simulated wind speed PSD on certain representative nodes on the transmission tower-line system.

TABLE 8: Comparison of the dynamic analysis results of the displacement at the top of the transmission tower for the single tower and the tower-line system under a wind speed of $U_{10} = 25.3$ m/s.

Node number	Maximum value			Average			Root mean square		
	TL	ST	TL/ST	TL	ST	TL/ST	TL	ST	TL/ST
<i>x</i> -direction displacement at the top of the tower (m)									
727	0.26	0.05	5.2	0.20	0.03	6.7	0.01	0.004	2.5
660	0.20	0.04	5.0	0.16	0.03	5.3	0.01	0.003	3.3
<i>z</i> -direction displacement at the top of the tower (m)									
727	0.07	0.0008	87.5	0.02	0.0004	50	0.02	0.0001	200
660	0.04	0.0008	50	0.01	0.0005	20	0.01	0.0001	100

Note. In the table, TL represents the response value of the tower in the tower-line system, and ST represents the response value of the corresponding single tower.

times that for the single tower. The displacement in the *z*-direction at the top of the tower can be as great as 7 cm, whereas in the corresponding single tower, this value is close to 0. The results presented in Table 9 demonstrate that the maximum acceleration and root-mean-square values in the

x-direction at the top of the tower in the tower-line system are less than the response values of the corresponding single tower, whereas the time history curves in Figures 20 and 21 reveal no obvious difference between the two. In addition, the maximum acceleration in the *z*-direction at the top of the

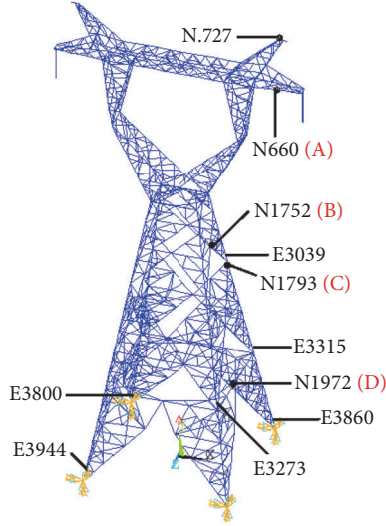


FIGURE 15: Measuring locations of the nodes and elements on transmission tower number 160.

TABLE 9: Comparison of the dynamic analysis results of the acceleration at the top of the transmission tower for the single tower and the tower-line system under a wind speed of $U_{10} = 25.3$ m/s.

Node number	Maximum value			Root mean square		
	TL	ST	TL/ST	TL	ST	TL/ST
<i>x</i> -direction acceleration at tower top (m/s^2)						
727	1.10	1.98	0.56	0.34	0.50	0.68
660	0.87	1.56	0.56	0.26	0.39	0.67
<i>z</i> -direction acceleration at tower top (m/s^2)						
727	0.59	0.10	5.9	0.13	0.03	4.3
660	0.45	0.08	5.63	0.09	0.03	3.0

Note. In the table, TL represents the response value of the tower in the tower-line system, and ST represents the response value of the corresponding single tower.

tower in the tower-line system is 5.9 times that in the corresponding single tower, and the root-mean-square response value is 4.3 times that in the single tower.

Similar to the results described in the previous section, we can also find that, from the frequency spectrum diagrams in Figures 20 and 21, the main frequency band of the tower vibration energy in the *x*-direction is narrow and the peak value is close to the fundamental natural frequency of the corresponding single tower in the *x*-direction, whereas the one in the *z*-direction is distributed in a wide range, with obvious peak values in the lower frequency range.

(2) *Stress Responses of the Tower Members.* The stress time history and the PSD at several different elements of the tower in the tower-line system under the design wind speed ($U_{10} = 25.3$ m/s) are shown in Figures 22 and 23, respectively.

Figure 22 shows that, under the design wind speed ($U_{10} = 25.3$ m/s), the maximum compressive stress of multiple members of the tower in the tower-line system can reach 310 MPa, close to the material design yield strength. Figure 23

demonstrates that the maximum stress of the main members of the tower in the tower-line system is caused by multimode vibration. The vibration energy is mainly distributed in the frequency band of 0-1 Hz, which is also far from the fundamental natural frequency of the corresponding single tower. Similarly, the frequency of the peak value of each high-order vibration model has an approximately multiplying relationship with the frequency of the peak value of its 1st-model.

To further understand the influence of the vibration of the transmission lines on the main members of the tower in the tower-line system, the steady-state time history response of the main members in the corresponding single tower under the design wind speed ($U_{10} = 25.3$ m/s) is calculated in this section. When calculating the dynamic response of the corresponding single tower, the wind loads are applied along the height of the tower, as shown in Figure 8. At the same time, the deadweights of the conductors, the ground wires, the insulators, and the fittings are applied on the hanging points of the tower. In addition, the wind loads sustained by the transmission lines under the design wind speed should also be applied on the hanging points of the tower simultaneously. The stress PSD of the main members of the corresponding single tower is also calculated (Figure 24).

Figure 24 shows that the peak frequencies corresponding to the stress PSD of elements number 3800 and 3944 in the single tower are 0.05 and 2.07 Hz, respectively. The vibration energy is mainly concentrated in the mode corresponding to 2.07 Hz, which is very close to the free vibration mode frequency of 2.1481 Hz, caused by the single tower bending along the *x*-direction, indicating that the stress increase in the members of the single tower is mainly caused by the wind load and the vibration of the tower itself.

Comparing Figures 23 and 24, the stress PSD of the tower in the tower-line system is mainly distributed in the range of 0-0.5 Hz, and the frequency corresponding to the peak of the PSD is close to the 1st-4th low-order natural frequencies of the tower-line system and far from the natural frequency of the single tower (see Table 4), thus indicating that the stress increase in the transmission tower in the tower-line system is mainly caused by the vibration of the transmission lines.

Table 10 presents a comparison of the dynamic stress of the tower in the tower-line system and the corresponding single tower under the design wind speed ($U_{10} = 25.3$ m/s). The results summarized in Table 10 demonstrate that, under the same design wind speed, the maximum stress of multiple members in the tower-line system can reach the design yield strength of the steel. The stress values in the tower-line system are much greater than those of the corresponding single tower. Therefore, under the design wind speed, the transmission tower in the tower-line system could be destroyed, but the corresponding single tower remains safe, demonstrating that the amplifying effect of the dynamic coupling between the transmission line and the transmission tower in the tower-line system on the dynamic response of the transmission tower cannot be neglected.

In general, the coupling effect between the transmission lines and the transmission tower is the intrinsic property of the tower-line system. Because of the coupling effect in the

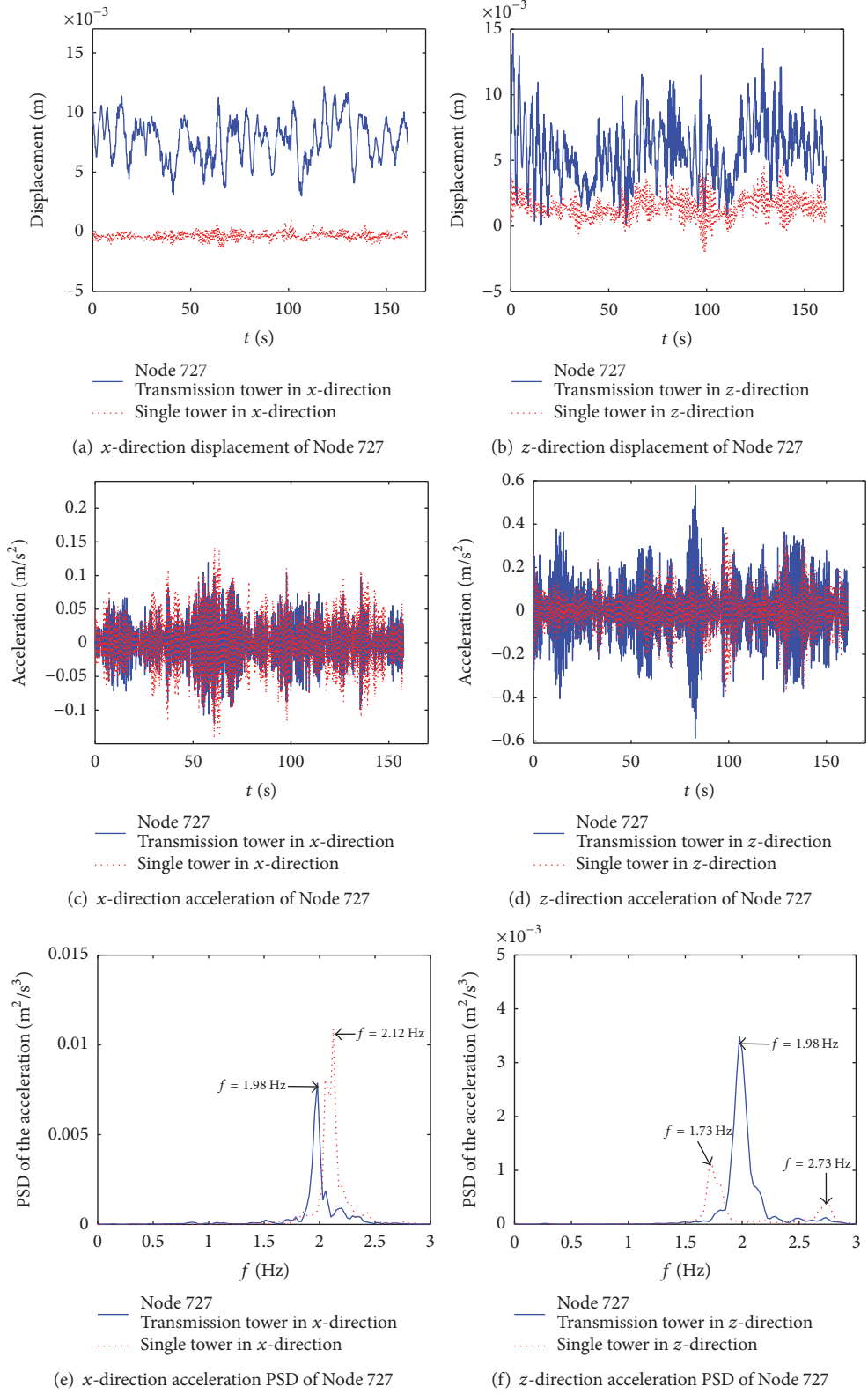


FIGURE 16: Steady-state response of Node 727 of the tower under a wind speed of $U_{10} = 6.03$ m/s.

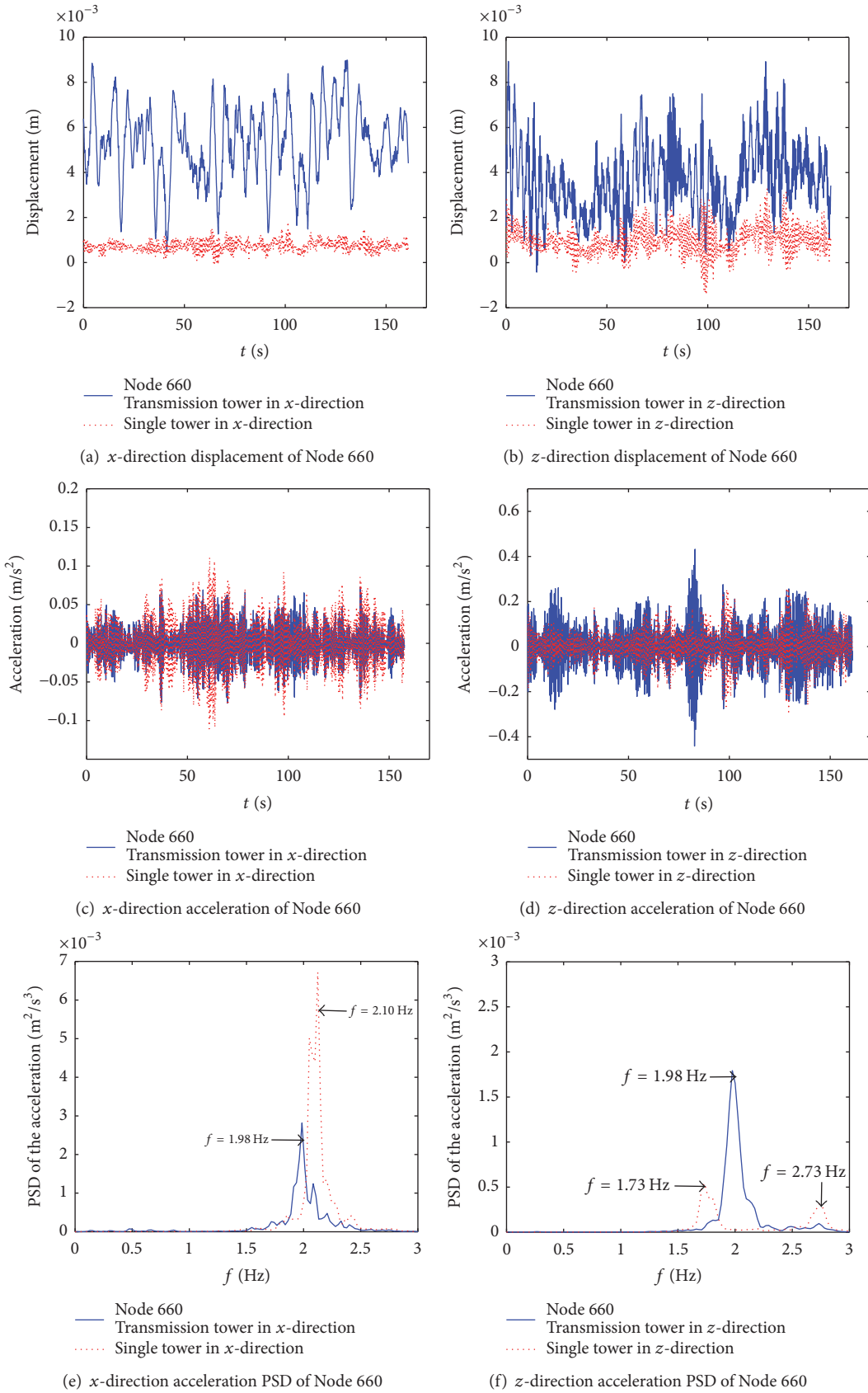


FIGURE 17: Steady-state response of Node 660 of the tower under a wind speed of $U_{10} = 6.03$ m/s.

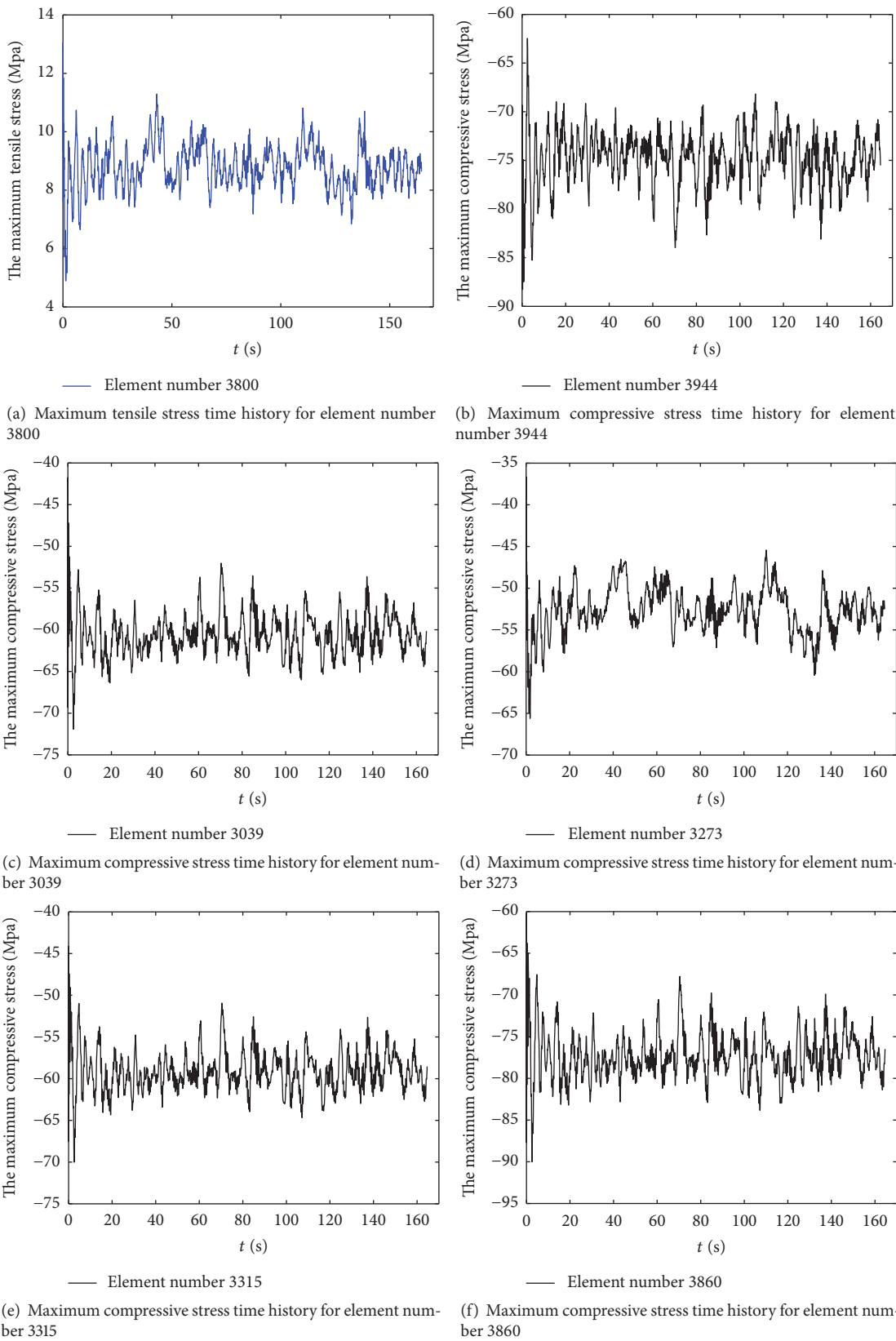


FIGURE 18: Stress time history of the main members of the transmission tower in the tower-line system under a wind speed of $U_{10} = 6.03$ m/s.

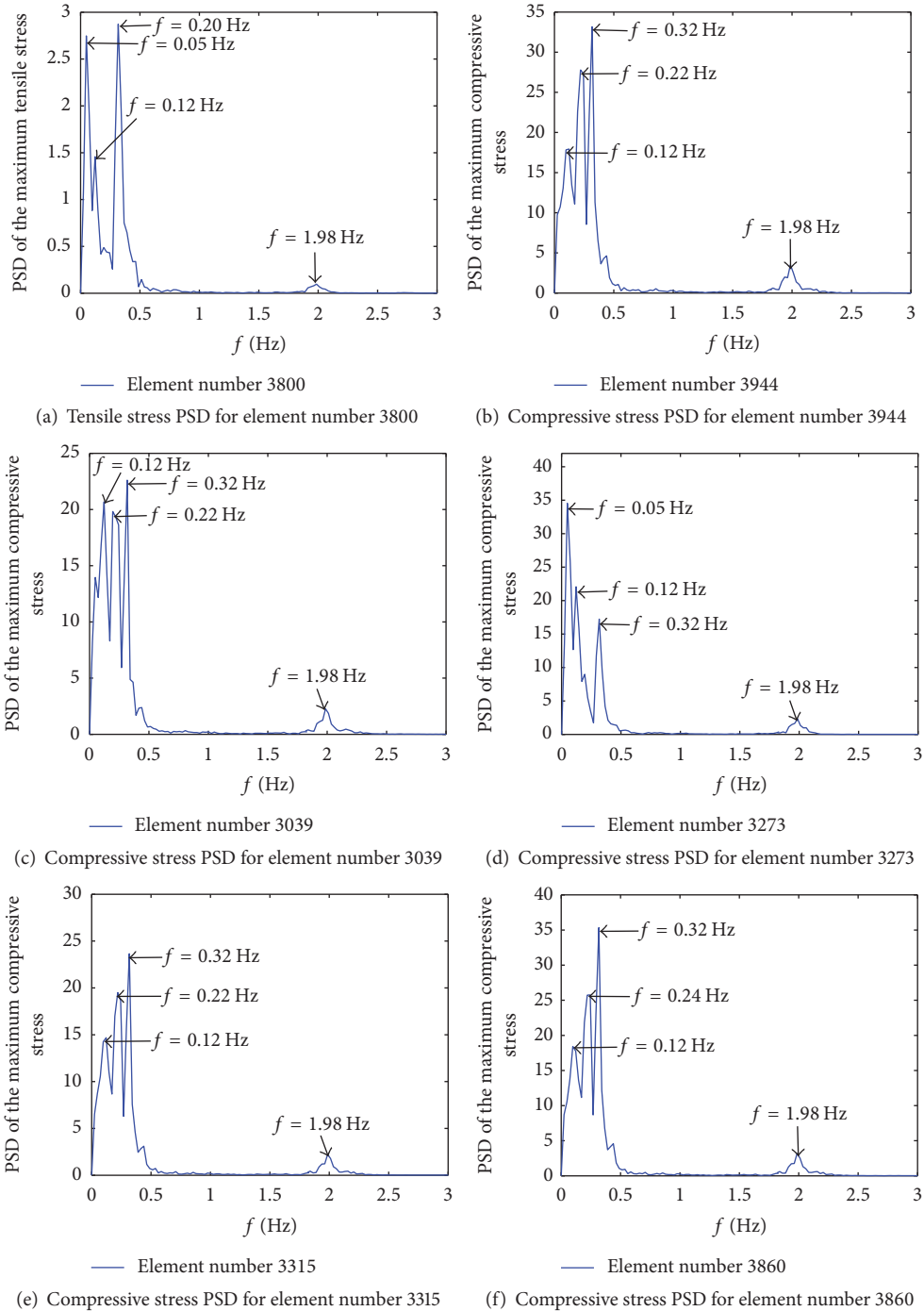


FIGURE 19: The stress PSD of the main members of the transmission tower in the tower-line system under a wind speed of $U_{10} = 6.03$ m/s.

tower-line system, the vibration of the transmission tower is more complicated and stronger in the tower-line system than in the single tower; that is, the coupling effect between the tower and the lines amplifies the vibration effect on the transmission tower. Comparing the frequency spectrum results in Figures 16, 17, 20, and 21, the coupling effect is less obvious under the low wind speed (i.e., $U_{10} = 6.03$ m/s) than that under the strong wind speed (i.e., $U_{10} = 25.3$ m/s). Although the results shown in Figure 19 demonstrate that

the maximum stress of multiple members of the tower in the tower-line system contains significant coupling vibration contributions, the coupling effect is too often neglected due to the small absolute value of the stress. However, under the strong wind speed (i.e., $U_{10} = 25.3$ m/s), the coupling effect on the responses of the tower becomes very prominent, resulting in the potential premature failure of the tower-line system, which indicates that wind speed plays an important role in the tower-line coupling effect.

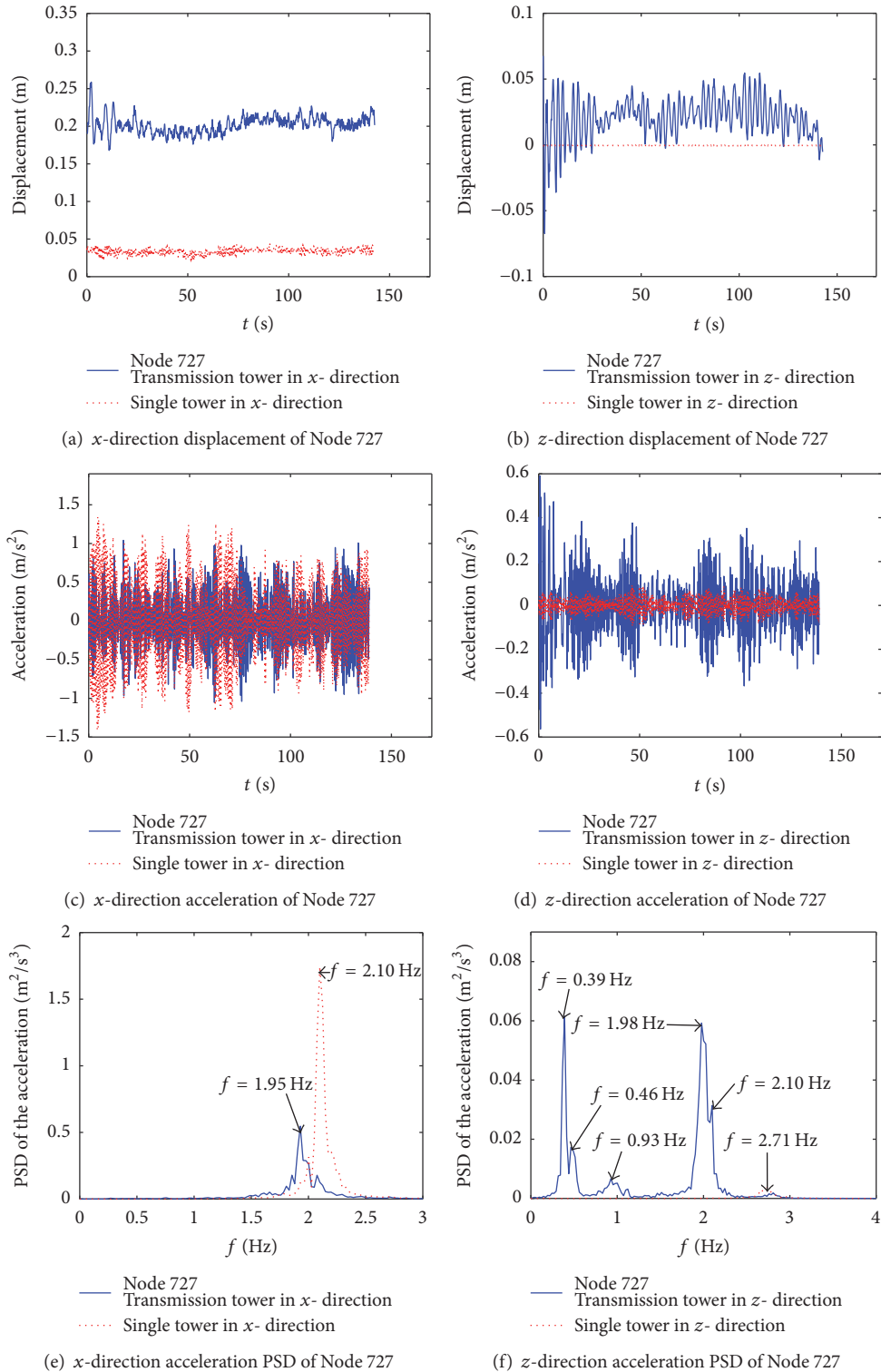


FIGURE 20: Steady-state response of Node 727 of the tower under the design wind speed ($U_{10} = 25.3$ m/s).

5.3. *The Comparative Analysis of the Wind-Induced Vibration Response of the Transmission Tower in the Tower-Line System and the Quasi-Static Response of the Corresponding Single Tower.* At present, in the structural design of transmission tower-line systems, the transmission tower is usually

separated from the transmission lines. In the design of a transmission tower, the quasi-static method is used. In this method, the wind loads sustained by the transmission lines are applied to the transmission tower as the external concentration force. The influence of the wind-induced vibration

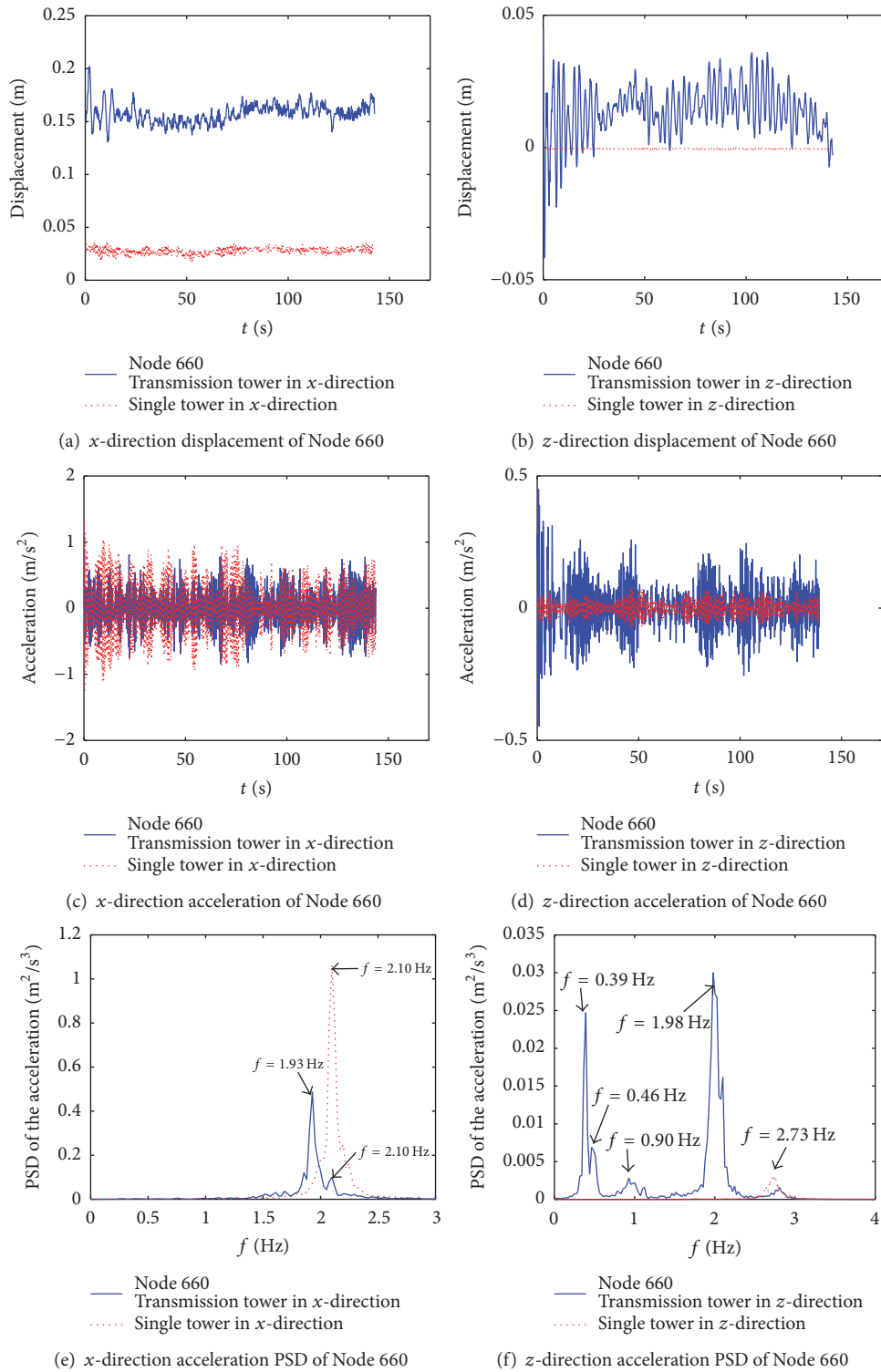


FIGURE 21: Steady-state response of Node 660 of the tower under the design wind speed ($U_{10} = 25.3$ m/s).

of the transmission lines on the dynamic characteristics of the transmission tower is disregarded. To quantitatively analyze the influence of the coupled vibration in the tower-line system on the structural design of the transmission tower,

based on the design method stipulated in China's "Technical Codes for Designing 110 kV–750 kV Overhead Transmission Lines" (GB50545-2010) [39], in this section, the wind loads of different strong wind speeds on the transmission lines are

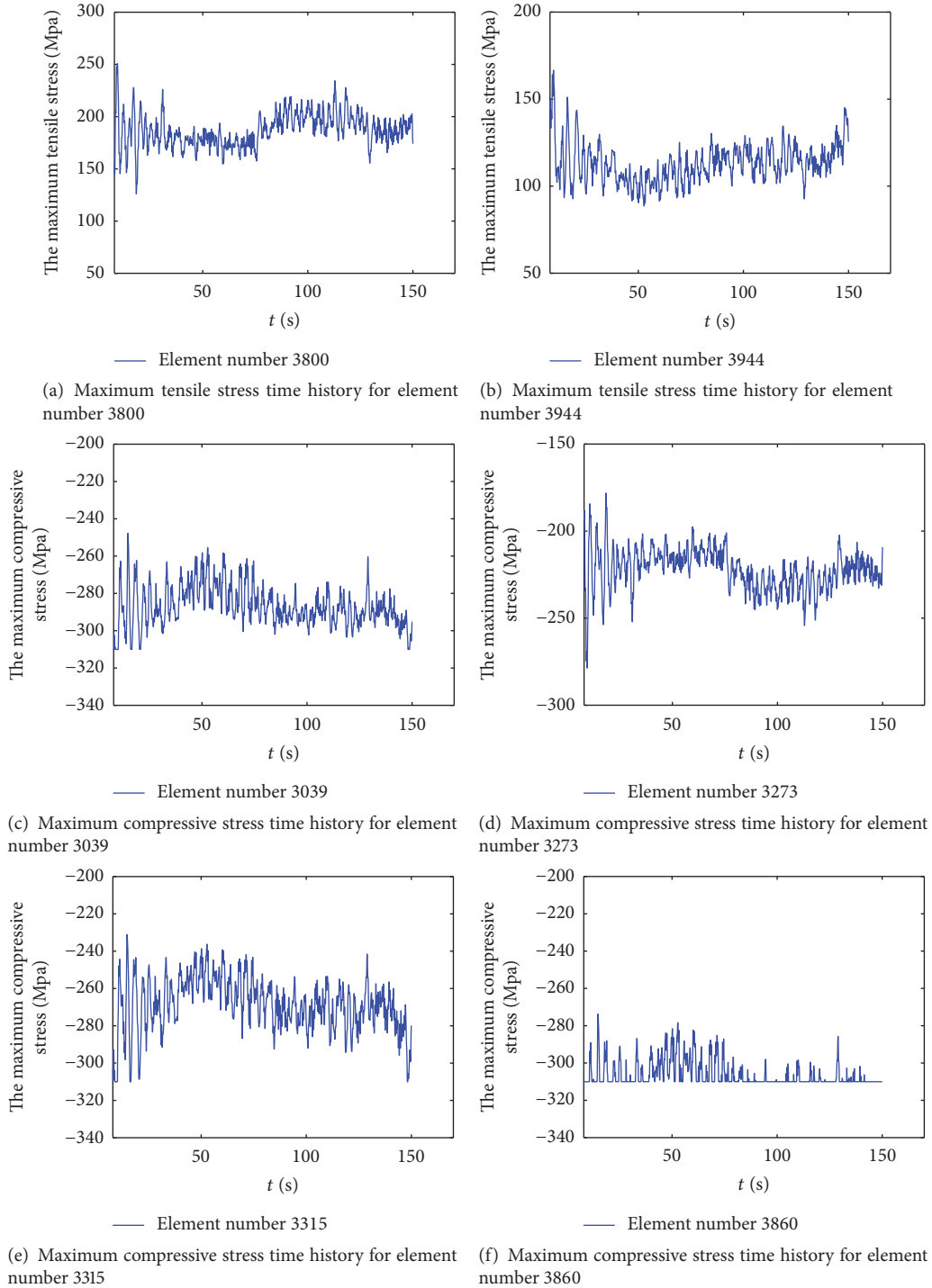


FIGURE 22: Stress time history response of the main members of the transmission tower in the tower-line system under the design wind speed ($U_{10} = 25.3$ m/s).

applied on the hanging locations of the transmission tower as external forces. The wind loads on the transmission tower are again divided into 8 segments, as shown in Figure 10.

The different wind speed conditions in the comparison include the following: average wind speeds at 10 m in height of 14, 16, 17, 18, 19, 20, 21, 22, 23, 24, and 25.3 m/s; to facilitate the identification of wind speed in the following analysis, the

following symbols are used: $U_{10} = 14$ m/s, $U_{10} = 16$ m/s, $U_{10} = 17$ m/s, $U_{10} = 18$ m/s, $U_{10} = 19$ m/s, $U_{10} = 20$ m/s, $U_{10} = 21$ m/s, $U_{10} = 22$ m/s, $U_{10} = 23$ m/s, $U_{10} = 24$ m/s, and $U_{10} = 25.3$ m/s, respectively.

In the actual environment, the directions of the wind loads are more complex, and various angles between the wind and transmission lines exist. Therefore, to understand the

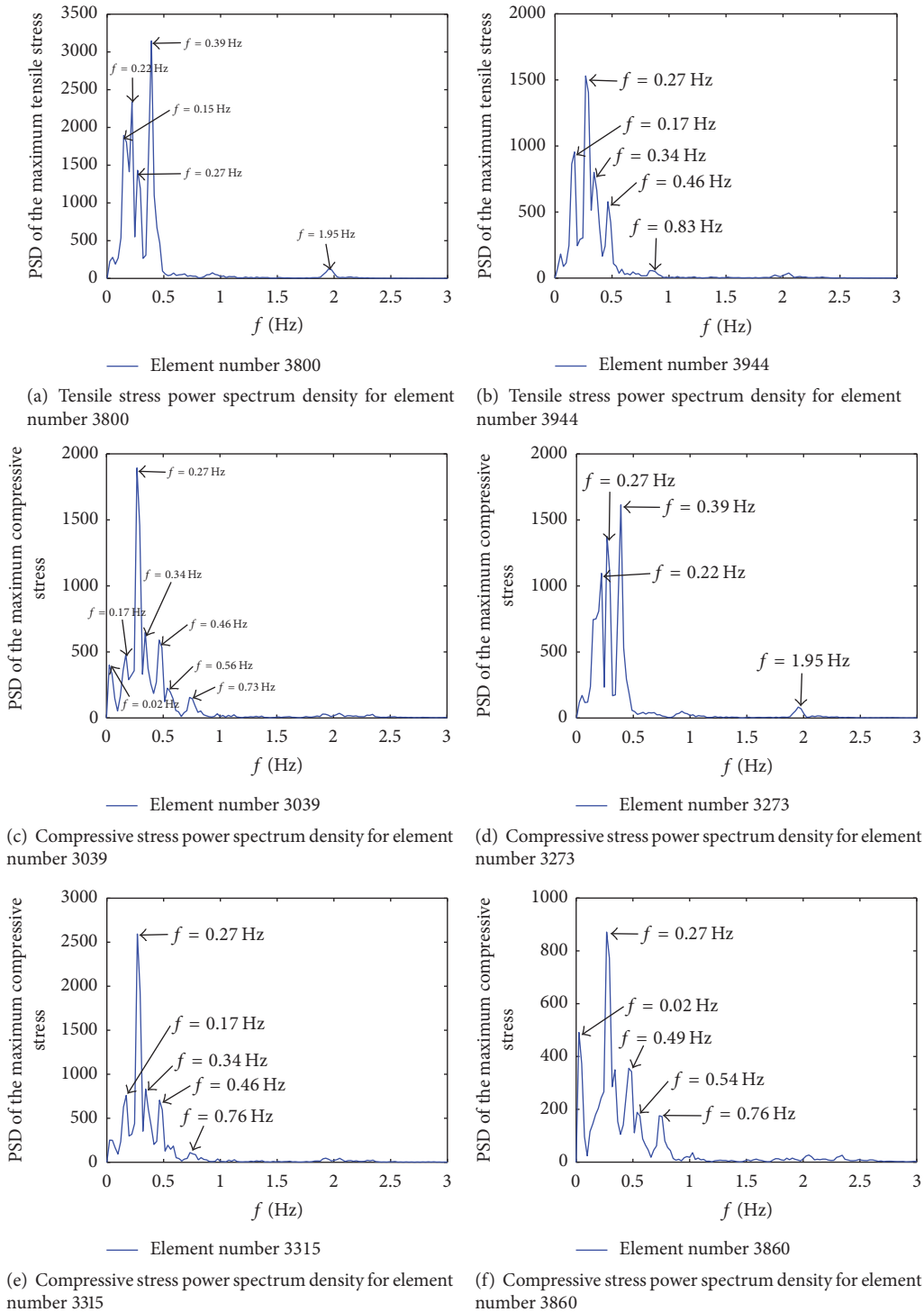


FIGURE 23: The stress PSD of the main members of the transmission tower in the tower-line system under the design wind speed ($U_{10} = 25.3$ m/s).

extent of the influence of the complexity of wind directions, in this section, the wind loads applied perpendicularly to the transmission line (i.e., wind angle of 90 degrees) is first calculated and analyzed, and the results are directly compared

to the dynamic calculation results of the tower-line system discussed previously. Then, wind direction angles of 60, 45, and 0 degrees (i.e., parallel to the transmission line direction) are analyzed and compared.

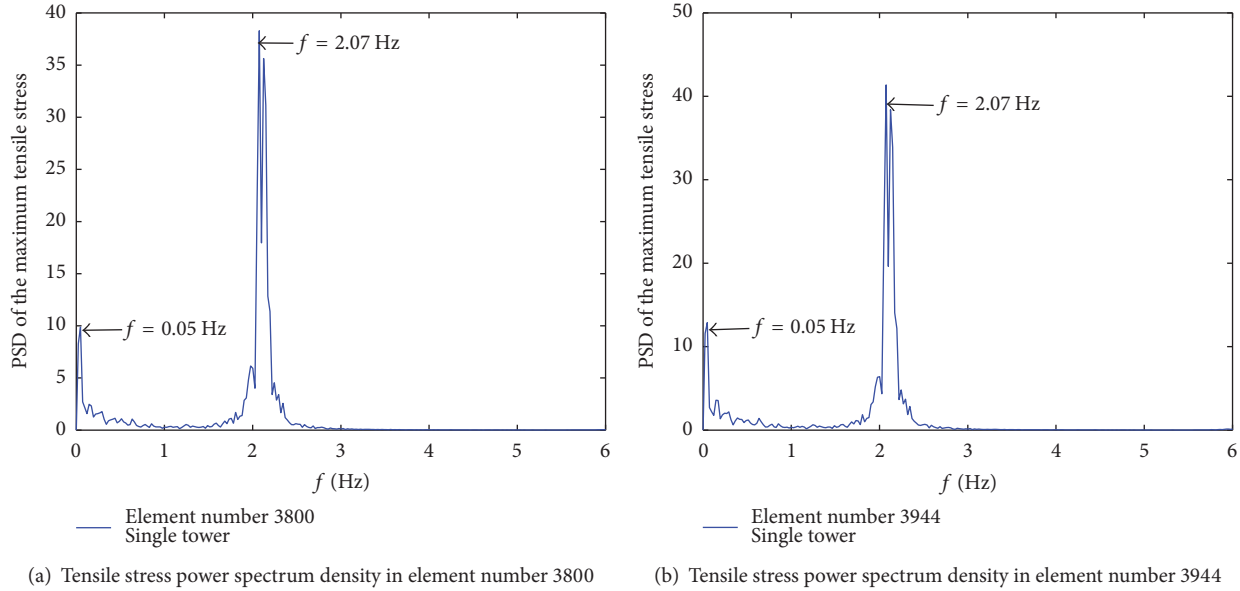


FIGURE 24: Stress PSD of the main members of the corresponding single transmission tower under the design wind speed ($U_{10} = 25.3$ m/s).

TABLE 10: Comparison of the dynamic stress results of the main members of the transmission tower in the tower-line system with the corresponding single tower under a wind speed of $U_{10} = 25.3$ m/s.

Element number	Stress of transmission tower members (MPa)								
	Maximum value			Average			Root mean square		
	TL	ST	TL/ST	TL	ST	TL/ST	TL	ST	TL/ST
3682	-310	-78.6	3.9	-246	-55	4.5	15.1	3.3	4.6
3800	251	30.5	8.2	187	27	6.9	15.7	2.9	5.4
3860	-310	-70.5	4.4	-306	-49	6.2	6.7	3.0	2.2
3944	167	41	4.1	113	10	11.3	11.2	3.2	3.5

Note. In the table, TL represents the response value of the transmission tower in the tower-line system, and ST represents the response value of the corresponding single tower. The minus sign stands for the compressive stress.

5.3.1. Comparison of the Wind-Induced Response of the Transmission Tower in the Tower-Line System and the Quasi-Static Response of the Corresponding Single-Tower under Different Wind Speeds. The results of the dynamic analysis of the tower in the tower-line system are compared with the quasi-static (QS) calculation results for the corresponding single tower under different wind speeds. A comparison of the displacements at the top of the tower is presented in Table 11. A comparison of the stress results of the tower members is provided in Table 12.

Tables 11 and 12 reveal that, under different wind speeds, the displacements at the top of the tower and the stress of tower members provided by the dynamic analysis of the tower-line system are greater than those of the quasi-static method for the corresponding single tower, demonstrating that coupling vibration between the transmission lines and the transmission tower occurs. This coupling effect increases both the lateral displacement of the tower and the axial compressive stress of the tower members. Therefore, the coupling vibration effect on the tower should be considered in the design of high-voltage transmission tower-line systems.

Because engineers are more concerned during the design process with the internal stress of the transmission tower members, to facilitate analysis, the ratio of the member stress of the tower by the dynamic analysis for the tower-line system and by the quasi-static (QS) calculation for the corresponding single-tower is defined as the dynamic amplifying coefficient, δ .

As evident from Table 12, when the wind speed is less than $U_{10} = 18$ m/s, at the tower bottom (0 m) and on the tower (a height of 19.8 m), the tower-line coupling effect increases with the wind speed. When the wind speed is greater than $U_{10} = 18$ m/s, δ decreases as the wind speed increases. When the wind speed reaches $U_{10} = 19$ m/s, the maximum axial compressive stress of the main member on compressive side of the tower bottom (0 m) reaches the design yield strength (310 MPa). When the wind speed reaches the design wind speed $U_{10} = 25.3$ m/s, the maximum compressive stress of more members reaches or exceeds the yield strength (310 MPa). At still higher wind speeds, δ decreases with increasing wind speed, likely because of the redistribution of the stress after the members yield. As the wind speed

TABLE 11: Comparison of the displacements of the tower calculated by dynamic analysis in the tower-line system and the displacement given by the quasi-static calculations for the corresponding single tower.

Wind speed	Node number	Displacement in the x -direction (m)			Displacement in the z -direction (m)		
		TL	QS	TL/QS	TL	QS	TL/QS
$U_{10} = 14$ m/s	727	0.091	0.071	1.28	-0.053	0.001	-53
	660	0.070	0.055	1.27	-0.032	0.0002	-160
$U_{10} = 16$ m/s	727	0.123	0.093	1.32	0.059	0.001	59
	660	0.096	0.072	1.33	0.036	0.0004	90
$U_{10} = 17$ m/s	727	0.145	0.105	1.38	0.080	0.001	80
	660	0.112	0.081	1.38	0.050	0.001	50
$U_{10} = 18$ m/s	727	0.170	0.117	1.45	0.102	0.001	102
	660	0.133	0.091	1.46	-0.062	0.001	-62
$U_{10} = 19$ m/s	727	0.202	0.131	1.54	-0.100	0.001	-100
	660	0.157	0.102	1.54	-0.062	0.001	-62
$U_{10} = 20$ m/s	727	0.192	0.145	1.32	0.116	0.001	116
	660	0.150	0.113	1.33	0.070	0.001	70
$U_{10} = 21$ m/s	727	0.221	0.160	1.38	0.096	0.002	48
	660	0.172	0.124	1.39	0.061	0.001	61
$U_{10} = 22$ m/s	727	0.258	0.175	1.47	-0.211	0.002	-105.5
	660	0.201	0.136	1.48	-0.129	0.001	-129
$U_{10} = 23$ m/s	727	0.286	0.186	1.54	-0.185	0.002	-92.5
	660	0.223	0.144	1.55	-0.116	0.001	-116
$U_{10} = 24$ m/s	727	0.301	0.202	1.49	-0.241	0.002	-120.5
	660	0.235	0.157	1.50	-0.151	0.002	-75.5
$U_{10} = 25.3$ m/s	727	0.426	0.225	1.89	-0.271	0.002	-135.5
	660	0.334	0.175	1.91	-0.168	0.002	-84

Note. In the table, TL represents the dynamic calculation results of the tower in the tower-line system, and QS represents the quasi-static calculation results as stipulated by the design code for the corresponding single tower.

increases, the stress of the main members by the quasi-static analysis continues to increase but remains within the elastic range. However, according to the dynamic time history analysis results, the stress of the corresponding members in tower-line system approaches or has already reached the material yield strength, and thus the range of stress increase is relatively small. Therefore, δ will decrease as the wind speed increases. Moreover, the stress distribution of the tower will result in the yielding of more members, especially the members near the tower bottom (0 m). For these reasons, δ for the tower bottom (0 m) will decrease further compared with that on the upper tower (e.g., height of 19.8 m).

In engineering design, the actual stress of main members plays decisive role. When the wind speed, U_{10} , increases from 14 to 18 m/s, even though the increasing magnitude of the stress of the main members caused by the coupling vibration effect in the tower-line system is pronounced (the corresponding δ value changes from 1.19 to 1.48), Table 12 indicates that the stress remains within the elastic range; that is, the tower remains safe. In such circumstances, even if the design is still based on the quasi-static method in the current design code, the results remain safe. When the wind speed is in the range of $U_{10} = 19$ to 25.3 m/s, the absolute value of the member stress caused by the effects of the tower-line coupling vibration is high (the corresponding δ value is

between 1.39 and 1.06). The stresses of some main members are approaching or have already reached the material yield strength, whereas the absolute stress values calculated by the quasi-static method stipulated in the design code show that the members remain within the elastic range. Therefore, the tower-line coupled vibration effect will cause the stress of the main members in the transmission tower to reach the material yield strength, even if the wind speed is lower than the design wind speed. In such circumstances, the design based on the quasi-static analysis method in the current design code is not safe. In other words, the transmission tower designed in accordance with the existing quasi-static method stipulated in the current design code can only nominally withstand the wind load equivalent to that of the design wind speed (i.e., $U_{10} = 25.3$ m/s), but in practice it can only withstand wind loads that are less than that of the design wind speed (i.e., $U_{10} < 25.3$ m/s).

Because the quasi-static analysis method in the current design codes is relatively simple, it is easy for designers to follow. Therefore, based on the present results, when designing transmission towers, to accommodate the adverse effects of tower-line coupling vibration, the results given by the quasi-static method in design code should simply be multiplied by the corresponding tower-line coupling effect dynamic amplifying coefficient, δ . As indicated in Table 12,

TABLE 12: Comparison of the stress at the top of the tower calculated by dynamic analysis in the tower-line system and by the quasi-static calculation for the corresponding single tower.

Wind speed	Distance from the tower bottom (m)	Element number	Axial compressive stress of the main members of the transmission tower (MPa)		
			TL	QS	$\delta = TL/QS$
$U_{10} = 14 \text{ m/s}$	0	3682	183.19	154.59	1.19
	9	3273	154.57	128.84	1.20
	15	2994	106.71	88.53	1.21
	19.8	2991	152.40	126.47	1.21
	23.4	2882	97.46	78.96	1.23
	25.8	2880	115.32	92.15	1.25
$U_{10} = 16 \text{ m/s}$	0	3682	221.35	179.40	1.23
	9	3273	187.72	150.63	1.25
	15	2994	131.50	104.96	1.25
	19.8	2991	185.81	148.35	1.25
	23.4	2882	121.75	94.06	1.29
	25.8	2880	145.17	109.63	1.32
$U_{10} = 17 \text{ m/s}$	0	3682	259.80	193.05	1.35
	9	3273	222.67	162.63	1.37
	15	2994	157.27	114.00	1.38
	19.8	2991	222.00	160.40	1.38
	23.4	2882	147.30	102.36	1.44
	25.8	2880	177.26	119.25	1.49
$U_{10} = 18 \text{ m/s}$	0	3682	306.27	207.47	1.48
	9	3273	262.84	175.31	1.50
	15	2994	187.08	123.55	1.51
	19.8	2991	262.94	173.13	1.52
	23.4	2882	176.51	111.11	1.59
	25.8	2880	214.15	129.40	1.65
$U_{10} = 19 \text{ m/s}$	0	3682	310.00	222.94	1.39
	9	3273	265.24	188.91	1.40
	15	2994	189.66	133.79	1.42
	19.8	2991	263.83	186.79	1.41
	23.4	2882	175.59	120.47	1.46
	25.8	2880	206.87	140.27	1.47
$U_{10} = 20 \text{ m/s}$	0	3682	310.01	239.17	1.30
	9	3273	276.54	203.18	1.36
	15	2994	197.09	144.52	1.36
	19.8	2991	276.08	201.12	1.37
	23.4	2882	185.27	130.29	1.42
	25.8	2880	225.51	151.67	1.49
$U_{10} = 21 \text{ m/s}$	0	3682	310.02	256.14	1.21
	9	3273	288.76	218.12	1.32
	15	2994	206.41	155.75	1.33
	19.8	2991	288.17	216.12	1.33
	23.4	2882	192.63	140.53	1.37
	25.8	2880	232.08	163.58	1.42

TABLE 12: Continued.

Wind speed	Distance from the tower bottom (m)	Element number	Axial compressive stress of the main members of the transmission tower (MPa)		
			TL	QS	$\delta = \text{TL}/\text{QS}$
$U_{10} = 22 \text{ m/s}$	0	3682	310.12	273.53	1.13
	9	3273	310.05	233.45	1.33
	15	2994	258.15	167.26	1.54
	19.8	2991	310.03	231.52	1.34
	23.4	2882	240.35	150.99	1.59
	25.8	2880	289.32	175.70	1.65
$U_{10} = 23 \text{ m/s}$	0	3682	310.18	286.04	1.08
	9	3273	310.11	244.57	1.27
	15	2994	280.94	175.59	1.60
	19.8	2991	310.07	242.66	1.28
	23.4	2882	265.35	158.47	1.67
	25.8	2880	304.39	184.38	1.65
$U_{10} = 24 \text{ m/s}$	0	3682	310.18	290.20	1.07
	9	3273	310.11	261.25	1.19
	15	2994	281.28	188.10	1.50
	19.8	2991	310.07	259.40	1.20
	23.4	2882	271.52	169.82	1.60
	25.8	2880	307.75	197.60	1.56
$U_{10} = 25.3 \text{ m/s}$	0	3682	311.69	294.05	1.06
	9	3273	310.74	284.45	1.09
	15	2994	310.07	205.48	1.51
	19.8	2991	310.47	282.72	1.10
	23.4	2882	310.00	185.53	1.67
	25.8	2880	304.34	215.91	1.41

Note. In the table, TL represents the dynamic calculation results for the tower in the tower-line system, and QS represents the quasi-static calculation results as stipulated by the design code for the corresponding single tower.

for example, under the designing wind speed ($U_{10} = 25.3 \text{ m/s}$), from the bottom to the top of the tower, the δ value is 1.06, 1.09, 1.51, 1.10, 1.67, and 1.41, corresponding to the tower members at heights of 0, 9, 15, 19.8, 23.4, and 25.8 m, respectively. Because the absolute stress value of the members near the tower bottom is large, it is the controlling stress of the design. Therefore, to meet these requirements, the quasi-static analysis result of the whole tower must be multiplied by the tower-line coupling effect dynamic amplifying coefficient, δ (e.g., $\delta \geq 1.06$), at the bottom of the tower.

5.3.2. Comparison of the Wind-Induced Response of the Transmission Tower in the Tower-Line System and the Quasi-Static Response of the Corresponding Single Tower under Different Wind Directions. In the actual environment, different angles exist between the directions of the transmission lines and the wind. To analyze the influence of these different wind directions on the stress of the main members of the tower, in this section, based on two engineering cases where the wind speed, U_{10} , is 20 m/s and 25.3 m/s, the axial compressive stresses of the main members (see Table 12) are calculated

using the dynamic analysis of the tower-line system under different wind direction angles (i.e., 90, 60, 45, and 0 degrees). The results are shown in Figure 25. As the wind direction angle increases, the axial compressive stress of the main members of the tower also increases. Therefore, the 90-degree wind angle creates the most adverse effects.

Because the members near the tower bottom (see Table 12) are usually dominant in design, the changes of the tower-line coupling effect dynamic amplifying coefficient, δ , under different wind directions (i.e., 90, 60, and 45) are also shown in Figure 26. As the wind direction angle decreases, δ also decreases, thus indicating that the amplifying effect of the tower-line coupling vibration is weakened. Overall, as the wind speed increases, the δ value curve develops, following a folding line-like pattern. However, at the design wind speed $U_{10} = 25.3 \text{ m/s}$, the δ values corresponding to the three wind directions are approximately equal, indicating that the tower-line coupling effect dynamic amplifying coefficient, δ , is more sensitive to wind speed changes. Therefore, the actual engineering design can be safely completed assuming a wind direction angle of 90 degrees.

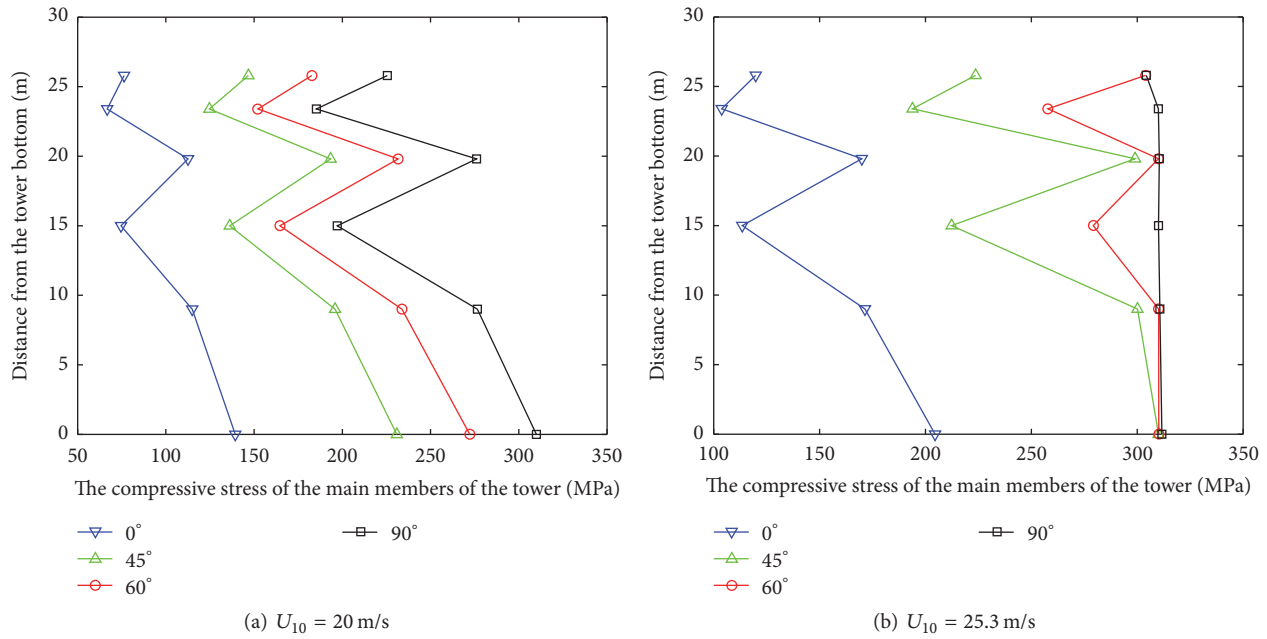


FIGURE 25: Comparison of the axial compressive stress of the main members of the tower in the tower-line system calculated using dynamic analysis under different wind directions.

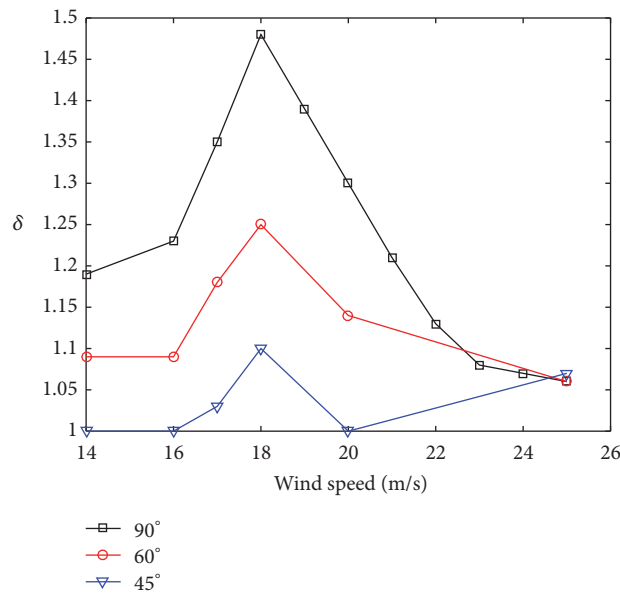


FIGURE 26: Comparison of the δ results of the members near the tower bottom under different wind speeds and wind directions.

6. Conclusions

In this study, a finite element model for transmission tower-line systems is established based on actual high-voltage transmission lines in East China. The wind-induced vibration responses of the tower-line system are analyzed using the established finite element model, and the accuracy of the finite element model is verified by comparing the results with field measurements. Based on the wind speed and wind pressure conversion theory and the modified *Davenport* spectrum, the wind load time history is simulated. The

dynamic responses of the transmission tower in the tower-line system under different wind speeds and directions are analyzed, and the results are compared with those calculated using the quasi-static method stipulated in China's "Technical Codes for Designing 110 kV–750 kV Overhead Transmission Lines" (GB50545-2010) for the corresponding single tower. The following are the main conclusions drawn from this study:

- (1) The coupling effect between the transmission lines and the transmission tower is an intrinsic property

of the tower-line system. When the transmission tower-line vibrates freely as a whole system, the fundamental natural frequency of the tower is much less than that of the corresponding single tower in the corresponding direction, and the overall vibrations of the tower and the lines are characterized by low frequencies and dense modes.

- (2) Wind speed plays an important role in the tower-line coupling effect. The wind-induced vibration of the transmission tower in the tower-line system is more complicated than that in the single tower because of the coupling effect. Under the low wind speed, the coupling effect is less obvious and can be neglected. However, under the strong wind speed (i.e., the average wind speed at a height of 10 m is greater than 10.8 m/s, corresponding to a Beaufort number greater than 6), the coupling effect on the responses of the tower gradually becomes prominent, possibly resulting in the risk of premature failure of the tower-line system.
- (3) Under the same design wind speed, the stress of the main members of the tower in the tower-line system increases more than that of the single tower. The maximum stress of the multiple members approaches or reaches the design yield strength of the steel. However, in the corresponding single tower, the stress of the members is much less than the design yield strength of the steel, and the tower remains safe. Under the same design wind speed, the member stress increase in the tower-line system is mainly caused by the vibration of the transmission lines due to the coupling effect, whereas the stress increase in the single tower is mainly caused by its self-vibration.
- (4) Under a 90-degree wind of varying speeds, the displacement of the tower top and the stress of the main members are greater than the results of the quasi-static analysis for the corresponding single tower, demonstrating that the amplifying effect of dynamic coupling on the response of the transmission tower cannot be neglected in the tower-line system. The member stress in the tower decreases as the wind direction angle decreases, thus indicating that the wind direction angle of 90 degrees (perpendicular to the direction of the transmission lines) is the most adverse wind direction.
- (5) The designs based on the quasi-static method stipulated in the current design code are unsafe because of the ignorance of the adverse impacts of coupling vibration on the transmission towers. In practical engineering, when the quasi-static method in the specifications is still used, the internal forces of the tower members given by the quasi-static analysis under the design wind speed can simply be multiplied by the tower-line coupling effect dynamic amplifying coefficient, δ , to approximate the adverse effects of the tower-line coupling on the transmission tower. For instance, the recommended value of δ is ≥ 1.06 based

on the design parameters of the tower-line system presented in this paper. Accordingly, the cross-section of the tower members should be designed based on the internal stress adjusted by using the amplifying coefficient to ensure the safety of the tower.

Conflicts of Interest

The authors declare that there are no conflicts of interest regarding the publication of this paper.

Acknowledgments

This research has been funded by the National Natural Science Foundation of China (Grants nos. 51578512 and 51108425) and Outstanding Young Talent Research Fund of Zhengzhou University (Grant no. 1521322004).

References

- [1] R. C. Battista, R. S. Rodrigues, and M. S. Pfeil, "Dynamic behavior and stability of transmission line towers under wind forces," *Journal of Wind Engineering & Industrial Aerodynamics*, vol. 91, no. 8, pp. 1051–1067, 2003.
- [2] Q. Xie and J. Li, "Current situation of natural disaster in electric power system and countermeasures," *Journal of Natural Disasters*, vol. 15, no. 4, pp. 126–131, 2006.
- [3] G. F. Zhao, *Research on Wind Induced Nonlinear Vibration of High Voltage Transmission Tower-Line Coupling System*, Tongji University, Shanghai, China, 2009.
- [4] A. Hamada and A. A. El Damatty, "Behaviour of guyed transmission line structures under tornado wind loading," *Computers & Structures*, vol. 89, no. 11-12, pp. 986–1003, 2011.
- [5] J. E. Mills, X. Ma, and Y. Zhuge, "Experimental study on multi-panel retrofitted steel transmission towers," *Journal of Constructional Steel Research*, vol. 78, pp. 58–67, 2012.
- [6] Z. Yan, J. E. Mills, and X. Ma, "Modeling of steel lattice tower angle legs reinforced for increased load capacity," *Engineering Structures*, vol. 43, no. 10, pp. 160–168, 2012.
- [7] C. Lu, X. Ma, and J. E. Mills, "The structural effect of bolted splices on retrofitted transmission tower angle members," *Journal of Constructional Steel Research*, vol. 95, pp. 263–278, 2014.
- [8] C. Lu, X. Ma, and J. E. Mills, "Modeling of retrofitted steel transmission towers," *Journal of Constructional Steel Research*, vol. 112, pp. 138–154, 2015.
- [9] H. Aboshosha, A. Elawady, A. El Ansary, and A. El Damatty, "Review on dynamic and quasi-static buffeting response of transmission lines under synoptic and non-synoptic winds," *Engineering Structures*, vol. 112, pp. 23–46, 2016.
- [10] T. P. Boudreaux, "Hurricane Carla vs. Transmission Lines," *Civil Engineering & Construction Review*, pp. 70–72, 1962.
- [11] H. S. Saffir, "Hurricane Hugo and Implications for Design Professionals and Code-Writing Authorities," *Journal of Coastal Research*, vol. 8, pp. 25–32, 1991.
- [12] <http://news.sina.com.cn/c/2009-11-17/152816622701s.shtml>.
- [13] K. R. Cooper, "Wind tunnel and theoretical investigations into the aerodynamic stability of smooth and stranded twin-bundled power conductors," Tech. Rep., National Research Council of Canada, 1973.

- [14] A. M. Loredou-Souza and A. G. Davenport, "Wind tunnel aeroelastic studies on the behaviour of two parallel cables," *Journal of Wind Engineering & Industrial Aerodynamics*, vol. 90, no. 4-5, pp. 407-414, 2002.
- [15] H. Z. Deng, S. Y. Zhu, X. M. Chen, and Z. M. Wang, "Wind tunnel investigation on model of long span transmission line system," *Journal of Tongji University (natural science)*, vol. 31, no. 2, pp. 132-137, 2003.
- [16] Y. Guo, B. N. Sun, Y. Ye, G. H. Shen, and W. J. Lou, "Wind tunnel test on aeroelastic model of long span transmission line system," *Journal of Zhejiang University (Engineering Science)*, vol. 41, no. 9, pp. 1482-1486, 2007 (Chinese).
- [17] F. Cluni, V. Gusella, and G. Bartoli, "Wind tunnel scale model testing of suspended cables and numerical comparison," *Journal of Wind Engineering & Industrial Aerodynamics*, vol. 96, no. 6-7, pp. 1134-1140, 2008.
- [18] Z.-P. Liang and Z.-L. Li, "An aeroelastic model design of ultra-high voltage power transmission line systems," *Chongqing Daxue Xuebao/Journal of Chongqing University*, vol. 32, no. 2, pp. 131-136, 2009.
- [19] G. Zhao, Q. Xie, S. Liang, and J. Li, "Wind tunnel test on wind-induced response of transmission tower and tower line coupling system," *Jianzhu Jiegou Xuebao/Journal of Building Structures*, vol. 31, no. 2, pp. 69-77, 2010.
- [20] M. Takeuchi, J. Maeda, and N. Ishida, "Aerodynamic damping properties of two transmission towers estimated by combining several identification methods," *Journal of Wind Engineering & Industrial Aerodynamics*, vol. 98, no. 12, pp. 872-880, 2010.
- [21] Q. Xie, C.-Y. Yan, and Y. Zhang, "Experiment and analysis on wind-induced dynamic tension of ice covered UHV conductors," *Gaodianya Jishu/High Voltage Engineering*, vol. 36, no. 8, pp. 1865-1870, 2010.
- [22] Y. M. Desai, P. Yu, N. Popplewell, and A. H. Shah, "Finite element modelling of transmission line galloping," *Computers & Structures*, vol. 57, no. 3, pp. 407-420, 1995.
- [23] G. H. Shen, G. H. Yuan, B. N. Sun, and W. J. Lou, "Dynamic impact effects on tower-line system due to Ice-shedding," *Engineering Mechanics*, vol. 27, no. 5, pp. 210-217, 2010.
- [24] Y. Zhang, C. Yan, and Q. Xie, "Wind tunnel test on wind-induced dynamic responses of icing ultra high voltage transmission tower-line coupling system," *Zhongguo Dianji Gongcheng Xuebao/Proceedings of the Chinese Society of Electrical Engineering*, vol. 30, no. 28, pp. 94-99, 2010.
- [25] F. Yang, J. Yang, and Z. Zhang, "Unbalanced tension analysis for UHV transmission towers in heavy icing areas," *Cold Regions Science and Technology*, vol. 70, pp. 132-140, 2012.
- [26] L. Zhou, B. Yan, L. Zhang, and S. Zhou, "Study on galloping behavior of iced eight bundle conductor transmission lines," *Journal of Sound and Vibration*, vol. 362, pp. 85-110, 2016.
- [27] M. J. He and B. F. Yang, "Site Vibration Experiment of Jiang Yin 500 kV Guyed Transmission Tower," *Structural Engineers*, no. 4, pp. 74-79, 2003.
- [28] M. J. He, X. M. Yan, and Y. G. Zhang, "Synchronous test study of two adjacent transmission tower undergoing ambient excitation," *Journal of Vibration and Shock*, vol. 28, no. 11, pp. 155-158, 2009 (Chinese).
- [29] Y. Momomura, H. Marukawa, T. Okamura, E. Hongo, and T. Ohkuma, "Full-scale measurements of wind-induced vibration of a transmission line system in a mountainous area," *Journal of Wind Engineering & Industrial Aerodynamics*, vol. 72, no. 1-3, pp. 241-252, 1997.
- [30] H. Yasui, H. Marukawa, Y. Momomura, and T. Ohkuma, "Analytical study on wind-induced vibration of power transmission towers," *Journal of Wind Engineering & Industrial Aerodynamics*, vol. 83, pp. 431-441, 1999.
- [31] M. Matsumoto, H. Shirato, T. Yagi, M. Goto, S. Sakai, and J. Ohya, "Field observation of the full-scale wind-induced cable vibration," *Journal of Wind Engineering & Industrial Aerodynamics*, vol. 91, no. 1-2, pp. 13-26, 2003.
- [32] J. Li, Q. Yan, Q. Xie, and J. Chen, "Wind field measurements and wind-induced vibration responses of transmission tower during typhoon wipha," *Journal of Architecture & Civil Engineering*, vol. 26, no. 2, pp. 1-8, 2009.
- [33] F. G. A. Al-Bermani and S. Kitipornchai, "Nonlinear analysis of transmission towers," *Engineering Structures*, vol. 14, no. 3, pp. 139-151, 1992.
- [34] F. Gani and F. Légeron, "Dynamic response of transmission lines guyed towers under wind loading," *Canadian Journal of Civil Engineering*, vol. 37, no. 3, pp. 450-464, 2010.
- [35] G. McClure and M. Lapointe, "Modeling the structural dynamic response of overhead transmission lines," *Computers & Structures*, vol. 81, no. 8-11, pp. 825-834, 2003.
- [36] N. Prasad Rao and V. Kalyanaraman, "Non-linear behaviour of lattice panel of angle towers," *Journal of Constructional Steel Research*, vol. 57, no. 12, pp. 1337-1357, 2001.
- [37] C. Klinger, M. Mehdianpour, D. Klingbeil, D. Bettge, R. Häcker, and W. Baer, "Failure analysis on collapsed towers of overhead electrical lines in the region Münsterland (Germany) 2005," *Engineering Failure Analysis*, vol. 18, no. 7, pp. 1873-1883, 2011.
- [38] H. J. Dagher and Q. Lu, "System reliability analysis of transmission lines," *Engineering Structures*, vol. 15, no. 4, pp. 251-258, 1993.
- [39] GB50545, *Technical Codes for Designing 110 kV-750 kV Overhead Transmission Lines*, National Standard of P.R. China, Planning Press, Beijing, China, 2010.
- [40] L. L. Zhang, *Research on Wind Stochastic Field and Analysis of Dynamic Reliability for High-Rise Building with Wind Loading*, Tongji University, Shanghai, China, 2006.
- [41] Q. G. Fei, Y. L. Xu, C. L. Ng, K. Y. Wong, W. Y. Chan, and K. L. Man, "Structural health monitoring oriented finite element model of Tsing Ma bridge tower," *International Journal of Structural Stability & Dynamics*, vol. 7, no. 4, pp. 647-668, 2007.
- [42] C. Dyrbye and S. O. Hansen, *Wind Loads on Structures*, John Wiley & Sons, 1996.
- [43] E. Simiu and R. H. Scanlan, *Wind Effects on Structures*, John Wiley & Sons, 1986.
- [44] GB50012, *Load Code for the Design of Building Structures*, National Standard of P.R. China, Architecture & Building Press, Beijing, China, 2012.

Research Article

Study on Vibration Reduction Method for a Subway Station in Soft Ground

Xian-Feng Ma,^{1,2} Ning-Ning Feng,¹ Guo-Bo Wang,³ and Xu Fang¹

¹Department of Geotechnical Engineering, Tongji University, Shanghai 200092, China

²Key Laboratory of Geotechnical and Underground Engineering of Ministry of Education, Tongji University, Shanghai 200092, China

³Hubei Key Laboratory of Roadway Bridge & Structure Engineering, Wuhan University of Technology, Wuhan 430070, China

Correspondence should be addressed to Guo-Bo Wang; wgb16790604@126.com

Received 28 July 2017; Accepted 23 October 2017; Published 14 November 2017

Academic Editor: Xing Ma

Copyright © 2017 Xian-Feng Ma et al. This is an open access article distributed under the Creative Commons Attribution License, which permits unrestricted use, distribution, and reproduction in any medium, provided the original work is properly cited.

With the rapid development of metro system in urban areas, vibration and its impact on adjacent structures caused by metro operation have drawn much attention of researches and worries relating to it have risen. This paper analyzed the vibration attenuation and the environment impact by a case study of a subway station in soft ground with adjacent laboratory building. A method of setting a compound separation barrier surrounding the station is checked and different materials used in the barrier have been tried and tested through numerical analysis. Key parameters of the material and the effects of vibration reduction are studied with the purpose that similar methodology and findings can be referenced in future practices.

1. Introduction

In the operation of large-scale metro system in modern cities around the world, vibration caused by running trains of metro system and its impact on environment have become increasingly problematic, especially in big cities with densely built structures and overcrowded population in both developed countries and emerging economies. Attentions of scholars in many countries have been drawn on this issue and vibration separation and reduction measures to tackle the subway vibration impact have been studied, among which barriers are usually assumed to be one of the effective ways.

Since 1960s, scholars including Barkan et al. [1–9] carried out researches on vibration isolation by barriers and proposed preliminary strategies relating to it. Qiu et al. [10] have also conducted relevant researches since 1998 in terms of efficiencies and environmental impacts of vibration barrier. Notwithstanding the above efforts, vibration barrier theory and some findings remain conditionally applicable, partly due to the complexity of the boundary value problems on site. Nowadays, researches on vibration isolation by barriers have been mainly based on numerical methods such as finite

element method and boundary element method, as well as indoor model tests or in situ tests. Useful findings have been obtained and some results have also been proposed on vibration isolation using barrier, but many of them still fall short of application on site due to insufficient calculation conditions or incomplete test cases on many occasions. On the other hand, in most of these researches, single material was employed in vibration isolation, while there are very few researches on the effect of using compound material in vibration isolation though there would be enough chances for compound material to be beneficial both technically and economically in vibration separation and reduction.

In this paper, a case study on vibration reduction methodology for a subway station in Shanghai is reported, aiming to answer the need of reducing the vibration impact on a physics laboratory building in close proximity to the station. The method includes a vibration separation trench surrounding the station structure and isolation materials that would be filled into the trench. The effects of different isolation materials were checked using numerical analysis and the results helped to guide the practice of vibration reduction for subway stations in Shanghai soft ground.

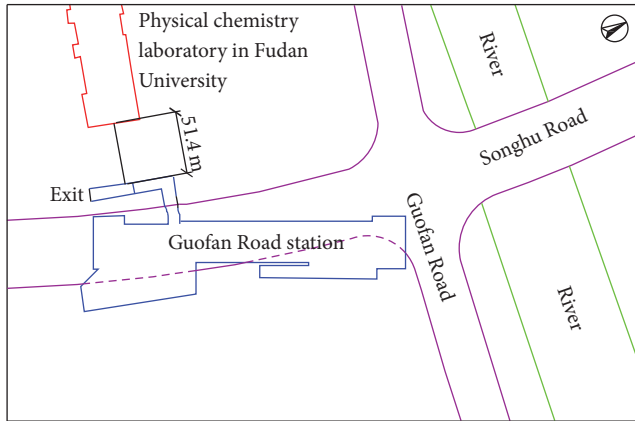


FIGURE 1: Layout of Guofan Road station and the adjacent building.

2. Subway Station Studied in This Paper

The station studied in this paper is Guofan Road subway station, which is under construction in phase two project of Shanghai Metro Line number 10. Due to the restrictions of the planning and site selection, Guofan Road station is set to be located at Songhu Road, and the west side is adjacent to New Jiangwan Campus of Fudan University, as shown in Figure 1. Inside the New Jiangwan Campus, there is a State Key Physical Chemistry Laboratory which is about 50 m away from the subway station. With consideration of strict vibration requirements for the surrounding environment needed for laboratory operation, measures have to be taken to ensure that there will be no adverse effect on daily operation of the laboratory after the station would be put into service. So the main issue is how to separate and reduce the vibration caused by the metro operation in the station.

3. Numerical Study on Vibration Separation Scheme

3.1. Comparison and Selection of Vibration Reduction Materials. After preliminary studies, it is decided to build a trench filled with soft materials surrounding the subway station wall to separate the vibration for the laboratory. Investigation on applicable materials that can be used in vibration reduction shows the following list: sand cushion, soil sandbag, STC reinforced sand, foam polyurethane, polymer, and foam concrete. Taking durability and cost aspect into consideration as well as the effect of reducing vibration, foam concrete and yellow sand were selected as the filling materials used in the trench separating Guofan Road station from surrounding ground. Several combinations of the two materials were studied in this research to achieve the required vibration reduction effect, while the cost could be controlled at the same time.

3.2. Barrier Filling Scheme for the Trench Surrounding the Station. In order to work out a reasonable filling scheme for the barrier to reduce and separate the vibration from the Guofan Road station, three alternatives were proposed for further

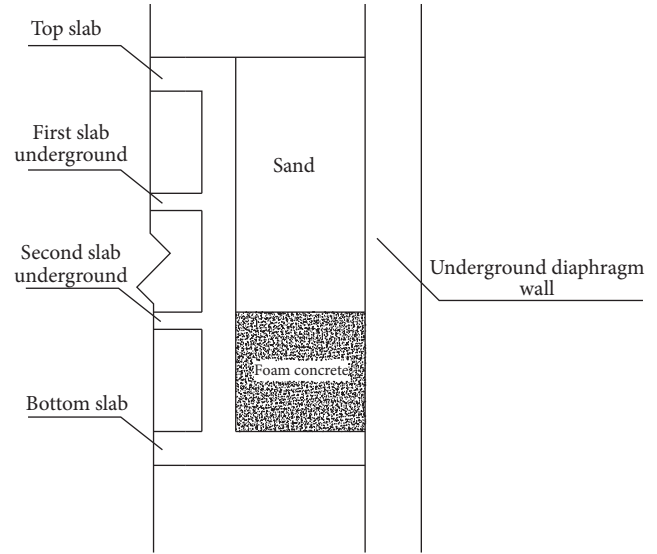


FIGURE 2: Sketch map of Scheme 1.

study, and selection was made based on comparison among them considering the feasibility of construction, economic aspect, and the effect of vibration isolation and reduction. The following part describes the three filling schemes for vibration reduction materials.

(1) *Scheme 1.* The space in trench between the side wall of the station structure and the diaphragm retaining wall will be filled by foam concrete at the depth of the third level of the station structure, and the rest space in the trench will be filled with sand, as shown in Figure 2.

(2) *Scheme 2.* The space in the trench at the depth of the second and third levels will be filled with foam concrete and the rest is filled with sand.

(3) *Scheme 3.* The space between the station structure's external walls and the diaphragm wall are all filled with sand.

During the process of numerical simulation, in order to acquire a better comparison among potential measures, some other schemes were added for further analysis. The added schemes include the following alternatives: all of the trench filled with foam concrete (Scheme 4); all trench filled with normal concrete (Scheme 5); and an open-air trench without any filling material (Scheme 6). Considering that the range of elasticity modulus of foam concrete is within 40 Mpa~1200 Mpa [11–13], the elasticity modulus is taken as parameters together with Poisson ration and the damping ration of foam concrete, for the purpose of carrying out parametric study to find out the more effective case. Each group of the parameters makes up one calculation case and thus there are six calculation cases altogether, and each of them includes six schemes of filling barrier material described above. So comparison between cases will help to decide which kind of foam concrete is more effective, while comparison between

TABLE 1: Calculation cases.

Cases	1	2	3	4	5	6
Parameters of foam concrete						
E (Mpa)	40	40	40	40	40	1000
c	0.05	0.5	0.95	0.05	0.05	0.05
ν	0.21	0.21	0.21	0.31	0.48	0.21

each scheme of a specific case is useful to decide which scheme is more effective and economical at the same time. Table 1 shows parameters in calculation cases.

3.3. Numerical Calculation Parameters. The excavation depth of the Guofan Road station is about 23.32 m with the width of about 21.5 m and the length of about 156.5 m. The thickness of the underground diaphragm wall is 1 m and its depth is 41.5 m. The soil layers encountered during the excavation of the station are as follows: layer ①1, layer ②1, layer ③, layer ④, and layer ⑤1, whose names are officially designated according to the sequence they are encountered from the surface to a deeper layer. Ground at the bottom level of the station is in the ⑤2 layer. According to the ground investigation report and the shear wave velocity of Shanghai soil layer in Table 3, the physical and mechanical parameters of soil layer in Shanghai can be obtained taking into consideration (1), as is shown in Table 2. The physical and mechanical parameters of C30 concrete which is used in the subway station, as well as the parameters of foam concrete, can be referred to Qiu-Huan et al.'s paper [14]. The parameters of medium sand refer to the literature [15, 16]. The constitutive relationship of soil, foam concrete, and medium sand is adopted as Mohr-Coulomb model, and the parameters are given in Table 3.

$$\begin{aligned}
 \lambda &= \frac{\nu E}{(1 + \nu)(1 - 2\nu)}, \\
 \mu = G &= \frac{E}{2(1 + \nu)}, \\
 E &= \frac{\nu(3\lambda + 2\mu)}{\lambda + \mu}, \\
 \nu &= \frac{\lambda}{2(\lambda + \mu)}, \\
 C_P &= \sqrt{\frac{\lambda + 2\mu}{\rho}}, \\
 C_S &= \sqrt{\frac{\mu}{\rho}} = \sqrt{\frac{E}{2(1 + \nu)\rho}}.
 \end{aligned} \tag{1}$$

It is well known that, in analyzing dynamic problems, in order to eliminate the adverse effect of the reflection of the vibration wave on the boundary, the artificial boundary condition should be set at the boundary. The boundary conditions for this numerical calculation are viscous-spring artificial boundaries, which can be referred to Gu et al.'s [17].

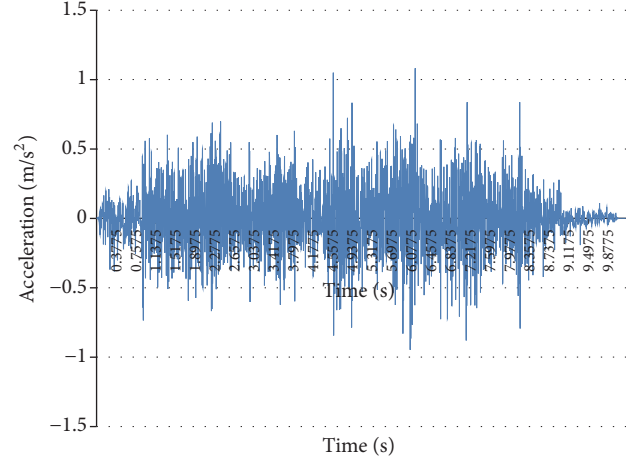


FIGURE 3: Acceleration time histogram.

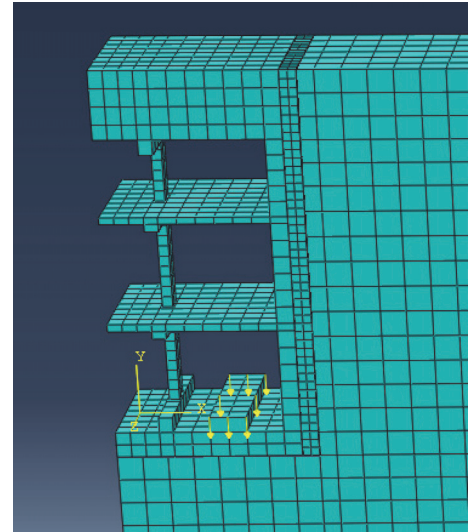


FIGURE 4: Details of station and location of acceleration.

3.4. Three-Dimensional Model, Applied Excitation, and Monitoring Nodes. The commercial software ABAQUS is used in this numerical calculation. Considering that the subway vibration is very small compared to the earthquake wave and thus no large relative displacement could be caused between soil and station structure, soil and diaphragm wall, and filling materials and surrounding structures, so these interfaces were assumed to be in displacement coordination condition, namely, binding constraints in the ABAQUS. Station, soil, diaphragm wall, and filling materials are modeled by solid element C3D8 in the software. The viscous-spring artificial boundary is applied to the boundary of the model, and the measured acceleration time-history at the rail ballast of a subway station in Shanghai was set to be the input excitation on the ballast (Figure 3). Based on the above model, filtering and spectrum analyses were performed. The excitation is applied by the boundary condition, and the applied position is shown in Figure 4. The finite element three-dimensional model with vertical depth of 60 m, horizontal length of

TABLE 2: Parameters of Shanghai soil.

Soil layers	Depth (m)	C_S (m/s)	E_d (MPa)	ρ (kg/m ³)	ν	c (kPa)	φ (°)
①1, ②1	6.9	101.80	52.43	1902.20	0.33	21	16
③, ④	10.6	136.22	84.64	1689.43	0.35	13	12.5
⑤1	4.8	178.65	155	1710	0.42	16	12.5
⑤2	13.9	211.21	218	1810	0.35	4	30.5
⑤3, ⑤4	4.1	275.94	379.68	1888.78	0.32	33	17
⑦1, ⑦2	4.8	335.61	556.5	1930	0.28	8	32.5
⑧1	8.9	352.06	589	1800	0.32	23	18
⑧2	6	376.39	685.1	1860	0.3	24	18.5

Note. C_S = shear wave velocity; E_d = dynamic modulus of elasticity; ρ = density; ν = Poisson ratio; c = cohesion; φ (°) = inner friction angle.

TABLE 3: Parameter of foam concrete, medium sand, and C30 concrete.

Materials	E (MPa)	ρ (kg/m ³)	ν	c (kPa)	φ (°)
C30 concrete	30000	2500	0.2	/	/
Foam concrete	40	600	0.21	1	15
Medium sand	448	1950	0.3	0.1	38

Note. E = modulus of elasticity.

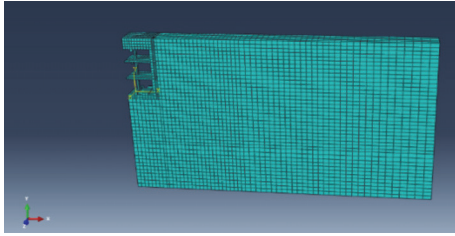


FIGURE 5: Three-dimensional model of Guofan Station.

112.77 m, and the longitudinal length of 8 m is established, as shown in Figure 5. The reason to take 8 m in longitudinal direction is that the longitudinal space of columns is 8 m, and building a 3D model in the whole length of 113.77 m would make computation time too long to be accepted in the analysis.

Considering the whole calculation model, monitoring nodes were set from the position of underground diaphragm wall till the location 60 m away from the underground diaphragm wall, with an interval of 5 m roughly between two neighboring points.

4. Calculation Results and Analysis

4.1. Calculation Results of Cases 1, 2, and 3. As seen from Table 1, it is clear that case 1 has a low Young's Modulus of about 40 MPa, a low damping of about 0.05, and a Poisson's ratio of 0.21. This case represented a relatively soft foam concrete. By monitoring the time domain and frequency domain results of the point, the acceleration level of each monitoring point can be calculated according to the vibration evaluation method. The relationship between the acceleration level and the distance from the vibration epicenter under the condition of case 1 is shown in Figure 6.

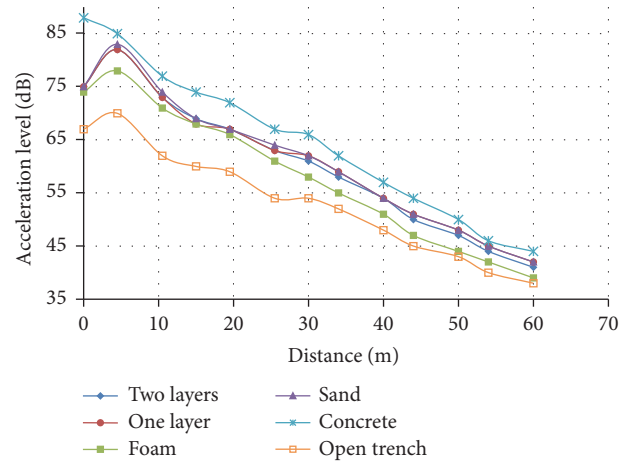


FIGURE 6: The relationship between the acceleration level and distance under case 1.

In order to facilitate the comparison among various results, Scheme 1 is renamed as one layer and Scheme 2 is renamed as two layers, while Schemes 3, 4, 5, and 6 are renamed as sand, foam concrete, concrete, and open trench, respectively. As seen from Figure 6, it is clear that vibration attenuates with the increase of distance. When the distance is about 60 m away from the vibration epicenter, the acceleration level of all the schemes falls below 45 dB. Comparison between schemes of case 1 shows that concrete trench scheme has the biggest vibration and open trench cut the vibration most effectively. Foam concrete trench performs better than the other two schemes left, while two-layer scheme is slightly better than one-layer sand scheme in terms of vibration reduction.

The relationship between the acceleration level and the distance under case 2 is shown in Figure 7, which shows a

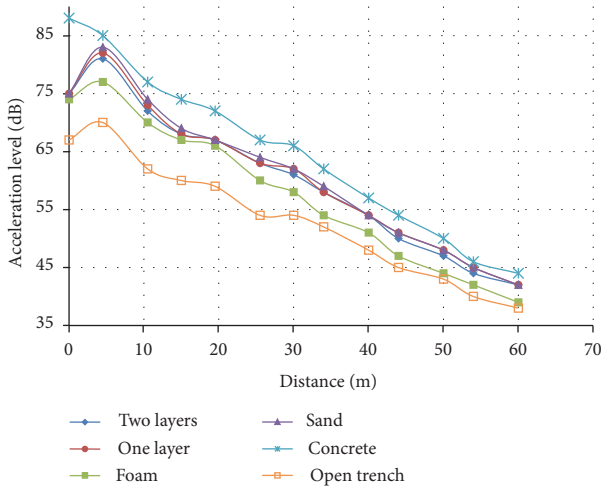


FIGURE 7: The relationship between the acceleration level and distance under case 2.

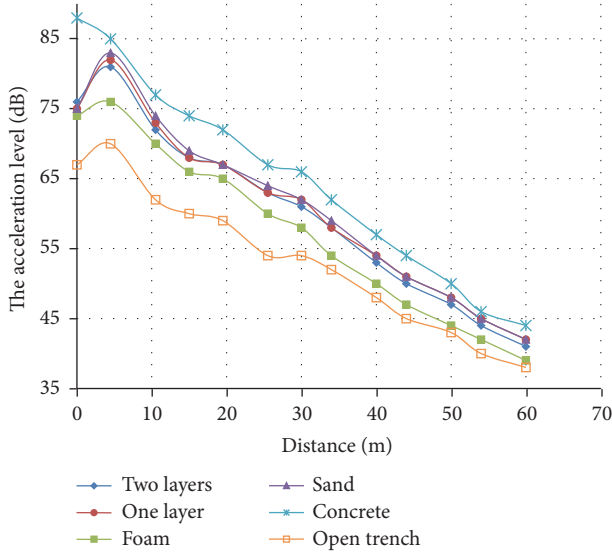


FIGURE 8: The relationship between the acceleration level and distance under case 3.

similar trend in case 1. This indicates that change of damping parameter of foam concrete did not change the calculation results much.

Figure 8 shows the relationship between the acceleration level and the distance from vibration epicenter under calculation case 3. Generally speaking, case 3 has a much bigger damping for foam concrete and thus has slightly more reduction of vibration especially for all foam concrete schemes.

4.2. Calculation Results of Case 4. The relationship between the acceleration level and the distance under the condition 4 is shown in Figure 9. Case 4 is slightly different from case 1 in that its Poisson's ratio is 0.31, which is slightly larger than 0.21 in case 1. While the general trend is the same as that in the above three cases, reduction degree seems to be bigger in

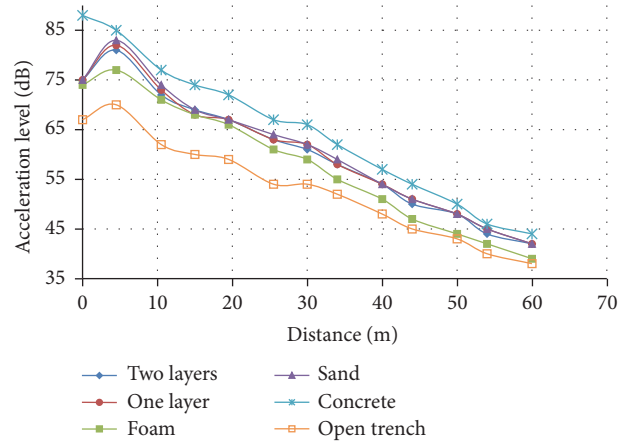


FIGURE 9: The relationship between the acceleration level and distance under case 4.

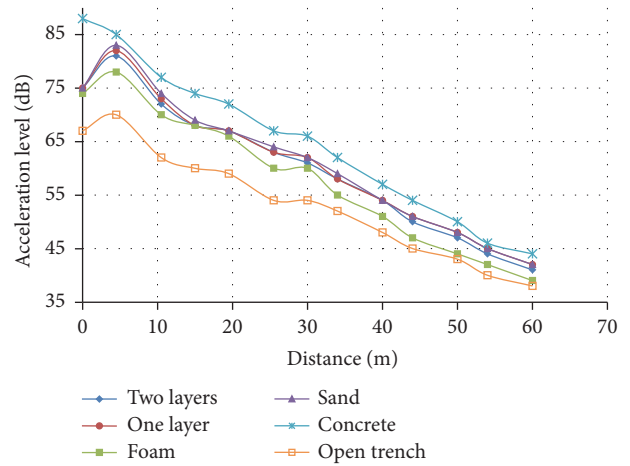


FIGURE 10: The relationship between the acceleration level and distance under case 5.

case 4 than that in case 1. The trend is that open trench has the highest effectiveness in reducing vibration, while trench filled with concrete has the highest acceleration level.

4.3. Numerical Result under Case 5. Case 5 (Figure 10) has the biggest Poisson's ratio for foam concrete, which is about 0.48. However, the trend among different schemes is the same as other schemes. Schemes 1, 2, and 4 which represent one layer, two layers, and no layer of foam concrete performed almost the same during the construction.

4.4. Numerical Result under Case 6. The relationship between the acceleration level and the distance under case 6 is shown in Figure 11. This case is another extreme situation, where the foam concrete's elastic rigidity is 25 times higher than other schemes in order to observe the effects of Young's Modulus on vibration reduction. It is clear that, in this case, vibration reduction curve is almost the same as that of Schemes 1 and 2. It means that stiff foam concrete is not so good in reducing vibration.

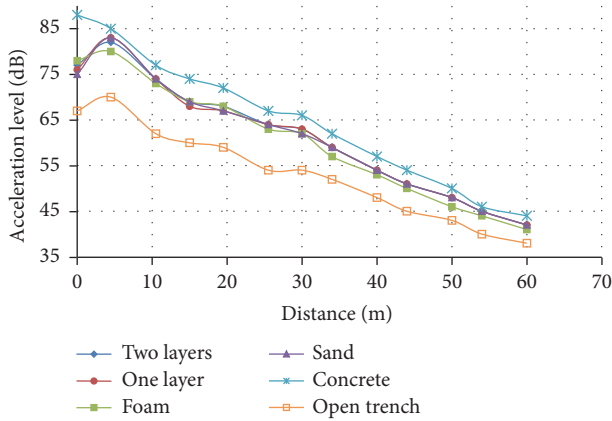


FIGURE 11: The relationship between the acceleration level and distance under case 6.

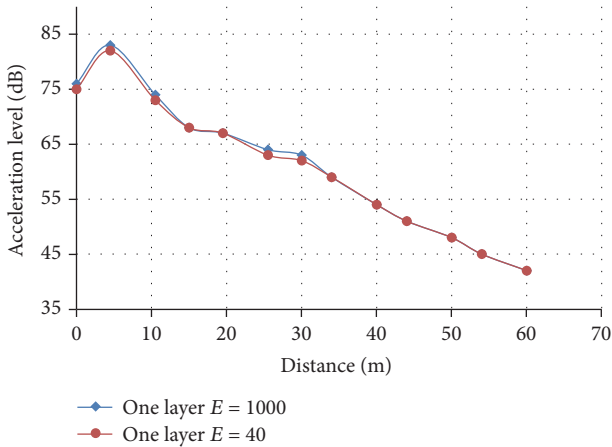


FIGURE 12: The comparison of acceleration between case 1 and case 6 in Scheme 1.

4.5. Parameter Sensitivity Analysis

4.5.1. Effect of Foam Concrete's Elasticity Modulus. The elasticity modulus of foam concrete is affected by the fabrication process, foaming agent, and other factors and will change within a larger range. Figures 12–14 checked the trends how the elasticity modulus of foam concrete influences the vibration reduction.

From Figures 12–14 it can be seen that the vibration reduction effect becomes lower as the elasticity modulus of the foamed concrete increases. This is because, with the increase of the elasticity modulus of the foam concrete, its wave impedance and wave impedance ratio both increase. The vibration reduction effect of different foamed concrete in Scheme 1 and Scheme 2 is slightly different, but there is a significant difference in Scheme 4. From Figures 6 and 11, it can be seen that when the elasticity modulus of the foam concrete increases, the difference in vibration reduction effect in Schemes 1, 2, and 3 basically disappeared. Besides, the wave impedance of foam concrete is closer to that of sand, meaning that when wave impedance ratio of materials is close, its vibration reduction effect is quite similar.

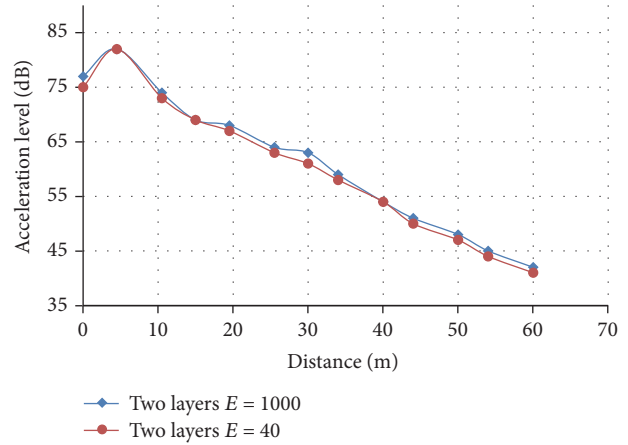


FIGURE 13: The comparison of acceleration level between case 1 and case 6 in Scheme 2.

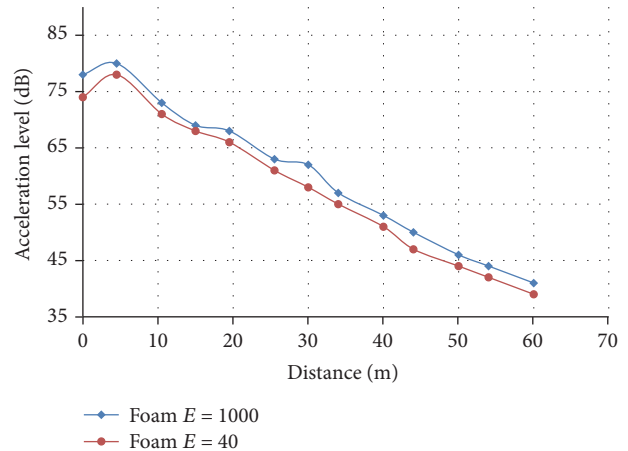


FIGURE 14: The comparison of acceleration between case 1 and case 6 in Scheme 4.

4.5.2. Effect of Foam Concrete's Poisson Ratio. In accordance with knowledge about wave impedance and wave impedance ratio, material's vibration reduction effect depends on these two parameters. The calculation of wave impedance is related to density, elasticity modulus, and Poisson Ratio of the material. The influence of the elasticity modulus of the concrete has been analyzed in the previous section. Since density of material can be uniquely determined, the effect degree of Poisson Ratio on the vibration reduction can thus be discussed here. The relationships between the acceleration level and the distance in Schemes 1, 2, and 4 under case 1, case 4, and case 5 are shown in Figures 15–17.

As can be seen from Figures 15–17, the change in Poisson's ratio of foam concrete has no significant effect on the vibration reduction effect in Schemes 1, 2, and 4. The wave impedance ratio under cases 1, 2, and 3 is very close, and the relation curve of acceleration level and the distance is basically coincident.

4.5.3. Effect of Foam Concrete's Damping Ratio. The effect of wave impedance ratio on the vibration reduction has been

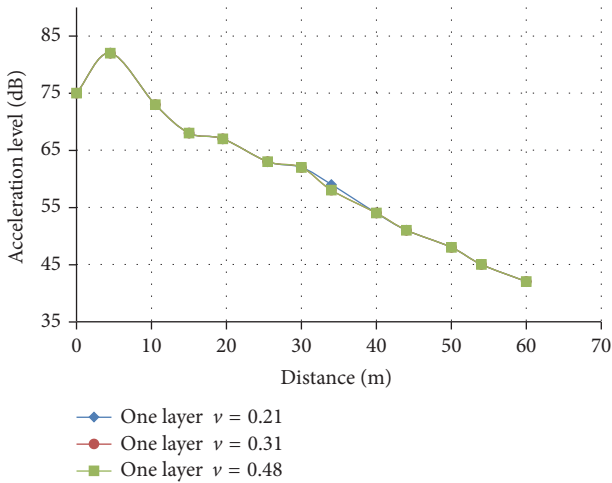


FIGURE 15: The comparison of acceleration level among cases 1, 4, and 5 in Scheme 1.

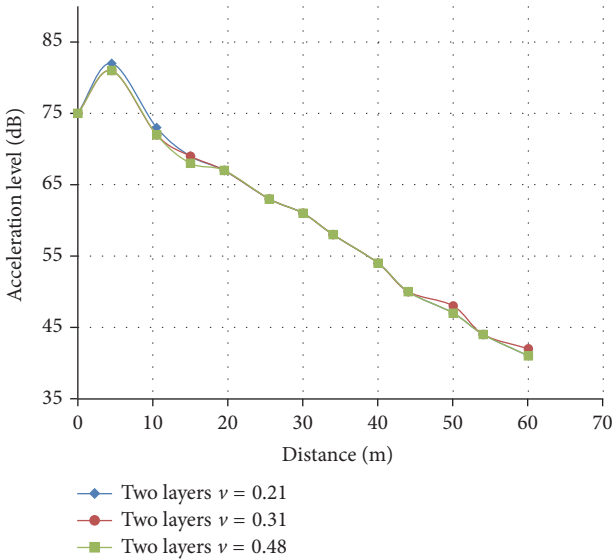


FIGURE 16: The comparison of acceleration among cases 1, 4, and 5 in Scheme 2.

analyzed in the previous two sections, and this section mainly examines the effect of damping ratio on the vibration reduction. Damping ratio of material is generally between 0 and 1, where the damping ratio of the foam concrete has been set, respectively, to be 0.05, 0.5, and 0.95, and the calculation results under cases 1, 2, and 3 are shown in Figures 18–20.

It can be seen from Figures 18–20 that, with the change of the damping ratio in Scheme 1 and Scheme 2, the relation curve of the acceleration level and distance has no significant difference, which means that the change of the damping ratio has little effects on vibration reduction. As for Scheme 4, the bigger the damping ratio of the foamed concrete, the better the vibration reduction effect, but the difference is not that large, which indicates that the damping ratio has only slight effect on the vibration reduction.

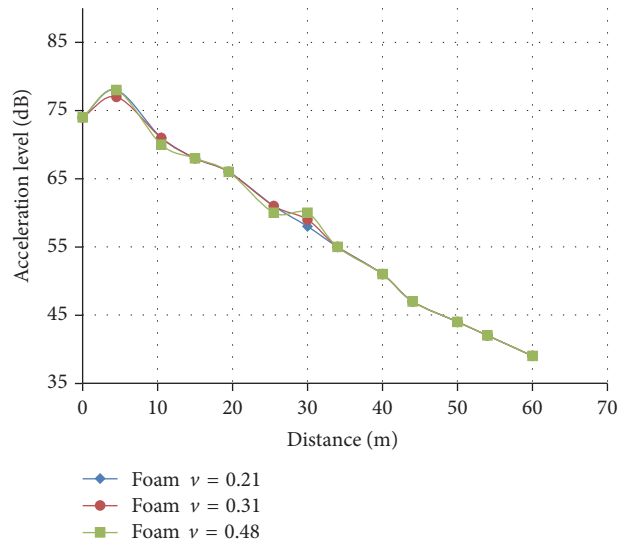


FIGURE 17: The comparison of acceleration level among cases 1, 4, and 5 in Scheme 4.

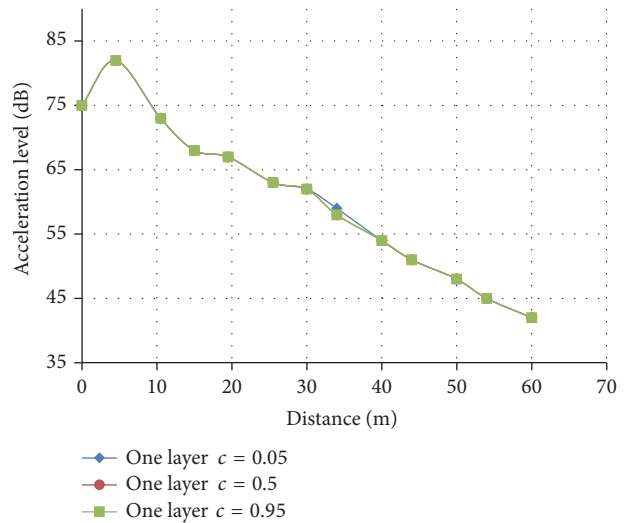


FIGURE 18: The comparison of acceleration level among cases 1, 2, and 3 in scheme 1.

It can be seen from the relation curve of acceleration level and distance from vibration epicenter in Figures 6–10 that, for Guofan Road station whose structure is surrounded by separated retaining wall, the vibration can be reduced by the trench between station structure and underground diaphragm wall, and the reduction effect is best with an open trench. The vibration reduction effect of the trench filled with foam concrete is obviously better than the trench filled with concrete; namely, Scheme 4 is obviously better than Scheme 5. The greatest reduction of acceleration level of the underground diaphragm wall is up to 14 dB, the average is about 8 dB, and the acceleration level decay is 9.4%. In addition, the vibration reduction effect in Scheme 1, Scheme 2, and Scheme 3 is better than that of Scheme 5 but worse than that of Scheme 4. The vibration reduction effect in Scheme

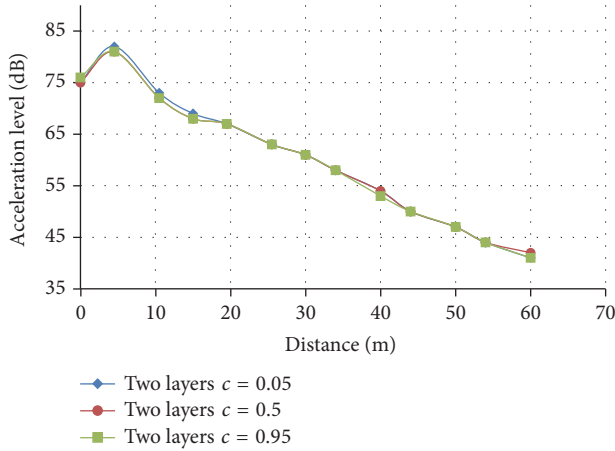


FIGURE 19: The comparison of acceleration level among conditions 1, 2, and 3 in Scheme 2.

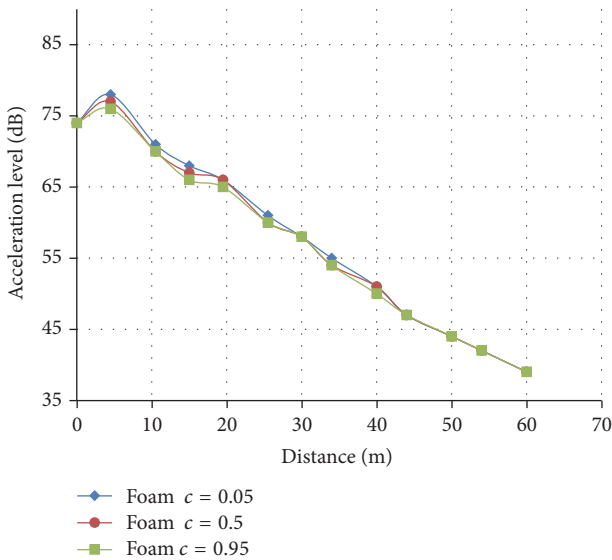


FIGURE 20: Comparison of acceleration level among cases 1, 2, and 3 in Scheme 4.

2 is slightly better than that in Scheme 1, and the vibration reduction effect in Scheme 1 is slightly better than Scheme 3, with about 2 dB decrement of acceleration level.

For this project, by filling vibration reduction material into the gap trench between station structure and underground diaphragm wall, vibration reduction and separation can be achieved. Several materials have been checked on their effect of reducing vibration and different parameters were considered. In this case where the gap trench is surrounded by concrete which has large wave impedance, filling in the trench with foam concrete which has relatively small wave impedance is most effective in reducing and separating vibration from the ground. In this meaning, Scheme 4 is the best filling scheme and can achieve a good vibration isolation and reduction effect. However, considering the balance between vibration reduction effect and the cost or

construction feasibility, one-layer scheme (Scheme 1) turned out to be the best one.

Based on the above analysis, Scheme 1 has been adopted in the design and construction work for Guofan Road station project. Further field measurement data is highly expected after the service start.

5. Conclusion

In this paper, the vibration separation and reduction effect of compound materials filled in a trench has been discussed in the scope of Guofan Road station in Shanghai Metro Line 10, phase two project. Foam concrete and sand materials are considered as barrier materials. Elasticity modulus, Poisson's ratio, and damping ratio of foam concrete are taken as sensitive parameters influencing the reduction effect, and series of numerical analysis have been conducted on different conditions to analyze their vibration reduction effect. The conclusions are as follows:

- (1) Separation trench surrounding subway station structures is effective in separating vibration of the station from adjacent environment. Foam concrete and sand can act as barrier materials.
- (2) In this project, when elasticity modulus, Poisson ratio, or wave impedance ratio of the foam concrete increases, the vibration reduction effect is lowered.
- (3) The changes of Poisson ratio show little influence on foam concrete's wave impedance and vibration reduction.

The damping ratio of foam concrete has an impact on vibration reduction but the impact is not obvious.

- (4) The barrier should be composed of a material with significant vibration reduction effect. When the barrier consists of two kinds of materials with different vibration reduction effect, the reduction effect depends on the material with the lower vibration reduction effect, and the combined effect will be obviously lowered.

Conflicts of Interest

The authors declare that they have no conflicts of interest.

References

- [1] D. D. Barkan and L. Drashevskaya, *Dynamics of bases and foundations*, McGraw-Hill, 1960.
- [2] D. Woods R, "Screening of Surface Wave in Soils," *Journal of the Soil Mechanics Foundations Division*, pp. 94–951, 1968.
- [3] F. E. Richart, *Vibrations of Soils and Foundations*, China Architecture Building Press, 1976.
- [4] W. A. Haupt, "Model tests on screening of surface waves," in *Proceedings of the 10th international conference on soil mechanics and foundation engineering*, vol. 3, pp. 215–222, 1981.
- [5] A. Haupt W, "Surface waves in nonhomogeneous half-space," *Dynamical methods in soil and rock mechanics*, pp. 335–367, 1978.

- [6] W. A. Haupt, "Numerical methods for the computation of steady-state harmonic wave fields," *Proc. of DMSR*, vol. 1978, no. 77, pp. 255–280, 2004.
- [7] G. Schmid, N. Chouh, and R. Le, "Shielding of structures from soil vibrations," *Soil Dynamics And Earthquake Engineering V*, pp. 651–662, 1991.
- [8] A. T. Peplow, C. J. C. Jones, and M. Petyt, "Surface vibration propagation over a layered elastic half-space with an inclusion," *Applied Acoustics*, vol. 56, no. 4, pp. 283–296, 1999.
- [9] H. Takemiya and F. Chen, "Enhanced seismic design of a pile foundation by cell-type wib," *Doboku Gakkai Ronbunshuu A*, vol. 62, no. 2, pp. 467–477, 2006.
- [10] C. Qiu, G.-Y. Gao, Z.-Q. Yue et al., "Research on the failure mechanism of barrier for isolating vibration," *Northwestern Seismological Journal*, vol. 25, no. 3, pp. 198–203, 2003.
- [11] L. S. Li, Q.-L. Xie, and L. Tang, "Influence Factors of Impact Reduction Performance of Foamed Concrete Backfill Layer," *Blasting*, vol. 03, pp. 166–171, 2015.
- [12] D. F. Zhao, W. W. Kong, and X. R. Song, "Testing method of elastic modulus of foamed concrete," *Concrete*, vol. 9, pp. 4–6, 2008.
- [13] X. Z. Yan and Q. F. Yao, "Experimental Study On The Mechanical Property of Foamed Concrete," *Industrial Construction*, vol. z1, pp. 962–964, 2007.
- [14] L. Qiu-Huan, L. Fang-yun, and W. Xiang-yun, "Study On Regulation Of Stress Wave Propagation In Rockmass With Compound Structures," *Chinese Journal of Rock Mechanics and Engineering*, vol. 22, no. 11, pp. 1832–1836, 2003.
- [15] Y.-K. Shen, *Study on The Propagation Laws of Subway-induced Vibration and Isolation of Reduction Methods of Build Vibration*, Tongji University, 2007.
- [16] J. L. Ma and H. P. Ding, "Comparative study on influence of different damping values in soil-layer seismic response analysis," *Journal of Disaster Prevention and Mitigation Engineering*, pp. 517–523, 2013.
- [17] Y. Gu, J.-B. Liu, and Y.-X. Du, "3D consistent viscous-spring artificial boundary and viscous-spring boundary element," *Journal of Engineering Mechanics*, vol. 24, no. 12, pp. 31–37, 2007.

Research Article

Study on Progressive Collapse Behavior of SRC Column-Steel Beam Hybrid Frame Based on Pushdown Analysis

Liusheng Chu,¹ Gaoju Li,¹ Danda Li,² and Jun Zhao¹

¹Zhengzhou University, Henan Province, China

²University of South Australia, Adelaide, SA, Australia

Correspondence should be addressed to Danda Li; danda.li@unisa.edu.au

Received 6 July 2017; Accepted 10 October 2017; Published 13 November 2017

Academic Editor: Songye Zhu

Copyright © 2017 Liusheng Chu et al. This is an open access article distributed under the Creative Commons Attribution License, which permits unrestricted use, distribution, and reproduction in any medium, provided the original work is properly cited.

To investigate the progressive collapse behavior of Steel Reinforced Concrete (SRC) column-steel beam hybrid frame after the failure of key structural elements, a PQ-Fiber model for an 8-storey structure is established in ABAQUS program. Nonlinear dynamic and static pushdown analysis are carried out after the failure and removal of the bottom-middle and bottom-corner columns. Numerical results of both methods agree well with each other. Results show that SRC column-steel frame has good resistance to progressive collapse under dynamic instantaneous load. After sudden removal of a bottom middle column, the development of structural collapse exhibits two mechanisms, the beam mechanism and the catenary mechanism. When the structure is within small deformation range, the collapse resistance of the residual frame is provided by the beam bending moment capacity, which is beam mechanism. For large deformation situation, the collapse resistance is mainly provided by the beam tensile strength, which is catenary mechanism. However, with the removal of a bottom corner column, the residual structure only undergoes the beam mechanism even for large deformations. For future practical applications, the influence of the steel ratio, steel section size, and the vertical position of the removed key components are investigated through a detailed parametric study.

1. Introduction

After the progressive collapse of the Ronan Point apartment due to gas explosion in London in 1968 [1], the structure progressive collapse behavior has attracted great interests from designers and researchers. ASCE07-05 [2] defined the progressive collapse behavior as the spread of an initial local failure between members, eventually resulting in collapse of large part or even entire of the structure. Apart from the United States, Britain, and Europe, other countries and regions also introduced the corresponding structure progressive collapse design specifications [2–7].

Many experimental and theoretical studies on the progressive collapse behavior of reinforced concrete frame and steel frame have been reported, including structural collapse mode and dynamic increasing factor. Tsai and Lin [8] conducted nonlinear static and nonlinear dynamic analyses on the progressive collapse behavior of the reinforced concrete building subjected to column failure. By using alternate path methods, J. Kim and T. Kim [9] studied the progressive

collapse-resisting capacity of steel frame. The results showed that the progressive collapse risk was highest when a corner column was suddenly removed. For practical applications, Liu [10] proposed an empirical formula through calculating the dynamic increasing factor (DIF), which can be used with nonlinear static analysis to assess the potential of progressive collapse for steel frames. Masoero et al. [11] presented an analytical model for the collapse of a 2D frame after column removal, which could be used to estimate the loads of collapse initiation. Based on DOD2010 [3] design process Liang et al. [12] investigated the progressive collapse behavior of a three-storey steel frame structure which was designed according to Chinese Design Code. Yi et al. [13] conducted a quasi-static test method to analyze the progressive collapse process of a RC frame structure after the failure of one of the bottom columns. Li et al. [14] conducted a nonlinear static pushdown analysis on the progressive collapse bearing capacity of the whole cast-in-place reinforced concrete frame loaded under different seismic intensities. The results showed that the seismic design improved the progressive collapse capacity of

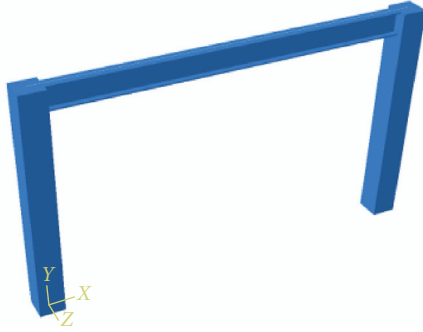


FIGURE 1: Finite element model of a hybrid frame.

the frame structure under the beam mechanism but has a limited increase when the structure is under the catenary mechanism. Fascetti et al. [15] proposed a new procedure from nonlinear static and dynamic analyses to evaluate the robustness of RC frame to progressive collapse after a sudden loss of vertical load carrying.

From the above literature, it can be seen that the current theory or experiment studies on progressive collapse are mostly about reinforced concrete structures (RC) and steel structures. In practical engineering, other than just steel structure or RC structures, more and more hybrid structures are developed to meet higher requirement of structure durability, performance, and economic and other aspects. A type of hybrid frame which consists of Steel Reinforced Concrete (SRC) column and structural steel beam is one of the widely used hybrid structures. It was proved to have good seismic performance and economic advantages compared with just structure steel frame or RC frame structure. However, there is little research on the progressive collapse ability of this SRC column-steel beam hybrid frame structure. It is most likely to occur under occasional impact loads such as explosion.

This paper addresses the progressive collapse behavior of SRC column-steel beam hybrid frame. An 8-storey hybrid frame structure was designed according to the current Seismic Code of China, and the pushdown analysis was carried out by using alternate path method under the occasional load. Based on the analysis results, the progressive collapse ability and collapse mechanism of the hybrid frame were studied, and the influence of the parameters such as the steel ratio of SRC column, steel section size, and the vertical position of removing key components were also investigated.

2. Calculation Method and Verification

2.1. FEM Modeling of Steel Reinforced Concrete (SRC) Column-Steel Beam Hybrid Frame Structure. In this study, ABAQUS program was employed for structure analysis. The hybrid frame components are all modeled by the two-dimensional plane element. This type of unit allows shear deformation, and takes into account the limited axial strain. The finite element model of a hybrid frame is shown in Figure 1. The reinforcing bars are defined by the * rebar keyword, and the number, position, and size of the each rebar are modeled

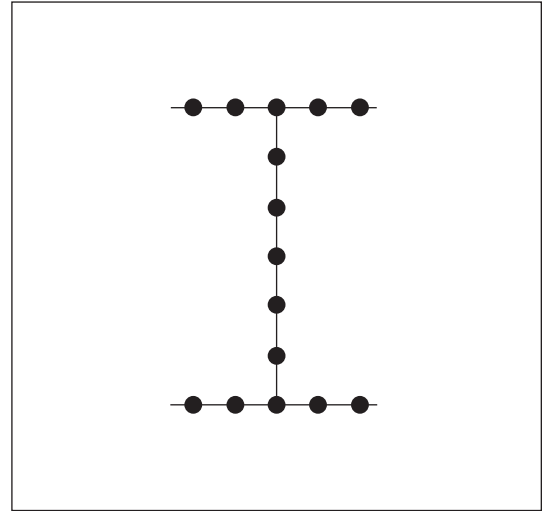


FIGURE 2: Discretization of the steel in the SRC column.

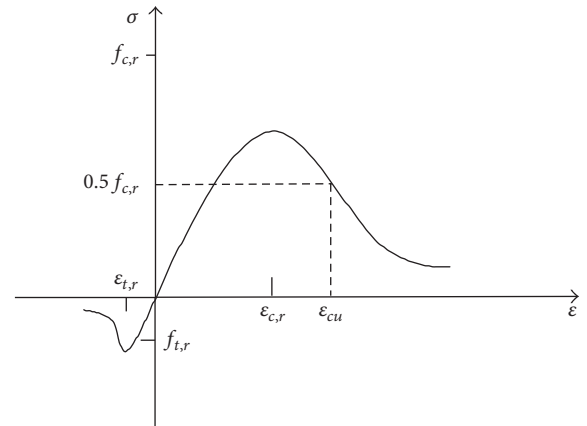


FIGURE 3: Stress-strain curve of concrete.

according to the actual situation. The steel in the SRC column will be separated into several steel fibers, as shown in Figure 2.

The concrete 03 in PQ-Fiber was used for the concrete constitutive model. This model is based on the concrete skeleton curve in current Chinese Code [16], in which the tensile strength of the concrete model can be considered. The stress-strain curve (Figure 3) of concrete under uniaxial tension can be determined by (1a), (1b), (1c), and (1d).

$$\sigma = (1 - d_t) E_c \varepsilon, \quad (1a)$$

$$d_t = \begin{cases} 1 - \rho_t [1.2 - 0.2x^5] & x \leq 1 \\ 1 - \frac{\rho_t}{\alpha_t (x - 1)^{1.7} + x} & x > 1, \end{cases} \quad (1b)$$

$$x = \frac{\varepsilon}{\varepsilon_{t,r}}, \quad (1c)$$

$$\rho_t = \frac{f_{t,r}}{E_c \varepsilon_{t,r}}, \quad (1d)$$

where d_t is tensile damage evolution parameters of concrete, α_t is decreasing parameters of concrete tensile constitutive curve, $f_{t,r}$ is uniaxial tensile strength of concrete, $\varepsilon_{t,r}$ is the concrete strain corresponding with $f_{t,r}$, and the parameter values in the formula are taken as in Chinese Code.

The stress-strain curves of concrete under uniaxial compression (Figure 3) can be determined by (2a), (2b), (2c), (2d), and (2e):

$$\sigma = (1 - d_c) E_c \varepsilon, \quad (2a)$$

$$d_c = \begin{cases} 1 - \frac{\rho_c n}{n - 1 + x^n} & x \leq 1 \\ 1 - \frac{\rho_c}{\alpha_c (x - 1)^2 + x} & x > 1, \end{cases} \quad (2b)$$

$$\rho_c = \frac{f_{c,r}}{E_c \varepsilon_{c,r}}, \quad (2c)$$

$$n = \frac{E_c \varepsilon_{c,r}}{E_c \varepsilon_{c,r} - f_{c,r}}, \quad (2d)$$

$$x = \frac{\varepsilon}{\varepsilon_{c,r}}, \quad (2e)$$

where d_c is the compressive damage evolution parameter, α_c is decreasing parameters, $f_{c,r}$ is uniaxial compressive strength of concrete, and $\varepsilon_{c,r}$ is the concrete strain at peak stress. The parameter values in the formula are taken as in Chinese Code [16].

USTEEL02 model of PQ-FIBER is used for the constitutive model of steel and rebar. Figure 3 shows the uniaxial stress-strain curve, where k is the hardening stiffness coefficient which represents the ratio of the second stage stiffness and the elastic modulus of the steel and is taken as 0.01 in this model.

In order to verify the applicability of the modeling in ABAQUS program of the SRC column-steel beam hybrid frame, the seismic behavior of the hybrid frame experiment conducted by Li and Zhao [17] was simulated. A one-way horizontal load is applied to the planar frame in the finite element model in Figure 1, with the analysis results shown in Figure 5. It indicated that the rigidity of the analysis curve is consistent with the stiffness of the test curve in the elastic stage. Beyond elastic stage the analyzed stiffness is slightly larger than the test value. The main reason is that the load on the structure in experimental test is cyclic load, while in the analysis it is monotonically horizontal load. Another possible reason is that the slip between the steel section and the concrete is not considered in the simulation, hence resulting in a faster drop in stiffness value than the tested value. However, it can be concluded that the two curves fit well.

The good agreement between the FEM method and the experimental results shows that it is feasible to carry out the elastoplastic simulation analysis to the SRC column-steel beam hybrid frame in the ABAQUS with PQ-FIBER.

2.2. Direct Dynamic Analysis. The straightforward progressive collapse capacity analysis of a frame is dynamic analysis on the remaining structure under the instantaneous load

from the force redistribution due to sudden collapse or failure of one column (Khandelwal and El-Tawil, 2011 [18]). However, the direct dynamic analysis method is time consuming and the massive data obtained during the analysis is not easy to interpret into design procedure. In this paper, a simplified pseudostatic analysis method is proposed to analyze the remaining structural system through applying a downward static load at the column collapsing point to represent the unbalanced reaction force from the column. This method is also named pushdown method. The direct dynamic analysis method here will be used as verification for the presented pushdown method.

2.3. Pushdown Method (Nonlinear Static Analysis). For the model considered in this paper, the material nonlinearity of steel and concrete needs to be considered in the analysis due to the large deformation estimated. In addition, due to the large number of elements involved in this model, the displacement-controlled nonlinear static method will be employed to improve the efficiency and accuracy of analysis. The structure dynamic effect will be considered and the dynamic increasing factor will be investigated.

In accordance with DOD2010 [3] and GSA2003 [4], after some structural components are removed and the initial destruction occurs, the residual structure damage is allowed. However, this damage should be restricted to avoid the progressive collapse damage in the residual structure. There is also a need to analyze the capacity of the remaining structure, and its progressive collapse ability.

According to US specification GSA2003 [4], if using the alternate load path method for progressive analysis, some of the specific vertical load-bearing components of structure need to be removed, and the overall structure damage should be controlled within the specified allowable range. In this paper, nonlinear static pushdown analysis of SRC column-steel beam hybrid frame is carried out using this method, removing SRC columns here in our case. In the pushdown analysis process, load is gradually applied to the structure and increased until the damage occurs. Then the relationship between structural resistance and deformation is able to be obtained, which will be used to determine the progressive ability of the structure.

Specifically in the ABAQUS program, the failure component is firstly removed by using life and death unit method, which can be achieved by the command of *MODELCHANGE, TYPE = ELEMENT, REMOVE. Then the linear load will be gradually applied to the beam until the final destruction of the structure.

As a verification pushdown method is used to simulate a 1/3 reinforced concrete frame experiment, which is designed according to the reinforced concrete design specification [13]. The gradual failure of the column in the bottom of the frame (Figure 6) is simulated by decreasing the load which was applied by jack. Based on concrete material model (the PQ-Fiber unit, in Figure 3) and steel constitutive model (Figure 4), the above-mentioned experimental progressive process was simulated by ABAQUS program. The middle column unloading force-unloading displacement curves of experimental and simulation are shown in Figure 6. It can be

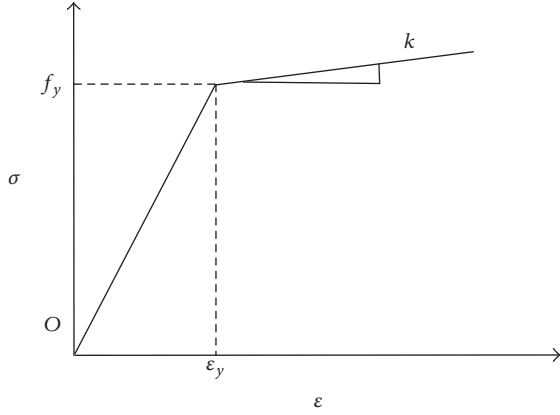


FIGURE 4: Stress-strain curve of steel.

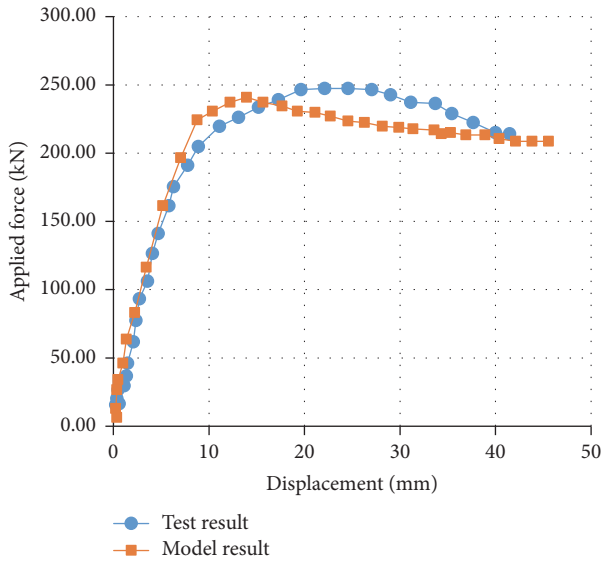


FIGURE 5: Load-displacement curve of SRC hybrid frame.

seen from the figure that the simulation results of both the elastic section and the plastic section are in good agreement with the experimental results, which shows that the progressive collapse of the structure can be effectively simulated, and the PQ-FIBER model can be used to simulate the progressive collapse behavior of concrete.

Assuming the relationship between applied load F_{FL} and the vertical deflection y at the collapse column point obtained from above static analysis is

$$F_{FL} = f(y). \quad (3)$$

The maximum dynamic displacement y_d after considering the impact effect due to sudden collapse of the column can be obtained through solving the following equation:

$$F_{FL}\bar{y}_d = \int_0^{\bar{y}_d} f(y) dy, \quad (4)$$

where the $F_{FL}\bar{y}_d$ on the left side of the equation means the work done by the applied load F_{FL} , and the integral term

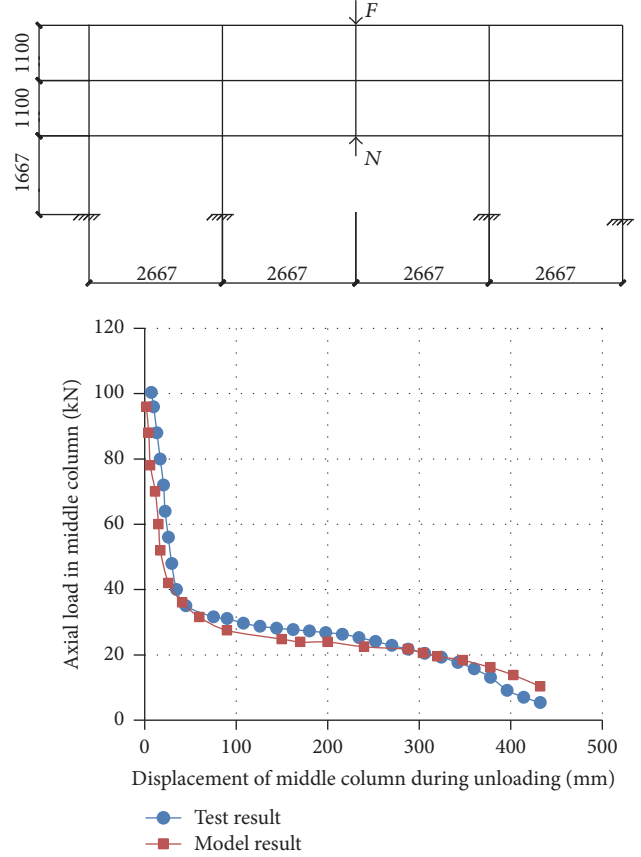


FIGURE 6: Load-displacement curves of pushdown analysis and test results.

$\int_0^{\bar{y}_d} f(y) dy$ on the right side means the deformational energy stored in the structure. Considering the damping effect, the maximum dynamic displacement y_d can be expressed as

$$y_d = \frac{[1 + e^{-\xi\pi}]\bar{y}_d}{2}, \quad (5)$$

where ξ is the damping ratio for the system, $\xi = 0.02$ for steel structures, and $\xi = 0.05$ for concrete structures. For the hybrid structure in this paper, 0.02 is used for damping ratio for conservative analysis.

In order to make the analysis result more clear, this paper adopts the concept of the load resistance coefficient proposed by Khandelwal and El-Tawil [18], which was defined as the ratio of the vertical incremental load on the beam to the normal load on it, as shown in the following formula:

$$F_{OL} = \frac{F_{FL}}{F_O}, \quad (6)$$

where F_{OL} is the load resistance coefficient, F_O is initial axial force in the collapsed column, and F_{FL} is the vertical incremental load on the beam.

Considering (6), (4) can be normalized as

$$F_{OL}\bar{y}_d = \int_0^{\bar{y}_d} f_{OL}(y) dy, \quad (7)$$

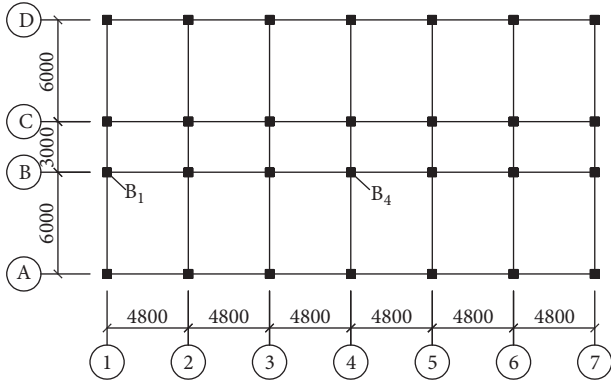


FIGURE 7: The planar arrangement of the hybrid frame structure.

where f_{OL} is the static relationship function between load resistance coefficient and vertical displacement at the collapse column point.

According to DOD2010 [3], the subsequent destruction of structural residual components should be strictly limited, which means that the residual structural components cannot exceed the ultimate plastic deformation of the component. In this paper, the progressive collapse failure criterion of the structure follows DOD2010 [3] requirement and the displacement difference at both ends of the steel beam is limited to 1/10 of span.

As for the removal of key components in progressive collapse analysis, GSA2003 [4] suggested four types of typical bottom frame columns, including internal columns, mid-column in long side, mid-column in short side, and corner columns. DOD2010 [3] also requires removal of the side column of the upper structure. This is because the bottom columns are more likely to have accidental loads, while the upper side columns are more likely to be exposed to gas explosion and the impact of flying objects. According to Chinese progressive collapse specification, bottom columns and upper floor columns where the cross sections change are the key components to be removed.

In this paper, pushdown analysis will be carried out by removing the bottom corner column and the middle column. Their effect on structure progressive collapse behavior was analyzed and parameters analysis was investigated.

3. Main Parameters and Calculation Principles

3.1. Design Parameters. The calculation model is 8-storey SRC column-steel beam hybrid frame structure. The plan drawing is shown in Figure 7. The storey height is 3.6 meters. There are 6 continuous spans along X direction and 3 span along Y direction. Column cross sections in storeys 1–4 are 550 mm × 550 mm and in storeys 5–8 are 500 mm × 500 mm. Concrete compressive strength is 40 MPa, and steel yield strength is 235 MPa.

3.2. Load and Member Details. Dead loads on both floor and roof are 5.0 kN/m², live loads on floor and roof are 2.0 kN/m² and 0.5 kN/m², respectively. The combination of load effects

TABLE 1: Cross section of SRC column.

SRC column	Section size (mm)	Steel size (mm) (height × width × web × flange)	Longitudinal reinforcement
1–4 storey	550 × 550	300 × 300 × 12 × 16	12Φ18
5–8 storey	500 × 500	240 × 240 × 10 × 17	12Φ16

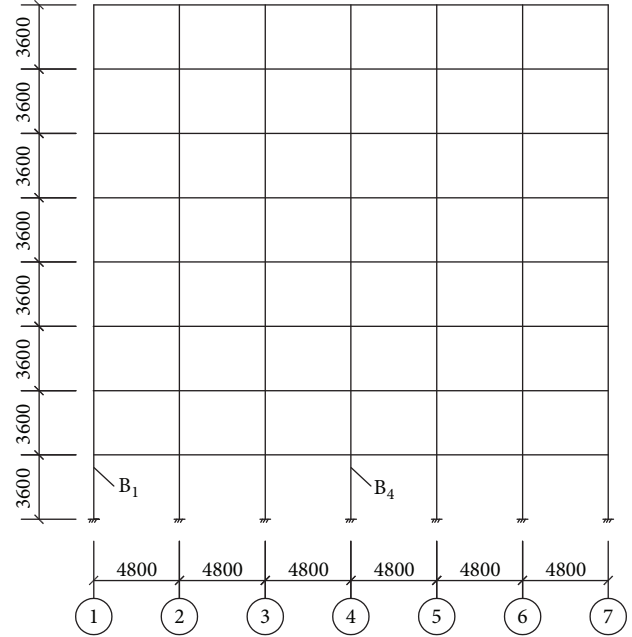


FIGURE 8: Elevation drawing of the hybrid frame structure.

in this paper is calculated according to the *Code for Anti-Collapse Design of Building Structures* [19] issued by the China Engineering Construction Association in 2014. The detail of the SRC column is listed in Table 1.

3.3. Analysis of Progressive Collapse Behavior. As shown in Figure 8, for the structure being considered, the bottom middle column B4 was removed and the structure was subjected to pushdown analysis. The second analysis is where the bottom corner column B1 was removed.

3.4. Progressive Collapse Behavior after Removal of Bottom Middle Column B4. The middle column B4 is removed from the frame and the column top is used as control node. Both dynamic analysis and pseudostatic pushdown analysis were carried out using ABAQUS program.

3.4.1. Dynamic Analysis Results. The dynamic displacement of the middle column upper node and the bending moment of the connecting beam are shown in Figures 9 and 10. It can be seen that the maximum dynamic response (at the beginning of the loading) is nearly double the value of the stable static response, which is similar to previous studies [10, 12, 14]. It

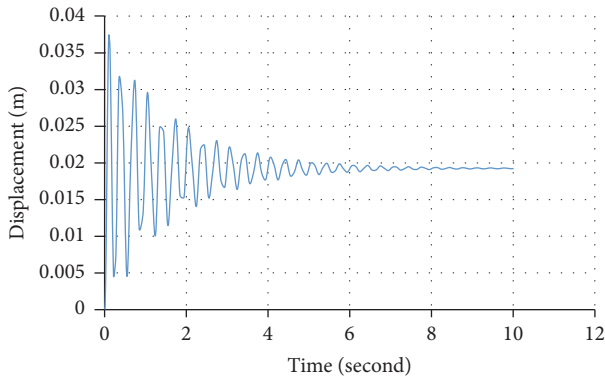


FIGURE 9: The displacement of middle column upper node versus time in dynamic model.

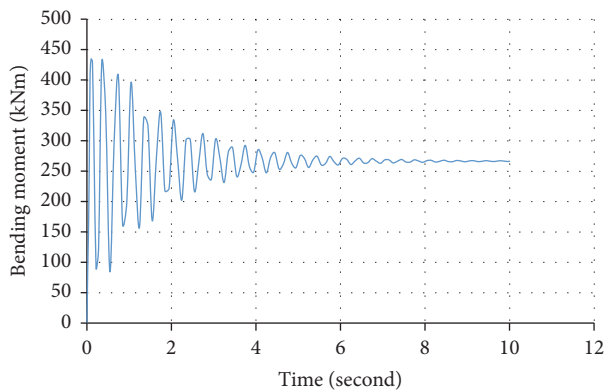


FIGURE 10: The bending moment of connecting beam to middle column upper node versus time in dynamic model.

indicates that the impact increasing effect cannot be ignored for structures with sudden column failure or collapse.

3.4.2. Pushdown Analysis Method. The deformation of frame after collapse of column B4 is shown in Figure 11. Figure 12(a) shows the relationship between the vertical displacement and the resistance coefficient of the column top node after the failure of the bottom middle column B1 from static analysis. Based on (5) and (7) and Figure 12(a), the dynamic displacement-resistance coefficient curve can be obtained as shown in Figure 12(b). It can be seen from the figure that the residual structure after removal of the column has a strong vertical stiffness and remaining capacity. The dynamic vertical displacement of the node is around 0.037 m, which is exactly the same as shown in the dynamic analysis results of Figure 8. Considering Figure 12(a), the pseudostatic load coefficient is 1.94. If the dynamic displacement reaches the standard limit of 0.48 m, which is equivalent to 1/10 of beam span, the load resistance coefficient is 2.62. It is obvious that the structure does not collapse after the removal of the column B1 from this SRC column-steel beam hybrid frame.

Figure 13 shows the bending moment-resistance coefficient curve of the steel beam which is connected with the removed column B4 after static analysis. It can be seen that

the bending moment of the steel beam increases abruptly with the increase of the resistance coefficient at the beginning of loading, with compressive axial force which increases linearly at a slow rate. The residual structure mainly depends on the bending capacity of the beam, and this stage is the beam mechanism stage. When the resistance coefficient is increased to 1.8 at the bending moment of 429.5 kNm the beam reaches its ultimate plastic moment. After that point, the bending moment gradually becomes more stable. Considering the fact that the pseudostatic load coefficient is 1.94 after removal of the column, the maximum dynamic ending moment within the steel beam can be considered as 430 MPa, which is exactly the same as the dynamic analysis result in Figure 10.

Figure 14 shows the axial force-resistance coefficient curve of the steel beam which is connected with the removed column B1. These figures show that, after resistance coefficient of 1.8, the slope of the curve becomes larger and the axial force in the beam increases rapidly. The hybrid frame enters the catenary phase gradually through the transition phase, and its anticollapse ability mainly depends on the axial tensile bearing capacity of the steel beam.

3.5. Progressive Collapse Behavior after Removal of Bottom Corner Column. The corner column B1 is removed from the frame and the column top is used as control node. Both dynamic analysis and pseudostatic pushdown analysis were carried out using ABAQUS program. From the pseudostatic pushdown analysis the deformation of overall structure is analyzed and shown in Figure 15.

Figure 16(a) shows the static analysis results for resistance coefficient-displacement curve of the frame after the bottom corner column is removed. Similar to the bottom middle column failure, the dynamic displacement-resistance coefficient curve for the corner column collapse mode can be obtained based on Figure 16(a) and (5) and (7) as shown in Figure 16(b). It can be seen from the figure that the residual structure after removal of the column has a strong vertical stiffness and remaining capacity. The dynamic vertical displacement of the node is around 0.065 m. Considering Figure 16(a), the pseudostatic load coefficient is 1.51 at the displacement of 0.065 m. If the dynamic displacement reaches the standard limit of 0.48 m, which is equivalent to 1/10 of beam span, the load resistance coefficient is 1.79 (Figure 16(b)). It is obvious that the structure does not collapse after the removal of the corner column from this SRC column-steel beam hybrid frame.

The relationships of the beam bending moment versus resistance coefficient of the structure after bottom corner column removed are given in Figure 17. It can be seen from Figure 17 that the moment of the beam at the beginning of the loading increases sharply, which shows a very obvious “beam mechanism.” Then, when the resistance coefficient increased to 1.01, the plastic hinge began to develop in the beam ends section with the bending moment changing more slowly. After this point the residual structure has been unable to continue to withstand more loads. Because the pseudostatic load coefficient is 1.51, the beam already comes into plasticity during the impact procedure due to sudden collapse of corner column.

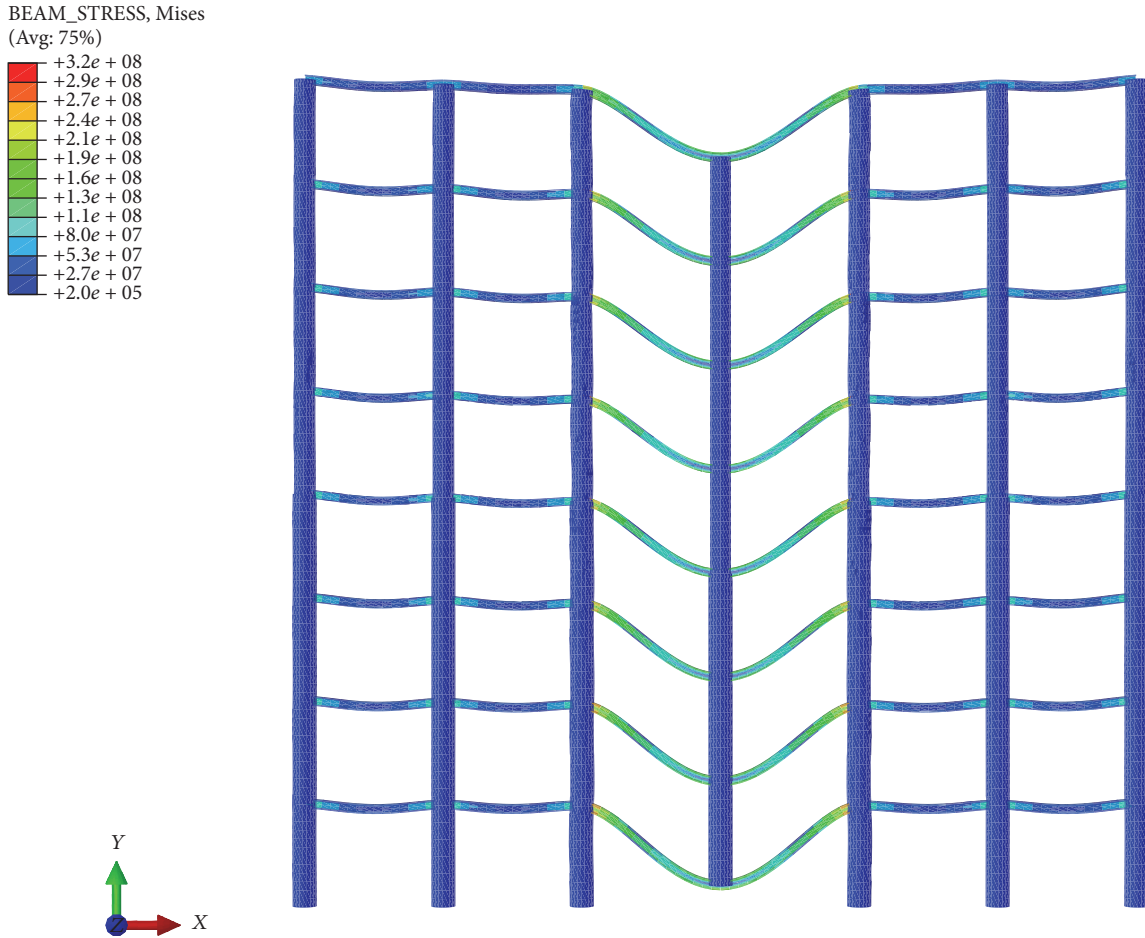


FIGURE 11: Deformation cloud diagram of the hybrid frame after the failure of the bottom middle column.

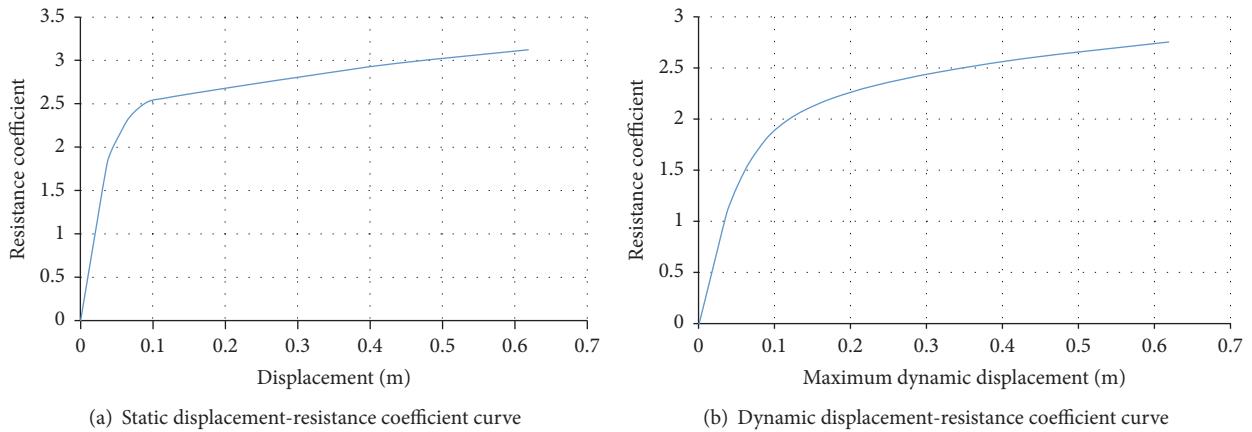


FIGURE 12: Vertical displacement-resistance coefficient curve of the hybrid structure after the failure of the bottom middle column.

The relationship of the axial force versus resistance coefficient of the structure after bottom corner column is removed is given in Figure 18. It can be seen that the beam is always in compression during the loading process, while in the bottom middle column removal case the beam is mainly in axial tensile strength (Figure 14). In summary, after the removal of

the bottom corner column, the upper residual structure (the part related to the removed column) becomes a geometrically variable system. When the bending moment of the beam reaches the ultimate moment, the residual structure cannot bear any more vertical load, and there is no “catenary mechanism” system formed after the “beam mechanism” stage.

TABLE 2: Different SRC column-steel ratio parameters for models (1)–(3).

Model	Steel size in 1–4 storeys (mm) (height × width × web × flange)	Steel size in 5–8 storeys (mm) (height × width × web × flange)	Steel ratio in 1–4 storeys (%)	Steel ratio in 5–8 storeys (%)
(1)	300 * 300 * 8 * 12	240 * 240 * 8 * 12	3.2	3.1
(2)	300 * 300 * 12 * 16	240 * 240 * 10 * 17	4.7	4.8
(3)	300 * 300 * 16 * 28	240 * 240 * 18 * 24	7.4	6.9

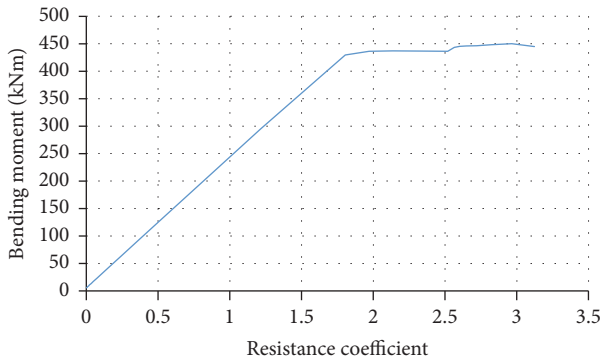


FIGURE 13: Bending moment-resistance coefficient curve of the steel beam connected with the removed middle column.

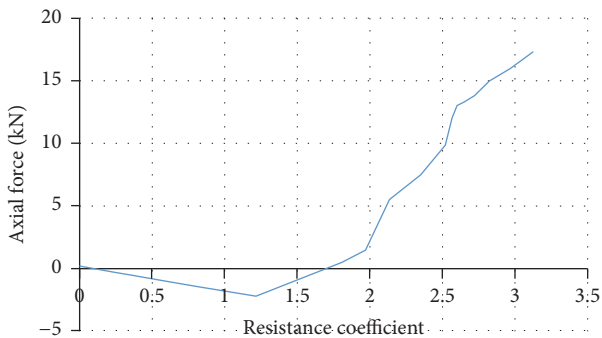


FIGURE 14: Axial force-resistance coefficient curve of the steel beam connected with the removed middle column.

From the above discussion, it can be seen that there are two stages in the progressive collapse process of SRC column-steel beam hybrid frame: “beam mechanism” and “catenary mechanism,” which is similar to the failure process of RC frame and steel frame [8, 9, 11–15]. As the catenary mechanism mainly depends on the tensile force of the steel beam, it is important to improve the tensile capacity of the beam section to improve the progressive collapse ability of the structure. At the same time, since the catenary mechanism can not be formed in the hybrid frame after the removal of the corner columns, its progressive collapse ability is weak. So the bottom corner column should be strengthened in the progressive collapse design.

4. Parametric Analysis of Progressive Collapse Behavior of SRC Column-Steel Beam Hybrid Frame

4.1. Effect of Steel Ratio of SRC Column. SRC column is the basic vertical load-bearing component in a hybrid frame. According to the design rules of steel composite structure [20]: the minimum steel ratio of SRC components is 3%, the appropriate steel ratio can be 5% to 8%, and thickness of steel component should be not less than 6 mm. Based on the above requirements, the steel ratio in this paper is increased by increasing the thickness of the flange plate and the thickness of the web without changing the flange width and section height. Table 2 shows the three different SRC column-steel ratio parameters for the model.

The SRC column-steel beam hybrid frame analysis model was established according to the three different column-steel ratio parameters in Table 2; then the SRC column of the same position was removed and the pushdown analysis was carried out, respectively.

4.1.1. Removing Bottom Middle Column. Figure 18 shows the displacement-resistance curve of the three hybrid frame models with different steel ratio after the bottom middle column was removed.

It can be seen from Figure 19 that when the limit of damage criterion is reached (i.e., the vertical displacement of 0.48 points), the resistance coefficients of the three models are 2.73, 3.02, and 3.36, respectively. This shows that the progressive collapse behavior of the system increases with the increase of steel ratio. This is because the vertical load is the main control load after the removal of vertical components. Increasing the steel ratio of SRC column can improve the overall stiffness of the structure and hence slightly improve the anticollapse bearing capacity of the structure.

4.1.2. Removing Bottom Corner Column. Figure 20 shows the displacement-resistance curve of the three models with different steel ratio after the bottom corner column was removed.

As can be seen from the figure, with the increase of steel ratio in the SRC columns, the resistance coefficient growth rate is very small. This is a similar conclusion as the removal of middle column. Increasing the steel ratio of the SRC column has a slight effect on the anticollapse ability of hybrid frame structure.

4.2. Effect of Cross Section Size of Steel Beam. The beam mechanism stage is the first stage of the progressive collapse

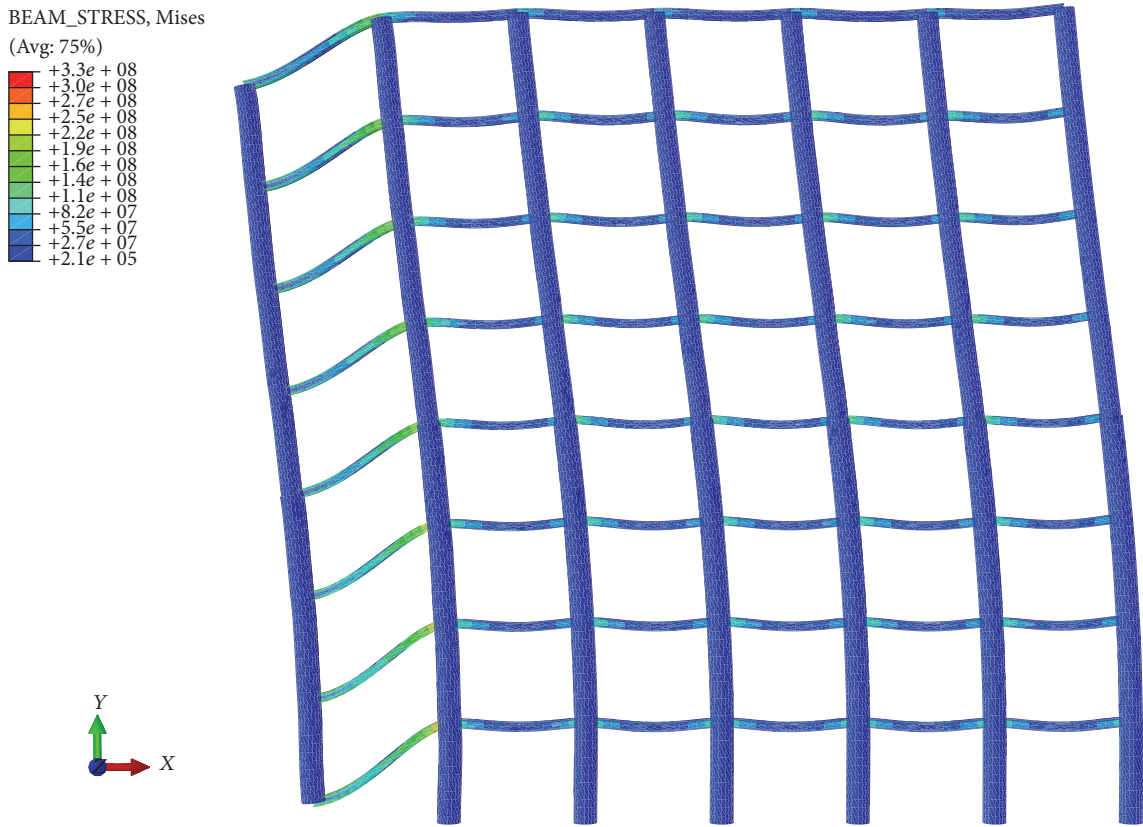


FIGURE 15: Deformation of the hybrid frame after the failure of the bottom corner column.

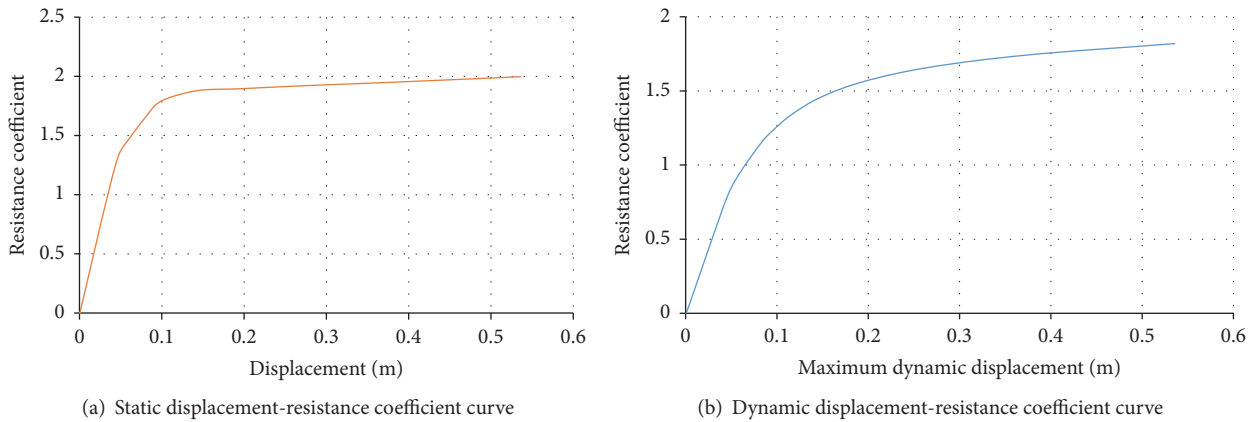


FIGURE 16: Vertical displacement-resistance coefficient curve of the hybrid structure after the failure of the bottom corner column.

process of the SRC column-steel beam hybrid frame. In that stage the anticollapse ability of the structure is mainly provided by the bearing capacity of the beam. Therefore the cross-sectional size of the beam has a direct effect on the progressive collapse of the structure. In addition, changing the beam cross-sectional dimensions, the beam-to-column linear stiffness ratio of the frame will also change. Also the beam-to-column linear stiffness ratio is an important factor in determining the integrity of the structure, which will affect the structure ductility, internal force distribution

and energy consumption, and other properties. Therefore, this paper presents a parametric analysis for the hybrid frame with different beam cross-sectional dimensions and corresponding beam-to-column linear stiffness ratios, which is shown in Table 3.

4.2.1. *Removing Bottom Middle Column.* The curves of the vertical displacement versus resistance coefficient of the hybrid frame with different beam parameters (Table 3) after

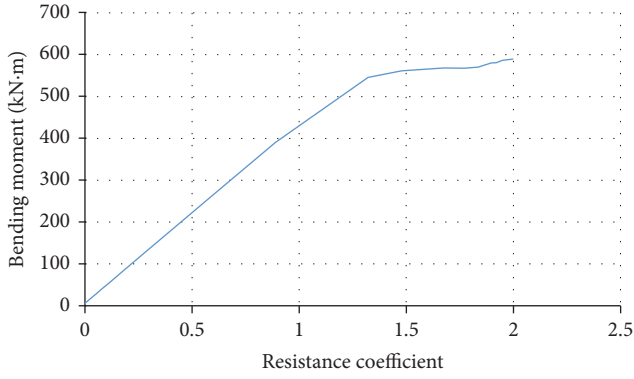


FIGURE 17: Bending moment-resistance coefficient curve of the steel beam connected with the removed corner column.

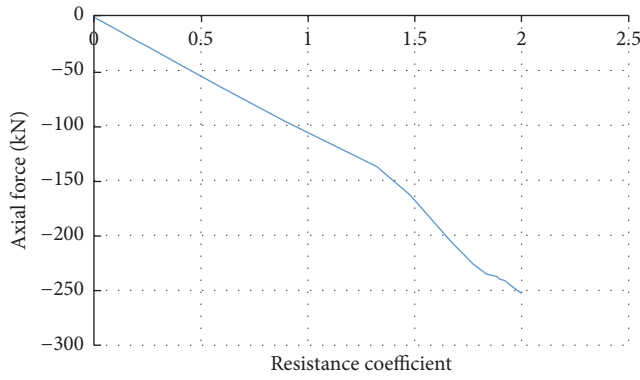


FIGURE 18: Axial force-resistance coefficient curve of the steel beam connected with the removed corner column.

TABLE 3: Beam dimension and corresponding beam-to-column linear stiffness ratios (models (4)–(7)).

Model	Beam dimension (mm) (height × width × web × flange)	Beam-to- column linear stiffness ratios in storeys 1–4 (i_b/i_c)	Beam-to- column linear stiffness ratios in storeys 5–8 (i_b/i_c)
(4)	350 * 250 * 12 * 16	0.143	0.218
(5)	400 * 250 * 14 * 16	0.195	0.292
(6)	400 * 250 * 16 * 24	0.266	0.401
(7)	450 * 250 * 16 * 24	0.421	0.562

removing the bottom middle column are presented in Figure 21.

It can be seen from Figure 21 that the trend of the four curves is consistent. When the structure reaches the failure criterion with the vertical displacement of 0.48 m, the resistance coefficients of the four models are 2.07, 2.58, 2.97, and 3.76, respectively. It indicates that the steel cross section size is closely related to the final progressive collapse bearing capacity of the hybrid frame. The larger the cross section is, the stronger the ultimate resistance of progressive collapse will be. The reason is that the ultimate progressive collapse bearing capacity of the hybrid frame is greatly influenced by

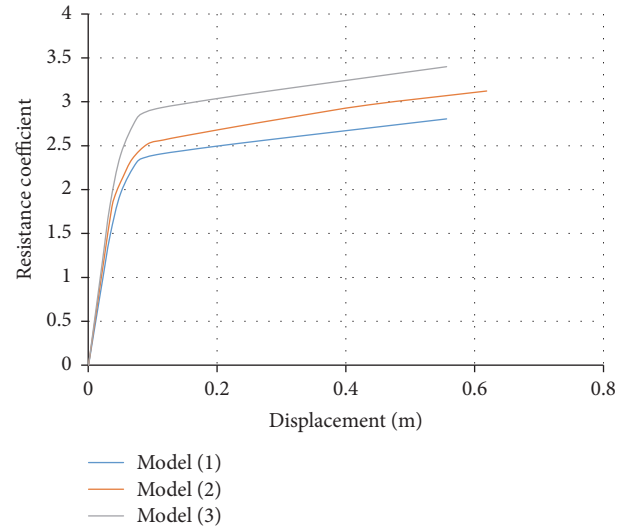


FIGURE 19: Displacement-resistance curve of the three models with different steel ratio after the bottom middle column was removed.

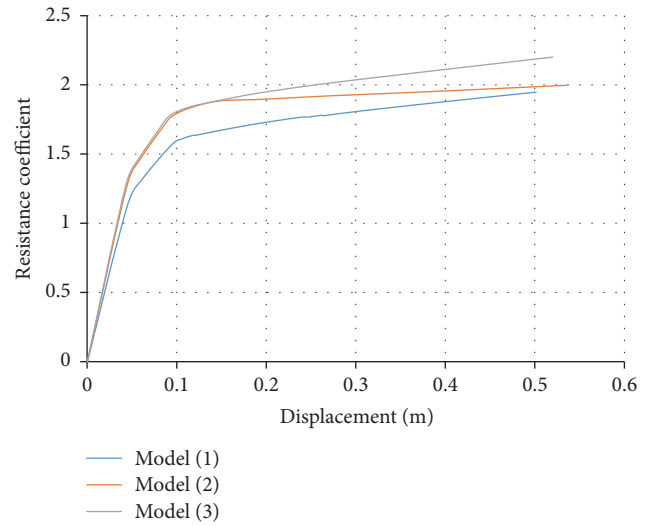


FIGURE 20: Displacement-resistance curve of the three models with different steel ratio after the bottom corner column was removed.

the ultimate moment of the “beam mechanism” stage, which is closely related to the beam section size.

4.2.2. *Removing Bottom Corner Column.* The curves of the vertical displacement versus resistance coefficient of the hybrid structure from the three models (Table 3) after removing the bottom corner column are given in Figure 22. It shows similar trend as Figure 21. With the increase of the cross-sectional dimension of the steel beam, the resistance coefficient of the model increases correspondingly, at values of 0.95, 1.47, 1.96, and 2.63 when the frame reaches the failure criterion. Again it indicates that the progressive collapse behavior of the SRC column-steel beam hybrid frame has a very close relationship with the cross section of the beam. It is worth noting that when the section of steel beam is

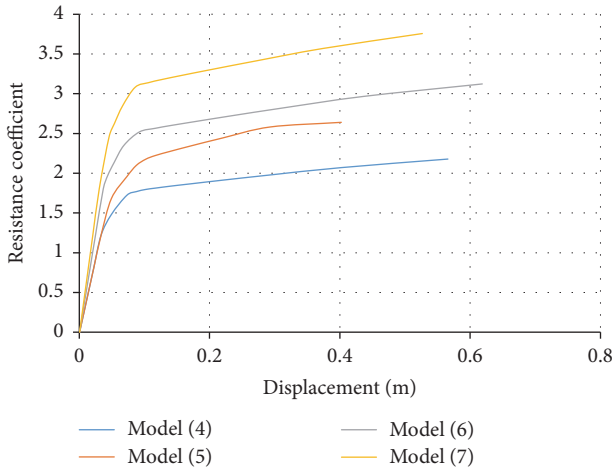


FIGURE 21: Vertical displacement-resistance coefficient relationship of models with different beam parameters after removing the bottom middle column.

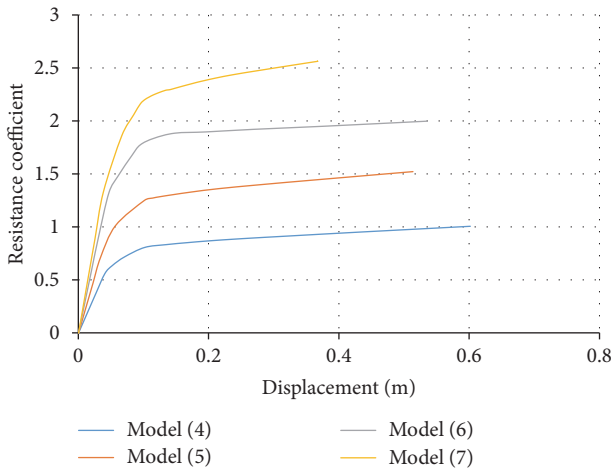


FIGURE 22: The vertical displacement-resistance coefficient relationship of models with different beam parameters after removing the bottom corner column.

350 * 250 * 12 * 16 (the stiffness ratio of beam and column is 0.143), the resistance coefficient is 0.95. That is, after removing the vertical member, the progressive collapse of the hybrid frame will occur under normal load.

4.3. Effect of the Different Vertical Demolition Positions. The effects of the removal of the middle column and the corner column on the progressive collapse behavior and the corresponding collapse mechanism are studied in the previous section; however, both analyses are about removal of the bottom storey column elements. To investigate more the effect of the vertical position of the removal column on the progressive collapse behavior, further pushdown analysis was conducted on the first, fourth, and seventh storey columns to represent the lower, middle, and upper parts of the structure.

Figures 23 and 24 are the curves of the vertical displacement versus the resistance coefficient at the control node for removal of the middle column and the corner column in

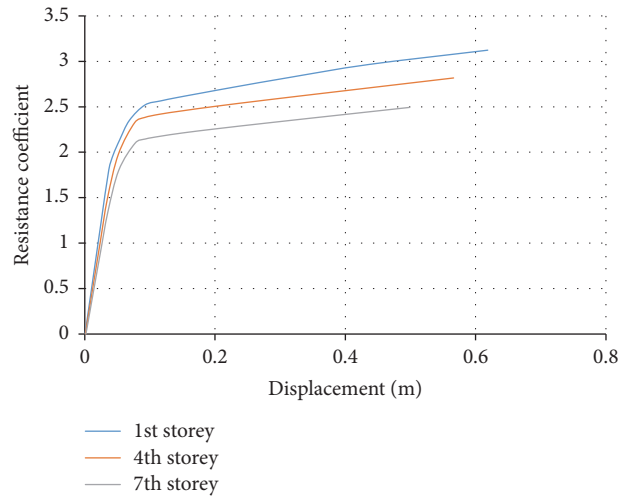


FIGURE 23: Vertical displacement-resistance coefficient curves obtained by removing the middle column in different floors.

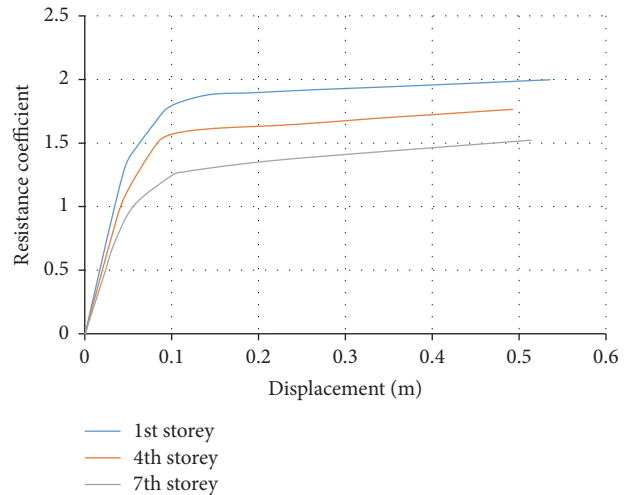


FIGURE 24: Vertical displacement-resistance coefficient curves obtained by removing the corner column in different storeys.

different floors. It can be seen from the curves that, for both middle column and corner column removal, the lower the vertical position of the removed column is, the greater the load resistance coefficient of the structure is at the limit of the failure criterion. It also indicates that the cross section of the column needs to be designed stronger if the lower columns are considered. In addition, the more the beam and column components which can form pull system are in the upper structure, the larger the redundancy is and the more the load transferring path that could be obtained is, and hence more elements can be involved in the process of internal force redistribution.

5. Conclusion

In this paper, the ABAQUS program is used to establish the SRC column-steel beam hybrid frame model, of which the

progressive collapse behavior is studied by both dynamic analysis and the pseudostatic pushdown method. The results of both methods agree well with each other. Some conclusions can be drawn from this investigation.

(1) For the bottom middle column removal case, the SRC column-steel frame has good resistance to progressive collapse under dynamic instantaneous load (impact effect from sudden column collapse). At the beginning of the loading, the progressive collapse resistance of hybrid frame is provided by the bending capacity of the steel beam (beam mechanism). And after the beam reaches its ultimate moment, the frame collapse resistance is provided by the tensile capacity of steel beam (catenary mechanism).

(2) For the bottom corner column removal case, the SRC column-steel frame does not collapse under dynamic instantaneous load (impact effect from sudden column collapse). But its resistance to progressive collapse is relatively smaller than that of middle column being removed. In addition, when the steel beam reaches the ultimate moment, the residual structure cannot bear any more vertical load, and there is no catenary mechanism system formed after the beam mechanism system.

(3) Increasing the steel ratio in the SRC column can slightly improve the progressive collapse bearing capacity of the SRC column-steel beam hybrid structure.

(4) Because the ultimate progressive collapse bearing capacity of the hybrid frame is greatly influenced by the ultimate moment of the “beam mechanism” stage, increasing the cross section of the steel beam can significantly improve the progressive collapse behavior of the hybrid frame.

(5) The lower the position of the removed column in the structure, the better the progressive collapse behavior of hybrid structure system and the greater the load resistance coefficient of the structure.

Conflicts of Interest

The authors declare that there are no conflicts of interest regarding the publication of this paper.

Acknowledgments

The first author would like to express gratitude to the National Natural Science Foundation of China for the financial support (Grant no. 51408556).

References

- [1] C. Pearson and N. Delatte, “Lessons from the progressive collapse of the Ronan Point apartment tower,” in *Proceedings of the 3rd Congress Forensic Engineering*, pp. 191–200, October 2003.
- [2] ASCE7-05, *Minimum Design Loads for Buildings and Other Structures*, American Society of Civil Engineers, Reston, Va, USA, 2005.
- [3] DOD2010, *Design of Structures to Resist Progressive Collapse*, Department of Defense, Washington, DC, USA, 2010.
- [4] United States General Service Administration (GSA), *Progressive Collapse Analysis and Design Guidelines for New Federal Office Buildings and Major Modernization Project*, 2003.
- [5] *Structural Use of Concrete. Part 1: Code of Practice for Design and Construction*, British Standard Institute, 1997.
- [6] D. B. Moore, “The UK and European regulations for accidental actions,” in *Proceedings of the Workshop on Prevention of Progressive Collapse*, National Institute of Building Sciences, Washington, DC, USA, 2002.
- [7] Daft prEN1991-1-7, *Eurocode 1: Actions on Structures. Part 1-7: General Actions—Accidental Actions*, European Committee for Standardization, 2005.
- [8] M.-H. Tsai and B.-H. Lin, “Investigation of progressive collapse resistance and inelastic response for an earthquake-resistant RC building subjected to column failure,” *Engineering Structures*, vol. 30, no. 12, pp. 3619–3628, 2008.
- [9] J. Kim and T. Kim, “Assessment of progressive collapse-resisting capacity of steel moment frames,” *Journal of Constructional Steel Research*, vol. 65, no. 1, pp. 169–179, 2009.
- [10] M. Liu, “A new dynamic increase factor for nonlinear static alternate path analysis of building frames against progressive collapse,” *Engineering Structures*, vol. 48, pp. 666–673, 2013.
- [11] E. Masoero, P. Darò, and B. M. Chiaia, “Progressive collapse of 2D framed structures: an analytical model,” *Engineering Structures*, vol. 54, pp. 94–102, 2013.
- [12] Y. Liang, X. Lu, and Y. Li, “Design method to resist progressive collapse for a three story RC frame,” *Journal of PLA University of Science and Technology*, vol. 8, no. 6, pp. 659–664, 2007 (Chinese).
- [13] W. Yi, Q. He, and Y. Xiao, “Collapse performance of RC frame structure,” *Journal of Building Structures*, vol. 28, no. 5, pp. 104–117, 2007 (Chinese).
- [14] Y. Li, X. Lu, L. Ye, and S. Chen, “Study on progressive-collapse resistance capacity of RC frame structures based on Pushdown analysis,” *Journal of Shenyang Jianzhu University (Natural Science)*, vol. 27, no. 1, pp. 10–18, 2011 (Chinese).
- [15] A. Fascetti, S. K. Kunnath, and N. Nisticò, “Robustness evaluation of RC frame buildings to progressive collapse,” *Engineering Structures*, vol. 86, pp. 242–249, 2015.
- [16] GB 50010-2010, *Code for Design of Concrete Structure*, China Construction Industry Press, Beijing, China, 2010 (Chinese).
- [17] F. Li and G. Zhao, “Study on seismic behavior of composite frame with SRC columns and steel beam,” *Industrial Construction*, vol. 40, no. 9, pp. 111–114, 2010 (Chinese).
- [18] K. Khandelwal and S. El-Tawil, “Pushdown resistance as a measure of robustness in progressive collapse analysis,” *Engineering Structures*, vol. 33, no. 9, pp. 2653–2661, 2011.
- [19] CECS392-2014, *Code for Design of Collapse Resistance of Building Structures*, China Planning Press, Beijing, China, 2014 (Chinese).
- [20] JGJ138-2001, “Technical specification for steel reinforced concrete composite structures,” Tech. Rep., China Architecture Industry Press, Beijing, China, 2002 (Chinese).

Research Article

Source Parameter Estimation Method for Assessment of Structural Resiliencies

Zijun Wang and Boming Zhao

School of Civil Engineering, Beijing Jiaotong University, Beijing, China

Correspondence should be addressed to Boming Zhao; bmzhao@bjtu.edu.cn

Received 21 July 2017; Accepted 1 October 2017; Published 30 October 2017

Academic Editor: Xing Ma

Copyright © 2017 Zijun Wang and Boming Zhao. This is an open access article distributed under the Creative Commons Attribution License, which permits unrestricted use, distribution, and reproduction in any medium, provided the original work is properly cited.

Assessing structural integrity and sustainability during natural hazards, for instance, strong earthquakes, is an effective way to reduce or even avoid large losses of life and property damage. With the established vulnerability relationships between source parameter and building damage, the seismic resilience of structures can be obtained after the source parameter is estimated in the early stage of an earthquake. For this purpose, we propose a method that employs the P wave displacement parameter to estimate earthquake magnitude in real time to quickly assess the structural resiliencies. By selecting period and amplitude parameter as comparisons, the magnitude estimation formulas are derived, respectively, where the proposed P wave displacement parameter method is of the highest precision. Through the evolutionary estimation of the P wave displacement parameter as a function of the time window used, we show that the existing regression relationships can be extended to the large earthquake. Therefore, this paper provides a quick earthquake magnitude estimation method for the establishment of a more reasonable and accurate resilience assessment system for structures.

1. Introduction

Assessing the structural integrity and sustainability during natural hazards, for instance, strong earthquakes, is an effective way to reduce or even avoid large losses of life and property damage. With the established vulnerability relationships between source parameter and building damage, if we can estimate the earthquake's magnitude before the high-intensity shaking occurs, the seismic resilience of structures can be obtained. Earthquake early warning systems [1–4] can provide alerts of impending ground motions within a few seconds to tens of seconds after an earthquake occurs so that appropriate measures can be immediately taken to mitigate seismic risks.

Strong earthquakes occur frequently in Mainland China, where more than 500 earthquakes with magnitude above 6.0 have occurred within 28 provinces from 1900 to the present day. Moreover, the region of earthquake occurrence has increased in size, and events occurred with greater intensity and frequency, meaning that the period of active earthquakes has arrived. These earthquakes destroy buildings and cause

severe losses of life and property. For example, more than eighty thousand deaths or disappearances occurred in the 2008 M_s 8.0 Wenchuan earthquake, which was a major tragedy for the Chinese people. Therefore, it is of great significance to seek an approach through scientific research to mitigate the potential threats associated with earthquake hazards.

In this paper, the P wave displacement parameter (MI_d) method, which uses data from a single station, is then proposed. We additionally select the representative period (τ_c) and the amplitude (P_d) parameters, and we compare the relationships between each of these 3 parameters and the magnitude of the aftershocks of the 2008 M_s 8.0 Wenchuan earthquake. In addition, magnitude estimation formulas are derived and the accuracy of these formulas is explored by comparing the estimated magnitude with the catalog magnitude. Furthermore, we investigate to what degree the initial parameters indicate the Wenchuan mainshock magnitude and analyze the relationships among the expanding time window, the proposed MI_d parameter, and the estimated magnitude. With the established vulnerability relationships

between magnitude and building damage, by quickly predicting the early structural antiseismic capacity from the estimated magnitude, this paper can provide a scientific basis for the establishment of a more reasonable and accurate resilience assessment system for structures.

2. Dataset

A robust input database is essential in identifying reliable regression functions for magnitude estimation using a statistical approach. According to the China Strong Motion Net Centre (CSMNC), after the M_s 8.0 Wenchuan earthquake on May 12, 2008, a total of 383 aftershocks were recorded by the end of 30 September 2008. These events were generated over a rupture length of approximately 300 km with focal depths ranging from 2 to 20 km, and the records were obtained by strong motion seismographs with a dynamic range of ± 2 g, which were mainly installed at free-field sites. The sampling rate was 200 sps.

In this study, we select the mainshock and 43 aftershocks of the 2008 M_s 8.0 Wenchuan earthquake. As criteria, we specify that the selected earthquakes should have magnitude greater than $M_s = 4.0$ and hypocentral distances less than 150 km. Furthermore, each selected event is required to have at least three records to ensure good station coverage and avoid the path effects. Thus, we use a total of 306 acceleration waveforms from the selected events, which demonstrate a large range of focal depths and mechanisms varying from thrust to strike slip.

Since correct picking of P arrivals and ensuring the exclusion of S waves from the analysis are prerequisites for accurately calculating the characteristic parameters, we use the three-step P phase detection method proposed by Wang and Zhao [5], and we double-check the arrival time via manual inspection for each waveform. After performing baseline error correction for the acceleration records, the signals are integrated to velocity records. Moreover, the velocity records are integrated to displacement records, which are required to calculate the parameter values. Then, for real-time applications, a high-pass recursive Butterworth filter with a cutoff frequency of 0.075 Hz is applied to the vertical components to remove the long-period drift that occurs after integration [6].

3. Source Parameter Estimation

3.1. Magnitude Estimation Method. The proposed P wave displacement parameter (MI_d) is defined as the integral of the squared high-pass filtered displacement of the vertical component ground motion, which ranges from 0 to 3 seconds of the initial P wave. The definition of MI_d shows that it is an integral of the squared displacement within the selected time window, which can reflect information with different periods carried by an advancing rupture on a fault plane. As a magnitude estimator, MI_d is a physically fundamental and source-dependent property. Nielsen [7] concluded that the flow rate of elastic energy controls earthquake fracture development and propagation. Fractures with higher initial

energy are more likely to continue propagating over long distances and grow into earthquakes with large magnitude.

To verify the validity of the proposed method, we select the two characteristic parameters that have so far proved to be the most robust, namely, τ_c and P_d [8, 9], for comparison. To correct the calculated MI_d and P_d values for the effects of distance, we normalize them to a reference distance of 80 km, which is the average of the hypocentral distances from the analyzed data set, as the way followed by Zollo et al. [10] and Festa et al. [11]. The final values of MI_d and P_d are referred to as MI_d^{Ref} and P_d^{Ref} , and they can be obtained after preliminary locations are available. Such locations can be determined using real-time procedures and data from a single station; for example, see the methods proposed by Odaka et al. [12] and Horiuchi et al. [13]. We average the characteristic parameters MI_d^{Ref} , τ_c , and P_d^{Ref} from the multiple observation records associated with each event and assume a linear regression model between the catalog magnitude M_s and the averaged parameters as $\log(\text{parameter}) = A + B \times M_s$, where A and B are constants that are to be determined from the regression analysis.

3.2. Relationships between Magnitude and MI_d , τ_c , and P_d . Using the current analytical form, the resulting best-fitting regression relationship between MI_d^{Ref} and the magnitude is given by

$$\log(MI_d^{\text{Ref}}) = -11.175 + 1.218 \times M_s \pm 0.399. \quad (1)$$

The individual data points and the average values of $\log(MI_d^{\text{Ref}})$ as a function of magnitude M_s are shown in Figure 1(a), where SDV means the standard deviation and R stands for the correlation coefficient (similarly hereinafter). The logarithm of the P wave displacement parameter shows a striking linear correlation with earthquake magnitude within the magnitude range considered ($4 \leq M_s \leq 6.5$).

The average period of ground motion τ_c is a measurement of the average period of the P wave within the first few seconds, which is frequently used to estimate magnitude [1]. According to the dataset, the regression relationship between τ_c and magnitude M_s is described by

$$\log(\tau_c) = -1.362 + 0.246 \times M_s \pm 0.148. \quad (2)$$

Since τ_c approximately represents the P wave pulse width, there is a good relationship between the average period of ground motion and the final earthquake magnitude in Figure 1(b).

As for the peak displacement amplitude P_d method, the linear regression relationship between the logarithm of P_d^{Ref} and earthquake magnitude M_s is established as follows:

$$\log(P_d^{\text{Ref}}) = -5.076 + 0.548 \times M_s \pm 0.275. \quad (3)$$

The regression curve in Figure 1(c) shows that P_d^{Ref} is well correlated with earthquake magnitude.

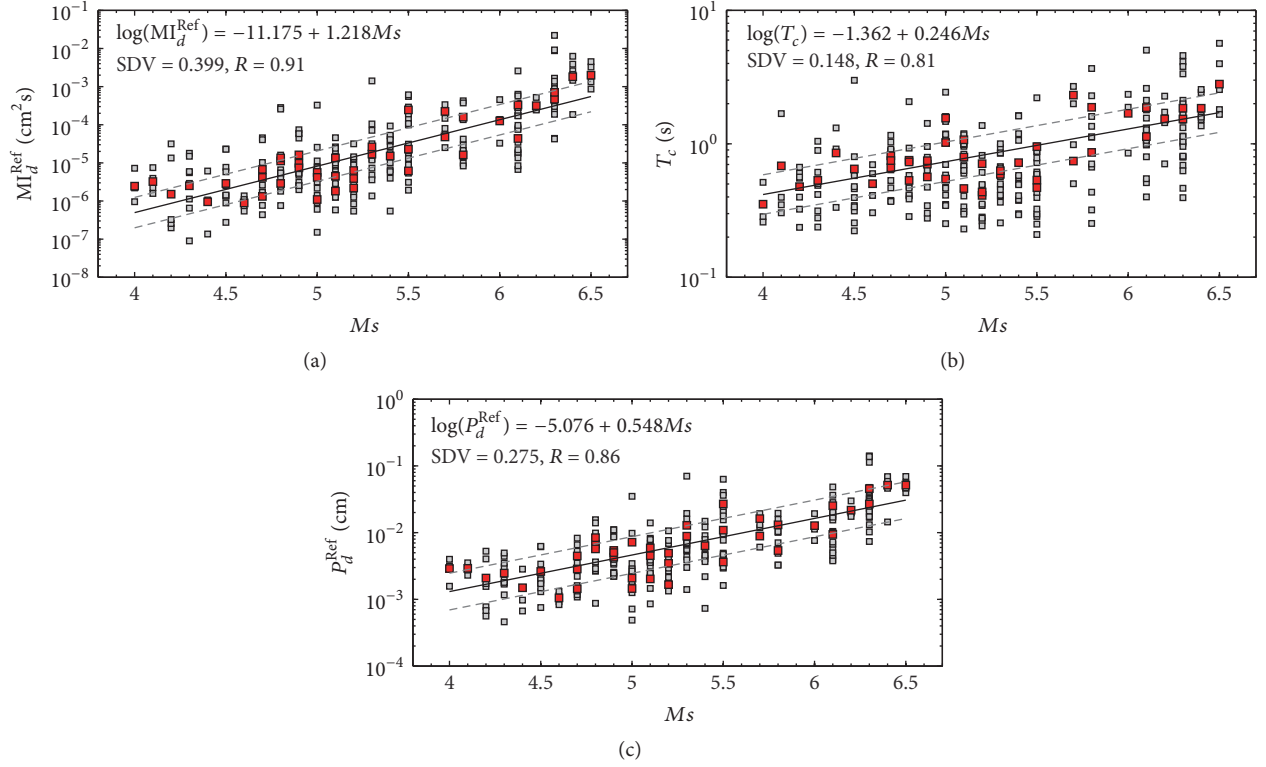


FIGURE 1: (a)–(c) show MI_d^{Ref} , τ_c , and P_d^{Ref} calculated from the first 3 seconds of P wave data (grey squares) and the averaged values (red squares). The magnitude regression relationships determined by this study are shown as solid lines, and the standard deviations are shown as dashed lines.

3.3. Estimated Magnitude Comparison. We can invert the regression results in (1)–(3) to obtain equations for estimating earthquake magnitude from the above 3 characteristic parameters as follows:

$$\begin{aligned}
 M_{MI_d^{\text{Ref}}} &= 9.175 + 0.821 \times \log(MI_d^{\text{Ref}}) \pm 0.328 \\
 M_{\tau_c} &= 5.537 + 4.065 \times \log(\tau_c) \pm 0.603 \\
 M_{P_d^{\text{Ref}}} &= 9.262 + 1.824 \times \log(P_d^{\text{Ref}}) \pm 0.502.
 \end{aligned} \quad (4)$$

We call these 3 estimated magnitude values M_e the P wave displacement parameter magnitude $M_{MI_d^{\text{Ref}}}$, the average period of ground motion magnitude M_{τ_c} , and the peak displacement amplitude magnitude $M_{P_d^{\text{Ref}}}$. Figure 2 shows that the M_e values calculated from (4) display approximately 1:1 relationships with the catalog magnitude M_s using the selected data.

On the 45° line, $M_e = M_s$, and the dashed lines illustrate the one-standard-deviation envelopes. Most of the estimated magnitude values fall within one standard deviation of the regression line. The proposed MI_d^{Ref} is associated with the smallest deviation, that is, 0.328, whereas the corresponding values for M_{τ_c} and $M_{P_d^{\text{Ref}}}$ are 0.603 and 0.502, respectively.

Based on the prediction equations (4), we calculate the differences Δ between the estimated and catalog magnitude values for each record (i.e., $\Delta = M_e - M_s$), which obey

normal distributions. Figure 3 shows histograms that reflect the corresponding frequency distributions. According to the computed probability density curves, the standard deviation associated with the proposed parameter MI_d^{Ref} is the lowest within the effective estimated range, demonstrating that the MI_d method displays the highest reliability and has apparent advantages over the τ_c and P_d methods.

4. Magnitude Estimation for Large Earthquakes

The results above imply that the parameters determined from the first 3-second P wave agree well with the catalog magnitude in the considered range ($4 \leq M_s \leq 6.5$); thus, the regression equations are practicable to estimate the magnitude for earthquakes under 6.5 reliably. However, for large earthquakes, the use of a limited portion of signals allows capturing only the slip contributions from a limited fault portion, which may result in the underestimation of final earthquake magnitude (i.e., the saturation problem) [11, 14].

For the 2008 M_s 8.0 Wenchuan mainshock, there were 32 records available within the criteria (hypocentral distance less than 150 km), which provided us with a unique opportunity to investigate the methodologies up to great earthquakes. We first check the extent to which these characteristic parameters could link the mainshock magnitude using the initial 3-second P wave. Then, we analyze the relationships among

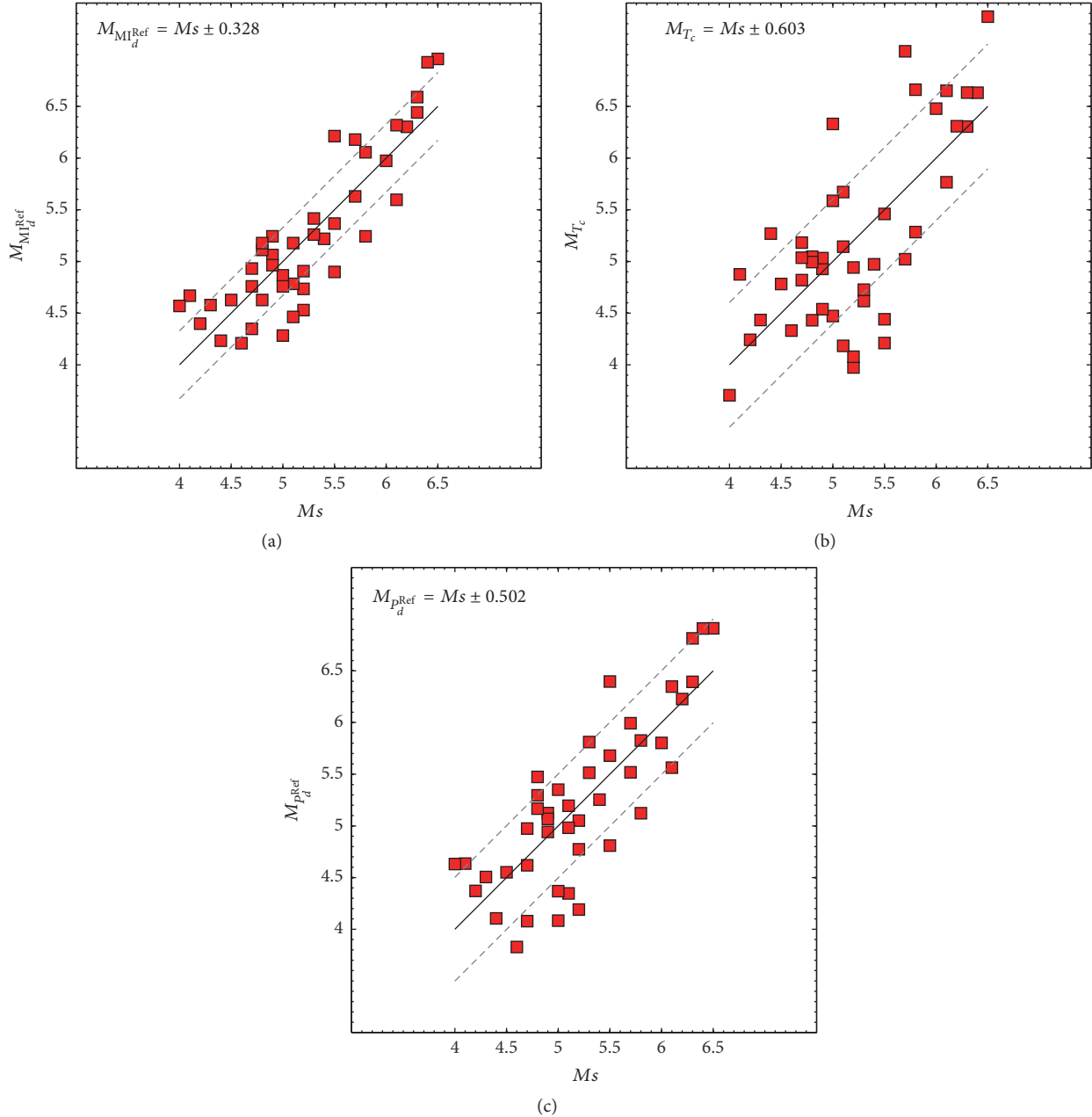


FIGURE 2: Magnitude determined using the 3 characteristic parameters versus the catalog magnitude M_s . Solid lines show the least squares fits, whereas the two dashed lines show the range of one standard deviation.

the increased time window, proposed MI_d , and predicted magnitude.

Together with the mainshock and aftershock records, we establish the correlations between MI_d^{Ref} , τ_c , P_d^{Ref} , and magnitude, respectively (see Figure 4), using the procedure discussed above. According to the regressions, the characteristic parameters derived for the mainshock using the 3-second P wave were all located without the one standard deviation and the anticipated magnitude values were calculated as $M_{MI_d}^{Ref} = 7.18$, $M_{T_c} = 7.05$, and $M_{P_d}^{Ref} = 6.91$, respectively. Although these three parameters all exhibited a saturation problem, the

proposed parameter MI_d was relatively more accurate and of the lowest standard deviation, meaning that it could be a reliable and robust magnitude estimator in the earthquake's early stage.

For the saturation problem in predicting large earthquakes, theoretically, a trade-off strategy between time and accuracy can be considered where better estimations could be obtained by enlarging the observation time window to update the characteristic parameters [15–17]. Since our proposed MI_d had the most accurate estimation for the mainshock with 3-second P wave compared with τ_c and P_d , we further

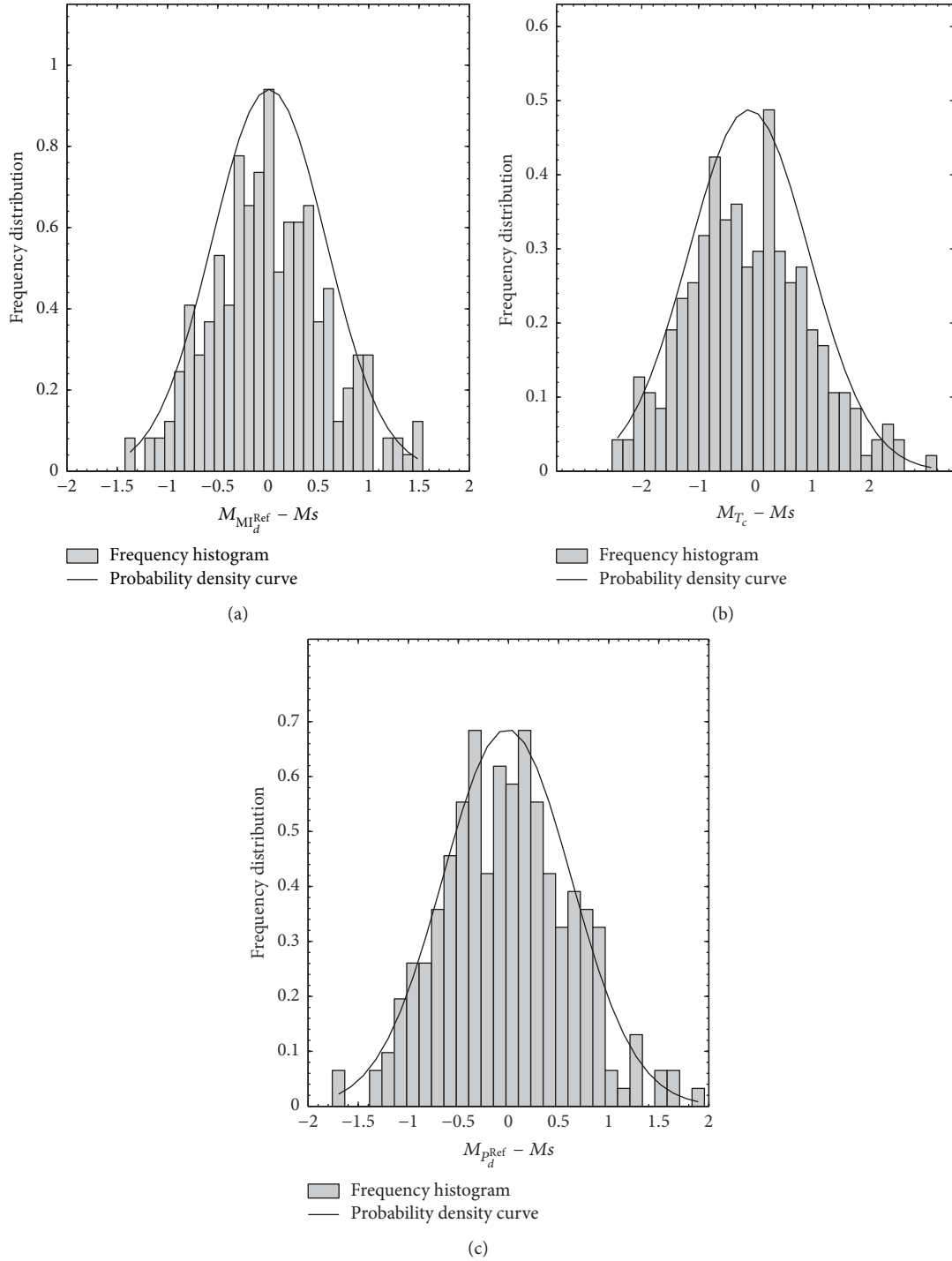


FIGURE 3: Frequency distribution histograms and the corresponding probability density curves of the estimated magnitude differences using each of the 3 characteristic parameters.

investigate MI_d using different time windows ranging from 3 to 10 seconds for all of the available records.

To avoid the S wave contamination while increasing the time window, we compute the theoretical S wave arrival times and exclude from our analysis all the stations for which the estimated S wave arrival occurred within the considered time window. Figure 5 shows that the MI_d^{Ref} magnitude

for the Wenchuan mainshock increases with the length of the P wave records used in determining MI_d^{Ref} . The MI_d^{Ref} growth pattern implies that MI_d^{Ref} determined from the first 6-7 seconds of P wave data may be sufficient to estimate the magnitude of earthquakes of magnitude 8.0. As the window length continues to grow, the magnitude converges at around 8.2. Since the magnitude is estimated only by the

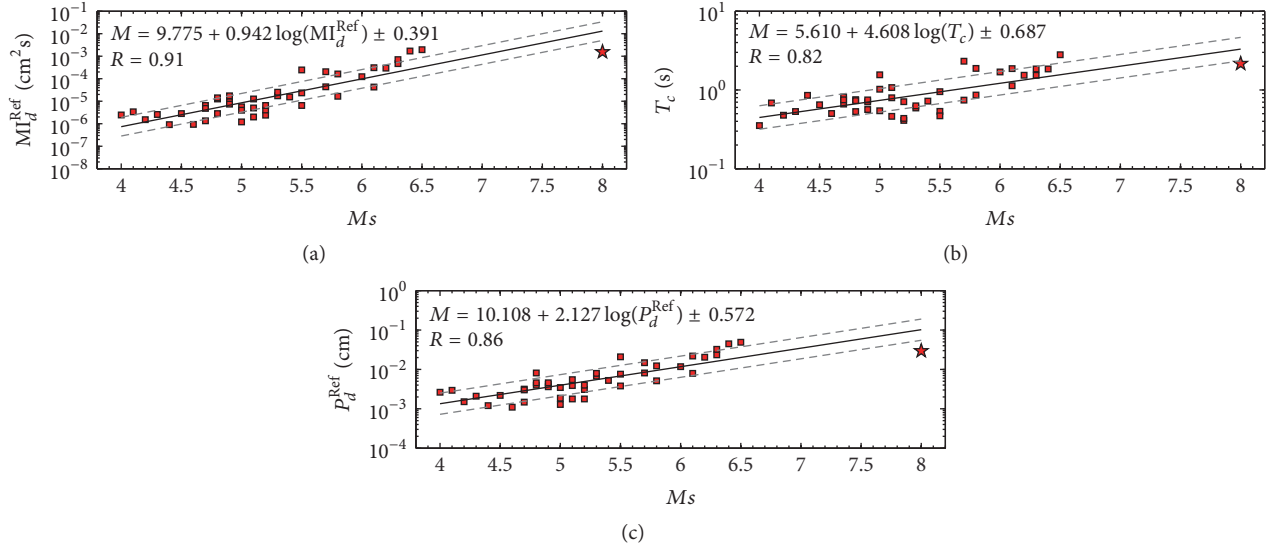


FIGURE 4: Reestablished regressions of catalog magnitude M_s with the 3 characteristic parameters (based on 3 seconds of P wave data) and considering the Wenchuan mainshock (red stars) concurrently. Solid lines show the least squares fits, whereas the two dashed lines show the one-standard-deviation envelopes.

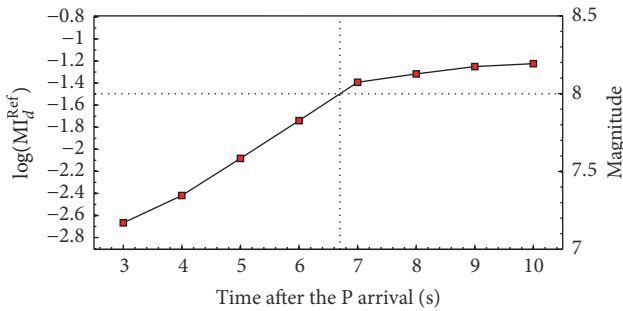


FIGURE 5: Growth in the MI_d^{Ref} parameter (averaged values) for the Wenchuan mainshock versus the lengths of the initial P wave records used. The corresponding magnitude scale is also represented; this scale is derived using the equation shown in Figure 4(a).

initial P wave, the results above illustrate that the parameter MI_d may be an accurate and rapid magnitude estimator for earthquakes with magnitude under 6.5. Moreover, it can also provide stable and accurate estimates for large earthquakes if an appropriately increased time window is used.

5. Discussion and Conclusion

We proposed a method in terms of the P wave displacement parameter (MI_d) to anticipate the magnitude in real time in order to quickly assess the seismic resilience of structures. The MI_d , τ_c , and P_d values for the 43 aftershocks of the 2008 Wenchuan earthquake were calculated and the magnitude estimation formulas from these 3 parameters were derived, respectively. Our result showed that the magnitude obtained from MI_d of 3-second initial P wave agreed well with the catalog magnitude, where the smallest uncertainty was acquired compared with those of τ_c or P_d . With the

established vulnerability relationships between magnitude and building damage, by quickly predicting the early structural antiseismic capacity from the estimated magnitude, this paper can provide a scientific basis for the establishment of a more reasonable and accurate resilience assessment system for structures.

Using only a small portion of the initial P wave signals may cause saturation problems in predicting large earthquakes [18]. In the case of the Wenchuan M_s 8.0 mainshock, using the first 3-second P wave may underestimate the magnitude by about 0.8 to 1.0 unit with the investigated parameters ($M_{MI_d^{\text{Ref}}} = 7.18$, $M_{\tau_c} = 7.05$, and $M_{P_d^{\text{Ref}}} = 6.91$); however, the proposed MI_d was of the best performance. To mitigate this problem, several methodologies use a longer time window of P wave to update magnitude estimates [17, 19]. The evolutionary estimation of MI_d as a function of the time window shows that the existing methodologies and regression relationships can be extended to large earthquakes, and the saturation effect can be removed through the use of time windows of approximately 6-7 seconds with the investigated MI_d parameter.

Conflicts of Interest

The authors declare that there are no conflicts of interest regarding the publication of this paper.

Acknowledgments

This research has been supported by the State Key Program of the National Natural Science Foundation of China (Grant no. U1434210), the National Natural Science Foundation of China (Grants nos. 51778046 and 51278045), and the Project of Shenzhen Metro Group Co., Ltd. (no. SZ-CGM-KY001/2014).

References

- [1] H. Kanamori, "Real-time seismology and earthquake damage mitigation," *Annual Review of Earth and Planetary Sciences*, vol. 33, no. 1, pp. 195–214, 2005.
- [2] G. Wurman, R. M. Allen, and P. Lombard, "Toward earthquake early warning in northern California," *Journal of Geophysical Research: Atmospheres*, vol. 112, no. B8, 2007.
- [3] R. M. Allen, P. Gasparini, O. Kamigaichi, and M. Böse, "The status of earthquake early warning around the World: an introductory overview," *Seismological Research Letters*, vol. 80, no. 5, pp. 682–693, 2009.
- [4] H. S. Kuyuk, R. M. Allen, H. Brown, M. Hellweg, I. Henson, and D. Neuhauser, "Designing a network-based earthquake early warning algorithm for California: ElarmS-2," *Bulletin of the Seismological Society of America*, vol. 104, no. 1, pp. 162–173, 2014.
- [5] Z. Wang and B. Zhao, "Automatic event detection and picking of P, S seismic phases for earthquake early warning and application for the 2008 Wenchuan earthquake," *Soil Dynamics and Earthquake Engineering*, vol. 97, pp. 172–181, 2017.
- [6] Y.-M. Wu and L. Zhao, "Magnitude estimation using the first three seconds P-wave amplitude in earthquake early warning," *Geophysical Research Letters*, vol. 33, no. 16, Article ID L16312, 2006.
- [7] S. Nielsen, "Can earthquake size be controlled by the initial seconds of rupture?" *Earthquake Early Warning Systems*, pp. 9–20, 2007.
- [8] M. Yamada and J. Mori, "Using τ_C to estimate magnitude for earthquake early warning and effects of near-field terms," *Journal of Geophysical Research: Solid Earth*, vol. 114, no. 5, p. B05301, 2009.
- [9] W. Wang, S. Ni, Y. Chen, and H. Kanamori, "Magnitude estimation for early warning applications using the initial part of P waves: A case study on the 2008 Wenchuan sequence," *Geophysical Research Letters*, vol. 36, no. 16, 2009.
- [10] A. Zollo, M. Lancieri, and S. Nielsen, "Earthquake magnitude estimation from peak amplitudes of very early seismic signals on strong motion records," *Geophysical Research Letters*, vol. 33, no. 23, Article ID L23312, 2006.
- [11] G. Festa, A. Zollo, and M. Lancieri, "Earthquake magnitude estimation from early radiated energy," *Geophysical Research Letters*, vol. 35, no. 22, Article ID L22307, 2008.
- [12] T. Odaka, K. Ashiya, S. Tsukada, S. Sato, K. Ohtake, and D. Nozaka, "A new method of quickly estimating epicentral distance and magnitude from a single seismic record," *Bulletin of the Seismological Society of America*, vol. 93, no. 1, pp. 526–532, 2003.
- [13] S. Horiuchi, H. Negishi, K. Abe, A. Kamimura, and Y. Fujinawa, "An automatic processing system for broadcasting earthquake alarms," *Bulletin of the Seismological Society of America*, vol. 95, no. 2, pp. 708–718, 2005.
- [14] C. Cauzzi, Y. Behr, J. Clinton, P. Kästli, L. Elia, and A. Zollo, "An open-source earthquake early warning display," *Seismological Research Letters*, vol. 87, no. 3, pp. 737–742, 2016.
- [15] P. Rydelek, C. Wu, and S. Horiuchi, "Comment on "Earthquake magnitude estimation from peak amplitudes of very early seismic signals on strong motion records" by Aldo Zollo, Maria Lancieri, and Stefan Nielsen," *Geophysical Research Letters*, vol. 34, no. 20, Article ID L20302, 2007.
- [16] I. Iervolino, M. Giorgio, C. Galasso, and G. Manfredi, "Uncertainty in early warning predictions of engineering ground motion parameters: what really matters?" *Geophysical Research Letters*, vol. 36, no. 5, Article ID L00B06, 2009.
- [17] S. Colombelli, A. Zollo, G. Festa, and H. Kanamori, "Early magnitude and potential damage zone estimates for the great Mw 9 Tohoku-Oki earthquake," *Geophysical Research Letters*, vol. 39, no. 22, Article ID L22306, 2012.
- [18] C. Satriano, Y.-M. Wu, A. Zollo, and H. Kanamori, "Earthquake early warning: Concepts, methods and physical grounds," *Soil Dynamics and Earthquake Engineering*, vol. 31, no. 2, pp. 106–118, 2011.
- [19] O. Kamigaichi, M. Saito, K. Doi et al., "Earthquake early warning in Japan: Warning the general public and future prospects," *Seismological Research Letters*, vol. 80, no. 5, pp. 717–726, 2009.

Research Article

Mitigation of Ground Vibration due to Collapse of a Large-Scale Cooling Tower with Novel Application of Materials as Cushions

Feng Lin and Qiheng Zhong

Department of Structural Engineering, Tongji University, Shanghai 200092, China

Correspondence should be addressed to Feng Lin; lin_feng@tongji.edu.cn

Received 18 May 2017; Revised 17 September 2017; Accepted 4 October 2017; Published 25 October 2017

Academic Editor: Mohamed ElGawady

Copyright © 2017 Feng Lin and Qiheng Zhong. This is an open access article distributed under the Creative Commons Attribution License, which permits unrestricted use, distribution, and reproduction in any medium, provided the original work is properly cited.

Ground vibration induced by the collapse of large-scale cooling towers in nuclear power plants (NPPs) has recently been realized as a potential secondary disaster to adjacent nuclear-related facilities with demands for vibration mitigation. The previous concept to design cooling towers and nuclear-related facilities operating in a containment as isolated components in NPPs is inappropriate in a limited site which is the cases for inland NPPs in China. This paper presents a numerical study on the mitigation of ground vibration in a “cooling tower-soil-containment” system via a novel application of two materials acting as cushions underneath cooling towers, that is, foamed concrete and a “tube assembly.” Comprehensive “cooling tower-cushion-soil” models were built with reasonable cushion material models. Computational cases were performed to demonstrate the effect of vibration mitigation using seven earthquake waves. Results found that collapse-induced ground vibrations at a point with a distance of 300 m were reduced in average by 91%, 79%, and 92% in radial, tangential, and vertical directions when foamed concrete was used, and the vibrations at the same point were reduced by 53%, 32%, and 59% when the “tube assembly” was applied, respectively. Therefore, remarkable vibration mitigation was achieved in both cases to enhance the resilience of the “cooling tower-soil-containment” system against the secondary disaster.

1. Introduction

A quantity of nuclear power plants (NPPs) will be built in inland China in the next several years to meet the rapidly increasing energy demand [1]. Consequently, cooling towers were planned for construction as indispensable heat rejection devices in inland NPPs. Most of these cooling towers are large-scale and adjacent to a nuclear island due to economic benefit and site limitations. Their heights have usually been designed to be more than 200 m and the typical spacing to the adjacent nuclear islands is about 300 m [2]. At present, the highest cooling tower worldwide is 200 m high and located at Niederaussem, Germany [3]. For safety's sake, it is reasonable to realize that these huge towers may collapse under accidental loads, for example, earthquakes or strong winds far beyond the design level [4]. The collapse of the towers can induce secondary disasters, for example, intensive ground vibrations featured with a mass of uncertain positions of vibratory sources distributing throughout a large area of

ground surface. For typical case using strongly weathered sandy slate as foundation soil, the maximum acceleration amplitude of ground vibration in radial direction at a distance of 350 m can reach as high as 0.29 g [4]. This will detrimentally affect the safe operation of the close-by nuclear-related facilities and have critical implications of nuclear accidents, as illustrated in Figure 1. However, these risks are not included in the current design concepts of NPPs in which cooling towers and nuclear-related facilities operating in a containment have been designed as fully isolated components [5, 6].

Vibration-related potential risks can be appropriately controlled by reducing the ground vibration to a limited level in the framework of a “cooling tower-soil-containment” system. In practice, several measurements are available to reduce impact-induced ground vibration, for example, soft soil acting as a cushion, an isolation trench, and a recipient isolator [7–9]. Among them, the application of soft materials acting as a cushion layer proved to be both efficient and economical under specific circumstances and was widely used in

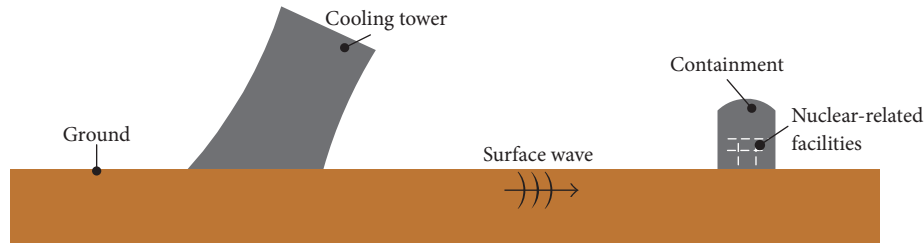


FIGURE 1: Secondary disaster of ground vibration after tower collapse in a “cooling tower-soil-containment” system.

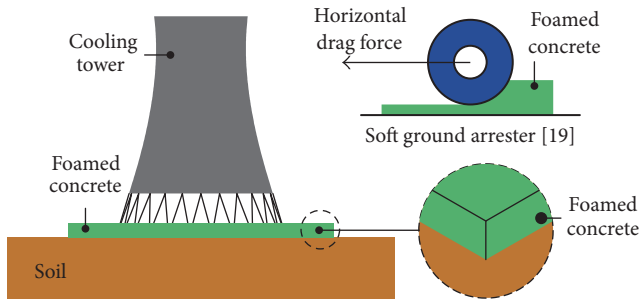


FIGURE 2: Foamed concrete was used as a cushion to reduce ground vibration.

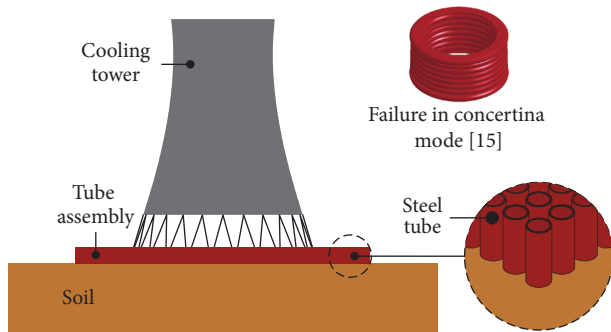


FIGURE 3: “Tube assembly” was used as a cushion to reduce ground vibration.

engineering. For instance, in high-speed railway engineering, rubber bearings were used as resilient elements to reduce train-induced vibrations transmitting to surrounding areas [10, 11]. In similar scenarios of shelters subjected to rock-fall impacts, the dynamic response of the shelters can be significantly reduced when sand cushion or used tire cushion layers were applied [12, 13].

To enhance the resilience of the “cooling tower-soil-containment” system in a disaster scenario, two energy dissipation materials were innovatively applied and acted as a cushion in this study. Figures 2 and 3 illustrate the schematic arrangement of the two materials, that is, foamed concrete and a “tube assembly,” which means a mass of thin-walled circular steel tubes were horizontally arranged to form a type of cellular material. Foamed concrete is a kind of porous material and has been used as soft ground

arresters for an aircraft overrunning the runway accident [19]. As illustrated in Figure 2, both the leading and trailing wheels were hindered by horizontal drag forces provided by the arrester bed. Compared to clay, sand, and water, foamed concrete is appropriate for arresting overrunning aircraft due to its stable mechanical properties over a broad range of temperature, negligible crushing-rebounding behavior, durability, and chemically inert composition [20, 21]. On the other hand, thin-walled circular steel tubes could buckle in a form of progressive folds and fail in concertina mode when subjected to uniaxial compression, as illustrated in Figure 3. The crushing behavior of tubes is associated with high energy absorption capacity [15, 22]. Plastic buckling and the resulting failure modes mainly depend on geometrical parameters, for example, ratios of height to diameter and diameter to thickness. In other words, different geometric parameters can result in failure modes rather than concertina mode, for example, diamond failure mode and Euler failure mode [23]. As far as the authors know, neither material has been used to mitigate impact-related ground vibration in civil infrastructure.

This paper presents a numerical study of novel application of two materials (i.e., foamed concrete and the “tube assembly”) acting as cushions to reduce collapse-induced ground. To achieve this, the behavior of the materials was first investigated. Then, numerical approach to build “cooling tower-cushion-soil” models was presented in detail. Using these models, the collapse of a cooling tower was finally simulated and comparative computation was performed to demonstrate ground vibration reduction by using each cushion. In the simulation, the commercial finite element program ANSYS/LS-DYNA was used [24].

2. Cushion Materials

The ground vibration reduction closely depends on the properties of the cushion material. In case of a cushion impacted by falling fragments of a collapsed tower, the stress-strain relationship of the cushion material under uniaxial compression is critical because the cushion is dominantly under vertical loads. In this study, proper stress-strain relationships of foamed concrete and the “tube assembly” were obtained based on experimental studies in the literature and trial computations using the models presented in Section 3 to achieve appropriate effect of vibration reduction. Cushion heights were adopted as 4 m and 2.4 m for foamed concrete and the “tube assembly,” respectively.

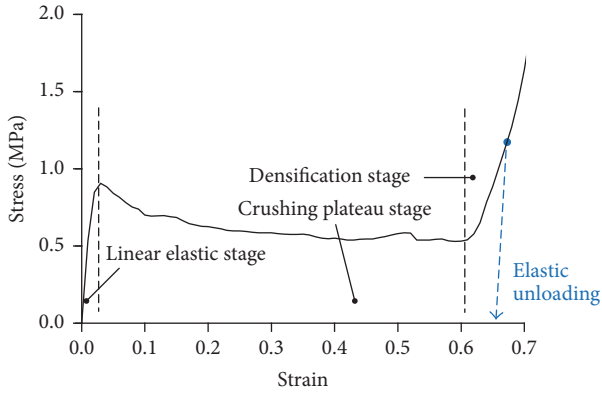


FIGURE 4: Stress-strain curve of foamed concrete under uniaxial compression in tests [14].

2.1. Foamed Concrete. Studies have indicated that the mechanical behavior of foamed concrete under uniaxial compression is primarily dependent on its density and temperature, while being insensitive to strain rate [14]. Foamed concrete with a density of 0.37 g/cm^3 in [14] was chosen for use in this study for vibration mitigation based on trial computations. Figure 4 illustrates the tested stress-strain curves under uniaxial compression, which was chosen for foamed concrete applied in this study. The curve was featured with three stages: the linear elastic stage, crushing plateau stage, and densification stage. The crushing plateau stage is not flat but actually has a negative slope.

A material model with the keyword `*MAT_CRUSHABLE_FOAM` was used, which was provided by the program ANSYS/LS-DYNA and especially applicable to crushable foam-like materials. Poisson's ratio and the damping coefficient of foamed concrete were both set to 0. Its tensile strength was adopted as 0.3 MPa based on the studies in [25]. Elastic behavior was assumed for unloading.

2.2. Tube Assembly. Different from foamed concrete, experimental data or expressions are presently not available to describe the stress-strain relationship of the "tube assembly" under uniaxial compression. Alternatively, its stress-strain relationship was obtained using a numerical approach including following four steps: (1) confirming the finite element method (FEM) based model of the thin-walled tube presented in [15]; (2) determining the material and dimension of an individual thin-walled tube used in the "tube assembly"; (3) understanding the mechanical behavior of individual thin-walled tube under uniaxial compression using the confirmed FEM model; (4) obtaining the stress-strain relationship of an "equivalent tube" in the form of a hexahedron which was actually used in models in Section 3 for the sake of numerical efficiency.

Step 1 (FEM model in [15]). A FEM-based model for small-scale thin-walled steel tubes under uniaxial compression was developed in [15] and verified using experimental results. The modelling approach was rebuilt by the authors to obtain a

TABLE 1: Material parameters for low carbon steel ST12 [15].

Parameter	Value
Density (g/mm^3)	7.85×10^{-3}
Elastic modulus (MPa)	2.1×10^5
Tangent modulus (MPa)	560
Yield strength (MPa)	285
Poisson's ratio	0.3
Parameter C in Cowper-Symonds model (ms^{-1})	2.6
Parameter P in Cowper-Symonds model	5.7

reliable numerical tool. Table 1 presents the material properties of low carbon steel ST12 used in [15]. As an example, Figure 5 compares the force-displacement curve simulated by the authors with the experimental results of the circular tube in [15]. It was found that the concertina failure mode was well simulated and both curves featured the folding or sawtooth form. This feature was due to axisymmetric and sequential folding starting at one end of the thin-walled steel tube under uniaxial compression [15, 23]. In general, the force magnitude in each folding and the amount of folding were well simulated and agreed well with the test data, indicating the efficiency of the FEM model.

Step 2 (material and dimension of individual thin-walled tube used in "tube assembly"). Large-scale thin-walled steel tubes were assumed to construct the "tube assembly" and have the identical material properties to those of low carbon steel ST12 in [15]. Each large-scale tube had an outer diameter of 850 mm, a wall thickness of 20 mm, and a height of 2400 mm. These dimensions were intentionally chosen to have almost identical geometric scales (i.e., ratios of height to diameter and diameter to thickness) to those of circular tubes in [15] to ensure the occurrence of the concertina mode of deformation.

Step 3 (mechanical behavior of individual thin-walled tube under uniaxial compression). The modelling approach in Step 1 was used to build a FEM model for the thin-walled steel tube in Step 2 to understand its mechanical behavior under uniaxial compression. Figure 6 illustrates the FEM model for the thin-walled tube with top and bottom rigid planes. Brick elements (SOLID164) were used to discretize the tube with reduced integration. To control zero energy mode, hourglass control type 4 was adopted with a coefficient set to 0.005. The tube was meshed into 150 vertical "levels," 160 circumferential "strips," and four "layers" in the thickness direction. This resulted in a maximum mesh size of about $16.0 \text{ mm} \times 16.7 \text{ mm} \times 5.0 \text{ mm}$. The material model with the keyword `*MAT_PIECEWISE_LINEAR_PLASTICITY` used in Step 1 was also applied for steel with consideration of strain rate effect. The bottom rigid plane was fixed and the top one was movable with constant downward velocities of 0.5 m/s, 20 m/s, 40 m/s, and 60 m/s, respectively. These velocities fully covered the velocity range of the fragments which impacted ground after the disintegration of the cooling tower in Section 3. The mass and thickness of

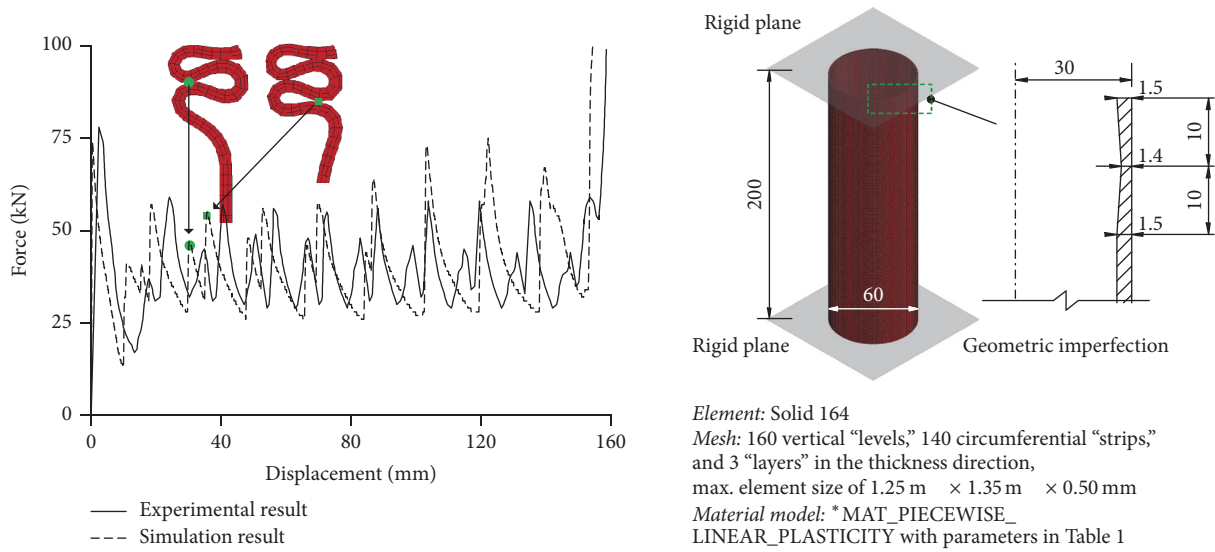


FIGURE 5: Comparison of force-displacement curve simulated by authors with experimental results of the circular tube in [15].

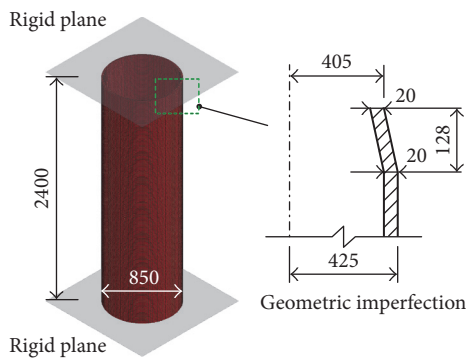


FIGURE 6: FEM model for thin-walled tube.

both planes were negligible. Automatic single surface contact (*CONTACT_AUTOMATIC_SINGLE_SURFACE) was defined between all the parts with friction coefficient set to 0.3 [15]. Figure 7 presents the force-displacement curves of the thin-walled tube under uniaxial compression at different velocities applied by the top plane. The force was the total response of the bottom plane which was critical for ground vibration in Section 3. Results found a regular fluctuation of the forces with increases in compressive deformation, which is a typical response for a thin-walled steel tube under uniaxial compression [15]. In addition, the forces generally increase with increases in compressive velocities, which was also confirmed in [15].

Step 4 (stress-strain relationship of an "equivalent tube"). It was not rational to directly incorporate the refined FEM model for thin-walled tubes in Step 3 in "cooling tower-cushion-soil" models established in Section 3, because this resulted in 4.6×10^9 elements of the cushion associated with enormous numerical consumption. Alternatively, a reasonable solution was to construct an "equivalent tube"

which had the characteristics of (1) discretization with fewer elements, (2) almost identical mechanical behavior to that of thin-walled tube under uniaxial compression, and (3) almost identical impact-induced ground vibration to that of thin-walled tube.

Figure 8(a) illustrates the profile of the "equivalent tube" in the form of a solid hexahedron with a dimension of 850 mm × 850 mm × 2400 mm. The density of the "equivalent tube" was set to 5.66×10^{-4} g/mm³ to ensure that the total mass of an "equivalent tube" was identical to that of a thin-walled tube. Figure 8(a) also presents the force-displacement curves for the "equivalent tube" under uniaxial compression at different velocities of 0.5 m/s, 20 m/s, 40 m/s, and 60 m/s, respectively. These curves are simplified from those in Figure 7 with consideration of (1) retaining the folding characteristic; (2) approximate amount of the folding; and (3) loading-speed-dependent responses. Based on Figures 8(a) and 8(b), the stress-strain curves of the "equivalent tube" under uniaxial compression at different velocities are illustrated.

Impact-induced ground vibrations were compared between the "thin-walled tube-soil" model and "equivalent tube-soil" model, which were illustrated in Figures 9(a) and 9(b), respectively. A rigid plane was set on each tube head with initial downward velocities of 20 m/s, 40 m/s, and 60 m/s, respectively. Their tube feet were tied to the soil surface using the keyword *CONTACT_TIED_SURFACE_TO_SURFACE. The thin-walled tube was modelled using the approach presented in Step 3. The "equivalent tube" was discretized using brick elements with full integration and divided into four elements in vertical direction, resulting in a mesh size of 850 mm × 850 mm × 600 mm. The soil model has a dimension of 120 m × 120 m in plane and 40 m thickness with its modelling strategy described in Section 3 in detail. As an example, Figure 9(c)

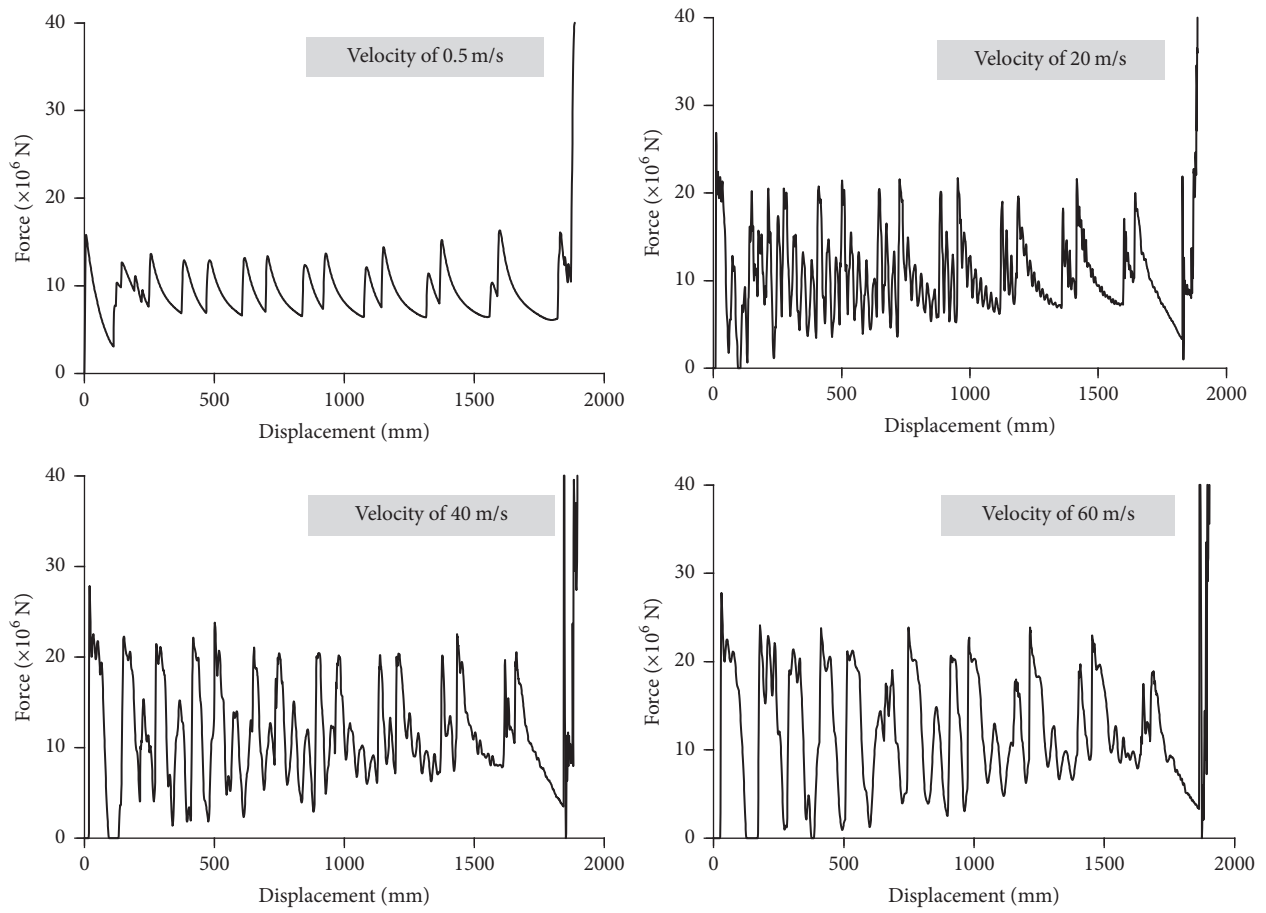


FIGURE 7: Force-displacement curves of thin-walled tube under uniaxial compression at different velocities applied by top plane.

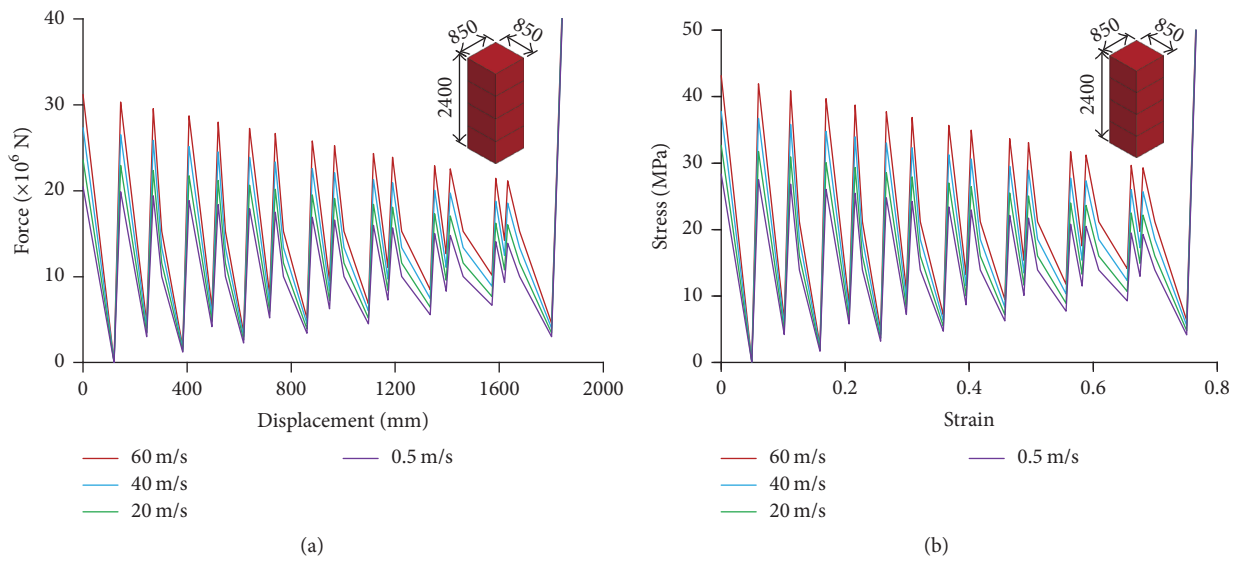


FIGURE 8: (a) Force-displacement curves and (b) stress-strain curves of “equivalent tube” under uniaxial compression at different velocities.

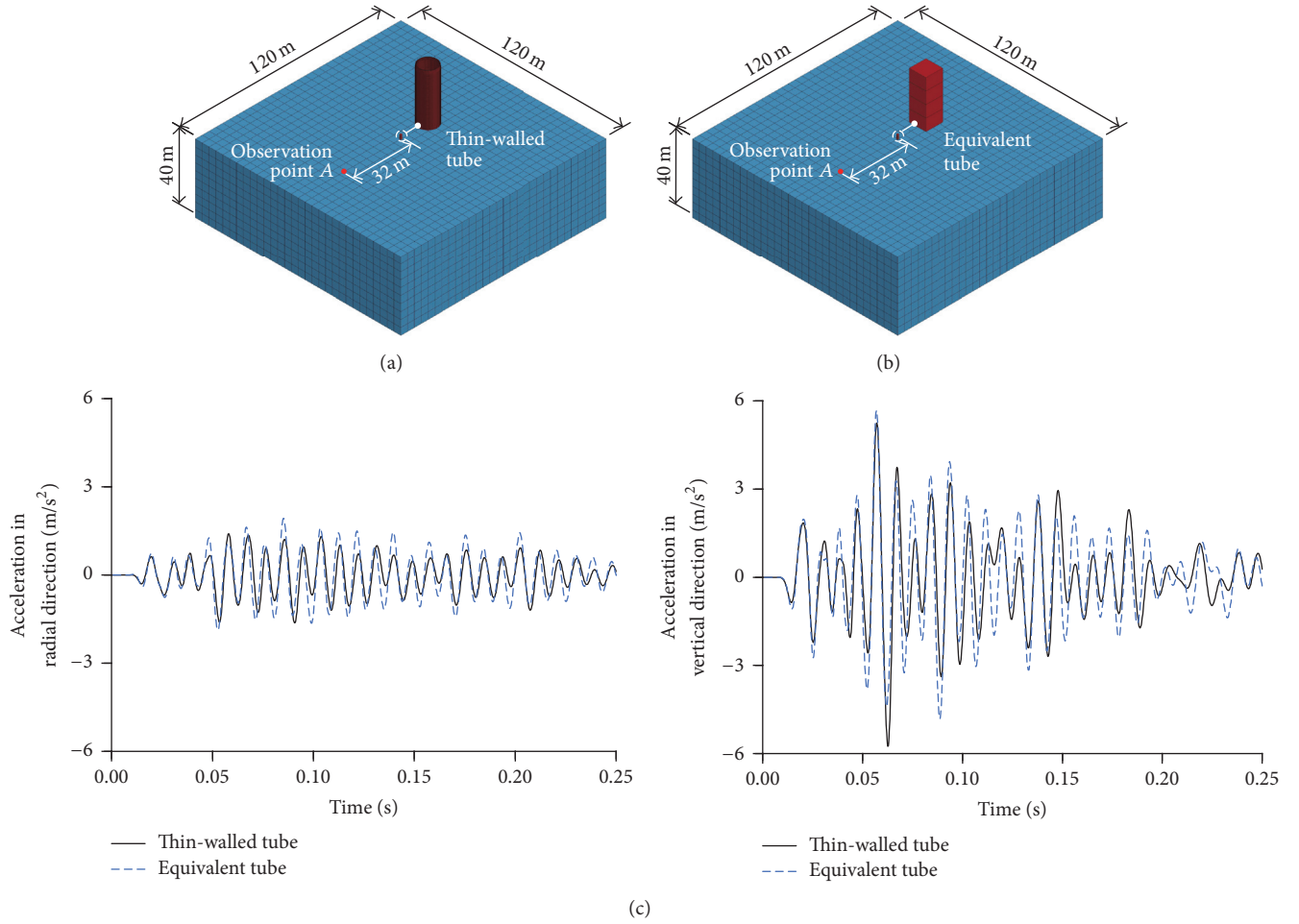


FIGURE 9: (a) “Thin-walled tube-soil” model; (b) “equivalent tube-soil” model; (c) acceleration histories of observation ground point A at a distance of 32 m in radial and vertical directions for the case of initial velocity of 60 m/s.

TABLE 2: Maximum accelerations of observation ground point A in radial and vertical directions at different initial velocities.

Number	Loading of rigid plane			Tube type	Max. acceleration (m/s ²)	
	Velocity (m/s)	Kinetic energy (J)	Mass (kg)		Radial	Vertical
1	20	1.80×10^7	9.00×10^4	Thin-walled tube	1.49	4.20
				Equivalent tube	1.49	4.20
2	40	1.80×10^7	2.25×10^4	Thin-walled tube	1.87	4.96
				Equivalent tube	1.56	4.73
3	60	1.80×10^7	1.00×10^4	Thin-walled tube	1.63	5.75
				Equivalent tube	1.93	5.68

illustrates the computed acceleration histories of observation ground point A at a distance of 32 m in radial and vertical directions for the case of initial velocity of 60 m/s. Table 2 presents the maximum acceleration of point A in radial and vertical directions at different loading velocities. Ground acceleration in tangential direction was too small due to central symmetry and thereby ignored. Results found that similar ground vibrations were achieved using the “thin-walled tube-soil” model and “equivalent tube-soil” model which meant that the “equivalent tubes” could be

incorporated in the “cooling tower-cushion-soil” model in Section 3 to replace the thin-walled tubes.

3. “Cooling Tower-Cushion-Soil” Model

3.1. *Computational Cases.* Three computational cases illustrated in Figure 10 were conducted to compare the vibration reduction by using two materials acting as cushions. Case 1 contained a cooling tower and homogeneous soil with finite dimension to provide a baseline of ground vibration.

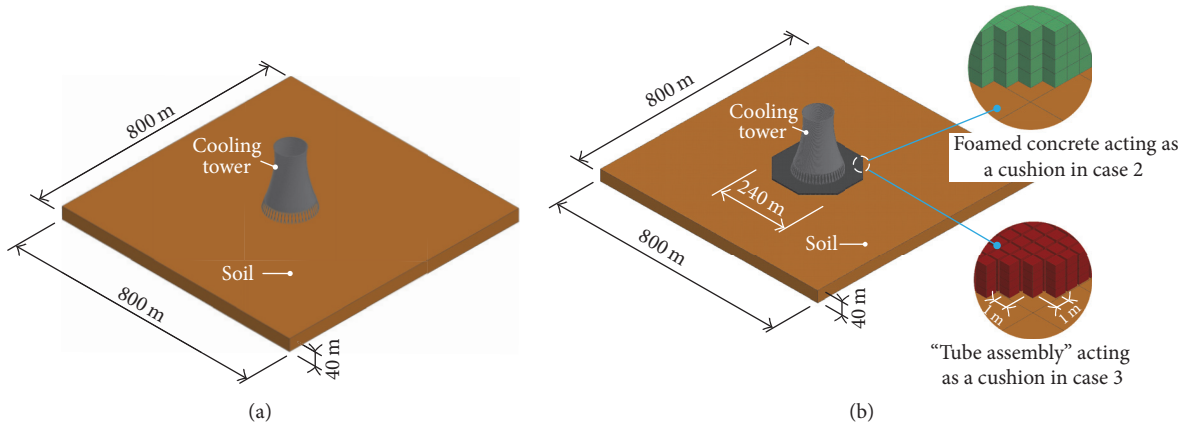


FIGURE 10: (a) Model for computational Case 1; (b) models for computational Cases 2 and 3.

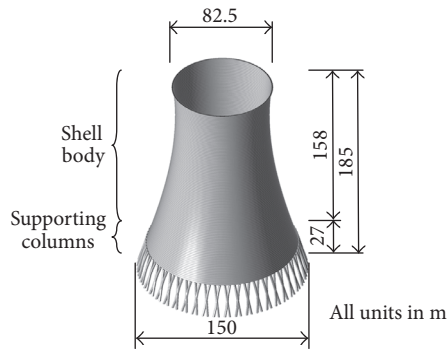


FIGURE 11: Profile of the cooling tower.

<i>Tower Information</i>	
<i>Geometry:</i>	shell thickness: 0.3~1.8 m
	Column: 48 pairs, 1.8 m in diameter
<i>Reinforcement:</i>	circumferential inner side: 0.13~0.74%
	Circumferential outer side: 0.16~1.02%
	Meridional inner side: 0.16~0.91%
	Meridional outer side: 0.18~1.00%
<i>Material: concrete:</i>	elastic modulus: 3.25×10^4 MPa
	Compressive strength: 27 MPa
	Tensile strength: 2.4 MPa
<i>Rebar:</i>	elastic modulus: 2.1×10^5 MPa
	Tangent modulus: 2.1×10^3 MPa
	Yield strength: 345 MPa

No cushion was used in Case 1, while in Cases 2 and 3 foamed concrete and the “tube assembly” were applied as cushion material, respectively. These models did not contain the modelling of nuclear-related facilities and a containment. Actually, a big model to describe the behavior of the integral “cooling tower-soil-containment” system could be built without technical difficulty, however, at the cost of enormous numerical consumption. Alternatively, the containment including nuclear-related facilities could be separately modelled using the ground vibration obtained from “cooling tower-cushion-soil” model as input data with less computational cost. This was beyond the study scope and not demonstrated in this paper.

Figure 11 illustrates the dimension and material parameters of a reinforced concrete cooling tower. The cooling tower was excerpted from a practical project as described in [26] at the Jidong Nuclear Power Station with a height of 185 m including a shell body and supporting columns. The cushions of foamed concrete and the “tube assembly,” with a height of 4 m and 2.4 m, respectively, were both in the planar form of an octagon with an in-circle radius of 120 m. The choice of the planar size was based on the debris area in the collapse simulation of the cooling tower. Foamed concrete was homogeneously constructed to build the cushion and lateral deformation was generally negligible for foamed concrete under uniaxial compression [27]. However, for the cushion

TABLE 3: Soil parameters.

Parameter	Value
Density (g/mm^3)	2.5×10^{-3}
Dynamic shear modulus (MPa)	5150
Poisson's ratio	0.33
Internal friction angle (rad)	0.64
Cohesion (MPa)	1.64
Damping ratio (%)	1.50

of the “tube assembly,” the thin-walled circular tubes with each diameter of 0.85 m were independently arranged with a center-to-center spacing of 1 m, resulting in a minimum gap of 0.15 m between two neighboring tubes, as illustrated in Figure 10. This gap was intentionally reserved so that (1) the folds of a tube under uniaxial compression could freely form without lateral restraint caused by neighboring tubes; thus, (2) the uniaxial compression state of “equivalent tubes” was properly achieved in numerical simulation. The soil belonged to the commonly used moderately weathered sandy slate [28]. Soil parameters are presented in Table 3.

3.2. *Modelling.* Two “cooling tower-cushion-soil” models were developed for Cases 2 and 3, respectively, based on a

TABLE 4: Brief description of “cooling tower-soil” model [2, 4, 8].

Region	Element	Material model	Meshing	Remark
Tower shell	SHELL163	Material models in Eurocode 2 Part 2.1	108 vertical “levels” and 384 meridional “strips,” max. size of 1.2 m × 1.5 m	Proper technique was used to connect shell elements in tower shell and solid elements in columns
Column				
Concrete	SOLID164	Holmquist-Johnson-Cook model	26 vertical “levels” and 4 elements in each “levels,” max. size of 0.6 m × 1.0 m × 1.3 m	Perfect bond between concrete and rebars
Rebar	BEAM161	Plastic kinematic model	Max. size of 1.3 m	
Soil	SOLID164	Drucker-Prager model	Sizes of 4 m × 4 m × 4 m were meshed in soil model with a dimension of 800 m × 800 m (plane) × 40 m (thickness)	Nonreflecting boundaries and damping were set in the soil model

“cooling tower-soil” model which was applicable to Case 1. Previously, the “cooling tower-soil” model was established by the first author and his collaborators to predict the collapse-induced ground vibration using the program ANSYS/LS-DYNA [2, 4, 8]. Table 4 briefly describes the modelling approach for the cooling tower and soil, and more details can be found in [2, 4, 8]. For modelling the cushion of foamed concrete, brick elements with full integration were used to achieve numerical stability with a mesh size of 1 m × 1 m × 1 m. The material model used in Section 2.1 was also applied. For modelling the cushion of the “tube assembly,” 47660 “equivalent tubes” were arranged with each dimension of 0.85 m × 0.85 m × 2.4 m and separated from each other with a center-to-center spacing of 1.0 m. The modelling approach was identical to that presented in Step 4 in Section 2.2. Poisson’s ratio of “equivalent tube” was set to 0. Each cushion was appropriately connected to the soil (*CONTACT_TIED_SURFACE_TO_SURFACE).

Several considerations were also addressed to make the calculation reasonable and efficient [2, 4, 8]. First, the column feet were numerically separated from the soil surface. By doing this, the earthquake wave was input at the element nodes on column feet. Second, collisions acted among shell fragments as well as between a shell fragment and soil during the collapse process. To simulate these, the commonly used penalty function method was used. The parameters were calibrated using impact test results of concrete blocks [29]. Third, for each tube, the top nodes were constrained (*CONSTRAINED_NODE_SET&*BOUNDARY_SPC_SET) so that they move simultaneously only in vertical direction. Fourth, reduced integration was applied in solid elements in the tower column and in the soil model to make the computation efficient, however, accompanied by undesired zero energy modes. To appropriately control these modes, hourglass control type 4 was applied. Finally, in a FEM-based dynamic analysis of wave propagation, the maximum mesh size of the soil model, l_e , should fit the following Eq. (1) [30]:

$$l_e \leq \left(\frac{1}{12} \sim \frac{1}{6} \right) \cdot \lambda_T = \left(\frac{1}{12} \sim \frac{1}{6} \right) \cdot \frac{v}{f_T}, \quad (1)$$

where λ_T is the wave length corresponding to the dominant wave frequency, f_T ; v denotes the propagation velocity of the wave under consideration.

Seven ground motion waves were individually used to cause the cooling tower to collapse and investigate the ground vibration. One of these waves was an artificial earthquake wave that is commonly used in nuclear engineering for seismic design in China. This earthquake wave matched the standard RGl.60 response spectrum proposed by the US Atomic Energy Commission [16] and was denoted as earthquake wave RGl.60 in this study. Figure 12 presents the acceleration history of the earthquake wave RGl.60 in two horizontal directions (X and Y) and vertical direction (Z) with the PGA normalized to 1.0 g. Other six earthquake waves were obtained from the Pacific Earthquake Engineering Research Center [31] with consideration of the soil properties commonly used in NPPs, that is, Coyote Lake (Gilroy Array #1 station), Kobe (Kobe University station), Loma Prieta (Gilroy Array #1 station), Northridge (LA Dam station), San Fernando (Pacoima Dam station), and Whittier Narrows (LA-Wonderland Ave station). The peak ground acceleration (PGA) of these earthquake waves in two horizontal directions and in the vertical directions was first set to 0.3 g, 0.3 g, and 0.2 g (g denotes the acceleration of gravity), respectively. The resulting ratio 0.3 : 0.3 : 0.2 = 1 : 1 : 0.67 was in agreement with the code GB 50267-97 [28]. Each earthquake wave was input on the bottom nodes of the elements on the column feet to shake the cooling tower model. Eventually, incremental inputs were performed gradually with a fixed step increment for PGAs of 0.1 g in two horizontal directions and 0.067 g in the vertical direction until the tower collapsed. In the computation, central difference method was used to solve the dynamic equations with time step controlled by the program and the maximum value of time step being 4×10^{-5} s.

3.3. Model Verification. The “cooling tower-soil” model was verified in several aspects, including (1) the collapse process analysis of a cooling tower model in a column failure test [32] and in a shaking table test [33]; and (2) the in situ monitoring of ground vibration caused by falling weight [8]. In addition, an on-site monitoring of ground vibration induced by the

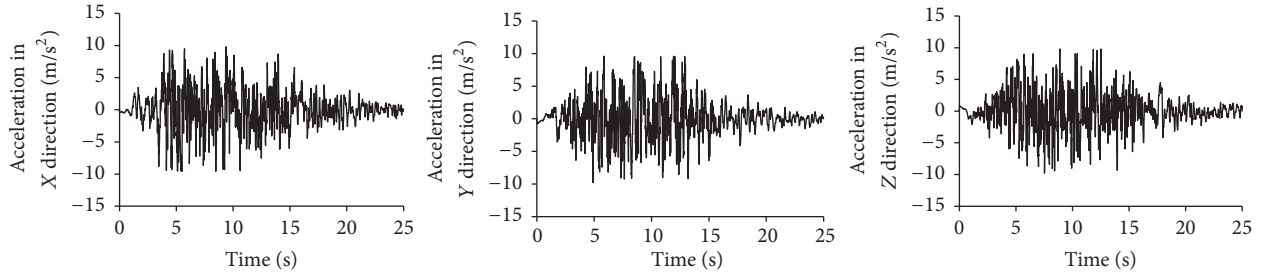
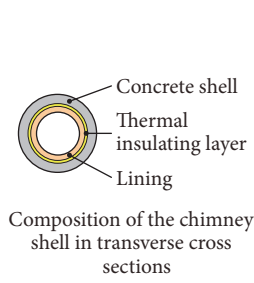
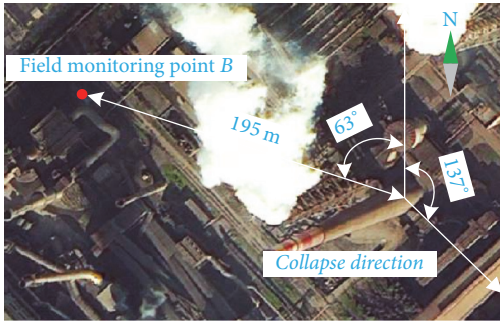


FIGURE 12: Artificial earthquake wave in accordance with RG1.60 response spectrum [16].



Height (m)	Outer radius (mm)	Chimney dimension		
		Concrete shell	Thickness (mm) Thermal insulating layer	Lining
0	9700	700	80	240
30	8500	500	80	240
50	7700	500	80	120
70	7100	400	80	120
110	5900	300	80	120
160	4600	200	80	120
200	3600	400	80	120

FIGURE 13: Profile of the chimney and the position of ground point B where ground vibration was measured [17].

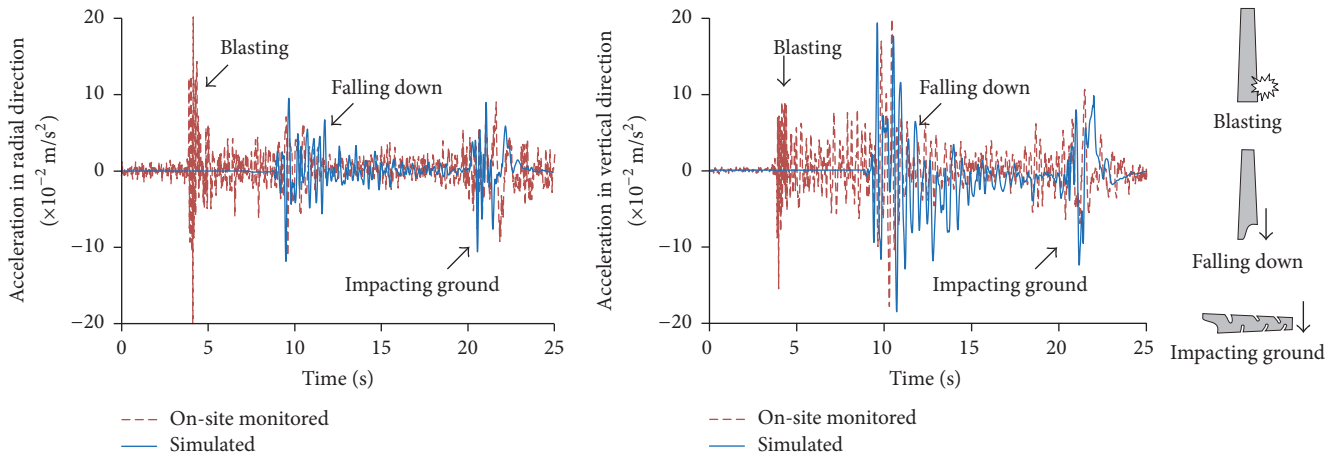


FIGURE 14: On-site monitored and simulated acceleration history of ground vibration at point B in radial and vertical directions [18].

demolition of a reinforced concrete chimney was recently performed by the first author and his collaborators and used herein for model verification [18]. The chimney, located in Shanghai, China, was 200 m high and demolished by controlled blasting. A “chimney-soil” model was built to predict the ground vibration using the identical modelling approach in the “cooling tower-soil” model. Figure 13 presents the bird’s eye view of the chimney, the chimney dimension, and the position of ground point B where ground vibration was monitored [17]. The uniaxial compressive strength of concrete was 23.4 MPa and the yield strength of the reinforcing steel bars was 400 MPa. The reinforcement ratios in the inner and outer sides in circumferential direction were 0.31%–1.1% and 1.1%–3.3%, respectively. Those in meridional

direction were 0.33%–1.3% and 1.1%–2.4%, respectively. The soil density, shear wave velocity, dynamic shear modulus, Poisson’s ratio, cohesion, and internal friction angle were 2200 kg/m³, 244 m/s, 190 MPa, 0.33, 1.64 MPa, and 36.42°, respectively. The chimney was meshed using 64 “levels” in vertical direction and 157 “strips” in meridional direction, resulting in total of 9678 shell elements. The soil model with a dimension of 600 m × 600 m × 35 m was discretized using 20000 solid elements. The elements actually destroyed by blasting were numerically achieved by a “killing” technique provided by the program ANSYS/LS-DYNA. Figure 14 compares the on-site monitored and simulated acceleration histories of ground vibration at point B. Table 5 presents the on-site monitored and simulated acceleration amplitudes of

TABLE 5: Comparison of the on-site measured and simulated maximum acceleration amplitudes of ground vibration at point B^* [18].

Direction	Stage	Amplitude ($\times 10^{-2}$ m/s ²)		
		On-site monitored	Simulated	Error [#]
Vertical	Falling down	19.10	19.65	2.88%
	Impacting ground	10.19	9.93	-2.55%
Radial	Falling down	-10.92	-11.16	2.20%
	Impacting ground	9.06	9.00	-0.67%

*The position of field monitoring point B was indicated in Figure 13. [#]Error = (simulated value – on-site monitored value)/on-site monitored value.

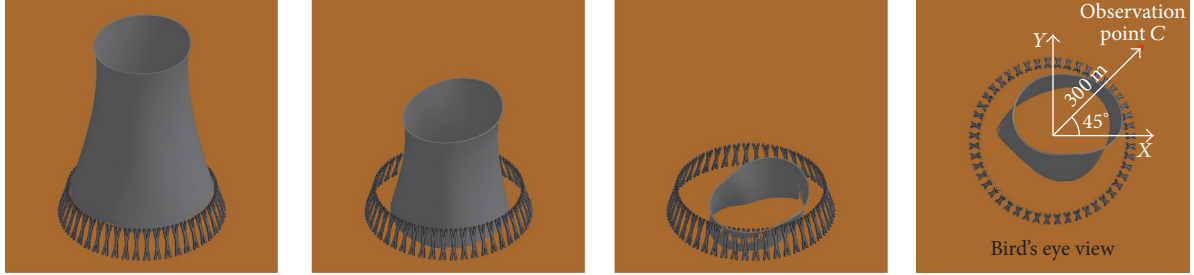


FIGURE 15: Collapse process of the cooling tower under the earthquake wave RG1.60.

ground vibration at point B . Results found that the vibration in the “falling down” and “impacting ground” stages was well predicted with the maximum error of acceleration amplitudes in a range from -2.55% to 2.88% . However, the comparison on the vibration in “blasting” stage was unavailable because the blasting effect was not simulated.

4. Vibration Mitigation

4.1. Collapse of Cooling Tower. The cooling tower survived until a certain PGA of an individual earthquake was reached. As an example, Figure 15 illustrates the collapse process of the cooling tower under the earthquake wave RG1.60 featured with the collapse mode of “collapse in integrity” [8]. A dominant collapse direction and point C at a distance of 300 m for observing ground vibration are also indicated in Figure 15.

4.2. Vibration Mitigation Effect. Figure 16 illustrates the acceleration histories of collapse-induced ground vibrations at point C in radial, tangential, and vertical directions in Cases 1, 2, and 3 for the cooling tower under the earthquake wave RG1.60. Table 6 compares the maximum acceleration amplitudes in radial, tangential, and vertical directions at different distances in Cases 1, 2, and 3 for the cooling tower under seven earthquake waves. In the computation, individual dominant collapse direction for the collapse of the cooling tower under each earthquake wave was used when evaluating ground vibration. Results found that collapse-induced ground vibration was remarkably reduced using each cushion. For the observation point C with a distance of 300 m, which is typical spacing between a cooling tower and adjacent nuclear island in China, the averaged maximum acceleration amplitudes were reduced by 91%, 79%, and 92% in radial, tangential, and vertical directions in Case 2 and 53%, 32%,

and 59% for those in Case 3, respectively. Evidently, in the concerned cases, foamed concrete was more effective than the “tube assembly.” In addition, the vibration reduction became weak with increases in distances.

4.3. Discussion. Three issues are discussed in this subsection, that is, mitigation effect of ground vibration, cushion heights, and comparison of mitigation effect with those in previous studies. The different mitigation effects are attributed to related physical properties (e.g., strength and deformability) and associated dynamic responses of the cushions (e.g., compaction height and energy absorption). Firstly, as illustrated in Figures 4 and 8(b), the strength of foamed concrete averaged about 0.61 MPa and the corresponding values approximately ranged from 13.6 to 20.8 MPa for the “equivalent tube” at different loading velocities. Both cushions had an ultimate strain of about 0.7. In appropriate conditions, a “soft” cushion (e.g., foamed concrete) commonly resulted in a better mitigation effect than a “hard” cushion (e.g., “tube assembly”) did. This has been generally accepted in engineering practice and was confirmed in [4]. In other words, the mitigation effect of two cushions will be similar if their related physical properties (e.g., strength and deformability) are comparable. However, detailed studies are beyond the scope of this study. Secondly and consequently, compaction heights of two cushions compressed by fallen shell fragments were significantly different. Figure 17 illustrates the distribution of compaction heights of two cushions for the cooling tower under the earthquake wave RG1.60. Foamed concrete with a height of 4 m was maximumly compacted by about 3.80 m which meant that the foamed concrete was almost fully compressed in the densification stage in certain places. However, the “tube assembly” was maximumly compacted by about 0.61 m which was remarkably less than the compaction height of the foamed concrete of 3.80 m. Thirdly, the energy

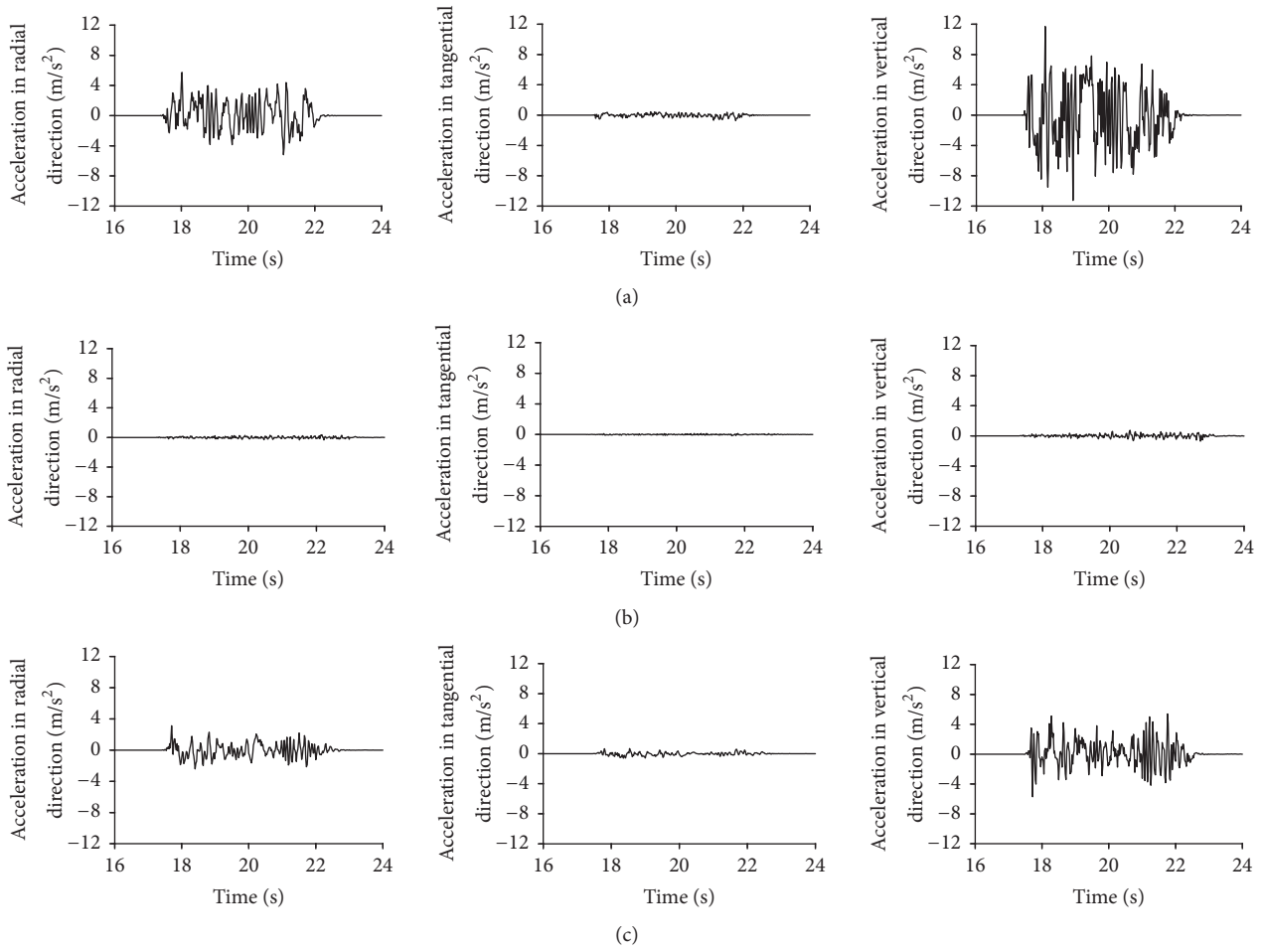


FIGURE 16: Acceleration histories of collapse-induced ground vibration at point C in radial, tangential, and vertical directions at a distance of 300 m in (a) computational Case 1; (b) computational Case 2; (c) computational Case 3 for cooling tower under earthquake wave RG1.60.

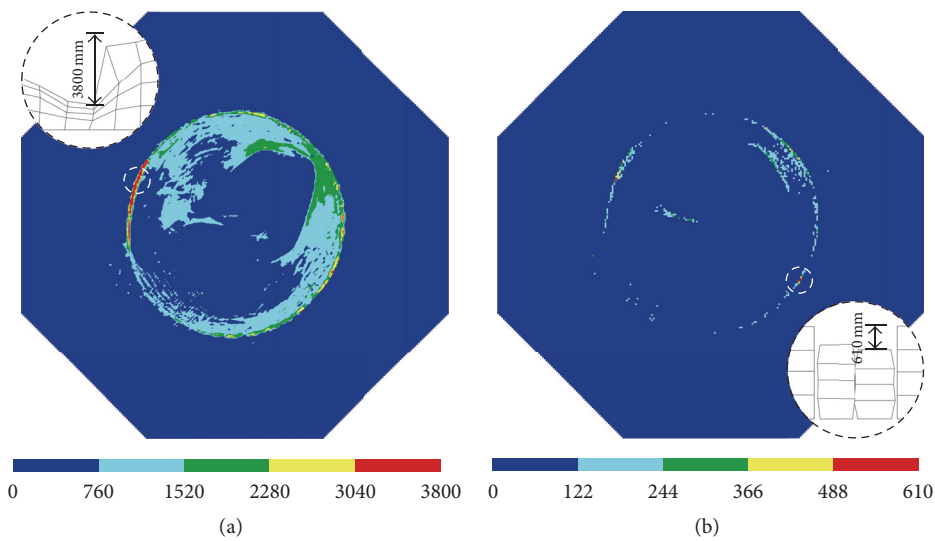


FIGURE 17: Distribution of compaction heights of cushions in (a) computational Case 2 and (b) computational Case 3 for cooling tower under earthquake wave RG1.60.

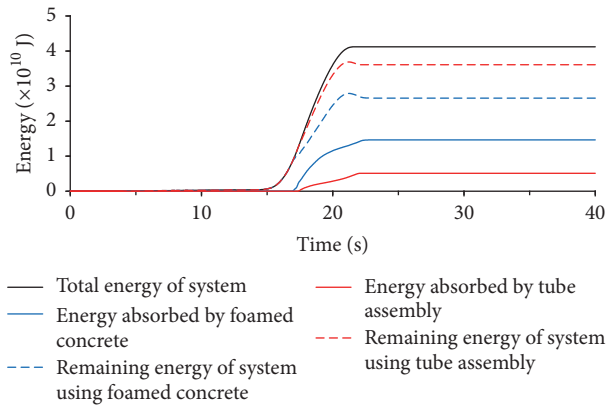


FIGURE 18: Development histories of total energy of the “cooling tower-cushion-soil” system, energy absorbed by cushions, and remaining energy of the system under earthquake wave RG1.60.

absorption capacities of the two cushions were different. Figure 18 illustrates the development histories of the total energy of the “cooling tower-cushion-soil” system, energy absorbed by each cushion, and the remaining energy of the system under the earthquake wave RG1.60. Results revealed that, in the concerned cases, foamed concrete had a higher energy absorption capacity and a less remaining energy than the “tube assembly” did, resulting in a more significant vibration reduction.

The cushion heights of 4 m for foamed concrete and 2.4 m for the “tube assembly” were chosen with consideration of the possible heights of cushions used in practice, available experimental data, and compaction heights impacted by fallen shell fragments. The height of the “tube assembly” was also in conformity with the geometrical parameters of tubes used in previous studies [15], that is, ratios of height to diameter and diameter to thickness. Variation of the geometrical parameters probably led to failure modes rather than concertina failure mode adopted in this study and, therefore, these geometrical parameters were not changed.

The effect of ground vibration reduction using foamed concrete was compared with that using other methods. In [4], a “soft” soil (clay) with a depth of 5 m acting as overlying soil above rock, an active isolation trench with a depth of 20 m, and a passive isolation trench with a depth of 20 m were used to reduce collapse-induced vibration, respectively. The maximum acceleration amplitudes were reduced in a range of 28%–54%, 39%–57%, and 12%–32% at a point with a distance of 350 m, respectively. Generally speaking, for one-time impact-induced ground vibration, the effect of vibration reduction using foamed concrete is more efficient than those using methods of overlying “soft” soil and isolation trenches.

5. Conclusions

A numerical study was performed to investigate the mitigation of collapse-induced ground vibration using two materials acting as cushions, that is, foamed concrete and the “tube assembly” to enhance the resilience of the “cooling tower-soil-containment” system against the postearthquake disaster

in NPPs. These two materials have high energy dissipation capacity and, however, were not found to be used in the field of vibration control. This study demonstrates the enormous potential of the two materials in vibration reduction using seven earthquake waves. For foamed concrete with a height of 4 m, collapse-induced ground vibration at the point at a distance of 300 m was reduced by 91%, 79%, and 92% in radial, tangential, and vertical directions. These values were 53%, 32%, and 59% for the “tube assembly” with a height of 2.4 m. Clearly, a remarkable effect of vibration mitigation was achieved. In the concerned cases, foamed concrete was more efficient than the “tube assembly” and other methods, for example, using overlying “soft” soil and isolation trenches in the previous studies.

An optimization approach is possible, for example, in terms of material properties and height of each cushion. This approach was not performed in this study and will be addressed in future research.

Conflicts of Interest

The authors declare that they have no conflicts of interest.

Acknowledgments

The authors would like to acknowledge financial support from the National Natural Science Foundation of China (Grant no. 51578399).

References

- [1] World Nuclear Association, Nuclear Power, <http://www.world-nuclear.org/information-library/country-profiles/countries-a-f/china-nuclear-power.aspx>.
- [2] F. Lin, H. Ji, Y. Li, Z. Zuo, X. Gu, and Y. Li, “Prediction of ground motion due to the collapse of a large-scale cooling tower under strong earthquakes,” *Soil Dynamics and Earthquake Engineering*, vol. 65, pp. 43–54, 2014.
- [3] D. Busch, R. Harte, W. B. Krätzig, and U. Montag, “New natural draft cooling tower of 200 m of height,” *Engineering Structures*, vol. 24, no. 12, pp. 1509–1521, 2002.
- [4] F. Lin, H. Ji, X. Gu, Y. Li, M. Wang, and T. Lin, “NPP planning based on analysis of ground vibration caused by collapse of large-scale cooling towers,” *Nuclear Engineering and Design*, vol. 295, pp. 27–39, 2015.
- [5] National Nuclear Safety Administration, General safety principles for design of nuclear power plants (HAD102/01), China Legal Publishing House, Beijing, China, 1989.
- [6] International Atomic Energy Agency (IAEA), Seismic design and qualification for nuclear power plants: safety guide, Safety Standards Series No. NS-G-1.6, Vienna, Austria, 2003.
- [7] G. Pflanz, K. Hashimoto, and N. Chouh, “Reduction of structural vibrations induced by a moving load,” *Journal of Applied Mechanics*, vol. 5, pp. 555–563, 2002.
- [8] F. Lin, Y. Li, X. Gu, X. Zhao, and D. Tang, “Prediction of ground vibration due to the collapse of a 235 m high cooling tower under accidental loads,” *Nuclear Engineering and Design*, vol. 258, pp. 89–101, 2013.

- [9] M. Srbulov, "Ground vibration engineering: Simplified analyses with case studies and examples," *Geotechnical, Geological and Earthquake Engineering*, vol. 12, pp. 1–230, 2010.
- [10] G. P. Wilson, H. J. Saurenman, and J. T. Nelson, "Control of ground-borne noise and vibration," *Journal of Sound and Vibration*, vol. 87, no. 2, pp. 339–350, 1983.
- [11] C.-M. Kuo, C.-H. Huang, and Y.-Y. Chen, "Vibration characteristics of floating slab track," *Journal of Sound and Vibration*, vol. 317, no. 3-5, pp. 1017–1034, 2008.
- [12] A. Q. Bhatti, "Falling-weight impact response for prototype RC type rock-shed with sand cushion," *Materials and Structures/Materiaux et Constructions*, vol. 48, no. 10, pp. 3367–3375, 2015.
- [13] J. Sun, Z. Chu, Y. Liu, W. Luo, and M. Wang, "Performance of Used Tire Cushion Layer under Rockfall Impact," *Shock and Vibration*, vol. 2016, Article ID 8760592, 2016.
- [14] H. Guo, W. Guo, and Y. Shi, "Computational modeling of the mechanical response of lightweight foamed concrete over a wide range of temperatures and strain rates," *Construction and Building Materials*, vol. 96, pp. 622–631, 2015.
- [15] X. Zhang, H. Zhang, and Z. Wen, "Axial crushing of tapered circular tubes with graded thickness," *International Journal of Mechanical Sciences*, vol. 92, pp. 12–23, 2015.
- [16] U.S. Atomic Energy Commission, Design Response Spectra for Seismic Design of Nuclear Plants (Regulatory Guide 1. 60), Washington, D.C., 1974.
- [17] Z.-X. Yang, "Controlled blasting scheme for reinforced concrete chimney," Department of Controlled Blasting of PLA University of Science and Technology, Nanjing, China, 2014.
- [18] W. Jiang and F. Lin, "Numerical simulation on ground vibration caused by the demolition of a 200 m high chimney," in *Vibroengineering PROCEDIA*, pp. 288–292, LVE International LTD., Kaunas, Lithuania, 2016.
- [19] Z. Q. Zhang, J. L. Yang, and Q. M. Li, "An analytical model of foamed concrete aircraft arresting system," *International Journal of Impact Engineering*, vol. 61, pp. 1–12, 2013.
- [20] R. F. Cook, "Soft-ground aircraft arresting systems," Tech. Rep. FAA/PM-87e27, Federal Aviation Administration, Washington, D.C., USA, 1987.
- [21] J. C. White and S. K. Agrawal, "Soft ground arresting system for airports," Tech. Rep. CT-93-80, Federal Aviation Administration, Washington, D.C., USA, 1993.
- [22] A. Pugsley and M. Macaulay, "The large-scale crumpling of thin cylindrical columns," *The Quarterly Journal of Mechanics and Applied Mathematics*, vol. 13, pp. 1–9, 1960.
- [23] K. R. F. Andrews, G. L. England, and E. Ghani, "Classification of the axial collapse of cylindrical tubes under quasi-static loading," *International Journal of Mechanical Sciences*, vol. 25, no. 9-10, pp. 687–696, 1983.
- [24] J. O. Hallquist Livermore Software Technology Corporation, Livermore, Calif, USA, 2006.
- [25] Y. H. Mugahed Amran, N. Farzadnia, and A. A. Abang Ali, "Properties and applications of foamed concrete; a review," *Construction & Building Materials*, vol. 101, pp. 990–1005, 2015.
- [26] Northeast Electric Power Design Institute Co., Ltd. of China Power Engineering Consulting Group, Study report on air cooling system and turbine of Jidong Nuclear Power Station. Changchun, China, 2016.
- [27] M. Avalle, G. Belingardi, and A. Ibba, "Mechanical models of cellular solids: Parameters identification from experimental tests," *International Journal of Impact Engineering*, vol. 34, no. 1, pp. 3–27, 2007.
- [28] *Standardization Administration of the People's Republic of China, Code for seismic design of nuclear power plants (GB 50267-97)*, China Planning Press, Beijing, China, 1998.
- [29] F. Lin and Y. Zhang, "An impulse-based model for impact between two concrete blocks," *International Journal of Impact Engineering*, vol. 107, pp. 96–107, 2017.
- [30] E. Kausel and G. Manolis, *Wave Motion in Earthquake Engineering*, WIT Press, Boston, USA, 2000.
- [31] The Pacific Earthquake Engineering Research Center, <http://ngawest2.berkeley.edu/T>, 2017.
- [32] X. Gu, Q. Yu, Y. Li, and F. Lin, "Collapse process analysis of reinforced concrete super-large cooling towers induced by failure of columns," *Journal of Performance of Constructed Facilities*, vol. 31, no. 5, 2017.
- [33] Q.-Q. Yu, X.-L. Gu, Y. Li, and F. Lin, "Collapse-resistant performance of super-large cooling towers subjected to seismic actions," *Engineering Structures*, vol. 108, pp. 77–89, 2016.

Research Article

Shake Table Study on the Effect of Mainshock-Aftershock Sequences on Structures with SFSI

Xiaoyang Qin and Nawawi Chow

Department of Civil and Environmental Engineering, The University of Auckland, 20 Symonds Street, Auckland, New Zealand

Correspondence should be addressed to Xiaoyang Qin; xqin009@aucklanduni.ac.nz

Received 10 July 2017; Accepted 19 September 2017; Published 23 October 2017

Academic Editor: Ivo Calò

Copyright © 2017 Xiaoyang Qin and Nawawi Chow. This is an open access article distributed under the Creative Commons Attribution License, which permits unrestricted use, distribution, and reproduction in any medium, provided the original work is properly cited.

Observations from recent earthquakes have emphasised the need for a better understanding of the effects of structure-footing-soil interaction on the response of structures. In order to incorporate the influences of soil, a laminar box can be used to contain the soil during experiments. The laminar box simulates field boundary conditions by allowing the soil to shear during shake table tests. A holistic response of a structure and supporting soil can thus be obtained by placing a model structure on the surface of the soil in the laminar box. This work reveals the response of structure with SFSI under mainshock and aftershock earthquake sequences. A large (2 m by 2 m) laminar box, capable of simulating the behaviour of both dry and saturated soils, was constructed. A model structure was placed on dry sand in the laminar box. The setup was excited by a sequence of earthquake excitations. The first excitation was used to obtain the response of the model on sand under the mainshock of an earthquake. The second and third excitations represented the first and second aftershocks, respectively.

1. Introduction

During an earthquake, the movement of soil causes movement of structures and this structural response, in turn, influences the movement of soil. This structure-footing-soil interaction (SFSI) can cause the seismic response of a structure to be different from that of an identical structure with an idealised fixed base assumption. This process may also cause the response of the soil to be different from what would be measured under free-field conditions, that is, without the structure. Observations from recent earthquakes, including those from the 2010-2011 Canterbury earthquakes, have identified a significant influence that the behaviour of soil can have on the overall seismic performance of structures.

By carrying out experiments, a more realistic simulation of the structural response with SFSI can be achieved. This not only allows researchers to understand the effects of SFSI but also it enables validation and improvement of numerical models. An early contribution to the understanding of SFSI was the presented example by Taylor et al. [1], where cyclic displacements were applied to a number of model footings seated on clay and sand. The results suggested that the soil

beneath the footing can be intentionally designed to deform beyond the elastic limit in strong earthquakes. This nonlinear soil behaviour can activate rigid body movements of the structure. As a consequent, a development of plastic hinge in the structure could be avoided. As discussed by Veletsos and Meek [2], the flexible ground can act as a damper by absorbing a large part of the vibration energy arising from earthquakes and thus can reduce the seismic response of a structure. Larkin [3] also concluded that the flexibility of the supporting soil can lengthen the vibration period of the structure-footing-soil system and result in a variation of structural response when compared to those obtained from analyses without considering SFSI.

On the other hand, the deformation of soil under footing rotation can sometimes result in the temporary uplift of footings. Deng et al. [4, 5] conducted centrifuge tests on single-degree-of-freedom (SDOF) bridge structures of various footing sizes, and Algie et al. [6] carried out dynamic field tests on a rocking shallow footing. The results of these investigations emphasised that footing uplift and nonlinear soil behaviour should be taken into consideration in seismic design. Recently, the effects of uplift on the response of liquid

storage tanks structures and nuclear plants have also been studied [7–11]. Qin et al. [12] studied the influence of footing uplift on the induced vibration of secondary structures. It was reported that footing uplift can not only reduce the response of structures but also reduce the induced vibrations of secondary structures. Larkin et al. [13] studied the response of structure considering adjacent structures.

Experimental simulation of the structural response with uplift on soil support depends on the correct replication of soil response during earthquakes. This can be achieved throughout the use of a laminar box. Laminar boxes are designed to simulate soil deformation conditions in situ and thus allow the soil to undergo shear deformation during a shake table test. Some of the characteristics that make laminar box tests preferable to other experimental methods, for example, field tests, are as follows [14]:

- (i) The ability to simulate boundary conditions of soil in situ
- (ii) The capacity to test soil specimens that are larger than the typical small-scale laboratory experiments like triaxial test
- (iii) Being able to explore the behaviour of soils in nonuniform, layered, and sloping sites
- (iv) The ability to reproduce the seismic response of structure and soil as one holistic system

Researchers have designed various types of laminar boxes in the past. A very simple laminar box was utilised by Latha and Krishna [15] in their study. This small box was rectangular in plan with internal dimensions of $0.5\text{ m} \times 1\text{ m} \times 0.8\text{ m}$. The box consisted of 15 laminar layers, constructed from pieces of hollow aluminium rectangular sections. The layers were separated by linear roller bearings to minimise friction. A more complicated laminar box was described by Ueng et al. [16]. This box was designed to undergo two-dimensional shaking and hence was called a biaxial laminar box. The box was rectangular in plan and had internal dimensions of $1.88\text{ m} \times 1.88\text{ m} \times 1.52\text{ m}$. It was made up of 15 horizontal layers and had a special sliding system which allowed movements in the horizontal plane. The layers were supported by a rigid steel structure which surrounded the entire box. The inside of this biaxial box was sealed with a 2 mm thick silicone rubber membrane which allowed for the testing of both dry and wet soils.

Study of structural response with SFSI focuses on the effect of the mainshock of the earthquake. Although the consequence of aftershock has been reported after many earthquake events, the structural response with SFSI in the aftershock event has not been studied. In this study, which is a part of the doctoral thesis of Qin [14], a laminar box large in horizontal areal extent was constructed. A SDOF model placed on sand in the box was considered. The responses of the model under the mainshock and aftershocks of an earthquake were compared.



FIGURE 1: The laminar box on the shake table.

2. Design of Large Laminar Box

A laminar box should accommodate the movement of soil and neither resists nor promotes soil displacement. The design of the large laminar box involved identification and consideration of the issues important to the performance of the box. These included inertia, friction, membrane effects, and boundary/corner effects [17]. The inertia of a heavy container can alter the movement of soil within the container that the soil-container system no longer simulates the soil movements in free-field condition. To minimise this effect, the laminar layers should be of relatively low mass [16]. In view of this, a lightweight material had to be chosen for the laminar layers. To ensure that the box would not resist soil movements, a sliding system had to be developed to allow the layers to move with as little frictional resistance as possible. Since the laminar box will also be used to test saturated soils to study the effect of soil liquefaction, a waterproof membrane was used. It had to be designed of sufficiently high flexibility to avoid any influence on the response of the soil [17].

The boundary effects are typically localised along the edges of the box. At the centre of the soil mass, the effects are usually not significant at the centre. Thus, the laminar box was designed with a large surface area to ensure that a suitable volume of soil at the centre of the overall mass would remain unaffected by boundary/corner effects. Other factors such as the availability of materials, cost, and ease of construction/repair were also considered during the design process. Active earth pressures [18, 19] were computed assuming that the entire box was filled with saturated soil. All components of the box were then designed to withstand the predicted loading. The final assembly of the large laminar box is shown in Figure 1. This box will be placed on a shake table and excited along its longitudinal axis. The final part of the design involved evaluating the structural integrity of all components of the box.

The laminar box has internal dimensions of $2\text{ m} \times 2\text{ m} \times 2\text{ m}$. Each laminar layer can move horizontally, in the direction of the excitation, up to 175 mm. The soil inside the box can undergo a maximum shear strain of approximately 9%, which is enough to simulate the in site epicentral displacement of soil under a large earthquake event. The box consists of three major components, that is, the base including barrier columns, the stack of laminar layers, and the membrane.

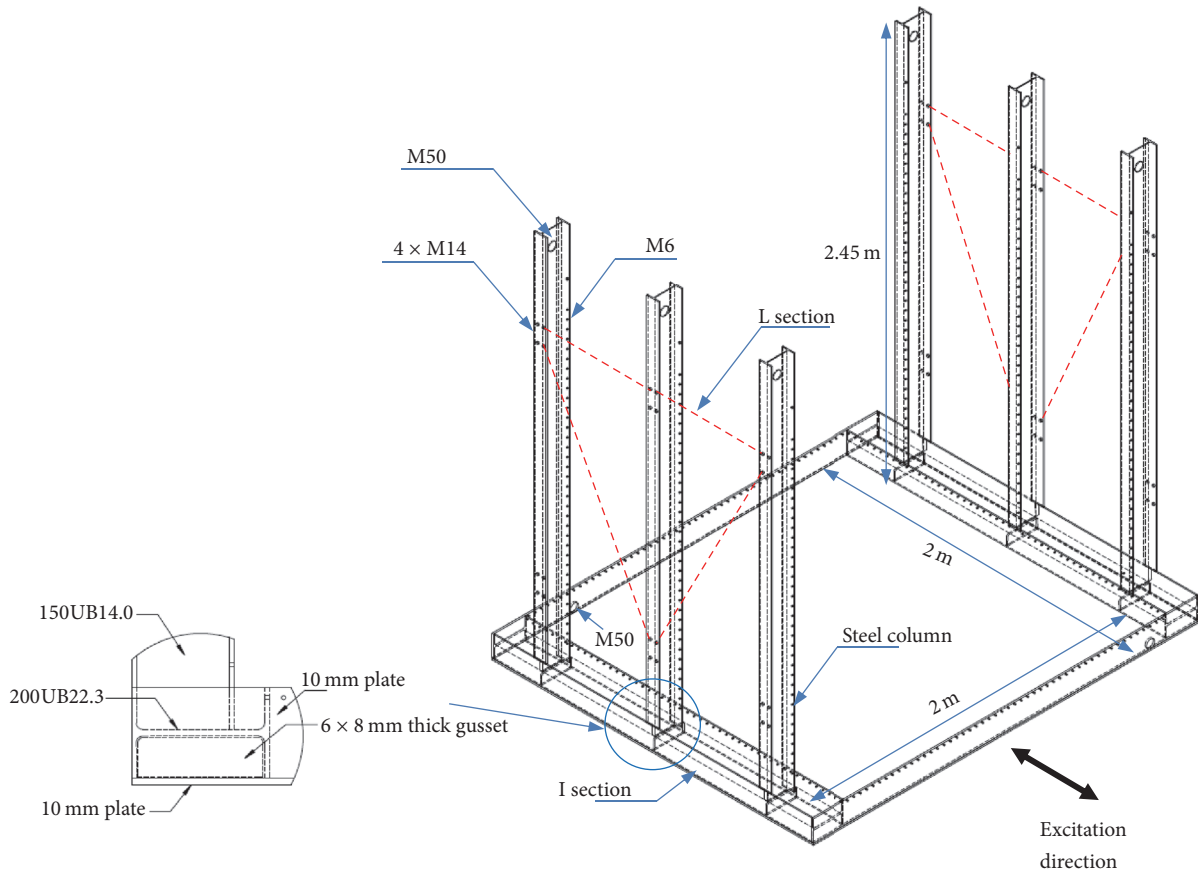


FIGURE 2: Details of the base and barrier columns.

2.1. Base and Barriers. The details of the base are shown in Figure 2. The base has internal dimensions of $2\text{ m} \times 2\text{ m} \times 0.235\text{ m}$ and is made of 10 mm steel plate. Steel I-sections (200UB22.3) are welded horizontally on the transverse sides of the base. Three columns are welded onto the I-sections. These 2.45 m high 150UB14.0 columns also provide the main structural strength of the box. This height is selected for the preparation of soil specimen (discussed in Section 2.4).

Rigid steel L sections brace the three columns (see red-dashed line in Figure 2). These members minimise vibration of the columns in the longitudinal shaking direction. A row of M6 holes, at 53 mm c/c, is drilled on the flange of the columns that face the inside of the box. Each hole will be used to fix a ball bearing for supporting a laminar layer. An 8 mm thick gusset is welded on the horizontal I-section directly under each column to facilitate load transfer to the base.

2.2. Laminar Layers. Thirty thin laminar layers are used. Each of these layers is composed of a lightweight aluminium alloy that minimises the mass. Figure 3 shows the construction of the laminar layers. Each laminar layer is a frame made of a combination of x-shaped sections and $250\text{ mm} \times 50\text{ mm} \times 3\text{ mm}$ rectangular hollow sections. It was decided to use x-shaped sections as these sections have built-in tracks in which ball bearings are used to support the laminar layer. In this way, ball bearings are not installed between laminar layers,

and the gap between the laminar layers is thus minimised. The x-shaped sections and rectangular hollow sections are bolted together using M12 bolts to form each layer.

Each layer is separated and supported by ball bearings fixed on the external columns. The ball bearings allow the layers to move relative to one other with little frictional resistance. A Teflon washer is provided between the x-shaped sections and the columns in order to reduce friction, thereby minimising resistance from the columns to the sliding of the laminar layers. As described in the previous section, the spacing between the holes for the ball bearings is 53 mm. The total thickness of the laminar layer is 50 mm (i.e., the height of the hollow section). Thus the gap between laminar layers is controlled to within 3 mm.

2.3. Membrane. The third major component of the large laminar box is the membrane that lines the inside of the box. While most other laminar boxes, such as the one developed by Ueng et al. [16], have utilised a silicone rubber membrane, the membrane in this box is made of a flexible and durable PVC fabric. It was chosen to minimise the resistance to the movement of sand during shear. The fabric was designed to fold/unfold as sand moves against it rather than to stretch like a conventional silicone rubber membrane. The membrane is made from a trapezium-shaped piece of fabric. The bottom of the trapezium has a length equal to the inner perimeter of the

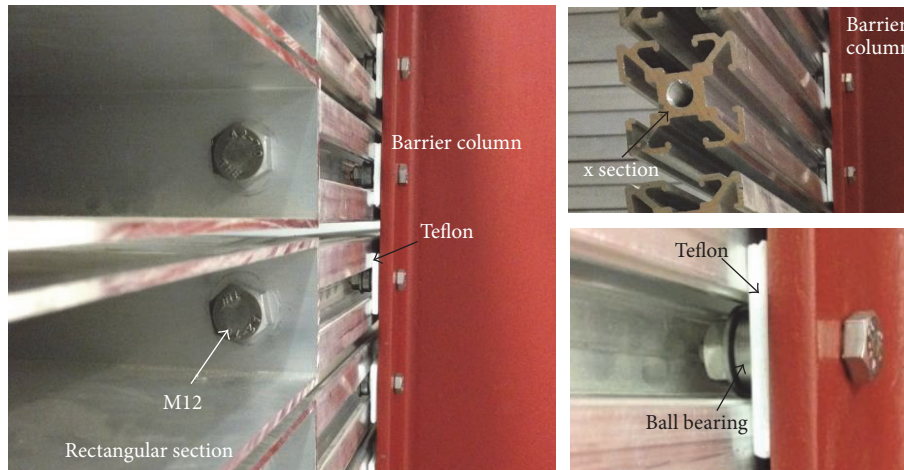


FIGURE 3: Construction of the laminar layers.

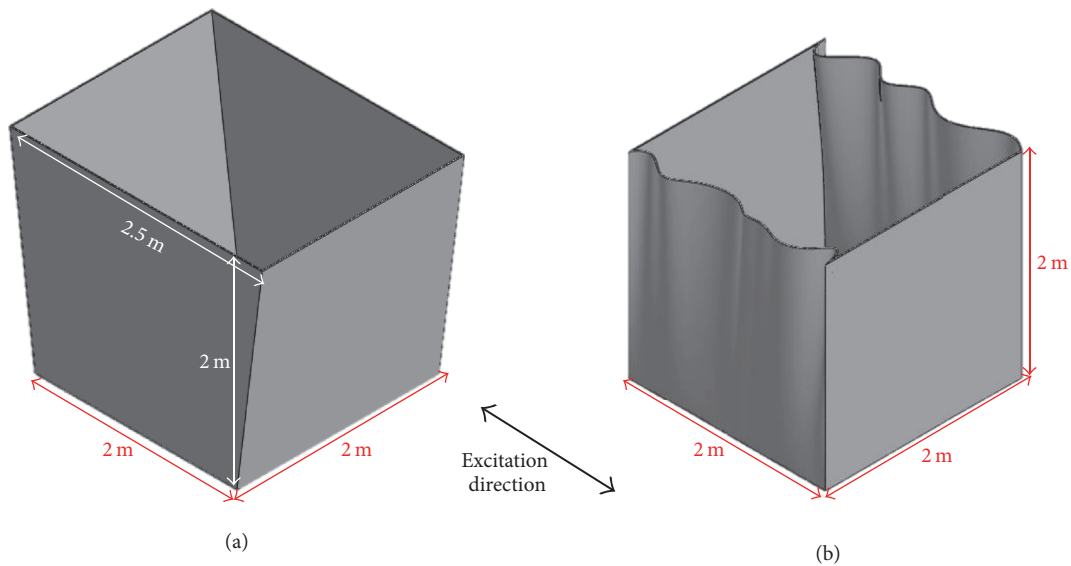


FIGURE 4: Size of the PVC fabric (a) before and (b) after being fitted into the laminar box.

box, while the top of the trapezium is about 1.25 times longer than the bottom (Figure 4(a)). The bottom of the fabric is clamped to the steel base of the box, while the top of the fabric is pegged to the top laminar layer. The result is a fabric system that has increasing leeway near the top of the box where the laminar layers are expected to move the most during testing (Figure 4(b)). This leeway allows the flexible membrane to fold/unfold easily to accommodate the movement of sand.

2.4. Preparation of the Sand. The laminar box was filled with 1 m depth of dry sand. This was achieved by raining the sand through a vertical distance higher than that required for the sand reaching terminal velocity (Figure 5(a)). Raining of sand is a common technique that is used to prepare sand samples for laboratory testing [16, 20]. A number of studies were conducted to calibrate this technique [21–23]. It was reported that raining sand above the terminal falling height,

determined to be above 400 mm, would allow for consistency in relative density at various locations of the sand layer [21, 22]. In this study, a timber box with a base area of 2 m × 2 m was used to rain the sand. The base of the box was drilled with 1800 holes of 9 mm diameter with *c/c* spacing of 40 mm. This means that 2.8% of the area of the base consists of openings (Figure 5(b)). During the raining process, the timber box was supported by the barrier columns of the laminar box. The maximum depth of sand in the laminar box is 2 m, and thus the clear distance between the base of the raining box and the maximum elevation of the sand surface is 450 mm. According to the data presented by both Rad and Tumay [22] and Vaid and Negussey [21], the relative density of the sand formed in the laminar box was about 35%. Figure 5(c) shows the particle size distribution of the sand. The parameters of the sand used in this study are shown in Table 1. The parameters were obtained according to NZS 4402 [24].

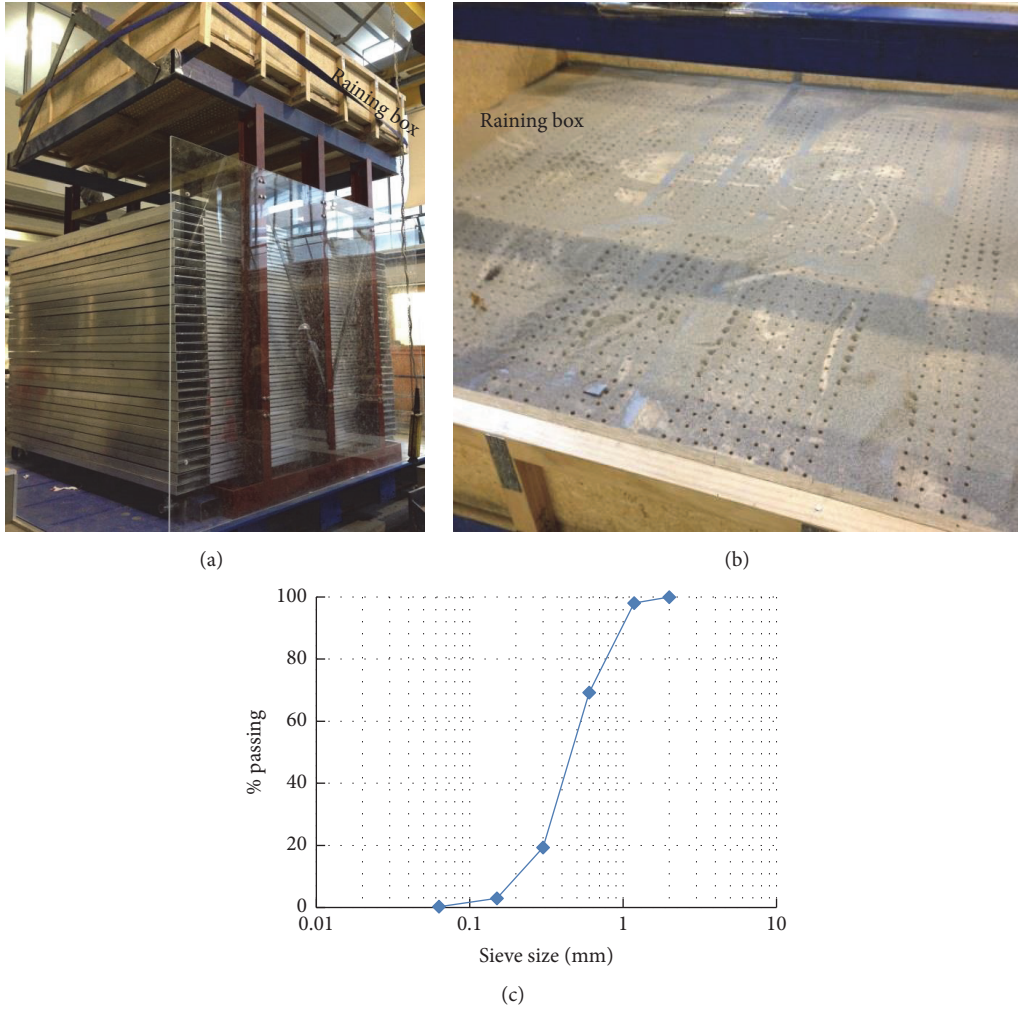


FIGURE 5: Test setup: (a) laminar box with (b) the raining box and (c) particle size distribution.

TABLE 1: Soil parameters.

Parameters	Quantities
Density (ρ)	1451 kg/m ³
Unit weight (γ)	14.2 kN/m ³
Max. void ratio (e_{\max})	0.93
Min. void ratio (e_{\min})	0.6
Specific gravity (G_s)	2.67

2.5. Shake Table Test Setup. The laminar box with 1 m depth of sand was placed on the shake table as shown in Figure 6. A frame model was placed on the sand surface. The model was assumed to be a SDOF model with a fixed base fundamental frequency of 2.8 Hz. The mass at the top was 19.2 kg and the height of the model was 580 mm. The footing size was 475 mm \times 475 mm. The footing was assumed to be rigid. Sand paper was attached under the footing to increase the friction at the footing-sand interface and thus minimise sliding. The accelerations at the top (a_T) and at the footing (a_F) of the model were measured. The acceleration of the sand beneath the model (a_S) was measured by embedding another

accelerometer in the sand directly beneath the centre of the footing of the model. Two laser transducers were used to measure the settlement at the sand surface and 250 mm away from the footing edge (Figure 6). The acceleration at the base of the laminar box (a_B) was also recorded. Strain gauges were attached at the base of the columns to measure the strain for calculating the bending moment development. The bending moments were used to calculate the base shears (V).

The excitation was simulated based on the Japanese Design Spectrum for a hard soil condition [25, 26]. Figure 7(a) shows the acceleration time history of the excitation. The peak ground acceleration (PGA) of the excitation is 0.79 g. The shake table used for this study was displacement controlled with a maximum allowable movement of ± 120 mm. The displacement time histories of the excitations were obtained by double integration of the acceleration time history (Figure 7(c)). Because the maximum ground displacement (335.57 mm) was larger than the allowable range of the shake table, it was decided to reduce the displacement of the excitation by a factor of four so that the maximum displacement of the ground motion is within the limit of the shake table. The ground acceleration is also reduced

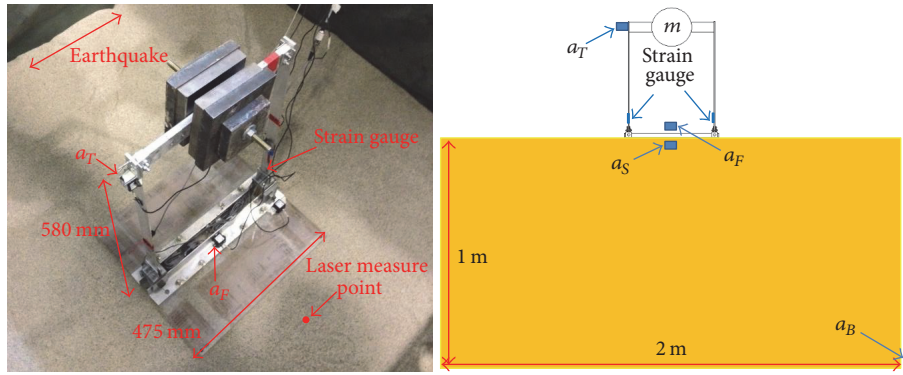


FIGURE 6: Setup of the model and instrumentation.

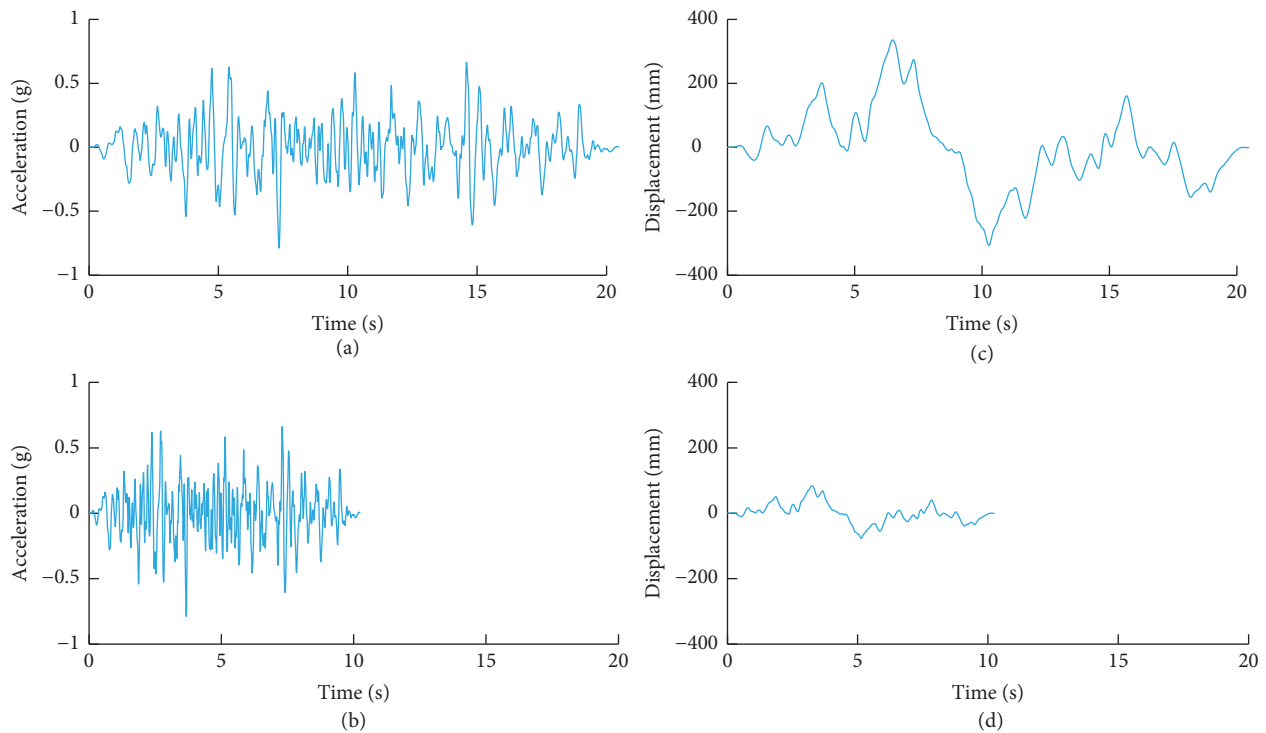


FIGURE 7: Ground excitation. ((a) and (c)) original and ((b) and (d)) scaled time history.

by a factor of four. The reduction leads to a loading that is not strong enough to excite the structure. To keep the magnitude of ground acceleration according to Buckingham π theory [27], the scale factor of the duration of the ground excitation needs to be two, because the scale factor of the ground acceleration depends on the dimension length and the dimension time power two. The relationship between the scale factors of length (S_L), times (S_T), and acceleration (S_a) is $S_T = \sqrt{S_L/S_a}$. To keep the acceleration magnitude, the acceleration scale factor needs to be 1. Consequently, the scale factor for time is $\sqrt{4/1} = 2$. After scaling, the magnitude of the ground displacement is only 25% of the original magnitude (see Figure 7(d)), while the magnitude of the ground acceleration time history has the same magnitude of the original ground acceleration (see Figure 7(b)). The duration

of the ground excitation is only 50% of the original duration (see Figures 7(b) and 7(d)). To investigate the effect of aftershock earthquake on the structure with soil, a sequence of three excitations was applied to the laminar box. The effect of mainshock was represented by the first excitation. The second and third excitations were used to represent the first and second aftershocks, respectively. For simplification, it is assumed that the time history of aftershocks is the same as that of the mainshock.

3. Accelerations of the Structure, Footing, and Soil

Figure 8, derived from the mainshock, shows the response spectrum of accelerations at three different locations. The

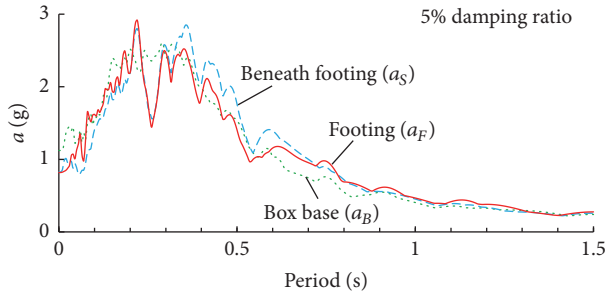


FIGURE 8: Response spectrum of accelerations at different locations.

dotted line represents the response spectrum at the base of the laminar box (a_B). The dashed and solid lines are the response spectra of acceleration at the centre (a_F) and immediately beneath (a_S) the footing, respectively. In the long period range (greater than 0.3 s), the spectrum values of a_S are larger than those of a_B . In contrast, in the short period range (less than 0.2 s), the spectrum values of a_S are lower than those of a_B .

Comparing the response spectrum of acceleration at the footing (a_F) and under the footing (a_S), the spectrum values of a_F are higher than those of a_S in the period range between 0.03 s and 0.2 s. In the long period range (greater than 0.7 s) the spectrum values of a_F and a_S are similar. Other than that, the spectrum values of a_F are lower than those of a_S .

The difference between the response spectrum values of a_F and a_S can be attributed to the interaction between the response of the model, the footing, and the soil. A part of the footing was observed to be temporarily separated from the supporting soil during all experiments. Because of the separation, the response spectrum values of a_F around the fixed base fundamental period of the model (0.36 s) reduce.

Figure 9(a) shows the acceleration of the soil beneath the model footing (a_S) during the mainshock and the first aftershock. While the solid line represents the case of the mainshock, the dashed line illustrates that of the first aftershock. As shown, the amplitude of the soil acceleration due to the mainshock was larger than that due to the aftershock. The maximum sand acceleration beneath the footing due to mainshock and the first aftershock was 0.75 g and 0.62 g, respectively, that is, a 17.33% difference. Figure 9(b) compares the acceleration of the soil beneath the model footing during the first (dotted line) and second (solid line) aftershocks. In general, the soil accelerations during the first and second aftershocks were similar. The maximum soil acceleration due to the second aftershock was 0.64 g. The difference in maximum soil acceleration between the first and second aftershocks was only 0.02 g. It is shown that acceleration of soil in the event of aftershocks is smaller than that in the mainshock, even though both mainshock and aftershocks have the same magnitude.

Figure 10 compares the response spectrum of the soil acceleration (a_S) under the footing during the mainshock and the aftershocks. The response spectra of a_S obtained from the aftershocks are very similar. However, some notable differences can be found when these response spectra are compared to those obtained from the mainshock. At periods

around 0.35 s and 0.6 s, the spectrum accelerations from the mainshock are higher than those of the aftershocks.

The difference in the response spectrum value of a_S among tests is attributed to the soil density being much higher in the aftershock events. Extensive soil settlement took place during the mainshock, and thus the soil density increased. Figure 11 shows the settlement at the soil surface in the mainshock and aftershocks. As shown, the final settlement at the soil surface due to the mainshock was 42.8 mm, while the final settlement caused by the first and second aftershocks was 7.4 mm and 6.2 mm, respectively. Most of the soil settlement took place during the mainshock. Thus, the soil densities in the events of the aftershocks were much higher than those of the mainshock. In the aftershocks, the settlements at the soil surface were very similar, leading to approximately equal changes of soil density. Consequently, the response spectrum values of a_S in the first and second aftershocks were similar (Figure 10). With lower soil density in the mainshock, the soil had the largest spectrum amplitude for periods in the vicinity of the fixed base fundamental period (0.36 s) of the structure.

Figure 12 compares the horizontal acceleration developed at the footing (a_F) during the mainshock and aftershocks. While Figure 12(a) shows the effect of aftershock by comparing the footing response obtained from the mainshock and the first aftershock, Figure 12(b) illustrates the effect of subsequent aftershock on the footing acceleration. Although the excitations were the same, the developments of footing acceleration during the mainshock and the first and the second aftershocks were different from each other. Figure 13 shows the response spectrum of soil and footing accelerations a_S and a_F obtained from the aftershocks. For most periods, the spectrum values of a_F are close to or larger than those of a_S . Except in the period range (approximately 0.3 s and 0.6 s) covering the fixed base fundamental period of the model (0.36 s), the spectrum value of a_F is smaller than that of a_S . This finding is consistent with the results of the mainshock.

Figure 14 shows a comparison of the horizontal acceleration at the top of the model (a_T). The acceleration of the model during the mainshock was larger than that during the aftershocks. The maximum horizontal acceleration at the top of the model in the mainshock and the first aftershock was 0.92 g and 0.67 g, respectively, that is, a 27% difference. On the other hand, the maximum horizontal acceleration at the top of the model during second aftershock was 0.68 g, similar to that of the first aftershock (see Figure 15(b)). The results show that, in the event of the aftershocks, the response of structure with SFSI can be reduced. This could be attributed to the fact that the density of sand of the aftershock was greater than that of the mainshock.

Figure 15 shows the Fourier spectrum of the structural horizontal acceleration due to the mainshock and the aftershocks. There is a noticeable difference between the Fourier amplitude of the mainshock and that of the first aftershock (Figure 15(a)). The maximum Fourier amplitude for case of the mainshock is 1.11 gs. However, the maximum Fourier amplitude obtained from the first aftershock was significantly lower (only 0.78 gs). Also, the majority of the Fourier amplitudes within the range of 1.6 Hz and 3 Hz obtained from the first aftershock were lower than those from

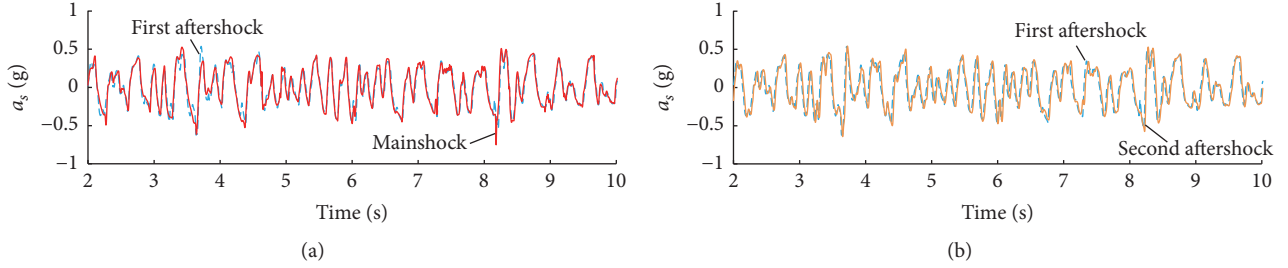


FIGURE 9: Effect of the earthquake sequence on the soil acceleration from beneath the footing.

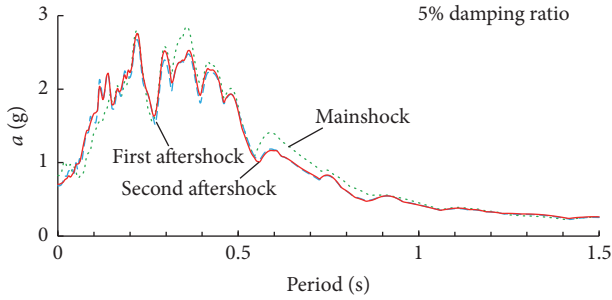


FIGURE 10: Effect of soil density on the spectrum acceleration of a_s .

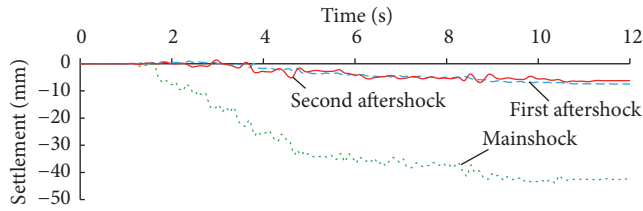


FIGURE 11: Settlement of the soil surface during the mainshock and aftershocks.

the mainshock. The Fourier amplitude obtained from the first aftershock was also significantly different from that obtained using the second aftershock (Figure 15(b)). This result shows that although the excitations of the mainshock and the first and the second aftershocks were assumed to be the same, the aftershock can cause amplification or reduction on the response of structure with SFSI.

4. Calculating the Base Shear of the Structure with SFSI

Strain gauge was used to measure the strain at the column base of the model. The development of base shear in the model during the earthquake can be calculated using the strain gauge measurement. Figure 16 shows a comparison of the base shear development in the model due to the mainshock and the aftershocks. As shown, the maximum base shear in the model due to the mainshock was larger than that due to the first aftershock. On the other hand, although the maximum horizontal acceleration at the top of the model due to the mainshock was the largest, the largest maximum

base shear (V) was found in the second aftershock event (Figure 16). The maximum base shear due to the mainshock was 169.5 N. The maximum base shear due to the first and second aftershocks was 159.2 N and 179 N, respectively. The maximum base shear due to the second aftershock was 5.6% and 12.4% larger than that due to the mainshock and the first aftershock, respectively. Although the mainshock and aftershock were the same, the development of maximum acceleration and base shear shows a different trend when subjected to the mainshock and the aftershocks.

Chopra and Yim [28] developed an equation of motion to calculate the response of a structure with a flexible support. The deformation of the support was modelled using two-spring support. They developed a set of formulas to calculate the maximum base shear (V_{\max}) of structures on flexible supports:

$$V_{\max} = V_{\text{cr}} \left\{ \frac{h^2}{R_o^2} + e^{-\xi\phi} \sqrt{\frac{b^4}{R_o^4} + \frac{b^2}{R_o^2} \left[\left(\frac{\tilde{S}_a}{g} \right)^2 \left(\frac{h}{b} \right)^2 e^{\xi\pi} - 1 \right]} \right\}, \quad (1)$$

where

$$\phi = \frac{\pi}{2} - \tan^{-1} \left\{ \frac{b}{R_o} \left[\left(\frac{\tilde{S}_a}{g} \right)^2 \left(\frac{h}{b} \right)^2 e^{\xi\pi} - 1 \right]^{-\frac{1}{2}} \right\}; \quad (2)$$

and b is half of the base width and h is the height of the model; g is the gravitational acceleration; $R_o = \sqrt{h^2 + b^2}$ and $V_{\text{cr}} = mg \times b/h$ is the base shear to initial footing uplift. \tilde{S}_a is the spectrum acceleration corresponding to the effective vibration period \tilde{T} .

The effective vibration period of a structure with a flexible support is

$$\tilde{T} = T \sqrt{1 + \frac{kh}{k_\theta}}, \quad (3)$$

where T is the fundamental period of the structure with a fixed base, k is the lateral bending stiffness of structure, and

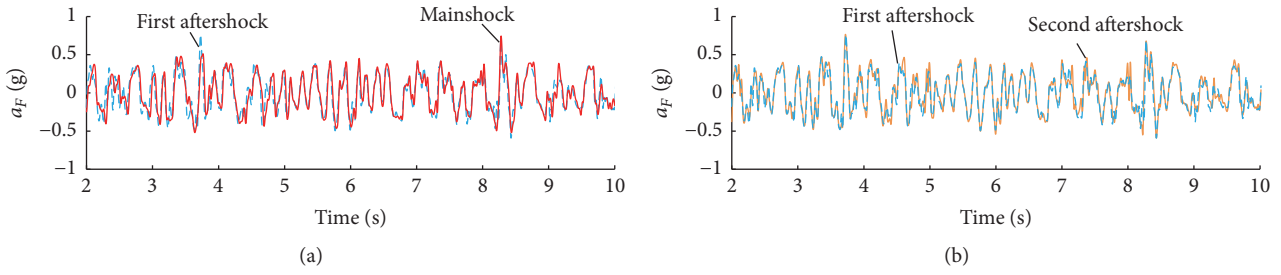


FIGURE 12: Effect of aftershock on the footing acceleration.

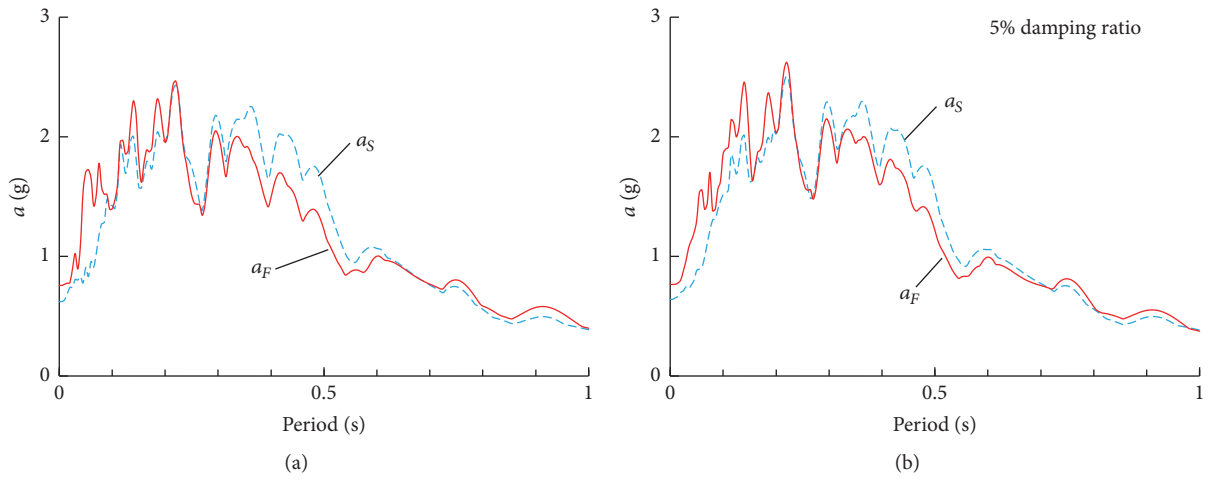


FIGURE 13: Response spectrum of soil and footing accelerations obtained from (a) the first aftershock and (b) the second aftershock.

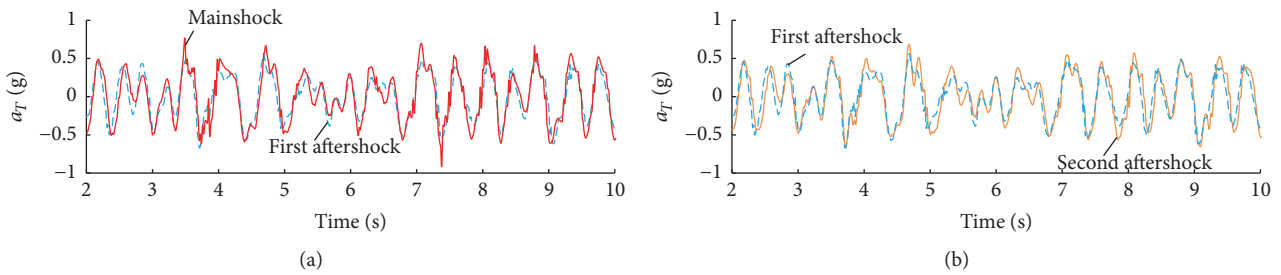


FIGURE 14: Effect of aftershocks on the structural acceleration.

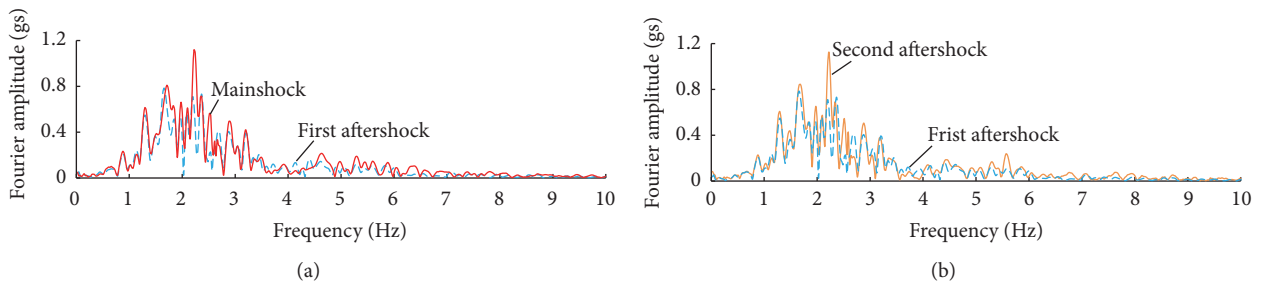


FIGURE 15: Frequencies content of structural top accelerations.

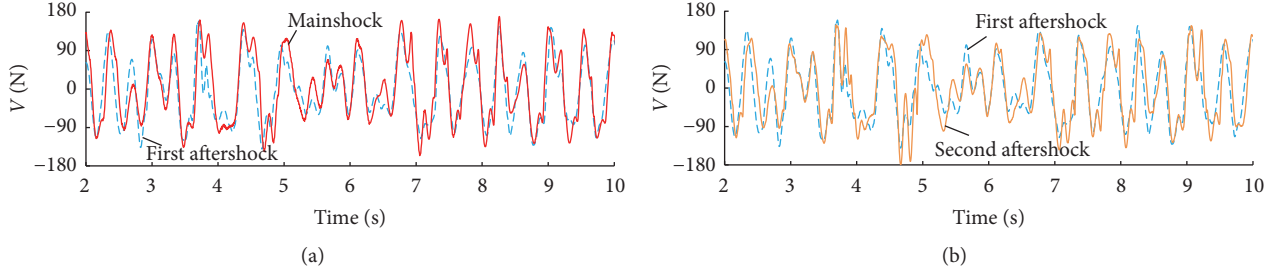


FIGURE 16: Base shear in the structure due to the mainshock and aftershocks.

k_θ is the rotational assumed static stiffness of the footing on uniform soil:

$$k_\theta = \frac{G\pi}{8(1-\nu)}B^2, \quad (4)$$

where G and ν are the shear modulus and Poisson's ratio of the soil, respectively; B is the base width ($2b$).

An empirical equation was developed by Larkin [29] such that the shear wave velocity (V_s) of sand can be calculated using the relative density (D_r), mass density (ρ), and mean effective confining stress (σ'_M):

$$V_s = \sqrt{\frac{D_r + 25}{100}} \times \left[\frac{\sqrt{0.422} \times 10^3 \times \sigma'_M}{\rho} \right]^{0.5}. \quad (5)$$

The shear wave velocity can be used to calculate the shear modulus of soil:

$$G = \rho V_s^2. \quad (6)$$

By combining (5) and (6), (7) can be obtained to estimate the shear modulus (G) of sand using the relative density D_r and effective confining stress σ'_M :

$$G = \frac{D_r + 25}{100} \times \sqrt{0.422} \times 10^3 \times \sigma'_M. \quad (7)$$

The shear modulus of the sand at depth of 59 mm is 0.45 MPa. This depth, calculated from 1/8 of the footing width, is the appropriate depth for a characteristic soil element to represent the stress conditions of soil involved in providing resistance to moment and shear [3]. The effective vibration frequency of the model on sand is calculated to be 2.74 Hz (see (3)). The effective vibration period of the model is very similar to the fixed base fundamental period. This is because, in shake table experiments, the sand cannot be scaled. As a consequence of this, the sand has larger stiffness than that of scaled sand. Consequently, the unscaled sand has a higher shear modulus, that is, higher sand stiffness.

Figure 17 shows a comparison of the maximum base shear (V_{\max}) of the model obtained using experimental data and (1). Strain gauge measurements are used to determine the maximum bending moment at the base of the model and thus the experimental maximum base shear can be calculated. The spectrum acceleration $\bar{S}_a(\bar{T})$ is derived from the acceleration measured in the soil beneath the footing (Figure 10). It

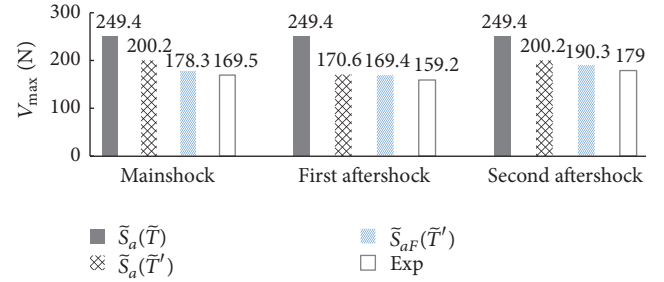


FIGURE 17: Calculation of the maximum base shear.

can be seen that (1) overestimates the maximum base shear of the model. The experimentally obtained maximum base shear for the model due to the mainshock and the first and the second aftershocks is 169.5 N, 159.2 N, and 179.0 N, respectively. With (1), the corresponding maximum base shear is 249.4 N. Equation (1) overestimates the maximum base shear of model by 47%, 57%, and 39%, respectively.

The accuracy of (1) is associated with the estimation of the effective vibration period of the model on sand. In (3), the rotational stiffness of footing on soil is modelled using elastic springs. Footing uplift and soil plastic deformation are not considered. Therefore, the effective vibrational period of the model is underestimated.

As shown in Figure 15, the maximum Fourier amplitude is found at 2.22 Hz considering the mainshock and the second aftershock. This indicates that the corresponding vibration periods (\bar{T}') are 0.45 s. Compared to the theoretical calculation ($\bar{T} = 0.36$ s), (3) underestimates the effective vibration period by 20%. For the case of the first aftershock, the maximum Fourier amplitude is found at 1.64 Hz, that is, 26% lower than that in the case of the mainshock. When \bar{T}' is used to obtain the spectrum value, the accuracy of (1) can be improved. The maximum base shear of the model due to the mainshock and the aftershocks, estimated using $\bar{S}_a(\bar{T}')$, is 200.2 N, 170.6 N, and 200.2 N, respectively. Although (1) overestimates the maximum base shears by 18%, 7%, and 12%, the calculations are closer to the experimental results. To further improve the accuracy of (1), the spectrum acceleration derived using footing acceleration (a_F) in conjunction with \bar{T}' can be used. The maximum base shear obtained from (1) using $\bar{T}'(\bar{T}')$ is 178.3 N, 169.4 N, and 190.3 N for the case of the mainshock, the first aftershock, and the second aftershock,

respectively. The corresponding errors reduce to 5%, 6%, and 6%.

5. Conclusions

This work addresses the response of a model structure on sand using a large laminar box which is square in plan. The laminar box can accommodate a depth of 2 m of soil, with a surface area of 4 m². The design and construction of the relatively large laminar box are presented. Shake table tests are conducted. An excitation was applied three times to simulate the effect of the mainshock and aftershocks of an earthquake.

The results reveal the following:

- (i) A relatively large laminar box can be used to investigate the structural response with SFSI and produce meaningful outcomes.
- (ii) The development of soil settlement in the mainshock was much larger than that in the aftershocks. As a result, the development of spectrum acceleration of soil acceleration was affected.
- (iii) Although the mainshock and aftershock were assumed to be the same, the densification of the sand in the aftershocks affects the development of structural top accelerations.
- (iv) With SFSI, the maximum horizontal acceleration in the structure when subjected to the mainshock was larger than that due to the aftershock. However, the maximum base shear of structure due to the aftershock can be larger than that due to the mainshock.
- (v) When comparing experimental results against those from an existing theoretical method, the accuracy of the method is sensitive to the effective vibration period of the SFSI system and the spectrum acceleration of the footing.

Disclosure

This paper is part of the doctoral thesis of Xiaoyang Qin.

Conflicts of Interest

The authors declare that they have no conflicts of interest.

Acknowledgments

The authors are grateful for the support by the Ministry of Business, Innovation and Employment through the Natural Hazards Research Platform under the Award 3708936 and by the Earthquake Commission under the Award 3704188.

References

- [1] P. W. Taylor, P. E. Bartlett, and P. R. Wiessing, "Foundation rocking under earthquake loading," in *Proceeding of the 10th International Conference on Soil Mechanics and Foundation Engineering*, vol. 3, pp. 313–322, Stockholm, Sweden, 1981.
- [2] A. S. Veletsos and J. W. Meek, "Dynamic behaviour of building-foundation systems," *Earthquake Engineering & Structural Dynamics*, vol. 3, no. 2, pp. 121–138, 1974.
- [3] T. Larkin, "Seismic response of liquid storage tanks incorporating soil structure interaction," *Journal of Geotechnical and Geoenvironmental Engineering*, vol. 134, no. 12, pp. 1804–1814, 2008.
- [4] L. Deng, T. Algie, and B. L. Kutter, "Innovative economical foundations with improved performance that is less sensitive to site conditions: centrifuge data report for LJD01," Tech. Rep. UCD/CGMDR-09/01, University of California, Davis, Calif, USA, 2009.
- [5] L. Deng, B. L. Kutter, and S. K. Kunnath, "Centrifuge modeling of bridge systems designed for rocking foundations," *Journal of Geotechnical and Geoenvironmental Engineering*, vol. 138, no. 3, pp. 335–344, 2012.
- [6] T. B. Algie, M. J. Pender, R. P. Orense, and L. M. Wotherpoon, "Dynamic field testing of shallow foundations subject to rocking," in *Proceedings of the New Zealand Society for Earthquake Engineering Annual Conference*, Wellington, New Zealand, 2010.
- [7] N. Saxena, D. K. Paul, and R. Kumar, "Effects of slip and separation on seismic SSI response of nuclear reactor building," *Nuclear Engineering and Design*, vol. 241, no. 1, pp. 12–17, 2011.
- [8] M. Ormeño, T. Larkin, and N. Chouw, "Evaluation of seismic ground motion scaling procedures for linear time-history analysis of liquid storage tanks," *Engineering Structures*, vol. 102, pp. 266–277, 2015.
- [9] M. Ormeño, M. Geddes, T. Larkin, and N. Chouw, "Experimental study of slip-friction connectors for controlling the maximum seismic demand on a liquid storage tank," *Engineering Structures*, vol. 103, pp. 134–146, 2015.
- [10] M. Ormeño, T. Larkin, and N. Chouw, "The effect of seismic uplift on the shell stresses of liquid-storage tanks," *Earthquake Engineering & Structural Dynamics*, vol. 44, no. 12, pp. 1979–1996, 2015.
- [11] Y. Chen, T. Larkin, and N. Chouw, "Experimental assessment of contact forces on a rigid base following footing uplift," *Earthquake Engineering & Structural Dynamics*, vol. 46, no. 1, pp. 1835–1854, 2017.
- [12] X. Qin, Y. Chen, and N. Chouw, "Effect of uplift and soil non-linearity on plastic hinge development and induced vibrations in structures," *Advances in Structural Engineering*, vol. 16, no. 1, pp. 135–147, 2013.
- [13] T. Larkin, X. Qin, and N. Chouw, "Effect of local site on SFSI of clustered structure," in *Proceedings of the International Workshop on Natural Hazards*, Azores, Portugal, April 2016.
- [14] X. Qin, *Experimental studies of SFSI effect on upliftable structures [Doctoral dissertation]*, ResearchSpace, Auckland, New Zealand, 2016, <https://researchspace.auckland.ac.nz/handle/2292/29301>.
- [15] G. M. Latha and A. M. Krishna, "Seismic response of reinforced soil retaining wall models: influence of backfill relative density," *Geotextiles and Geomembranes*, vol. 26, no. 4, pp. 335–349, 2008.
- [16] T.-S. Ueng, M.-H. Wang, M.-H. Chen, C.-H. Chen, and L.-H. Peng, "A large biaxial shear box for shaking table test on saturated sand," *Geotechnical Testing Journal*, vol. 29, no. 1, pp. 1–8, 2006.
- [17] S. K. Prasad, I. Towhata, G. P. Chandradhara, and P. Nanjundaswamy, "Shaking table tests in earthquake geotechnical engineering," *Current Science*, vol. 87, no. 10, pp. 1398–1404, 2004.

- [18] N. Mononobe and O. Matsuo, "On the determination of earth pressure during earthquakes," in *Proceedings of the World Engineering Congress*, vol. 9, pp. 179–187, Tokyo, Japan, 1929.
- [19] M. Matsuo and S. Ohara, "Lateral earth pressures and stability of quay walls during earthquakes," in *Proceedings of the 2nd World Conference on Earthquake Engineering*, Tokyo, Japan, 1960.
- [20] X. Qin, W. M. Cheung, N. Chouw, T. Larkin, and S. W. C. Ching, "Study of soil-structure interaction effect on ground movement using a laminar box," in *Proceedings of the New Zealand Society for Earthquake Engineering Annual Conference*, Wellington, New Zealand, 2013.
- [21] Y. P. Vaid and D. Negussey, "Relative density of pluviated sand samples," *Japanese Society of Soil Mechanics and Foundation Engineering*, vol. 24, no. 2, pp. 101–105, 1984.
- [22] N. S. Rad and M. T. Tumay, "Factors affecting sand specimen preparation by raining," *ASTM Geotechnical Testing Journal*, vol. 10, no. 1, pp. 31–37, 1987.
- [23] M. Okamoto and S. Fityus, "An evaluation of the dry pluviation preparation technique applied to silica sand samples," in *Proceedings of the International Symposium on Geomechanics and Geotechnics of Particulate Media*, pp. 33–39, Taylor and Francis, London, UK.
- [24] NZS 4402, *Methods of Testing Soil for Civil Engineering Purposes*, Standard Association of New Zealand, Wellington, New Zealand.
- [25] Japan Society of Civil Engineers, *Earthquake Resistant Design Codes in Japan*, Maruzen, Tokyo, Japan, 2000.
- [26] N. Chouw and H. Hao, "Study of SSI and non-uniform ground motion effect on pounding between bridge girders," *Soil Dynamics and Earthquake Engineering*, vol. 25, no. 7-10, pp. 717–728, 2005.
- [27] E. Buckingham, "On physically similar systems; Illustrations of the use of dimensional equations," *Physical Review A: Atomic, Molecular and Optical Physics*, vol. 4, no. 4, pp. 345–376, 1914.
- [28] A. K. Chopra and S. C.-S. Yim, "Simplified earthquake analysis of structures with foundation uplift," *Journal of Structural Engineering (United States)*, vol. 111, no. 4, pp. 906–930, 1985.
- [29] T. Larkin, "DENSOR—a computer program for seismic response analysis of nonlinear horizontal soil layers," Tech. Rep. 51508/6, Norwegian Geotechnical Institute, 1978.

Research Article

Numerical Study on the Seismic Response of Structure with Consideration of the Behavior of Base Mat Uplift

Guo-Bo Wang,¹ Xin Zhou,¹ Xian-Feng Ma,^{2,3} and Jun Wu⁴

¹Hubei Key Laboratory of Roadway Bridge & Structure Engineer, Wuhan University of Technology, Wuhan 430070, China

²The Key Laboratory of Geotechnical and Underground Engineering of the Ministry of Education, Tongji University, Shanghai 200092, China

³Department of Geotechnical Engineering, Tongji University, Shanghai 200092, China

⁴School of Urban Railway Transportation, Shanghai University of Engineering Science, Shanghai 201620, China

Correspondence should be addressed to Xian-Feng Ma; xf.ma@tongji.edu.cn

Received 12 June 2017; Accepted 31 July 2017; Published 3 October 2017

Academic Editor: Xing Ma

Copyright © 2017 Guo-Bo Wang et al. This is an open access article distributed under the Creative Commons Attribution License, which permits unrestricted use, distribution, and reproduction in any medium, provided the original work is properly cited.

The foundation might be separated from the supporting soil if the earthquake is big enough, which is known as base mat uplift. This paper proposed a simplified calculation model in which spring element is adopted to simulate the interaction between soil and structure. The load-deformation curve (F - D curve) of the spring element can be designated to represent the base mat uplift, in which the pressure can be applied while tensile forces are not allowed. Key factors, such as seismic wave types, seismic wave excitation directions, seismic wave amplitudes, soil shear velocities, structure stiffness, and the ratio of structure height to width (H/B), were considered in the analysis. It is shown that (1) seismic wave type has significant influence on structure response due to different frequency components it contained; (2) the vertical input of seismic wave greatly affected structure response in vertical direction, while it has little impacts in horizontal direction; (3) base mat uplift is easier to take place in soil with higher shear velocity; (4) structure H/B value has complicated influence on base mat uplift. The outcome of this research is assumed to provide some references for the seismic design of the structure due to base mat uplift.

1. Introduction

There have been two ways to deal with the soil-structure interaction (SSI) effect in seismic design of structures: one is treating the soil as rigid medium and neglecting the SSI effect; the other is assuming the foundation to be fully bonded to soil so that the foundation uplift cannot occur. However, the importance of the SSI in the dynamic response of structure has been realized recently by researchers, though foundation uplift has not gotten enough attention yet, partly due to the fact that interfacial behavior between foundation and soil cannot be directly observed after earthquake. However, the phenomenon of foundation uplift can be verified indirectly in some earthquakes such as that of Chile 1960, Alaska 1964, San Fernando 1971, Kocaeli 1999, and Athens 1999 [1], in which snow was observed under the structural base mat.

Housner [2] found that several golf-ball-on-a-tee type of elevated water tanks survived from ground shaking whereas the reinforced concrete structures of elevated water tanks were severely damaged during the Chilean earthquake in 1960. Motivated by this phenomena, Housner further investigated dynamic response of rigid block rocking on rigid horizontal base to establish the relationship between structure and foundation uplift. After that, the impact of foundation uplift on the dynamic response of structures had attracted much interest of earthquake related researchers. Early research works focused on rigid block rocking on rigid base [3] or elastic/Winkler base [4, 5], in which the influence of structure flexibility on dynamic response of structure is neglected. Later, calculation models for flexible blocks/structure rocking on rigid base [6, 7] and elastic base [8, 9] were proposed (see Figure 1).

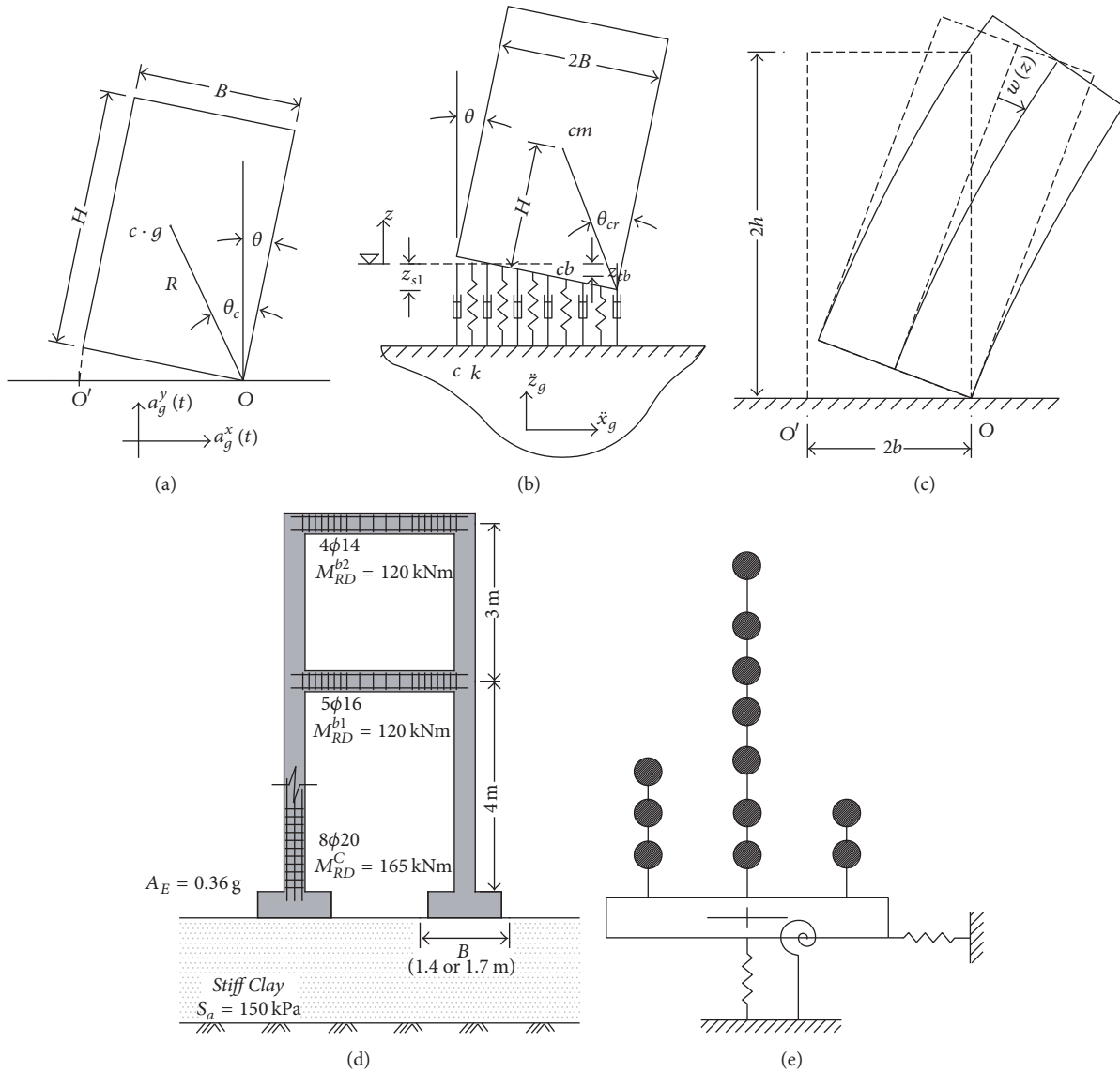


FIGURE 1: Four calculation models. (a) Rigid block rocking on rigid base [3]; (b) rigid block rocking on Winkler base [4]; (c) flexible block rocking on rigid base [6]; (d) practical structure rocking on elastic base [8]; (e) SR model [10].

With the construction of nuclear power plant (NPP) structures in Japan and America, much attention had been paid to the impact of base mat uplift on the seismic response of structure. The SR (Away-Rocking) model (as shown in Figure 1(e)) was developed and used widely for the analysis of the dynamic response of NPP due to its complicate property. Kennedy et al. [13] established a simplified dynamic mathematical model for a typical High Temperature Gas-cooled Reactor (HTGR) plant. The results showed that linear analysis may be used to determine all structural response for rock sites even when there is substantial base slab uplift. However, for soil sites, nonlinear analyses on structure should be conducted if base mat uplift occurs. Taking a reactor building of Pressurized Water Reactor (PWR) plant as an example, Sotomura and Kase [10] investigated the impact of the vertical and horizontal ground motion on

the seismic response of structure due to base mat uplift. With the development of computing resource, numerical simulation methods have been employed to conduct the three-dimensional nonlinear calculation. Naohiro et al. [14] established a three-dimensional nonlinear FEM model to calculate the seismic response of a nuclear power plant with consideration of base mat uplift during earthquake. The ultimate displacement of structure and its fragility were then evaluated. Bolisetti and Whittaker [15] analyzed the influence of adjacent structures on foundation uplift in NPP structures by finite element method, in which the contact element or joint element was used to represent the behavior of the base mat uplift. Yabushita et al. [16] and Naohiro et al. [17] studied the nonlinear behavior of base mat uplift by arranging joint elements between the reactor building base mat and the underneath soil in 3D FE model. However, such

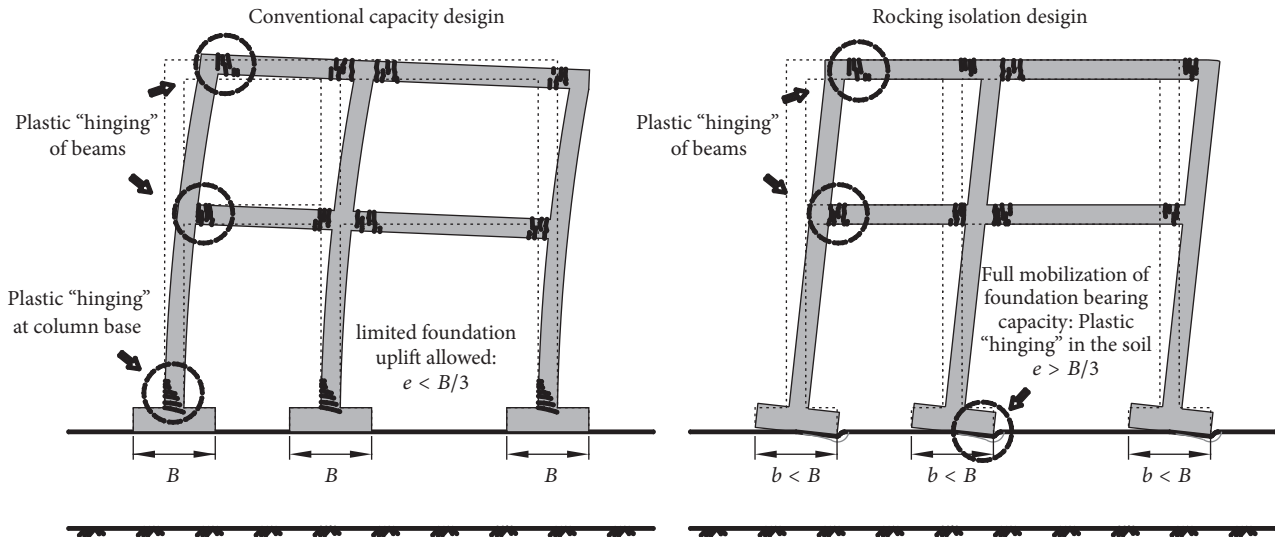


FIGURE 2: The principle of the new idea “rocking isolation” [11, 12].

FE method suffered two key problems, that is, the difficulty in determination of constitutive models for contact/joint element and convergent issue in FE analysis.

Recently, Gazetas et al. [11, 12] proposed a concept of rocking isolation, in which the influence of foundation uplift on seismic response of structure can be investigated. Preliminary results showed that foundation uplift was beneficial to dynamic behavior of structure during earthquake. Compared to the current prevailing “capacity design” philosophy, Gazetas proposed the idea of rocking isolation, taking advantage of the nonlinear characteristics of surrounding soil in the phenomenon of SSI, and then they intentionally induced the plastic hinging in the element of foundation and soil (as shown in Figure 2) to mobilize the strength of the surrounding soil. Anastasopoulos et al. [18, 19] analyzed the impact of rocking isolation on an asymmetric frame structure and a retrofitted three-story building, and it is observed that the rocking isolation in structure can offer increased safety margins. Gazetas et al. [11, 12] suggested that seismic safety factors can be reduced to 1 by adopting the idea of rocking isolation.

From the initial study on the rigid block rocking at the rigid base to the up-to-date conception of rocking isolation, one crucial problem has not been solved perfectly, that is, how to establish a suitable calculation model to compute seismic response of block/structure due to base mat/foundation uplift. It is obvious that the nonlinear property of surrounding soil cannot be considered in the traditional analysis model as shown in Figures 1(a), 1(b), and 1(c), and the three-dimensional effect cannot be included in the SR model as shown in Figure 1(e). The real three-dimension FE model, as given in Figures 1(d) and 2, might overcome the above shortcomings; however, there are highly demanding computational time and resource, and hence it is unsuitable for practical designers. Most importantly, the rocking system is a time varying system, which means the stiffness, frequency, period, and damping are changing with the amount and area of foundation uplift. In order to establish a robust calculation

method with consideration of the foundation uplift, the “stress redistribution phenomenon” must be considered. In this paper, a spring element method is proposed to avoid the convergence issue in the contact/joint element method and then the seismic response of structure due to the foundation uplift can be analyzed systematically. Although this method cannot consider nonlinear character of surrounding soil, the research work here can give some insight to the seismic response of structure due to foundation uplift and then provides the theoretical foundation for further work with consideration of the nonlinear property of soil. At same time, some key factors impact on the seismic structural response and foundation uplift ratio are also discussed.

2. New Computational Method Using Spring Element

2.1. Traditional Method. The development of the calculation method for seismic response of structure considering base mat uplift has experienced three stages. The first stage was focusing on block rocking on soil surface. Chopra and Yim [20] established analytic formulae for a rigid and flexible body rocking on rigid foundation, from which the classic Winkler foundation model and simplified two-element foundation model were proposed. The SR model was then proposed in the second stage to analyze the linear seismic responses of structure [21]. It should be noticed that only 2D analyses were conducted in first two stages. The 3D FE method was employed in the third stage, in which the contact element or joint element was used to consider the soil-structure interaction and the behavior of base mat uplift [17, 22]. It should be mentioned that the 3D FE model can be used to conduct nonlinear analysis since the nonlinear property of material and geometry can be incorporated in a 3D FE model.

2.2. The Basic Principle of the New Method. The computation efficiency for contact element and joint element is usually

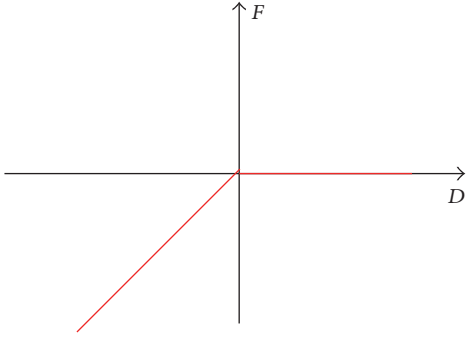


FIGURE 3: F - D curve for COMBIN39 element.

very low due to the difficulty of convergence in nonlinear analysis. In order to overcome this deficiency, a new computational method is suggested in this paper, in which the contact or joint element is replaced by spring element. The spring elements, COMBIN39 in the FE software ANSYS, can provide pressure by setting its load-deformation curve (F - D curve) as shown Figure 3, and the tensile forces are not allowed. It is obvious that the base mat uplift will occur if the vertical displacement of node at base mat is larger than zero. The values of spring stiffness and damping ratio or damping coefficient can be determined by classic empirical formulae for soil impedance, which will be given in the following section.

2.3. Implementation of the New Method. The spring element in FE software ANSYS has the feature of “no length,” which means that the two nodes at each end of the spring element will locate at the same position. It should be noticed that the nodes in Figure 4 are layered deliberately for the sake of explanation of the occurrence of base mat uplift. The process of simulation can be classified into four phases.

(a) *Before the Phase of Computation.* The point O is set as the original coordinate to establish the FE model of structure, in which the positive direction is assumed to be upwards (Figure 4(a)).

(b) *Phase of Static Analysis.* The spring element will be compressed under the self-weight of the structure and reach the static equilibrium at certain position (see the dotted line in Figure 4(a)).

(c) *Phase of Seismic Excitation.* The structure will rock left and right under the seismic excitation. Critical state is defined as the situation when the vertical displacement of the corner node at base mat is equal to zero (see Figure 4(b) and node 1 in Figure 6).

(d) *Phase of Base Mat Uplift.* The vertical displacement of base mat will increase with the increase of the amplitude of input seismic wave, and, accordingly, the base mat uplift will occur due to no tensile force being allowed in the spring element (see Figure 4(c)).

The base mat will touch the soil again if the peak acceleration of the seismic wave passes through. It should be

noted that the shock effect between soil and base mat will not be considered here for the sake of simplicity.

3. Calculation Model

3.1. Simplified Calculation Model. In current study, a four-story frame structure (as shown in Figure 5) is taken as a typical structure in the analysis. The base mat is 12 m square and the height of each story is 3 m. The section of each column is 0.6 m in both width and length. The mass density of the concrete is set to 2600 Kg/m^3 , modulus of elasticity is 36 GPa, and the Poisson ratio is 0.2. The total weight of the structure is calculated to be $7.38 \times 10^6 \text{ N}$.

In the FE model, the beam is simulated with BEAM188 element, and the wall and slab are represented by SHELL181 element. The total number of element and node are 2274 and 1326, respectively. The axes of X and Z are set in horizontal directions and Y is in vertical direction.

3.2. Soil Model. Soil is modelled by spring-damping element (COMBIN39 element), which has six degrees of freedom in each node: two horizontal directions, one vertical direction, two rocking directions, and one torsion direction. The shear wave velocity, mass density, and Poisson ratio of the soil are 1100 m/s , 2350 Kg/m^3 and 0.4, respectively.

3.3. Soil Impedance Computation. In current research, the rigid foundation is considered to be rested on the surface of a half space. The embedded depth of foundation H is neglected for a conservative treatment.

The formulae suggested by Veletsos and Verbic [23] are employed in this research as the expressions are frequency-dependent, which is much more rational. The formulae are given in Tables 1 and 2, and the calculation results are listed in Table 4.

The recommended formulae in ASCE code (Table 3) are also used to verify Table 2's calculation results.

It can be seen from Table 4 that the calculated stiffness and damping by two methods are almost the same.

3.4. Damping. The damping in a soil-structure interaction system mainly consists of two parts: soil damping and structure damping. Soil damping can be calculated by soil impedance functions, that is, the formulae listed in Table 1 or Table 3. According to the results from Rotaru et al. [25] and German standards [26], it is suggested that if the calculated damping values of soil are too big, the damping value in horizontal and vertical direction for soil can be cut off by 15% and 30%, respectively. Structure damping is considered to be Rayleigh damping, which can be expressed by the following formulae:

$$\begin{aligned}
 C &= \alpha [M] + \beta [K], \\
 \alpha &= \frac{2\omega_1\omega_2\xi}{\omega_1 + \omega_2}, \\
 \beta &= \frac{2\xi}{\omega_1 + \omega_2},
 \end{aligned} \tag{1}$$

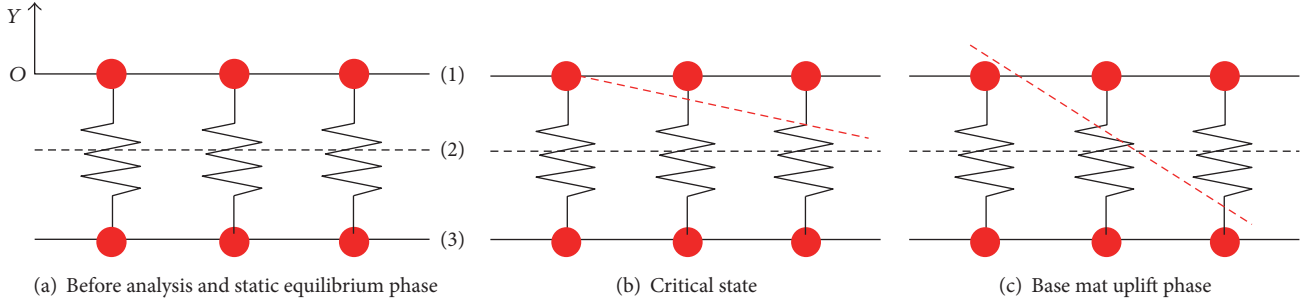


FIGURE 4: Schematic diagram of the working state of spring element. (1) base mat plane, (2) static equilibrium plane, and (3) copied plane (for the establishment of spring element).

TABLE 1: Soil impedance functions for circular foundation on a half-space [23].

Mode	K_{st}	k	c
Horizontal	$\frac{8GR}{2-\nu}$	$k_x = k_y = 1$	$c_x = c_y = \alpha_1$
Vertical	$\frac{4GR}{1-\nu}$	$k_z = 1 - \gamma_1 \frac{(\gamma_2 a_0)^2}{1 + (\gamma_2 a_0)^2} - \gamma_3 a_0^2$	$c_z = \gamma_4 + \gamma_1 \gamma_2 \frac{(\gamma_2 a_0)^2}{1 + (\gamma_2 a_0)^2}$
Rocking	$\frac{8GR^3}{3(1-\nu)}$	$k_\psi = 1 - \beta_1 \frac{(\beta_2 a_0)^2}{1 + (\beta_2 a_0)^2} - \beta_3 a_0^2$	$c_\psi = \beta_1 \beta_2 \frac{(\beta_2 a_0)^2}{1 + (\beta_2 a_0)^2}$
Torsion	$\frac{16GR^3}{3}$	$k_\theta = 1 - 0.425 \frac{(0.687 a_0)^2}{1 + (0.687 a_0)^2}$	$c_\theta = 0.425 \times 0.687 \frac{(0.687 a_0)^2}{1 + (0.687 a_0)^2}$

α_1 , β_1 , and γ_1 are numerical coefficients which depend on Poisson's ratio ν as shown in Table 2.

TABLE 2: Values for fitting parameters of α_1 , β_1 , and γ_1 [23].

Quantity	$\nu = 0$	$\nu = 1/3$	$\nu = 0.45$	$\nu = 0.5$
α_1	0.775	0.65	0.6	0.6
β_1	0.8	0.8	0.8	0.8
β_2	0.525	0.5	0.45	0.4
β_3	0	0	0.023	0.027
γ_1	0.25	0.35	—	0
γ_2	1.0	0.8	—	0
γ_3	0	0	—	0.17
γ_4	0.85	0.75	—	0.85

where ξ is the damping ratio and ω_1 and ω_2 are system natural frequencies. Generally, the damping is set to be 0.05, and structure first-order natural frequency and the tenth-order natural frequency are selected for ω_1 and ω_2 in current study.

3.5. Computation Time Step. As high frequency contents will be generated in the occurrence of base mat uplift, the time step is selected to be 0.002 s, which is small enough to consider the influence of high frequency contents.

4. Influencing Factors

There are many factors that impact the seismic response of structure, like velocity of shear wave, type and amplitude of seismic wave, structure stiffness, the ratio of structure height

to width, and so on. The following factors are considered in this papers.

(1) *Amplitude of Seismic Wave.* According to Chinese code [27], the amplitude of seismic wave in terms of ultimate safety in ground motion is 0.15 g and should not be bigger than 0.5 g for seismic design of nuclear power plants. Therefore, three amplitudes are considered: 0.15 g, 0.5 g, and 1 g (1 g is for the sake of comparison).

(2) *Direction of Seismic Waves.* According to Chinese code, the direction of input seismic wave in model should be applied at two horizontal and one vertical direction simultaneously. Due to the symmetry of the structure, the seismic waves are input only in one horizontal (X) and one vertical (Y) directions in current study. The amplitude of seismic wave in vertical direction is set to be two-thirds of that in horizontal direction. Furthermore, in order to analyze the influence of vertical seismic wave on the dynamic response of structure, the case having only horizontal seismic wave input is also considered.

(3) *Type of Seismic Wave.* EL-Centro wave is selected as first input wave, and Songpan wave is used as the second one, which is recorded in Wenchuan earthquake in 2008 in China, and Taft wave is then used for comparison purpose. The time history and Fourier spectrum curves for above three types of seismic wave are illustrated in Figure 7, and their amplitudes are scaled to be 0.15 g, 0.5 g, and 1 g, respectively.

TABLE 3: Soil impedance functions recommended in ASCE code [24].

Motion	Equivalent spring constant	Damping coefficient
Horizontal	$K_x = 32(1-\nu) \frac{GR}{7-8\nu}$	$C_x = 0.576K_x R \sqrt{\frac{\rho}{G}}$
Rocking	$K_\psi = \frac{8GR^3}{3(1-\nu)}$	$C_\psi = \frac{0.3}{1+B_\psi} K_\psi R \sqrt{\frac{\rho}{G}}$
Vertical	$K_z = \frac{3GR}{1-\nu}$	$C_z = 0.85K_z R \sqrt{\frac{\rho}{G}}$
Torsion	$K_t = \frac{16GR^3}{3}$	$C_t = \frac{\sqrt{K_t I_t}}{1+2I_t/\rho R^5}$

Note. ν , G , and ρ are soil Poisson ratio, shear modulus, and mass density and R is the equivalent radius of structure base mat. $B_\psi = [3(1-\nu)I_0]/(8\rho R^5)$, in which I_0 is the mass moment of inertia about the rocking axis at structure base mat and I_t is structure polar mass moment of inertia.

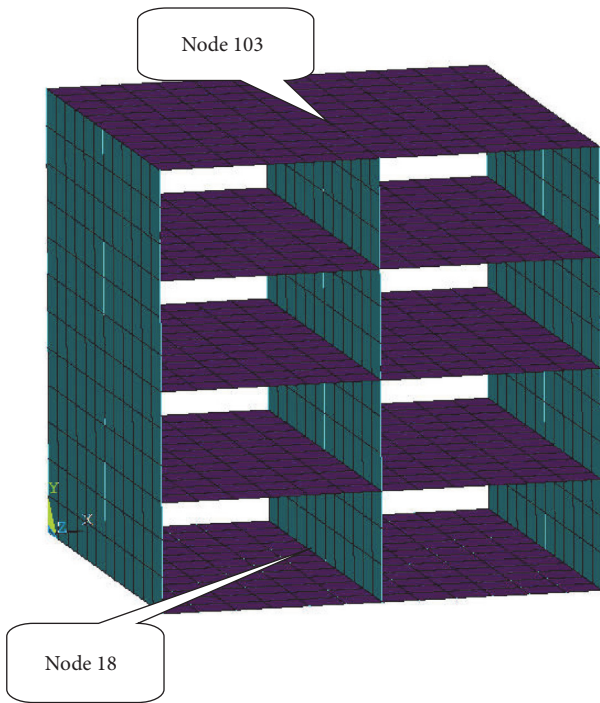


FIGURE 5: Computation model.

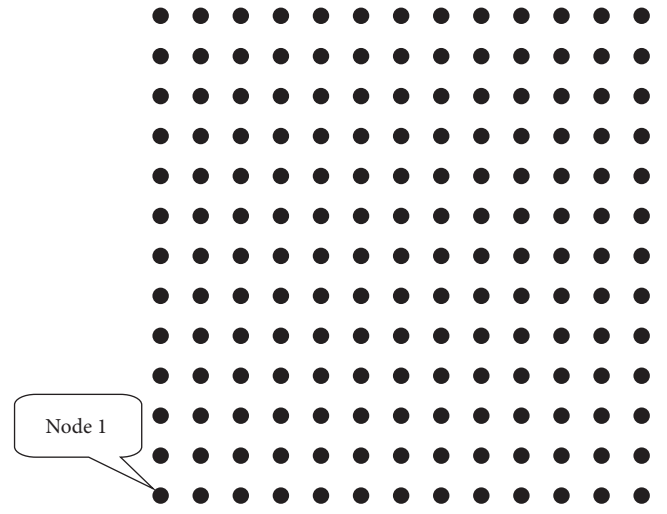


FIGURE 6: Plan view of base mat.

TABLE 4: Calculation results comparison between two methods.

Motion	K		c	
	Veletsos	ASCE	Veletsos	ASCE
Horizontal/N/m	9.01E10	9.73E10	0.63	0.58
Rocking/N*m	1.96E12	1.81E12	0.15	0.11
Vertical/N/m	8.97E10	9.63E10	0.83	0.72
Torsion/N*m	2.33E12	2.09E12	0.16	0.12

(4) *Soil Parameters*. Based on Chinese code, the soil-structure interaction effect can be neglected if the velocity of shear wave in soil is bigger than 1100 m/s. In this study, three velocities of shear wave in soil are considered: 2000 m/s, 1100 m/s, and 400 m/s.

5. Modal Analysis

Modal analysis is firstly conducted on structure system. The first five natural frequencies and their corresponding vibration modes are given in Table 5.

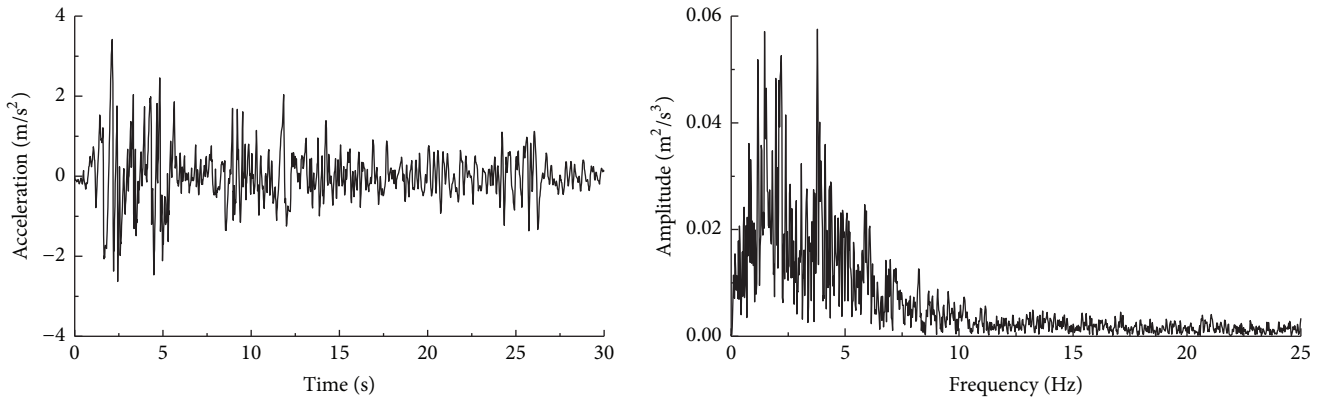
6. Analysis of the Standard Case

The standard case is defined as that where the structure is excited by the EL wave in horizontal direction with peak acceleration of 0.5 g and vertical direction with peak acceleration of 0.33 g simultaneously (labeled as HV case), and the velocity of shear wave is set to be 1100 m/s.

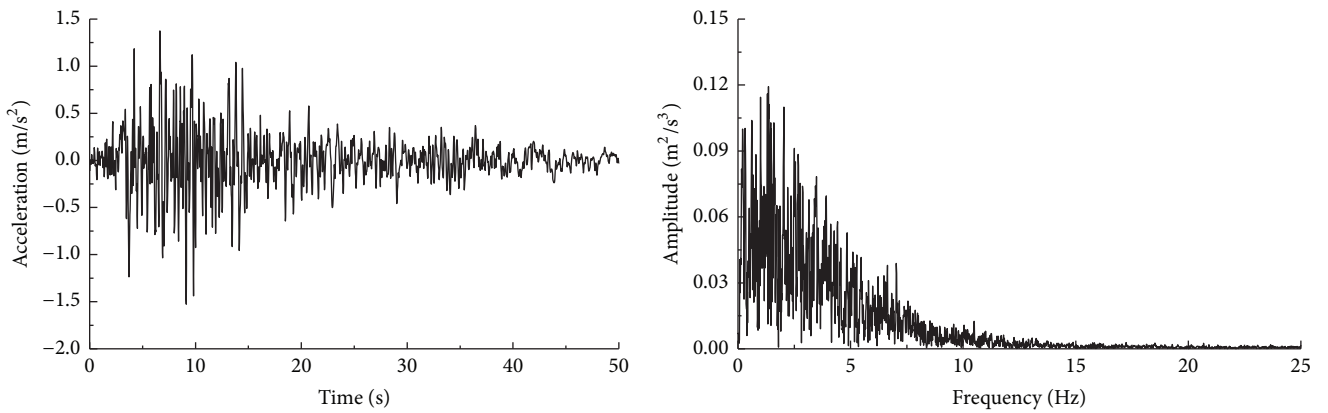
6.1. Floor Acceleration and Corresponding Fourier Spectrum. The time history of horizontal and vertical acceleration and its corresponding Fourier spectrum curves for the fourth floor (the node 103 in Figure 4) and the first floor (node 18 in Figure 4) are given in Figures 8 and 9, respectively. It is observed that the amplitudes of acceleration are different for different floors, and the amplitude of acceleration increases with the structure height. It is also found that horizontal acceleration

TABLE 5: The first five natural frequencies and corresponding vibration mode.

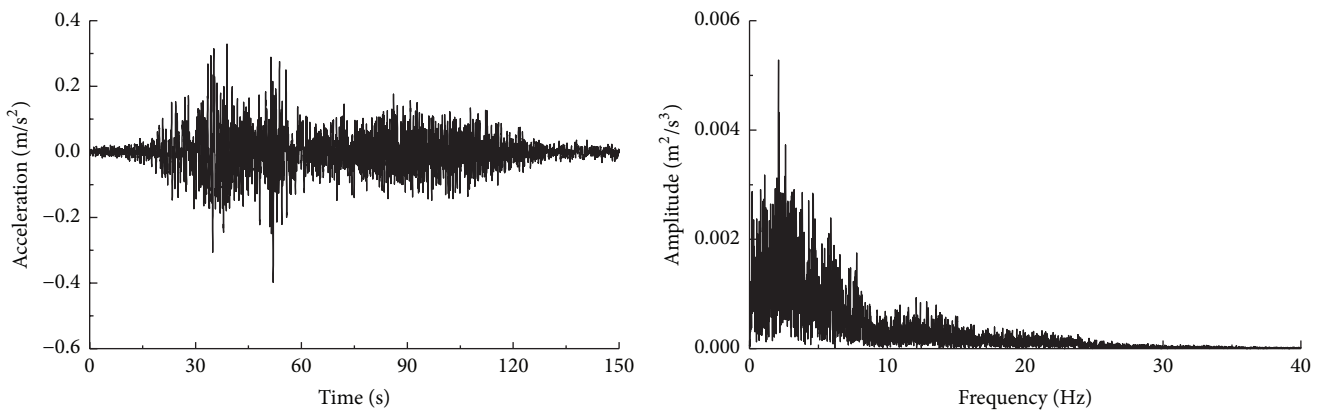
Order	1	2	3	4	5
Frequency/Hz	1.9581	7.4998	10.961	12.309	14.572
Vibration Mode	Horizontal	Horizontal	Structure torsion about vertical axis	Floor torsion about vertical axis	Vertical



(a) El-Centro wave



(b) Taft wave



(c) Songpan wave

FIGURE 7: Time history and Fourier spectrum curves of input waves.

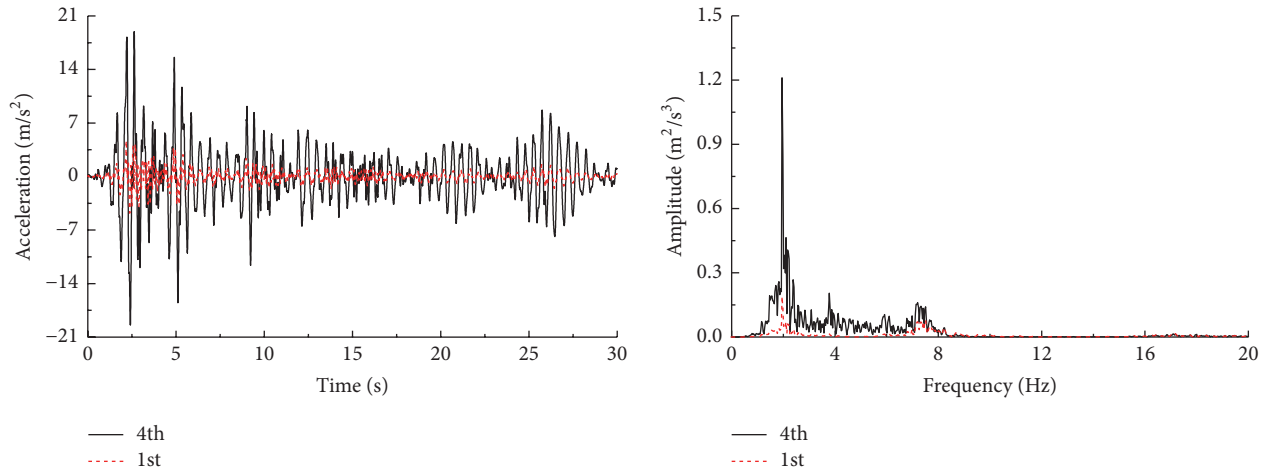


FIGURE 8: Horizontal acceleration time history and corresponding Fourier spectrum curves at node 103 on the 4th floor and node 18 on the 1st floor under standard case (HV).

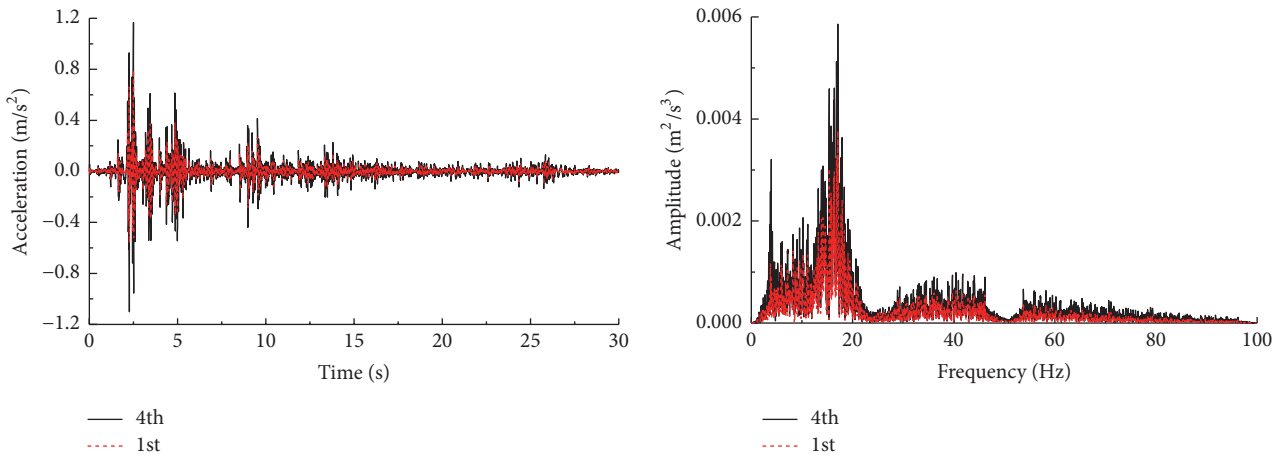


FIGURE 9: Vertical acceleration time history and corresponding Fourier spectrum curves at node 103 on the 4th floor and node 18 on the 1st floor under standard case (HV).

is mainly concentrated in low frequency, especially at the structure natural frequency (1.958 Hz), while the spectrum of the frequency for vertical acceleration is much wider than that of horizontal acceleration.

6.2. Floor Response Spectrum. Figure 10 reports the response spectrum curves of horizontal and vertical acceleration for the fourth and first floor. The predominant period of horizontal acceleration (as shown in Figure 10(a)) is much longer than that of the vertical acceleration (as shown in Figure 10(b)). From Figure 10, it is also found that, in lower floor, the predominant period is shorter, which is consistent with the result obtained from Figures 8 and 9.

6.3. Base Mat Vertical Displacement and Rotation. According to the prescribed method shown in Figure 4, the base mat will be separated from the underlying soil if the vertical displacement at node 1 (See Figure 4) is larger than zero. The uplifted time and its related uplifted amount can be seen in

Figure 11 for foundation corner. The peak vertical displacement at node 1 under the HV case is 0.334 mm with the trigger time at 2.4549 s, and, accordingly, it can be calculated that the rotation angle of foundation is $0.334/12000$, which is so small that the influence of base mat uplift on seismic response of structure can be neglected. The above result can also be verified by the time history curves of horizontal acceleration and its corresponding Fourier spectrum curves for node 103 for the case of base mat uplift allowed and restricted (Figure 12). From Figure 12, it is found that for both cases the curves are almost identical.

6.4. Uplift Area Ratio. The ratio of uplift area is defined as the ratio of the maximum uplifted area to the total area of base mat. This value is a key parameter to evaluate the effect of base mat uplift on the seismic response of structure. In current study, the maximum uplifted area can be determined by the following procedures: (a) extract the time history curve of vertical displacement at node 1; (b) determine the trigger time

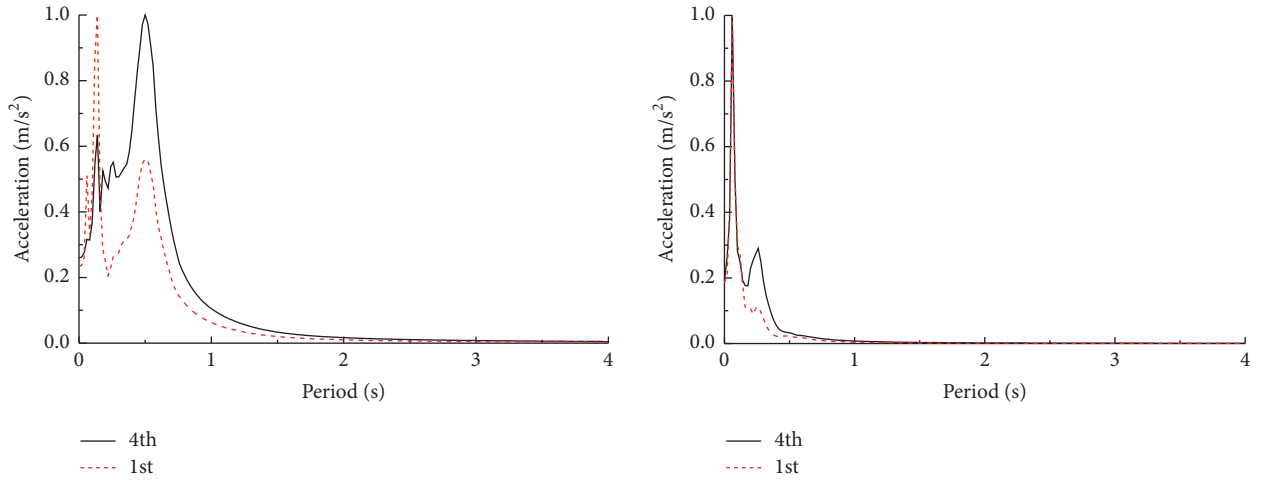


FIGURE 10: Horizontal and vertical acceleration response spectrum curves of the fourth and first floor under standard case (HV).

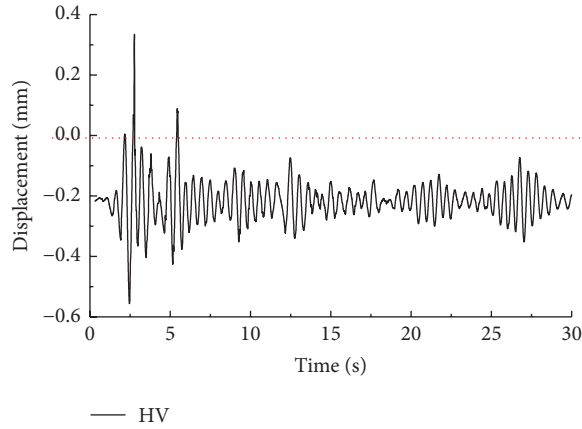


FIGURE 11: Vertical displacement at the corner of base mat under standard case (HV).

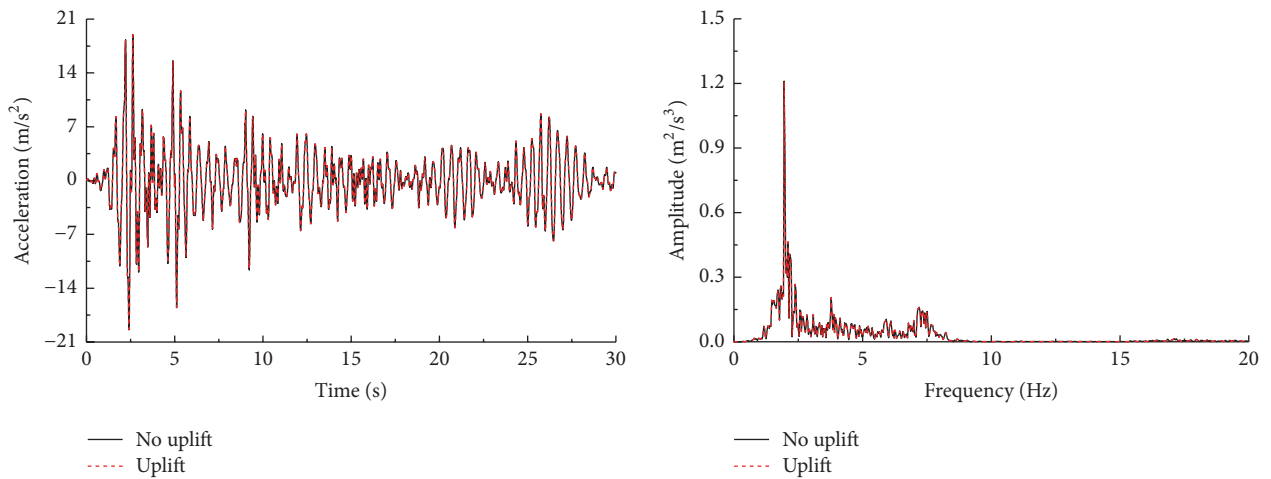


FIGURE 12: Horizontal acceleration time history and its Fourier spectrum curves at node 103 on the fourth floor under standard case (HV).

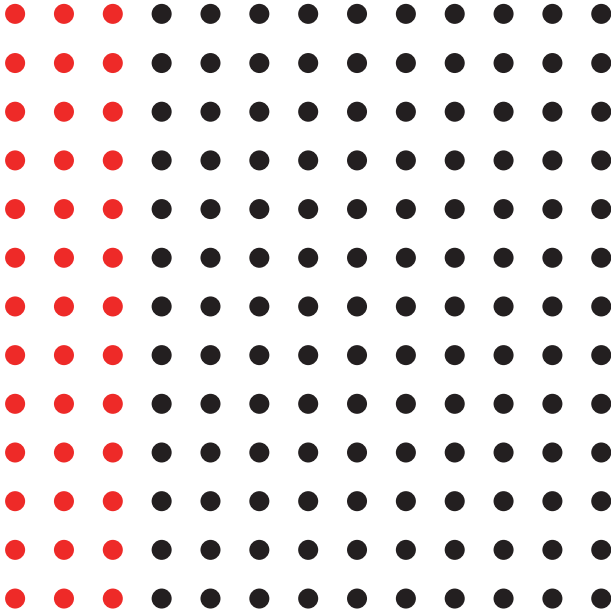


FIGURE 13: Schematic diagram of uplifted nodes under standard case: 52 nodes uplifted and uplift area ratio is 25.0%.

of the base mat uplift; and (c) select the nodes whose vertical displacement is bigger than zero at this time or substep. These selected nodes are seen as the uplifted nodes and the area consisted by these nodes is then defined as the maximum uplifted area.

Figure 13 is the selected uplifted nodes at the base mat for the standard case (HV case). It can be observed that there are 52 uplifted nodes and hence the uplift area ratio is calculated as 25% for the HV case.

7. Analysis of Influence Factors

Key factors affecting the dynamic response of structure are analyzed in this section, including seismic wave (input direction, amplitude, and type), velocity of shear wave in soil, and structure related factors (stiffness and the ratio of height to width, H/B). The calculated results are compared with those of the standard case (HV case). For the sake of simplicity, the H case represents the one that the structure is merely excited in horizontal direction.

7.1. Influence of Input Seismic Wave Directions. Figure 14 shows the time history curve of horizontal acceleration and its corresponding Fourier spectrum curves at node 103 both for the H case and the HV case. It can be seen that the horizontal acceleration and spectrum curves for both cases are almost the same, which means the seismic wave input at vertical direction has little impact on the structural response at horizontal direction.

From Figure 15, it is found that the vertical acceleration is greater in HV case than that in the H case. The higher frequency contents are observed for the HV case due to the base mat uplift as shown in Figure 16.

Figure 17 illustrates the horizontal and vertical acceleration response spectrum curves at node 103 on the fourth floor for HV and H cases.

Figure 18 is the time history curves of vertical displacement at node 1 (see Figure 4) for the HV and H cases. It can be seen that the variation of vertical displacement response under two cases is identical, and there are only small difference in peak values for both cases. It is found that the peak value for the H case is 0.189 mm at time of 2.4089 s, while the peak value for HV case is 0.334 mm at the time of 2.4549 s, which is almost twice of that in the H case.

Figures 19 and 13 are the uplifted nodes at the base mat for H case and HV case, respectively. It can be seen that there are 39 uplifted nodes and the uplift area ratio is about 16.7%, while for HV case the uplift area ratio is 25%.

Based on above analysis, it can be concluded that the seismic wave input at vertical direction has little influence on structural response at horizontal direction, while mainly having impact on the structural response at vertical direction and the maximum base mat uplift area ratio.

7.2. Influence of Input Seismic Wave Amplitudes. The maximum vertical displacements at node 1 for the HV case with amplitudes of 0.15 g, 0.5 g, and 1 g are -0.42 mm, 0.334 mm, and 2.91 mm, respectively, and its corresponding maximum uplift area ratios are determined as 0%, 25%, and 75%, respectively. It can be seen that the maximum vertical displacement at base mat is negative in the case that the amplitude of seismic wave is small (0.15 g), which means the base mat uplift does not occur. Meanwhile, for the HV case with the amplitude of 0.4 g, the maximum vertical displacement at node 1 is found to be 0.02 mm, which can be treated as the critical amplitude for the base mat uplift in current study.

7.3. Influence of Input Seismic Wave Types. It is well known that the different seismic waves have different frequency components and in turn generate different seismic responses of structure. In this section, three types of seismic waves are selected with consideration of the distance effect, that is, the EL wave (near-field wave), Taft wave (middle-distance wave), and Songpan wave (long-distance wave) which is recorded during the Wenchuan earthquake in 2008 in China. Their acceleration time history and Fourier spectrum curves are shown in Figure 7.

Due to the difference in computational times (EL wave 30 s, Taft wave 50 s, and Songpan wave 150 s), the results from different seismic waves are shown separately. Figures 8, 20, and 21 show the time history curve of horizontal acceleration and its corresponding Fourier spectrum curves at node 103 under EL, Taft, and Songpan waves (with HV input), respectively. It can be seen that for Songpan wave the acceleration has bigger value (22.09 m/s²) while the acceleration for Taft wave is smaller (18.44 m/s²). This is reasonable as the dominant frequency of Songpan wave is about 2 Hz (as shown in Figure 7), which is very close to structural first natural frequency of 1.96 Hz. And from Table 4, it is observed that the first-order vibration mode for structure is horizontal vibration.

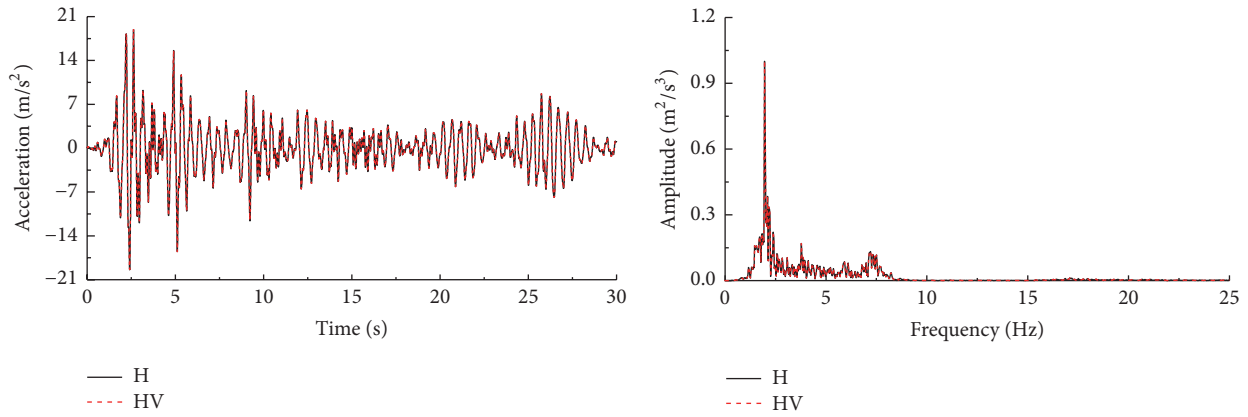


FIGURE 14: Horizontal acceleration time history and spectrum curves at node 103 under EL wave for H and HV case.

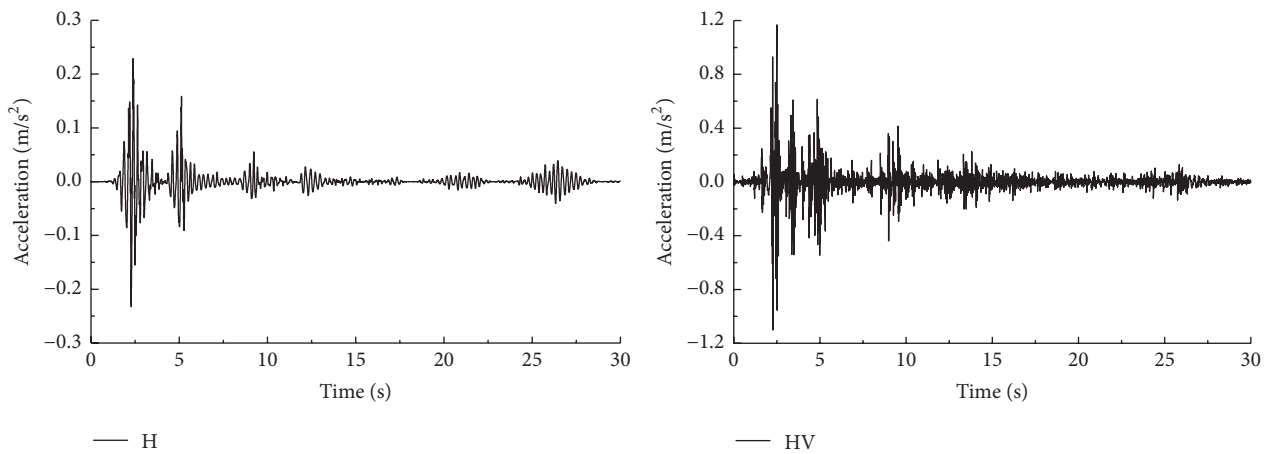


FIGURE 15: Vertical acceleration time history at node 103 under EL wave for H case and HV case.

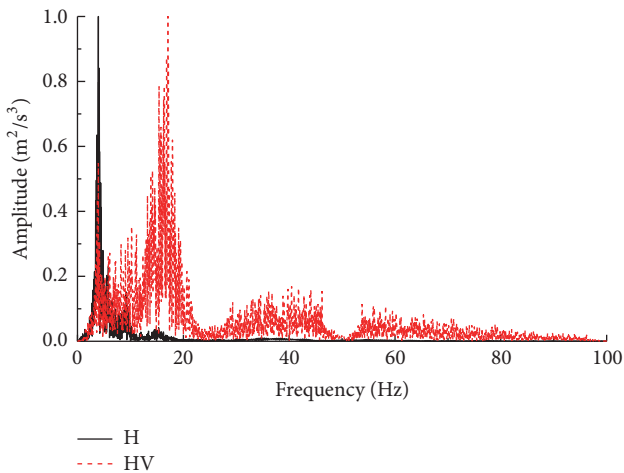


FIGURE 16: Normalized vertical acceleration Fourier spectrum curves at node 103 under EL wave for H case and HV case.

The vertical displacement response at node 1 (Figure 22) under Songpan wave has bigger value of 0.436 mm, while, for the Taft wave, smaller value is observed (0.0488 mm),

which is only one-tenth of that in the case of Songpan wave. However, more importantly, based on the red dotted line in Figure 22, it is found that the vertical displacements under the EL and Taft wave exceeded zero value at several moments, while for Songpan wave, the vertical displacement went beyond zero value at concentrated moments. It can be postulated that under Songpan wave the base mat uplift occurs at concentrated moment, while base mat uplift happens at several moments under the EL and Taft wave.

Figures 23, 24, and 25 report the time history curve of vertical acceleration and its corresponding Fourier spectrum curves at node 103 for the case of EL, Taft, and Songpan waves with the standard HV input wave, respectively. It can be seen that the acceleration under Songpan wave is bigger while the acceleration under EL wave is smaller. From the figure, it is also observed that the Fourier spectrum curve under Songpan wave consists of many higher frequency components between 40 Hz and 100 Hz, at which the bigger uplift displacement occurred.

Figures 13, 26, and 27 give the schematic diagrams of uplifted nodes under EL, Taft, and Songpan wave with the standard HV input, respectively. From Figure 27, it is found that the maximum uplifted area ratio under Songpan wave

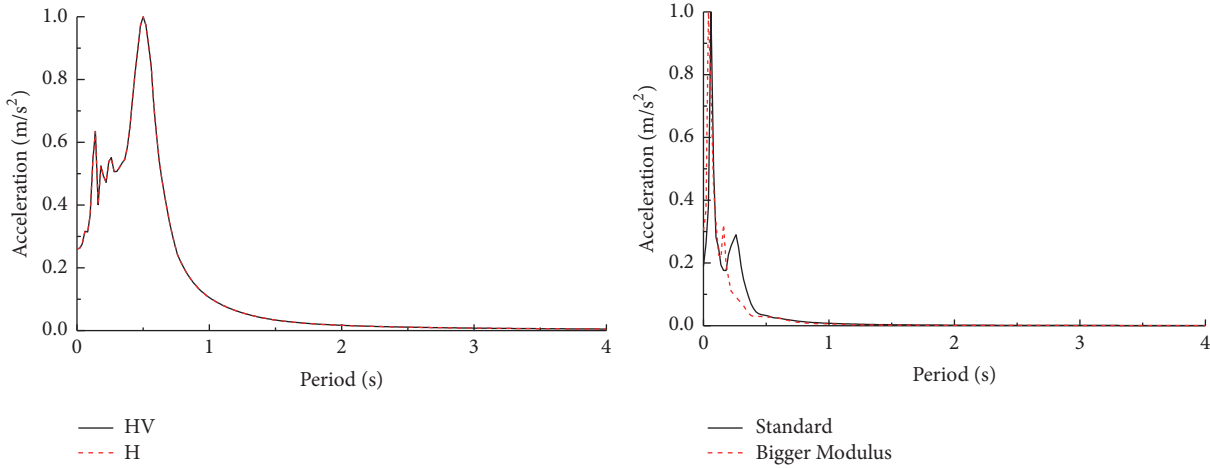


FIGURE 17: Normalized horizontal and vertical acceleration spectrum curves at node 103 under EL wave for HV and H case.

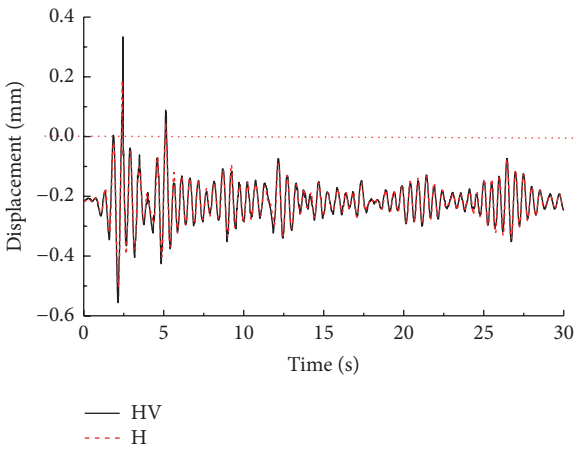


FIGURE 18: Vertical displacement time history curves at node 1 under EL wave for H case and HV case.

has a bigger value of 25.6%, while the ratio under Taft wave is as small as 5.6%.

From the above analysis, it can be concluded that the different seismic waves have a significant influence on the dynamic response of structure due to different frequency components from each seismic wave. When the predominant frequency of seismic wave is closer to that of the natural frequency of structure, the seismic response of structure will be excited significantly.

7.4. Influence of Shear Wave in Soil. Figures 28, 13, and 29 illustrate the schematic diagrams of uplifted nodes under the EL wave with the velocity of shear wave in soil of 400 m/s, 1100 m/s, and 2000 m/s, respectively. The maximum uplifted area ratios under the above three velocities are found to be 5.6%, 25%, and 33.3%, respectively, which means that the stiffer the soil, the easier the occurrence of the base mat uplift.

7.5. Influence of Structure Stiffness. Two cases were considered in this section. For the first case, the stiffness of the

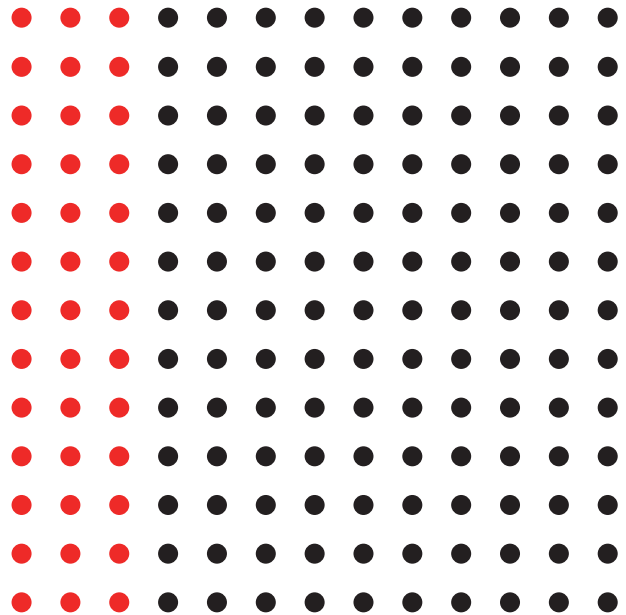


FIGURE 19: Schematic diagram of uplifted nodes under H case: 39 nodes uplifted and uplift area ratio is 16.7%.

structure is increased: the thickness of side wall is increased from 0.2 m to 0.4 m, and the section of the column is enhanced from 0.6 m * 0.6 m to 1.0 m * 1.0 m. Consequently, the structural natural frequency is increased from 1.958 Hz to 3.033 Hz. For simplicity, this case is labeled as Bigger Section. Figure 30 reports the time history curve of vertical displacement at node 1 on the base mat for the Bigger Section case. It can be found that the vertical displacement is less than zero during all time, which means that the base mat was not uplifted during the earthquake. This is because that the increase of structural section size will significantly increase the total mass of the structure, and in turn the heavier weight of structure will be beneficial to resist the occurrence of base mat uplift. For the second case, in order to investigate

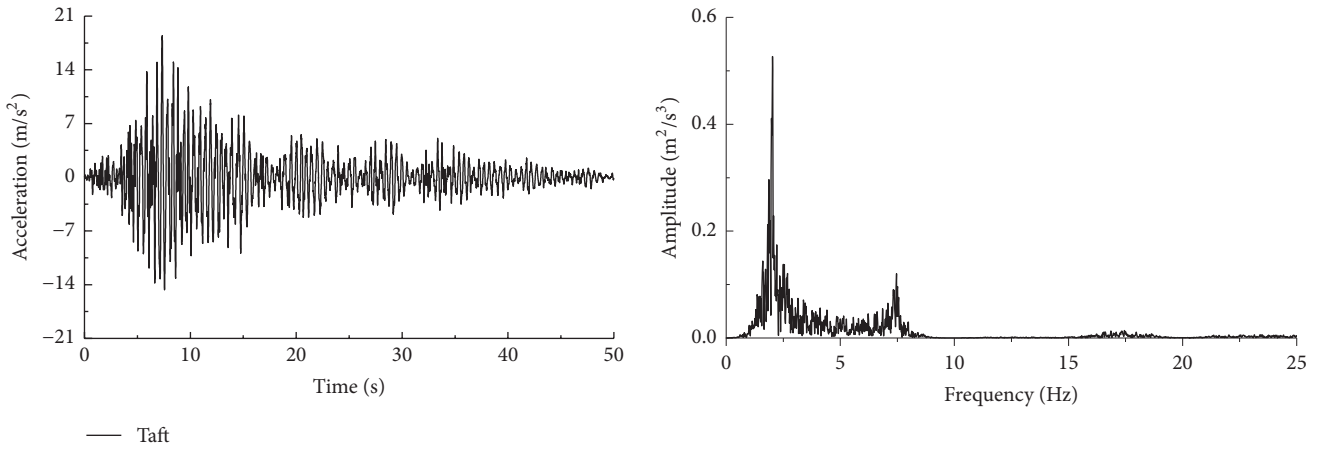


FIGURE 20: Horizontal acceleration time history and Fourier spectrum curves at node 103 under Taft wave (HV case).

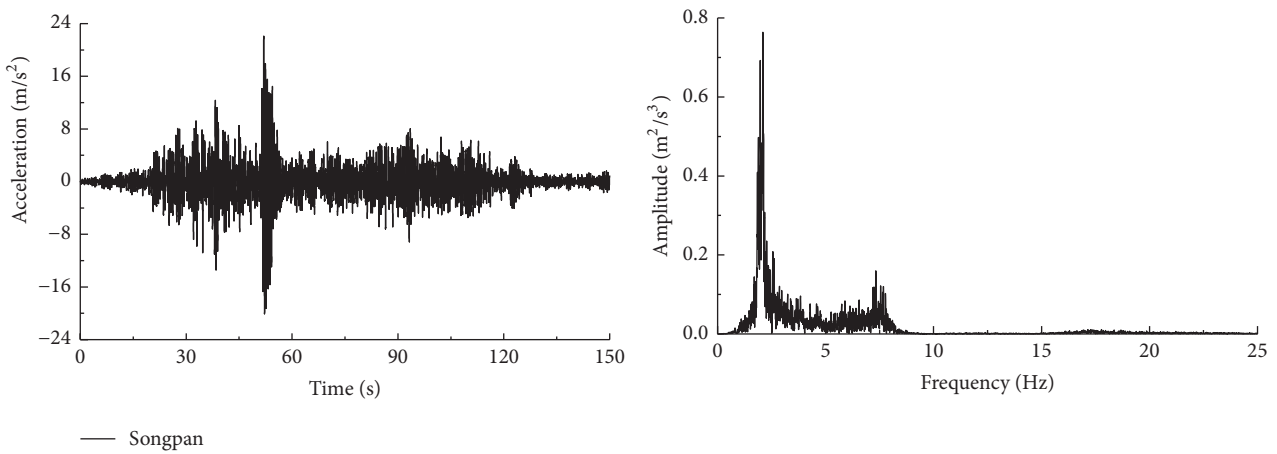


FIGURE 21: Horizontal acceleration time history and Fourier spectrum curves at node 103 under Songpan wave (HV case).

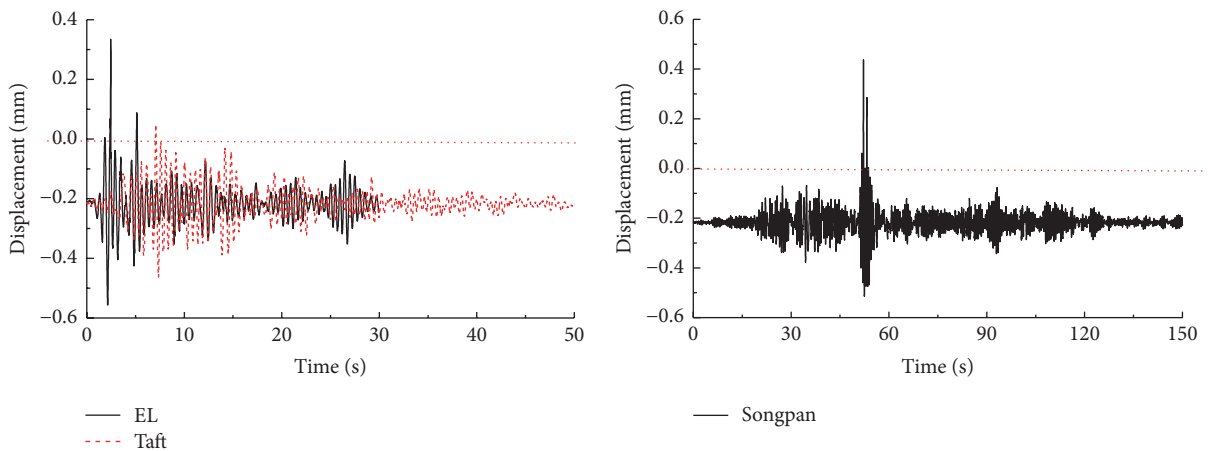


FIGURE 22: Comparison of vertical displacement time history curves at node 1 under EL, Taft, and Songpan waves.

the influence of structure stiffness on the dynamic response of structure, the total structural mass remains unchanged, while the structural stiffness is strengthened by increasing material modulus. In this case, the modulus of material is set to 75 GPa after using trial and error method to make the natural frequency of structure close to that in the first case.

The second case is labeled as Bigger Modulus. From Figure 30, it is found that the base mat uplift occurs. Hence, it can be concluded that the base mat is easier to occur under bigger structural stiffness.

The spectrum curves of horizontal and vertical acceleration at node 103 on the fourth floor for Standard and Bigger

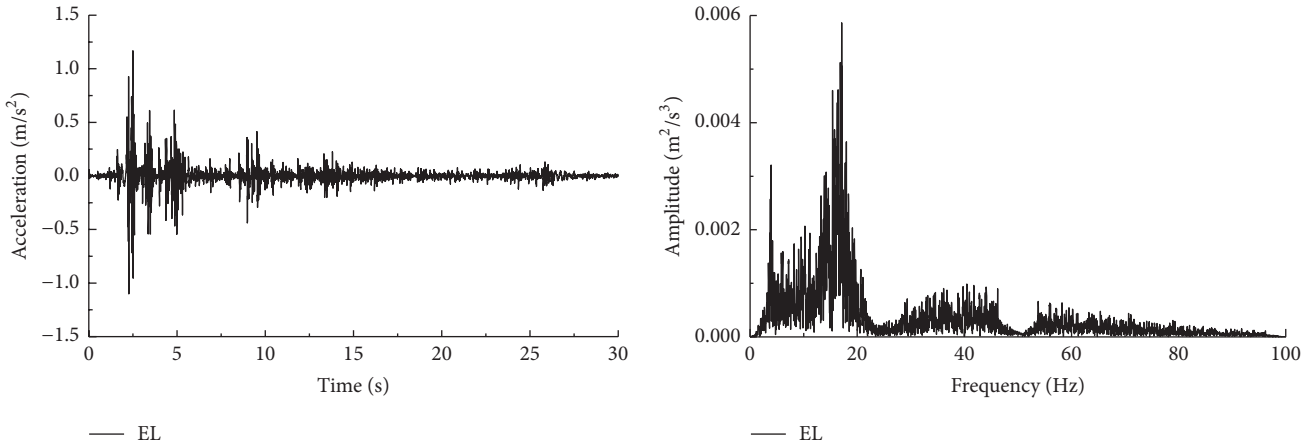


FIGURE 23: Vertical acceleration time history and Fourier spectrum curves at node 103 under EL wave (HV case).

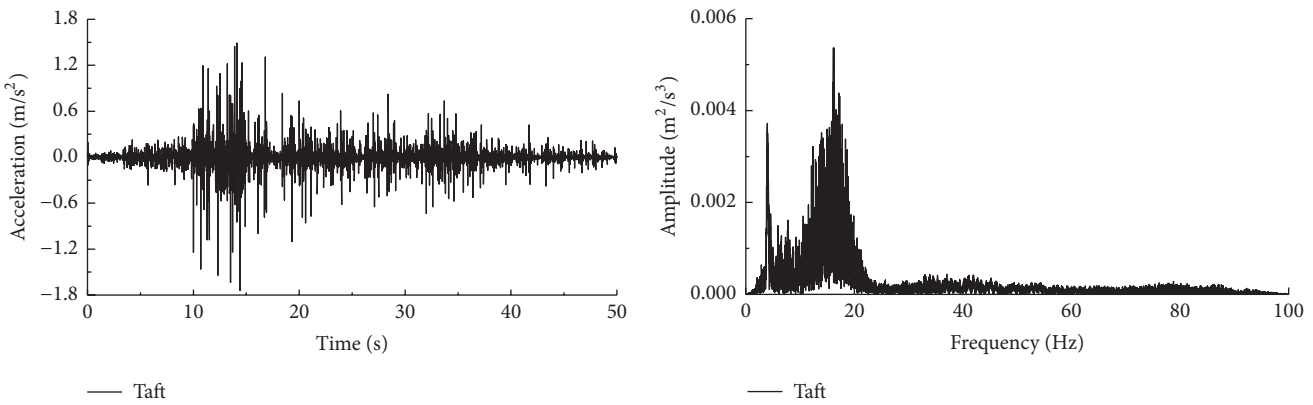


FIGURE 24: Vertical acceleration time history and Fourier spectrum curves at node 103 under Taft wave.

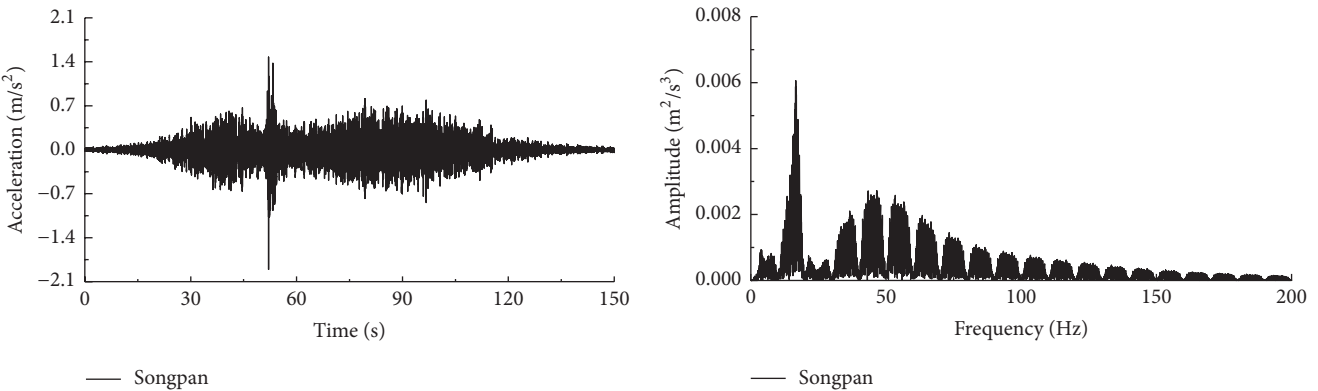


FIGURE 25: Vertical acceleration time history and Fourier spectrum curves at node 103 under Songpan wave.

modulus case are given in Figure 31. From the figure, it can be found that the structural stiffness affects the horizontal acceleration in shorter period, while it impacts on the vertical acceleration in longer period.

The schematic diagram of uplifted nodes under the case of Bigger Modulus is given in Figure 32. It can be seen that only 34 nodes were uplifted and then the maximum uplift area ratio is found to be 12.5%, which is much smaller than that in standard case (52 uplifted nodes with the maximum uplift area ratio of 25%).

7.6. Influence of the Ratio of Structure Height to Width. The ratio of structural height to width (H/B) is set to 1 in the standard case. In this section, the values for H/B are set to 0.5 and 2 by modifying the structure to two-story and eight-story, respectively. And other material parameters remain the same as those in Standard case. The time history curves of vertical displacement for two H/B values are given in Figure 33. It is observed that the base mat uplift did not occur for these two cases; however, the base mat uplift is relatively easier to occur for smaller H/B value.

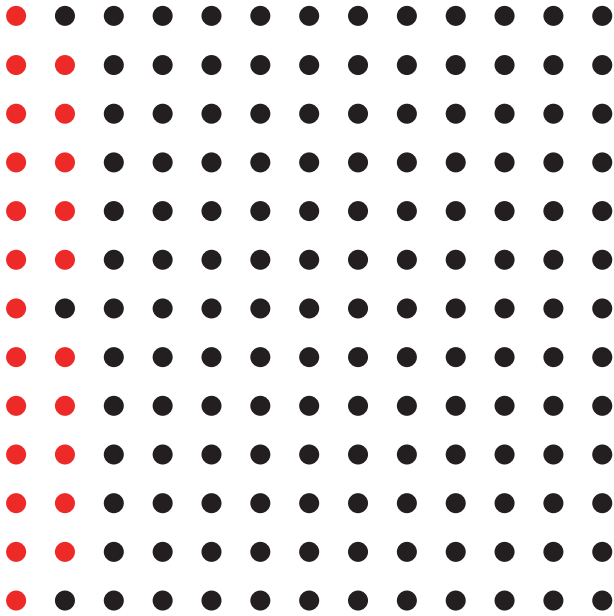


FIGURE 26: Schematic diagram of uplifted nodes under Taft wave for HV case (23 nodes uplifted and uplift area ratio is 5.6%).

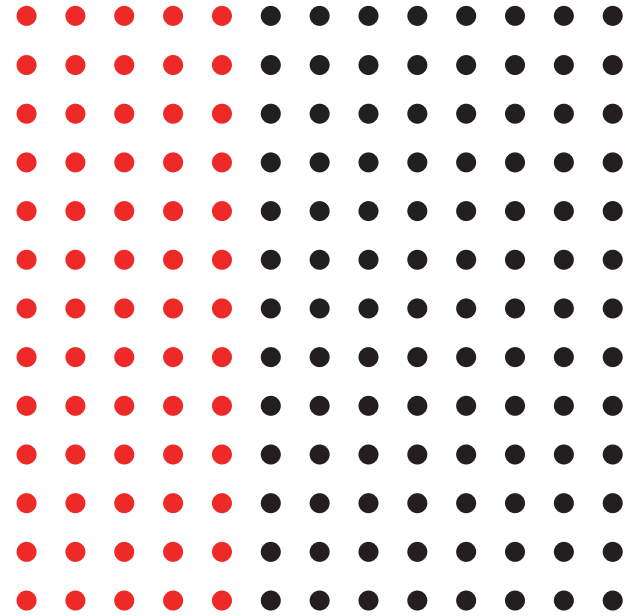


FIGURE 28: Schematic diagram of uplifted nodes with the soil shear wave 2000 m/s under EL wave for HV case (65 nodes uplifted and uplift area ratio is 33.3%).

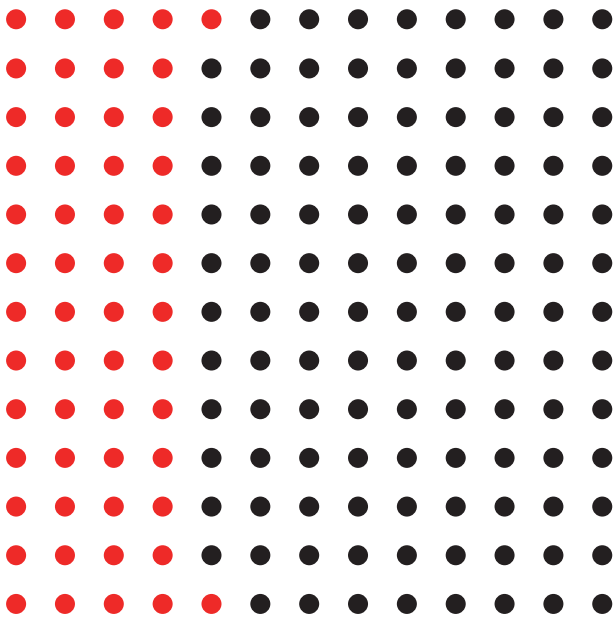


FIGURE 27: Schematic diagram of uplifted nodes under Songpan wave for HV case (54 nodes uplifted and uplift area ratio is 25.6%).

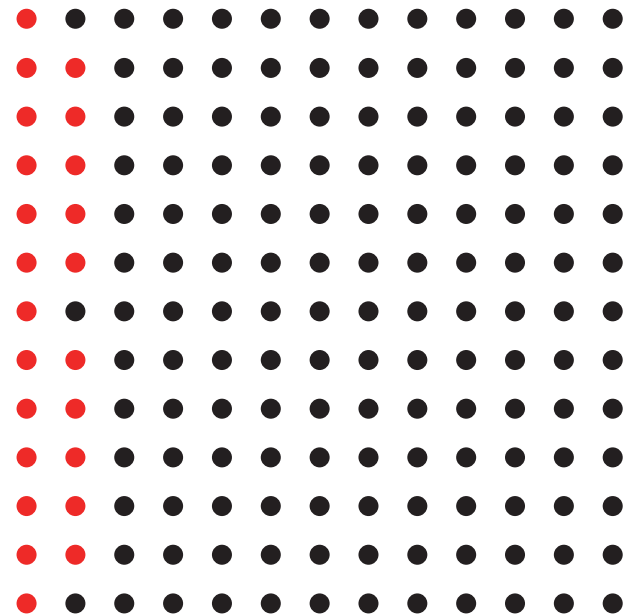


FIGURE 29: Schematic diagram of uplifted nodes with the soil shear wave 400 m/s under El wave for HV case (23 nodes uplifted and uplift area ratio is 5.6%).

The comparisons of the structural natural frequency and its related structural stiffness are also conducted. The first natural frequencies for H/B values of 2, 1, and 0.5 are found to be 0.851 Hz, 1.958 Hz, and 4.746 Hz, respectively, and their related masses are $1.363e6$ Kg, $7.375e5$ Kg, and $4.249e5$ Kg, respectively. Therefore, based on the empirical formula $k = m * (2\pi f)^2$, the corresponding structural stiffness for different H/B values can be calculated as $3.9e7$ N/m, $11.16e7$ N/m, and $37.79e7$ N/m, respectively. It is obvious that with the increase

of H/B ratio, the structural masses increase while the first-order natural frequency decreases. It is then postulated that the structure tended to be softer with the increase of H/B ratio.

The base mat uplift is found easier to occur for small H/B ratio value by comparing the case of H/B ratio of 0.5 and 2, while the conclusion is contrary by comparing the case of H/B ratio of 0.5 and 1. This can be explained in two aspects:

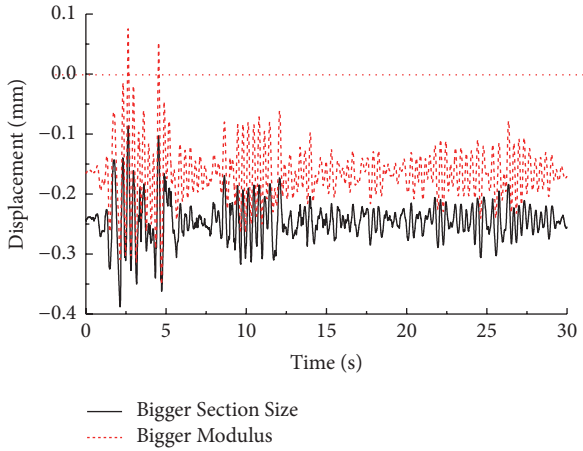
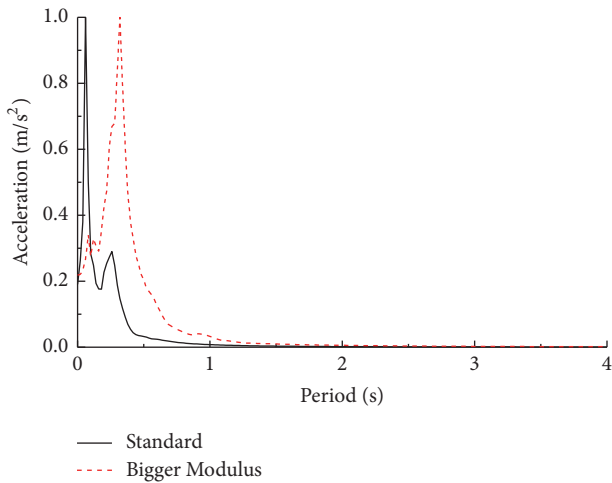
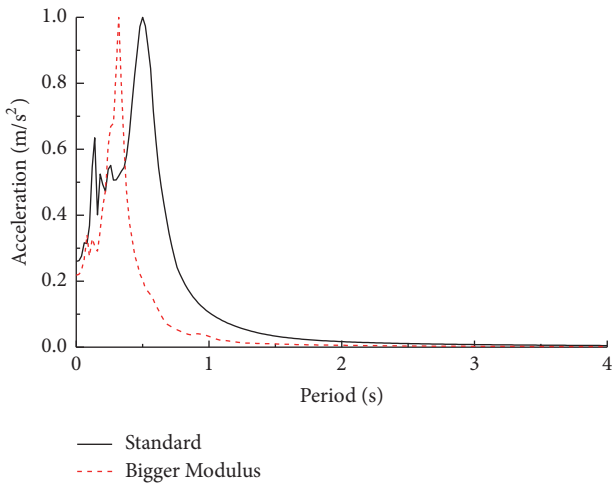


FIGURE 30: Vertical displacement time history curves at node 1 on the structure base mat under two cases: Bigger Section Size case and Bigger Modulus case.



(a) Horizontal acceleration



(b) Vertical acceleration

FIGURE 31: Spectrum curves of horizontal and vertical acceleration at node 103 under standard case and Bigger Modulus case.

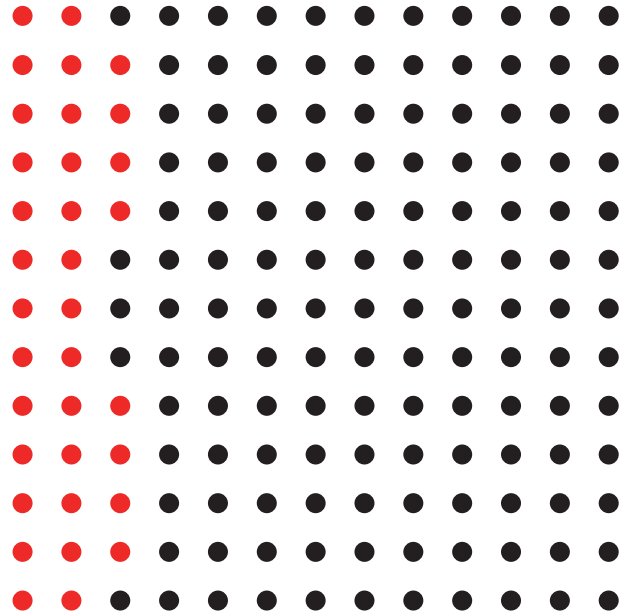


FIGURE 32: Schematic diagram of uplifted nodes under the Bigger Modulus case (34 nodes uplifted and the maximum uplift area ratio is 12.5%).

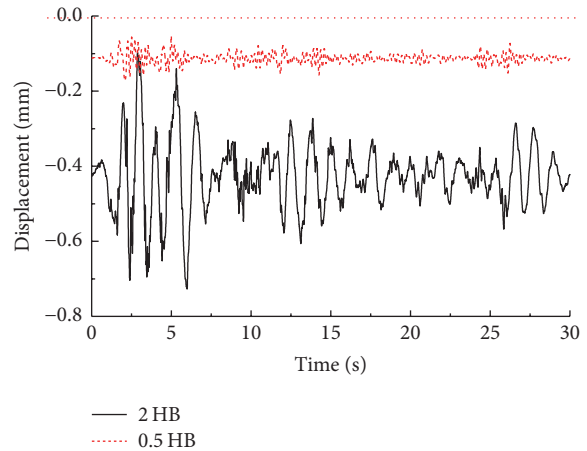


FIGURE 33: Vertical displacement time history curves at node 1 on the structure base mat under two cases: structure H/B ratios are equal to 0.5 and 2.

firstly, the bigger inertial force and overturning moment tend to be generated for higher structure and then result in the uplifting of base mat. Secondly, it is well known that the structure will perform more stable for larger width, which is beneficial to resist the occurrence of base mat uplift.

7.7. Influence of the Concentrated Mass. It should be noted that the existence of the machine, furniture, or accessory equipment can be simplified as a concentrated mass on the floor in general. Theoretically, the influence of concentrated mass on the base mat uplift should be investigated in three aspects: firstly, greater inertial force will be applied on the structure, and hence the base mat uplift is easier to

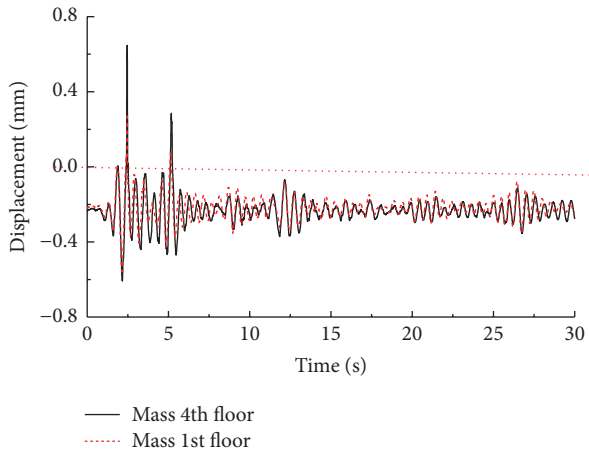


FIGURE 34: Vertical displacement time history curves at node 1 on the structure base mat under two cases: concentrated mass located on the fourth and first floor.

occur. Secondly, the concentrated mass has little influence on structural stiffness, and then the heavier structure can prevent base mat uplift. Thirdly, the structure will be assumed to be an unsymmetrical structure and then the torsion force will affect the dynamic response of structure. However, the effect of torsion force is decided by the weight of the concentrated mass. This means whether the base mat uplift can be prevented or not is determined by the weight and location of the concentrated mass. However, the influence of the location of concentrated mass is discussed in this section because the weight can be changed a lot in the practical situation.

A concentrated mass with the one-tenth of the total weight of the structure is located on the middle point in the fourth and the first floor, respectively. The time history curves of vertical displacement for the two cases are shown in Figure 34. It is observed that the maximum vertical displacements for the Mass on 4th Floor and Mass on 1st Floor are about 0.647 mm and 0.2836 mm, respectively, and its corresponding maximum uplift ratios are found to be 33.3% (65 uplifted nodes as shown in Figure 35) and 22.2% (49 uplifted nodes as shown in Figure 36), respectively, while, for the standard case (No Concentrated Mass), the maximum vertical displacement is found to be 0.334 mm with the maximum uplift ratio of 25% (52 uplifted nodes). It can be found that the location of concentrated mass on the higher floor (4th floor) tends to make the base mat uplift easier to occur, while the existence of concentrated mass on the lower floor (1st floor) will prevent the base mat uplift. The final result depends on which factor is dominant: the overturning moment caused by inertial force or structure total weight.

8. Conclusions

In order to overcome the computational convergence issue in traditional contact and joint element method, a new method based on the spring element is proposed in this paper to consider the impact of base mat uplift on the seismic response

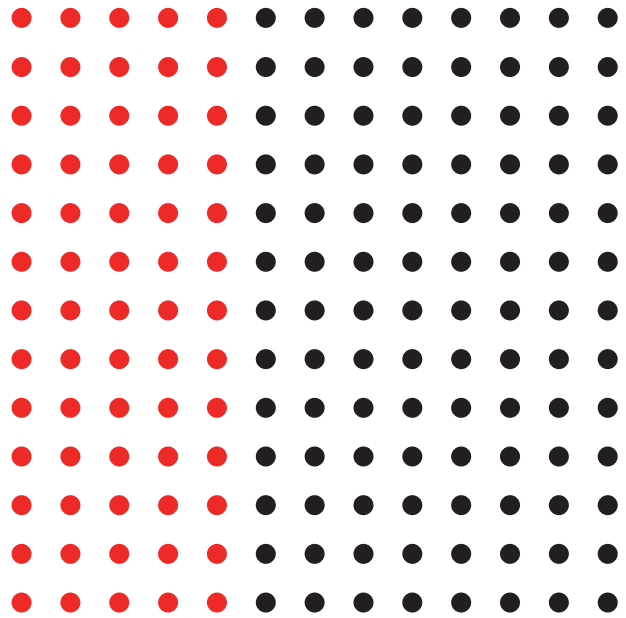


FIGURE 35: Schematic diagram of uplifted nodes under the concentrated mass located on the fourth floor (65 nodes uplifted and the maximum uplift area ratio is 33.3%).

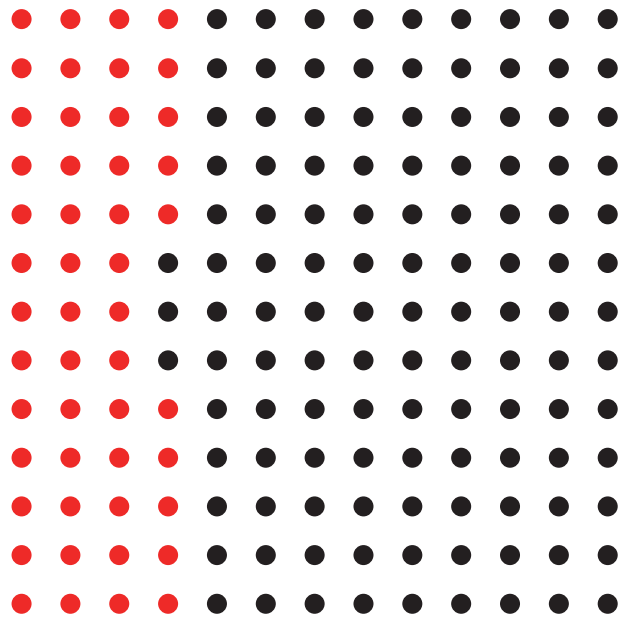


FIGURE 36: Schematic diagram of uplifted nodes under the concentrated mass located on the first floor (49 nodes uplifted and the maximum uplift area ratio is 22.2%).

of structure. Some key factors, such as seismic waves, velocity of shear wave in soil, and structural characters, are analyzed and discussed. The following conclusions can be drawn from the above analysis and comparison:

- (1) The vertical direction of input seismic wave has little influence on the seismic response of structure at horizontal direction, while it significantly affects the seismic response of structure in vertical direction, and the maximum uplifted

area ratio of structure. This result is consistent with the earlier research results by Joe (1993) and Kennedy et al. (1976) and in turn verified the rational of the proposed method in current study.

(2) The seismic response of structure tends to be larger with the increase of the amplitude of input seismic wave.

(3) The type of seismic wave has a notable effect on structural responses. Regarding the structure and selected seismic waves in current paper, the seismic response of structure for the long-distance Songpan wave turns out to be tensor due to the fact that the dominant frequency of the seismic wave is very close to the natural frequency of structure.

(4) The velocity of shear wave in soil has certain influence on seismic response of structure. It is found that the stiffer the soil is, the easier the occurrence of the base mat uplift is.

(5) The ratio of structural height to width (H/B) has a complicated influence on the base mat uplift. It is found that higher structure with smaller width theoretically tends to make base mat uplift easier. However, in higher structure, the structural stiffness tends to decrease and total weight of structure tends to increase, which in turn prevents the base mat uplift. Therefore, the net effect will be determined by the factor which is dominant.

(6) The influence of auxiliary equipment on the seismic response of structure mainly depends on its weight and location.

As has been stated previously, simulation of rocking system in seismic analysis obviously involves nonlinearity of soils and the interface between structure and soil in terms of both stress-strain relationship and geometry aspects. For the sake of simplicity, only geometry nonlinearity has been considered in this paper. In case of strong earthquake where nonlinear stress-strain relationship is prominent in material response, such property will absorb certain amount of energy and thus benefit the structure in terms of earthquake-proof capability. Further analysis should be carried out in light of more accurate simulation on nonlinearity in future researches.

Conflicts of Interest

The authors declare that they have no conflicts of interest.

Acknowledgments

The authors are thankful for the support from the Natural Science Foundation of China (nos. 51208406, 51678465) and Scientific Research Foundation for Chinese Ministry of Education for Returned Overseas Researchers.

References

- [1] M. Apostolou, G. Gazetas, and E. Garini, "Seismic response of slender rigid structures with foundation uplifting," *Soil Dynamics and Earthquake Engineering*, vol. 27, no. 7, pp. 642–654, 2007.
- [2] G. W. Housner, "The behavior of inverted pendulum structures during earthquake," *Bull. Seism. Soc.*, vol. 53, pp. 403–417, 1963.
- [3] C. S. Yim, A. K. Chopra, and J. Penzien, "Rocking response of rigid blocks to earthquakes," *Earthquake Engineering & Structural Dynamics*, vol. 8, no. 6, pp. 565–587, 1980.
- [4] A. S. Koh, P. D. Spanos, and J. M. Roesset, "Harmonic rocking of rigid block on flexible foundation," *Journal of Engineering Mechanics*, vol. 112, no. 11, pp. 1165–1180, 1986.
- [5] C. W. Harden and T. C. Hutchinson, "Beam-on-nonlinear-winkler-foundation modeling of shallow, rocking-dominated footings," *Earthquake Spectra*, vol. 25, no. 2, pp. 277–300, 2009.
- [6] M. F. Vassiliou, K. R. Mackie, and B. Stojadinović, "Dynamic response analysis of solitary flexible rocking bodies: Modeling and behavior under pulse-like ground excitation," *Earthquake Engineering and Structural Dynamics*, vol. 43, no. 10, pp. 1463–1481, 2014.
- [7] S. Acikgoz and M. J. DeJong, "The rocking response of large flexible structures to earthquakes," *Bulletin of Earthquake Engineering*, vol. 12, no. 2, pp. 875–908, 2014.
- [8] F. Gelagoti, R. Kourkoulis, I. Anastasopoulos, and G. Gazetas, "Rocking isolation of low-rise frame structures founded on isolated footings," *Earthquake Engineering and Structural Dynamics*, vol. 41, no. 7, pp. 1177–1197, 2012.
- [9] I. Anastasopoulos, G. Gazetas, M. Loli, M. Apostolou, and N. Gerolymos, "Soil failure can be used for seismic protection of structures," *Bulletin of Earthquake Engineering*, vol. 8, no. 2, pp. 309–326, 2010.
- [10] K. Sotomura and H. Kase, "Nonlinear response analysis on reactor building subject to horizontal and vertical ground motion simultaneously," in *Inproceedings of the 7th International Conference on Structural Mechanics in Reactor Technology (SMiRT7)*, pp. 341–348, Chicago, 1983.
- [11] G. Gazetas, I. Anastasopoulos, and E. Garini, "Geotechnical design with apparent seismic safety factors well-below 1," *Soil Dynamics and Earthquake Engineering*, vol. 57, pp. 37–45, 2014.
- [12] G. Gazetas, "4th Ishihara lecture: Soil–foundation–structure systems beyond conventional seismic failure thresholds," *Soil Dyn. Earthq.*, vol. 68, pp. 23–39, 2015.
- [13] R. P. Kennedy, S. A. Short, D. A. Wesley, and T. H. Lee, "Effect on non-linear soil-structure interaction due to base slab uplift on the seismic response of a high-temperature gas-cooled reactor (HTGR)," *Nuclear Engineering and Design*, vol. 38, no. 2, pp. 323–355, 1976.
- [14] N. Naohiro, A. Shodo, S. Takuya et al., "Study of ultimate seismic response and fragility evaluation of nuclear power building using nonlinear three-dimensional finite element model," *Nucl. Eng. Des.*, vol. 240, pp. 3551–3560, 2010.
- [15] C. Bolisetti and A. S. Whittaker, "Seismic structure-soil-structure interaction in nuclear power plant structures," in *Proceedings of the 21th International Conference on Structural Mechanics in Reactor Technology (SMiRT21)*, p. 11, New Delhi, India, 2011.
- [16] N. Yabushita, N. Nakamura, T. Suzuki et al., "Analyses of reactor by 3D nonlinear FEM models considering basement uplift for simultaneous horizontal and vertical ground motions," in *Inproceedings of the 19th international conference on Structural Mechanics in Reactor Technology (SMiRT19)*, pp. 1–8, Toronto, 2007.
- [17] N. Naohiro, I. Susumu, Y. Naoto, S. Takuya et al., "Analyses of reactor building by 3D nonlinear FEM models considering base mat uplift for simultaneous horizontal and vertical ground motions," *Nucl. Eng. Des.*, vol. 238, pp. 166–180, 2008.
- [18] I. Anastasopoulos, F. Gelagoti, A. Spyridaki, J. Sideri, and G. Gazetas, "Seismic rocking isolation of an asymmetric frame on

- spread footings,” *Journal of Geotechnical and Geoenvironmental Engineering*, vol. 140, no. 1, pp. 133–151, 2014.
- [19] I. Anastasopoulos, V. Drosos, and N. Antonaki, “Three-storey building retrofit: Rocking isolation versus conventional design,” *Earthquake Engineering and Structural Dynamics*, vol. 44, no. 8, pp. 1235–1254, 2015.
- [20] A. K. Chopra and S. C. Yim, “Simplified Earthquake Analysis of Structures with Foundation Uplift,” *Journal of Structural Engineering*, vol. 111, no. 4, pp. 906–930, 1985.
- [21] H. Tanaka, I. Maeda, K. Moriyama, and S. Watanabe, “Study on Horizontal Vertical Interactive SR Model for Base mat Uplift (Part 1 Formulation on Non-linear Characteristics of Soil Spring),” in *Inproceedings of the 13th International Conference on Structural Mechanics in Reactor Technology (SMiRT13)*, pp. K08-1–K08-6, 1995.
- [22] H. Masaeli, F. Khoshnoudian, and M. Hadikhan Tehrani, “Rocking isolation of nonductile moderately tall buildings subjected to bidirectional near-fault ground motions,” *Engineering Structures*, vol. 80, pp. 298–315, 2014.
- [23] A. S. Veletsos and B. Verbic, “Vibration of viscoelastic foundations,” *Earthquake Engineering & Structural Dynamics*, vol. 2, no. 1, pp. 87–102, 1973.
- [24] American Society of Civil Engineers Standard, “Seismic analysis of safety - related nuclear structures and commentary,” *ASCE*, pp. 4–98, 1998.
- [25] I. Rotaru, V. Serban, N. Krutzik, D. Papandreou, and W. Schütz, “Reanalysis and evaluation of the seismic capacity of the CANDU 700 MW NPP CERNAVODA,” *Nuclear Engineering and Design*, vol. 212, no. 1-3, pp. 381–393, 2002.
- [26] “Design of Nuclear Power Plants against seismic events part 4,” in *Proceedings of the Requirements for procedures for verifying the safety of mechanical and electrical components against earthquakes (KTA 2201. 4 (6/90))*, vol. 4, 1990.
- [27] Code for seismic design of buildings, in Chinese.

Research Article

Computation of Rayleigh Damping Coefficients for the Seismic Analysis of a Hydro-Powerhouse

Zhiqiang Song and Chenhui Su

State Key Laboratory Base of Eco-Hydraulic Engineering in Arid Area, Xi'an University of Technology, Xi'an 710048, China

Correspondence should be addressed to Zhiqiang Song; szhiq2004@126.com

Received 12 April 2017; Accepted 27 July 2017; Published 30 August 2017

Academic Editor: Xing Ma

Copyright © 2017 Zhiqiang Song and Chenhui Su. This is an open access article distributed under the Creative Commons Attribution License, which permits unrestricted use, distribution, and reproduction in any medium, provided the original work is properly cited.

The mass and stiffness of the upper and lower structures of a powerhouse are different. As such, the first two vibration modes mostly indicate the dynamic characteristics of the upper structure, and the precise seismic response of a powerhouse is difficult to obtain on the basis of Rayleigh damping coefficients acquired using the fundamental frequencies of this structure. The damping ratio of each mode is relatively accurate when the least square method is used, but the accuracy of the damping ratios that contribute substantially to seismic responses is hardly ensured. The error of dynamic responses may even be amplified. In this study, modes that greatly influence these responses are found on the basis of mode participation mass, and Rayleigh damping coefficients are obtained. Seismic response distortion attributed to large differences in Rayleigh damping coefficients because of improper modal selection is avoided by using the proposed method, which is also simpler and more accurate than the least square method. Numerical experiments show that the damping matrix determined by using the Rayleigh damping coefficients identified by our method is closer to the actual value and the seismic response of the powerhouse is more reasonable than that revealed through the least square method.

1. Introduction

With the exploitation of water resources in southwest China, large-scale hydropower stations have been established in regions frequently hit by earthquakes. The antiseismic safety of powerhouses is essential for water turbine generators and operators in powerhouses. The seismic responses of powerhouse structures are often analyzed with time history method. For example, structural dynamic time history analysis includes modal superposition and step-by-step integration methods. Multi-degree-of-freedom vibration is decoupled in multiple single-degree-of-freedom vibrations in modal superposition method. Single-degree-of-freedom systems can be subjected to a precise dynamic response analysis through Duhamel's integration. With this method, input damping is accurate and high-speed calculation is achieved. However, modal superposition time history analysis method is only applicable to linear elastic structure systems because a structure possesses different decomposition modes at various times due to nonlinear structural material, nonlinear

contact state, and other parameters. Therefore, a step-by-step integration dynamic time history analysis method can be used for a nonlinear system, which requires damping matrix establishment.

Unlike the formation of stiffness and mass matrixes, the formation mechanism of damping is complicated; that is, a damping matrix can be calculated by using a construction method but cannot be directly determined by identifying the material, size, and characteristics of structures [1]. Consequently, different damping matrix construction theories have been proposed [2–9]. For instance, a Rayleigh damping model is widely used because of its excellent advantages [10–13]. (1) In this model, the damping matrix of a structure is a linear combination of mass and stiffness matrixes. As such, Rayleigh damping models can provide a clear physical meaning and present a convenient expression. Thus, these models can be easily applied. (2) A Rayleigh damping matrix must be orthogonal to mode shapes. Consequently, decoupling the dynamic equations of multiple degree-of-freedom systems via mode superposition become convenient.

Mode damping ratios can be directly used in single degree-of-freedom systems (generated by decoupling) dynamic response calculation. Therefore, damping input shows an enhanced accuracy and a reduced calculation scale. (3) Rayleigh damping coefficients can be determined by the orthogonality of a damping matrix for a modal shape. (4) With appropriate Rayleigh damping coefficients, results of a dynamic response analysis of a multi-degree-of-freedom system are the same as experimental data. A damping model is also embedded in commercial finite element software, and Rayleigh damping models are considered as a basis for damping matrix construction commonly utilized in the seismic time history analysis of hydraulic structures.

The damping matrix of a structure is the linear combination of the mass and stiffness matrixes of a Rayleigh damping model:

$$[C] = \alpha [M] + \beta [K], \quad (1)$$

where α and β , respectively, represent the mass and stiffness proportional damping coefficients, which are collectively known as Rayleigh damping coefficients. $[M]$, $[C]$, and $[K]$ are the mass, damping, and stiffness matrixes, respectively. In traditional methods, two reference vibration modes (i - and j -order) are selected, and their damping ratios ζ_i and ζ_j obtained through measurement or reliable test data estimation and their frequencies ω_i and ω_j are used to calculate α and β :

$$\begin{Bmatrix} \alpha \\ \beta \end{Bmatrix} = \frac{2\omega_i\omega_j}{\omega_j^2 - \omega_i^2} \begin{pmatrix} \omega_j & -\omega_i \\ -\frac{1}{\omega_j} & \frac{1}{\omega_i} \end{pmatrix} \begin{Bmatrix} \zeta_i \\ \zeta_j \end{Bmatrix}. \quad (2)$$

This equation can be simplified as follows when $\zeta_i = \zeta_j = \zeta$:

$$\begin{Bmatrix} \alpha \\ \beta \end{Bmatrix} = \frac{2\zeta}{\omega_i + \omega_j} \begin{Bmatrix} \omega_i\omega_j \\ 1 \end{Bmatrix}. \quad (3)$$

Two orders of the reference frequency can be easily and appropriately selected to determine Rayleigh damping coefficients when the degree of freedom of a structure is low or the dynamic response of this structure is controlled by some low-order modes. For example, the first two orders are generally obtained as reference frequencies in traditional methods. For complex structures and structures with a number of modes that contribute greatly to dynamic responses, difficulties in selecting two orders of reference frequencies to obtain reasonable Rayleigh damping coefficients α and β are encountered. If damping coefficients are chosen inappropriately, a slight difference in damping may seriously distort the calculation of the seismic response of a given structure [14–17].

Many scholars investigated the calculation of Rayleigh damping coefficients. Pan et al. [18] proposed a constrained optimization method to determine Rayleigh damping coefficients for the accurate analysis of complex structures. An objective function is defined as a complete quadratic combination of the modal errors of a peak base reaction

evaluated through response spectral analysis. An optimization constraint is enforced to determine the exact damping ratio of modes that contribute greatly to dynamic responses. This method is based on Duhamel's integral formula, which is suitable for linear elastic systems. Yang et al. [19] studied the application of a multi-mode-based computation method in single-layer cylindrical latticed shells because the traditional two-mode Rayleigh damping method is unsuitable. Yang et al. [19] also suggested that the multi-mode-based computation method is preferable when many dominant modes are distributed loosely and found in a wide range of frequencies under some ground motions. Jehel et al. [20] comprehensively compared the initial structural stiffness and updated tangent stiffness of Rayleigh damping models to allow a practitioner to objectively choose the type of Rayleigh damping models that satisfy his needs and be provided with useful analytical tools for the design of these models with good control on their damping ratios during inelastic analysis. Erduran [21] evaluated the effects of a Rayleigh damping model based on the engineering demand parameters of two steel moment-resisting frame buildings. Rayleigh damping models, which combine mass and stiffness proportional components, are anchored at reduced modal frequencies, which create reasonable damping forces and floor acceleration demands for both buildings but do not suppress higher-mode effects. Zhe et al. [22] developed an improved method to calculate Rayleigh damping coefficients for the seismic response time history analysis of powerhouse structures by considering the spectrum characteristics of the ground motion and the frequency characteristics of these structures. Using the improved method, Zhe et al. [22] obtained calculation results that are consistent with experimental findings.

Hongshi [23] initially compared and analyzed several methods of calculating Rayleigh damping coefficients and subsequently proposed the least square method to minimize the difference between the calculated damping ratio and the actual damping ratio within the cutoff frequency. Li et al. [24] then established the corresponding method for the seismic response analysis of powerhouse structures by calculating the proportional damping coefficient through the weighted least square method.

Analyzing the seismic dynamic response of long-span arch bridges and super high structures with long periods, Lou [15, 25] found that Rayleigh damping coefficients determined by traditional methods involving the first two orders of frequencies as reference frequencies inaccurately reflect the actual damping effect of long-period structures in a dynamic process and even create a large deviation. Hence, calculation methods of the Rayleigh damping coefficients of long-period structures in dynamic processes should be further discussed.

The definition of long- and short-period structures is a relative concept depending on the relationship between the basic period of a structure and the characteristic period of dynamic loads. A short-period structure is characterized as a structure whose basic period is less than or close to the

characteristic period of external loads. Otherwise, a given structure is called a long-period structure. The basic characteristic period is usually 10^{-1} s or higher because the stiffness of the upper frame structure is relatively weak. Therefore, this weak structure is also described as a long-period structure because of the characteristic period of seismic waves. The mass and stiffness of the upper and lower structures of powerhouses are different. As such, the first two modes of vibration often indicate the dynamic characteristics of the upper structure. The damping matrix obtained by traditional methods of calculating Rayleigh damping coefficients does not easily reveal the actual damping of the whole powerhouse structure. Hence, the influence of the calculation methods of Rayleigh damping coefficients on the dynamic response of a powerhouse under seismic actions should be investigated. In this study, the calculation of Rayleigh damping coefficients is examined to analyze the seismic responses of a powerhouse.

To calculate Rayleigh damping coefficients, Chopra [1] suggested that “in dealing with practical problems, it is reasonable to select the modes of vibrations i and j with specific damping ratios to ensure that the damping ratios of all modes of vibration that contribute greatly to the dynamic response are reasonable.” Differences in the mass and stiffness of the upper and lower structures of a powerhouse remarkably create the dynamic characteristics of a powerhouse structure. The first two vibration modes often involve the relatively soft upper structure of the powerhouse, whose mode participation mass is quite smaller than that of the whole powerhouse. The damping of these buildings under seismic actions is mainly due to various interior frictions and deformations of components and the ones between them. Therefore, mode participation mass should be considered as a key factor affecting the calculation of damping. The modes that contribute greatly to dynamic responses are found on the basis of mode participation mass. In this study, the Rayleigh damping coefficient is calculated.

This paper is organized as follows. Section 2 introduces the finite element models of a powerhouse and several methods of calculating Rayleigh damping coefficients. The two modes that remarkably affect the dynamic responses are determined on the basis of mode participation mass, and the Rayleigh damping coefficients are calculated. Section 3 presents the results of the dynamic response obtained by different methods. Numerical results show that the proposed method accurately reveals the two modes contributing to the dynamic response of the powerhouse, and the calculated Rayleigh damping coefficients are consistent with actual results. The calculated results are also closer to the exact solutions and even higher than those acquired by the least square method. Section 4 provides the conclusion.

2. Seismic Analysis Model of Powerhouses and Calculation Method of Rayleigh Damping Coefficients

2.1. Three-Dimensional Finite Element Model and Seismic Inputs. In Figure 1, the three-dimensional finite element model of a typical unit of the hydropower station is established. The depth of the foundation is about twice the

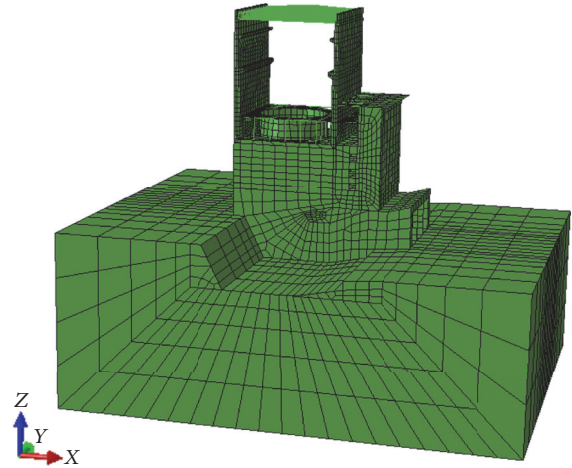


FIGURE 1: Finite element model of the powerhouse.

height of the powerhouse, and the upstream and downstream and the left and right sides extend twice the height of the powerhouse because of the elastic coupling effect of the foundation. The foundation boundary condition is that the bottom is fixed and the four boundaries are normally constrained. Turbine generators, cranes, roof loads, and hydrodynamic pressures are simulated as the additional mass at corresponding locations. A linear elastic model is used in the structure, and the local strengthening effects of the volute steel plate and the seating ring are neglected. The damage cracks of the concrete around the volute are also disregarded. Zhang et al. [26] observed that cracks on thin parts of the concrete of a volute greatly change the local stiffness of the volute but slightly alter the displacement, speed, and acceleration of the upper structure compared with those without cracks. The nonmass foundation, which does not affect the response peaks of the structure, is adopted for calculation convenience.

In engineering designs, a single seismic time history does not generally influence the dynamic response of a structure. Different factors, such as site characteristics, fortification intensity, and probability of ground motion, should be considered in accordance with the requirements of the antiseismic codes of various types of structures. Therefore, seismic time history is simulated in this paper according to the response spectrum of the standard design in literature [27].

Under actual conditions, the site type is I_0 , the characteristic period T_s is 0.02 s, the representative of the maximum value of the response spectrum of the standard design is 2.25, the seismic intensity is increased from degrees 7 to 8 according to requirements of the grade and importance of structures, the peak acceleration of the horizontal ground motion is increased from 0.05 g to 0.1 g, the time step of the ground motion is 0.01 s, and the total time is 20 s. Figure 2 shows the generated seismic time histories, in which the correlation coefficients of x and y directions, x and z directions, and y and z directions are 0.0011, 0.1737, and 0.0002, respectively. These coefficients are less than 0.3, which

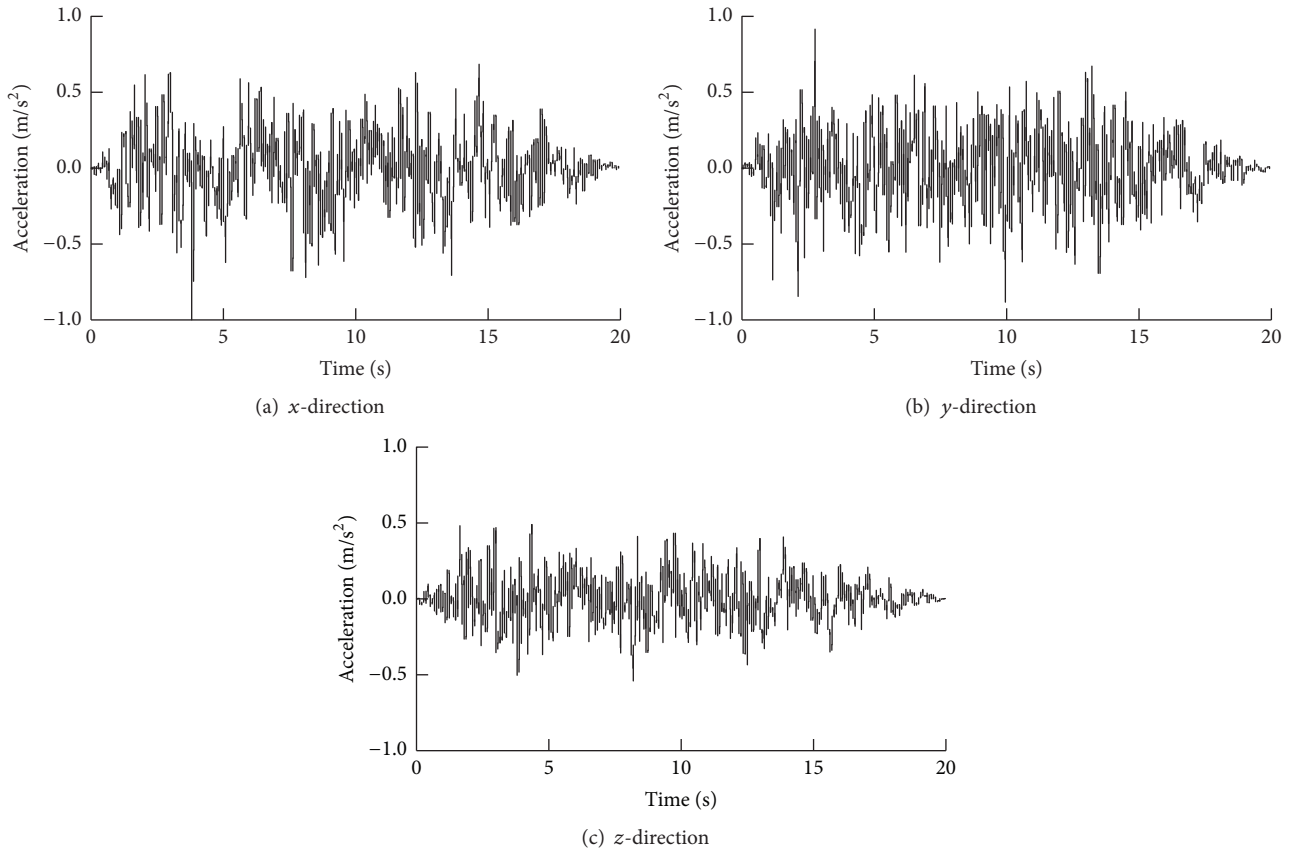


FIGURE 2: Calculation of the time history of seismic acceleration.

satisfies the requirements [26] that the time histories in the three directions should be independent of one another.

2.2. Calculation Method of Rayleigh Damping Coefficients.

A reasonable proportional damping matrix based on the Rayleigh damping model is necessary when the step-by-step integration method is used to conduct dynamic time history analysis. In this case, Rayleigh damping coefficients directly affect the results of dynamic analysis.

A linear elastic powerhouse structure is presented as an example and the response of the modal superposition time history method (referred to as modal method thereafter) is used as a reference, which is the standard of measurement, to evaluate the influence of various Rayleigh damping coefficients obtained by different methods on the seismic response in the step-by-step integration method. The relevant specification [27] requires that the damping ratio of the powerhouse under the action of ground motion is 0.07, which is substituted into the following Rayleigh damping coefficients to obtain the corresponding damping matrix of each method and then applied to the step-by-step integration method to solve the seismic response of the powerhouse.

The finite element model of the powerhouse is initially analyzed to determine the natural frequency of some orders of the structure, which is required for the calculation of Rayleigh damping coefficients. The first 80 orders are

obtained. The mode participation masses of x , y , and z directions are 92.1%, 90.8%, and 91.0% of the total mass of the model, respectively. These values are more than 90% of the total mass of the model and thus satisfy the requirement of calculation accuracy. Figure 3 illustrates some orders of the vibration modes of the hydro-powerhouse and the typical vibration characteristics of the ground-type powerhouse structure. The frequencies are low and dense, and the frequencies of the first 10 orders range from 0.55 Hz to 6.21 Hz. The natural period of the vibration of the first order is 1.83 s, which is much larger than the characteristic period of a seismic wave, and this finding indicates that the powerhouse is a long-period structure. The first-order vibration mode is mainly the vibration of the frame columns and roof grids in the upstream and downstream directions. Most of the modal shapes of the low orders are mainly the bending and torsional vibration of the upper frame structure and the vibration of the weak parts of the generator floor and windshield. The two-order vibration modes with the largest mode participation masses of the three directions are the 13th (7.72 Hz) and 25th (12.81 Hz), whose mode participation masses are 14.6% and 25.3%, respectively. The vibration modes correspond to the whole vibration of the powerhouse and the higher-order bending vibration of the superstructure.

According to the natural frequency of the structure of the powerhouse and the characteristic of each mode of vibration,

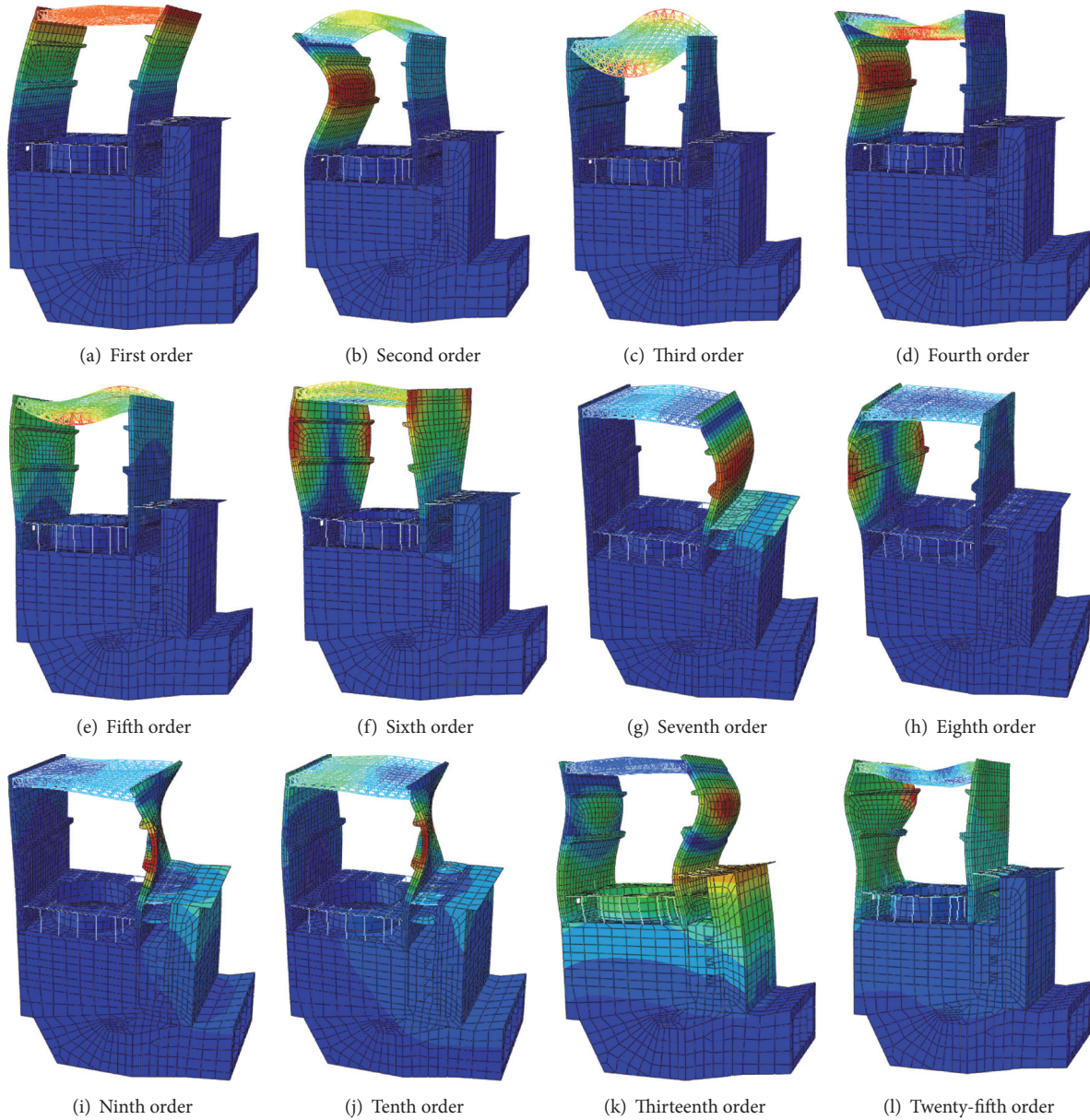


FIGURE 3: Vibration modes of the hydro-powerhouse.

the methods widely used and the proposed calculation method of Rayleigh damping coefficients can be summarized as follows:

(1) In method 1 or the traditional method, the first two orders of natural frequency are used to determine Rayleigh damping coefficients. This method is based on the assumption that low-order vibration modes contribute greatly to structural dynamic responses. Many orders of vibration modes are also complex, and low-order modes mainly correspond to the vibrations of the weak parts of the upper structure. Therefore, this assumption is inapplicable. The damping ratios of the vibration modes obtained in this method are too large, but the first two orders are equal to the actual values. Consequently, the contributions of the third-order vibration modes to dynamic responses become weakened and induce a low total structural response. Designing

an antiseismic powerhouse based on these response results is risky. The first two natural frequencies are 0.55 and 2.96 Hz according to the calculation of the finite element structure of the powerhouse. The damping coefficients obtained by method 1 are $\alpha_1 = 0.4053$ and $\beta_1 = 0.0064$ (3).

(2) In method 2, the frequency band of interest is selected; that is, the natural frequencies of the first order and the last order (80th order) are used as the parameters. The mode participation masses of x , y , and z directions are larger than 90% of the total mass of the model and thus satisfy the calculation accuracy requirements. The natural frequency of the 80th order is 27.96 Hz. According to (3), the damping coefficients acquired by this method are $\alpha_2 = 0.4709$ and $\beta_2 = 0.0008$.

According to the calculation principle of Rayleigh damping coefficients, the frequencies ω_i and ω_j of the two constants

TABLE 1: Rayleigh damping coefficients obtained by different methods.

Methods	α	β	According to	Involved orders
Modal methods	\	\	Constant damping ratio: 0.07	1–80
Case 1	0.4053	0.0064	First and second orders	1, 2
Case 2	0.4709	0.0008	First and last orders	1, 80
Case 3	0.9553	0.0010	Optimization by least square method	1–80
Case 4	0.5286	0.0012	Weighted least squares, weight coefficients: $1/\omega_i$	1–80
Case 5	0.4064	0.0063	Weighted least squares, weight coefficients: $\exp(-\omega_i)$	1–80
Case 6	4.2364	0.0011	Two orders have largest mode participation masses	13, 25
Case 7	0.7878	0.0015	Weighted least squares, weight coefficients: m_i/M	1–80

α and β should cover the target frequency band in the structural analysis. The calculation of the specific frequency band should be considered in terms of the frequency components of the loads acting on a particular structure and the dynamic characteristics of this structure.

However, this method may cause several problems. (1) The selection of target frequency band relies on experience. (2) The set damping ratios within the band may be too small. As such, the calculated structural response may be excessively large and inappropriate if the deviation is overly large.

(3) In method 3, the least square method without weighting coefficients is used. The damping coefficients are calculated by applying the least square method to determine the least square sum of the difference between the calculated damping ratio of each order and the actual damping ratio within the cutoff frequency. The formula is expressed as follows:

$$\min_{\alpha, \beta} \sum_{i=1}^n \left(\frac{\alpha}{2\omega_i} + \frac{\beta\omega_i}{2} - \zeta \right)^2. \quad (4)$$

(4) In method 4, given weighting coefficients, the orders that contribute greatly to the damping effect will become more dominant, while the ones that contribute a little are less important. The objective function is

$$\min_{\alpha, \beta} \sum_{i=1}^n \frac{1}{\omega_i} \left(\frac{\alpha}{2\omega_i} + \frac{\beta\omega_i}{2} - \zeta \right)^2. \quad (5)$$

The weighting coefficient is the reciprocal of the natural frequency of each order. Therefore, low orders correspond to high weight coefficients and contribute to the dynamic responses of structures.

(5) Method 5 is almost the same as method 4. These methods differ in terms of their weight coefficients; that is, the weight coefficient of method 5 is the negative exponential function of the natural frequency of each order:

$$\min_{\alpha, \beta} \sum_{i=1}^n \exp(-\omega_i) \left(\frac{\alpha}{2\omega_i} + \frac{\beta\omega_i}{2} - \zeta \right)^2. \quad (6)$$

(6) Method 6 is our proposed approach. The orders that contribute greatly to the responses are selected on the basis of mode participation mass. The two orders with the largest total mode participation masses in the three directions are considered as references to calculate the damping coefficients.

According to the results of the self-vibration characteristics of the structure of the powerhouse, these two orders are the 13th (7.72 Hz) and 25th (12.81 Hz), and their masses are 14.6% and 25.3%, respectively.

(7) Method 7 is based on method 6, and the least square method involving mode participation masses as coefficients is established and expressed as follows:

$$\min_{\alpha, \beta} \sum_{i=1}^n \frac{m_i}{M} \left(\frac{\alpha}{2\omega_i} + \frac{\beta\omega_i}{2} - \zeta \right)^2. \quad (7)$$

The mode orders and damping coefficients obtained by each method are shown in Table 1.

3. Seismic Analysis of Different Rayleigh Damping Coefficients Obtained Using Various Calculation Methods for the Powerhouse

Five typical points in the powerhouse are selected to reveal the representative seismic response of the powerhouse comprehensively: 8079 in the middle of the top of the downstream wall, 6636 in the middle of the joint between the generator floor and the downstream wall, 8255 in the mid-span of the generator floor, 8088 in the downstream side of the cover fan, and 2889 in the downstream side of the seating ring. The relative peak acceleration of each typical point determined by different calculation methods is listed in Table 2, and the direction of acceleration is disregarded and the maximum absolute value is considered. The peak acceleration of each point acquired by the modal superposition method is set as the standard value. The results of methods 1 to 7 are normalized and the percentages of deviation from the results acquired by the modal superposition method are obtained (Figure 4).

In Table 2 and Figure 4, different calculation methods of damping coefficients significantly affect the calculation results of the seismic response of the powerhouse.

In method 1, the relative peak acceleration of each typical point in different directions is smaller than the exact values because the damping ratios of the 1st and 2nd orders of the vibration modes are equal to 0.07 and the damping ratios of the 3rd to the 80th orders are greater than 0.07. These findings indicate that damping ratios increase significantly as the order increases and thus yield high damping ratios and

TABLE 2: Peak accelerations of typical points determined by different methods (m/s²).

Node	Direction	Modal method	Case 1	Case 2	Case 3	Case 4	Case 5	Case 6	Case 7
2889	<i>x</i>	0.482	0.423	0.732	0.623	0.603	0.424	0.483	0.535
	<i>y</i>	1.368	1.239	1.835	1.680	1.675	1.245	1.437	1.617
	<i>z</i>	0.442	0.380	0.834	0.725	0.707	0.383	0.558	0.641
6636	<i>x</i>	2.947	2.193	5.407	4.665	4.642	2.208	3.133	4.108
	<i>y</i>	2.186	1.996	2.898	2.522	2.595	1.999	2.112	2.357
	<i>z</i>	1.360	0.852	2.333	2.031	1.929	0.860	1.559	1.706
8079	<i>x</i>	3.971	2.807	7.310	5.983	5.944	2.829	4.179	5.139
	<i>y</i>	4.163	3.457	4.971	4.902	4.913	3.475	3.892	4.831
	<i>z</i>	2.844	1.534	4.898	4.459	4.354	1.555	3.395	3.901
8088	<i>x</i>	1.919	1.541	3.349	2.999	2.989	1.551	2.212	2.707
	<i>y</i>	1.864	1.744	2.757	2.421	2.465	1.747	1.811	2.239
	<i>z</i>	1.167	0.792	1.703	1.556	1.534	0.800	1.233	1.422
8255	<i>x</i>	2.830	2.141	5.207	4.501	4.483	2.156	3.030	3.971
	<i>y</i>	2.168	1.967	2.955	2.557	2.622	1.971	2.077	2.370
	<i>z</i>	1.666	1.060	2.536	2.301	2.243	1.069	1.798	2.060

Note. *x* represents the upstream and downstream direction, *y* shows the direction perpendicular to the stream direction, and *z* denotes the vertical direction.

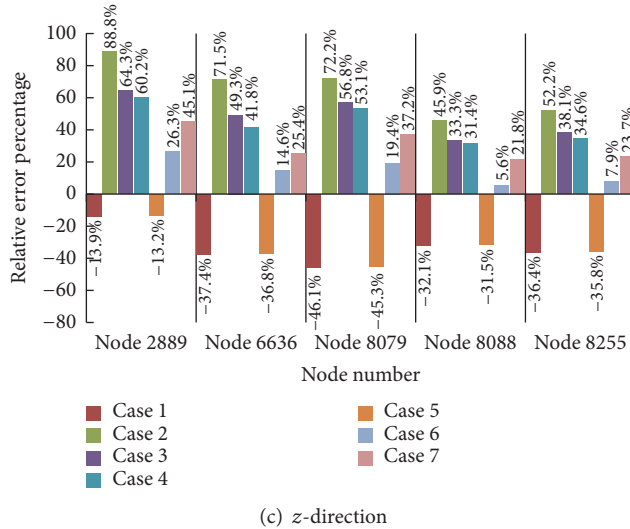
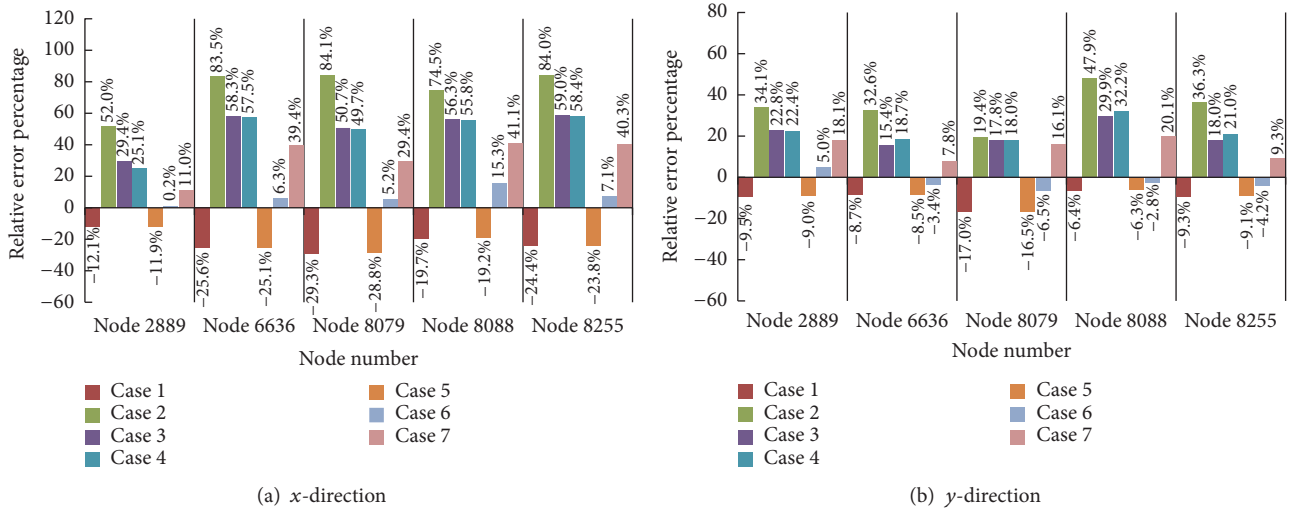


FIGURE 4: Error of the peak acceleration.

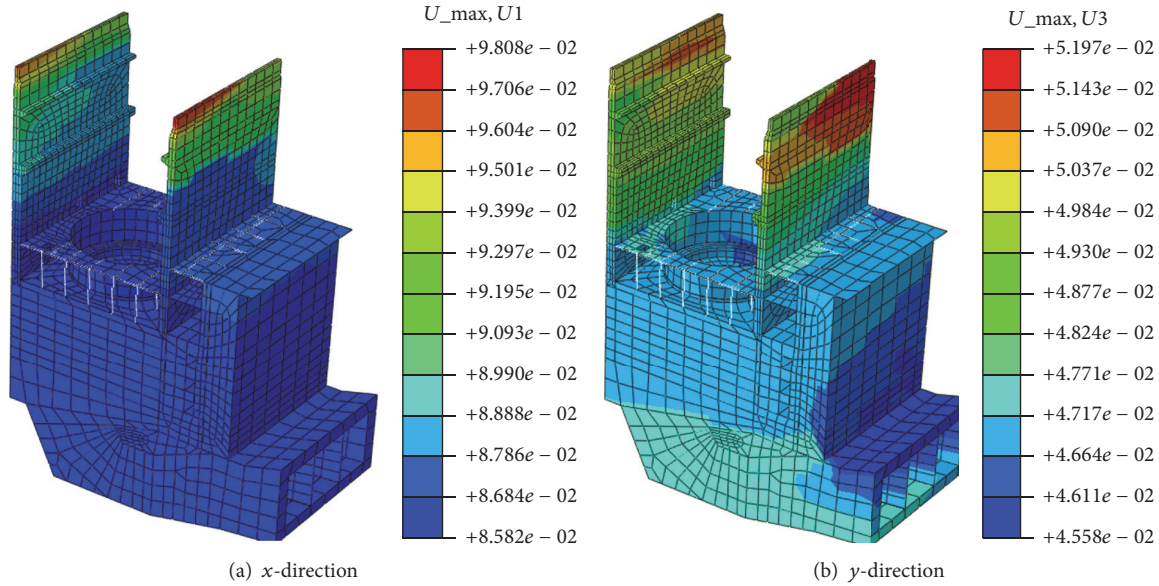


FIGURE 5: Displacement envelope figures of the whole powerhouse.

low seismic responses. Low-order modes, such as the first and second orders, are not the main contributors to the structural dynamic response when the mass and stiffness of the upper and lower structures of the powerhouse differ greatly. The low-order modes of vibration often indicate the dynamic characteristics of the upper structure because of the low mode participation mass. Therefore, designing an antiseismic powerhouse by using the results calculated with this method is risky. In the example, the acceleration in the z direction differs from the exact solution to a greater extent than those in the x and y directions. The relative peak acceleration in the z direction of the point in the middle of the top of the downstream wall also deviates from the exact value by up to 46%.

In method 2, the relative peak acceleration of each typical point in different directions is greater than the exact value because the damping ratios of the 1st and 80th orders of the vibration mode are equal to 0.07 and the damping ratios of the 2nd to the 79th orders are smaller than 0.07. Therefore, low damping ratios and high seismic responses are obtained. In the example, the relative peak acceleration in the z direction of the point in the downstream side of the seating ring deviates from the exact value by up to 89%. Numerous solutions that are greater than the exact values account for the increase in construction costs, which fail to satisfy the current requirements of performance-based antiseismic designs.

Method 3 is based on the least square method. In the example, the relative peak acceleration of each point in different directions is larger than the exact solutions, but the overall deviation is lower than that of method 2. The relative peak acceleration in the z direction of point 2889 deviates from the exact value by up to 64%.

Method 4 is based on the weighted least square method. In the example, the relative peak acceleration of each point in different directions is larger than the exact solutions

and slightly lower than that of method 3. The solutions obtained by this method are closer to the exact values, and the numerical distribution is similar to that in method 3. Similarly, the relative peak acceleration in the z direction of point 2889 deviates from the exact value by up to 60%.

Method 5 is also based on the weighted least square method. In the example, the relative peak acceleration of each point in different directions is close to and slightly larger than those acquired in method 1 and is less than the exact solutions. The seismic response is lower than the exact value. The relative peak acceleration in the z direction of point 8079 also deviates from the exact value by up to 45%.

In method 6, the mode orders with a remarkable contribution to the structure dynamic responses are selected according to the mode participation mass. The mode participation mass is the most important factor that influences the damping coefficients of the powerhouse. The 13th and 25th orders yield the largest vibration mode participation mass. The Rayleigh damping model shows that the damping ratios of the 13th and 25th orders are 0.07, the damping ratios of the 1st–12th and the 26th–80th orders are greater than 0.07, and the damping ratios of the 14th–24th orders are less than 0.07. The relative peak acceleration of each typical point in different directions is quite close to the exact values; that is, the differences from the exact data of most of the points are within 10%. The relative peak acceleration in the z direction of point 2889 deviates from the exact value by 26%.

The displacement envelope figures of the whole powerhouse in the x and y directions via method 6 are presented in Figure 5. The peak displacement of the lower structure appears uniform. The peak displacement of the upper structure is larger because of the whiplash effect. The larger stiffness of the powerhouse transversal to the flow direction leads to a smaller peak displacement than that along the flow direction.

In method 7, the damping coefficients are obtained on the basis of the weighted least square method. In contrast to methods 4 and 5, method 7 considers the mode participation masses as the weighting coefficients; that is, the orders that contribute greatly to the dynamic response are selected on the basis of the mode participation mass. The damping coefficients of most of the modes obtained by this method are closer to the exact values, whereas the damping coefficients of the modes that contribute greatly to the dynamic response are less accurate. The relative peak acceleration of each typical point in different directions is closer to the exact solution determined by method 7 than those obtained by methods 2–5 but less accurate than the one acquired by method 6.

The relative peak acceleration of each typical point in different directions obtained by methods 3, 4, 5, and 7, which were based on the least square method, is closer to the exact value than that identified by methods 1 and 2. Therefore, the solutions provided by the least square method or the weighted least square method are more accurate than those established by methods 1 and 2. Methods 4 and 5 are based on the weighted least square method and on the assumption that low-order modes contribute greatly to seismic responses. However, the results calculated by the two methods differ greatly. In particular, the response of the powerhouse acquired by method 4 is greater than the exact value, whereas the response determined by method 5 is smaller than the exact finding. The relative peak acceleration of point 8079 detected by method 4 is also 2.8 times greater than that revealed by method 5. The mode participation mode is thus regarded as an important factor influencing the damping coefficients of the powerhouse in methods 6 and 7. By comparison, the solutions from method 7 are less accurate than those from method 6.

These comparisons and analyses reveal that the drawbacks of the least square method and the weighted least square method are inevitable. On the one hand, the weight coefficients remarkably influence the calculation results. Therefore, the damping coefficients of all orders can be considered to reduce the uncertainty caused by the two chosen modes, but the uncertainty attributed to the selection of the weight coefficients cannot be removed. On the other hand, we have yet to verify importance of the orders that contribute greatly to the response during calculation to obtain the optimal objective function in the least square method and the weighted least square method. The accuracy of the damping ratios of the orders that remarkably contribute may be severely reduced. Therefore, the least squares method and the weighted least squares method are slightly uncontrollable and should be used cautiously in practical engineering.

Table 3 and Figure 6 show the relative peak displacements for each typical point obtained by different methods, in which the direction of displacement is disregarded and the maximum absolute value is considered, and the percentage of deviation from values obtained by modal superposition method. The relative peak displacements of the points in different directions are similar to those of the relative peak acceleration analyzed in the preceding sections. Only few values obtained by methods 1 and 5 are closer to the exact values because changes in damping affect the distribution of

the relative displacements of the structure in time history under the same seismic input. As such, peak displacements are influenced cumulatively. Overall, the results determined by method 6 are still the closest solutions to the exact values because they are more stable and reliable than those identified by other methods. In the example, the largest deviations from the exact relative peak acceleration determined by methods 1–7 in different directions are -28.39% , 63.61% , 41.59% , 41.44% , 27.83% , 30.37% , and 28.67% , respectively.

The solutions obtained by method 6 are slightly larger than and closer to the exact values. The modes that contribute greatly to the dynamic response are found on the basis of the mode participation mass, and the damping coefficients are calculated using method 6. These findings are consistent with the calculation method of Rayleigh damping coefficients proposed by Chopra [1]: “In dealing with practical problems, it is reasonable to select the modes of vibration i and j with specific damping ratios to ensure that damping ratios of all modes of vibration that contribute greatly to the dynamic response are reasonable.” Therefore, we verify that mode participation mass is related to the contribution of orders to seismic responses. Our numerical experiments demonstrate that the Rayleigh damping coefficients determined by this method are closer to the actual values and the seismic response of the structure is more reasonable.

4. Conclusions

Calculation methods of Rayleigh damping coefficients greatly affect the results of the seismic responses of powerhouses and buildings with similar structural characteristics. In method 1 or the traditional method, the damping ratios except the first two values are larger than the exact ratios. As a result, the structural dynamic response is significantly smaller. The first two vibration modes often indicate the dynamic characteristics of the upper structure, not the whole structure. The damping ratios of most of the vibration modes in the middle are smaller than the exact values. As such, the structural dynamic response in method 2 is significantly larger than that in method 1. To obtain the optimal objective function, we can use the least square method and the weighted least square method for an accurate calculation of damping coefficients. However, whether the orders that contribute greatly to responses play an important role in the calculation remains uncertain. The errors of the damping ratios of the orders with a significant contribution may be severely increased. Thus, the dynamic response of a structure is unable to satisfy the required accuracy in practical engineering.

In the method proposed in this study, the mode orders that influence the dynamic responses are found on the basis of mode participation mass, and Rayleigh damping coefficients are determined by using the natural frequencies of the two mode orders, whose mode participation masses are the largest. The seismic response distortion attributed to large differences in Rayleigh damping coefficients caused by improper modal selection is avoided by using the proposed method, which is also simpler and more accurate than the least square method. Our numerical experiments show that the damping matrix determined by using Rayleigh damping coefficients in this method is closer to the actual value, and the seismic response of the powerhouse is more acceptable.

TABLE 3: Peak displacements of each point obtained by different methods (cm).

Node	Direction	Modal method	Case 1	Case 2	Case 3	Case 4	Case 5	Case 6	Case 7
2889	<i>x</i>	0.020	0.022	0.027	0.026	0.025	0.022	0.026	0.024
	<i>y</i>	0.121	0.112	0.138	0.137	0.136	0.113	0.133	0.134
	<i>z</i>	0.016	0.015	0.025	0.022	0.022	0.015	0.019	0.020
6636	<i>x</i>	0.134	0.120	0.214	0.187	0.187	0.120	0.173	0.170
	<i>y</i>	0.191	0.188	0.230	0.209	0.213	0.188	0.218	0.206
	<i>z</i>	0.033	0.026	0.054	0.046	0.045	0.026	0.037	0.040
8079	<i>x</i>	6.882	7.287	7.429	6.164	7.116	7.289	7.739	6.431
	<i>y</i>	0.527	0.502	0.597	0.583	0.580	0.503	0.541	0.573
	<i>z</i>	0.302	0.307	0.326	0.278	0.308	0.308	0.317	0.287
8088	<i>x</i>	0.093	0.082	0.143	0.129	0.128	0.082	0.118	0.117
	<i>y</i>	0.164	0.157	0.194	0.180	0.181	0.157	0.184	0.177
	<i>z</i>	0.028	0.021	0.043	0.038	0.038	0.021	0.032	0.034
8255	<i>x</i>	0.129	0.116	0.208	0.182	0.182	0.116	0.168	0.166
	<i>y</i>	0.186	0.183	0.228	0.205	0.212	0.183	0.212	0.201
	<i>z</i>	0.042	0.030	0.065	0.058	0.058	0.030	0.045	0.052

Note. *x* represents the upstream and downstream direction, *y* corresponds to the direction perpendicular to the stream direction, and *z* indicates the vertical direction.

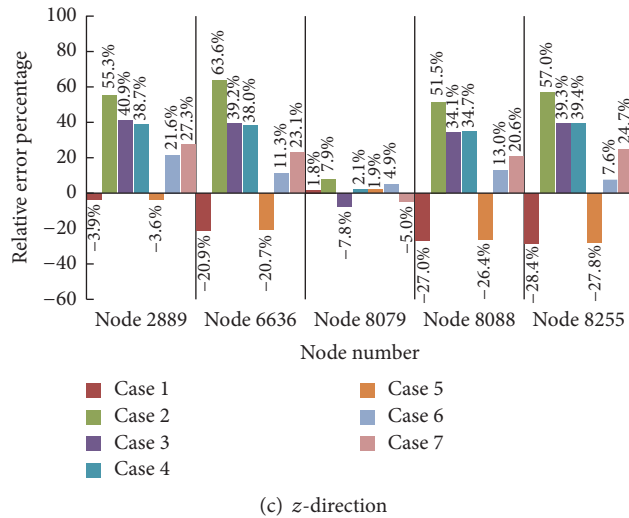
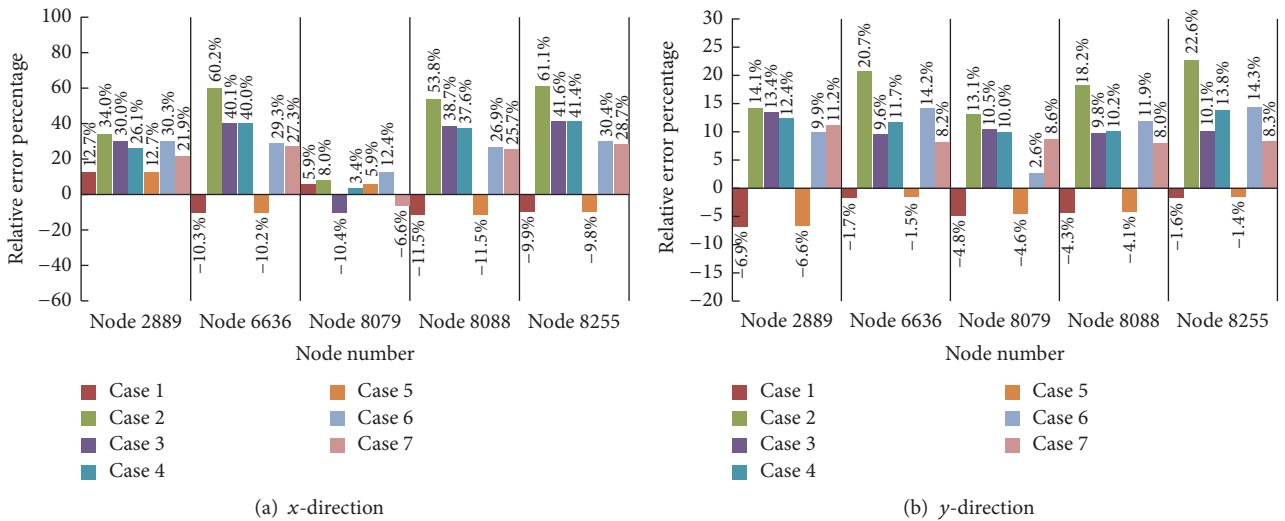


FIGURE 6: Error of peak displacements.

Conflicts of Interest

The authors declare that there are no conflicts of interest regarding the publication of this paper.

Acknowledgments

This research was supported by the National Natural Science Foundation of China (51479165) and State Key Laboratory Base of Eco-Hydraulic Engineering in Arid Area Independent Research Project (2016ZZKT-1).

References

- [1] A. K. Chopra, *Dynamics of structures: Theory and applications to earthquake engineering*, Upper Saddle River: Prentice Hall, 2011.
- [2] T. K. Caughey and M. E. O'Kelly, "Classical normal modes in damped linear dynamic systems," vol. 32, pp. 583–588, 1965.
- [3] Z. Liang and G. C. Lee, "Representation of damping matrix," *Journal of Engineering Mechanics*, vol. 117, no. 5, pp. 1005–1020, 1991.
- [4] H. Zongming, B. Shaoliang, and L. Ming, "Review on the damping in earthquake response time-history analysis of structures," *Earthquake Engineering and Engineering Vibration*, vol. 16, no. 2, pp. 95–102, 1996.
- [5] J. Dong, H. Z. Deng, and Z. M. Wang, "Studies on the damping models for structural dynamic time history analysis," *World Information on Earthquake*, vol. 16, pp. 63–69, 2000.
- [6] S. Adhikari, "Damping modelling using generalized proportional damping," *Journal of Sound and Vibration*, vol. 293, no. 1-2, pp. 156–170, 2006.
- [7] D. Danhui and S. Limin, "Damping modeling and evaluation of structural dynamic finite element analysis," *Journal of Vibration and Shock*, vol. 26, no. 2, pp. 121–124, 2007.
- [8] J. E. Luco, "A note on classical damping matrices," *Earthquake Engineering and Structural Dynamics*, vol. 37, no. 4, pp. 615–626, 2008.
- [9] H.-D. Zhang and Y.-F. Wang, "Study on seismic time-history response of structures with complex damping," *Gongcheng Lixue/Engineering Mechanics*, vol. 27, no. 1, pp. 109–115, 2010.
- [10] D. R. Pant, A. C. Wijeyewickrema, and M. A. ElGawady, "Appropriate viscous damping for nonlinear time-history analysis of base-isolated reinforced concrete buildings," *Earthquake Engineering & Structural Dynamics*, vol. 42, no. 15, pp. 2321–2339, 2013.
- [11] J. Wang, "Rayleigh coefficients for series infrastructure systems with multiple damping properties," *JVC/Journal of Vibration and Control*, vol. 21, no. 6, pp. 1234–1248, 2015.
- [12] R. E. Spears and S. R. Jensen, "Approach for selection of rayleigh damping parameters used for time history analysis," *Journal of Pressure Vessel Technology*, vol. 134, no. 6, 2012.
- [13] Y. Li, Y. Sun, B. Li, and Z. Xu, "Penalty function-based method for obtaining a reliability indicator of gravity dam stability," *Computers and Geotechnics*, vol. 81, pp. 19–25, 2017.
- [14] American Society of Civil Engineers, *Seismic Analysis of Safety-Related Nuclear Structures and Commentary*, ASCE 4-98 Standard, 2000.
- [15] L. Menglin, S. Lei, and S. Fei, "Effect s of damping matrix modeling on seismic response of super high-rise structures," *Structural Engineers*, vol. 29, no. 1, pp. 55–61, 2013.
- [16] D.-G. Zou, B. Xu, and X.-J. Kong, "Study of influence of different methods for calculating Rayleigh damping coefficient on high earth-rock dam seismic response," *Yantu Lixue/Rock and Soil Mechanics*, vol. 32, no. 3, pp. 797–803, 2011.
- [17] D.-G. Pan and L.-L. Gao, "Comparison of determination methods for Rayleigh damping coefficients and effects on seismic responses of structures," *Gongcheng Lixue/Engineering Mechanics*, vol. 32, no. 6, pp. 192–199, 2015.
- [18] D. G. Pan, G. D. Chen, and L. L. Gao, "A constrained optimal Rayleigh damping coefficients for structures with closely spaced natural frequencies in seismic analysis," *Advances in Structural Engineering*, vol. 20, no. 1, pp. 81–95, 2017.
- [19] D.-B. Yang, Y.-G. Zhang, and J.-Z. Wu, "Computation of Rayleigh damping coefficients in seismic time-history analysis of spatial structures," *Journal of the International Association for Shell and Spatial Structures*, vol. 51, no. 164, pp. 125–135, 2010.
- [20] P. Jehel, P. Léger, and A. Ibrahimbegovic, "Initial versus tangent stiffness-based Rayleigh damping in inelastic time history seismic analyses," *Earthquake Engineering and Structural Dynamics*, vol. 43, no. 3, pp. 467–484, 2014.
- [21] E. Erduran, "Evaluation of Rayleigh damping and its influence on engineering demand parameter estimates," *Earthquake Engineering and Structural Dynamics*, vol. 41, no. 14, pp. 1905–1919, 2012.
- [22] L. Zhe, W. Gongxian, and H. Yong, "Application of improved calculation method of Rayleigh damping coefficients to seismic response analysis on quay crane structure," *Journal of South China University of Technology Natural Science Edition*, vol. 43, no. 6, pp. 103–109, 2015.
- [23] L. Hongshi, "Relative errors and determination of Rayleigh damping scale coefficient," *Journal of Hunan institute of Engineering*, vol. 11, no. 3-4, pp. 36–38, 2001.
- [24] X.-J. Li, C.-L. Hou, R. Pan, G.-L. Zhou, and Y. Yang, "Effect of damping matrix selection on seismic response of nuclear power plant structures," *Zhendong yu Chongji/Journal of Vibration and Shock*, vol. 34, no. 1, pp. 110–116, 2015.
- [25] L. Menglin and Z. Jing, "Discussion on damping models for seismic response analysis of long-span bridge," *Journal of Vibration and Shock*, vol. 28, no. 5, pp. 22–25, 2009.
- [26] Y.-L. Zhang, Z.-Y. Ma, Y. Wang, and J. Chen, "Effect of cracks on dynamics characteristics of hydropower house," *Journal of Hydraulic Engineering*, vol. 39, no. 8, pp. 982–986, 2008.
- [27] National Energy Administration of China, *Code for seismic design of hydraulic structures of hydropower project*, NB 35047-2015, 2015.